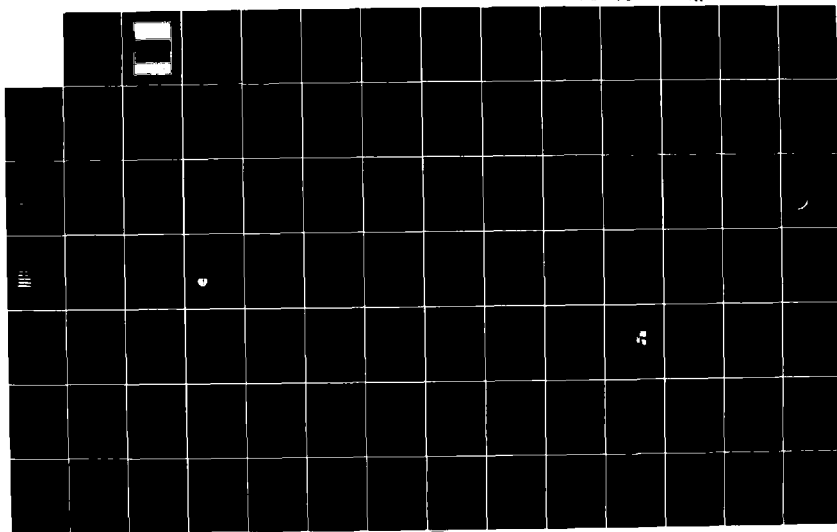AD-A124 280 PREDICTION OF AERODYNAMIC LOADS ON ROTORCRAFT(U) 1/4
ADVISORY GROUP FOR AEROSPACE RESEARCH AND DEVELOPMENT
NEUILLY-SUR-SEINE (FRANCE) SEP 82 AGARD-CP-334
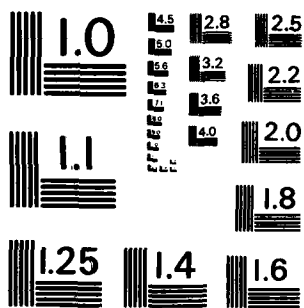
UNCLASSIFIED   F/G 1/2   NL

MICROCOPY RESOLUTION TEST CHART

NATIONAL BUREAU OF STANDARDS-1963-A

AGARD-CP-334

AGARD

ADVISORY GROUP FOR AEROSPACE RESEARCH & DEVELOPMENT

7 RUE ANCELLE 92200 NEUILLY SUR SEINE FRANCE

AD A 124260

AGARD CONFERENCE PROCEEDINGS No. 334

Prediction of Aerodynamic Loads on Rotorcraft

DTIC
ELECTE

FEB 9 1983

H

NORTH ATLANTIC TREATY ORGANIZATION

**DISTRIBUTION AND AVAILABILITY
ON BACK COVER**

83 02 09 059

NORTH ATLANTIC TREATY ORGANIZATION

ADVISORY GROUP FOR AEROSPACE RESEARCH AND DEVELOPMENT

(ORGANISATION DU TRAITE DE L'ATLANTIQUE NORD)

AGARD Conference Proceedings No.334

PREDICTION OF AERODYNAMIC LOADS ON ROTORCRAFT

Papers presented and discussions held at the Fluid Dynamics Panel Specialists' Meeting
held at Church House, London, United Kingdom, 17–18 May 1982.

THE MISSION OF AGARD

The mission of AGARD is to bring together the leading personalities of the NATO nations in the fields of science and technology relating to aerospace for the following purposes:

— Exchanging of scientific and technical information;

— Continuously stimulating advances in the aerospace sciences relevant to strengthening the common defence posture;

— Improving the co-operation among member nations in aerospace research and development;

— Providing scientific and technical advice and assistance to the North Atlantic Military Committee in the field of aerospace research and development;

— Rendering scientific and technical assistance, as requested, to other NATO bodies and to member nations in connection with research and development problems in the aerospace field;

— Providing assistance to member nations for the purpose of increasing their scientific and technical potential;

— Recommending effective ways for the member nations to use their research and development capabilities for the common benefit of the NATO community.

The highest authority within AGARD is the National Delegates Board consisting of officially appointed senior representatives from each member nation. The mission of AGARD is carried out through the Panels which are composed of experts appointed by the National Delegates, the Consultant and Exchange Programme and the Aerospace Applications Studies Programme. The results of AGARD work are reported to the member nations and the NATO Authorities through the AGARD series of publications of which this is one.

Participation in AGARD activities is by invitation only and is normally limited to citizens of the NATO nations.
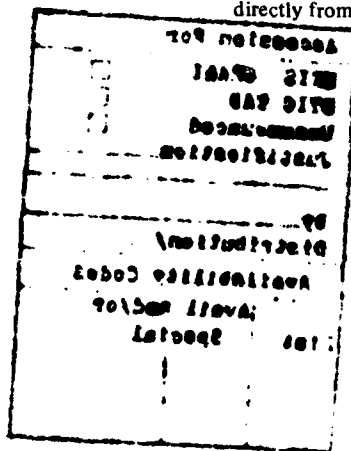
EXECUTIVE SUMMARY

A wide range of aerodynamic phenomena contribute to the airloads on rotorcraft, and the accurate prediction of these loads represents a major challenge to the helicopter technical community. This Specialists' Meeting was organized for the purpose of identifying and assessing recent developments in this field. The primary theme of the meeting was the prediction and experimental verification of the steady and unsteady aerodynamic forces on the rotor blades of modern helicopters and related devices, such as wind turbines.

The Meeting consisted of four main sessions that addressed recent advances in rotor airloads prediction methods, including the evolution to the present state of the art, the capabilities and limitations of the current methodology, and the specific areas that need further effort. Nineteen invited papers were presented in the following four sessions:

I. ROTOR BLADE AERODYNAMIC CHARACTERISTICS: The current engineering prediction techniques for airfoil and rotor blade planform shapes were outlined. These methods draw from a variety of analytical, numerical, and experimental sources, especially the latter. New, more advanced methods were also described for predicting the section characteristics and performance of rotor airfoils, including dynamic stall, transonic effects, and three-dimensional corrections.

II. WAKES AND AERODYNAMIC INTERFERENCE EFFECTS OF ROTORCRAFT AND WIND TURBINES: This session included methods of predicting the wake vortex structure of an isolated rotor in hover and related measurements of the induced velocity field. Airloads and stresses resulting from blade-vortex interactions and from aerodynamic interactions between the main rotor, fuselage, tail rotor, and engine inlet were described, along with adaptations of predictive techniques to horizontal-axis wind turbines.

III. ROTOR AIRLOADS PREDICTION PROGRAMS: Individual aerodynamic modules, generally simpler than the ones described in Sessions I and II, have been combined with structural dynamic models and assembled into large prediction codes. Current programs were outlined, including their capabilities and limitations, and a progress report was given on a comprehensive new interdisciplinary analysis system that is under development.

IV. EXPERIMENTAL CORRELATIONS AND VERIFICATIONS. Data from model and flight tests were analyzed and compared with predictions, with varying degrees of success. New data management systems and data analysis techniques were also described.

In addition to the contributing authors, two rotorcraft specialists with broad backgrounds and experience in each of the relevant technical areas were invited to assess and critique the papers in the four sessions and to comment on advances in the state of the art in predictive capability. Written remarks by seven of these Commentators are included in these Proceedings.

Significant advances have been made in recent years towards understanding and predicting the individual aerodynamic effects discussed in Sessions I and II. However, much of this new information has yet to be incorporated into the large prediction codes described in Session III. Similarly, the comprehensive and sophisticated analyses have generally not been tested rigorously against the most complete and advanced sets of experimental data. Furthermore, none of the data sets appears to include all the information that would be needed to completely validate the latest global computer models.

Nevertheless, the current generation of helicopter airloads prediction programs represent considerable evolutionary progress over the past decade. Although present analyses use aerodynamic modules that are based on earlier technology, they have been fine-tuned and "validated" on the basis of previous experience. Significantly better structural dynamic models are now included, and new, powerful scientific computers are being used to greater advantage. The greatest limitation seems to be in extrapolating a given program to a new or unrelated rotor design.

The information presented at this Specialists' Meeting indicates that significant additional improvements in predictive capability can be achieved in the following three main ways:

(1) Incorporating the new fundamental aerodynamic developments into future prediction codes. This has to be in the simplest and most practical manner possible so as to minimize the additional computational expense.

(2) Performing more systematic and thorough experimental correlations and verifications. Additional and more comprehensive data are needed, but even the existing measurements tend to be under-utilized.

(3) Structuring and managing the future codes in a more unified and organized manner, using modern software methodology. The overall program should consist of modular subsystems that can be individually modified to allow new technology to be introduced or corrections to be made with minimum effort and expense.

The efforts required to implement such improvements are considerable, but the potential benefits to the NATO community are even greater. Therefore, the specialists in helicopter airloads predictions should be encouraged by AGARD to continue the exchange of information and ideas that was begun at this meeting.

W.J.McCROSKEY
Chairman, Programme Committee

AGARD FLUID DYNAMICS PANEL

M. l'Ing. en Chef B.Monnerie
Chef de la Division d'Aérodynamique Appliquée
ONERA
29, Avenue de la Division Leclerc
92320 Châtillon — France

Dr L.Roberts
Joint Institute for Aeronautics & Acoustics
Department of Aeronautics and Astronautics
Stanford University
Stanford
California 94305 — USA

PROGRAM COMMITTEE MEMBERS

Dr.W.J.McCroskey N202A-1 (Chairman)
Senior Staff Scientist
Ames Research Center
Moffett Field
CA 94035 — USA

Professor Dr Ir. J.A.Steketee
Department of Aerospace Engineering
Delft University of Technology
Kluyverweg 1
2629 HS Delft — Netherlands

Dipl. Ing. P.W.Sacher
Messerschmitt-Bolköw-Blohm GmbH, UF-FE 122
Postfach 80 11 60
D-8000 München 80 — FRG

Dr Ing. U.Sacerdote
Direttore Affari Generali
Aeritalia
Via Panama 52
Rome — Italy

M. l'Ing. de l'Armement M.Vergne
STPA/EG
4 Avenue de la Porte d'Issy
75996 Paris Armées — France

Dr D.J.L.Smith
Head of Aerodynamics Department
Royal Aircraft Establishment
Farnborough
Hants GU14 6TD — UK

CONTENTS

THE ROLE OF ANALYSIS IN THE AERODYNAMIC DESIGN

OF ADVANCED ROTORS

By

L. Dadone

Engineering Specialist, Aerodynamics
Boeing Vertol Company
Boeing Center
P.O. Box 16858
Philadelphia, PA 19142
USA

SUMMARY

Although significant advances have been recently made in all the areas of aerodynamics and fluid dynamics concerning the understanding of the flow field of helicopter rotors, the key to the definition and validation of advanced rotor designs still rests substantially with wind tunnel and flight test, guided to a growing extent, but generally not dictated by analysis.

As two-dimensional flows received a great deal of attention in recent years, it is not surprising that some of the most successful contributions of analysis to advanced rotors have been the result of airfoil optimization. Rotor airload prediction methods, corbining the relevant aerodynamic and dynamic phenomena, have been used in the definition of the design objectives and have provided the guidelines necessary to make use of improved rotor sections. It is not clear to what extent sectional optimization can be used to further improve advanced rotors, but the design of better rotor sections may still be feasible.

This paper reviews from a manufacturer's point of view the extent to which flow analysis has influenced rotor design, it suggests an interim method to define tip geometries for high speed flight until rotor blades can be modeled more rigorously, and it addresses the potential value of new computational methods in improving the aerodynamic efficiency of helicopter rotors.

INTRODUCTION

Advanced rotors will allow rotorcraft to fly faster and more efficiently. In a narrow sense, the objective of the aerodynamic optimization of rotors and wings is the suppression of flow separation and minimization of induced power.

As the limits of the helicopter flight envelope have been expanded, and as a requirement for increased efficiency has been prompted by recent energy problems, the quest for rotors with improved aerodynamic characteristics, "advanced rotors", has received a new impetus. An additional incentive has been the need to quantify the true operational limits of conventional rotors, a knowledge which will have significant influence in determining whether helicopters are adequate for a number of future commercial and military applications.

The potential value of pure helicopters, i.e., helicopters employing conventional rotors for lift and propulsion, is compared to other helicopter alternatives and to the tilt-rotor in Figure 1. The comparison is based on a transport mission that defines payload to gross weight ratios for a range in speed capability. The potential for high speed operation beyond 180 knots has already been demonstrated[1] and further gains are within reach pending the suppression of the vibratory loads associated with flight regimes near and beyond 200 knots, assuming that this can be achieved with minimum weight and performance penalties.

New methods resulting from the availability of large computers have recently been developed and have already had a significant impact on fixed wing applications of analysis[2]. But even before the advent of Computational Fluid Dynamics, computers have changed the role of the average engineer. Some have turned into "developers", and many more into "users" of computer programs. Fortunately or not, "analysis" today implies the definition and use of computer programs, with the added dimension that now we can, if not careful, generate many more wrong answers using far more complex computation methods, and faster than ever before.

With all their drawbacks, however, computers have made a significant difference in the way we approach the understanding of physical phenomena. Recent advances in computational methods have been so substantial that, particularly in industry, it is difficult to reach and maintain a proper perspective on the role of analysis. While at times it is easy to be accused of relying too much on computations, an excessively down-to-earth approach might cause us to under-utilize existing resources and lose some of whatever technical competitive advantage we have.

As the objective of advanced rotor design is the definition of faster and more fuel efficient helicopters, the development of analysis can be justified only within the context of its application to this objective. The potential benefits to be derived from the aerodynamic improvement of rotors have been quantified in various ways. For

instance, at the 1980 HAA/NASA meeting[3] F. McHugh offered the following perspective on the value of advanced rotor research:

"As part of NASA's research, a study[4] was conducted to determine the payoff in fuel reduction resulting from estimated levels of improvement potentially available from advanced technology. The three major improvements were light weight structure, rotor lift/effective drag ratio and hover figure of merit in addition to regenerative engines. The combined improvement of all the technology improvements was 30 to 40 percent (Figure 2). To determine which of the technologies would provide the largest fuel saving per dollars spent in development, an additional study was made to assess the cost of research and development required to provide the level of technology improvement used in the study. As shown in Figure 3, drag reduction provided the largest fuel saving per development dollar with figure of merit and rotor lift/effective drag ratio as the next two major areas. Light weight structure and engine development were assessed, at that time, as having high development costs and thereby lower energy savings per development dollar."

It has long been recognized that, away from rotor limits, even simple analysis will yield fairly accurate trends in terms of the effect of twist and planform variation on performance. Simple analysis can show that twist will improve aerodynamic efficiency in hover, and that reducing the planform where more is lost from drag than gained from lift will also improve efficiency. Twist and planform variations imply consequences in forward flight performance and loads which cannot be generally quantified analytically, but which can be quantified experimentally. Beyond the calculation of basic twist and planform trends, the use of analysis in improving helicopter rotors has been limited because analysis has been substantiated only over known flight regimes and cannot be safely used to extrapolate characteristics beyond 20 to 40 knots. However, testing has been accomplished very recently[1] up to 231 knots in the lifting and propelling mode for conventional rotors of varying solidity, blade number, tip planform and structural characteristics. This new information will aid in the substantiation of up to date forward flight codes. Analysis will then permit the assessment of the requirements for a rotor design optimized for high speed flight.

PAST AERODYNAMIC ANALYSIS DEVELOPMENTS AT BOEING VERTOL

Milestones in the development and introduction of methods of analysis which influenced the aerodynamic design of Boeing Vertol rotor systems are shown in Table I.

Following is a brief chronology of main developments since the early 1960's.

o **Introduction of Camber on CH-47 Rotor Blades**

Starting from the early 1960's, research was undertaken on rotors which would increase the efficiency and expand the flight envelope of the CH-46 and CH-47 helicopters. Eventually, this research led to the introduction of the V23010-1.58 airfoil on CH-47B and C blades, and of a slightly modified V23010 airfoil on the CH-46. This rotor system modification was part of extensive changes to the CH-46 and CH-47 models, made in conjunction with more powerful power plants. The key change on the rotor blades was the replacement of a symmetrical section with a cambered one.

The research leading to the CH-47B rotor blades was carried out over several years, and it involved a series of airfoil tests in the Transonic Wind Tunnel at Boeing Seattle. Since at that time the methods airfoil analysis did not allow the prediction of sectional characteristics at all the conditions necessary to assess rotor blade airloads, during the early 1960's the choice of airfoils was determined mostly by systematic wind tunnel measurements. Besides the methods described by Abbott and VonDoenhoff[5], the basis for airfoil contour variation was the information available on the overall characteristics of NACA airfoils, and the requirement that the new CH-47 sections be a contour modification easily applied over the existing CH-47A symmetrical contour, without major re-tooling.

Even as the first cambered blades were being flight tested, thought was being given to further improvement. The basic tradeoff between maximum lift characteristics at intermediate Mach numbers, necessary to delay stall over the retreating side, and the need to reduce advancing blade power was proposed by F. Davenport in 1966[6], on the basis of the "dagger model" (AR = 5.5) data from the Boeing Transonic Wind Tunnel.

o **Early Airfoil Analysis Methods**

New methods became available during the late 1960's and early 1970's to aid in the analytical evaluation of the sectional characteristics necessary to improve helicopter rotors. These methods combined potential flow solutions for two-dimensional airfoils with boundary layer analysis. The methods were not new, but their application to systematic airfoil studies had not been practical until they were adapted to local computers.

While not meant for and not valid at conditions involving separation, by correlation with 2-D data these potential flow/boundary layer interaction methods allowed the prediction of the maximum lift, at M = 0.4, of airfoils whose stall was characterized by L.E. or T.E. separation (no thin airfoil stall, involving laminar bubbles).

Potential flow analysis for subcritical flow had also been successfully combined with observations on the drag rise characteristics of airfoils at high subsonic Mach numbers[7]. The outcome was an empirical method based on the evaluation of the conditions at which the flow becomes locally sonic at the "crest" of an airfoil, hence "crest-line" theory. The combination of potential flow/boundary layer interaction methods and crest-line theory allowed the analytical review of airfoil sections which would meet the criteria set by Davenport, the only difference in the approach being the replacement of the Mach number at which a drag coefficient level would be reached, with the Mach number for drag divergence at zero lift.

o **"Lifting-Line" Rotor Analysis and Unsteady Aerodynamic Methods**

The 1960's also saw the development of lifting-line/strip-analysis computer codes for non-elastic articulated rotors. These methods were based on the interpolation of detailed two-dimensional airfoil characteristics and on the use of prescribed wake models to calculate the induced velocities along a rotor blade, either in hover (B-92) or in forward flight (B-67), thus allowing the evaluation of a non-uniform flow field more representative of the rotor environment than possible by momentum ("uniform downwash") methods. Oscillating airfoil tests were conducted starting in 1966 and, by 1968, the data from the oscillating airfoil tests were used to assess dynamic stall delay effects on airfoil characteristics[8]. By 1969 a more comprehensive lifting-line/strip-analysis method became operational, the B-67DD code. This method did not require any empirical adjustments to the sectional data because of the introduction of an unsteady aerodynamic formulation to account for dynamic stall delay effects and to approximate the increase in mean profile drag. Although retaining the old kinematic wake model, the new code included a modal representation of blades flexible flatwise and in torsion.

The B-67DD forward flight analysis, its hover counterpart, B-92, and simpler codes used to carry out trim analysis, were the basis for systematic trend studies to determine the most efficient planform, twist and airfoil combinations necessary to support the growth of the CH-47 and other prototype helicopters programs. Except for an advanced geometry blade involving a small amount of taper distributed from root to tip (the "AGB" blade), and a "hatchet" tip configuration, defined on the basis of simple local sweep considerations and flight tested on the Model 347 helicopter, all blades considered up to the early 1970's were of rectangular planform, with airfoils tapered in thickness and camber as necessary to reduce advancing blade drag, and with twist defined to gain the best hover performance, while minimizing forward flight performance penalties.

The lack of fundamental methods to understand unsteady aerodynamics combined with flow separation led to a few misconceptions as to the nature of dynamic stall delay. A significant amount of time was spent searching, by means of oscillatory airfoil tests and rotor tests, for an airfoil which would overcome by unsteady aerodynamic effects its poor quasi-steady performance at the Mach numbers encountered during retreating blade stall, and still have outstanding transonic drag characteristics.

o **Heavy Lift Helicopter Rotor Airfoils**

The early 1970's saw the development of new rotor blades first for the Heavy Lift Helicopter (HLH) and later for the Utility Tactical Transport and Support (UTTAS) helicopter. Besides the improved structural characteristics due to composite materials, both rotors employed sections which had been designed almost entirely on the basis of established advancing/retreating blade criteria where, however, more elaborate design objectives were set for different spanwise locations along the blade. Additional restrictions were also imposed on the two-dimensional pitching moment coefficients as a result of rotor tests which quantified the dependence of blade torsional loads and pitch link loads on the level of the sectional pitching moments.

The overall definition of blade requirements was determined analytically, with emphasis on hover performance. Airfoil design was guided by airloads analysis to establish the correct balance of camber, thickness and trailing edge reflex. However, the final rotor blade configurations, particularly regarding the correct amount of T.E. reflex, were determined by wind tunnel tests of model rotor blades. The background of these developments is discussed in references (9), (10) and (11).

o **More Advanced Lifting-Line Rotor Analysis Methods**

The late 1970's saw the introduction of the models of two important phenomena into the B-67 airloads analysis. The first was in response to the need to quantify the difference between two- and three-dimensional flow effects near the tip ("tip relief" effects). The second was a definition of the dependence of the spanwise location of the rolled-up tip vortex on the instantaneous blade loading, without the complexity of a free wake (tried, with disappointing results, in 1969). The version of B-67 with a kinematic wake rolled up by Betz criteria was identified as B-65. Tip relief effects on drag were introduced as proposed by LeNard[12], while lift and pitching moment corrections, initially based on existing data on low aspect ratio wings tested at transonic speeds, were further improved on the basis of more recent experimental and analytical evidence. As shown in Table I, during the mid 1970's a derivative of the B-67 analysis was defined to include sweep

effects. This code, called B-66, is currently undergoing final checkout and corre-
lation with model rotor test data.

o Recent Advanced Rotor/Airfoil Design

Although tip modifications were attempted during the 1970's, primarily to improve
hover performance, the blades considered for production were all limited to a rec-
tangular planform, including the fiberglass blades for the CH-47D, which utilize
the VR-7 and VR-8 airfoils originally designed for the HLH.

The last airfoil design based on requirements not involving blade sweep, discussed
in Reference (11), was carried out in 1978 during efforts to define a conventional
rotor optimized for 180 knot cruise speed without severe performance and loads
penalties. Two of the airfoils defined and tested in 1978, the VR-12 and VR-15,
are shown in Figure 4 and there compared to airfoils on Boeing Vertol helicopters
in current use. The performance of selected helicopter sections is compared in
Figure 5.

The VR-12 and VR-15 represent the best compromise possible, within the limits of
the methods used, for the maximum lift capability at $M = 0.4$, and the drag diver-
gence Mach number at zero lift, while meeting hover drag requirements and restrict-
ing the sectional pitching moments to levels shown to be necessary by previous test
experience. The two-dimensional tests confirmed the predicted sectional perform-
ance and demonstrated that current methods of airfoil analysis can be successfully
used to design and optimize helicopter rotor airfoils.

The new sections were designed entirely analytically by means of a potential flow/
boundary layer interaction analysis[13] and a viscous transonic analysis[14], both
calibrated with data from the two-dimensional transonic insert of the Boeing Super-
sonic Wind Tunnel. Details of the methods used are outlined in Reference (11).
The VR-12 and VR-15, employed on a number of advanced rotor configurations, have
been the subject of exhaustive model rotor tests to determine the rotor performance
for flight beyond 180 knots. Several rotor configurations tested in the most
recent advanced rotor test are described in Reference (1).

Hover and forward flight performance for some of the configurations employing the
new airfoils are shown in Figures 6, 7 and 8. Figure 8 shows the benefits possible
by introducing planform taper in combination with advanced airfoils. Figure 9
illustrates the growth in blade loads with increasing speed, as measured during one
of the recent Boeing Vertol advanced rotor tests. The growth in advancing blade
loads is the main cause of rotor limits, as far as performance is concerned; how-
ever, the torsional fluctuations associated with retreating blade stall, while not
always limiting performance, are a significant source of higher harmonic vibratory
loads.

It is interesting to note that during the mid-1960's limitations in the theory and
restrictions in the experimental set-up convinced us of intrinsic limitations in
the range of usefulness of conventional rotors. This prejudice took years to over-
come. In fact, both theory and test seemed to point to insurmountable limits for
conventional articulated rotors at high speeds. As shown by F. McHugh[15,16] and
confirmed by current analysis (B-65), we can operate at speeds well beyond 200
knots with the rotor providing the lift and propulsive force representative of an
advanced helicopter, with some increase in loads.

The question now is: How should we alter the geometry and, if necessary, the
structural properties of a rotor blade to improve efficiency and to extend the high
speed capability?

PRESENT ROLE OF ANALYSIS

As illustrated in Figure 8, the introduction of sweep did not produce an improvement in
forward flight performance at high speeds over the level achieved by an advanced rotor
configuration employing just tip taper. As the methods of analysis available when the
test was planned did not allow a comprehensive assessment of all the implications of tip
sweep, sweep was introduced on several model blades so that key trends could be deter-
mined experimentally.

The results of the test show that there are fundamental aspects of the aerodynamic and
dynamic behavior of swept rotor blades that we still need to understand. This under-
standing will probably not be a result of any advanced technique of flow analysis, at
least during the immediate future. In the near term, the useful limits of advanced
rotors will be assessed as the result of:

(a) Empirical means to account for 3-D tip relief effects. Although the approach
    used at this time is based on the "complementary" wing formulation by
    LeNard[12], the tip relief evaluation procedure may be improved by means of
    recently developed rotor blade panel methods[17,18,19]. An example of 3-D
    "relieved" environment by the method of Reference (12) is compared to airfoil
    drag divergence boundaries in Figure 10.

(b) Approximations of local sweep effects, to be used in evaluating first order
    aerodynamic sweep requirements. Typically, these effects may be expressed by

a function of the quarter-chord sweep angle, $(\cos \Lambda)^n$, and be combined with tip relief assessment methods.

(c) Two-dimensional airfoil analysis and design methods. Besides the potential flow/ boundary layer interaction and viscous transonic flow analysis methods[13,14], today airfoil analysis can be carried out by two-dimensional codes which include a model of the separated wake[20,21]. Airfoil contours can be also optimized by computer assisted procedures tied in with a 2-D transonic analysis code[22,23].

(d) Lifting line performance and loads analysis methods incorporating relatively simple but correctly coupled aerodynamics and dynamics, such as the B-66 analysis, a modification of the B-65 analysis, mentioned earlier, having provisions for planform sweep.

The near-term process used in defining advanced rotor configurations which combine airfoils integrated with planform and sweep requirements, can be described as follows:

(1) Combine three-dimensional Mach "relief" methods, such as the LeNard method[12], with a simple formulation describing the nominal local Mach number environment for a rotor in forward flight. When linked with a local sweep geometry generation scheme, as illustrated in Figure 11, the "inverse" tip-relief analysis can be used to line up two-dimensional airfoils along curved boundaries, while taking into account the first order flow deflection effects due to the physical size of the tip and local drag divergence requirements. Examples of the result of this process are shown in Figures 12 and 13. In the first example, Figure 12, the planform was iterated upon to obtain a straight trailing edge. In the second, Figure 13, a swept forward trailing edge. The conditions on which these designs were based are described in the figures.

(2) Having obtained candidate shapes based on preliminary lift and drag divergence requirements, the newly defined planforms can be then analyzed by means of complete lifting line analysis methods incorporating rotor wake models, unsteady aerodynamics effects, planform effects, sweep (in the aerodynamic sense, and by introducing the correct lift offset), 2-D airfoil data, tip relief approximations, elastic blade effects and blade dynamics. This can be accomplished by means of the B-65/B-66 codes mentioned earlier, within the range of conditions for which the codes have been validated, which now includes flight speeds up to 231 knots.

(3) With revised and, after the first iteration, more detailed lift/Mach number requirements from the airloads analysis, it is possible to re-enter the inverse sweep solution and update the planfrom or airfoil distribution on the basis of new local drag divergence Mach number boundaries.

(4) The inverse sweep/airloads analysis cycle can be repeated for the desired design conditions until the conclusion is reached that either an airfoil/planform combination is possible, or that the requirements exceed the means available to meet them. At that point, in order of increasing complexity, the following choices are possible:

    o Change blade torsional stiffness,

    o Further relax the sweep or planform/taper requirements,

    o Investigate the value of changing or redesigning the airfoils.

More comprehensive methods may also be employed to refine the planform geometry from an aerodynamic point of view, possibly with the aid of induced velocity information from the lifting-line airloads analysis. The Tauber/Arieli and Caradonna/Chattot codes[17,18,19], should be tried to assess whether airfoil/planform combinations as, for instance, in Figures 12 and 13, can be altered as three-dimensional surfaces to improve their transonic characteristics, although it is not clear whether these codes can be used for such a specific application. However, at this time any clue would be useful because potential contour change benefits can be later refined and verified experimentally.

In order to achieve flight speeds beyond 200 to 220 knots with conventional helicopter rotors planform sweep is probably a necessity because, in terms of Mach number penetration, airfoils and unswept planforms may have been exploited to the point of diminishing returns even after all three-dimensional effects are properly taken into account. Some further extension may be obtained by reducing camber and thickness, but although potentially capable of very high drag divergence Mach numbers, sections which are too thin would have very poor off-design performance and would not produce enough lift where needed at Mach numbers below drag divergence.

Even sweep, however, has its limitations. Figures 14 and 15 compare the nominal Mach number environment of two blade planforms, the first rectangular and the second swept. While sweep reduces the nominal local Mach number at $\psi = 90$, the encounter with higher local Mach numbers is delayed to azimuth positions beyond 90° in proportion to the magnitude of the local sweep angle built into the blade.

As shown in Figure 10, three-dimensional tip relief practically vanishes inboard 0.85R on a rectangular planform with airfoils 8% to 10% thick. Rotor tips employing thin airfoils and/or chord taper would experience a further reduction in tip relief, so that any improvement in Mach number penetration inboard of 85% of the radius would have to be obtained by sweep. An increase in airfoil drag divergence by $\Delta M = 0.05$, from a current $M_{DD} = 0.8$ to $M_{DD} = 0.85$ for an average advanced "working section" at the zero lift level, would allow an increase in flight speed by almost 33 knots, assuming that changes in blade drag divergence Mach number can be converted directly into flight velocity. It is not likely, however, that sweep could be successfully employed inboard of 85% of radius for local Mach number reduction alone, because even by a conservative estimate $(\cos \Lambda)$ the effect of sweep may be too weak to be worth the complexity of planform sweep over a substantial portion of span. Although nominally optimized for the advancing side, a swept tip blade will have to be able to provide lift and fly through the retreating side of the rotor disc without stalling too severely, while providing the necessary thrust, propulsive force and acceptable blade/control loads. If this can be achieved, it will probably result in the following significant changes in airfoil design objectives:

(1) As blade torsional moments and elastic windup may be as much a function of tip sweep as of sectional pitching moments, the current nose-up pitching moment requirements may be relaxed, allowing the use of sections without the T.E. reflex with negative camber which characterizes most current advanced helicopter rotor airfoils. Positive camber at the trailing edge would allow an increase in the maximum lift and drag divergence boundaries beyond the level of the VR-12 to VR-14 sections of Figure 5.

(2) It is not clear at this time what effect sweep would have on dynamic stall, although it may be speculated that, if not excessive, the elastic windup due to sweep may help in reducing stall effects by reducing the angle of attack. At any rate, different maximum lift objectives would have to be set for the inboard sections not involved in sweep (inboard of 80% to 85% of span) and the tip sections. If it could be demonstrated that sweep attentuates dynamic stall and hence reduces the $C\ell_{max}$ requirement at $M = 0.4$, a very firm requirement up to now in designing Vertol rotor airfoils, it would be possible to reduce overall camber and provide better Mach number penetration at low lift levels.

FUTURE APPLICATIONS

Having reviewed the means presently available to evaluate by analysis changes in blade geometry which will result in improved aerodynamic efficiency, one must reach the conclusion that while not quite representative of the actual flow along a rotor blade, the two-dimensional definition of blade sections is the area in which analysis has been most useful.

What needs to be addressed is the fact that while advanced methods of analysis generally take a long time to be substantiated and find their way into applications, in the long term the definition of improved rotor systems would become prohibitively costly, if not impossible, without the guidance of adequately developed methods of analysis.

The problem can be summarized as follows: on one side we have well described phenomena which are applicable to the prediction of rotor airloads only if we make bold assumptions as to their validity in the rotor flow environment (airfoil theory, for instance). On the other side we have analytical models of separate phenomena which would be well suited to reveal details of the rotor flow field, but which will not be useful in rotor optimization unless they can (a) be expanded to a higher degree of resolution, (b) be integrated within comprehensive methods of rotor analysis which properly combine and couple all the elements involved, and (c) can be substantiated by correlation with test data, i.e., airloads from blade pressure measurements, blade loads and overall performance.

Given the choice of an analysis which combines relatively simple models of the individual phenomena, correctly coupling all the most important aerodynamic and structural/dynamic effects, and an analysis which describes in great detail a phenomenon removed from the helicopter rotor, at present the engineer attempting rotor optimization would be forced to use the more comprehensive, if less accurate, method to guide the process. The role of advanced analytical models of the individual phenomena will depend on our willingness and ability to introduce them into the rotor analysis codes.

Potential of New Methods of Analysis

Of the advanced methods of analysis currently under development, the following have the potential for a significant impact on the aerodynamic design of future helicopter rotors:

(1) Lifting surface rotor analysis methods, for both subcritical and transonic flow regimes, which are being progressively expanded to include more comprehensive wake models and unsteady aerodynamics effects.

(2) Fixed wing/fuselage 3-D panel analysis, utilizing potential flow models, which may later be extended to helicopters.

(3) Euler and Navier-Stokes codes.

The first group includes the adaptation of FLO22 to the rotating environment[17], and transonic small disturbance methods extended to helicopter rotor blades[18,19].

The development of advanced panel methods and of the Euler and Navier-Stokes codes has been motivated by the need to improve the efficiency of fixed wing aircraft. Before deciding how useful these methods would be to helicopters, we should understand how useful they have been to the fixed wing community so far.

In recent years, fixed wing methods of analysis have evolved to a state of "mature technology" so that more of the optimization of aircraft components, as well as the integration of components, can be carried out prior to experimental confirmation. In absence of flow separation, the analytical techniques are so well trusted that local changes in fuselage contour may be assessed entirely analytically, and accepted without further verification.

In Reference (2), L. Miranda reached the conclusion that potential flow models appear to be "quite adequate" for the majority of airplane applications, "provided that appropriate viscous corrections are incorporated in the transonic regime". For the future "greater gains in effectiveness are likely to come from the expansion of the geometrical capabilities of full potential flow codes, rather than from the introduction of more accurate flow models, as Euler and Navier-Stokes solvers". And "finally, that" computational aerodynamics and wind tunnel testing should not be viewed as competing technologies...but rather should be used in a complementary fashion". Concluding that wind tunnel testing, for the foreseeable future will remain the best tool for verification and validation.

These comments could apply as well to the modeling of rotor blades, except that the application of panel methods to helicopter rotors is not close to the degree of "maturity" of the fixed wing methods.

The adequacy of the geometric representation of the surfaces involved is of course an issue. Although "low-order" panel methods have been proposed, it is not clear to what extent details of the rotor surface may be quantified by analysis. No matter how useful these methods will be in the future, near term applications are not quite within reach.

It is possible that a considerable insight into unsteady aerodynamics and tip flow phenomena may be eventually gained by Navier-Stokes and Euler finite difference methods, but the careful coupling of panel methods and wake models, backed by specific wind tunnel tests, will probably yield usable trends before the more fundamental flow analysis methods produce any directly applicable results.

Although the analysis of tip flows has significantly progressed during the last few years, it is not time to call an end to airfoil optimization. The emphasis, however, should be on the right combination of camber, thickness and tip shape for established families of airfoil shapes rather than on the optimization of airfoil contours on the basis of high lift and high Mach number penetration. This will be accomplished by analysis of the rotor flow environment carried out in conjunction with planform optimization based on lifting-line/strip-analysis methods. The results of more sophisticated methods of flow analysis will be needed to define empirical models of specific phenomena necessary to make comprehensive rotor analysis codes both practical and successful.

CONCLUSIONS

(a) Until now, the basis for most progress in the aerodynamic optimization of rotor blades has been the combination of strip analysis methods and two-dimensional airfoil optimization, substantiated by test data (airfoil and rotor).

(b) The benefits of new rotor designs at the extremes of the flight envelope cannot yet be quantified by analysis in a consistent and reliable manner.

(c) With no exceptions, experiment has been the real source of data for both development and verification of final rotor designs. In this sense helicopters do not differ much from fixed wing aircraft, but the methods of analysis for fixed wing applications have reached a greater level of maturity.

(d) The prediction of rotor airloads requires the combination and the coupling of the analytical models of different phenomena.

(e) For the near future, the definition of advanced rotors will continue to depend on two-dimensional optimization guided by rotor airload analysis and confirmed by test. However, the level of sophistication needed in furthering the state of the art may soon exhaust this approach.

(f) Lifting line methods combined with empirical means to account for transonic effects and unsteady aerodynamics near the tip of rotor blades will be used to continue sectional and planform optimization until rotors can be better modeled as complete surfaces.

(g) If we consider the degree of resolution necessary to model even relatively simple two-dimensional flow fields, we must conclude that it will be indeed a long time before we can model the flow field of a rotorcraft in all its complexity. However, we do not need to know the flow field in every detail. What we must understand

thoroughly are the ways in which all main aerodynamic and dynamic phenomena are interrelated.

(h) The two most important items to be defined are:

    (1) What is an acceptable balance between simplification and sophistication?

    (2) What are the specific design criteria for airfoil/planform optimization?

REFERENCES

1. McVeigh, M. A. and McHugh, F. J., "Recent Advances in Rotor Technology at Boeing Vertol". Presented at the 38th Annual AHS National Forum, Anaheim, CA, May 1982.

2. Miranda, L. R., "A Perspective of Computational Aerodynamics from the Viewpoint of Airplane Design Applications". AIAA 82-0018. Presented at the AIAA 20th Aerospace Sciences Meeting, Orlando, Florida, January 1982.

3. Proceedings of the HAA/NASA Advanced Technology Workshop, Palo Alto, CA, December 2-5, 1980.

4. Wiesner, W., and Snyder, W. J., "Efficient Civil Helicopters: The Payoff of Directed Research". Presented at the 33rd Annual AHS National Forum, Washington, D.C., May 1977.

5. Abbott, I. H., and VonDoenhoff, A. E., "Theory of Wing Sections", McGraw Hill Book Company, 1949.

6. Davenport, F. J., and Front, J. V., "Airfoil Sections for Rotor Blades - A Reconsideration", presented at the 22nd Annual Forum of the American Helicopter Society, Washington, D.C., May 12, 1966.

7. Royal Aeronautical Society Transonic Aerodynamics Committee, "A Method of Estimated Drag-Rise Mach Number for Two-Dimensional Airfoil Sections", Transonic Data Memorandum 6407, July 1964.

8. Gross, D. W., and Harris, F. D., "Prediction of Inflight Stalled Airloads from Oscillating Airfoil Data". Presented at the 25th Annual National Forum of the American Helicopter Society, Washington, D.C., May 1969.

9. Benson, R. G., Dadone, L. U., Gormont, R. E., and Kohler, G. R., "Influence of Airfoils on Stall Flutter Boundaries of Articulated Helicopter Rotors", presented at the 28th Annual Forum of the American Helicopter Society, Washington, D.C., May 1972.

10. Dadone, L. U., and Fukushima, T., "A Review of Design Objectives for Advanced Helicopter Rotor Airfoils", presented at the AHS Symposium on Helicopter Aerodynamic Efficiency, Hartford, Connecticut, March 1975.

11. Dadone, L. U., "Rotor Airfoil Optimization: An Understanding of the Physical Limits", 34th Annual AHS Forum, Washington, D.C., May 1978. Preprint 78-4.

12. LeNard, F. and Boehler, G. D., "Inclusion of Tip Relief in the Prediction of Compressibility Effects on Helicopter Rotor Performance", USAAMRDL TR73-71, December 1973.

13. Stevens, W. A., Goradia, S. H., and Braden, J. A., "Mathematical Model for Two-Dimensional Multi-Component Airfoils in Viscous Flow", NASA CR 1843, July 1971.

14. Bauer, F., Garabedian, P., Korn, D., Jameson, A., "Supercritical Wing Sections II", Lecture Notes in Economics and Mathematical Systems, Volume 108, Springer-Verlog (New York), 1975.

15. McHugh, F. J. and Harris, F. P., "Have We Overlooked the Full Potential of the Conventional Rotor?". Presented at the 31st Annual National Forum of the AHS, Washington, D.C., May 1975.

16. McHugh, F. J., "What are the Lift and Propulsive Force Limits at High Speeds for the Conventional Rotor?". Presented at the 34th Annual National Forum of the AHS, Washington, D.C., May 1971.

17. Arieli, R., and Tauber, M. E., "Analysis of the Quasi-Steady Flow About an Isolated Lifting Helicopter Rotor Blade". Joint Institute for Aeronautics and Acoustics, JIAATR-24, August 1979.

18. Caradonna, F. X., and Tung, C., "Experimental and Analytical Studies of a Model Helicopter Rotor in Hover". Presented at the Sixth European Rotorcraft and Powered Lift Aircraft Forum, Bristol, England, September 16-19, 1980.

19. Chattot, J. J., "Calculation of Three-Dimensional Unsteady Transonic Flows Past Helicopter Blades", NASA TP1721, October 1980.

20. Henderson, M. L., "A Solution to the 2-D Separated Wake Modeling Problem and Its Use to Predict $C\ell_{max}$ of Arbitrary Airfoil Sections", AIAA 16th Aerospace Sciences Meeting, Huntsville, Alabama, January 1978.

21. Maskew, B., Dvorak, F. A., "Investigation of Separation Models for the Prediction of $C\ell_{max}$", presented at the 33rd Annual National Forum of the American Helicopter Society, Washington, D.C., May 1977.

22. Hicks, R. M., and McCroskey, W. F., "An Experimental Evaluation of a Helicopter Rotor Section Designed by Numerical Optimization", NASA TM78622, March 1980.

23. Blackwell, J. A., and Hinson, B. L., "The Aerodynamic Design of an Advanced Rotor Airfoil", NASA CR2961, 1978.
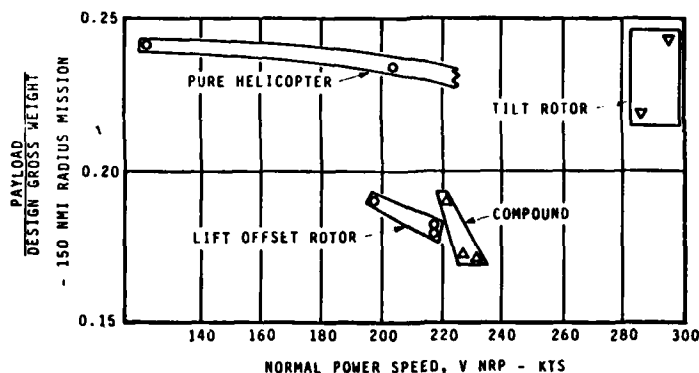
Figure 1. Rotary Wing Transport Aircraft Weight
Trend with Speed.
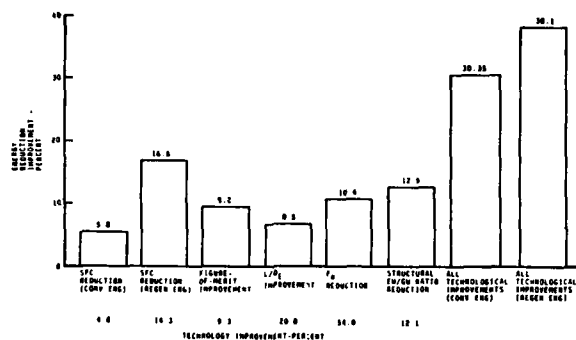
Figure 2. Results of NASA Sponsored Study
of Advanced Technology Features
to Reduce Fuel Consumption.
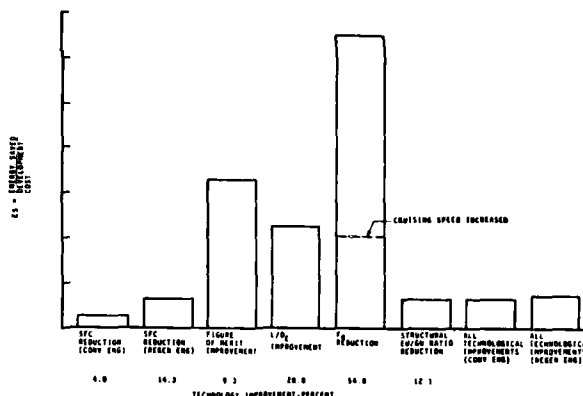
Figure 3. Comparison of Payoff Levels
Resulting from Helicopter Energy
Research.
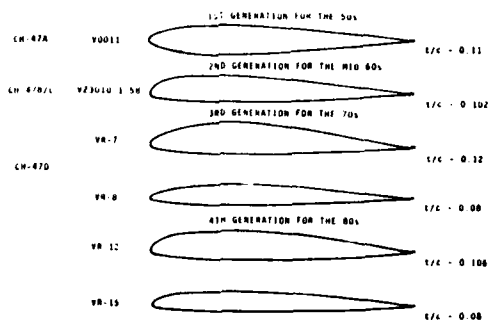
Figure 4. Boeing Vertol Helicopter Airfoil
Development.
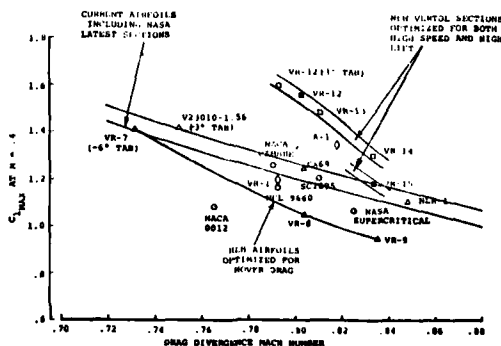
Figure 5. Comparison of Helicopter Rotor
Airfoils.
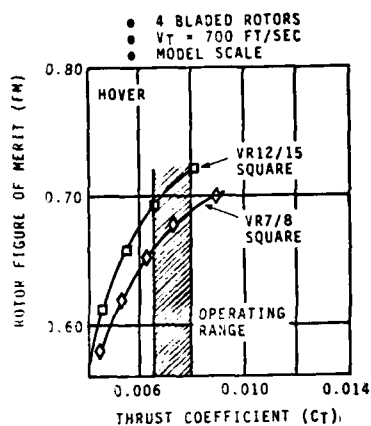
Figure 6. Improvement in Hover Perform-
ance Due to Advanced Airfoils.
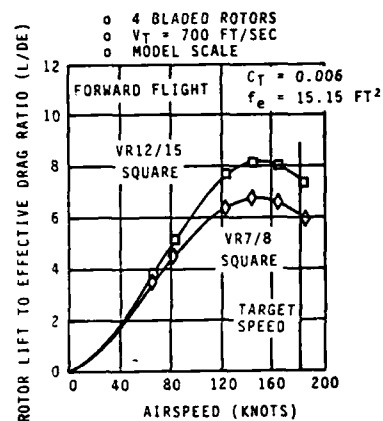
Figure 7. Improvement in Forward Flight
Performance Due to Advanced
Airfoils.
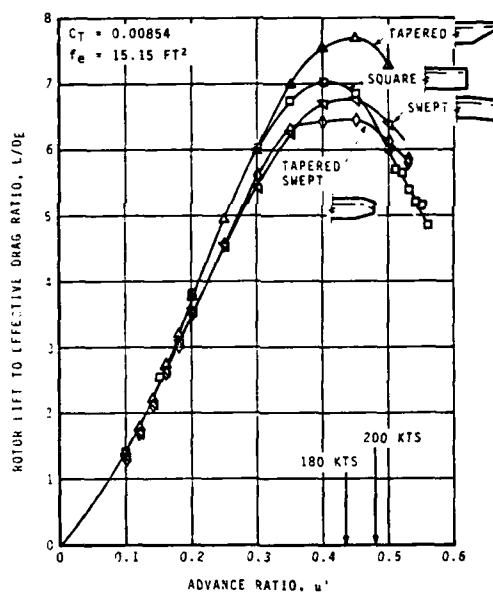
Figure 8. Effect of Planform on Performance.
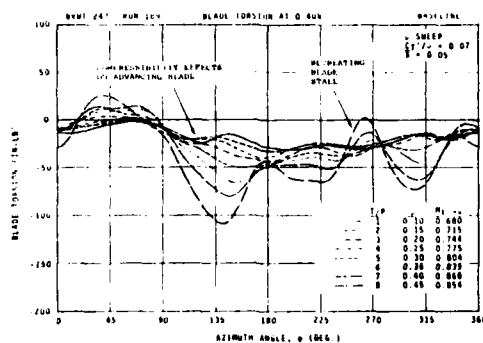
Figure 9. Effect of Advance Ratio on Blade Loads.
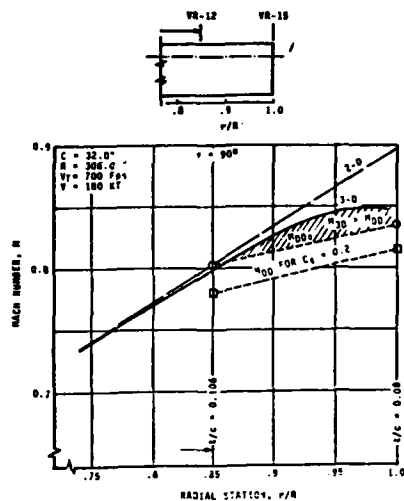
Figure 10. Local Mach Number Environment Near the Tip of a Rectangular Planform Rotor Blade.
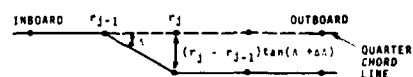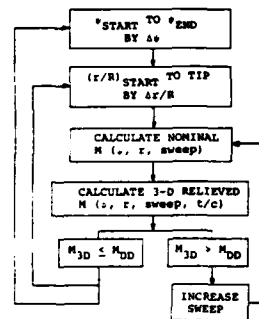
Figure 11. Step by Step Deployment of Local Sweep Used in Altering the Blade Quarter Chord Line to Meet Prescribed Mach Number Requirements.
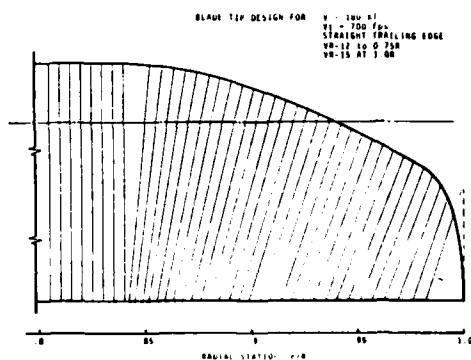
Figure 12. Example of Tip Planform Designed to Meet Prescribed Mach Number Requirements. Continuous Straight Trailing Edge.
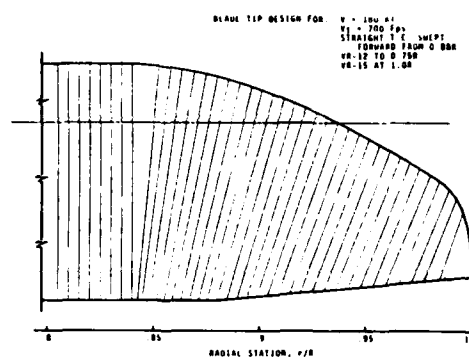
Figure 13. Example of Tip Planform Designed to Meet Prescribed Mach Number Requirements. Straight Swept-Forward Trailing Edge.
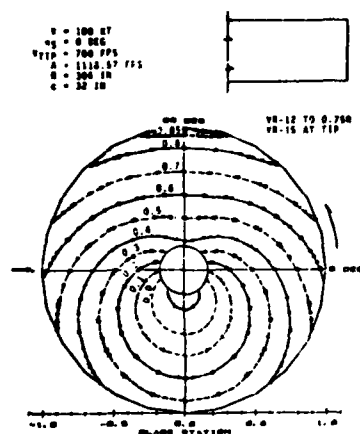
Figure 14. Mach Number Environment of a Rectangular Planform Blade, Including 3-D Tip Relief.
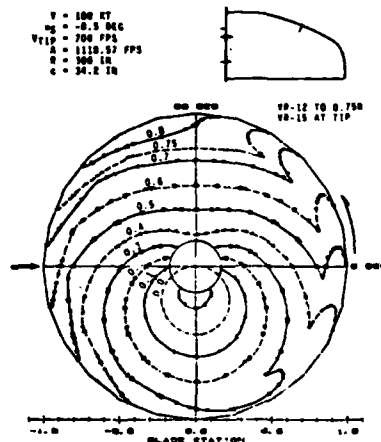
Figure 15. Mach Number Environment of a Swept Tip Rotor Blade, Including 3-D Tip Relief.

<u>TABLE I</u>

SUMMARY OF METHODS OF ANALYSIS USED IN THE
AERODYNAMIC OPTIMIZATION OF BOEING VERTOL ROTOR SYSTEMS

Year	Airfoil/Blade Analysis	Rotor Analysis	Rotor System
1965	Vortex polygon methods	Hover, B-92	CH-47B with V23010-1.58 airfoil, -3°T.E. Tab. (Modification of CH-47A blades)
1966		Forward flight, B-67MC	
1967/68	Definition of dynamic stall delay method[8].		CH-47C with V23010-1.58 airfoil and revised T.E. tab configuration
1969	"Peaky" airfoil methods - Crest line theory	Definition of elastic blade version of B-67, with unsteady aerodynamics, B-67DD. "Free-Wake" version of B-67MC	
1970	Potential flow/ boundary layer interaction analysis TEA267 (Boeing Seattle)	Tandem rotor methods	
1971	Transonic analysis by Murman/Krupp (BSRL)		Design of the VR-7 and VR-8 for the HLH rotor
1972		Advanced B-92 hover code	Defined VR-9 for UTTAS blade tip
1974		Initial formulation of B-65 (Betz rollup) and B-66 (quarter-chord sweep) forward flight codes.	
1975	Potential flow/ boundary layer interaction[13] and viscous transonic[14] codes transferred to Vertol from Boeing Seattle	Started development of lifting surface hover code (B-20)	VR-7 and VR-8 used on CH-47D blades
1978			VR-12/VR-15 defined for 180 KT mission
1979		Inverse LeNard[12] solution	
1980	Tauber/Arieli[17] code (Acquired from NASA)		
1981	(2-D) Separated flow analysis available at Vertol (Henderson)[20]	B-65 operational. Acquisition of HOVERS and ROTAIR codes from AMI	
1982	Planned attempt to use Caradonna/Chattot Code[18,19]	B-66 operational. Integration of airfoil and swept tip design	Definition of high speed rotor requirements

REPRESENTATION OF AIRFOIL BEHAVIOUR

by

T.S. Beddoes
Senior Research Specialist
Westland Helicopters
Yeovil, Somerset BA20 2YB
UK

SUMMARY

A time delay model for dynamic stall was generated several years ago. It is discussed with regard to current applications in rotor analysis programs and the shortcomings of the model are highlighted to illustrate the objectives for an improved approach. Subsequent effort involving airfoil tests and analysis has provided a basis for closer identification and modelling of the phenomena involved up to the limit of the high subsonic Mach numbers achieved by the rotor in forward flight. Even at low Mach numbers supercritical flow is established at high lift and shock-boundary layer interaction governs separation. The possible shock configurations have been examined and a criterion derived empirically to correlate the critical shock upstream pressure prior to reversal of shock motion. The criterion has been extended to the dynamic regime by modelling the time dependent relationship between the peak pressures and the lift coefficient and, for application, the procedure is further simplified by utilising a modified value of the lift coefficient.

In addition to leading edge or shock induced separation significant non-linearities in airfoil behaviour can be identified with trailing edge separation. To represent this phenomenon a simplified form of the solution for Kirchhoff flow is applied and provides a means for reconstructing static test data in a simple and straightforward manner. The significance of this approach lies in the identification of the flow separation point which enables dynamic effects on trailing edge separation to be implemented. By making use of some detailed calculations on turbulent boundary layer flow reversal it is shown how dynamic terms may be included in the model without undue complication. In many cases the dynamic delay in trailing edge separation results in a premature encounter of critical leading edge or shock pressures and when this happens the consequences are simulated by accelerating the progression of the separation point. In conjunction with the latter phenomenon vortex shedding occurs and immediately has a large effect on the pitching moment but the eventual loss of lift is delayed. It is shown how the modelling of the above features may be incorporated in an overall structure suitable for inclusion in a rotor analysis.

INTRODUCTION

Theoretical methods for predicting the force and moment characteristics of airfoils are continually being improved. Most approaches use a boundary layer solution to define the boundary condition for an outer potential flow. These solutions are capable of producing good results up to the point where flow separation becomes significant but are unable to define adequately the maximum lift and associated pitching moment beyond this point which for most practical cases involve a region of supercritical flow. For rotor loads and performance prediction it is essential to incorporate representation of airfoil behaviour in the regime involving both partial and complete flow separation. This regime is greatly influenced by unsteady conditions which are present on the rotor blade. Consequently, many experimental studies have been performed to define the dynamic behaviour of a range of airfoils through a large angle of attack range and means sought to generalise the results in a form which may be implemented within an analysis of rotor loads.

The evaluation of lift, drag and pitching moment at a particular location on the blade constitutes the innermost loop in any rotor calculation which includes radial, azimuth and control loops. A not untypical rotor load calculation involving a trim convergence may require 30,000 passes through the subroutine for generating airfoil data. Thus there is a premium on brevity though not at the expense of realism because, in conjunction with improved structural and wake modelling, it is becoming posssible to predict with greater confidence the non linear rotor behaviour near the flight boundaries. The latter attribute is important in the early design stage to ensure the minimum rotor size for the specified requirements.

The purpose of this paper is to present a formulation for a second generation model for unsteady airfoil behaviour. This involves the identification and representation of, trailing edge and leading edge or shock induced separation together with vortex shedding, where appropriate, all within the constraints imposed by computational requirements. Bearing in mind that a modern blade design is likely to incoporate several airfoil sections optimised for different radial locations, it is desirable that the model should be structured around the physics of the various flow regimes encompassed. Otherwise, in interpolating between the defined sections, and Mach number it is likely that inconsistencies will arise. The overall model is structured around the solution for time dependant fully attached flow. For a sampled solution which follows from the azimuth stepping procedure of the rotor calculation, the most appropriate form is the indicial response function for which standard solutions are available. The use of indicial response functions is covered in available literature, e.g. reference 1 and is discussed here only briefly.

In the current context there is obviously no possibility of performing an iterative potential solution and boundary layer calculation, even in a constrained form. An open loop calculation must be performed which incorporates the influence of separation on the potential solution and for this purpose the formulation for Kirchhoff flow is used in an approximate form. Force and moment behaviour are thus related to the location of the separation point which is treated as a degree of freedom in the solution.
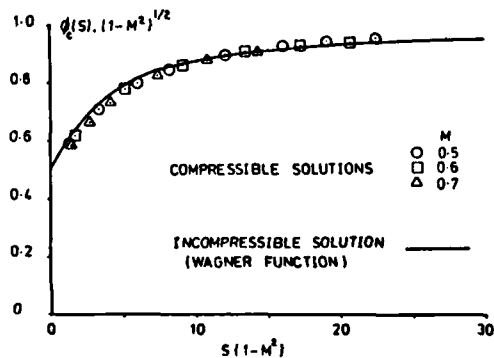
FIG.1. GENERALISATION OF THE INDICIAL LIFT FUNCTION

RESPONSE TO SINGLE STEP :

$$C_L = 2\pi . \Delta\alpha . \phi_c(s') = C_{L_\alpha}\alpha_\varepsilon(s')$$

where $\phi_c(s') = (1 - A_1 e^{-b_1 s'} - A_2 e^{-b_2 s'})(1-M^2)^{-1/2}$

$s' = s(1 - M^2)$

$A_1 = 0.165$, $A_2 = 0.335$, $b_1 = 0.0455$, $b_2 = 0.3$

FOR A CONTINUOUS SAMPLED SYSTEM :

$$C_L = C_{L_\alpha}\alpha_\varepsilon(t)$$

$$\alpha_\varepsilon(t) = \alpha_{(n=0)} - X_n - Y_n + \sum_1^n \Delta\alpha_n$$

where

$$X_n = X_{(n-1)} e^{-b_1 \Delta s'} + A_1 . \Delta\alpha_n$$

$$Y_n = Y_{(n-1)} e^{-b_2 \Delta s'} + A_2 \Delta\alpha_n$$

$$\Delta s' = \Delta t . \frac{2V}{c}(1 - M^2)$$

FIG.2. APPLICATION OF THE INDICIAL LIFT FUNCTION

AN EXISTING MODEL

A time delay model for generating unsteady airfoil characteristics is in routine use at Westland Helicopters and at RAE. It is described here briefly for two reasons. Firstly, for comparitive purposes, to illustrate the structure of what may be termed a 'first generation' model, and secondly, to provide a background for some of the comparisons of rotor loads calculations with experiment, which are presented elsewhere in this meeting. For the attached flow regime the unsteady loads are calculated via a generalised indicial lift function, based on the Wagner function which was derived for incompressible flow. By appropriately scaling the ordinates of this function (figure 1) the compressible solution for the indicial response (as presented in reference 2) may be shown to correspond closely except for the first semi-chordlength of travel. The response to a continuously varying angle of attack is constructed by treating the time history as an accumulating series of step functions for which the solution is obtained by super-position. At any instant in time, the difference between the instantaneous value of lift and what would be the steady state value may be viewed as a lift deficiency. As the indicial lift function is expressed using exponential terms, then in the absence of further forcing, the lift deficiency will decay in an exponential manner whose rate is independent of the magnitude of the lift deficiency. This property facilitates a simple form of numerical solution which is presented in figure 2.

To accomodate pitching motion the angle of attack is defined at the 3/4 chord location thus, depending on the pitch axis location, a component of pitching velocity is included and appropriate virtual mass terms are added.

To extend the model to the separated flow regime recourse is made to static wind-tunnel test data. For each Mach number the angle of attack (α_1) which delimits attached flow is determined by the break in pitching moment and a further angle (α_2) is used to represent the condition where flow separation and hence centre of pressure has stabilised.
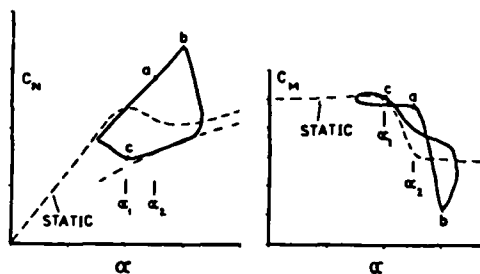
STATIC DATA IDEALISED:

C_M BREAK AT α_1, SEPARATION STABILISED AT α_2

DYNAMIC STALL PROGRESSION:

EXCEED α_1 WITHOUT SEPARATION, START TIME DELAY.

(a) TIME DELAY (τ_1) EXCEEDED. VORTEX SHED FROM L.E.

LIFT MAINTAINED, MOMENT DIVERGES ~ C.P. = $f(\alpha, t)$

(b) TIME DELAY (τ_2) EXCEEDED. VORTEX PASSES T.E.

LIFT DECAYS ~ REFLECTED IN MOMENT VARIATION.

(c) FLOW REATTACHES FOR $\alpha < \alpha_1$.

FIG. 3. TIME DELAY MODEL
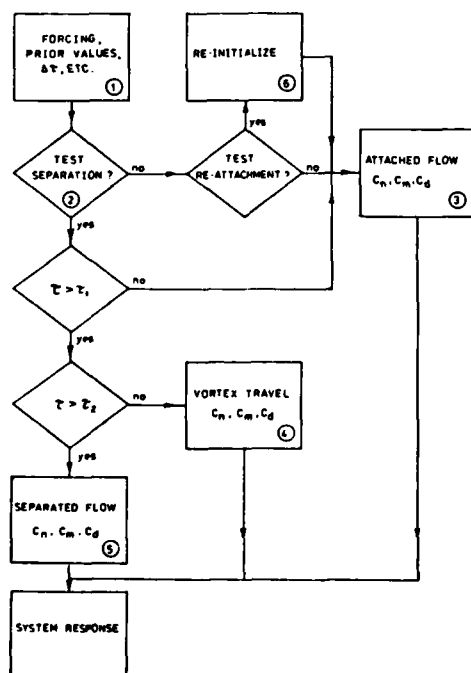
FIG. 4. CALCULATION PROCEDURE

In application, when the local value of angle of attack exceeds α_1 the onset of separation is assumed to be delayed for a finite period of time (τ_1) during which the lift and moment behave as appropriate for attached flow. When this time delay is exceeded flow separation is assumed to be initiated by the shedding of a vortex from the surface of the airfoil and after a further period of time (τ_2), during which the vortex traverses the chord, it passes free of the surface. In this interval lift is generated by the vortex and the overall level maintained equivalent to that for fully attached flow but the centre of pressure moves aft as a function of both angle of attack and time. When the vortex passes free of the surface the lift decays rapidly to a value appropriate to fully separated flow assuming that the angle of attack is still sufficiently high. If and when the angle of attack reduces below the value α_1 re-attachment of the flow is represented by the attached flow model, re-initialised to account for the current lift deficiency. This sequence of events and the corresponding behaviour of lift and pitching moment is illustrated by figure 3 and the logic of the calculation procedure is shown in figure 4.

To accomodate the non-linearities in pitching moment and drag exhibited by test data for the region $\alpha < \alpha_1$, these characteristics are represented by a simple curve fit procedure and re-generated to simulate values appropriate for attached flow. Not only does the centre of pressure calculation provide the large pitching moment excursion for separated flow but also provides a measure of separation which is used to modify the calculation of drag which in the extreme case tends to the value $C_N \sin \alpha$.

The model is described in more detail in reference 3 which includes several comparisons with test data. Extensive correlation studies have been performed using test data for many different airfoils and various modes of dynamic forcing. From these studies some general conclusions can be drawn by categorising the airfoils into two groups based on their behaviour during static stall. Firstly, airfoils exhibiting a gradual stall resulting from progressive trailing edge separation (trailing edge stall) and secondly, those airfoils exhibiting a fairly abrupt stall resulting either from leading edge (or short bubble) stall or rapid progression of trailing edge stall triggered by leading edge reseparation (leading edge stall). In general, the correlation is good for leading edge stall airfoils but not always good for trailing edge stall airfoils. This problem (see figure 5) arises from the changing nature of the stall under dynamic conditions insofar as the tendency for trailing edge stall is suppressed by significant rates of change and the stall becomes dominated by leading edge or shock induced separation. There are two ways to compensate for this behaviour. By observing the dynamic stall characteristics for low frequency the chosen value of α_1 may be modified so that the model will produce satisfactory results. A better approach (discussed in reference 4) makes use of a leading edge pressure criterion to initiate the dynamic stall process. The latter is limited to low Mach numbers where, however, the problem is most often encountered.
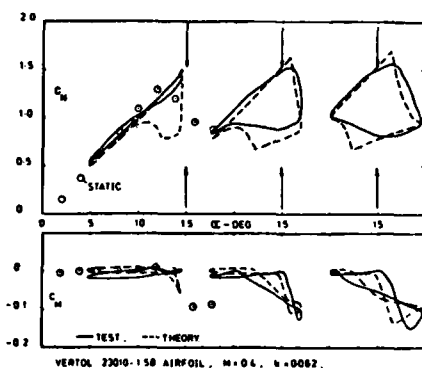
FIG.5. LIMITATIONS OF INITIAL TIME DELAY MODEL

Alternatively, the leading edge pressure criteria may be used to redefine α_1.

Even with its limitations this model of dynamic stall, in conjunction with flexible blade representation, has produced valuable results in reproducing rotor behaviour in the region of the flight boundary, both in hover and forward flight. The level of confidence thus generated has enabled the analysis to be applied to optimise both the aerodynamic and structural design of new rotors. The introduction of moulded composite construction facilitates the use of varying airfoil section geometry along the blade and has prompted effort to design new sections optimised for specific lift and Mach number ranges. To support these designs dynamic testing has become routine and is extended to high subsonic Mach number. Consequently, considerable variation in behaviour has been encountered and provides incentive to improve the modelling of dynamic stall.

SEPARATION IN SUPERCRITICAL FLOW

At low Mach number a combination of local velocity and velocity gradient provides a criterion to identify the onset of leading edge separation. This is equivalent to a critical pressure and pressure gradient and has prompted examination of test results at higher Mach number to correlate features of the pressure distribution with the lift and pitching moment breaks which denote significant separation. Qualitatively, the sequence of events accompanying increasing angle of attack may be summarised thus:-

The region of supercritical flow on the upper surface is terminated by a shock wave which strengthens and moves aft as incidence is increased. At some point the conditions at the shock are sufficient to promote local separation which re-attaches forming a bubble. Eventually, the separation increases in severity and extent and the shock moves forward. Under static conditions the latter event coincides with trailing edge separation and pressure divergence. Initially, the force and moment vary in a regular manner with only minor deviation as the bubble develops behind the shock. The major change occurs when the shock motion reverses, at which point breaks in lift and/or moment occur; figure 6 serves to illustrate this behaviour.

In some cases the combined effect on the boundary layer of the local behaviour of the shock and the pressure recovery over the remaining portion of the chord are sufficient to induce premature separation at the trailing edge and gradual divergence of trailing edge pressure but it appears that the single most important factor is the pressure rise at the shock itself. Thus it is useful to examine and correlate shock reversal (or gross separation) with the shock pressure rise. The equations governing shock pressure rise are:

$$\frac{P_2}{P_1} = \frac{7 M_1^2 \sin^2\theta - 1}{6}$$

$$\frac{\Delta P}{P_\infty} = \frac{P_2 - P_1}{P_\infty} = \frac{P_1}{H_0}\left(\frac{P_2}{P_1} - 1\right)\frac{H_0}{P_\infty}$$

$$= \left(\frac{1 + 0.2\, M_\infty^2}{1 + 0.2\, M_1^2}\right)^{3.5} \cdot \frac{7(M_1^2 \sin^2\theta - 1)}{6}$$

NOW

$$7 M_1^2 \sin^2\theta_{s_{max}} = 3M_1^2 - 5 + [3(3M_1^4 + 4M_1^2 + 20)]^{\frac{1}{2}}$$

AND

$$7 M_1^2 \sin^2\theta_{s_{cr}} = 3M_1^2 - 2 + [3(3M_1^4 - 4M_1^2 + 13)]^{\frac{1}{2}}$$
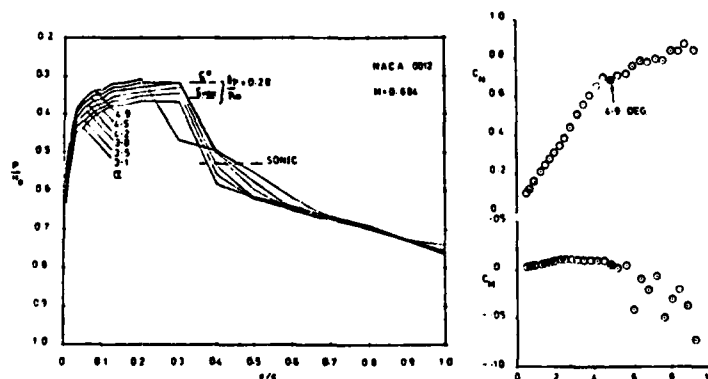
FIG.6. SEPARATION AT HIGH MACH NUMBER
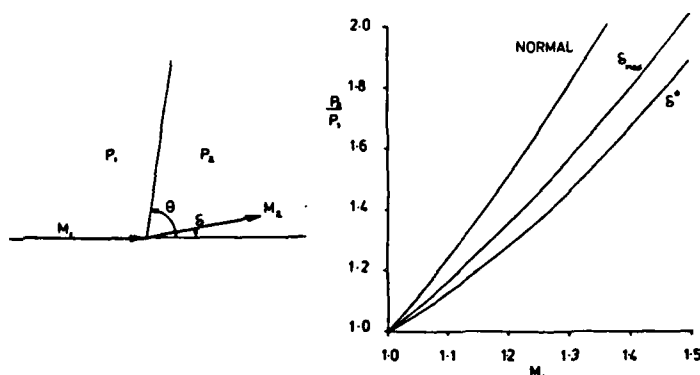
FIG.7. SHOCK CONFIGURATION AND PRESSURE RISE

FIG.8. HYPOTHETICAL LIMITS FOR SHOCK PRESSURE RISE

where the shock configuration, parameters and results are shown in figure 7.

Thus the shock pressure rise depends on the shock angle θ and, flow deflection angle δ. For $\delta = o$, $\theta = 90°$ (normal shock) and this is the configuration which is appropriate when the shock pressure rise does not significantly disturb the boundary layer. With boundary layer thickening or local separation there is progressive deflection of the flow and the shock wave becomes oblique. Reference 5 discusses the relationships involved and application to the calculation of viscous transonic flows. In the present context two physically significant combinations of θ and δ are of particular interest. For a given upstream Mach number, as the flow deflection angle increases the shock becomes oblique and weakens up to a point at which the flow deflection angle reaches a maximum ($\delta = \delta_{MAX}$). Further weakening of the shock occurs as it becomes more oblique but the flow deflection angle decreases and eventually the point is reached where the downstream flow becomes sonic; the deflection angle is then denoted by δ. The difference between δ and δ_{MAX} is small but for a subsonic freestream, supersonic flow behind the (single) shock is incompatible with attached flow. From measured pressure distributions on the NACA 0012 the conditions ahead of the shock were noted which corresponded to the onset of the bubble behind the shock and to the forward movement of the shock. When these are plotted against freestream Mach number (figure 8a) they are seen to follow the same trend given by the locus of constant shock pressure rise for the conditions corresponding to δ_{MAX} and δ. A critical shock pressure rise $\Delta P/P_\infty$ of slightly less than 0.3 is indicated; the upstream pressures corresponding to $\Delta P/P_\infty = 0.28$ have been superimposed on figure 6 and match the onset of bubble formation (δ_{MAX}) at $\alpha = 3.5$ and shock reversal (δ) at $\alpha = 4.5$.

Similar results have been obtained from tests of other helicopter airfoils but, in order to extend the scope of the correlation, data from tests on the NLR 7301 airfoil have been included (figure 8b). The geometry of this airfoil differs significantly with respect to thickness and camber and the test Reynolds numbers are roughly a third of the NACA 0012 values, the data shown correspond to free transition with the exception of the solid symbols. For a Mach number of 0.6 and above the correlation is good but deteriorates for M = 0.5 where the shock is around 6% chord and possibly interacting with a laminar or transitional boundary layer. Greater variability is also noted for the other airfoils where similar conditions exist and in tests involving low Reynolds number and artificially induced transition when the shock is ahead of or in the vicinity of the transition strip. Even for naturally turbulent boundary layers at moderate or high Reynolds numbers some variation in the critical shock pressure rise and shock configuration must be anticipated but the differences observed thus far appear to be of second order (approximately $\pm.02$ on $\Delta P/P_\infty$). Subsequent to the onset of shock reversal the local Mach number ahead of the shock continues to increase temporarily but no attempt has been made to correlate this phenomenon.
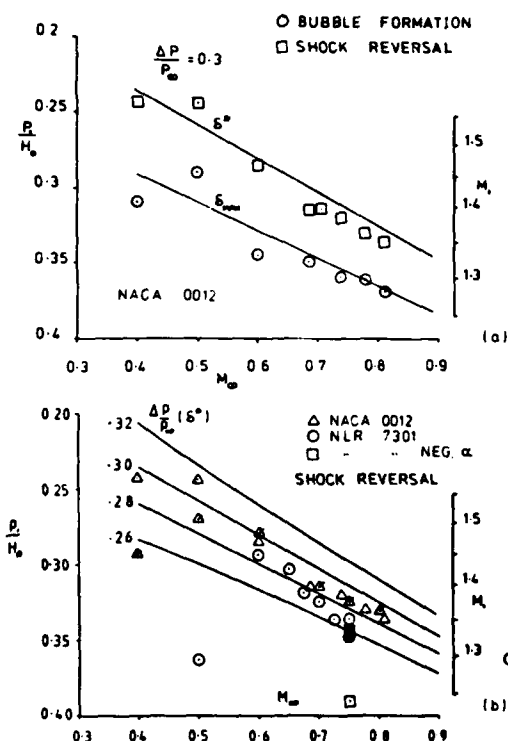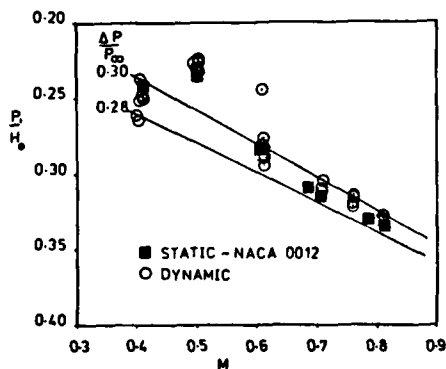
FIG. 9. COMPARISON OF STATIC AND DYNAMIC SHOCK REVERSAL

PEAK UPPER SURFACE PRESSURE , VARYING x/c
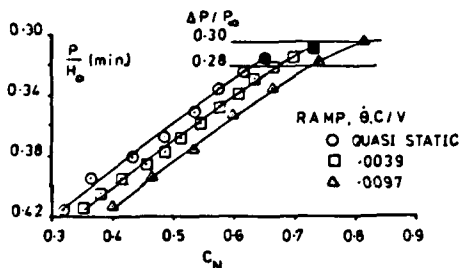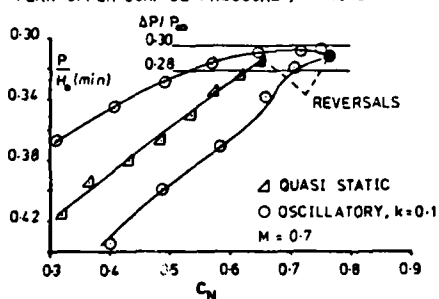
FIG.10. SHOCK REVERSAL — DYNAMIC BEHAVIOUR

Correlation of critical shock pressure rise has been extended to the dynamic regime. For a given time history of forcing via angle of attack there is a phase shift in the lift response and a further phase shift in the pressure response. Nevertheless, the critical pressure ahead of the shock for shock reversal is roughly the same (see figure 9) and, as for the static data, the initiation of the pitching moment break is closely related to this event; i.e. there is no significant further delay in the pitching moment response. The dynamic response of the peak upper surface pressure (at varying x/c) to varying C_N is shown in figure 10 for harmonic oscillation and ramp motion and is compared with the quasi static relation. For increasing C_N there is a significant lag in the peak pressure response which results in the critical pressure being achieved at a C_N higher than the static value. Combined with the lag of the C_N response with respect to α this results in an overall significant delay in pitching moment break. It is apparent, then, that a single criterion is adequate for both static and dynamic behaviour for the purpose of identifying the pitching moment divergence. Application of this criterion requires a means of relating the dynamic pressure response to the forcing. In the context of rotor load calculation this relationship has to be simple in order to be practical.

UNSTEADY PRESSURE RESPONSE

For the purpose of invoking the critical pressure criterion only the peak pressures just ahead of the shock are of concern and a first order relationship between pressure and C_N is required.

From frequency response tests at low Mach number it can be established that the phase lag of leading edge pressure with respect to C_N (ϕ_{PN}) is linear with reduced frequency in the range of interest. This implies that the relationship can be represented by a first order lag which, at M = 0.3, yields a time constant (T_p) equivalent to 1.7 semi chord-lengths of travel.

Thus it is possible to relate P(t) and C_N(t) to the static relation. Furthermore, it is possible to obviate the need for calculating pressures by transfering the calculation to the C_N domain. This may be accomplished by applying the compensation to C_N(t) thus producing an ersatz value C_N'(t) such that whatever properties may be attributed to p(t) are equally appropriate to C_N'(t). Under static conditions $C_N'=C_N$(static). From observation of the test data a critical value of $C_N' = C_N$(static) may be obtained which corresponds to the critical pressure at the appropriate Mach number.

The value of C_N'(t) may be obtained at the same time as C_N(t) by implementing the transfer function

$$\frac{C_N'(p)}{C_N(p)} = \frac{1}{1+T_p.P}$$
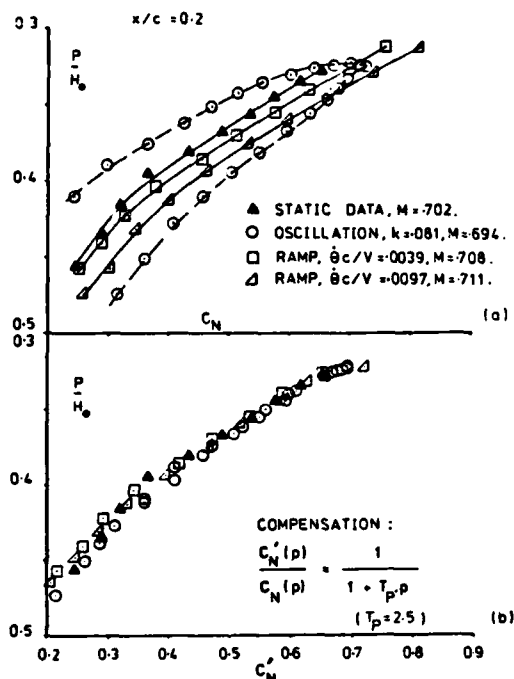
FIG 11. COMPENSATION OF TIME DEPENDENT PRESSURES.

COMPENSATION :

$$\frac{C_N'(p)}{C_N(p)} = \frac{1}{1 + T_p \cdot p}$$

$(T_p = 2.5)$

STATIC DATA, M = .702.
OSCILLATION, k = .081, M = .694.
RAMP, $\dot{\theta}c/V$ = .0039, M = .708.
RAMP, $\dot{\theta}c/V$ = .0097, M = .711.

x/c = 0.2

KIRCHHOFF FLOW

$\frac{x_{sep}}{c} = f$

streamline

$K = \frac{C_L (separated)}{C_L (attached)} = 0.25(1 + f^{1/2})^2$

O TEST
(NACA REP 446)
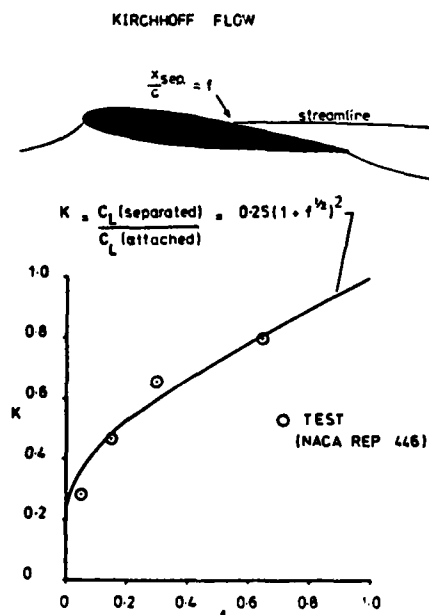
FIG 12. TRAILING EDGE SEPARATION

At higher Mach number the relationship between pressure and C_N becomes non-linear but the same form of compensation remains appropriate. To illustrate this, the examples of figure 10 (for M = 0.7) which comprise static, oscillatory and ramp data have been replotted as a composite in figure 11(a) in terms of the pressure at x/c = 0.2 versus C_N. When the C_N time history for each case is compensated using the above transfer function the pressures may be replotted versus C_N' (fig 11b). Using a value of T_p equivalent to 2.5 semi-chords of travel the dynamic pressures correlate with the static pressures to within experimental accuracy and repeatability. It is apparent that the value of T_p increases with increasing Mach number but further analysis of test results is required before any specific relationship can be justified. An advantage of monitoring the parameter C_N' is avoidance of the necessity to vary the x/c location for critical pressure with angle of attack and Mach number. The ability to generalise dynamic effects on the critical aspects of the pressure distribution provides a useful means for implementing the criteria for leading edge and shock induced separation.

TRAILING EDGE SEPARATION

Trailing edge separation is involved to some degree in almost all examples of airfoil stall. Even when the primary source of separation is at the leading edge or at the shock wave the associated boundary layer disturbance is generally sufficient to promote some separation at the trailing edge. The associated loss of circulation introduces non-linearities in the lift and pitching moment and may delay the onset of critical conditions elsewhere to a higher angle of attack. Among the theories for two dimensional flows which encompass separated regions, that due to Kirchhoff is reviewed in reference 6. The particular case of a flat plate at incidence is included and it is shown that the solution for C_L may be approximated quite simply in terms of the separation point x/c = f.

$$C_L = 2 \pi \alpha (\tfrac{1}{2} + \tfrac{1}{2} f^{\frac{1}{2}})^2$$

This may be interpreted as implying that the ratio of the actual lift to the potential value for unseparated flow is equal to $\tfrac{1}{4}(1 + f^{1/2})^2$ and provides a simple means for evaluating lift if the flow separation point can be determined. In reference 8 some results of test on an NACA 0012 airfoil are presented for which the airfoil was modified by the addition of protuberances to promote separated flow. For a limited range of angle of attack separation was stabilised at each protuberance location and provides data which compare favourably with the Kirchhoff flow approximation (figure 12).

In the dynamic case, in addition to temporal effects on the pressure distribution, the boundary layer development is time dependent. No experiments are available which enable these two aspects to be studied independently and systematically but the problem has been approached theoretically in reference 7.
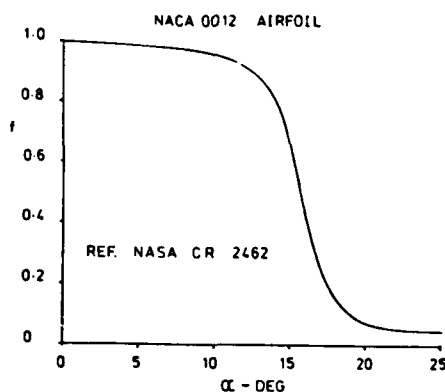
FIG.13. CALCULATED FORWARD MOVEMENT OF TURBULENT FLOW REVERSAL POINT.
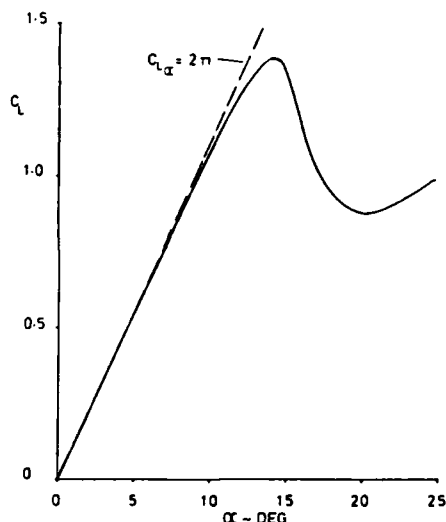
FIG.14 APPLICATION OF KIRCHOFF LAW TO CALCULATED SEPARATION (REVERSAL) POINT.
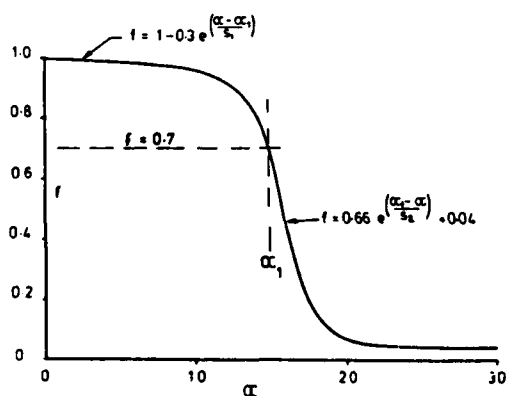
FIG.15. GENERALISATION OF FLOW SEPARATION

Recognising the limitations inherent in the attempt to model developing flow separation via a coupled potential flow and turbulent boundary layer analysis, the study of reference 7 utilises the onset of boundary layer flow reversal as a measure of unsteady effects. A finite difference scheme is used to integrate the unsteady boundary layer equations, which are coupled at each instant of time to a fully unsteady and nonlinear potential flow analysis. The calculations are extended to high angle of attack but do not include representation of flow separation in the potential flow analysis and hence the C_L values are unrealistic where separation would be implied. However the approach makes it possible to study the unsteady effects on pressure and boundary layer development either independently or in conjunction and to interpret the results in terms of the forward progression of the turbulent boundary layer flow reversal point.

The calculated forward movement of the flow reversal point for the static condition is shown in figure 13 and in this circumstance there should be a close relationship with the flow separation point. If this is assumed and the Kirchhoff flow expression is applied, the resulting variation of lift with angle of attack can be derived (figure 14). The result is sufficiently encouraging to suggest application of the procedure as a general means for reproducing the non-linear behaviour caused by trailing edge separation. To accomplish this the form of the relationship between f and α is generalised as shown in figure 15 so that it is comprised of two curves which exponentiate to the fully attached and fully separated conditions from a breakpoint at f = 0.7 for which the corresponding α is denoted by α_1. The curve is thus defined by three parameters, α_1, and the two exponential factors S_1 and S_2. Variation of f with α may be deduced from static test data using the Kirchhoff law and the zero lift value of the lift curve slope. Values of α_1, S_1 and S_2 may be curve fitted to these results and the lift curve reconstructed for any value of α. The results obtained from a set of tests on the NACA 0012 are shown in figure 16. Thus the variation of lift may be obtained using a potential calculation which neglects separation (represented by the zero lift value of the lift curve slope) and an independent representation of the flow separation point.

Pitching moment and drag may also be related to the deduced flow separation point in the following manner. The centre of pressure at any angle of attack may be obtained from the relation C_M/C_N (allowing for the value of C_{M_0} when appropriate). The variation is plotted versus the corresponding deduced value of f and curve fitted to the form

$$\frac{C_M}{C_N} = k_0 + k_1 f + k_2 f^4$$

Reconstruction of test data for NACA 0012 is shown in figure 17.

Reference 6 also presents an approximation for pressure drag in Kirchhoff flow but comparison with test data is not favourable, so an alternative empirical relation has been generated thus:

$$C_D = C_{D_0} + 0.035 C_N \sin\alpha + K_D C_N \sin(\alpha - \alpha_{DD})$$

IMPLIED SEPARATION POINT

$$\frac{C_m}{C_n} = k_0 + k_1 f + k_2 f^4$$
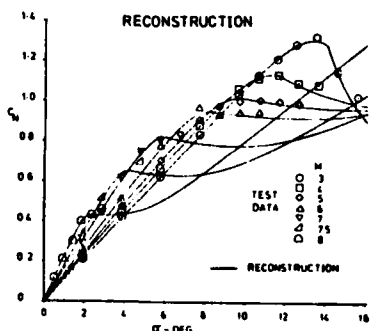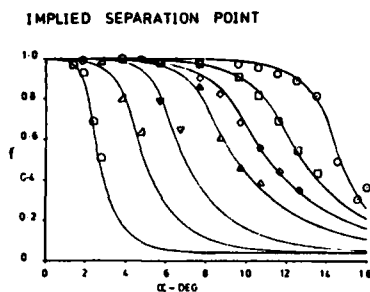
RECONSTRUCTION

FIG.16. RECONSTRUCTION OF LIFT
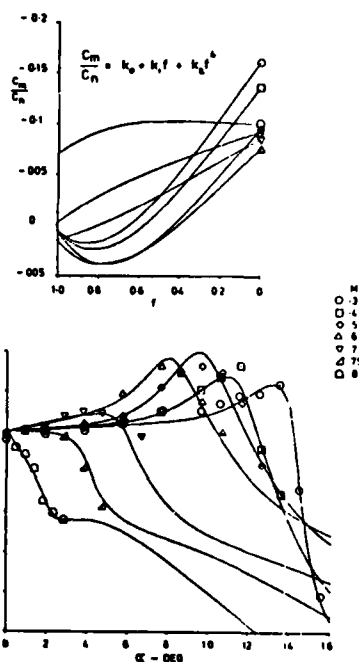
FIG.17. RECONSTRUCTRUCTION OF PITCHING MOMENT
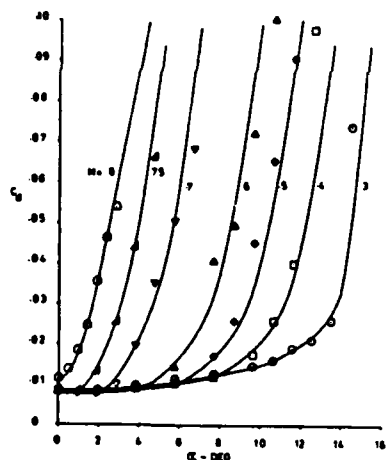
FIG.18. RECONSTRUCTION OF DRAG DATA

TABLE 1.

PARAMETER VALUES FOR RECONSTRUCTION OF NACA 0012 TEST DATA.

M	0·3	0·4	0·5	0·6	0·7	0·75	0·8
$C_{l\alpha}$	·108	·115	·1225	·1345	·158	·1785	·2225
α_1	14·0	11·6	9·8	8·3	6·1	4·3	2·3
s_1	1·4	1·7	1·6	1·2	0·8	0·6	0·4
s_2	1·4	3·2	3·6	3·3	2·3	1·7	1·0
k_0	-·16	-·135	-·095	-·075	-·085	-·092	-·10
k_1	·28	·26	·235	·195	·115	·070	-·01
k_2	-·115	-·12	-·135	-·105	-·015	·02	-·04
C_{d_0}	·0065	·0080	·0077	·0078	·0078	·0078	·0114
α_{DD}	10·3	7·9	6·1	4·5	2·2	0·9	0
d_f	4·0	3·3	2·8	2·5	1·5	1·0	0·5

where α_{DD} represents a drag divergence angle obtained from test for each Mach number. For $\alpha < \alpha_{DD}$, $K_D = 0$; otherwise $K_D = 2.7$ e^{d_f} where d_f is a function of Mach number. Drag variation reconstructed on the above basis is compared with test in figure 18 and table 1 presents the coefficient used in the reconstruction of lift, drag and moment.

The above formulation for static force and moment data provides a compact structure for the reproduction of non-linear behaviour but, more importantly, by utilising a representation of trailing edge separation it provides a means for extending the modelling to the dynamic regime. For this purpose, the results of the analysis of reference 7 provide a basis for evaluating dynamic effects on trailing edge separation, using the location of boundary layer flow reversal as an indicator.

A series of systematic calculations are presented in reference 7 for increasing values of ramp rate ($\theta c/v$) and repeated using the following combination of constraints.
(1) Steady potential flow – unsteady boundary layer
(2) Unsteady potential flow – steady boundary layer
(3) Unsteady potential flow – unsteady boundary layer

For the purpose of this discussion the behaviour of the flow reversal point will be assumed to represent the separation point.

When steady potential flow is assumed, the variation of pressures with time follow the variation with α as generated by the static solution, thus the boundary layer possesses the only timewise degree of freedom. From the results it is observed that the forward

(a) STEADY POT. FLOW
UNSTEADY B.L.

$T_P = 0, \ T_F = 3$

$\dot{\theta}c/V$
0
.005
.02
.04

(a)

--- NASA CR 2462
— MODEL

(b) UNSTEADY POT. FLOW
STEADY B.L.

$T_P = 1.7, \ T_F = 0$

(b)

(c) UNSTEADY POT. FLOW
UNSTEADY B.L.

$T_P = 1.7, \ T_F = 3$

$\dot{\theta}c/V$
0
.005
.02
.04

(c)

FIG 19 TRAILING EDGE SEPARATION - DYNAMIC MODEL

progression of the flow reversal point lags significantly behind the static variation with α.

The simplest representation of this behaviour is given by a first order lag for which the operational equation is

$$\frac{f'(p)}{f(p)} = \frac{1}{1 + T_F p}$$

where $f(p)$ represents the response to the pressure distribution and $f'(p)$ incorporates the additional boundary layer response. A value for T_F of 3 (semi chords) models the results of reference 7 quite well for the initial progress of the reversal point up to $f' = 0.7$. Beyond this point the reversal speeds up and can be matched by halving the time constant (figure 19(a)).

To model the result for unsteady potential flow and steady boundary layer, the boundary layer lag may be removed by setting $T_F = 0$. The boundary layer response is then determined by the pressure time history which, as already noted, can be related to the dynamic C_N by another first order lag. At low Mach number the peak pressure time constant $T_P = 1.7$ was obtained from the prior frequency response analysis. Thus an equivalent angle of attack (α_f), which represents the quasi static α for the same peak pressure, can be used to generate the reversal point f; i.e.

$$\alpha_f = \frac{C_N'}{C_{N_\alpha}} \quad \text{where} \quad \frac{C_N'(p)}{C_N(p)} = \frac{1}{1 + T_p p}$$

Using the specified forcing of α the dynamic values of C_N (potential), C_N' and α_f may be evaluated using indicial methods and the variation of f evaluated. The result which is shown in figure 19(b), is in good agreement with reference 7 and, indirectly, substantiates the value of T_P obtained independently and the assumption that the peak pressures dominate the boundary layer development.

From the above comparison substantiation has been obtained for the modelling of the two components which contribute to the overall delay in boundary layer reversal. When these are combined the result may again be compared with the calculation of reference 7. To obtain the comparison shown in figure 19(c) it was found necessary to halve again the time constant T_F for values of $f'(t)<0.7$.

The analysis of reference 7 and the correlation shown assume a progression of the flow reversal (and implicitly, separation) from the trailing edge forward. From test results it is observed, for moderate Reynolds numbers and for both low and high subsonic Mach number, that separation may suddenly originate near the leading edge or at the shock location. The critical pressures associated with this behaviour have been discussed already and to implement the phenomenon it is sufficient to overide the above calculation procedure to accelerate the progression of flow separation.

The objective in modelling the location of flow separation is to provide a means for extending the evaluation of forces and moments into the dynamic regime via application of the Kirchhoff flow approximation. To complete the model requires the addition of another important physical feature, namely vortex shedding. As the separation point progresses, vorticity is shed locally and is convected aft over the surface. Consequently the initial loss of lift is zero but grows rapidly. For a sampled system the vortex lift may be modelled as follows. The increment in vortex lift is evaluated from the shift of the separation point in the current interval according to the Kirchhoff approximation. At the same time the total vortex lift is allowed to decay exponentially with time using a time constant equivalent to about six semi chords of travel. Consequently, when rate of change of angle is low, vortex lift is being dissipated as fast as it accumulates. The abrupt changes which occur when the critical

FIG. 20. RESPONSE TO RAMP FORCING

conditions for leading edge or shock induced separation are reached are assumed to terminate the vortex lift buildup as soon as the associated vortex reaches the trailing edge region; i.e. after a suitable time delay. Associated with the latter event an increment in pitching moment is obtained by allowing the centre of pressure of the vortex lift to move aft during the interval.

The significance of leading edge separation and vortex lift are illustrated in figure 20 which presents an experimental time history of lift and moment in response to, ramp forcing which builds up to a rate of $\theta c/v = 0.026$ at about 15°. The collapse of leading edge pressure is indicated by a solid symbol and the static test data are included for comparison. Application of the theoretical model described is shown with and without the influence of leading edge separation and the associated vortex (figure 20). Using the model of trailing edge separation only it can be seen that the break in pitching moment is delayed too much, that the characteristic overshoot is missing and that maximum lift is underpredicted. The addition of leading edge separation and vortex lift rectifies these errors but as rate is reduced the characteristics revert smoothly to the non linear behaviour of the static data.

CONCLUSION

A model for dynamic stall has been constructed which allows closer identification of the interacting phenomena involved. Individual features are modelled in a manner that can be readily integrated within the overall calculation procedure and compatible with the sampled system and indicial method of implementation. The features comprise:
(1) A criterion for shock induced separation
(2) Dynamic effects on the critical features of the pressure distribution
(3) A model for trailing edge separation including dynamic effects
(4) A means of relating force and moment characteristics to the location and progression of the separation point
(5) Superposition of leading edge or shock induced separation when appropriate.
(6) Addition of vortex lift in conjunction with (5) above.

REFERENCES

(1) Various Authors; A special course in unsteady aerodynamics. AGARD Report 679, June 1980.

(2) Bisplinghoff, R.L., Ashley, H., Halfman, R.L. Aeroelasticity, Addison - Wesley 1955.

(3) Beddoes, T.S. A synthesis of unsteady aerodynamic effects including stall hysteresis, Proc. 1st European Rotorcraft Forum. September 1975.

(4) Beddoes, T.S. Onset of leading edge separation effects under dynamic conditions and low Mach number. American Helicopter Society Annual Forum 1978, Preprint 78-63.

(5) Jou, W.H., Murman, E.M. A phenomenological model for displacement thickness effects of transonic shock wave-boundary layer interactions AGARD CP291, 1980.

(6) Thwaites, B. Incompressible aerodynamics. O.U.P. 1960.

(7) Scruggs, R.M., Nash, J.F., Singleton, R.E. Analysis of dynamic stall using unsteady boundary layer theory. NASA. CR-2462, Oct. 1974.

(8) Jacobs, E., Airfoil section characteristics as affected by protuberances. NACA Report 446, 1932.

ETUDES DE PROFILS ET D'EXTREMITES
DE PALE D'HELICOPTERE

par
J.J. THIBERT et J.J. PHILIPPE
Office National d'Etudes et de Recherches Aérospatiales (ONERA)
92320 CHATILLON - FRANCE

RESUME

L'amélioration des performances des rotors d'hélicoptères suscite de nombreux travaux dans le monde entier, dans les domaines de l'aérodynamique, de l'aéroélasticité, des matériaux et de l'acoustique.

Pour ce qui est de l'aérodynamique, l'ONERA a entrepris, il y a quelques années, en collaboration avec l'Aérospatiale, un programme de recherches à long terme avec pour objectifs d'améliorer la connaissance de l'écoulement autour des pales ainsi que les méthodes de prévision des performances et de définir des pales optimisées pour les futurs hélicoptères. L'objet de cette communication est de présenter les résultats obtenus à ce jour pour deux thèmes du programme de recherche que sont la définition de nouveaux profils et l'étude des extrémités de pale.

Dans la première partie, la méthode de définition d'une nouvelle famille de profils sera exposée et les performances de cette famille seront comparées à celles d'autres familles connues ainsi qu'aux prévisions par les méthodes de calculs.

Dans la seconde partie, les études expérimentales et théoriques des écoulements sur différentes extrémités de pale seront présentées. On s'intéressera plus particulièrement à la définition de nouvelles formes en plan qui peuvent améliorer le fonctionnement des extrémités dans le secteur de la pale avançante et aussi les performances globales du rotor.

STUDIES OF AEROFOILS AND BLADE TIPS
FOR HELICOPTERS

SUMMARY

A lot of work is being done in the world in order to improve rotor performances. The main areas of research are aerodynamics, aeroelasticity, materials and acoustics.

In 1974, in France, ONERA and Aérospatiale, undertook jointly an aerodynamic long term research program to get a better knowledge of the flow around the blades and to improve the performances prediction codes. The main objective is the design of optimized blades for new helicopters. This paper presents the results obtained up to now for two points of this research program which are the design of new aerofoils and the study of blade tips.

In the first part the design methodology of a new family of aerofoils is presented and the performances of these aerofoils deduced from wind tunnel tests are compared with those of other known airfoils and with the theoretical predictions.

In the second part, theoretical and experimental studies of the flow around several blade tips are presented. Emphasis is put on the design of new blade tips in order to improve the advancing blade behaviour and so the total rotor performances.

1 - INTRODUCTION -

Le développement et l'application sur hélicoptère des matériaux composites a permis d'accroître les performances globales des machines en réduisant notablement leur coût à l'achat et en opération. Cette augmentation des performances des nouveaux rotors est due principalement à l'utilisation de nouveaux profils non symétriques à épaisseur relative variable en fonction de l'envergure, à un vrillage plus accentué et à de nouvelles formes d'extrémités des pales. Ceci a été rendu possible par la maîtrise de la technologie des pales composites mais également grâce aux travaux de recherches en aérodynamique effectués ces dix dernières années dans de nombreux pays par les organismes de recherche et les constructeurs.

L'objet de la présente communication est de présenter les principaux résultats obtenus à ce jour à l'ONERA, dans le cadre d'un programme de recherches à long terme, mené en collaboration avec l'Aérospatiale, dans les domaines des profils et des extrémités de pales.

Dans la première partie, la méthode de définition d'une nouvelle famille de profils sera exposée. Les principales caractéristiques aérodynamiques de ces profils, déduites d'essais bidimensionnels, seront présentées et comparées à celles d'autres profils ainsi qu'aux prévisions des méthodes de calculs. Les performances de rotors maquette et grandeur utilisant ces nouveaux profils seront ensuite comparées à celles de rotors classiques équipés de profils NACA.

Dans la seconde partie, les études expérimentales et théoriques des écoulements sur différentes extrémités de pale seront présentées. On s'intéressera plus particulièrement à la définition de nouvelles formes en

plan qui peuvent améliorer le fonctionnement des extrémités dans le secteur de la pale avançante et aussi les performances globales du rotor.

2 - *DEFINITION ET PERFORMANCES D'UNE NOUVELLE FAMILLE DE PROFILS POUR PALE D'HELICOPTERE -*

2.2 - *Historique des profils pour pales d'hélicoptères -*

Un examen des profils utilisés sur les pales (fig. 1) fait apparaître la même évolution, avec un certain décalage, que pour les ailes d'avions. Ainsi sur les premières machines les pales sont constituées de profils minces puis entre 1930 et 1945 les profils sont issus des séries Göttingen ou NACA (G 770, NACA 0012, NACA 23012 - 23015). Dans les années 1950, la mode des profils laminaires s'étend aux hélicoptères (NACA 63 A 012 - 63 A 015 - 9 H 12) mais les performances obtenues sont décevantes et l'on assiste dans les années 60 à un retour aux classiques profils NACA ou dérivés. Il faut également souligner que pendant toute cette période, les pales métalliques sont équipées du même profil, quelle que soit la position en envergure.

2.2 - *Intérêt de profils modernes adaptés aux hélicoptères -*

La récente évolution vers des pales à profils évolutifs s'explique aisément lorsqu'on examine sur le disque rotor les lignes iso-Mach et iso-incidence calculées et dont un exemple simplifié est présenté figure 2. Les profils, au cours d'une rotation de la pale sont alternativement soumis à de faibles incidences et des vitesses élevées puis à de fortes incidences et des vitesses modérées. Les niveaux de Mach et d'incidence rencontrés par les profils étant fonction de leur position en envergure, l'optimisation des performances du rotor conduit à définir une pale à profil évolutif en envergure. Les principaux domaines de fonctionnement des profils sont donc :

- Mach élevé et faible C_z ;

- faible Mach et C_z élevé.

Un troisième domaine est également à retenir en considérant le vol stationnaire par lequel les conditions d'attaque des profils sont quasi-stationnaires et correspondent sensiblement à :

- Mach 0,6 et C_z 0,6.

Tout gain de performances des profils dans ces trois domaines conduira à une amélioration des qualités aérodynamiques du rotor. Ainsi les résultats d'une étude paramétrique effectuée par l'Aérospatiale [1] présentés figure 3 montrent que :

- une augmentation du C_z max retarde le décrochage en pale reculante et entraîne un gain de traction à vitesse constante ou un gain de vitesse à traction constante ;

- un recul du nombre de Mach de divergence de traînée (Mdx) permet une augmentation de la vitesse de rotation et donc une diminution du C_z de fonctionnement de la pale pour tous les azimuts, ce qui retarde le décrochage en pale reculante et conduit également à un gain de traction à vitesse constante ;

- outre l'augmentation des possibilités maximales du rotor la diminution de la puissance nécessaire en vol de palier stabilisé conduit à des économies de carburant. Or un bilan de puissance montre qu' à 300 km/h par exemple, la traînée des pales absorbe plus de 40 % de la puissance totale ; toute diminution du Cx des profils soit en pale reculante en retardant le décrochage soit en pale avançante par recul du Mdx permettra donc des gains substantiels.

Compte tenu de cette analyse des conditions de fonctionnement des profils, on peut établir un cahier des charges pour les différentes sections le long de la pale. Celui présenté figure 4 a été établi par l'Aérospatiale. La pale a été divisée en trois parties :

- partie interne r/R $<$ 0,8 ;

- partie intermédiaire 0,8 $<$ r/R $<$ 0,9 ;

- partie externe r/R $>$ 0,9.

Deux séries de spécifications ont été proposées pour les sections internes et externes de la pale, l'une étant plus orientée vers la recherche de C_z max élevés, l'autre vers l'obtention de Mach de divergence de traînée élevés. Les chiffres de la figure 4 montrent que les performances visées sont bien supérieures à celles du profil de référence NACA 0012 dont les principales caractéristiques déduites des essais à la soufflerie S3 Modane de l'ONERA à un nombre de Reynolds de 7 x Mo x 10^6 sont :

- C_z max à Mo = 0,4 : 1

- Mdx à C_z = 0 : 0,79.

Il faut également souligner que les contraintes en Cmo sont extrêmement sévères même pour les sections internes de la pale afin de réduire la torsion des pales et de minimiser les efforts sur les biellettes de commande de pas.

2.3 - *Méthode de définition de la nouvelle famille de profils -*

Cinq profils ont été définis pour répondre à ces cahiers des charges. Leur appellation est OA2XX, OA2 désignant le nom de la famille et les deux derniers chiffres l'épaisseur relative qui varie de 6 à 13 %.

2.3.1 - *Profil de base de la famille -*

Le premier profil a été défini pour la section intermédiaire de la pale. Ce profil, appelé OA209, a été défini en choisissant la répartition des vitesses à faible Mach et $C_z \sim$ 0, figure 5, la forme du profil étant calculée par une méthode inverse [2]. Cette technique permet un contrôle direct des survitesses intrados et extrados et par conséquent de la traînée ainsi que du Cmo. Les essais de ce profil à la soufflerie S3 Modane de l'ONERA ayant montré des gains importants par rapport au profil NACA 0012 dans tous les domaines :

- C_z max = + 11 % à Mo = 0,3, + 21 % à Mo = 0,5 ;
- Mdx = + 0,06 à C_z = 0 ;
- C_z/C_x = + 25 % à Mo = 0,6 et C_z = 0,6 ;
- /Cmo/ < 0,005 jusqu'au Mdx.

ce profil a été retenu comme profil de base de la famille.

2.3.2 - Profils pour les sections externes de la pale -

Deux profils ont été définis pour répondre aux deux cahiers des charges de l'Aérospatiale. Ces profils ont été dérivés géométriquement du profil OA 209 (fig. 6). Pour le premier (OA 207) de 7 % d'épaisseur relative, la partie avant du profil de base a été conservée jusqu'au maître couple, de manière à obtenir de bonnes performances en C_z max à faible Mach, et une affinité sur la partie arrière a permis de définir un profil de 7 % d'épaisseur relative en vue d'obtenir un faible niveau de C_x et un Mdx élevé à C_z = 0.

Pour le second profil d'extrémité l'accent étant mis sur les performances à Mach élevé, une épaisseur de 6 % a été retenue. Ce profil OA 206 a été défini en conservant la loi d'épaisseur du profil OA 209 et en la portant par affinité à 6 % et en choisissant une loi de cambrure permettant d'assurer les performances en C_z max conjointement avec un faible Cmo.

2.3.3 - Profils pour les sections internes de la pale -

La contrainte essentielle pour les profils de cette région de la pale porte sur les C_z max. Le niveau de C_z max recherché dépendant toutefois de la classe de l'hélicoptère et de sa mission, l'Aérospatiale a établi 2 cahiers des charges, l'un orienté vers l'obtention de bonnes performances dans tous les domaines de vol, l'autre vers de forts C_z max à faible Mach. Les deux profils correspondant ont été appelés respectivement OA212 et OA213.

Le profil OA212 a été défini en utilisant la même technique que pour le profil OA206. La loi d'épaisseur du profil OA209 a été portée à 12 %, dans le but d'obtenir un bon comportement du profil à faible Cz et Mach élevé, et la loi de cambrure a été dérivée de celles des profils NACA de la série 6 avec modification dans la région de bord de fuite pour réaliser conjointement les niveaux de C_z max et de Cmo demandés (fig.7).

Le second profil OA213 devant posséder essentiellement de forts C_z max a été par contre défini par méthode inverse comme le profil OA209. La répartition des pressions a été choisie à Mo = 0,5 et C_z = 1 ; elle a été déduite de celle du OA212 avec réduction de la survitesse et modification de la loi de recompression à l'extrados à l'aval du profil.

Les dessins de ces 5 profils sont présentés figure 8. Leurs performances ont été estimées à l'aide d'un programme de calcul résolvant l'équation complète du potentiel à l'aide d'un schéma non conservatif. Les effets visqueux sont pris en compte par une technique de couplage faible, l'épaisseur de déplacement étant ajoutée au profil initial [3]. Ce programme de calcul a été validé à l'aide des résultats expérimentaux obtenus dans la soufflerie S3 Modane de l'ONERA sur de nombreux profils. Les comparaisons calcul-expérience effectuées ont montré que la plupart des performances étaient correctement prévues (Cx, Mdx, répartitions des pressions, Cm) à l'exception toutefois du C_z max qui ne peut être évalué, la technique de couplage faible excluant tout calcul précis sur une configuration présentant un décollement. L'estimation du C_z max des différents profils a donc été effectuée sur la base d'une estimation du Kp mini à l'extrados au décrochage déduite des essais en soufflerie pour des profils à faible Cmo, le Kp mini ainsi estimé étant fonction du nombre de Mach et de l'épaisseur relative.

2.4 - Performances de la famille de profils OA2XX -

2.4.1 - Essais bidimensionnels -

Les essais des cinq profils de la famille ont été effectués à la soufflerie S3 Modane de l'ONERA sur des maquettes de 210 mm de corde et pour des nombres de Reynolds égaux à 7 x Mo x 10^6. Les performances de ces profils ont été publiées en [4] [5] et [6]. La figure 9 compare leurs principales caractéristiques aérodynamiques à celles du profil NACA 0012 mesurées dans les mêmes conditions. La famille OA2XX couvre un domaine de Mach de divergence de traînée à C_z = 0 allant de 0,75 (OA213) à 0,91 (OA206) et de C_z max variant de 0,97 (OA206) à 1,46 (OA213) pour Mo = 0,3. Signalons en outre que les niveaux de Cmo sont extrêmement faibles puisque pour tous les profils l'on a - 0,01 < Cmo < 0,005 jusqu'au Mdx. La figure 10 présente quelques comparaisons entre les résultats des calculs et les résultats expérimentaux sur les profils OA207 et OA212. On notera la bonne prévision des polaires et de l'évolution du Cx avec le Mach à C_z constant. Quelques écarts apparaissent toutefois dans la prévision du Cmo à fort Mach et du niveau de survitesse à fort C_z du fait de la technique de couplage faible utilisée et de l'absence de traitement du proche sillage dans la méthode de calcul. Les nouvelles méthodes de calcul en cours de développement et utilisant des techniques de couplage fort [7] et [8] devraient permettre d'améliorer encore les prévisions.

A titre indicatif les performances de la famille OA2XX sont comparées figure 11 à celles publiées des profils VRXX développés par BOEING-VERTOL. Les évolutions des C_z max et des Mach de divergence de traînée des profils des deux familles ont été tracées en fonction de l'épaisseur relative. La comparaison est toutefois à faire avec prudence, les conditions d'essais étant différentes (soufflerie, Reynolds). De plus pour une même épaisseur relative le cahier des charges n'est pas nécessairement identique, les objectifs pouvant être orientés soit vers les C_z max, soit vers les Mdx, et les contraintes en Cmo pouvant également être plus ou moins sévères. La figure 12 qui élimine le paramètre épaisseur relative donne une idée plus précise de l'évolution obtenue par rapport au profil de référence NACA 0012 sous l'aspect C_z max et Mdx. Elle montre en outre que les performances atteintes par la famille OA2XX sont voisines des objectifs du cahier des charges.

Ces essais bidimensionnels stationnaires ont été complétés par des essais en instationnaire basses vitesses dans la soufflerie S10 du CEAT à Toulouse en vue de préciser le comportement de ces nouveaux profils dans

des conditions plus proches de celles rencontrées sur une pale d'hélicoptère [9]. Des essais complémentaires en instationnaire ont également été effectués en écoulement transsonique à la soufflerie S3 Modane de l'ONERA [10].

2.4.2 - Essais sur rotor maquette -

Compte tenu des résultats obtenus en bidimensionnel, l'Aérospatiale a poursuivi les essais de ces profils sur rotor maquette. Quatre rotors quadripales de 4,20 m de diamètre et de 140 mm de corde, utilisant les profils OA2XX ont été essayés sur le banc d'essais d'hélicoptère de la soufflerie S1 Modane de l'ONERA. Les définitions géométriques de ces rotors ainsi que celle du rotor de référence utilisant le profil NACA 0012 et des profils Aérospatiale dérivés de la famille NACA 131XX sont présentées figure 13.

Les essais de ces rotors [11] ont permis de vérifier que les gains obtenus en bidimensionnel se retrouvaient effectivement sur rotor. L'influence bénéfique d'un affinement en bout de pale et de l'utilisation pour les sections internes de la pale de profils à C_z max élevés a également été constatée. La figure 14 présente l'évolution de la figure de mérite en vol stationnaire en fonction de la traction du rotor et de la vitesse périphérique pour les rotors 5, 6A et 6B. Les nouveaux profils donnent un gain d'environ 3 % pour la traction nominale, de plus l'affinement en bout de pale du rotor 6B conduit, pour des vitesses périphériques élevées, à moins de pertes sous fortes charges que dans le cas du rotor 5. L'utilisation des profils OA213 et OA206 sur le rotor 7B améliore sensiblement les performances du rotor en vol d'avancement. Ainsi, figure 15, le gain sur le coefficient de puissance atteint 9 % pour la poussée nominale à Λ = 0,4 (Vo = 300 km/h).

2.4.3 - Essais en vol -

Deux rotors, l'un utilisant le profil OA209, l'autre le profil OA212 jusqu'à 0,75R puis affiné au profil OA207 en bout de pale (pales 3e génération), ont été essayés en vol, le premier rotor sur un SA 360 Dauphin, le second sur les versions bimoteurs SA 365 C et SA 365 N.

Les résultats d'essais en vol [5] et [12] ont confirmé dans les 2 cas les gains obtenus sur rotor maquette.

Le rotor OA209 a ainsi permis d'obtenir par rapport à un rotor NACA 0012 :

- en vol stationnaire un gain de masse décollable de 2 % à iso-puissance ;

- un élargissement de l'enveloppe de vol en vol d'avancement, la portance du rotor étant accrue de 10 % quelle que soit la vitesse pour la puissance maxi (fig. 16) ;

- des gains en vitesse à iso-puissance variant de 5 km/h jusqu'à 50 km/h à 4 000 m (fig. 17) ;

- une réduction importante du niveau vibratoire en vol d'avancement.

Pour le rotor à profil évolutif les gains comparés à un rotor NACA 0012 sont les suivants :

- augmentation de l'efficacité du rotor en vol de croisière économique et à grande vitesse (fig. 18) ;

- élargissement de l'enveloppe de vol en vitesse et en masse (fig. 19) ;

- en vol stationnaire un gain de masse décollable de 100 kg à iso-puissance maximale.

Des rotors utilisant les profils OA213 et OA206 n'ont pas encore été essayés en vol. Toutefois, compte tenu des résultats d'essais à S1 Modane, les gains de performances devraient encore être supérieurs.

3 - ETUDE DES EXTREMITES DE PALE -

Les performances globales d'un rotor d'hélicoptère peuvent être également améliorées par l'utilisation de formes d'extrémité de pale autres que la forme rectangulaire qui équipe encore un très grand nombre d'hélicoptères. Une extrémité de pale d'hélicoptère joue un rôle aérodynamique beaucoup plus important qu'une extrémité d'aile d'avion. Quelle. que soit la configuration du rotor en vol stationnaire ou en vol d'avancement et donc quel que soit l'azimut considéré, la vitesse d'attaque y est la plus grande ($V = \omega z + Vo \sin \psi$) et la circulation est le plus souvent maximale dans cette région de la pale. De plus ces extrémités émettent des tourbillons marginaux qui perturbent le fonctionnement des autres pales du rotor. On peut en outre estimer qu'en vol stationnaire et en vol d'avancement à grande vitesse la plus grande partie de la puissance à fournir au rotor est due aux traînées des extrémités de pale entre 0,8 R et R qu'il faut vaincre pour faire tourner le rotor à vitesse constante.

Les buts poursuivis à l'ONERA pour les recherches concernant les extrémités de pale sont :

- la connaissance de leurs conditions de fonctionnement ;

- l'établissement de programmes de calcul de prévision de celles-ci ;

- la définition d'extrémités de pale plus performantes que celles utilisées jusqu'à présent ;

- l'essai sur rotor maquette en soufflerie et éventuellement en vol.

Ces différentes étapes sont systématiquement explorées à la Direction de l'Aérodynamique de l'ONERA depuis 1974 en étroite collaboration avec l'Aérospatiale mais aussi dans le cadre de collaborations internationales avec l'US Army RTL d'Ames, la NASA à Ames et le RAE pour certaines de ces recherches à caractère fondamental.

3.1 - Fonctionnement en pale avançante -

Les conditions de fonctionnement d'une extrémité de pale sont particulièrement sévères dans le secteur de la pale avançante puisqu'on y trouve les nombres de Mach d'attaque les plus élevés et souvent à la limite des nombres de Mach de divergence de traînée de chacun des profils équipant l'extrémité, lorsque la vitesse de l'appareil devient suffisamment grande.

3.1.1 - *Cas du rotor non portant* -

Les incidences sur les extrémités de pale au voisinage de l'azimut 90° sont souvent proches de zéro, soit légèrement positives, soit légèrement négatives selon la vitesse d'avancement de l'hélicoptère (fig. 2). Les extrémités de pale sont d'abord soumises à des nombres de Mach incidents croissants et à des attaques en flèche positives avant 90°, puis à des nombres de Mach incidents décroissants et des attaques en flèche négatives après l'azimut 90° et il convient donc de connaître les conséquences de ces conditions de fonctionnement tridimensionnelles et instationnaires.

Le cas d'un rotor non portant est plus facile à analyser. Aussi l'ONERA a-t-il effectué d'abord des essais sur un rotor bipale non vrillé avec mesure des répartitions de pression absolue à 0,85 R - 0,9 R et 0,95 R. Les essais ont permis de bien mettre en évidence les effets instationnaires et les effets des écoulements radiaux que F.X. Caradonna et M.P. Isom [13] avaient découverts par le calcul dans le cas d'une pale droite.

J.J. Chattot a poursuivi cette étude théorique, qui consiste à résoudre l'équation des petites perturbations transsoniques instationnaires, en mettant en oeuvre un programme de calcul des répartitions de pression sur une pale à extrémité de forme quelconque [14]. Ce programme de calcul est maintenant utilisé de façon courante à l'ONERA et est décrit en détail dans la référence 15. La figure 20 montre d'abord une comparaison entre résultats de calcul et résultats des essais précités sur le rotor à extrémité droite. L'accord entre la prévision et l'expérience est particulièrement bon. La figure 20 met également clairement en évidence la très nette dissymétrie des répartitions de pression de part et d'autre de l'azimut 90° caractériséepar exemple par des recompressions sans choc à 60° et des chocs très intenses à 120°. L'association d'un nombre de Mach croissant et d'une attaque en flèche positive avant 90° retarde donc l'apparition des troubles transsoniques, alors que celle d'un nombre de Mach décroissant et d'une attaque en flèche négative les aggrave. Les calculs "quasi-stationnaires" effectués pour une position figée de la pale permettent, par comparaison aux résultats des calculs instationnaires, de séparer les effets instationnaires et d'écoulements radiaux. La figure 21 montre en particulier que l'attaque en flèche négative (écoulement radial vers le centre du rotor après 90°) tend à atténuer la détente de bord d'attaque et donc à réduire les zones d'écoulement supersonique et l'intensité des chocs de recompression.

Les effets purement instationnaires peuvent être également mis en évidence par des calculs bidimensionnels en considérant un écoulement par tranche comme l'a montré une étude US Army-ONERA [16] mais lorsqu'on s'approche de l'extrémité de la pale, seuls des calculs tridimensionnels instationnaires peuvent permettre de bien décrire les phénomènes observés expérimentalement.

3.1.2 - *Les extrémités en flèche* -

La mise en flèche d'une extrémité de pale vient très naturellement à l'esprit lorsqu'on veut, comme pour une aile d'avion, diminuer le nombre de Mach incident normal au bord d'attaque.

Les écoulements y sont cependant beaucoup plus complexes que sur une extrémité droite et l'ONERA a donc d'abord effectué des essais sur un rotor bipale non vrillé avec une extrémité en flèche à 30°. L'analyse des répartitions de pression mesurées a montré que ce type d'extrémité, qui peut améliorer les performances d'un rotor à grande vitesse, n'est en fait favorable que sur une partie seulement du secteur de la pale avançante [17]. La figure 22 montre bien que l'accord calcul-expérience est encore suffisamment bon, pour se servir du programme de calcul décrit précédemment, pour étudier de façon systématique l'influence de la forme en plan sur les performances d'une extrémité de pale dans le secteur de la pale avançante.

Ces deux séries d'essais sur pale à extrémité droite et à extrémité en flèche à 30° dans le cas fondamental d'un rotor non portant ont également servi à la NASA [18] et au RAE [19] à valider leurs propres programmes de calcul.

La figure 23 qui fournit les lignes iso-Mach calculées pour les azimuts 60° et 120°, montre que ce type d'extrémité en flèche à corde presque constante est le siège de fortes détentes sur une bonne partie de leur envergure. Il convient donc de voir quels sont les paramètres géométriques qui jouent sur la présence ou l'absence de ces survitesses, qui ne peuvent que dégénérer en chocs générateurs de traînée et de bruit.

La figure 24 montre l'évolution en envergure des nombres de Mach locaux maximaux sur des pales :

- rectangulaire ;

- à extrémite en flèche à 30° et à corde constante ;

- à extrémité en flèche à 30° pour la ligne de bord d'attaque mais à bord de fuite aligné avec celle de la partie courante de la pale ;

- à extrémité parabolique en flèche définie à l'ONERA.

Dans ces calculs, les pales sont d'allongement 7 et la loi d'évolution des profils NACA 00XX qui les équipent est conservée pour toutes les formes. Les calculs sont effectués à l'azimut 90° dans l'approximation quasi-stationnaire. On voit qu'il n'y a pas intérêt à garder une ligne de bord de fuite rectiligne si l'on veut diminuer les survitesses locales mais qu'il est toujours bon de mettre une ligne de bord d'attaque en flèche. L'adoption d'une ligne de bord d'attaque parabolique en flèche permet de réduire considérablement toutes les survitesses et fait pratiquement disparaître tout écoulement transsonique important dans ce cas de calcul, comme le confirment les lignes iso-Mach calculées (fig. 25). Cette forme parabolique en flèche permet en fait de faire évoluer la flèche locale de la ligne de bord d'attaque jusqu'à des valeurs importantes de l'ordre de 80°. Sa définition est précisée sur la figure 26 et explicitée dans les références 15 et 20. L'évolution progressive de cette flèche locale de ligne de bord d'attaque est surement un des facteurs importants qui permet d'optimiser la mise en flèche d'une extrémité de pale d'hélicoptère.

3.2 - *Amélioration des performances globales d'un rotor avec des pales équipées d'extrémités paraboliques en flèche* -

L'extrémité parabolique en flèche définie précédemment doit donc améliorer le comportement de l'extrémité de

la pale dans le secteur de la pale avançante mais il n'est pas évident a priori qu'elle soit bonne pour tous les azimuts et quelle que soit la configuration du rotor. Aussi a-t-on effectué des essais sur un rotor tripale vrillé à la soufflerie S2 de Chalais-Meudon (fig. 26). Les résultats ont confirmé qu'une extrémité de pale "optimisée" pour les seules conditions de la pale avançante améliore globalement les performances d'un rotor. La figure 27 montre l'évolution de la puissance à fournir au rotor en fonction de la vitesse de vent Vo dans la soufflerie pour deux niveaux de portance, le rotor assurant la traction nécessaire pour vaincre la traînée d'un fuselage caractérisé par un (CxS)/Sσ de 0,1. L'extrémité parabolique en flèche est meilleure que l'extrémité droite puisque pour une vitesse Vo fixée, le rotor qui en est équipé a besoin de moins de puissance que celui qui est équipé d'extrémités droites. Le gain de puissance peut atteindre de 5 à 8 % dans les conditions de soufflerie.

Des améliorations ont été obtenues dans toutes les configurations étudiées (quels que soient les niveaux de portance ou de traction demandés au rotor et même en vol stationnaire [21]).

Au vu de ces résultats, l'Aérospatiale a décidé d'essayer ces extrémités de pale en vol sur un appareil Dauphin, pour confirmer l'intérêt de telles formes sur un rotor réel [11] et [22]. Cette expérimentation sera des plus intéressantes car de nombreuses différences demeurent entre les pales que l'on peut essayer sur maquette de rotor de faible dimension et celles d'un rotor réel, notamment les déformations que subissent les pales.

3.3 - *Etudes liées aux phénomènes tourbillonnaires* -

Les études théoriques précédentes ont surtout été basées sur l'amélioration des conditions de fonctionnement des extrémités de pale dans le secteur de la pale avançante pour lequel une hypothèse d'absence de portance pouvait être envisagée.

Dans le cas réel d'un rotor portant, l'extrémité de pale émet un tourbillon marginal qui, en passant à proximité des pales suivantes, perturbe fortement leur fonctionnement.

3.3.1 - *Le vol stationnaire* -

Dans cette configuration, le tourbillon marginal lâché par une pale se retrouve très proche de la pale suivante et il induit donc en extrémité de pale des variations significatives d'incidence.

Une simulation en soufflerie de ces phénomènes d'interaction tourbillonnaire a été réalisée à la soufflerie S3 de Chalais-Meudon en plaçant une demi-aile à proximité du tourbillon marginal émis par une autre demi-aile placée en amont perpendiculairement à la première. La figure 28 montre les répartitions en envergure des portances locales en absence ou en présence du tourbillon perturbateur. L'interaction tourbillonnaire augmente les portances locales du côté de l'extrémité de la demi-aile et les diminue vers l'emplanture. Globalement cela se traduit par une augmentation de traînée globale de la demi-aile de près de 40 % dans cette configuration d'essai [23] pour laquelle le niveau de portance globale est conservé égal à 0,5.

Le programme de calcul de petites perturbations transsoniques permet aussi de traiter le cas d'une pale isolée portante. La prise en compte d'un tourbillon perturbateur a été incluse dans ce programme, suivant la méthode développée par F.X. Caradonna [24]. La méthode consiste à imposer un saut du potentiel correspondant à la circulation du tourbillon sur un demi-plan infini partant de l'axe de ce tourbillon. Les figures 28 et 29 montrent la validité d'une telle approche théorique puisqu'elle permet de retrouver avec une bonne approximation les répartitions de pression et les portances locales mesurées expérimentalement.

Le cas d'un rotor en vol stationnaire est plus complexe. Des mesures du champ des vitesses induites par un rotor tripale vrillé ont été effectuées à la soufflerie S2 de Chalais-Meudon à l'aide d'un vélocimètre laser à 2 composantes. La figure 30 montre l'évolution en envergure des composantes verticales des vitesses induites à différentes distances en dessous du disque rotor et la trajectoire du tourbillon qui en a été déduite. Ces essais ont permis à l'Aérospatiale de valider son programme de mise en équilibre du sillage pour les calculs de performance du rotor en vol stationnaire [25]. Ils serviront aussi de bases de comparaison pour les calculs futurs qui seront menés lorsque le programme de calcul sur pale isolée de rotor permettra de tenir compte de la présence des autres pales.

3.3.2 - *Le vol d'avancement* -

Des interactions tourbillonnaires peuvent se produire également en vol d'avancement et elles affectent des secteurs azimutaux très différents selon la valeur du paramètre d'avancement. A forte vitesse on s'intéressera plus particulièrement à celles qui se produisent en pale avançante où la présence de tourbillons provenant de la pale précédente ne peut que compliquer la prévision par le calcul des charges locales instantanées.

Des mesures par vélocimétrie laser ont également été effectuées à la soufflerie S2 de Chalais-Meudon sur un rotor tripale en vol d'avancement en se limitant, pour commencer, au plan radial Ψ = 90°. La figure 31 illustre l'évolution temporelle des 2 composantes des vitesses mesurées et on remarquera les perturbations amenées par le passage de la pale au voisinage du point de mesure. La figure 32 montre le champ des composantes verticales de vitesse lorsque la pale passe à l'azimut 90°. Elle permet d'identifier la position du tourbillon lâché par la pale précédente ; dans cette configuration d'essai il ne se trouve qu'à environ 0,55 C au-dessous de la pale. Il sera donc nécessaire de prendre en compte, sous des formes plus ou moins sophistiquées, dans les calculs relatifs en vol d'avancement, la présence de ces tourbillons lâchés par les autres pales.

Ces mesures complètent aussi celles des pressions absolues effectuées précédemment sur les extrémités des pales du rotor tripale de la soufflerie S2 de Chalais-Meudon [20]. Les résultats de ces mesures de pression avaient permis de préciser les conditions de fonctionnement (portance, nombre de Mach incident) des extrémités de pale suivant les valeurs de la vitesse de l'écoulement dans la soufflerie, les niveaux de portance et de traction demandés au rotor. Toutes ces mesures serviront dans le futur à valider l'extension au cas portant du programme ONERA de petites perturbations transsoniques instationnaires sur pale isolée de rotor.

3.4 - *Evolution des programmes de recherche -*

L'objectif principal à court terme est de commencer à calculer des répartitions de pression sur une pale portante de rotor d'hélicoptère, même si cela doit se faire avec des approximations plus ou moins grossières pour tenir compte de la présence des autres pales ; en particulier, on s'intéressera à vérifier que les formes d'extrémité de pale définies à portance nulle pour minimiser les troubles transsoniques en pale avançante restent suffisamment performantes dans les différentes configurations où elles fonctionnent avec une portance non négligeable. On pourrait alors envisager par exemple un premier calcul d'optimisation entre le vol stationnaire et le vol d'avancement rapide en définissant un vrillage non linéaire des pales et une forme en plan en flèche appropriée.

La prise en compte des effets visqueux demeure aussi un objectif très important. Des calculs couplés fluide parfait-fluide visqueux ont déjà été effectués à l'ONERA dans le cas d'écoulements bidimensionnels instationnaires sur profil ou dans le cas d'écoulement par tranche sur pale de rotor d'hélicoptère [26] et [27]. L'effort se poursuit actuellement en tridimensionnel, en utilisant à cet effet un programme de calcul par méthode intégrale des couches limites tridimensionnelles instationnaires développé par le CERT [28] . La figure 33 montre par exemple l'évolution des épaisseurs de quantité de mouvement et du coefficient de frottement local sur la section à 0,95 R de différentes extrémités de pales pour lesquelles certains résultats de calcul de fluide parfait ont déjà été présentés sur les figures 24 et 25. Ce type de calcul permettra donc une estimation des traînées de frottement. La traînée globale des pales s'obtiendra en ajoutant à cette traînée de frottement une traînée de choc dans le cas des écoulements transsoniques. On devrait ainsi arriver à chiffrer le gain total potentiel des différentes formes d'extrémités de pale en tenant compte des surfaces mouillées réelles. Des calculs couplés fluide parfait-fluide visqueux en écoulement tridimensionnel sur pale de rotor sont donc envisageables dans l'avenir mais ils nécessiteront des moyens informatiques puissants.

L'étude aéro-acoustique des extrémités de pale sera également abordée en se consacrant en priorité au bruit impulsif généré à grande vitesse et pour lequel les nouvelles formes en flèche pourraient être une source de progrès.

4 - CONCLUSIONS -

- L'utilisation de nouveaux profils a permis d'améliorer très nettement les performances des rotors d'hélicoptères. Il faut souligner toutefois que ces profils ont été définis sur la base de critères stationnaires. En conservant ce même type de critères les gains potentiels que l'on peut encore espérer sont sans doute faibles. Seule une réduction de la contrainte sur le Cmo permettrait d'accroître sensiblement les performances des profils en C_z max et en finesse au prix bien entendu d'un accroissement des efforts de torsion sur la pale et sur les biellettes de commande de pas. Toutefois les progrès des méthodes de calcul en instationnaire et l'amélioration de la compréhension des phénomènes de décrochage instationnaire permettront sans doute dans un avenir proche la définition de profils sur la base de critères instationnaires plus proches des conditions réelles de fonctionnement des profils.

- L'étude des extrémités de pale entreprise à l'ONERA n'a pas encore apportée des résultats aussi complets et spectaculaires que ceux des nouveaux profils OA. L'évaluation d'une nouvelle forme d'extrémité parabolique en flèche est cependant en cours ; les premiers résultats obtenus en soufflerie sont très encourageants mais devront être confirmés lors d'essais en vol prévus en 1982 par l'Aérospatiale. L'étude expérimentale des écoulements sur des extrémités de pale de forme différente et la mise en place de programmes de calculs, de plus en plus sophistiqués, tridimensionnels quasi-stationnaires ou instationnaires non portants ou portants, même sur pale isolée de rotor d'hélicoptère, devraient dans l'avenir permettre des optimisations plus rigoureusesde ces extrémités de pale à partir de cahiers des charges à établir en étroite liaison avec les constructeurs.

REFERENCES -

[1] P. FABRE - Nature et importance des problèmes aérodynamiques des hélicoptères-6e Colloque d'Aérodynamique Appliquée - Toulouse - Novembre 1969.

[2] Y. MORCHOISNE - Méthode de calcul inverse en écoulement compressible -AAAF,12e Colloque d'Aérodynamique Appliquée (1975).

[3] J. BOUSQUET - Calculs bidimensionnels transsoniques avec couche limite - AAAF, 11e Colloque d'Aérodynamique Appliquée (1974).

[4] J.J. THIBERT and J. GALLOT - A new family for rotor blades - Paper presented at 3th European Rotorcraft and Powered lift Aircraft Forum, 1977. T.P. ONERA 1977-131.

[5] J.J. THIBERT and J. GALLOT - Advanced research on helicopter blade airfoils, Paper presented at 6th European Rotorcraft and Powered Lift Aircraft Forum, Sep 1980, T.P. ONERA 1980-93.

[6] J.J. THIBERT and J.M. POURADIER - Design and tests of an helicopter rotor blade with evolutive profile. Twelfth I.C.A.S. Congress. Munich (Germany), Oct. 1980, T.P. ONERA 1980-125.

[7] J.C. LE BALLEUR - Couplage visqueux-non visqueux : méthode numérique et application aux écoulements transsonique et supersoniques. La Recherche Aérospatiale n° 1978-2, p. 67-76.

[8] J.C. LE BALLEUR - Calcul des écoulements à forte interaction visqueuse au moyen de méthodes de couplage AGARD CP on Computation of viscous inviscid interaction, Colorado-Springs, 29/9 - 1/10 1980.

[9] J. RENAUD and J. COULOMB - 2D simulation of unsteady phenomena on a rotor. Fourth European Rotorcraft and Powered Lift Aircraft Forum, Stresa (Italy), Sept. 1978.

3-8

[10] E. SZECHENYI - An experimental study of the dynamic forces acting on fixed and vibrating two-dimensional aerofoils. Third European Rotorcraft and Powered Lift Aircraft Forum, Aix-en-Provence (France), Sept.1977.

[11] J.P. SILVANI et A. VUILLET - Aerospatiale survey of wind tunnel testing of small and large scale rotors Seventh European Rotorcraft and Powered Lift Aircraft Forum, Garmish - Partenkirchen (Germany), Sept. 1981.

[12] P. ROESCH - Aerodynamic Design of the Aerospatiale AS 365 N Dauphin 2 Helicopter - 6th European Rotorcraft and Powered Lift Aircraft Forum - Bristol - September 1980.

[13] F.X. CARADONNA, M.P. ISOM - Numerical calculations of unsteady transonic flow over helicopter rotor blades. AIAA Journal, Vol. 14 n° 4, April 1976.

[14] J.J. CHATTOT - Calculation of three-dimensional unsteady transonic flow past helicopter blades. NASA TP AVRADCOM TR 80-A 2 (A.M.). 1980.

[15] J.J. CHATTOT, J.J. PHILIPPE - Calcul des répartitions de pression sur une pale d'hélicoptère symétrique en vol d'avancement à portance nulle. La Recherche Aérospatiale n° 1980-6, p. 317-330.

[16] F.X. CARADONNA, J.J. PHILIPPE - The flow over a helicopter blade tip in the transonic regime. Vertica, vol 2, n° 1 (1978).

[17] B. MONNERIE, J.J. PHILIPPE - Aerodynamic problems of helicopter blade tips. Vertica, Vol. 2, p. 217-231.

[18] R. ARIELLI, M.E. TAUBER - Computation of subsonic and transonic flow about lifting rotor blades. AIAA paper n° 79 - 1667.

[19] J. GRANT - The prediction of supercritical pressure distributions on blade tips of arbitrary shape over a range of advancing blade azimuth angles. 4th European Rotorcraft and Powered Lift Aircraft Forum, Stresa, Italia, Sept. 1978.

[20] J.J. PHILIPPE, J.J. CHATTOT - Experimental and theoretical studies on helicopter blade tips at ONERA. 6th European Rotorcraft and Powered Lift Aircraft Forum - Bristol, Sept. 1980. ONERA TP n° 1980-96.

[21] J.J. PHILIPPE, P. LAFON - Amélioration des performances d'un rotor d'hélicoptère par utilisation d'une extrémité de pale parabolique en flèche. La Recherche Aérospatiale n° 1981-5, p. 345,346.

[22] R. LYOTHIER - Les extrémités de pale d'hélicoptère - 18e Colloque d'Aérodynamique Appliquée -AAAF, Novembre 1981

[23] J.J. PHILIPPE, C. ARMAND - ONERA Aerodynamic Research Work on Helicopters - AGARD CP 233 - 1977. Aussi dans la Recherche Aérospatiale n° 1978-6, p. 287-304.

[24] F.X. CARADONNA - The transonic flow on a helicopter rotor. Ph. D. Dissertation, Stanford University, March 1978.

[25] J.M. POURADIER, E. HOROWITZ - Aerodynamic study of a hovering rotor. 6th European Rotorcraft and Powered Lift Aircraft Forum, Bristol, Sept. 1980.Vertica, vol. 5, n° 4, 1981, p. 301-315.

[26] A. DESOPPER, R. GRENON - Couplage fluide parfait - fluide visqueux en écoulement instationnaire bidimensionnel incompressible et transsonique. AGARD CP 291 (1980).

[27] A. DESOPPER - Influence of the Laminar and Turbulent Boundary Layers in Unsteady Two-Dimensional Viscous-Inviscid Coupled Calculations. IUTAM Symposium, Toulouse, France 1981. Unsteady Turbulent Shear Flows.

[28] J. COUSTEIX, R. HOUDEVILLE - Etablissement et application d'une méthode intégrale de calcul d'une couche limite turbulente en écoulement tridimensionnel instationnaire, incompressible. R.T. ONERA 28/2259 AND, Février 1980.

1907-1930 PROFILS MINCES

1930-1945 PROFILS GOETTINGEN OU NACA

    KELLETT KD1 (1935) GOETTINGEN 770

    SIKORSKY YR4 (1943) NACA 0012

    NACA 23015 ,

    PIASECKI PV2 (1945) NACA 0012.6

    NACA 23012.6

    NACA 23015

1950-1960 PROFILS LAMINAIRES

    SERIE 6 (65-412 – 63A012 – 63A015)

    SERIE H (9 H 12)

1960-1970 PROFILS NACA ET DÉRIVÉS

1970 DÉFINITION DE PROFILS ADAPTÉS
    AUX HÉLICOPTÈRES

KELLETT KD-1
AUTOGYRE

KELLETT KD-1

NACA 0012

NACA 23012

NACA 65, - 412

NACA 9-H-12

Fig. 1 – Historique des profils utilisés.

Fig. 2 – a) Lignes iso-Mach et iso-angle de flèche pour
$\mu = 0,335$ ($V_0 = 73,7$ m/s, $\omega R = 220$ m/s).

b) Lignes iso-incidence pour le rotor du Dauphin
365. (masse : 3 T ; altitude de vol $\simeq$ 2000 m).

a) $V = 220$ m/s
$\sigma = 0,0545$
$m = 1500$ Kg.
$z = 0$ $t = 15°C$

Cz max = 1.55
1.35
1.15

b) $m = 1500$ Kg
$\sigma = 0,0545$
$z = 0$ $t = 15°C$

V = 220 m/s
V = 208 m/s
V = 195 m/s
V = 170 m/s

Puissance (KW)

700 - à 300 km/h.

- Puissance de traînée des pales 43 %
- Puissance des traînées parasites 44,5 % } 87,5 %
- Puissance rotor anticouple 5 %
- Puissance transmission 5 %
- Puissance induite 2,5 %

Puissance totale

Puissance de traînées de pales

Puissances des traînées parasites

Puis. Rotor anticouple
Puis. Transmission
Puis. Induite

Fig. 3 – a) Influence du Cz max.

b) Influence de la vitesse en bout de pale

c) Puissance nécessaire en vol horizontal.

Fig. 4 – Cahier des charges pour pale d'hélicoptère.

Conditions de vol	Coefficient Aérodynamique prépondérant		SECTION 1	SECTION 2	SECTION 3	
vol d'avancement	Mach à Cz=0	>	0.75	0.80	0.85	0.90	0.90
	(Cmo)	≤	0.01	0.01	0.01	0.01	0.01
vol stationnaire	Finesse à Mo=0.6 Cz=0.6	>	60	75	80	85	85
manœuvre	Mo=0.3	>		1.5	1.6		
	Cz max Mo=0.4	>	1.6	1.3	1.3	1.0	0.95
	Mo=0.5	>		1.3			
contraintes supplémentaires	e/c	~	13	12	9	7	6

$C_z - 0$

V/V_0

Intrados

X/C

0   0,5   1

OA 209

Fig. 5 – Définition du profil OA 209.

OA 209

Partie avant conservée   Affinité sur la partie arrière

Loi épaisseur OA 209

affinité 2/3

Loi épaisseur OA 206 + Loi de cambrure NACA 131 modifiée

PROFIL OA 207
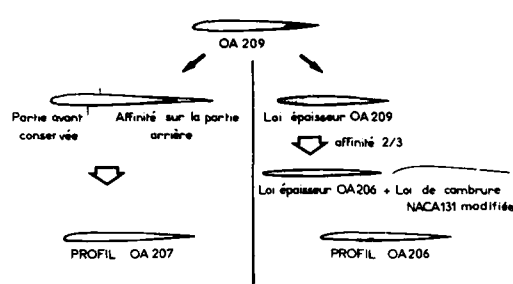
PROFIL OA 206

Fig. 6 – Définition des profils OA 207 et OA 206.

OA 212

OA 209

Loi épaisseur OA 209

Affinité 4/3

Loi épaisseur OA 212 + Cambrure dérivée NACA série 6

OA 212

OA 213

Répartition de vitesse a Mo=0.5 Cz~1

M

1,0

0.4

X/C

Programme inverse Morchoisne
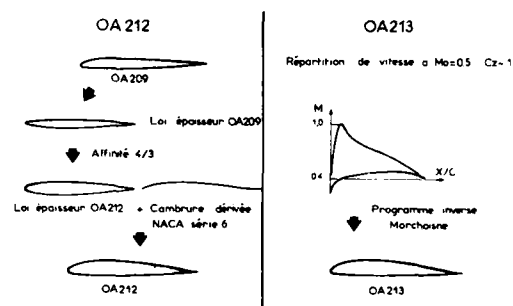
OA 213

Fig. 7 – Définition des profils OA 212 et OA 213.

OA 209

OA 207

OA209

OA212

OA 213
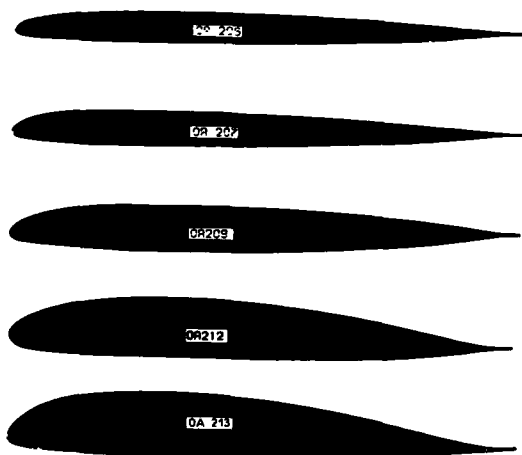
Fig. 8 – Dessin de la famille de profils.

Fig. 9 – Performances de la famille de profils.

C_Z max

M_{DX}

M_{DX}

0,9

1,6

C_Z max (M=0.4)

1,4

NACA 0012

C_Z max (M=0,3)

0,8

1,2

NACA 0012

M = 0.3

1,0

M = 0.5

C_Z max (M=0,5)

0,8

0,7

6   7   8   9   10   11   12   13

e/c %

a) Prévision des polaires

c) Prévision du C_mo
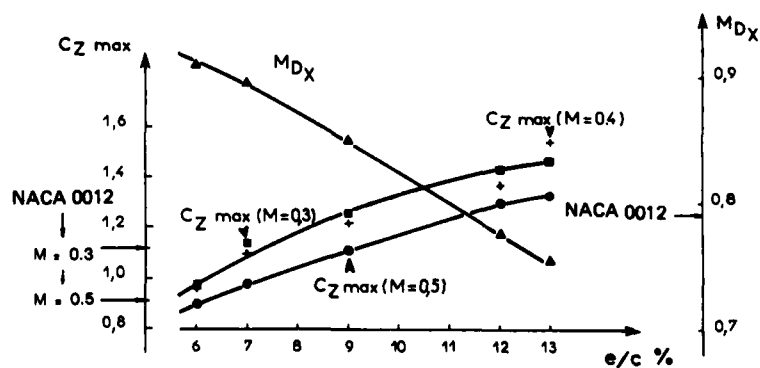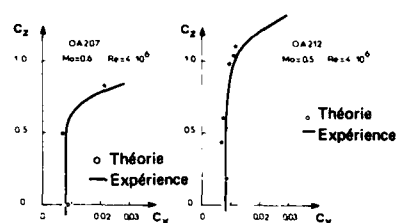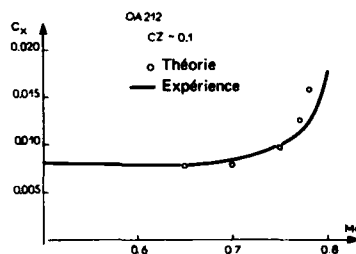
b) Prévision du C_x à C_z constant
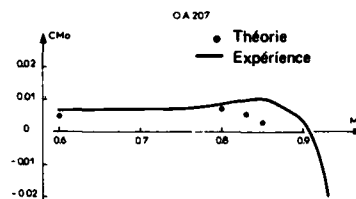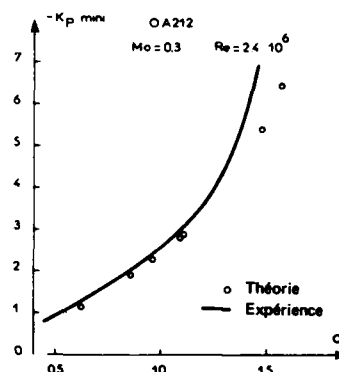
d) Prévision de la survitesse au bord d'attaque

Fig. 10 – Comparaisons calcul expérience.

b) Evolution du M_DX en fonction de l'épaisseur relative.
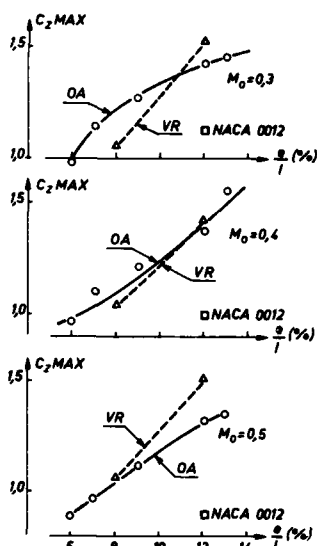
a) Evolution du Cz max en fonction de l'épaisseur relative

Fig. 11 – Comparaison des familles OA et VR
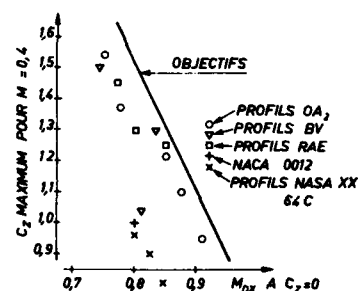
Fig. 12 – Comparaison série OA-autres profils.

Fig. 13 – Définition des rotors maquettes.
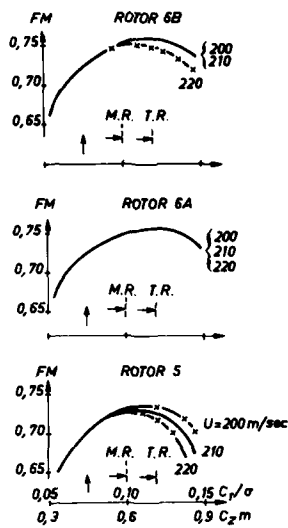
Fig. 14 — Evolution de la figure de mérite des différents rotors. Essais Modane.
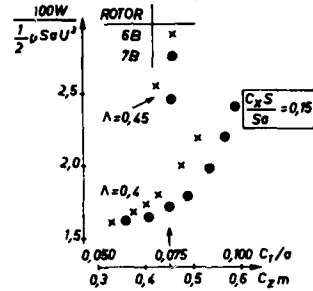
Fig. 15 — Influence du choix des profils sur le coefficient de puissance.
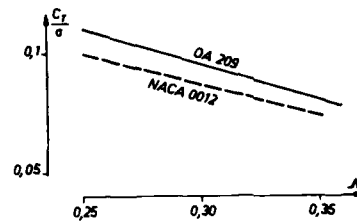
Fig. 16 — Accroissement de l'enveloppe de vol.
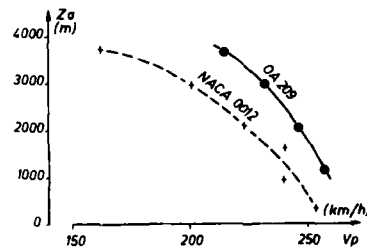
Fig. 17 — Augmentation de la vitesse maximale.
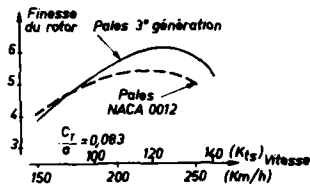
Fig. 18 — Amélioration de la finesse du rotor.
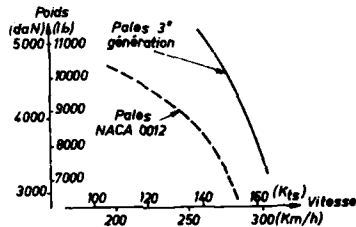
Fig. 19 — Extension de l'enveloppe de vol.
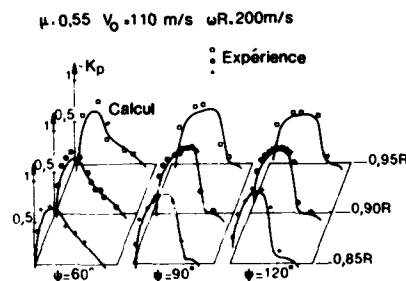
Fig. 20 — Comparaison calcul-expérience sur l'extrémité droite.
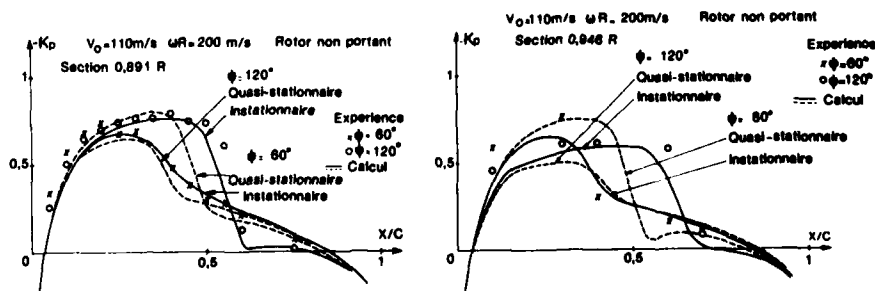
Fig. 21 — Comparaison calculs instationnaires et quasi-stationnaires avec l'expérience. Section 0,891 R et 0,946 R.
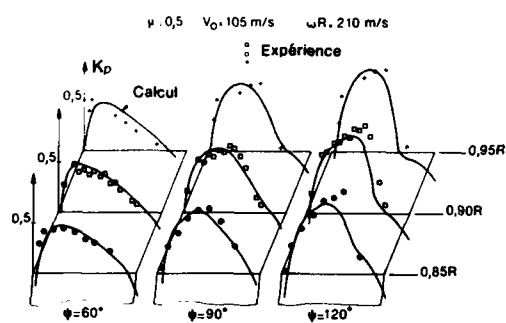
Fig. 22 — Comparaison calcul-expérience sur l'extrémité en flèche.

Fig. 24 — Evolution du nombre de Mach maximal sur la pale à extrémité en flèche.

Rotor non portant

Fig. 23 — Lignes iso-Mach sur une pale à extrémité en flèche à 30°.

Rect   F 30   F 30 A   PF 2
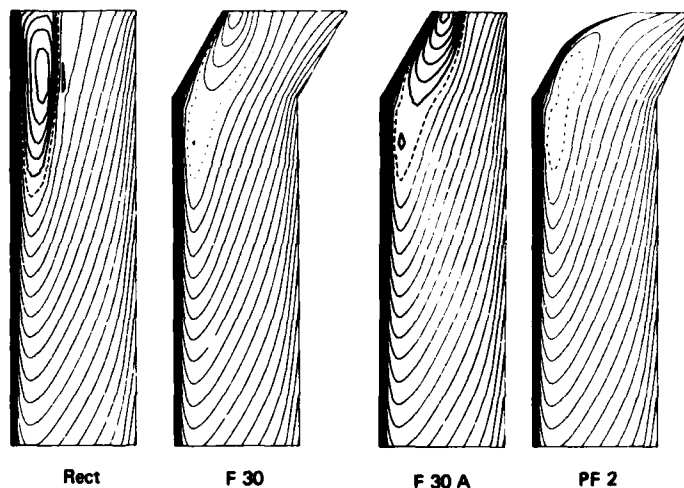
Fig. 25 — Lignes iso-Mach · $\psi = 90°$ · $\mu = 0,4$ $M_{\omega}R = 0,64$ · calculs Q-S.
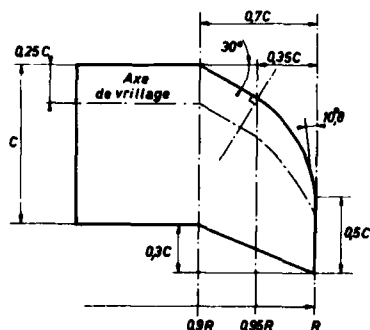
Fig. 26 — Forme en plan de l'extrémité parabolique en flèche et vue du rotor en soufflerie.
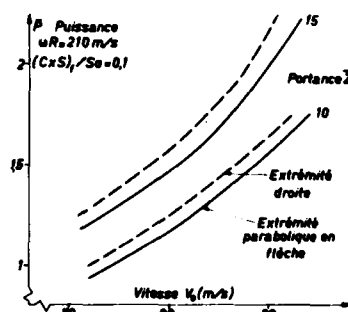
Fig. 27 — Puissance à fournir au rotor en fonction de la vitesse d'avancement.
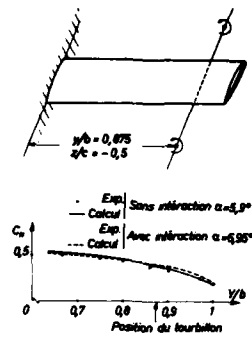
Fig. 28 — Demi-aile à la paroi avec ou
sans interaction tourbillon-
naire. (M∞ = 0,6 Cz = 0,5).
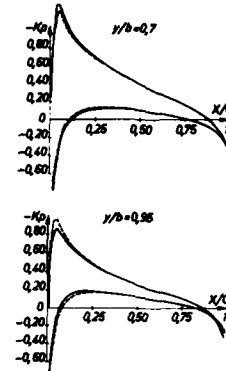
Fig. 29 — Répartitions de pression
calculées sans interaction
tourbillonnante (———) ou
avec interaction tourbil-
lonnante (———).
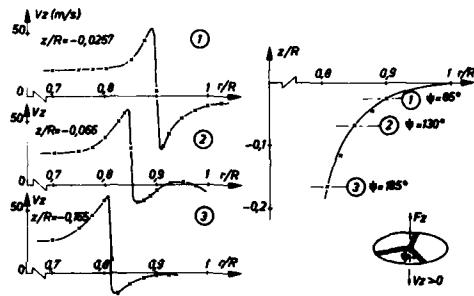
Fig. 30 — Vitesses induites par un rotor en vol stationnaire.
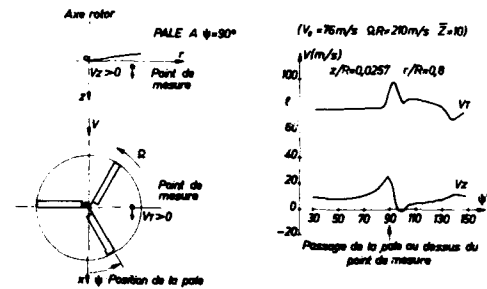
Fig. 31 — Mesure des vitesses autour d'un rotor en vol d'avancement.
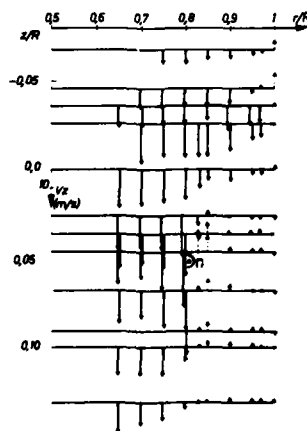
Fig. 32 — Vitesse induite verticale (plan x = 0)
pour un azimut de pale $\psi = 90°$.
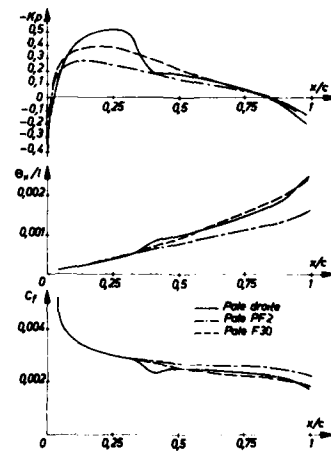
Fig. 33 — Evolution des épaisseurs de quantité de
mouvement et des coefficients de frot-
tement sur différentes extrémités de
pale (section à 0,955 R).

CALCULATION OF 3D UNSTEADY
TRANSONIC FLOW AROUND ROTOR BLADES

by

H. Stahl

Messerschmitt-Bölkow-Blohm GmbH
Postfach 801140
8000 München 80, Germany

SUMMARY

The aerodynamics of the rotary wing present one of the strongest challenge within the aerodynamic sciences. Severe operational limitations of the helicopter stem from the fact, that the lifting system is subject to transonic phenomena, which result from the specific flow field around the advancing side of the rotor disc. Furthermore, it is seen that unsteadiness and the three-dimensional nature of the flow are two further important parts of the problem. The understanding, the accurate prediction, and the control of the transonic aerodynamic phenomena are essential preconditions for further improvement of rotary-wing aircraft.

In view of the significant influences of transonic flow on rotor operation, the adequate modelling of the fundamental physics and the calculation of the main consequences is of utmost importance. Thereby, the calculation requirements are extreme, and are differing considerably from these of the fixed wing aircraft. The most efficient rotor blade flow calculation techniques at present use the relaxation method for solving the finite difference approximation of the small disturbance equations, however, the disadvantage of extremely large computational times prevents from using these methods within complete rotor aerodynamics and loads analyses.

The paper will describe the work currently done at MBB, concentrating on the application and adaptation of classical wing methods to the special requirements of rotor blade tip flow. This gives the possibility to overcome the limitations of the current methods, such as large computational times. The problem is split up into two principal categories, the 3-D steady flow, and the 2-D unsteady case.

The unsteady calculation is carried out by a finite difference method for the 2-D case considering both the angle of attack and the Mach number variation. The 3-D calculation is based on a finite element model for fixed wings, which is adapted for the rotor blade application by a linearly varying velocity distribution over the blade radius. Hereby only the outer 25% of the radius are taken into account. The final lift and moment distributions on the blade are determined by superposition of 3-D steady and 2-D unsteady results.

The final objective of the present work is the improvement of existing rotor theories, which are usually based on blade element theory with insufficient representation of tip effects. By adaptation of these semi-empirical results in the rotor models their applicability can be improved especially for the advancing blade, but also over the whole azimuth angle region.

NOTATIONS

c	chord length of a profile		κ	isentropic exponent
r	local radius position		μ	advance ratio
t	time		ρ	density
u,v,w	velocity components		ω	angular velocity
x,y,z	coordinates		Φ,ϕ	potential
K	$= \dfrac{\omega \cdot c}{U_\infty}$ - reduced frequency		ψ	azimuth angle
M_0	medium Mach number			
M	Mach number		**Subscripts**	
M_∞	free stream Mach number		ξ,ζ	partial derivative with respect to the indicated coordinates
ΔM	Mach number amplitude			
R	rotor radius		τ	partial derivative with respect to nondimensional time
U_∞	free stream velocity			
α	angle of attack (pitch angle)			
α_0	medium pitch angle			
$\Delta\alpha$	amplitude of pitch angle			
ξ,ζ	nondimensional coordinates			

1. INTRODUCTION

There exist fundamental differences in the flow around the wing for fixed-wing and rotary wing aircraft. Already in steady forward flight these differences mainly concern Mach numer, angle of attack, and yaw angle distributions that depend upon the radial position along the blade as well as upon azimuth angle in the case of the rotor and are therefore unsteady.

In recent years the speed of helicopters has increased. Thereby, new problems arose because of strong flow separation on the retreating rotor blade and transonic effects on the advancing blade. As a result the helicopter power consumption, vibration, and noise emission are also severly affected.

The present major problem of interest is the advancing blade, especially the blade tip where the highest velocities occur. Thus the blade tip may enter the transonic flow regime where the aerodynamic coefficients change appreciably due to compressibility effects and occurence of shock waves. These influences must be understood for further improvement of the aerodynamic behavior and thus the design of the blade tip.

A frequently used method for calculating the airloads of rotors is the blade element theory (two-dimensional). But for calculations close to the blade tip it is less useful because three-dimensional effects become very important. Therefore other calculation methods become necessary that include all these effects.

In the literature several authors considered the flow around the blade tip. Due to the restricted capacity of the available computers the problem had to be simplified. One of the most common simplifications is the application of potential theory for this flow. The potential equation is modified to include the linear velocity gradient of the rotor, and it is solved numerically by finite difference or finite volume techniques. Two methods shall be mentioned that attacked this problem with some success. One method developed by Caradonna [1] concerns the steady flow and the other procedure, developed by Caradonna and Isom [2] treats the unsteady flow under the assumption of zero lift. For industrial purposes, however, the computational time of these methods is much too high.

From the mathematical point of view the application of potential theory to the flow around a rotor blade tip is not exact. This problem is considered in more detail in [3].

Considering the flow around the blade tip the assumption of irrotational flow is made. Calculation time is further reduced when the problem is split up into two parts, the three-dimensional steady case and the two-dimensional unsteady case. For both cases computer codes are available from the fixed wing technology. However, in the original form they are not applicable to the rotor flow conditions, so they have to be modified.

2. ADAPTATION OF EXISTING COMPUTER MODELS

2.1 THE TWO-DIMENSIONAL UNSTEADY PROCEDURE

For the unsteady case a computer code developed by Eberle [4] is used. It is a method for calculating transonic flow over a profile with a sinusoidally oscillating trailing edge flap. The numerical procedure uses a finite difference scheme and applies the TSP-ADI-method (Transonic potential – alternating direction implicit). The computational time needed is about 2 min on IBM 3033 for one case.

The transonic potential equation of the unsteady flow is of the form

$$- M_\infty^2 \; K^2 \; \phi_{\tau\tau} - 2 \; M_\infty^2 \; K\phi_{\xi\tau} + \{1 - M_\infty^2 - M_\infty^2 \; [3 + M_\infty^2 \; (\kappa - 2)] \; \phi_\xi\} \; \phi_{\xi\xi} + \phi_{\zeta\zeta} = 0$$

Small perturbations are assumed and K (reduced frequency) must be smaller than unity. For achieving mass conservation at sonic lines and shocks a numerical viscosity is introduced, so that the numerical stability in supersonic regions is guaranteed.

For introducing the unsteady pitch angle motion the flap hinge is blocked and the pivot point is moved to any point desired, so the whole profile can oscillate around this point. Normally the point will be fixed at c/4. The pitching motion is defined by

$$\alpha = \alpha_o \cdot \sin \omega t.$$

In fig. 1 the lift and pitching moment coefficients and the resulting center of pressure are shown over one period. For comparison the steady curves are also presented. In the unsteady case the maximum value of the lift coefficient occurs at smaller azimuth positions ψ than expected by steady state analysis. The same effect can be observed for the pitching moment. Only the unsteady curve of the center of pressure is very different from the steady one because the values of the lift and moment coefficients are rather small.

A further unsteady effect is the Mach number variation on the blade due to forward flight of the rotor. The local Mach number perpendicular to the leading edge is defined by

$$M(t,r) = (\mu \cdot \sin \omega t + \frac{r}{R}) \cdot M_O(R)$$

with μ as the advance ratio and $M_O(R)$ the hovering blade tip Mach number. The result for a pure Mach number variation is shown in fig. 2. Here the lift coefficient, pitching moment coefficient and center of pressure are drawn over one period. For comparison he result for the steady state case is indicated, too. Due to the unsteady flow the maximum value of the lift coefficient is moved to a higher azimuth angle. The same tendency can be observed for the pitching moment coefficient. The curve for the center of pressure does not show an appreciable deviation from the steady one, contrary to the angle of attack variation.

The calculation of the unsteady flow is split up into three steps:

      1. Start of the flow from rest ($\alpha = 0$)

      2. Start of the unsteady motion

      3. Final state of unsteady motion.

As a result unsteady pressure distributions, lift coefficients and pitching moment coefficients are obtained.

RESTRICTIONS

Not every effect can be taken into account. The velocity and pitching angle variation can be considered like a two-dimensional influence. Only the velocity component perpendicular to the leading edge, however, affects the two-dimensional calculation. The yawing angle is a three-dimensional effect only and cannot be considered here. Also all motions of the blade due to elasticity are neglected.

Other limitations are due to the theory applied. These are:

      a) The reduced frequency must be $K < 1$

      b) The Mach number $M_\infty = 1$ cannot be exceeded

      c) Only weak shocks are permitted

      d) Slender profiles should be used.

2.2 THE THREE-DIMENSIONAL STEADY PROCEDURE

This procedure is also developed by Eberle [5]. The underlying theory is the potential theory with its boundary conditions. For the numerical procedure the finite element method is used. It is developed for wings and wing/body combinations and is applicable to transonic flow with $M_\infty < 1$.

The basic equation is:

$$\iiint \rho \left(u \frac{du}{d\phi} + v \frac{dv}{d\phi} + w \frac{dw}{d\phi} \right) = 0$$

The procedure uses a numerical viscosity to guarantee the numerical stability, thereby allowing shocks to be generated. In performing the calculation advantage is taken of the symmetry of a plane. In this way much computational time is saved.

The most important three-dimensional effects are the influence of the angular velocity of the rotor and yaw angle distribution over the blade radius.
However, to handle the procedure and to modify it for the rotor flow some idealizations have to be made [3]. One is the assumption that it is possible to calculate the rotor flow for each azimuth angle ψ like a steady flow. This is not according to the real flow but it can be assumed as an approximation. Another assumption concerns the applicability of potential theory for the flow around the rotor blade tip since the rotor flow is not irrotational at all.

Firstly, the linear velocity gradient is to be introduced into the far field condition. The relation for the velocity is accordingly

$$u = \omega \cdot r + U_\infty \cdot \sin \psi$$

In this case the velocity U_∞ represents the advance velocity of the rotor. The result of such a flow is shown for the advancing blade ($\psi = 90^\circ$) in fig. 3. Here chordwise pressure distributions are shown for the outer 25 percent of the radius. The influence of the blade tip can be seen as well as the effect of the decreasing velocity farther inboard.

Due to the assumption that oncoming stream lines have to be parallel to the plane of symmetry the yaw angle cannot be calculated directly. One way to solve the problem is the application of a geometrical transformation. This can be assumed as an approximation to the real flow and is based on the following considerations:

When the wing makes a yaw angle with the flow the stream lines meet another aerofoil section. Compared with an aerofoil section perpendicular to the leading edge, the chord is enlarged and the relative thickness is smaller. The flow is no longer symmetrical to any plane. The aerodynamic coefficients are not distributed symmetrically with respect to the geometric plane of symmetry (formerly chosen as the aerodynamic reflection plane).

If the yaw angles are assumed to be small, the effect due to asymmetry may be neglected as a first approximation. Then it is possible to position the aerofoil sections parallel to the stream lines by introducing a sweep angle. In this way the aerodynamic yaw angle is transformed into a geometrical sweep angle with the corresponding chord.
As the yaw angle on a rotor blade is not constant along the radius, this transformation results in a curved leading edge of the blade, shown in _fig. 4._

RESTRICTIONS

a) Due to the assumption of symmetrical wing the yawing angle β must be zero.

b) The oncoming stream lines have to be parallel to the plane of symmetry.

c) The Mach number M_∞ cannot exceed unity.

d) Only small perturbations (i.e. weak shocks) are allowed.

3. INVESTIGATIONS OF THE TWO-DIMENSIONAL UNSTEADY EFFECTS

Considering the two-dimensional unsteady flow around a profil several paramters govern the flow:

- the form of the airfoil section

- the time dependent Mach number variation $M(t)$

- the pitch angle oscillation $\alpha(t)$

For the case of a harmonically varying Mach number and pitch angle, as at a rotor blade, the time dependent parameters can be specified more accurately. Then there are

- the medium Mach number M_O

- the amplitude of the Mach number ΔM

- the medium pitch angle α_O

- the amplitude of the pitch angle $\Delta\alpha$

- the reduced frequency K

The amplitude of the Mach number is related to the advance ratio by

$$\mu = \frac{\Delta M}{M_O}$$

3.1 PARAMETRIC STUDIES

3.1.1 THE INFLUENCE OF THE ADVANCE RATIO

In fast forward flight there occur transonic effects on the advancing blade tip. To get the dependence of the Mach number the pitch angle and its amplitude is set zero ($\alpha = \Delta\alpha = 0^O$). The pure influence of the Mach number variation upon the aerodynamic coefficients like C_L, C_m was already shown in fig. 2. The deviation from the steady case was indicated, too. Another result for a NACA 0012 profile is shown in fig. 5. The maximum Mach numbers reached at $\Psi = 90^O$ are 0.73, 0.76, 0.79, 0.81 corresponding to an advance ratio of μ = 0.4, 0.45, 0.5, 0.55, respectively. It can be seen that for the chosen rotor tip speed of ωR = 200 m/s the flow is subsonic over the whole half-period of the advancing blade at μ = 0.4 and 0.45 (r/R = 0.89). Compressibility effects such, as shocks, can be observed, firstly, at higher advance ratios. Characteristic is the asymmetry of the pressure distributions with respect to $\Psi = 90^O$. The shocks are stronger in the region after $\Psi = 90^O$ caused by the unsteadiness of the flow.
Remark. The investigated advance ratios correspond to model rotor experiments shown in fig. 12.

3.1.2 THE INFLUENCE OF THE AMPLITUDE OF THE PITCH ANGLE

The influence of the amplitude of the pitch angle $\Delta\alpha$ on the coefficients is very strong. In fig. 6 lift and pitching moment coefficients and the center of pressure are shown for $\Delta\alpha = 0^O$ as reference and $\Delta\alpha = 1^O$ ($\alpha_O = 2^O$). The advance ratio is assumed to be μ = 0.36. As the figure shows the deviation due to the oscillating pitch angle is very large compared with the steady case, and the tendencies due to $\Delta\alpha$ are just inverse to that of a pure Mach number variation. However, it can be seen that the effects due to the

oscillating angle dominates the effects due to Mach number variation. Also the center of pressure for $\Delta\alpha = 1°$ deviates appreciably from the curve of $\Delta\alpha = 0°$ (pure Mach number variation).
The effect of a pure pitch angle motion on the aerodynamic coefficient was already shown in fig. 1.

3.1.3 THE INFLUENCE OF THE REDUCED FREQUENCY

In fig. 7 the pressure coefficient behaviour of the advancing blade is shown for several frequencies ($x/c = 0.233$, $\alpha = 0°$). The decreasing values of the reduced frequency correspond to the flow over aerofoil sections of a rotor blade, from inboard to outboard, of the outer 25 percent radius. The advance ratio ($\mu = 0.445$) and the pitch angle ($\alpha = \Delta\alpha = 0°$) are kept constant. The diagram fig. 7a corresponds to a full-scale rotor ($\omega = 42$ s^{-1}) and fig. 7b corresponds to a 1/7 model ($\omega = 266.7$ s^{-1}).

The minimum pressure occurs at the lowest frequencies. At higher frequencies it dimishes and is shifted to higher azimuth angles. At $K = 0.0084$ the maximum starts to divide into two maxima.
In fig. 7b at $K = 0.0325$ the maximum is distributed from $\Psi = 60°$ to $\Psi = 120°$. In this region the pressure coefficient is almost constant. Then it happens the same as before. The maximum is shifted to higher value. But here the front part increases first, the rear part of the maximum sets up at small frequencies ($K = 0.0279$).

The most interesting feature is the influence of the reduced frequency. The smaller frequency is about one tenth below the higher one. But this difference causes a total different time dependent flow over the rotor span. Also the medium Mach number changing as indicated has an influence not to be neglected.

3.1.4 THE INFLUENCE OF THE MEDIUM PITCH ANGLE

In fig. 8 the influence due to the medium pitch angle is shown for advance ratios $\mu = 0.275$ and 0.36 ($\Delta\alpha = 0°$). It can be observed that a higher angle α_0 causes stronger compressibility effects around $\Psi = 90°$. Only the center of pressure is uneffected by the angle α_0.

3.2 COMPARISON WITH MEASUREMENTS

The most useful test data available for comparison are measurements on a model rotor [6] with a diameter of 1,50 m and a tip speed of 200 m/s. The blades are tapered and have airfoil sections of the NACA 00XX series with a NACA 0014.5 profile at 0.8 R and a NACA 0009 profile at $r/R = 1$. The blades are untwisted. Pressure data were measured at 85.5, 62.2, and 94.6% radius of the rotor. The last one is very close to the tip where three-dimensional effects are no longer negligible. In this connection it should be noted that the comparison is made with two-dimensional calculations.
In fig. 9, 10, 11 pressure distributions are shown over half a period for a maximum tip speed of $\omega R = 200$ m/s for 85.5, 89.2, and 94.6% radius, respectively. The corresponding maximum Mach numbers are 0.841, 0.863, and 0.888. The chordwise stations are $x/c = 0.3$, 0.5, and 0.4. Good agreement between measurement and theory is achieved at $x/c = 0.3$ for increasing velocity ($\Psi < 90°$). At the inboard stations measurement and theory compare relatively well, at the outer section at 94.6% R the comparison is poor due to three-dimensional effects. In fig. 12 chordwise pressure distributions are shown for maximum sectional Mach numbers of $M = 0.73, 0.76, 0.79, 0.81$ corresponding to advance ratios of $\mu = 0.4, 0.45, 0.5, 0.55$, respectively, at azimuth angles of $\Psi = 60°$ and $120°$. Although in this case (89.2% R) three-dimensional effects are not negligible the agreement between theory and measurement is very good.

3.3 REMARKS ABOUT SIMILARITY LAWS

For model rotor tests in most cases the same tip speed and foreward flight speed is used as for full-scale rotors to achieve Mach number similarity. By a simultaneous accurate geometrical scaling Reynolds number similarity is not attainable due to the different blade chord.
If Reynolds number similarity is desired, the model rotor blade chord must be of the same size as the full-scale blade chord. This leads to a reduced aspect ratio of the model rotor blade. Through that and due to the higher velocity gradient along the blade radius the change of the reduced frequency over the radius is much higher for the model rotor.
In fig. 13 the reduced frequency trend over the blade radius is shown for a full-scale ($R = 5$ m) and a model rotor ($R = 0.75$ m) for different values of blade chord length.

For the same blade chord ($c = 0.2$ m) the K-gradient at the blade tip is

$$\Delta K/\Delta R = -0.444 \text{ m}^{-1} \text{ (model rotor)}$$
$$\Delta K/\Delta R = -0.010 \text{ m}^{-1} \text{ (full-scale rotor)}$$

The ratio between these values of 44.4 is reduced to 7.4 by accurate geometrical scaling (same aspect ratio). The influence of these three-dimensional effects are not fully known, but should be investigated. In general similarity parameters especially for the rotor should be defined, because the parameters of the wing theory are no longer sufficient.

4. PARAMETRIC INVESTIGATIONS OF THE THREE-DIMENSIONAL MODEL

4.1 INFLUENCE OF THE ANGLE OF ATTACK

The influence of the angle of attack is shown in fig. 14 by the three-dimensional pressure distribution on the blade tip. Angles of attack are 1° and 2° and the tip Mach number is $M_T = 0.8$. Due to the higher angle of attack the inner border of the supersonic region is shifted from about 0.85 radius to 0.8 radius, that means to a lower local Mach number. Also the shock strength is more than doubled on the outer 10% of the blade radius.

4.2 INFLUENCE OF THE AZIMUTH POSITION

In fig. 15a and b the lift and pitching moment distributions and the center of pressure are shown for azimuth positions of $\Psi = 60^\circ$, 90°, and 120°. The maximum tip Mach number of $M_T = 0.8$ at 90° corresponds to $M_T = 0.78$ at $\Psi = 60^\circ$ and 120°, whereas the angle of attack is 1° for all three cases. Compared with the 90° position, for the yawed blade the lift and pitching moment coefficients are reduced in the near tip region, but farther inboard they are beyond the 90° values. The most remarkable changes occur for the center of pressure. Generally, it is shifted towards the leading edge due to the three-dimensional effects, but it moves back with increasing azimuth angle.

5. COUPLING OF THREE-DIMENSIONAL AND UNSTEADY EFFECTS

To achieve the real airload distributions (lift and pitching moment) in the tip region the three-dimensional and unsteady effects are superposed in a suitable manner. In addition to the lift and pitching moment coefficient the drag would be of interest in this case also, but it cannot be predicted by the potential theory, which is used in both numerical methods. For the coupling of the three-dimensional and unsteady effects the method shown in fig. 16 has been developed.

The underlying concept is as follows: By means of the three-dimensional procedure the aerodynamic coefficients will be determined. Then the difference between the two-dimensional steady and unsteady calculation is determined for a given radial position at the outer 25 percent radius. This difference will be added to the three-dimensional value at the same radius location. From this value a ratio can be defined with which all three-dimensional coefficients are to be multiplied. In this way the unsteady effect can be introduced.

The application to the lift coefficient leads to

$$C_{Lu}(r) = C_L(\text{unsteady}, r) = \frac{C_{LS}}{C_{LO}} (C_{LO} + \Delta C_{Lu})$$

Herein ΔC_L is defined as

$$\Delta C_{Lu} = C_L(\text{2d, unsteady}) - C_L(\text{2d, steady})$$

C_{LO} is the lift coefficient at a given radius location and

C_{LS} is the lift coefficient along radius from the steady calculation.

6. CONCLUSION

The application of three-dimensional computation methods in rotor aerodynamics has become necessary because the requirements for extending necessitating a more deep understanding of the flow around the rotor blades. By aerodynamically optimizing the blade tip an improvement is possible. However, the two-dimensional computation methods are no longer sufficient especially near the tip and thus three-dimensional computer programmes are required. From the foregoing discussion the following conclusions can be drawn:

- The problem of the flow in the vicinity of the tip of a rotor blade has already been investigated in the literature using the potential theory. The agreement between theory and experiment is acceptable. However, the procedures are limited either to hover or to nonlifting flow. Also, the computation time is inacceptably high for industrial purposes.

- A programme for unsteady two-dimensional flow has been modified for an oscillating free stream Mach number and angle of attack. The effects of these parameters and additionally the influence of the reduced frequency and the medium angle of attack are studied.

- A programme for steady three-dimensional flow over a fixed wing has been modified for a rotating blade by taking into account the velocity variation over the blade

radius and the yawing angle. Calculations with this programme provided results as expected on a rotor blade tip.

- A model has been developed in order to couple the three-dimensional effects with the unsteady two-dimensional ones.

- Subjects for further investigations with this model are

  o the determination of the induced angle of attack due to the velocity down wash of the foregoing blade

  c the influence of the tip vortex of the preceeding blade

  o the application of the calculated aerodynamic coefficients of the blade in rotor computer models

7. REFERENCES

1. F.X. Caradonna   "The Transonic Flow on a Helicopter Rotor",
                          Dissertation, March 1978

2. F.X. Caradonna   "Numerical Calculation of Unsteady Transonic Potential
    M.P. Isom   Flow over Helicopter Rotor Blades",
                          AIAA Journal, Vol. 14, No. 4, 1976

3. H. Stahl   "The Problem of Calculation of the Flow around Helicopter
                          Rotor Blade Tips",
                          Seventh European Rotorcraft and Powered Lift Aircraft
                          Forum, Garmisch-Partenkirchen, Germany, Sept. 8-11, 1981

4. A. Eberle   "Ein instationäres TSP-Verfahren für Profile mit schwin-
                          genden Klappen",
                          MBB-UFE122-AERO-MT-495, 1980, MBB

5. A. Eberle   "Erweiterung des transsonischen 2-D-Panelverfahrens auf
                          die Berechnung gepfeilter Tragflügel",
                          UF 1451, 1978, MBB

6. F.X. Caradonna   "The flow over a Helicopter Bade Tip in the Transonic
    J.J. Philippe   Regime",
                          Second European Rotorcraft and Powered Lift Aircraft
                          Forum, Bückeburg, Germany, Sept. 20-22, 1976

7. J.J. Philippe   "ONERA Aerodynamic Research Work on Helicopter",
    C. Armand   92330 Châtillon (France), 1977

8. D.S. Dulikravich   "Finite Volume Calculation of Transonic Potential Flow
                          Through Rotors and Fans",
                          FDA-80-03, March 1980

9. R. Stricker   "Instationäre, drei-dimensionale, transsonische Umströ-
    S. Wagner   mung der Rotorblattspitze",
    V. Mikulla   MBB GmbH, UD-263-78, Januar 1979

10. E. Truckenbrodt   "Strömungsmechanik",
                          Springer-Verlag, Berlin, Heidelberg, New York, 1968.
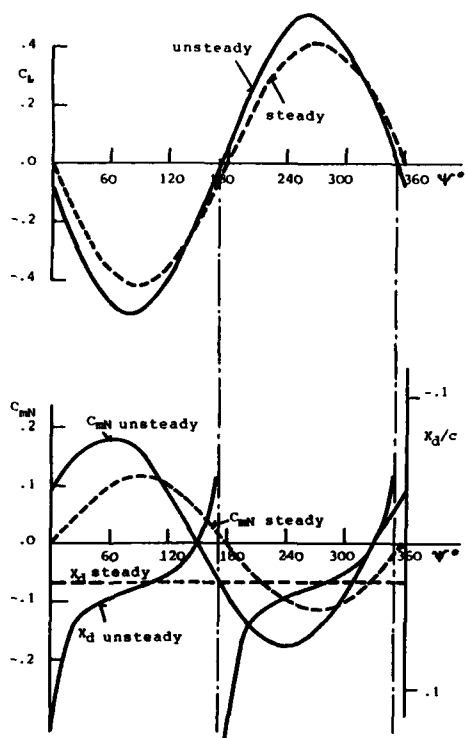
Fig.1 The trend of lift, pitching moment co-
efficient and center of pressure over one
period at $M_\infty = 0.6$, $\alpha = 0°$, $\Delta\alpha = 3.78°$ (NACA
0006, $K = 0.434$, $\mu = 0$)

Fig.3 Chordwise pressure distribution at
$M_T = 0.85$, $\mu = 0.31$, $\alpha = 0°$ (NACA 0012)
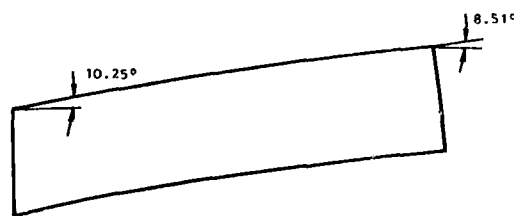
Fig.4 Transformed blade tip, $\beta = \beta(r)$, $\mu = 0.4$,
$\psi = 120°$, $\omega R = 220$m/s
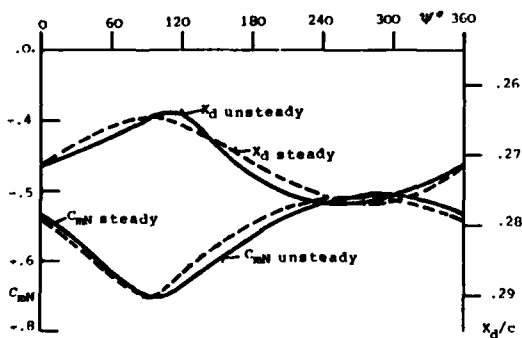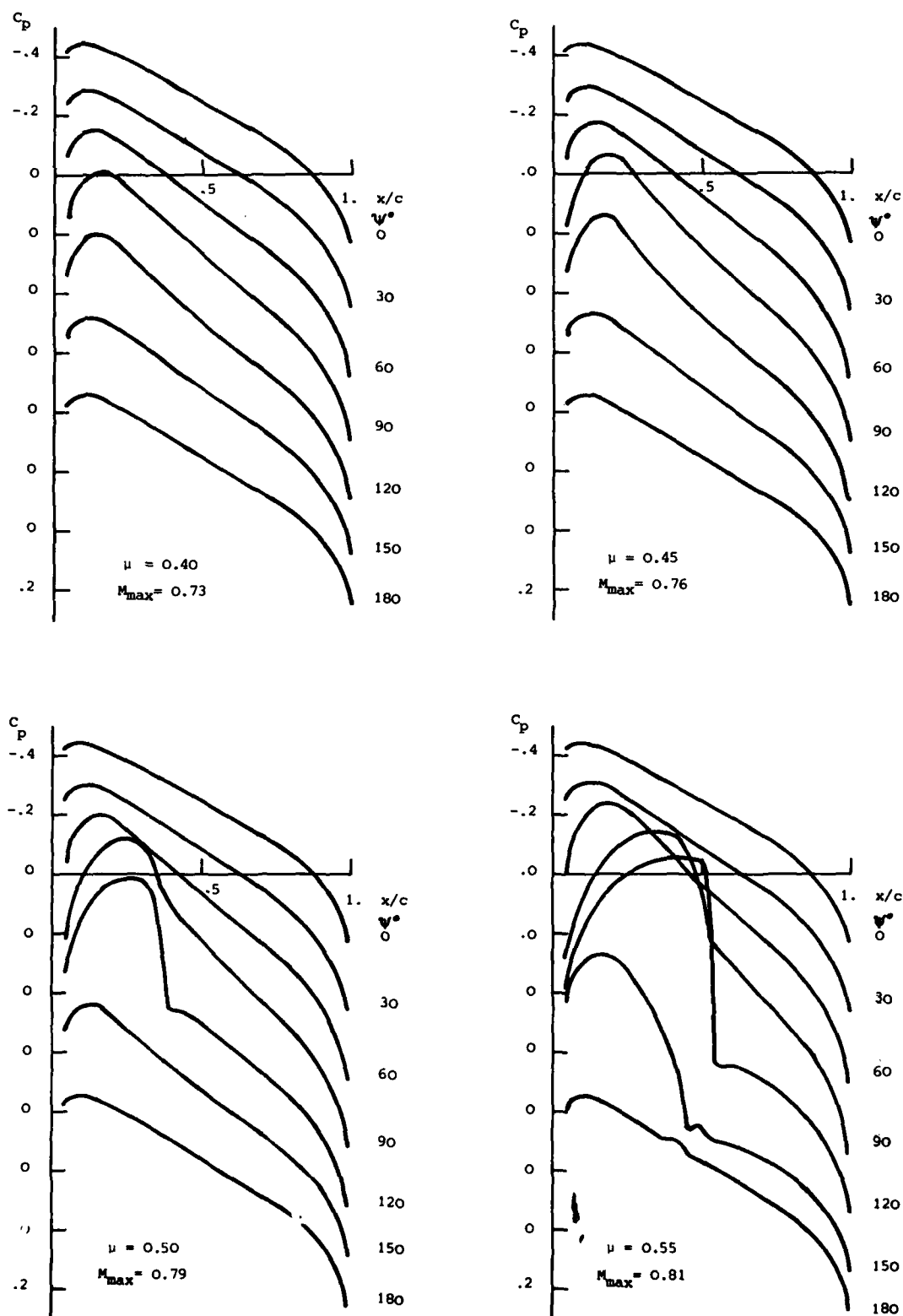
Fig.2 The trend of lift, pitching moment co-
efficient and center of pressure over one
period at $M_0 = 0.49$, $\alpha_0 = 2°$, $\mu = 0.36$ (NACA
0012, $\Delta\alpha = 0°$)

Fig.5 Chordwise pressure distributions for several advance ratios for M_0= 0.52 (NACA 0012, α_0= $\Delta\alpha$ = 0°)
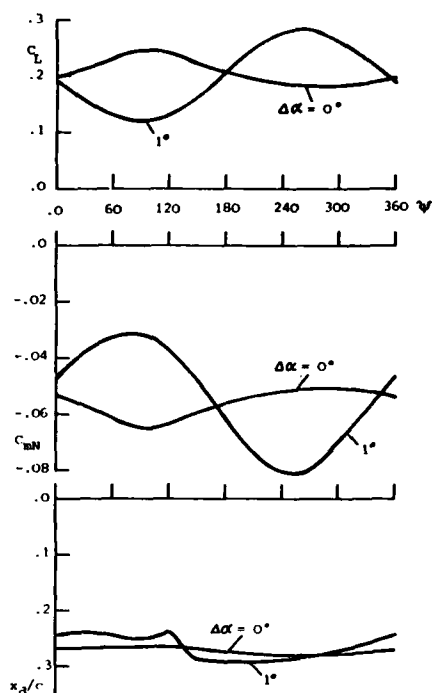
Fig.6 Aerodynamic coefficients over one period for two pitch angle amplitudes for $M_0 = 0.49$, $\alpha_0 = 2°$, $\mu = 0.36$ (NACA 0012)
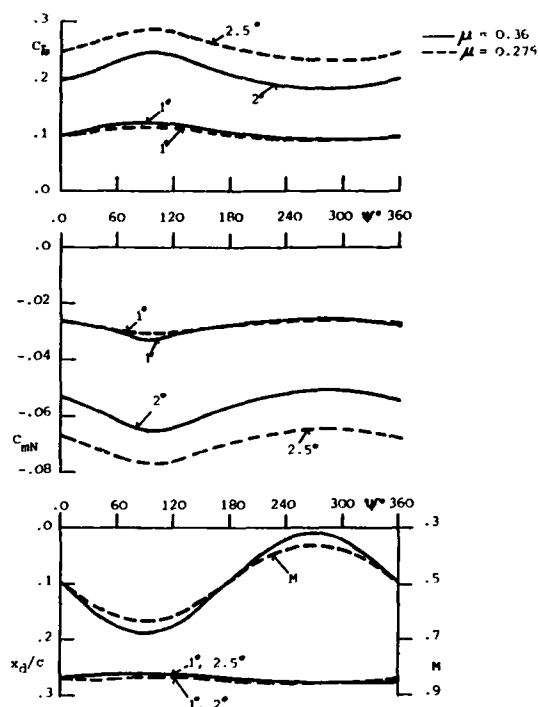
Fig.8 Aerodynamic coefficients over one period for $M_0 = 0.49$ (NACA 0012, $\Delta\alpha = 0°$)

$$M_0 = \frac{4.68 \cdot 10^{-3}}{K}$$
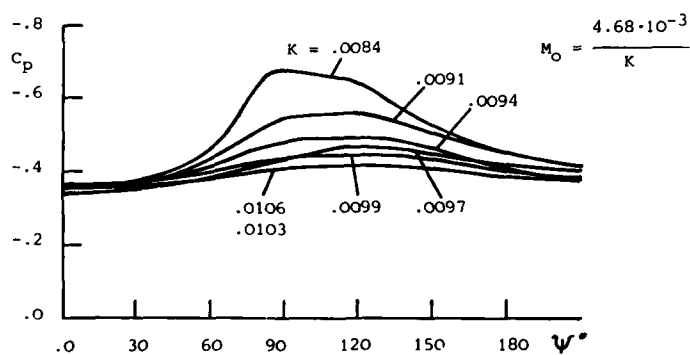
a) full-scale rotor

b) model rotor

$$M_0 = \frac{1.44 \cdot 10^{-2}}{K}$$
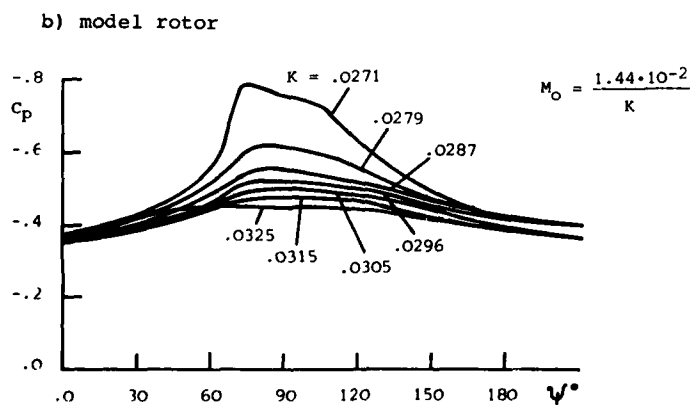
Fig.7 Pressure coefficients over half a period for $\mu = 0.445$ (NACA 0012, x/c = 0.233)
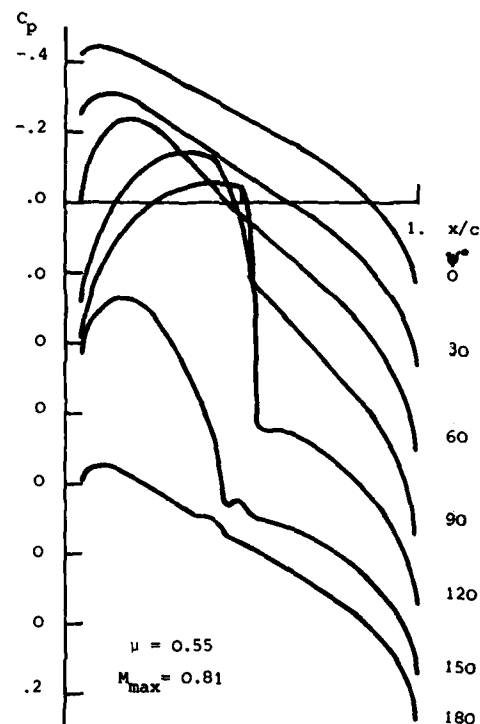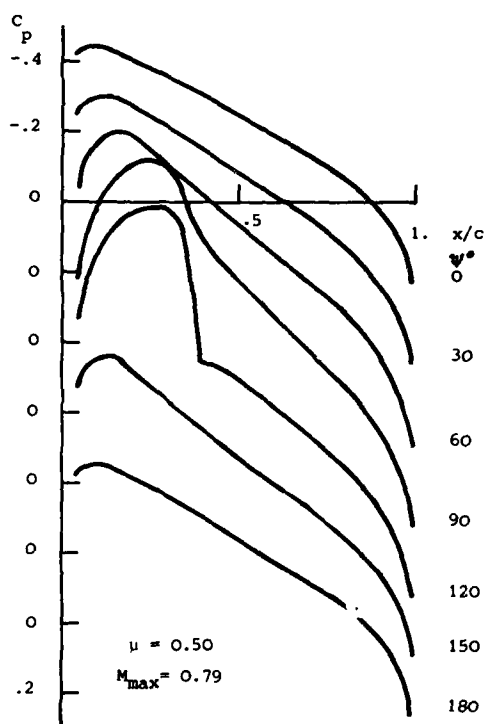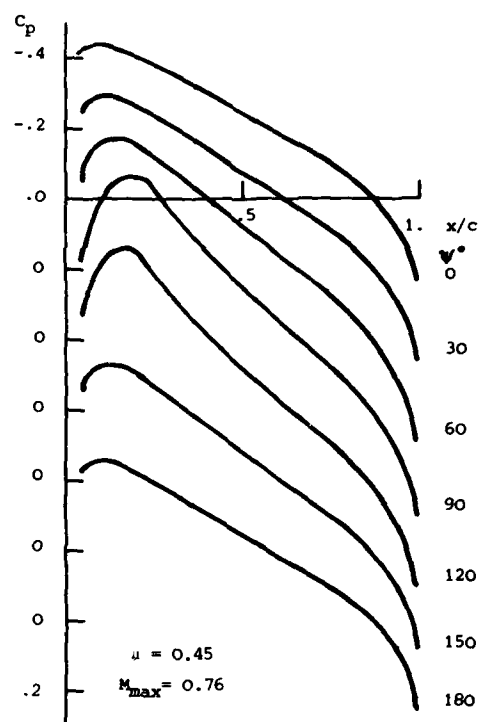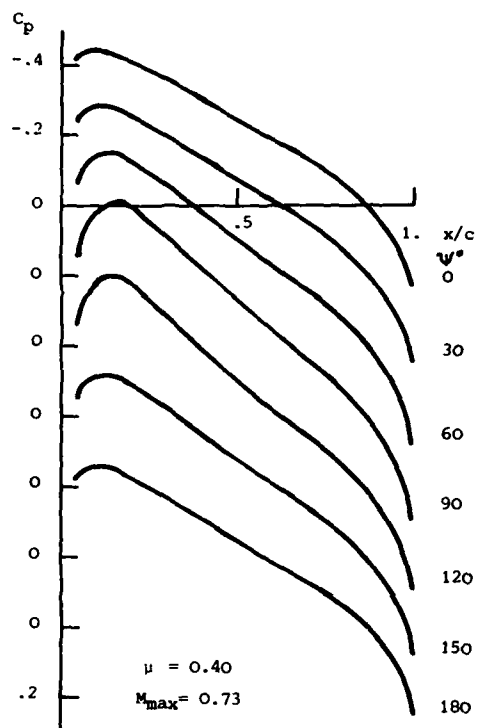
Fig.5 Chordwise pressure distributions for several advance ratios for $M_0 = 0.52$ (NACA 0012, $\alpha_0 = \Delta\alpha = 0°$)
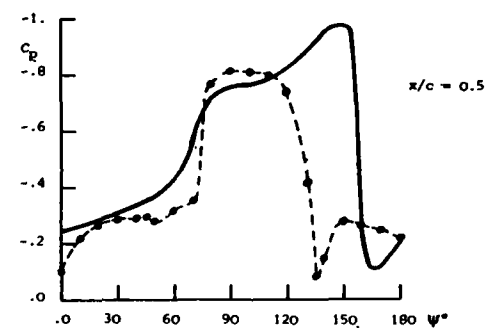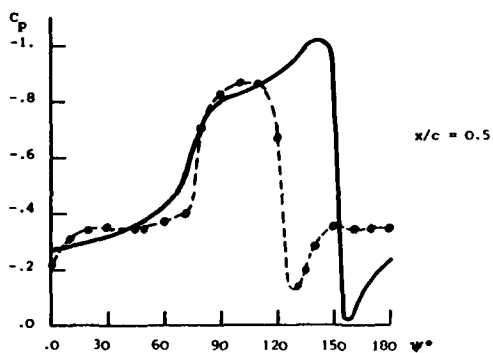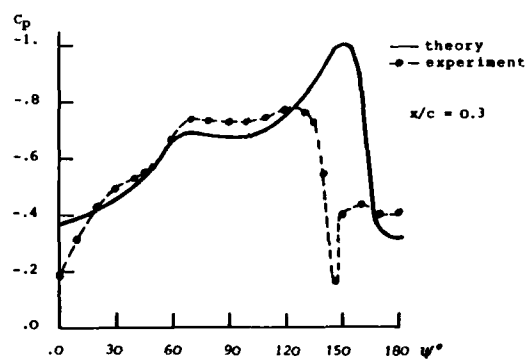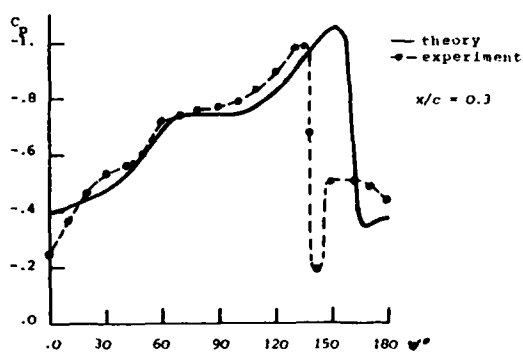
Fig.9 Comparison between theoretical and experimental pressure coefficients at 85.5% R, M_0= 0.54, μ = 0.55 (NACA 0013, α_0= $\Delta\alpha$ = 0°)

Fig.10 Comparison between theoretical and experimental pressure coefficients at 89.2% R, M_0= 0.55, μ = 0.55 (NACA 0012, α_0= $\Delta\alpha$ = 0°)
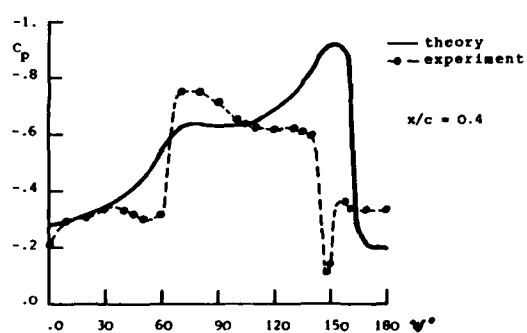
Fig.11 Comparison between theoretical and experimental pressure coefficients at 94.6% R, M_0= 0.57, μ = 0.55 (NACA 0010.5, α_0= $\Delta\alpha$ = 0°)
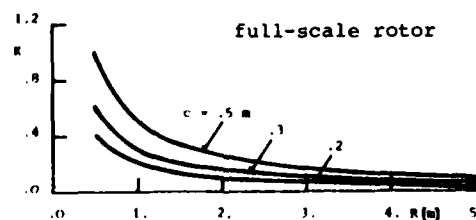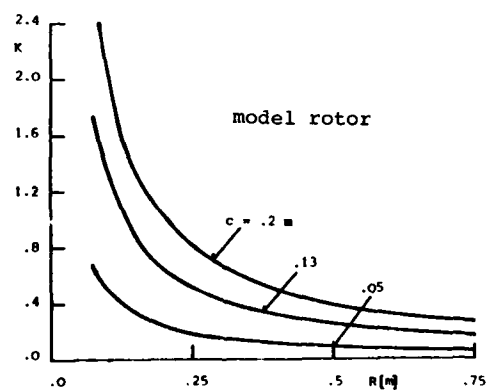
Fig.13 Dependence of the reduced frequency on radius and blade chord for a model rotor and a full-scale rotor
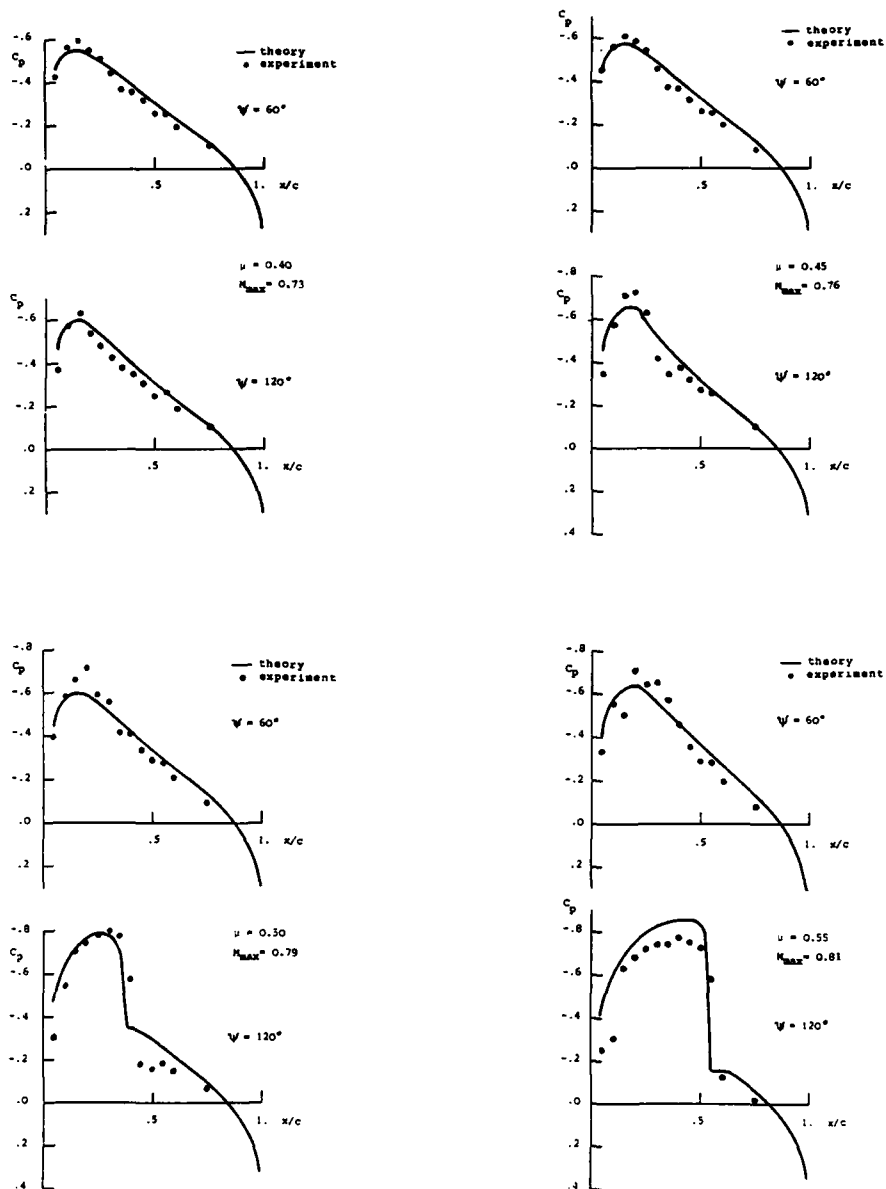
Fig.12 Comparison between theoretical and experimental pressure coefficients for several advance ratios, M_0= 0.52 (NACA 0012, α_0= $\Delta\alpha$ = 0°)

a) Lift coefficient vs radius

b) Pitching moment coefficient vs radius
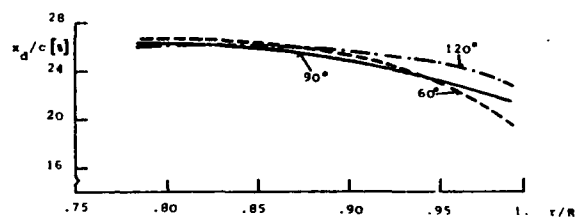
c) Center of pressure vs radius

Fig.15 Aerodynamic coefficients on the blade tip for several azimuth angles ψ for $M_T(90°)=$ 0.8 (NACA 0012, $\mu = 0.36$, $\alpha = 1°$)
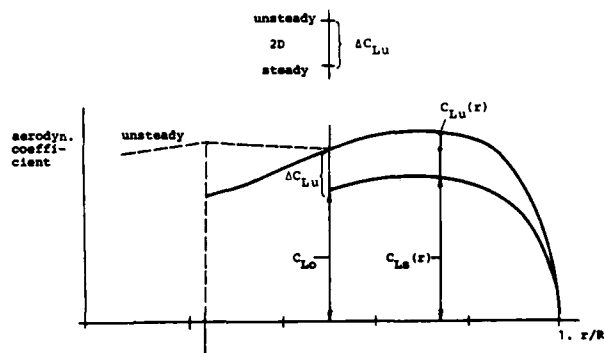
Fig.16 Model for coupling three-dimensional and unsteady effects on the blade tip

Fig.14 Chordwise pressure distributions for $M_T=$ 0.8 (NACA 0012, $\mu = 0.36$, $\alpha = 1°$)

COMMENTS ON SESSION No. 1
«ROTOR BLADE AERODYNAMIC CHARACTERISTICS»
by
J. GALLOT
Société Nationale Industrielle Aérospatiale
B.P. 13
Marignane
13725
France

Complementary articles dealing with analysis and synthesis of unsteady aerodynamic phenomena influence (stall, compressibility, tridimensional, etc ...) on the behaviour of a rotor were presented during this session which evidenced the manufacturers' concern not to develop hardly operational and verifiable computer codes leading to prohibitive computation times. The experimental approach is retained to control optimization of a mathematically designed rotor and determine the limits of existing methods. Efforts applied in basic research of unsteady stall and unsteady, compressible tridimensional effect must be continued even if manufacturers only retain the most simple and essential part of such research in their computer codes.

Every article states that rotor performance optimization will prove profitable for the manufacturers while new airfoils development and blade tip definition must be emphasized. A pure helicopter flying at more than 200 kts   could certainly be designed in the near future if present research efforts are kept up.

1. THE ROLE OF ANALYSIS IN THE AERODYNAMIC DESIGN OF ADVANCED ROTORS
by L. DADONE - Boeing Vertol - U \

This article thoroughly describes changes in methods and ideas at Boeing Vertol from 1965 till now shows that helicopter manufacturers made large progress in their understanding of the rotor's aerodynamic behaviour. Experimental research proceeds and helicopter design methods are developed along a course parallel to that of airplanes, with some delay however, considering the greater complexity of aerodynamic flows along blades.

The rotor optimization approach recommended by the present writer is quite realistic ; it is based on the use of relatively simplified computer codes taking essential effects into consideration :

— Lifting line theory + bidimensional characteristics of airfoils

— Prescribed wake model

— Unsteady aerodynamic effects

— Plan form, sweep effect, tip relief approximation

— Blade aeroelasticity

The need to verify theoretical optimization results with appropriate experiments in flight or wind tunnel and to set the validity limits of prediction tools is emphasized ; meanwhile, basic research must be continued for detail analysis of fundamental phenomena (Unsteady aerodynamics and aerodynamic flow at blade tips) and computer codes, specific to a particular problem, must be processed to define the parameters used in solving such problem.

A helicopter flying at more than 200 knots could be designed only by close, interrelated optimization of plan form at blade tip and selection of airfoils in the same area as shown in Fig. 8 describing plan form influence on performance in level flight.

This paper also raises a very old question : Could the present C_{m_o} limit be extended to improve maximum lift and drag divergence characteristics ; Could a sweptback tip extend C_{m_o} and would this tip really have beneficial effects on dynamic stall ?

One could only agree with the idea that rotor optimization in hover and forward flight is a profitable field of research (see Fig. 3) provided :

— an acceptable compromise is found between simplification and sophistication of prediction methods,

— the same compromise applies between basic research, experimentation in flight or in wind tunnel and results processing with computer codes,

— technological aspects inherent to such optimization are not neglected.

2. REPRESENTATION OF AIRFOIL BEHAVIOUR
by T.S. BEDDOES - W.H.L. - UK

The conventional «time delay» method used to synthetize dynamic stall of an airfoil is perfectly adapted to a rotor computer code. Such method is not accurate enough however in the case of airfoils stalling indifferently at trailing or leading edge depending upon instant operating conditions.

Following a detail analysis of bidimensional steady and unsteady airfoil tests, the present writer succeeded in representing non linearities resulting from separation of leading edge or induced by shock, the effect of trailing edge separation and the influence of a vortex flowing along the airfoil. The method used in this case requires knowing 10 constants per Mach number deduced from steady, bidimensional tests ; the above mentioned constants as well as three time constants are used to reevaluate the three airfoil characteristics (C_z, C_m, C_x) in unsteady air flow. Results thus obtained (see Fig. 20) are quite satisfactory and it would be interesting to verify the accuracy of this synthetizing method on airfoils other than NACA 0012.

The interest of this synthetizing method is that it is based on the analysis of aerodynamic phenomena dictating the unsteady behaviour of an airfoil ; its principles could possibly be used to develop an inverse method applied to the definition of an airfoil meeting unsteady specifications.

3. HELICOPTER AIRFOILS AND BLADE TIPS DESIGNS
by J.J. THIBERT and J.J. PHILIPPE - ONERA - France

This article written by a group of ONERA scientists is very interesting in that it presents the results of a research programme initiated approximately 10 years ago.

The advantages of close cooperation between scientific organizations and manufacturers as well as the need to extend such cooperation to rotor aerodynamic research at an international level are also mentioned.

– The ONERA group studied an airfoil family 0A2XX whose performance is close to specification requirements (see Fig. 12) and comparable to the results obtained by other scientists (see Article 1). A more accurate comparison of results obtained on airfoils tested in various wind tunnels with various Reynolds Numbers would probably prove quite useful to define the state of the art as it now stands and to answer the following question : «Can we expect significant gains in rotor performance as a result of improvements in helicopter blade airfoils ? » It is essential to develop yet further our understanding of unsteady aeroelastic phenomena (stall, compressibility, etc ...) to optimize airfoils with, perhaps, higher C_{m_0} values while considering unsteady criteria closer to effective operating conditions on helicopter blades.

– As concerns blade tips, a theoretical and experimental approach evidenced the need to include unsteady effects and radial flow effects and emphasized the importance of tridimensional effects beyond 0.95 R. Computer codes developed to study blade tips ought to consider vortex interactions and should, in the short run, be capable of processing lift, even in an approximate manner, and providing drag data for a new tip shape.

Application of already existing methods allowed developing a rather promising (parabolic sweptback) blade tip PF2 that should give a 5 to 8 % rotor power gain as compared to a straight tip (see Fig. 27) ; this gain remains to be confirmed by full scale experimentation that is more representative of the blade's aeroelasticity aspects.

It is not unnecessary to remind, outside the framework of the present article, how difficult it is to form an objective opinion on the contradictory results obtained by different scientists in the blade tip research field while there probably are multiple causes for such discrepancies (Performance measurements accuracy, aeroelasticity influence, blade technology . . .).

4. CALCULATIONS OF 3D UNSTEADY TRANSONIC FLOW AROUND ROTOR BLADES
by H. STAHL - MBB - Germany

This article is an indication of the manufacturers' concern in integrating tridimensional, unsteady aerodynamic effects with the least expense into their rotor aerodynamic computer codes; to do so, they derive such codes from conventional codes applied to aircraft. A simplified method is suggested to associate a 3D steady analysis taking a radial speed gradient into account with a 2D unsteady lift analysis (variable Mach No and incidence). It is envisaged, as a future extension, to include deflection and vortex influence of the previous blade in this method.

The final objective : application of aerodynamic coefficients (C_z, C_m) calculated with this method to a rotor model, is still far off. It is regrettable that no indication is given as to C_x evaluation, such evaluation is essential from a performance standpoint, or as to computation times expected in the ultimate version.

A rather interesting remark is made concerning the need to study similarity rules applicable to unsteady tridimensional effects ; ignoring these rules might lead to an erroneous interpretation of results obtained after mockup tests in wind tunnel (different aspect ratio, reduced frequency and, chiefly, different reduced frequency gradients spanwise).

Commentary on Session I

Design and Prediction for Rotor Blade Aerodynamics

by

Warren H. Young, Jr.
Structures Laboratory, USARTL (AVRADCOM)
NASA Langley Research Center
Hampton, Virginia 23665

SUMMARY

The state of rotor blade aerodynamic calculation methods is reviewed. Two factors that limit the accuracy of these methods for design of airfoils and blade tips and the primary factor limiting the prediction of rotor performance are identified. A survey of the future demands on blade aerodynamics leads to the prediction that a sharp upturn in the results expected from aerodynamicists is imminent.

INTRODUCTION

The importance of separated flow to rotor performance has long been recognized. Figure 1 was published by Frank Harris in 1969.[1] Based on oscillating airfoil tests and simple yaw corrections, the thrust of a heavily stalled rotor was predicted at low advancing tip Mach numbers. This result was a significant advance in rotor prediction capability. The four papers[2-5] presented in this session on rotor blade aerodynamics do not represent an attempt to improve the analyses of 12 years ago. Instead, they are a response to new requirements. The helicopter aerodynamicist is now expected to not only improve performance but also to design airfoils and blades that minimize separated flow and reduce dynamic blade loads.

The acceptance in 1969 of rotor calculations for heavily stalled rotors was a turning point for aerodynamicists. Aerodynamicists began to be expected to "predict with greater confidence the non-linear rotor behavior near the flight boundaries."[3] Not only performance but also unsteady control system loads and rotor stability calculations are now demanded of the aerodynamicist. An increase in expectations has also taken place in the area of design based on analyses. New helicopters now have airfoils and tip shapes that are aerodynamically designed specifically for the mission of that particular helicopter. The four papers presented in this session are the basis for the argument that another sharp increase in the demands on and expectations from the aerodynamicist is imminent.

DISCUSSION

Areas of Research

The four papers in this session demonstrate the two major thrusts of current work in rotor blade aerodynamics, transonic tips and airfoils. Table I categorizes the four papers by areas of application.

TABLE I.   AREAS OF RESEARCH OF SESSION PAPERS

	2D Unstalled	Dynamic Stall	Transonic Tips
Understand Phenomena		Beddoes	
	Thibert and Phillipe		Thibert and Phillipe
Design Blades	Dadone		Dadone
Predict Airloads	Stahl	Beddoes	Stahl

The columns indicate that the blade is being analyzed in two pieces: two-dimensional analyses on the inboard section of the blade and three-dimensional tip analyses. Stahl[5] clearly recognizes the importance of integrated blade analysis but uses two analysis schemes for computational efficiency. The rows of Table I divide the papers into categories of: basic research or understanding the physical flow phenomena, blade design, and prediction of the aerodynamics of a complete rotor. The demand for lower cost per case increases dramatically from top to bottom. For example, in order to understand the flow processes at work in dynamic stall Beddoes[3] uses data from very expensive model tests. However, he must construct very efficient computer models because a rotor analysis may require an estimated 30,000 dynamic stall calculations. The papers by Dadone[2] and by Thibert and Phillipe[4] are aimed primarily at design. Both authors use the best available analysis (almost regardless of computer cost), but not the more expensive method of parametric experiments. However, the need for more accurate analyses and the need for more confidence in the calculated performance of the blade after it is installed on the rotor have been made clear by these papers.

Limitations on Accuracy

Two of the immediate problems that limit the accuracy of blade aerodynamics involve separated flow. The first problem is dynamic stall prediction. Figure 2 shows results from a tunnel spanning model in the United Technolog as main wind tunnel.[6] The wing is swept 30° and is oscillated in pitch

to generate dynamic stall data. The significant differences in stall behavior caused by blade yaw are illustrated in figure 2. This result can probably be modeled by Beddoes' method. However, data are available for only one airfoil at one sweep angle, and this is insufficient experimental data to allow confident airfoil design. Either more experimental data or a viscous flow calculation scheme that incorporates unsteady sweep is needed.

A second problem involving a separated flow phenomenon that cannot be adequately modeled[7] is shown in figure 3. The tip vortex begins with boundary layer separation of the flow around the tip as far forward as the quarter-chord point for rectangular tips. The low pressure area caused by this vortex moves inboard as it extends to the trailing edge. This causes an area of high lift and nose-down pitching moment near the tip. Figure 4 is a calculation by Maskew[8] using an incompressible panel method to model the tip vortex flow over the upper surface of a rectangular wing. This method has been correlated with some experimental results for rectangular tips, but the effect of tip shape on the size, shape, and location of the tip vortex is almost unknown. Research on tip shapes is being carried out by a cooperative NASA/DFVLR program designed to describe the unsteady pressures about four tip shapes (figure 5) that are oscillating in pitch. This research will yield much information about the effect of blade planform on tip vortex size, shape, and location over the upper surface of the blade just downstream of the trailing edge.

These two separated flow problems illustrate that research on airfoil aerodynamics and blade tip design is not complete. However, no matter how accurate the calculations for the design of the airfoil or the tip, these components must be made part of the calculation scheme for an entire rotor. Rotor calculations have a limit in accuracy that is independent of the accuracy of the calculations for airfoil alone or blade alone.

The primary problem faced by aerodynamicists who apply new airfoils to blades with non-rectangular planforms is uncertainty about the blade angle of attack. The angle of attack of the blade is controlled by the vortices in the wake; the vortices are controlled by the blade lift and planform; and the blade lift is controlled by the angle of attack. The weak links in this computational circle are the effect of blade planform on vortex size and location and the uncertainties in the position of the wake vortices. Table II is an attempt to summarize the state of the art in the calculation of the

TABLE II. ROTOR BLADE SURFACE PRESSURE CALCULATION STATUS FOR ADVANCED TIP SHAPES

Rotor Blade Pressure as a Function of:	Inboard Part of Blade		Tip Region	
	Limitations	Accuracy	Subsonic	Transonic
Mean value, x/c, r/R	Wake flow	±5%		Fixed wing code
1-per-rev, x/c, r/R	Components only	±5%	Only one uncorrelated code; includes tip vortex	Limited correlation
N-per-rev, x/c, r/R	Wake in development – subsonic stall uncorrelated			No correlation
Vortex interaction, t	Unstalled, subsonic ±20%		No work	No work

chordwise and spanwise distribution of pressure. Such pressure distributions are required for calculation of noise, gust response, blade loads, and even stability. The accuracy estimates do not apply to rectangular planformsbut they do apply to advanced blade tip shapes. Several analyses which have proved accurate for rectangular planforms are expected to differ by 5% even for the simple case of prediction of lift in hover when applied to advanced tip shapes. The inboard portion of the blade is calculable by two-dimensional strip theories except for close interaction with vortices from other rotor blades. The limitation on accuracy is the uncertainty in wake prediction. For example, there is no analysis available that accounts for the effect on the blade of shed vorticity in the wake due to lift variations at frequencies above 1-per-rev. However, such calculations are routinely performed for fixed-wing flutter calculations. The purpose of these arguments is not to discourage the development of better calculations for airfoils or blade tips, but to encourage the development of wake models that are consistent with even the present accuracy of blade aerodynamic calculations.

The importance of integrating the design of airfoils and blade shapes has been demonstrated by Bingham.[9] The idea of integrated design is to first define the performance requirements for one particular rotor that operates in a known flight envelope. The basic calculation tool is an array of rotor performance programs for both hover and forward flight. Iterative calculations for combinations of blade chord, shape, twist, and airfoils are used to design the blade. This iterative procedure is required by the interdependence of the parameters that affect rotor performance. The success of this design procedure has been validated by wind tunnel testing.[10] The primary limitation on this method is uncertainty about the rotor wake models.

Future Requirements

Just as there was a rise in expectations of the results of aerodynamic calculations after 1969, there will soon be another dramatic increase in the results demanded of aerodynamicists. Figure 6

depicts, in an oversimplified manner, the inputs received by the blade aerodynamicist and the outputs required. The solid line represents the present computational cycle. Aerodynamic solutions for blades are expected to define forces for a rotor with a wake that is representative of trim in order to calculate rotor performance, dynamic loads, and stability. The broken lines represent new computational loops that will put expanded demands on the blade aerodynamic calculations. The use of active controls such as higher harmonic control, multicyclic control, dynamic stall suppression, or gust alleviation control will require higher frequency unsteady aerodynamics. The dashed loop indicates that better rotor wake calculations will require more precise descriptions of both the shed wake and the tip vortices that are generated by the blade. Eventually noise theories will need time histories of pressure distributions on the blade and even the flow field surrounding the blade. Thus the impression that there are multiple methods available for blade design and that only a few capabilities need to be added to existing analyses breaks down when the total array of tasks confronting the blade aerodynamicist is examined.

CONCLUSIONS

The papers in the session demonstrate that analytical and empirical methods are very effective in three areas of blade aerodynamics: (1) design of airfoils below stall by two-dimensional, steady analyses, (2) prediction of unsteady airfoil performance including dynamic stall, and (3) design of transonic tips without separated flow. The need is immediate for adding three-dimensional effects to dynamic stall empirical methods, for adding dynamic stall criteria to airfoil design, and for adding tip vortex models to transonic tip design. At present, the application of blade aerodynamics to rotors is limited by uncertainties in the rotor wake models for unsteady flow and advanced tip shapes. Furthermore, the future demands on aerodynamicists will include detailed, unsteady pressure distributions for the calculation of noise, gust response, response to active controls, and blade-vortex interaction.

REFERENCES

1. Harris, Franklin D.; Tarzanin, Frank J., Jr.; and Fisher, Richard K.: Rotor High Speed Performance, Theory vs. Test, J. Am. Hel. Soc., Vol. 15, July 1970, pp. 35-44.

2. Dadone, L.: The Role of Analysis in the Aerodynamic Design of Advanced Rotors, AGARD CP-334, London, U. K., May 1982.

3. Beddoes, T. S.: Representation of Airfoil Behaviour. AGARD CP-334, London, U. K., May 1982

4. Thibert, J. J. and Philippe: Etudes de Profils et d'Extremites de Pale d'Helicoptere. AGARD CP-334, London, U. K., May 1982.

5. Stahl, H.: Calculation of 3D Unsteady Transonic Flow Around Rotor Blades. AGARD CP-334, London, U. K., May 1982.

6. St. Hilaire, A. L.; Carta, F. O.; and Jepson, W. D.: Influence of Sweep on the Aerodynamic Loading on an Oscillating NACA 0012 Airfoil, NASA CR-3092, 1979.

7. Gray, R. B.; McMahon, H. M.; Shenoy, K. R.; and Hammer, M. L.: Surface Pressure Measurements at Two Tips of a Model Helicopter Rotor in Hover, NASA CR-3281, May 1980.

8. Maskew, B.: Influence of Rotor Blade Tip Shape on Tip Vortex Shedding--An Unsteady, Inviscid Analysis, presented at the 36th Annual Forum of the American Helicopter Society, Preprint No. 80-6, May 1980.

9. Bingham, Gene J.: The Aerodynamic Influences of Rotor Blade Airfoils, Twist, Taper, and Solidity on Hover and Forward Flight Performance. Proceedings of the 37th Annual Forum, American Helicopter Soc., May 1981, pp. 37-50.

10. Berry, John D.: Performance Testing of a Main Rotor System for a Utility Helicopter at 1/4 Scale, NASA TM-83274 (AVRADCOM TR 82-B-3), April 1982.
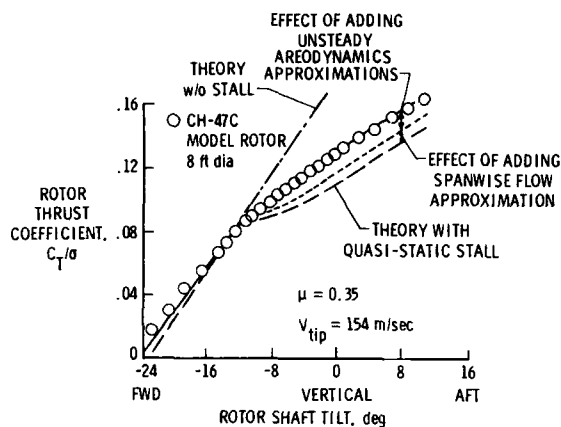
Figure 1. The incorporation of yaw and dynamic stall into the performance calculation of a heavily stalled rotor (Ref. 1).
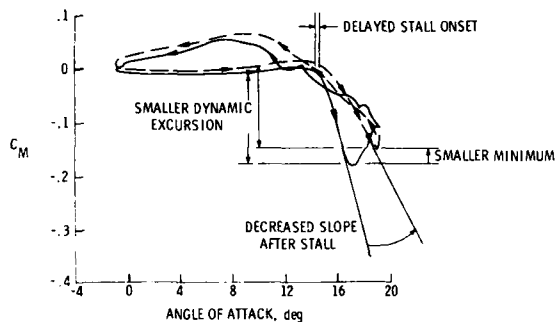
Figure 2. Summary of the effects of yaw (Dotted line is 30° yaw, and solid line is unyawed) on dynamic stall pitching moment hysteresis (ref. 6).
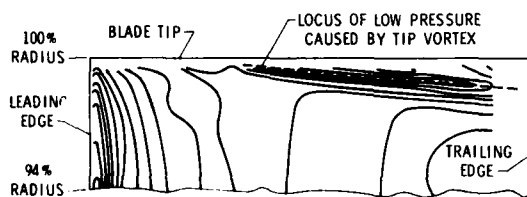
Figure 3. Measured pressure contours on the upper surface of a rotor blade in hover (Ref. 7).
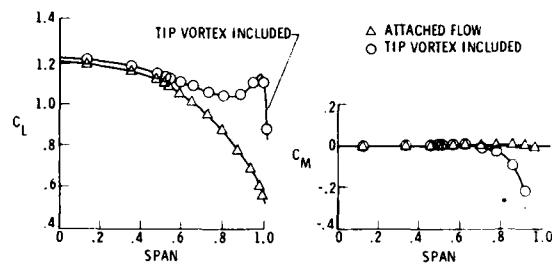
Figure 4. Calculation of the effect of tip vortex formation on the lift and moment of a rectangular wing (Ref. 9)
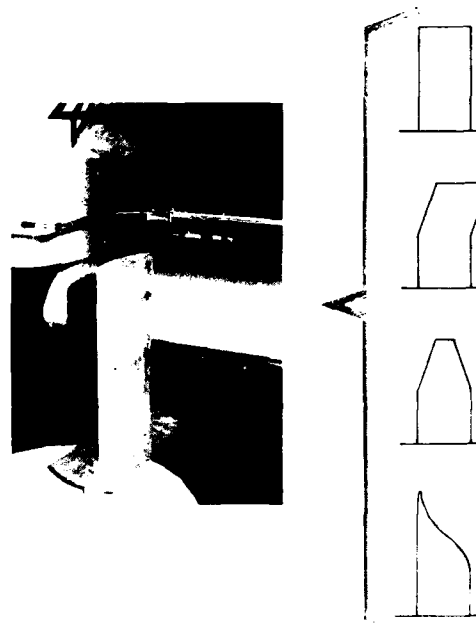
Figure 5. Four tip shapes instrumented for unsteady pressure measurements for tip vortex formation and the DFVLR oscillating wing mount.

ENVIRONMENT OF BLADE AERODYNAMICS CALCULATIONS
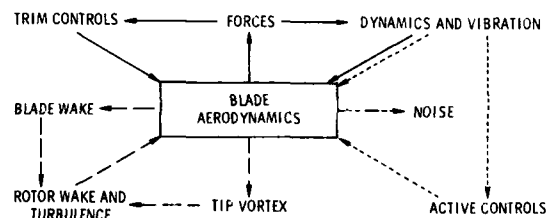
Figure 6. Present (solid lines) and future demands on blade aerodynamic calculations.

AERODYNAMIC RESEARCH ON TIPVANE WINDTURBINES

by
G.J.W. van Bussel
Th. van Holten
G.A.M. van Kuik
Delft University of Technology
Department of Aerospace Engineering
Kluyverweg 1
2629 HS DELFT
The Netherlands

SUMMARY

Tipvanes are small auxiliary wings mounted at the tips of windturbine blades in such a way that a diffuser effect is generated, resulting in a mass flow augmentation through the turbinedisc. For the prediction of aerodynamic loads on the tipvane wind turbine use is made of the accelerationpotential, on which an expansion method is applied. In its simplest form, this method can essentially be classified as a lifting line approach, however, with a proper choice of the basic loaddistributions of the lifting line, the numerical integration of the pressurefield becomes one dimensional. The integration of the other variable can be performed analytically.

This method based on a mainly analytical approach has the advantage of giving a better insight in the peculiarities of a specific configuration.

The complete analytical expression for the pressure field consists of two series of basic pressure fields. One series is related to the basic load distributions over the turbineblade, and the other series to the basic load distribution over the tipvane. In addition another basic pressure field related to a triangular loaddistribution over the turbineblade and the tipvane was needed, in order to take care of the "lift transfer" from turbineblade to tipvane.

The coefficients in these pressure field expressions are a priori unknown, and are determined by a boundary condition requiring the flow to be tangential on both turbineblade and tipvane. A numerical procedure then yields the coefficients of the basic pressure fields.

1. Introduction

The research on tipvaneturbines aims at a process improvement of the wind energy conversion system, which is more than component improvement such as efficient aerofoils and optimized transmission systems.

These latter developments make it possible for a modern windturbine to approach the Betz maximum power coefficient. However, process improvements are possible based on flow phenomena which are not consistent with the assumptions made in Betz theory. Power coefficients far above the Betz maximum value are possible when for example forces are applied perpendicular to the winddirection and when viscous effects play an important role.

At the Delft University of Technology, the windenergy group investigates the effect of tipvanes, which are small auxiliary wings at the end of the turbine blades (fig. 1), inducing a mass flow augmentation by the creation of a Venturi flow.

At the Cambridge and Amsterdam BHRA Wind Energy System meetings (ref. 1 and 2) papers have been presented concerning the tipvane concept. There the principal flow mechanisms from theoretical considerations and as observed in flow visualization studies were reported and also test results of tipvane drag reduction were shown. The present status of the research is that the main flow mechanisms are understood, and the principal problems have been solved. A short survey will be given in this paper, whereafter one of the research fields is treated more in detail: the analytical aerodynamic work, accompanied by experimental verification.

2. Present status of the tipvane research

Since the demonstration of the mass flow augmentation (ref. 2) the following other important results have been obtained:

- the tipvane drag can be reduced to a nearly twodimensional level, as will be shown in the next chapter. The phenomenon of side edge suction, a suction force acting on the tips of the tipvane, comparable with leading edge suction, appeared to have a great influence on the drag.
  Fig. 2 shows that due to an asymmetric lift distribution on the tipvane, and due to the fact that the relative flow direction does not coincide with the rotational direction, the side edge suction can have a component in drag direction (a force tangential to the disc plane of the rotor). A proper adjusting of the tipshape can eliminate this effect (ref. 3).
- Experiments with screens of various porosities, simulating (by dissipation) the energy extraction by turbine blades, showed that the amount of energy is really extractable. Gross C_p values of 1.5 are measured which is about 2.5 times the Betz maximum (ref. 4).
- A very promising development has been started with the beneficial use of viscous effects: for the energy extraction by diffuser type windturbines, such as shrouded turbines and tipvane turbines, values have been measured which are about 25% higher than can be expected by potential theory. This is due to an energy transport from the outer flow into the wake behind the turbine, by turbulent mixing in the region where this wake is diffusing. This extra energy can be extracted by the rotor: according to theoretical extrapolations for a tipvane turbine with artificially stimulated mixing, power augmentation factors in the order of 10, when compared with conventional turbines, must be possible. Refs.4 and 5 describe this phenomenon more in detail.
- Theoretically as well as experimentally the main flow mechanisms are understood and the next step will be the verification in atmospheric conditions.
  Therefore, and in order to carry out aeroelastic experiments, a field test installation is planned. In a later stage the installation can be modified into a first prototype.

The aerodynamic work on the tipvane rotor has comprised several branches. Many qualitative and quantitative experiments have been carried out on a modelscale. Simultaneously various theoretical models have been developed in order to get better understanding of the experimental results and to obtain design methods for forthcoming full scale applications.

Special emphasis is given in this paper to the theoretical analyses, yielding aerodynamical loads on the tipvane windturbine, with references to theoretical and experimental verifications.

3. Governing equations

3.1 The method of the velocity potential

The basic governing equations for incompressible inviscid flows have been established already in the 18th century by Leonhard Euler, who developed the well known Euler equations expressing the conservation of momentum in the fluid, as well as the equation of continuity expressing the conservation of mass. These equations take the form:

$$\text{div } \underline{V} = 0 \quad \text{(continuity)} \tag{3-1}$$

and

$$\rho \frac{D\underline{V}}{Dt} = - \text{ grad } p \quad \text{(Euler equation)} \tag{3-2}$$

Both Lagrange and Laplace have developed the method of solving this set of equations, by introducing the concept of the velocity potential. The velocity potential $\phi(x,y,z)$ is defined as a scalar function such that

$$\underline{V} = \text{grad } \phi \tag{3-3}$$

It is easily shown that such a scalarfunction $\phi(x,y,z)$ always exists in flow regions where the rotation of the fluid particles is zero:

$$\text{rot } \underline{V} = 0 \tag{3-4}$$

or

$$\frac{\partial u}{\partial y} - \frac{\partial v}{\partial x} = 0, \quad \frac{\partial u}{\partial z} - \frac{\partial w}{\partial x} = 0, \quad \frac{\partial v}{\partial z} - \frac{\partial w}{\partial y} = 0 \tag{3-5}$$

Writing the equation of continuity in terms of the velocity potential by substituting (3-3) into (3-1) results in the equation of Laplace:

$$\text{div grad } \phi = 0 \tag{3-6}$$

or

$$\frac{\partial^2 \phi}{\partial x^2} + \frac{\partial^2 \phi}{\partial y^2} + \frac{\partial^2 \phi}{\partial z^2} = 0 \tag{3-7}$$

3.2 The method of the acceleration potential

Prandtl indicated in 1936 an alternative way to treat three-dimensional flows in which the velocity perturbations are small compared with the undisturbed velocity w. The assumption that all higher order perturbations may be neglected is directly used to simplify the basic flow equations (3-1) and (3-2). For incompressible, inviscid flows this simplification works out as follows. Substituting the equations (3-5) expressing rot $\underline{V} = 0$ into the Euler equations leads to:

$$\frac{\partial u}{\partial t} + 1/2 \frac{\partial}{\partial x} (u^2 + v^2 + w^2) = - \frac{1}{\rho} \frac{\partial p}{\partial x}$$

$$\frac{\partial v}{\partial t} + 1/2 \frac{\partial}{\partial y} (u^2 + v^2 + w^2) = - \frac{1}{\rho} \frac{\partial p}{\partial y} \tag{3-8}$$

$$\frac{\partial w}{\partial t} + 1/2 \frac{\partial}{\partial z} (u^2 + v^2 + w^2) = - \frac{1}{\rho} \frac{\partial p}{\partial z}$$

Now writing

$$u = u' \quad , \quad v = v' \quad , \quad w = W + w' \tag{3-9}$$

where u', v' and w' are small perturbations, substituting this into (3-8), linearizing and using the linearized expression rot $\underline{V} = 0$, leads to:

$$\frac{\partial u'}{\partial t} + W \frac{\partial u'}{\partial z} = - \frac{1}{\rho} \frac{\partial p}{\partial x} \quad , \quad \frac{\partial v'}{\partial t} + W \frac{\partial v'}{\partial z} = - \frac{1}{\rho} \frac{\partial p}{\partial y} \quad , \quad \frac{\partial w'}{\partial t} + W \frac{\partial w'}{\partial z} = - \frac{1}{\rho} \frac{\partial p}{\partial z} \tag{3-10}$$

The first of these equations is then partially differentiated with respect to x, the second with respect to y, and the third with respect to z. Summing and using the linearized continuity equation

$$\frac{\partial u'}{\partial x} + \frac{\partial v'}{\partial y} + \frac{\partial w'}{\partial z} = 0 \tag{3-11}$$

then yields:

$$\frac{\partial^2 p}{\partial x^2} + \frac{\partial^2 p}{\partial y^2} + \frac{\partial^2 p}{\partial z^2} = 0 \tag{3-12}$$

which is Laplace's equation, where the Laplace operator div grad works upon the pressure p. Eq. (3-12) is valid in steady as well as unsteady flowfields, if as assumed during the derivation, the undisturbed velocity W is a constant, independent of the space- and time coordinates. Instead of the pressure p, one can also put the pressure perturbation p' = p - p_∞ in (3-15). For simplicity the notation p(x,y,z) will in the following always be used for the field of pressure perturbations. The field p(x,y,z) is a characteristic scalar function for the flow field, just like the velocity potential ϕ(x,y,z). The essential difference between p and ϕ is the fact that in incompressible flows the function p(x,y,z) can never exhibit discontinuities in the free flow away from the physical boundaries, in contrast to the function ϕ(x,y,z) that does show discontinuities.

4. Asymptotic considerations

In the derivation of solutions of the Laplace eqs (3-7) and (3-12), use can be made very often of asymptotic expansion techniques. Although the application of asymptotic theory in aerodynamics seems to be a rather recent development it has already been used, at least in an intuitive way, by Ludwig Prandtl.
When he developed his lifting line theory for the determination of lift and drag on a straight wing in steady parallel flow, there where undisputably asymptotic considerations present. The "far field" viewpoint in this theory is evident, it has even supplied the name "lifting line" theory. Far from the wing, assuming a reasonable large aspect ratio, the forces on it are thought to be concentrated along a straight line. But also the "near field" philosophy was present expressed in the application of two-dimensional aerofoil theory within the lifting line model of Prandtl.
In the modelling of the flow phenomena of the tipvane windturbine the asymptotic approach has proven to be succesful. It is often possible to reduce a complex flow problem into several parts, each with two characteristic length scales. It is then possible to find a solution in terms of an asymptotic expansion. Such a solution consists of "near field" terms, "far field" terms and "common field" terms.
The "near field" terms have been derived by asymptotical considerations close to the lifting surface, and the "far field" terms by application of asymptotics for the flow far away from the aerodynamical active surface(s).
The "common field" terms in the solution are introduced by the simple fact that the "near field" terms in the solution do have a "far field" effect and vice versa. With the common field terms the "far field" effect of the "near field" is cancelled and simultaneously the "near field" effect of the far field terms.

With these asymptotic expansions, models have been developed for the flow around the tipvanes, for the conventional horizontal axis windturbine in steady parallel flow, for T-tail interference of two lifting surfaces and finally a first order model for the complete tipvane configuration. These models will be discussed in more detail in the following chapters.

5. First order solution for the flowfield of isolated tipvanes

5.1 The boundary value problem for an isolated rotating tipvane
The various coordinate systems used in this chapter are depicted in figs. 3, 4, 5, 6, 7 and 8.

The (x_r, y_r, z_r) coordinate system rotates at a radius R with the tipvane (Fig. 3). The (x_T, y_T, z_T) coordinate system of the tipvane is defined with respect to the (x_r, y_r, z_r) system in such a way that it can be obtained by rotating the (x_r, y_r, z_r) around the y_r-axis over a "sweepangle" Λ, followed by a rotation around the already swept x_r-axis (fig. 4). In this way the tipvanecoordinate system is obtained, and the tipvane is defined by

$$|x_T| \leqslant \frac{c_T}{2} \; , \quad y_T = (R - \gamma z_T) - [(R - \gamma z_T)^2 - x_T^2]^{\frac{1}{2}} + y_{T_C}(x_T, y_T) \; , \quad |z_T| \leqslant \frac{b_T}{2} \qquad (5\text{-}1)$$

The right hand side of this formula consists of two parts. The first part represents in linearized theory the curvature of the circular track covered by the tipvane and the second part $y_{TC}(x_T, z_T)$ gives the camber relative to this aerodynamical ineffective circular curvature.
The boundary value problem for this isolated rotating tipvane yields

$$\frac{\partial^2 p}{\partial x^2} + \frac{\partial^2 p}{\partial y^2} + \frac{\partial^2 p}{\partial z^2} = 0 \qquad (5\text{-}2)$$

with boundary conditions

1. $p \to 0$ for $x^2 + y^2 + z^2 \to \infty$ $\qquad (5\text{-}3)$

2. $\dfrac{1}{\rho\Omega^2 R}\dfrac{\partial p}{\partial y} = R\dfrac{\partial^2 y_{TC}}{\partial x_T^2}$ $\qquad (5\text{-}4)$

on the tipvane at the time t = 0. The tipvane is at t = 0 assumed to be at azimuthal position $\psi = \frac{\pi}{2}$, given by

$$x = x_t + \Lambda z_t \; , \quad y = R - \gamma z_t - y_T(x_T, z_T) \; , \quad z = \Lambda x_T - z_T \qquad (5\text{-}5)$$

where $|x_T| \leqslant \frac{c_T}{2}$ and $|z_T| \leqslant \frac{b_T}{2}$

With this boundary condition the particles of air moving over the tipvane surface obtain the correct accelerations to fit the curvature of the tipvane.

3. p singular on the leading edge ($x_T = - c/2$) in such a way that

$$\left(\frac{v}{\Omega R}\right) = - \frac{\partial y_{TC}}{\partial x_T} + \Lambda \frac{z_T}{R} + \left\{\gamma + \frac{\partial y_{TC}}{\partial z_T}\right\} \left(\frac{w}{\Omega R}\right) \tag{5-6}$$

on the midchord line of the tipvane: $x_T = y_T = 0$, $|z_T| \leqslant \frac{b_T}{2}$ and at the time $t = 0$.
This is the tangential flow condition for the tipvane. Because of condition (5-4) this condition has to be fulfilled on one spanwise line. A convenient choice is the midchordline.

5.2 The asymptotic solution in the near field

In the vicinity of the tipvane it becomes convenient to write the Laplace equation for the pressure (equation (5-2)), in terms of the local tipvane coordinate system (x_T, y_T, z_T):

$$\frac{\partial^2 p}{\partial x_T^2} + \frac{\partial^2 p}{\partial y_T^2} + \frac{\partial^2 p}{\partial z_T^2} = 0 \tag{5-7}$$

On physical grounds it seems justifiable to state that in the immediate vicinity of the tipvane, staying away from its tipregions, the characteristic length of spanwise pressure variation is of the order of the span b_T, whereas chordwise pressure variation are of the order of the chord c_T.

Substitution of the nondimensionalized coordinates $\frac{x_T}{c_T/2}$; $\frac{y_T}{c_T/2}$ and $\frac{z_T}{b_T/2}$ into (5-7) yields

$$\frac{\partial^2 p}{\partial \left(\frac{x_T}{c_T/2}\right)^2} + \frac{\partial^2 p}{\partial \left(\frac{y_T}{c_T/2}\right)^2} = - \frac{1}{A_T^2} \frac{\partial^2 p}{\partial \left(\frac{z_T}{b_T/2}\right)^2} \tag{5-8}$$

where $A_T = b_T/c_T$ is the aspect ratio of the tipvane.
Suppose a solution p_1 of the boundary value problem has been found in asymptotic theory which obeys equation (5-8) up to the order A_T^{-1}. This solution also satisfies, in the immediate vicinity of the tipvane, the differential equation

$$\frac{\partial^2 p_1}{\partial \left(\frac{x_T}{c_T/2}\right)^2} + \frac{\partial^2 p_1}{\partial \left(\frac{y_T}{c_T/2}\right)^2} = 0 \tag{5-9}$$

of course up to the order A_T^{-1}.

With an accuracy up to this same order the solution p_1 obtained from asymptotical theory can then be replaced, but only in the vicinity of the tipvane, by a solution P_{near} satisfying (5-9) throughout the whole field.
Since p_{near} and p_1 coincide close to the tipvane (in the "near field"), p_{near} must also satisfy the boundary conditions (5-4) and (5-5) applicable in the near field.

The third boundary condition (5-3) is not necessarily satisfied by p_{near} since this condition is imposed upon p_1 in the far field; and in this far field p_1 and p_{near} are no longer identical up to the order A_T^{-1}.

According to reference 6, the general solution P_{near} for a thin aerofoil of arbitrary mean line and arbitrary angle of attack (including bladetwist) yields, in terms of elliptic cylinder coordinates:

$$\frac{P_{near}}{\frac{1}{2}\rho(\Omega R)^2} = - \frac{C_{\ell_1}\left(\frac{z_T}{b/2}\right)}{\pi} \frac{\sin \varphi}{\cosh\eta + \cos\varphi} - \frac{1}{\pi} \sum_{n=1}^{\infty} a_n \left(\frac{z_T}{b/2}\right) e^{-n} \sin(n\varphi) \tag{5-10}$$

Here the index 1 has been used in the liftcoefficient C_ℓ since the second term on the right hand side also may contribute to the lift. In linearized theory, the boundary conditions on the tipvane may be replaced by the same conditions on the projection of the tipvane on the x_T, z_T plane. With boundary condition (5-5) the coefficients a_n can be determined:

$$\sum_{n=1}^{\infty} n \, a_n \left(\frac{z_T}{b_T/2}\right) \frac{\sin n\varphi}{\sin\varphi} = - \pi c \frac{\partial^2 y_{TC}}{\partial x_T^2} \qquad \text{on the tipvane.} \tag{5-11}$$

It is assumed now that the camberfunction of the tipvane $y_T(x_T, z_T)$ consists of a curvature due to its circular path (see equation (5-1)) plus an angle of attack θ, which may vary along the span.
Substitution of $y_{TC}(x_T, z_T) = - \theta(z_T)x_T$ into (5-11) yields

$$\sum_{n=1}^{\infty} n \, a_n\left(\frac{z_T}{b/2}\right) \frac{\sin n\varphi}{\sin \varphi} = 0 \tag{5-12}$$

all over the tipvane,

and so

$$a_n = 0 \qquad n = 1,2,3,\ldots. \tag{5-13}$$

5.3 The asymptotic solution in the far fields

The second step in the application of the asymptotic expansion method is the consideration of the behaviour of p_1 in the far field. At a distance of the order of the span b_T of the tipvane it is reasonable to state that all pressure variations have the same characteristic length scale.

Since relative errors of the order $A_T^{-2} = (c_T/b_T)^2$ are neglected here, the tipvane chord seems thus to have shrunk into one single line carrying discrete singularities. So the solution p_1 is now, in the far field and upto the order A_T^{-1}, identical to the pressure field of a lifting line p_{far}.
For p_{far} the determining equations yield:

$$\frac{\partial^2 p_{far}}{\partial \left(\frac{x_T}{b_T/2}\right)^2} + \frac{\partial^2 p_{far}}{\partial \left(\frac{y_T}{b_T/2}\right)^2} + \frac{\partial^2 p_{far}}{\partial \left(\frac{z_T}{b_T/2}\right)^2} = 0 \tag{5-14}$$

$$p_{far} \to 0 \qquad x^2 + y^2 + z^2 \to \infty \tag{5-15}$$

By the assumption that the tipvane boundary conditions may considered to be located on the projection of the vane on the y_T plane, the pressure field p_1 is antisymmetric with respect to this y_T plane. Then the final boundary condition for p_{far} has been generated:

$$p_{far} \text{ singular on the line } x_T = y_T = 0, \ |z_T| \leqslant \frac{b_T}{2} \tag{5-16}$$

and antisymmetric with respect to the plane $y_T = 0$

The general solution satisfying (5-14), (5-15) and (5-16) given in prolate spheroidal coordinates using associate Legendre functions of the first and second kind, yields according to references 6 and 7:

$$\frac{p_{far}}{\frac{1}{2}\rho(\Omega R)^2} = \sum_{m=1}^{\infty} \sum_{n=1}^{\infty} \left\{ A_{mn} \, P_n^m(\cos\theta) \, Q_n^m(\cosh\nu) \, \sin m\chi \right\} \tag{5-17}$$

5.4 The introduction of a common field expression

At this moment two representatives have been found for p_1: p_{near} corresponding with p_1 in the near field, and p_{far} corresponding with p_1 in the far field.
Summation of p_{near} and p_{far} then yields a competent candidate for the first order solution p_1 of the complete boundary value problem, at least at first sight. This would only be true however, if the contribution of p_{near} in the far field is neglectible with respect to p_{far}, and vice versa. According to equation (5-16) one knows that p_{far} shows a singular behaviour near the midchordline of the tipvane. Thus it is clear that here p_{far} is not neglectible with respect to p_{near}.
So the solution p_1 is not obtained by simply summing up p_{near} and p_{far}, and more work has to be done to obtain a solution satisfying all conditions.
Suppose a pressure field would exist that has the following features: in the near field it equals p_{far}, to the required order of accuracy, and in the far field this pressure field is identical to p_{near} (to the right order). By addition of p_{near} and p_{far}, and the subtraction of this field, the "common" pressure field" p_{common}, a first order solution would have been obtained:

$$p_1 = p_{near} + p_{far} - p_{common} \tag{5-18}$$

The common field can evidently be obtained by observation of the asymptotic expansion behaviour of both p_{near} and p_{far}. The near field solution p_{near}, asymptotically expanded for $r_T = O(b_T)$ up to the order A_T^{-1} yields:

$$\frac{p_{near}}{\frac{1}{2}\rho(\Omega R)^2} \approx \frac{C_{\ell_1}\left(\frac{z_T}{b_T/2}\right)}{\pi} \frac{c_T/2}{r} \sin\chi \text{ for } r_T \to \text{order } O(b_T) \tag{5-19}$$

Thus p_{common} yields

$$\frac{p_{common}}{\frac{1}{2}\rho(\Omega R)^2} = \frac{C_{\ell_1}\left(\frac{z_T}{b_T/2}\right)}{\pi} \frac{c_T/2}{r_T} \sin\chi \tag{5-20}$$

Comparison of p_{common} with p_{far} (eq. (5-17)) immediately shows that the terms in (5-17) with $\sin m\chi$ for $m > 1$ must vanish, since otherwise the condition

$$p_{common} = (p_{far})_{r_T} \to \text{order } O(c_T) \tag{5-21}$$

cannot be satisfied.
With $A_n = A_{1n}$ the asymptotic expansion of p_{far} for $r_T = O(c_T)$ up to the order A_T^{-1} yields:

$$\frac{p_{far}}{\frac{1}{2}\rho(\Omega R)^2} \approx -\frac{\sin\chi}{\pi} \frac{b_T/2}{r_T} \left\{1 - \left(\frac{z_T}{b_T/2}\right)^2\right\}^{\frac{1}{2}} \sum_{n=1}^{\infty} A_n \, P_n^1 \frac{z_T}{b/2} \tag{5-22}$$

$$\text{for } r_T \to \text{order } O(c_T)$$

5.5 The complete asymptotic solution

By the matching condition:

$$(p_{near}) \qquad \approx p_{common} \approx (p_{far}) \tag{5-23}$$
$$r_T \to 0(b_T) \qquad\qquad r_T \to 0(c_T)$$

the following relation between C_{ℓ_1} and the coefficients A_n is obtained:

$$C_{\ell_1}\left(\frac{z_T}{b_T/2}\right) = A_T \left\{1 - \left(\frac{z_T}{b_T/2}\right)^2\right\}^{\frac{1}{2}} \sum_{n=1}^{\infty} A_n P_n^1\left(\frac{z_T}{b_T/2}\right) \tag{5-24}$$

The complete pressure field p_1 now follows from substitution of p_{near} (eq. (5-10) with (5-13)), p_{common} (eq. (5-20)) and p_{far} into (5-18):

$$\frac{p_1}{\frac{1}{2}\rho(\Omega R)^2} = -\frac{C_{\ell_1}\left(\frac{z_T}{b_T/2}\right)}{\pi} \frac{\sin\varphi}{\cosh\eta + \cos\varphi} + \frac{C_{\ell_1}\left(\frac{z_T}{b_T/2}\right)}{\pi} \frac{c_T/2}{r_T} \sin\chi +$$

$$+ \frac{\sin\chi}{\pi} \sum_{n=1}^{\infty} A_n P_n^1(\cos\theta) Q_n^1(\cosh\nu) \tag{5-25}$$

In the above expression, the liftcoefficient C_{ℓ_1} is still indetermined. With the remaining boundary condition (5-6) this indeterminatess can be removed. By substitution of $\frac{\partial v}{\partial t} = -\frac{1}{\rho}\frac{\partial p}{\partial y}$ (which follows from the linearized Euler equation) equation (5-6) yields

$$\frac{-1}{\frac{1}{2}\rho(\Omega R)^2} \int_{-\infty}^{0} \frac{\partial}{\partial(y/R)} p(x,y,z,t) \Omega dt = 2\left[\theta(z_T) + \Lambda\frac{z_T}{R} + \gamma\frac{W}{\Omega R}\right] \tag{5-26}$$

for a particle of air arriving at the midchordline of the tipvane at $t = 0$.

Substitution of p_1 in (5-26) then yields the final boundary condition. The evaluation of this final one dimensional integral equation is done numerically, using a collocation-point method.
The method proceeds with the introduction of n_o basic pressure distributions and their corresponding basic liftcoefficient distributions. The m'th $(m = 1, .. n_o)$ basic distribution is obtained from (5-25) and (5-24) respectively by substitution of $A_n = 0$ $n \neq 0$ and $A_m = 1$.

5.6 Complications in oversynchronous operation of the tipvane

The stability of the numerically obtained solution with respect to variation of number and position of the collocation points and further parameters in the numerical procedure, appears to be quite satisfactory in undersynchronous states of operation. The term undersynchronous is used when a tipvane is not yet situated in the direct wake of the preceding one (fig. 9a).
However, the method developed as yet is not capable of dealing with oversynchronous situations (fig. 9b). This is caused by the singular behaviour of the induced velocity field generated by the upstream tip of the tipvane, which is felt by its successor. This gives rise to a special kind of singularity not met in ordinary aircraft aerodynamics. The source of the problems appeared to be of a rather fundamental character (ref. 8). An explanation can be given when one considers the implicit assumptions made for the spanwise lift distribution in the model.

In undersynchronous situations the tipvane is travelling through a regular velocity field and thus the tipvane lift distribution is also regular.
But in oversynchronous situations the tipvane experiences the singular tipvortex of the preceding one, and thus irregularities in the lift distribution are present at the point where the vortex hits the tipvane (the point of overlap). In the original method only regular lift distributions are considered and therefore the procedure breaks down in the oversynchronous situations.
A solution is found by involving also lift distributions having a kink at the point of overlap.
With such a kink in the spanwise lift distribution it is possible to generate a singular self induced velocity field.
Provided that the jump in the spanwise derivative has a correct magnitude the singularity in this self induced velocity field exactly cancels the singularity in the induced velocity field of the preceding tipvane. Then the complete induced velocity field is not singular anymore at the tipvane, which is the only acceptable solution from the physical point of view (fig. 10).
Consider the liftdistribution over the tipvane to be composed out of two parts. One part is identical to the assumed liftcoefficient distribution of (5-24) and is directly correlated to the pressure field p_1 of equation (5-25). This part indicates the spanwise liftdistribution over the complete tipvane. The second part consists of an extra liftdistribution over the interfering part only (the part indicated by $\frac{b_T}{2} - 2\pi\frac{W}{\Omega} > z_{T_0} > -\frac{b_T}{2}$) of the same character as the first part (5-24):

$$C_{\ell_1 cur}(\zeta) = \frac{b_{Tcur}}{b_T} \{1 - \zeta^2\}^{\frac{1}{2}} \sum_{n=1}^{\infty} B_n P_n^1(\zeta) \tag{5-27}$$

where

$$\zeta = \frac{2}{b_{Tcur}}\{z_T + \pi\frac{W}{\Omega}\} \text{ and } b_{Tcur} = b_T - 2\pi\frac{W}{\Omega}.$$

In order to obtain a non-singular velocity distribution over the tipvane, the kink in the liftcoefficient distribution obtained by addition of (5-24) and (5-27) at the point of overlap $z_T = \frac{b_T}{2} - 2\pi \frac{W}{\Omega}$ must have the correct value. This implies the following relation for the coefficients A_n and B_n:

$$\sum_{n=1}^{\infty} n(n+1)A_n + \frac{1}{2} \sum_{n=1}^{\infty} n(n+1) B_n = 0 \qquad (5-28)$$

as is derived in reference 8.

The extra liftcoefficient distribution (5-27) is of course correlated with an extra pressure field p_{cur}. This extra pressure field p_{cur} should also satisfy, on account of the linearity of the problem the eqs. (5-2) through (5-6). Then a first order solution p_{1cur} is found, completely analogous to (5-25). The choice of the n_0 basic pressure distributions, and thus liftcoefficientdistributions in the oversynchronous situation is more arbitrary. Based upon the experience reported in reference 8 the following selection has been made:

$$\frac{p_{basic}(x,y,z,t,n)}{\frac{1}{2}\rho(\Omega R)^2} = - \frac{C_\ell(\frac{z_T}{b/2},n)}{\pi} \frac{\sin\varphi}{\cosh\eta + \cos\varphi} + \frac{C_\ell(\frac{z_T}{b/2},n)}{\pi} \frac{c_T/2}{r_T} \sin\chi +$$

$$+ \frac{\sin\chi}{\pi A_T} P_n^1 (\cos\theta)\, Q_n^1 (\cosh\nu) +$$

$$+ \frac{C_{\ell_{cur}}(\zeta,n)}{\pi} \frac{\sin\varphi_{cur}}{\cosh\eta_{cur}+\cos\varphi_{cur}} + \frac{C_{\ell_{cur}}(\zeta,n)}{\pi} \frac{c_T/2}{r_T} \sin\chi_{cur} + \qquad (5-29)$$

$$- n(n+1) \frac{\sin\chi}{\pi A_T} P_1^1 (\cos\theta_{cur})\, Q_1^1 (\cosh\nu_{cur})$$

with

$$C_\ell(\frac{z_T}{b_T/2},n) = \left\{1 - (\frac{z_T}{b_T/2})^2\right\}^{\frac{1}{2}} P_n^1 (\frac{z_T}{b_T/2}) \qquad (5-30)$$

and

$$C_{\ell_{cur}}(\zeta,n) = - n(n+1) \frac{b_{Tcur}}{b_T} \left\{1-\zeta^2\right\}^{\frac{1}{2}} P_1^1 (\zeta)\right]_{\left[\frac{b_T}{2} - 2\pi \frac{W}{\Omega}, - \frac{b_T}{2}\right]} \qquad (5-31)$$

And the basic liftcoefficientdistributions:

$$C_{\ell_{basic}} (\frac{z_T}{b_T/2},n) = C_\ell(\frac{z_T}{b_T/2},n) + C_{\ell_{cur}}(\zeta,n) =$$

$$= \left\{1 - (\frac{z_T}{b_T/2})^2\right\}^{\frac{1}{2}} P_n^1 (\frac{z_T}{b_T/2}) - n(n+1) \frac{b_{Tcur}}{b_T} \left\{1 - \zeta^2\right\}^{\frac{1}{2}} P_1^1(\zeta)\right]_{\left[\frac{b_T}{2} - 2\pi \frac{W}{\Omega}, - \frac{b_T}{2}\right]} \qquad (5-32)$$

Note that by the choice of (5-30) and (5-31), the condition (5-28) to be opposed upon the coefficients of the liftcoefficientdistribution in oversynchronous situations already is satisfied.

5.7 Results

Typical results for a modelconfiguration frequently used are shown in fig. 11. Notice the steady increase in total lift with decreasing lateral spacing of the tipvanes (increasing tipspeed ratio). Up to the synchronous state (where the upstream tipvortex of the tipvane exactly hits the downstream tip of the following vane) the character of the lift distribution does not change very drastically (fig. 11a). But in oversynchronous conditions the character suddenly changes (fig. 11b). Notice the abrupt decrease of lift at the spanwise location where the overlapping region starts. Here the counter vortex is generated that annihilates the tipvortex from the preceding vane.

Once the synchronous tipspeedratio is exceeded the flow itself autosynchronizes the aerodynamically effective span, and the overlapping region becomes inefficient.

In fig. 12 the induced drag is depicted versus the amount of lateral space (tipspeed ratio). It can be seen that when the overlapping has started, the induced drag becomes practically zero. Besides this result proves that in oversynchronous situations the vortex annihilation is almost perfect (no induced drag!).

Thus according to theory it is sufficient to take into account only viscous drag effects of the tipvane(s) when calculating the net power output for an optimal tipvane turbine.

6. Aerodynamic loads on the turbineblade

With the matched asymptotic expansion method based upon the acceleration method applied on the turbine blade configuration, one assumes a finite number of blades throughout the whole analytical procedure. This is in contrast to the classical methods where the momentum theory (infinite number of blades!) is within the

procedure modified for a finite number of blades (tip correction factors).

Therefore the method described here yields a better description of the tipflow effects.

On the other hand it must be realised that application of the acceleration potential implies the assumption of small velocity perturbations.

In the linear theory as initiated by the eqs. (3-12) through (3-17) the pressure gradients are determined that would have acted upon a particle of air if it was forced to follow a straight path with a constant velocity equal to the unperturbed velocity W. Then the assumption is made that the particle following its real perturbed (but a priori unknown) path feels the same pressure gradients.

When the method is now applied to the windturbine situation, yielding the integration of a pressure field quite analogue to the eqs. (5-25) and (5-26) by means of a collocation point method for basic distributions it turns out to give incorrect results.

The reason for it is that windturbines operate in heavily loaded conditions and this implies significant induced velocities near the discplane of the windturbine.

But with a partial delinearization in the method good results were obtained. This delinearization is applied as follows.

In the linear method the position of a particle of air arriving at the time $t = 0$ at the turbineblade location (x_0, y_0, z_0) is assumed to be given by

$$x = x_0 \quad , \quad y = y_0 \quad , \quad z = z_0 + Wt \tag{6-1}$$

In the delinearized method the eqs. (6-1) are replaced by

$$x = x_0 \quad , \quad y = y_0 \quad , \quad z = z_0 \ (W + v(x_0, y_0, z_0))t \tag{6-2}$$

where $v(x_0, y_0, z_0)$ indicates the velocity at the point (x_0, y_0, z_0) found in the linear method.

In this way the method is iteratively delinearized such that the deviations of the assumed travelling velocity, which is constant in time, from the velocities in the discplane of the rotor is small.

Physically the partial delinearization is explained as follows:

In the linearized method the wake is assumed to be rigid and non-diverging. With this delinearization an axial deformation of the wake is allowed. It should be realized that this method does not lead to an exact delinearization since the pressure field is still determined by the Laplace equation (5-2) which was derived by linearization. It is rather more a convenient engineering procedure to deform the flowfield in such a way that some of the most important effects can be included.

In the numerical evaluation of this procedure, only the particles arriving at $t = 0$ in the collocationpoints have to be considered.

Since these collocationpoints are assumed to be situated on the midchordline of the blade (cf boundary condition (5-31)) and since at $t = 0$ the midchordline of the blade ($y_r = 0$) coincides with the y-axis the equation (6-2) yield:

$$x = 0 \quad , \quad y = r_i \quad , \quad z = z_j(t) \ (W + v_{i,j-1})t \tag{6-3}$$

Where r_i denotes the radial position of the i'th collocationpoint and $v_{i,j-1}$ the calculated induced velocity in the j-1'th iteration at the i'th collocation point.

In practical application only two iterations are necessary. Even one iteration is sufficient if one starts with $v_{i,0} = -0,333$, the value obtained for the ideal windturbine operating in optimal conditions.

In the present method the viscous effects are included by the implication of two-dimensional aerofoil characteristics. This is done in the ultimate performance calculation. First an inviscid liftcoefficient-distribution over the turbineblade is calculated by means of the predescribed method. Then the corresponding angle of attack distribution is derived using the relation $\alpha = C_\ell/2\pi$. From this angle of attack distribution a new liftcoefficientdistribution, as well as a dragcoefficientdistribution is formed, using the two-dimensional aerofoil characteristics of the sections used.

As an example the performance of the rotor depicted in fig. 13 is calculated. This specific rotor has been tested in the 2.2 m diameter open jet windtunnel of Delft University of Technology. Furthermore, measurements were done at DUT on the curved plate "aerofoils" used in this rotor (ref. 9), so good comparison of theory with experiments was possible. Fig. 14 shows the result. A good agreement is established between theory and measurements apart from the point at a tipspeedratio $= 6.6$. But at this point strong vibrations were observed, which may be the explanation for the discrepancy. For this result 10 collocation points were used, evenly distributed along the span of the rotorblade. Typical computing time for one iterationstep and 10 collocation points is in the order of 10 to 15 seconds (Amdahl 470) for double precision calculations (16 decimal digits).

7. The interference between turbine blade and tipvane

7.1 The pressure field of a T-tail

The study of the interference effects (ref. 10) has started with the most simple configuration: two lifting surfaces in a steady flow. The load distribution on each surface is again represented by a series of basic load distributions. The interference effects are formulated as extra conditions to be satisfied by the coefficients of the basic load distributions. Two steps appeared to be necessary in order to formulate the problem uniquely: the introduction of an extra basic lift distribution, having a non-zero jump at the junction of the two surfaces (fig. 15) and the introduction of a "mirror-condition" stating that the slope of the vertical surface lift distribution near the junction must be zero. Without this last condition, a solution as shown in fig. 16 is, mathematically, a possible one.

The transport of loading from the vertical to the horizontal surface is something that must be established explicitly, by formulating this mirror-condition: the upper part of the vertical surface feels the horizontal surface as an end plate, and reflects itself. Thus a non-zero loading must be possible at the junction, while the slope of the vertical surface lift distribution must be zero at that point.

7.1.1 The pressure field of the vertical surface

As the load distribution on the vertical surface is known to have the character as shown in fig. 15, it is convenient to compose the loaddistribution of a triangle part, and the remaining part which makes the definite shape. The particular solution of the Laplace equation for the far field, which represents the triangle part is given by:

$$\left\{\frac{P_{far}}{\frac{1}{2}\rho U^2}\right\}_{triangle} = -\frac{C_o}{\pi} \cdot \frac{\sin\chi_v \cdot \sin\theta_v}{\sinh\nu_v \cdot (\cosh\nu_v - \cos\theta_v)} \tag{7-1}$$

This particular solution of the far field Laplace equation (cf. (5-14)) has also consequences for the structure of the near and the common field. Apart from the general first order structure of the pressure field of a lifting surface cf. (5-25) three extra terms must be included in order to represent the triangle distribution or the vertical surface. When the matching procedure as worked out in chapter 5 is applied correctly this leads to the following expression for the pressure field on the vertical surface:

$$\frac{P_{1v}}{\frac{1}{2}\rho U^2} = -\frac{\sum_{n=1}^{\infty} c_{\ell_v}^n (\frac{y_v}{b_v/2})}{\pi} \frac{\sin\varphi_v}{\cosh\eta_v + \cos\varphi_v} + \frac{\sum_{n=1}^{\infty} c_{\ell_v}^n (\frac{y_v}{b_v/2})}{\pi} \frac{c_v/2}{r_v} \sin\chi_v +$$

$$+\frac{\sin\chi_v}{\pi} \sum_{n=1}^{\infty} C_n P_n^1 (\cos\theta_v) Q_n^1 (\cosh\nu_v) + \tag{7-2}$$

$$-\frac{c_{\ell_v}^o (\frac{y_v}{b_v/2})}{\pi} \frac{\sin\varphi_v}{\cosh\eta_v + \cos\varphi_v} + \frac{c_{\ell_v}^o (\frac{y_v}{b_v/2})}{\pi} \frac{c_v/2}{r_v} \sin\chi_v - \frac{\sin\chi_v}{\pi} C_o \frac{\sin\theta_v}{\sinh\nu_v(\cosh\nu_v - \cos\theta_v)}$$

where

$$c_{\ell_v}^n = \frac{b_v/2}{c_v} \left\{1 - (\frac{y_v}{b_v/2})^2\right\}^{\frac{1}{2}} C_n \cdot P_n^1 (\frac{y_v}{b_v/2}) \qquad n = 1,2,... \tag{7-3}$$

and

$$c_{\ell_v}^o = \frac{b_v/2}{c_v} \cdot 2 C_o (1 + \frac{y_v}{b_v/2})$$

The carthesian coordinates systems used for the T-tail are depicted in fig. 17.

7.1.2 The pressure field of the horizontal surface

The pressure field of the horizontal surface is constructed from the same components as the vertical surface pressure field: a summation of basic loaddistributions, characterized by the Legendre functions P_n^1, and triangle loaddistributions, which now are based on half the span, instead of the whole span as in the previous section. Therefore, the pressure fields, due to these triangle loaddistributions are written in their own half span coordinate systems, see fig. 17.

Now in the first order approximation of the pressure field, the near field contribution is zero outside the span, or, in other terms: this near field contribution is of a higher order. For example the near field of the left triangle loaddistribution ($z_h > 0$) has no contribution in the region $z_h < 0$. However, on physical grounds some trouble may be expected for $z_h \to 0$. Looking at the matching condition cf (5-23), it is justified to replace the complete pressure field of a lifting surface by the far field only, if the distance to the mid-chord line is a chord length or more. So, if the region

$|\frac{z_h}{c_h}| < 1$ is excluded, the complete pressure field can be assumed to have the following form:

$$\frac{P}{q} = \left\{\frac{P}{q} near + \frac{P}{q} far - \frac{P}{q} common\right\}_{\text{basic loaddistributions}} + \left\{\frac{P}{q} far \atop \text{left triangle} + \frac{P}{q} far\right\}_{\text{right triangle}}$$

$$+ \left\{\frac{P}{q} near - \frac{P}{q} common\right\}_{\text{left triangle}} \Big|_{\left[0 \leqslant \left|\frac{z_h}{b_h/2}\right| \leqslant 1\right]} + \left\{\frac{P}{q} near - \frac{P}{q} common\right\}_{\text{right triangle}} \Big|_{\left[0 \geqslant \frac{z_h}{b_h/2} \geqslant -1\right]} \tag{7-4}$$

The complete expressions for the liftcoefficientdistribution and the pressure field can now be written using eq. (7-4) and the analogous expressions of the vertical surface pressure field, whereby the triangle-loaddistributions are assumed to be antisymmetric with respect to z_h.

7.1.3 The pressure field of the complete T-tail

The pressure field of the complete T-tail is just a summation of the expressions for the horizontal and the vertical surface. However, some simplifications have to be made. The same problems with the near field terms of the pressure field, as indicated in the previous section arise when the pressure is calculated in a point $|2y_v/b_v| > 1$. Then the first order vertical surface pressure field contributes to the pressure only by the far field terms because the near field terms are restricted to $|2y_v/b_v| < 1$. Therefore the assumption is made that a particle, which follows a path towards the horizontal surface, sees the vertical surface as a lifting line. This is the same assumption as has been made for two triangle loaddistributions in the previous section. It is consistent now, to represent the horizontal surface pressure field by a lifting line pressure

field, if a particle follows a path towards the vertical surface. The result is that instead of one expression for the complete pressure field two approximate expressions will be used. For a particle travelling to the horizontal surface the total pressure field experienced from the T-tail is thus given by

$$\frac{P_{lh}}{\frac{1}{2}\rho U^2} + \left(\frac{P_{lv}}{\frac{1}{2}\rho U^2}\right)_{far}$$ and for a particle travelling to the vertical surface the total pressure field yields:

$$\frac{P_{lv}}{\frac{1}{2}\rho U^2} + \left(\frac{P_{lh}}{\frac{1}{2}\rho U^2}\right)_{far} \quad .$$

Where

$$\left(\frac{P_{lv}}{\frac{1}{2}\rho U^2}\right)_{far} = \frac{\sin\chi_v}{\pi}\left[\sum_{n=1}^{\infty} C_n\, P_n^1(\cos\theta_v)\, Q_n^1(\cosh\nu_v) - C_o\, \frac{\sin\theta_v}{\sinh\nu_v\,(\cosh\nu_v - \cos\theta_v)}\right] \qquad (7\text{-}5)$$

and

$$\left(\frac{P_{lh}}{\frac{1}{2}\rho U^2}\right)_{far} = \frac{\sin\chi_h}{\pi}\sum_{n=1}^{\infty} D_n\, P_n^1(\cos\theta_h)\, Q_n^1(\cosh\nu_h) + \frac{\sin\chi_{h\ell}}{\pi}\, D_o\, \frac{\sin\theta_{h\ell}}{\sinh\nu_h\,(\cosh\nu_{h\ell} + \cos\theta_{h\ell})} +$$

$$+ \frac{\sin\chi_{hr}}{\pi}\, D_o\, \frac{\sin\theta_{hr}}{\sinh\nu_{hr}\,(\cosh\nu_{hr} + \cos\theta_{hr})} \qquad (7\text{-}6)$$

It should be realised that the complete expression $\frac{P_{lh}}{\frac{1}{2}\rho U^2} + \frac{P_{lv}}{\frac{1}{2}\rho U^2}$ is completely equivalent to the expressions

$$\frac{P_{lh}}{\frac{1}{2}\rho U^2} + \frac{P_{lv}}{\frac{1}{2}\rho U^2}\bigg|_{far} \quad \text{and} \quad \frac{P_{lh}}{\frac{1}{2}\rho U^2}\bigg|_{far} + \frac{P_{lv}}{\frac{1}{2}\rho U^2}$$

for particles travelling to the horizontal (resp. vertical) lifting surface, as long as their distance to the vertical (horizontal) surface is in the order of the span of the horizontal (vertical) wing (cf the matching condition (5-23)).

In fig. 15 a schematical representation of the loaddistribution is given, for the case that the horizontal tailplane has no angle of incidence. It is clear, that the whole vertical surface loading which is present at the junction, must be carried over to the horizontal plane and is spread symmetrically. So the magnitude of the discontinuity in the horizontal plane loading must be equal to the vertical surface loading at the junction. This must of course also be true, when the horizontal plane has an angle of incidence, and generates its own loaddistribution.

Strictly spoken this statement is anticipating the solution, so it is not a boundary condition. But as it simplifies the calculation procedure, and is really evident, it will be treated as such:

$$\left\{\Delta(C_\ell \cdot c_h)_h\right\}_{\frac{z_h}{b_h/2} = 0} = \left\{(C_\ell - c_v)_v\right\}_{\frac{y_v}{b_v/2} = 1} \qquad (7\text{-}7)$$

From eq. (7-3) and the equivalent expression for $C_{\ell_h}^n$ it follows:

$$\left\{\sum_{n=1}^{\infty} C_{\ell_v}^n \cdot c_v\right\}_{\frac{y_v}{R/2} = 1} = 2\, C_o\, b_v \qquad (7\text{-}8)$$

$$\left\{\sum_{n=1}^{\infty} C_{\ell_h}^n \cdot c_h\right\}_{\frac{z_h}{b_h/4} = \frac{z_{hr}}{b_h/4} = -1} = 2\, D_o\, b_h \qquad (7\text{-}9)$$

so with eq. (7-6) it follows

$$C_o \cdot b_v = D_o\, b_h \qquad (7\text{-}10)$$

In the expressions for the pressure field there is now one extra indeterminateness left when compared to the expression (5-30), in the unknown coefficient C_o.

By the above mentioned mirror-condition, this indeterminateness can be removed.
The mirror condition states that the very last part of the vertical surface $\left(\frac{y_v}{b_v/2} \to 1\right)$ "feels" the

horizontal plane as an infinite plane in which the aerodynamic loading must be reflected without any discontinuity. Thus this yields:

$$\frac{\delta(C_\ell \cdot c_v)_v}{\delta\left(\frac{y_v}{b_v/2}\right)} = 0 \quad \text{for} \quad \frac{Y_v}{b_v/2} \to 1 \qquad (7\text{-}11)$$

Substituting (7-3) into (7-11) eventually leads to

$$C_o = \sum_{n=1}^{\infty} C_n \sum_{m=1}^{\infty} m \qquad (7\text{-}12)$$

The lift distributions of the horizontal and vertical surface are then determined by two integral equations analogous to eq. (5-26), one for the particles arriving at the horizontal surface, and one for the vertical surface.
Since in these equations the integrand contains the unknown liftdistributions of both the horizontal and the vertical surface (explicitely or in the form of the coefficients C_n and D_n) they must be solved simultaneously.
Again this is done numerically using a similar method as described in chapter 5.
A result is shown in fig. 18, where the present method is compared with the results of ref. 11. This is a lifting line method, restricted to arrangements with constant induced sidewash. The agreement between the vertical surface load distributions is very good, which is not so on the horizontal surface. The latter is due to the chord distribution of the horizontal surface (assumed in ref. 10). Near the junction the chords are very large in order to get constant induced sidewash, but this violates the linearization assumption in the acceleration potential method.
Fig. 19 shows a typical result of a situation with horizontal surface incidence: on one half of the horizontal surface the load distribution has become very small, while on the other half, the interference augments the load distribution.

7.2 The pressure field of the complete tipvane rotor

The difference between the pressure field expression for a T-tail and for a rotating tipvane rotor is small, at least in undersynchronous situations. The only difference felt in the method is the path that the particles follow with respect to the T-tail, or more precisely the continuously changing position of the tipvane rotor with respect to the straight path of the particles of air. This induces the introduction of many coordinate transformations but since they are not relevant now they will not be given. Furthermore the evaluation of the final boundary condition of (5-26) implies the partial differentiation of the pressure field in the y-direction (fig. 3) for the tipvane, and in the z-direction for the turbineblade. But within the local T-tail coordinate system, this means a differentiation in the x_h-y_h plane and in the z_h direction. This does not give any problem because the pressure field is not singular anywhere, except at the lifting surface itself.
In the oversynchronous situations there are some changes in the structure of the complete pressure field. Due to the effects mentioned in chapter 5 it is now necessary to modify the pressure field of the horizontal surface, which now plays the tipvane role according to the expression (5-29). This means that the pressure field of the tipvane is given by

$\dfrac{P_{1T}}{\frac{1}{2}\rho(\Omega R)^2} + \dfrac{P_{1Tcur}}{\frac{1}{2}\rho(\Omega R)^2}$. Here the expression $\dfrac{P_{1T}}{\frac{1}{2}\rho(\Omega R)^2}$ is equivalent to the expression for the horizontal sur-

face. Only the dynamic pressure $\frac{1}{2}\rho U^2$ has been replaced by $\frac{1}{2}\rho(\Omega R)^2$ since the undisturbed flowvelocity felt by the tipvane equals $((\Omega R)^2 + W^2)^{\frac{1}{2}} \approx \Omega R$ for large tipspeedratios $\lambda = \frac{\Omega R}{W}$, instead of U felt by the T-tail.

The expression for $\dfrac{P_{1Tcur}}{\frac{1}{2}\rho(\Omega R)^2}$ is completely analogous to the one derived in chapter 5-2, for the oversynchro-

nous state of operation of the isolated rotating tipvane.

A typical result of the complete method in an oversynchronous situation is depicted in figure 20. In this present calculation 9 collocation points were chosen on the tipvane, and also 9 collocation points on the turbine blade. Notice the jump in the liftcoefficient distribution over the tipvane at the junction. Also notice the peak in this distribution on the downstream side of the tipvane at $2z_T/b_T = -0,70$.
At this position the tipvane meets the trailing vortex tip emanated from the upstream tip of the previous tipvane.
The present configuration is two-bladed. The expressions given in this paper described the one-bladed configuration. But addition of extra blades is quite simple. Consider a particle of air travelling along its assumed straight path towards the turbineblade or the tipvane. Then the experienced accelerations must be integrated, but now not only those caused by the tipvane turbine blade on which it arrives at $t = 0$, but also the accelerations caused by the presence of the other blades. The extension of the method from one tipvane (turbineblade , tipvaneturbine blade) to N tipvanes (turbine blades, tipvane turbine blades) is simply done by some extra coordinate transformations, which rotate the tipvane (turbineblade, tipvane-turbine blade) over $\frac{2\pi}{N}$, $2 \cdot \frac{2\pi}{N}$, ... (N-1) $\frac{2\pi}{N}$ radians with respect to the first tipvane.

The accelerations felt by the above mentioned particle from the situation with N tipvanes (turbine blades, tipvane turbine blades) are then obtained from the addition of (N-1) pressure fields to the pressure field of one tipvane (turbine blade, tipvane turbine blade).
All these pressure fields are identical, but rotated over $\frac{2\pi}{N}$, $2\frac{2\pi}{N}$, ..., (N-1) $\frac{2\pi}{N}$ with respect to the field of the first tipvane (turbine blade, tipvane turbine blade).
Since the tipvane concept is simultaneously developed with the prediction methods no comparisons can be made with other extensive prediction methods for the complete configuration. Comparison with time-averaged momentum theories do give similar results, but these agreements do consider only global effects such as average axial forces, average radial forces etc.
At the moment no models are available on which more detailed information, such as liftdistributions can be obtained.

8. Conclusions

The analytical method, developed to calculate the flow field of a tipvane rotor, seems to give satisfactory results. As far as comparisons with experiments and other analytical methods are available, for conventional turbines and isolated tipvanes, they show reliable results. Particular difficulties, such as the interference of tipvane and turbine blade, and the interaction of the tipvortices are taken into account in a correct way.

9. References

1. Th. van Holten — "Windmills with diffusor effect induced by small tipvanes", paper E-3, Int. Symp. on Wind Energy Systems, Cambridge, U.K., September 1976.

2. Th. van Holten — "Tipvane research at the Delft University of Technology", paper F-2, 2nd Int. Symp. on Wind Energy Systems, Amsterdam, The Netherlands, October 1978.

3. M.M. van Beek-Derwort, Th. van Holten, G.A.M. van Kuik — "Work done by the tipvane group of the Delft University of Technology for the National Research Program Windenergy" period: January 1979 / April 1979, Delft Univ. of Techn., Dept of Aerospace Eng. Memorandum M-331, May 1979.

4. M.M. van Beek-Derwort, Th. van Holten — "Progress report of the tipvane group at the Delft University of Technology", period: October 1979 / January 1980, Delft Univ. of Techn., Dept. of Aerospace Eng. Memorandum M-364, February 1980.

5. M.M. van Beek-Derwort, P.C. Hensing, Th. van Holten — "Work done by the tipvane group of the Delft University of Technology for the National Research Program Windenergy", period: October 1978 / January 1979, Delft Univ. of Techn., Dept of Aerospace Eng. Memorandum M-322, February 1979.

6. Th. van Holten — "The computation of aerodynamic loads on helicopter blades in forward flight, using the method of the accelerationpotential", Delft Univ. of Techn., Dept of Aerospace Eng. Report VTH-189, 1975.

7. G.J.W. van Bussel — "First order calculation of drag- and liftdistribution on isolated rotating tipvanes", Delft Univ. of Techn., Dept. of Aerospace Eng. Memorandum M-290, November 1979.

8. G.J.W. van Bussel — "Analysis of mutual interference of wings in a plane, staggered formation", Delft Univ. of Techn., Dept of Aerospace Eng., Memorandum M-315, November 1978.

9. D.F. Volkers — "Preliminary results of windtunnel measurements on some airfoil sections at Reynolds numbers between 0.6×10^5 and 5.0×10^5", Delft Univ. of Techn., Dept of Aerospace Eng. Memorandum M-276, June 1977.

10. G.A.M. van Kuik — "An asymptotic lifting line approach to T-tail interference problems", Delft Univ. of Techn., Dept of Aerospace Eng. Memorandum M-332, June 1979.

11. J. Weber, A.C. Hawk — "Theoretical loaddistributions on fin-body-tailplane arrangements in a side wind", A.R.C. Technical Report R & M no 2992, London, 1957.

Fig. 2: Interfering of trailing vorticity causes an asymmetrical lift distribution on the tipvane. Then a net side edge suction force remains.
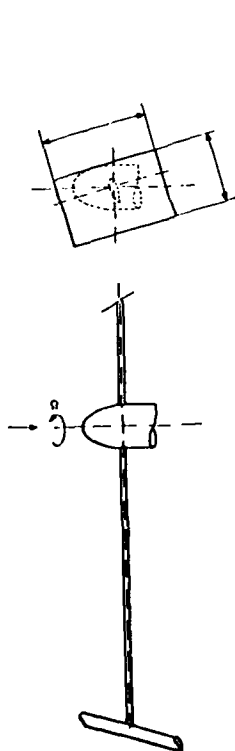
Fig. 1: Tipvane windturbine.
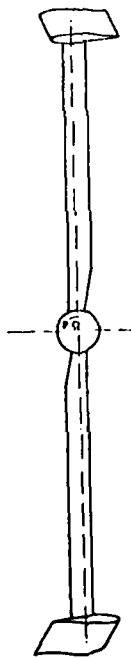
Fig. 3: Basic reference coordinate system.
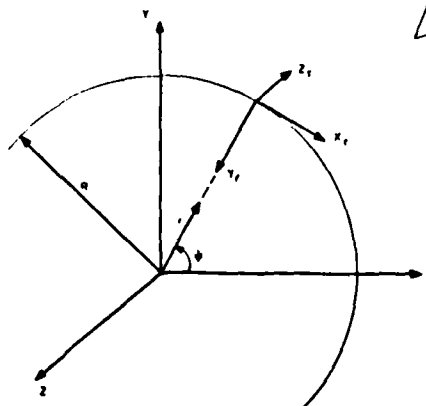
Fig. 4: Tipvane coordinate system.

Z_T

Z_r

c_B

X_T

b_T

X_r

Y_T

r_T

X

X_T

c_T

b_B

Y_T

a. Tipvane   b. Rotorblade

Fig. 6: Cicular cilinder coordinate system.

Fig. 5: Notations.

Y_r

Z_T

$\eta \to \infty$

Y_T

$\varphi = \frac{\pi}{2}$

$\eta = $ constant

Y_T

$-\frac{b}{2}$

X

$\varphi = \pi$

$\eta = 0$

$\varphi = 0$

X_T

$-\frac{c}{2}$

$\upsilon = 0$

X_T

$\frac{b}{2}$

$\upsilon = $ constant

$\varphi = \frac{3\pi}{2}$

Z_T

Fig. 8: Prolate spheroidal coordinate system.
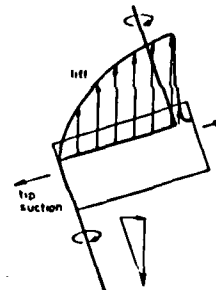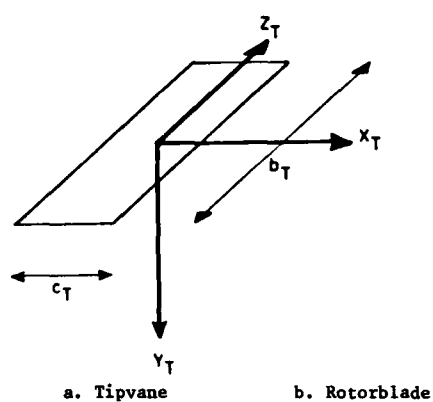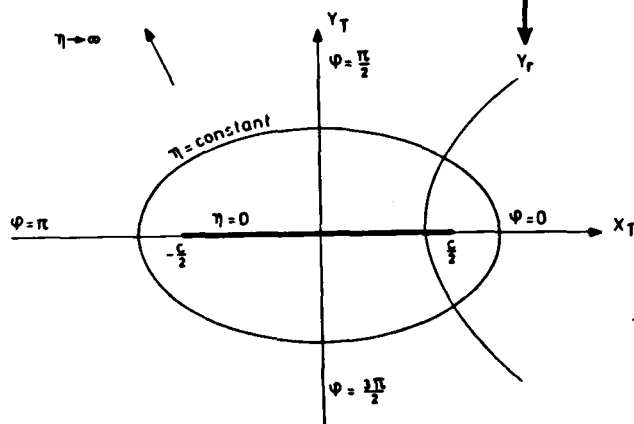
Fig. 7: Elliptical coordinate system.

$\theta = $ constant

z_r

z_T

x_T x_r

outwash   inwash

radial outflow   radial inflow

x_T x_r

outwash   inwash

observed vortex system

c_t

a. Undersynchronous situation   b. Oversynchronous situation

Fig. 10: Autosynchronization caused by ineffectiveness of the overlapping region.

Fig. 9: Operation modes of the tipvane
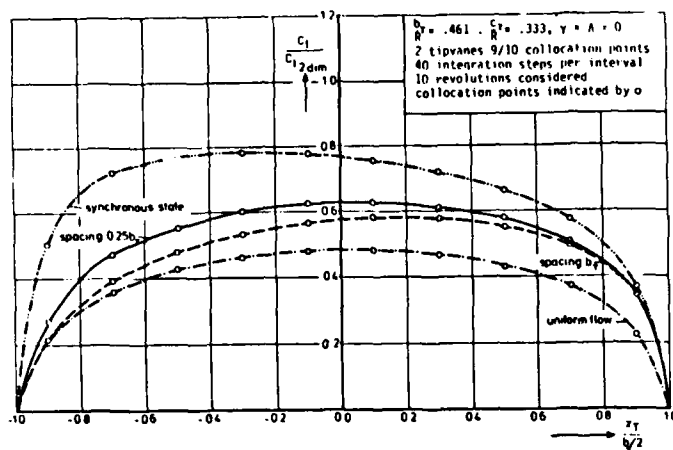
Fig. 11a: Liftcoefficient distributions over the tipvane in undersynchronous and synchronous states.
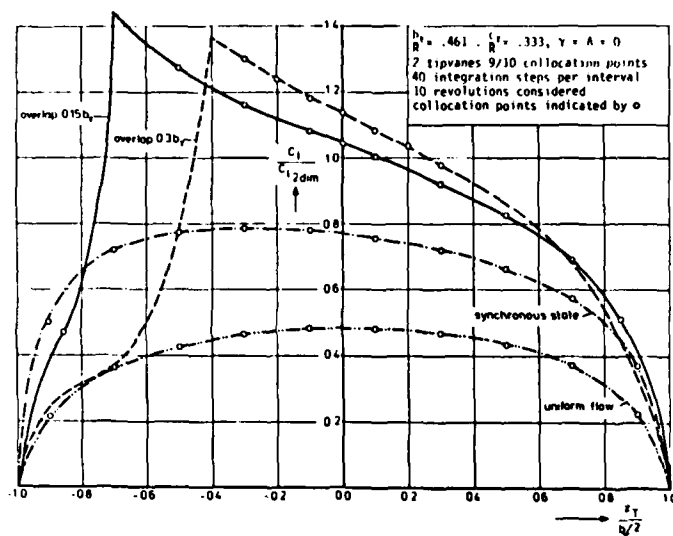
Fig. 11b: Liftcoefficient distributions over the tipvane in synchronous and oversynchronous states.
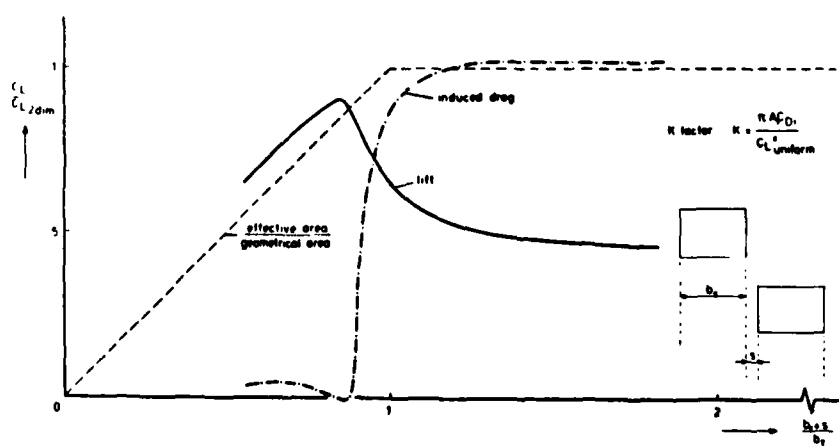
Fig. 12: Calculated lift and induced drag versus amount of lateral spacing for the same configuration as in figure 11.
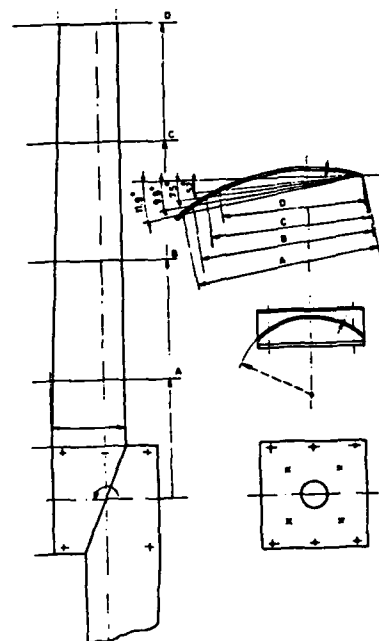
Fig. 13: Curved plate windturbine rotor.
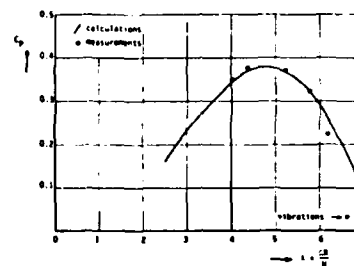
Fig. 14: Measured and calculated performance of the rotor depicted in fig. 13.
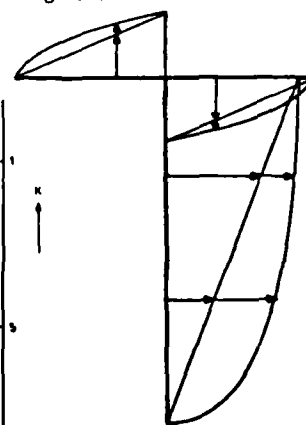
Fig. 15: Schematic loaddistribution on a T-tail with zero horizontal plane incidence angle.
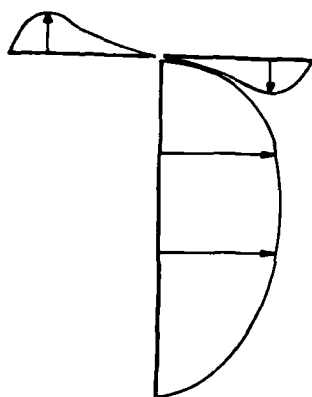
Fig. 16: Schematic load distribution on a
T-tail without "end plate" con-
dition. No horizontal plane in-
cidence angle.
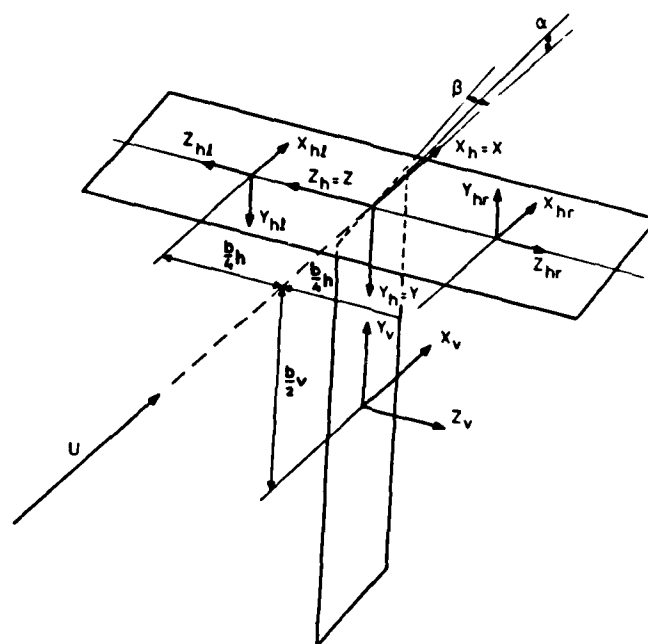
Fig. 17: Notations for the T-tail configuration.

$A_v = 8$

$A_h = 4$

$\bar{c}_v = 1$

$\bar{c}_h = 2$

---- Weber
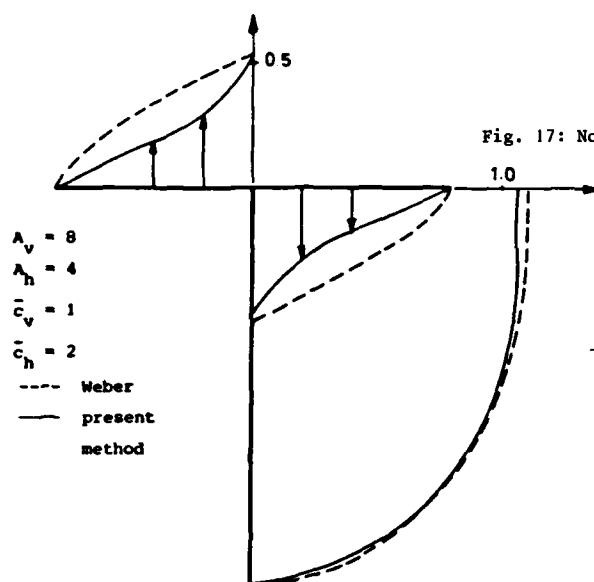
—— present
method

Fig. 18: Comparison of $C_\ell \cdot c/\bar{c}_v$ distribution from
present method, with the method of Weber
and Hawk, reference 11.

$A_v = A_h = 3$

$\bar{c}_v = \bar{c}_h = 1$
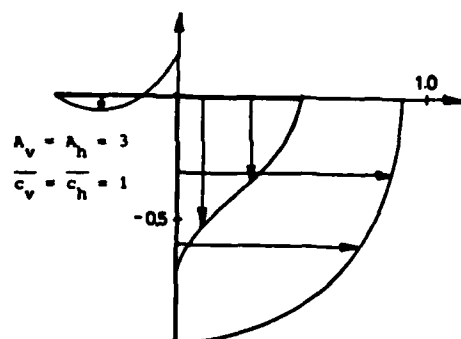
Fig. 19: $C_\ell \cdot c/\bar{c}_v$ distribution of T-tail with a
horizontal surface incidence angle.

downstream side   upstream side

$\zeta_T/(B.2)$

C_1

TIPVANE

tip

BLADE

root

C_1
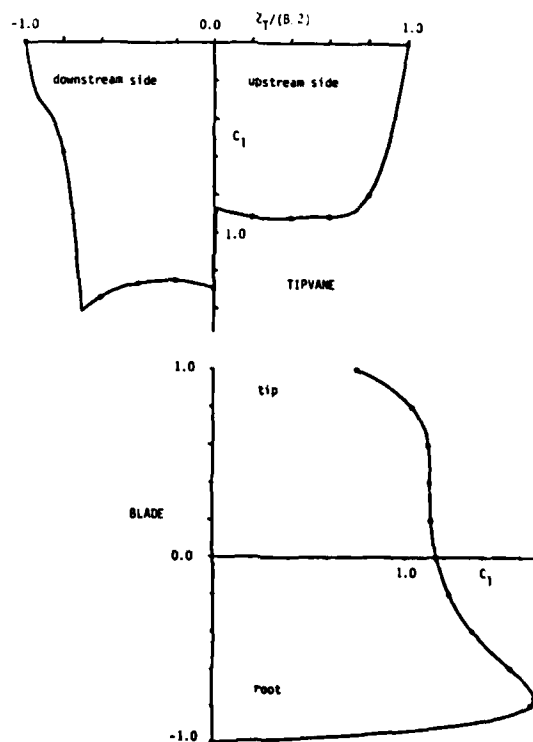
Fig. 20: Typical distribution of liftcoefficients along
turbine blade and tipvane.

AERODYNAMIC LOAD CALCULATION ON
HORIZONTAL AXIS WIND TURBINE IN NON UNIFORM FLOW
by
Elio Lupo, Dr.Eng.
Energy Sector
AERITALIA Soc.Aerospaziale Italiana p.Az.
Corso Marche, 41 - 10146 TORINO
ITALY

SUMMARY

The Energy Sector of AERITALIA S.A.I.p.A. has been working for
the past years in the field of horizontal axis wind generator.
During the preliminary design it is important to understand the
source of the aerodynamic loading which plays a critical role
in the design and it is necessary to have a rapid evaluation of
variable loads on the blades due to nonuniform flow.
In order to make the above calculations of blade loads an aero-
dynamic computer program, applicable to upwind rotors, has been
developed.
This program takes into account the atmospheric boundary layer
the variation in wind direction and tower reflection.
This program performes an aerodynamic analysis based on a combi
nation of momentum and blade element equations and calculates
the aerodynamic conditions and the airloads for 36 azimuth posi
tions of a rigid blade during its rotation.
The inputs of the program are the geometric characteristics of
the rotor and blades, the aerodaynamic characteristic of the
airfoil sections, the wind shear expression, the yaw and tilt
angle with wind direction and the rotor-tower diameter ratio for
cylindrical towers.

LIST OF SYMBOLS

a	axial induction factor
a'	tangential induction factor
A	empirical factor
B	number of blades
C	empirical factor
c	local chord of blade element (m)
C_D	$D/(1/2 \rho U\pi R)$=rotor drag coefficient
C_d	profile drag coefficient of blade element
C_{dt}	drag coefficient for a cylindrical tower
C_L	lift coefficient of blade element
C_m	moment coefficient of blade element
C_N	$N/(1/2 \rho U\pi R)$=normal force coefficient of one blade
C_p	$P/(1/2 \rho U\pi R)$=power coefficient
C_T	$T/(1/2 \rho U\pi R)$=tangential force coefficient of one blade
d_m	Distance between center of rotor and tower axis (m)
D	Rotor drag
F	tip loss factor
H	height above the ground (m)
H_h	hub height (m)
H_o	surface roughness length(m)
H_{ref}	reference height for wind shear (m)
N	Normal force on one blade (N)
MB	flatwise moment (Nm)
MC	chordwise moment (Nm)
MT	torsion moment (Nm)
MY	tilting moment (Nm)
MZ	Yaw moment (Nm)
P	Power (Kw)
R	radius of rotor (m)
R_T	Tower radius
r	local radius of blade element (m)
T	Tangential force one blade (N)
U	wind velocity (m/sec)
$U_x-U_y-U_z$	components of wind velocity respect to x y z axis (m/sec)
U_{ref}	reference wind velocity at H_{ref} (m/sec)
X	$\Omega r/U$ local tip speed ratio
α	angle of attack of the blade element (degrees)
θ	angle between rotor plane and relative velocity element (degrees)
λ	tip speed ratio $\Omega R/U$
ρ	density of the air (kg/m^3)
σ'	$Bc/2\pi r$ local solidity ratio of the rotor
Ω	angular velocity of the rotor (rad/sec)
δ	exponent of power law wind shear
γ	rotor axis tilt angle (degrees)
ϵ	yaw angle (degrees)
Y	lateral force on the rotor
Z	vertical force on the rotor

1. INTRODUCTION

During the preliminary design of a wind turbine it is normal to determine performance and static loads on the blades considering the rotor in a steady, homogenous and non-turbulent wind stream. However, it is also necessary to know the unsteady load distribution. An actual wind turbine infact is operating in nonuniform flow (vertical increase of the average wind velocity so called wind shear, fluctuations in space and time, change on wind direction and tower interference).

This paper presents a study developed by AERITALIA Energy Sector on a horizontal axis wind turbine in nonuniform flow. Turbolence is not taken into account because the fluctuations in space and time depend strictly on the site where the wind turbine will be installed and because the turbolence is considered in relation to the turbine control.

The paper is referred to an horizontal axis wind turbine with upwind rotor, two blades and cylindrical tower, which can be considered the best trade-off between different configurations (up- or down-wind rotor, cylindrical or truss tower) considering cost of design and construction, aerodynamic, structural and aeroelastic problem.

2. THEORY AND REMARKS

Fig.1 shows the reference axes, and Fig.2 the sign convenction for Ω (rotational speed) and ψ blade azimuth position. For the blade a second system of axes is defined in Fig.3 x'y'z', where the y'axis is directed along the blade axis on the 25% of chord.

The theory based on a combination of momentum and blade element equations (ref.1-2) has been applied for the present study. We have selected these simple equations in order to have a rapid evaluation of the blade loads for several different configurations and because for the preliminary design it is not necessary to apply a more complicated theory, as free wake theory.

The model for the rotor in nonuniform flow is derived from momentum theory and consists in subdividing the blades in several elements (ref.3); for each element the induced velocities are calculated in the plane of the rotor, considering the element under calculation equivalent to a blade element of a rotor in uniform flow. With this assumption it is possible to apply the same relation derived for the rotor in uniform flow. In order to calculate these velocities the average values are estimated from momentum considerations (ref.4). From the induced velocity relative to the blade element the angle of attack and the effective velocity are calculated. The local lift and drag can be derived from the data on two-dimensional airfoil sections (C_L vs α, C_d vs α). In order to estimate the "tip-losses" the Prandtl correction (ref.5) has been used

$$F = (2/\pi) \arccos \left[\exp{-(B/2)(1-r/R)/((r/R)\sin\vartheta)} \right] \tag{2.1}$$

where B is the number of blades
   r/R non dimensional station along the blade
   R rotor radius
   ϑ angle from relative velocity to plane of rotation

In operating conditions the momentum theory leads contradictory results when the induced velocities in the rotor plane become larger than one half of the wind velocity. The increase of the induced velocities is coupled with an increase of the wake width behind the rotor (continuity equation). At a certain moment the wake structure breaks down into turbolence and it is not more possible to apply the momentum theory. In order to calculate the turbulent wake state some empirical relations between the axial force and the average velocity through the rotor disk (ref.6 - ref.1) has been incorporated in the mathematical model. By the momentum theory the relation between the induced axial velocity at the rotor disk (aU) and the axial force of the rotor (D) can be written in non-dimensional form:

$$C_D = 4a (1-a) \tag{2.2}$$

This parabolic relation is plotted in Fig.4, but for $(1-a) < 0.5$ it is not applicable. Ref.6 proposes for $(1-a) < 0.6$ the empirical relation also plotted in fig.4 which can be linearized by the following expression:

$$C_D = A - C (1-a) \tag{2.3}$$

where

   A = 1.6 and C = 1.066

Assumed that (2.3) is also valid for each blade element, it has been introduced on the relation C_L versus ϑ of the single element for $(1-a) < 0.6$.

The relation between C_L and ϑ is (momentum theory - ref.5)

$$\sigma' C_L \cos\vartheta \ (U_{rel}/U)^2 = 4 F \sin\vartheta \cos\vartheta \ (\sin\vartheta + X\cos\vartheta)(\cos\vartheta - X\sin\vartheta) \tag{2.4}$$

which is plotted in fig.5 for one value of the local tip speed ratio $X = \Omega r/R$. Considering the simple theory the operating point of the blade element is determined by the intersection between this curve and the airfoil lift versus aerodynamic angle of the blade element. If ϑ is less than ϑ_1 $((1-a) < 0.6)$ it is necessary to introduce the relation derived from experimental data. For ϑ_1 corresponding to $(1-a)=0.6$, C_{L1} is calculated by the equation (2.4). The second point C_{L2} for $\vartheta = 0$ is determined considering that the

lift C_L has a non tangential component and that there is no tangential velocity (a'=0). The linear expression for C_L vs θ is:

$$C_L = (C_L)_2 - \left[(C_L)_2 - (C_L)_1 \right] \theta/\theta_1 \tag{2.5}$$

At this point it is possible to calculate the operating point of the blade element in the turbulent wake state.

The coefficients of the normal force, tangential force and power for the blade element can be calculated from the following equations:

$$dC_N = 1/\pi\, C_L(c/R) \cos\theta \, (\sin\theta + X\cos\theta)^2 \left[1 + (C_d/C_L)\,tg\,\theta \right] d(r/R) \tag{2.6}$$

$$dC_T = 1/\pi\, C_L(c/R) \sin\theta \, (\sin\theta + X\cos\theta)^2 \left[1 - (C_d/C_L)\,cotg\,\theta \right] d(r/R) \tag{2.7}$$

$$dC_P = X dC_T \tag{2.8}$$

considering the local tip speed ratio, which depends on the radial and azimuth position of the blade element, derived from local wind and tip speed due to a nonuniform flow.

By performing integration along the blade, considering the local wind speed, the following loads can be determined for the complete blade at ψ position: normal force N (x' axis), tangential force T (z'axis), flatwise moment M_B (z'axis), chordwise moment M_C (x'axis) and torsion moment M_T (y'axis). The integration of 2.8 along the blade provides the power extraction from the wind for one blade at the ψ azimuth position. Considering the different loads for each azimuth angle of the blade, the resultant force on the rotor along the y and z axis and the tilting and lateral moment My, Mz can be calculated.

3. VERTICAL WIND SHEAR

The variation of the average wind velocity with height due to the ground friction is known as the vertical wind shear and it is a typical example of wind nonuniformity (ref.8). The exact variation with height depends upon the ground surface roughness characteristics. The vertical wind shear can be represented by two mathematical expressions: a power law or a logarithmic law (ref.9).

In most cases it is possible to consider a more or less linear velocity increase between the top and the bottom of the rotor, because the wind turbine is placed at some height above the ground (fig.6). In this case the following comments can be made:

- The force along x axis or drag (D) and the torque are not affected by a linear shear for rotors with two or more blades.

- The side force (Y) and the tilting moment (MY) vary as $\sin^2\psi$ in case of one or two blades rotors; they have a constant non zero value for three or more bladed rotors and the sign do not change during rotation.

- The vertical force (Z) and the yawing moment (MZ) vary as $\sin\psi\cos\psi$ in case of one or two bladed rotors and they are equal to zero for three of more bladed rotors.

To obtain a more valid result the wind speed variation can be expressed by one of the two following mathematical expressions (3.1 e 3.2). One is the power law relationship:

$$U/U_{ref} = (H_i/H_{ref})^{\delta} \tag{3.1}$$

where the U ref. is the wind velocity at the reference height Href. and the exponent δ depends on the surface type:

Flat open country	ice	0.09
	show	0.10
	sea	0.11
Low roughness	meadow	0.10
	crops	0.14 ÷ 0.18
Rough	wooded	0.10
	city suburbs	0.28
Very rough	urban center	0.24 ÷ 0.35

The reference height is normally 10 meters. The relation 3.1 is very important in the performance analysis of the wind turbine rotor and it yields conservative results for the power extraction.

For conservative results of the airloads on the blades it is better to use the second mathematical expression based on a logarithmic law:

$$U/U_{ref} = \ln(H/H_0) \, / \, \ln(H_{ref}/H_0) \tag{3.2}$$

where H_0 is the surface roughness length. For engineering applications, a value of $H_0 = 0.2$ meters is recommended for the surface roughness length.

4. TOWER DISTURBANCE

The tower produces a disturbance in the wind flow of the rotor blades. In the case of an upwind rotor (tower reflection) the disturbance velocities are due to the obstruction represented by the tower. These velocity variations can be calculated from the potential flow theory employing polar coordinates with respect to the tower axis. It is possible to calculate the effective wind velocity of the blade element for each azimuth angle ψ and for each position along the blade, considering the distance of the element under calculation from the tower axis.

In the case of down-wind rotor the blade is subjected to aerodynamic shadow of the tower. In this case it is difficult to represent the velocity distribution of tower wake with a mathematical expression. During the preliminary design it is possible to compute this wake as a function of the tower drag coefficient. For symmetrical bodies, such as a cylindrical tower we can calculate the velocity distribution with the following relationship (ref.10):

$$U_x/U = 1 - K_1 \, e^{\, K_2 \,(r/R \, \sin\psi)} \tag{4.1}$$

where K_1 and K_2 are:

$$K_1 = 4\cdot10^{-4}\cdot C_{dt} \cdot (RN)^{.5} \; (R_T/x)^{.5}$$

$$K_2 = 2.5\cdot10^{-6} \; (RN) \; (R/R_T)^2 \cdot R_T/x$$

where RN is the Reynolds number for the complete tower.

Taking into account the initial choise of an up-wind configuration, the aerodynamic program for the airloads calculation considers only the case of tower reflection. The disturbance is considered only when the blade passes near the tower for azimuthal positions from 140° to 220°.

5. CROSS FLOW

In several operating conditions rotor is working in cross flow conditions, such as in presence of sidegust or changes in wind direction not sufficient or rapid enough to be compensated by rotation of the rotor axis. The lateral flow and the variations in wind direction produce rotor moments that are function of the inflow angle and wind lateral velocity. In many cases the misalignment of the rotor axis with the wind speed vector is present in normal operation, because in the design a tilt angle is introduced to move the blade away from the tower (fig.7).

If the cross flow component is of the same order of magnitude as the axial component it cannot be analysed by simple methods, but it requires complex free wake analyses. When the rotor is operating under cross flow condition, it is subjected to conditions similar to helicopter blades during forward flight: the experimental and theoretical results indicate that the flow is highly nonuniform. The primary effect of cross flow is to generate time varying loads on the rotor containing all harmonics of rotational speed, in particular a first harmonic (once per revolution) component is important to consider for the airloads.

During the preliminary design and in absence of an adequate experimental basis, for estimating these blade loads, a reasonable first approximation may be made neglecting the nonuniformity of the flow perpendicular to the rotor plane and considering only the effect of the cross flow velocity component in the plane of the rotor (ref.11). The blade sees a time varying velocity during its rotation, the velocity component of the cross flow in the rotor plane is added to the rotational velocity on one side of disc (advanced blade) and subtracted on the other side (returned back blade). Two inflow angles are introduced in the program to consider the cross flow. They describe the misalignment of the rotor axis with the wind direction: one in the vertical plane γ (tilt angle) and the other in the horizontal plane ε (yaw angle); for the sign of the two angles see fig.6-7. Considering these angles we have two velocity components in the plane of the rotor disc: along the y axis and z axis (yaw and tilt angles respectively)

$$U_y = U\sin(\varepsilon) \qquad U_z = U\sin(\gamma) \tag{5.1}$$

The local tip speed of the element is calculated by the relation:

$$V = \Omega \, r - U_y\cos\psi - U_z\sin\psi \tag{5.2}$$

On the basis of this consideration it is possible to calculate flatwise and chordwise blade moments depending on the azimuth position of the blade. They cause a tilting and lateral moment (MY, MZ) on the rotor.

6. PROGRAM DESCRIPTION

To determine the aerodynamic loads of the blades a computer program based on the theory previously described has been developed. The wind turbine modelled in this program is a two blade horizontal axis type with a central hub. The blades are assumed identical and can present any given twist and chord distribution. The entire rotor assembly is assumed to be rigid and turning at a constant angular velocity. Each blade is divided into 20 spanwise sections, equal in length, between the tip and root sections; the region of the rotor hub is modelled by a simple cut-out of each blade.

By an interative procedure the program calculates the aerodynamic conditions of the blade elements and the loads on the blade and on the rotor for 36 azimutal positions. All calculations are made with non dimensional relations but the outputs are in dimensional form because the rotor dia. and rotor speed are defined.

The program can make the required calculations for a defined wind speed range and for various blade configuration angles; for example it is also possible to calculate the blade loads in nonuniform flow for the tip controlled rotor. This control type is applied in the large horizontal axis wind turbines, the portion of the blade with a variable pitch is normally 35-30% of the radius at the blade tip.

The program calculates the rotor performance and characteristics according to the following flow chart representation.

FLOW CHART

```
                    ┌─────────────┐
                    │   START     │
                    └─────────────┘
                  ┌─────────────────┐
                  │  READ INPUT     │
                  └─────────────────┘
        ┌──────────────────────────────────────┐
        │ WRITE GEOMETRICAL DATA OF THE BLADE   │
        └──────────────────────────────────────┘
          ┌──────────────────────────────────┐
          │ START LOOP OF THE WIND VELOCITY   │
          └──────────────────────────────────┘
             ┌──────────────────────────┐
             │ START LOOP OF AZIMUTAL    │
             │ POSITION 10≪ψ<360°        │
             └──────────────────────────┘
            ┌────────────────────────────┐
            │ START LOOP OF BLADE ELEMENT │
            │ ALONG THE BLADE RADIUS      │
            └────────────────────────────┘
            ┌──────────────────────────────────┐
            │ CALCULATION OF WIND               │
            │ VELOCITY RELATIVE TO THE ELEMENT  │
            └──────────────────────────────────┘
       ┌───────────────────────────────────────────┐
       │ SETTING ANGLE AND ELEMENT CHORD CALCULATION│
       └───────────────────────────────────────────┘
          ┌──────────────────────────────────────┐
          │ ITERATIVE PROCEDURE TO CALCULATE      │
          │ THE INDUCED VELOCITY, $\vartheta$ ,$c_L$│
          └──────────────────────────────────────┘
      ┌────────────────────────────────────────────────┐
      │ AERODYNAMIC COEFFICIENT PROFILE CALCULATION     │
      └────────────────────────────────────────────────┘
             ┌──────────────────────────────┐
             │ END LOOP OF THE ELEMENT       │
             └──────────────────────────────┘
             ┌──────────────────────────────┐
             │ CALCULATION OF THE POWER      │
             │ EXTRACTION AT THIS ψ ANGLE    │
             └──────────────────────────────┘
          ┌────────────────────────────────────┐
          │ LOADS CALCULATION ALONG THE BLADE   │
          └────────────────────────────────────┘
       ┌──────────────────────────────────────────────┐
       │ OUTPUT OF LOADS IN FLATWISE AND CHORDWISE     │
       │ AND AERODYNAMIC CONDITION ALONG THE BLADE     │
       └──────────────────────────────────────────────┘
            ┌────────────────────────────────────┐
            │ TILTING AND LATERAL MOMENT          │
            │ AND FORCE CALCULATION Y, Z, MY, MZ  │
            └────────────────────────────────────┘
                  ┌──────────────────────┐
                  │ END LOOP OF  ψ        │
                  └──────────────────────┘
        ┌──────────────────────────────────────────────┐
        │ POWER CALCULATION                             │
        │ CONSIDERING THE TWO BLADES AT EVERY ψ POSITION│
        └──────────────────────────────────────────────┘
          ┌────────────────────────────────────────┐
          │ AVERAGE CALCULATION FOR EACH LOADS      │
          └────────────────────────────────────────┘
            ┌──────────────────────────────────┐
            │ END LOOP OF WIND VELOCITY         │
            └──────────────────────────────────┘
         ┌────────────────────────────────────────┐
         │ OUTPUT OF THE ROTOR PERFORMANCE,        │
         │ BLADE LOADS AT THE ROOT, MOMENTS        │
         │ AND FORCES RESPECT TO THE x y z         │
         │ AXIS FOR EACH AZIMUTAL POSITION         │
         │ AND FOR EACH WIND VELOCITY              │
         └────────────────────────────────────────┘
                ┌──────────────────────┐
                │ PLOTTING RESULTS      │
                └──────────────────────┘
                    ┌─────────────┐
                    │   END       │
                    └─────────────┘
```

The inputs data necessary to run the program may be subdivided in five sections:

Section 1 : dimensional data

- Rotor diameter (m)
- Rotational speed R.P.M.
- Tip pitch angle of the blade tip section (degrees)
- Root pitch angle of the blade root section (only for a tip controlled rotor) (degrees)
- Tilt angle γ (degrees)
- Coning angle

Section 2: geometrical data of blade and tower (non dimensionalized by the rotor radius)

- Coefficients of the linear or parabolic expression of the taper ratio and blade twist
- Reference height H_{ref}/R
- Hub height H_O/R
- Distance between center of rotor and tower axis dm/R

Section 3: wind characteristics

- Range of the wind speed under calculation (m/sec)
- Exponent of power law of wind shear or surface roughness length H_O
- Cross flow angle of the rotor axis & (yaw)   (degrees)

Section 4: aerodynamic characteristics of the airfoil section along the blade

- Coefficients of the mathematical expressions of the C_L, C_d, C_m versus α

Section 5: flags for the control program option

- Wind shear with power or logarithmic law
- "long printout" or "short printout"
- no or yes results plotter.

7. RESULTS AND CONCLUSIONS

Using the program herein described we have investigated a wind turbine with the following configuration:

N^O of blades	= 2
Rotor Dia.	= 32 m
Rotational speed	= 40.6 RPM
Tip chord	= 2.5 m
Taper ratio	= Linear
Twist angle	= 6°
Hub Dia.	= 3.2 m
Coning angle	= 4°
Hub height	= 26 m
Tower Dia.	= 1.6 m
Rotor distance from tower axis	= 3.5 m
Rotor configuration	= upwind
Tilt angle	= 6°
Tip pitch angle for the whole blade	= 1°
Airfoil section	= NACA 44XX

The wind turbine is evaluated for a nonuniform flow considering the logarithmic law for the wind shear with H_O = 0.2 m, H_{ref} = 10 m, and a cross flow angle of 5°. The wind speeds evaluated at the hub height were 8-9-10 m/sec. These speeds correspond to the reference height (10 m) respectively to 6.5 - 7.3 - 8.1 m/sec.

In this paper we have included only the graphic results of the load calculation (fig.8-14)but with the option of a "long printout" it is possible to have the loads and the aerodynamic characteristics along the blade. From the diagrams it is clear that the rotor loads (drag D, lateral moment MZ, tilting moment MY) and the power present a period of twice per revolution while the first harmonic of the blade loads is one per revolution. In the diagrams of the blade loads at the root (MB, MC, MT) the influence of the wind shear can be observed. At the bottom azimuth position (Ψ = 180°), it is also possible to see the influence of the tower reflection. In the present case the tower disturbance is not large because the turbine has an up-wind rotor and the distance between the blade and the tower has been optimized. The average values of the moments at the blade root are:

wind speed (m/sec)	8	9	10
MB (Nm)	- 100424.0	-116704.0	-132130.0
MC (Nm)	10273.0	14452.0	19013.0
MT (Nm)	4596.0	5967.0	7413.0

The difference between the maximum and minimum value during the rotation in percent of average value is:

wind speed (m/sec)	8	9	10
MB (%)	42	43	44
MC (%)	80	79	78
MT (%)	46	40	38

These variations are very important for the blade design considering the fatigue life.

To investigate the importance of each type of flow non uniformity it is possible to use the program considering separately wind shear, cross flow and tower disturbance. For example in the last   diagram the lateral force Y due only to the tower reflection is shown.

The results obtained from this theoretical analysis must be compared with the experimental data. Preliminary wind tunnel test results concerning the distribution of loads along the blade will be available in the next future. Moreover we are waiting for the experimental campaign with the actual wind turbine in order to have sufficients available data for a good comparison.

LIST OF REFERENCE

- 1   Stoddard F.S.   Momentum theory and flow states for wind mills.
                         Wind Technology Journal, 1,1 (Spring 1977) pp. 3-9.

- 2   Wilson R.E.
      Lissaman PBS   Applied aerodynamics of Wind Power Machines.
                         Oregon States Univ. Report NSF/RA/N-74113 (July 1974).

- 3   De Vries O.   Fluid Dynamic aspects of wind energy conversion AGARDograph
                         No. 243 (July, 1979).

- 4   De Vries O.   The aerodynamic performance of a horizontal-axis wind turbine
                         in a stationary parallel flow. Discussion of existing theories,
                         of a parameter study and of consequences for a wind tunnel mo-
                         del design.
                         NLR TR 780 84 L (July 1978).

- 5   Prandtl L.
      Betz A.   Vier Abhandlungen zur hydrodynamik und Aerodynamik (Göttingen,
                         1927) p. 68.

- 6   Miller R.H.
      et al.   Wind energy conversion (final report, February 1975 - Octobre
                         1976) NSF/RA 760569 (Octobre 1976), pp II -54 through II -56.

- 7   Glauert H.   Windmills und Fans. Aerodynamic Theory (ed. W.F. Durand) Chapter
                         XI, Div. L. (Dover Publ. Inc., N.Y. 1963).

- 8   Frost W.   Engineering handbook on the Atmospheric Environmental Guidelines
                         for Use in Wind Turbine Generator Development.
                         Proc. Third Biennal Conf. and Workshop on Wind Energy Conversion
                         Systems (Wash. D.C. 19-21 Sept. 1977).
                         JBF Scient. Corp. CONF. 770921 (Sept. 77).

- 9   Lumley J.L.
      Panofsky H.A.   The structure of Atmospheric Turbolence.
                         (J. Wiley & Sons Inc. 1964).

- 10 Miller R.H.
      Dugundji J.
      Martinez-Sanchez H.
      Gohard J.
      Chung S.
      Wendell J.   Doe, Wind Energy Conversion, Sept. 1978, Report COO-4131-Tl, Vol.1

- 11 Glauert H.   Miscellaneous Airscrew. Problems Aerodynamic Theory (ed. W.F. Durand)
                         Chapter XII, Div. L (Dover Publ. Inc.; N.Y. 1934).
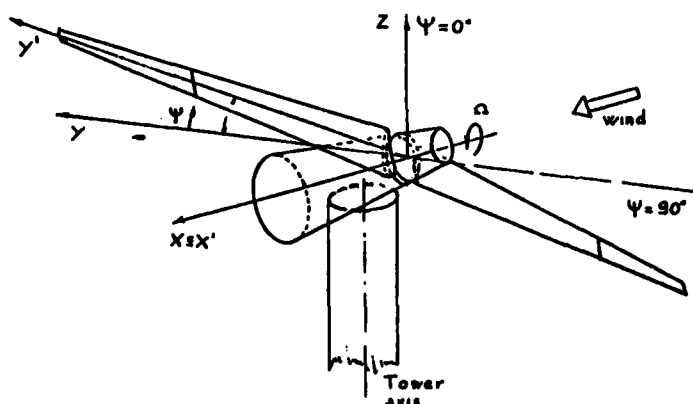
FIG. 1

Rotor axes
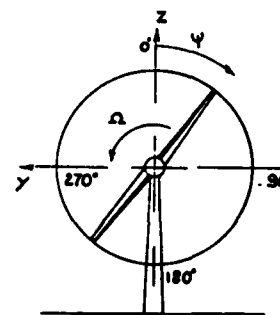
FIG. 2

Azimuth position and rotor speed
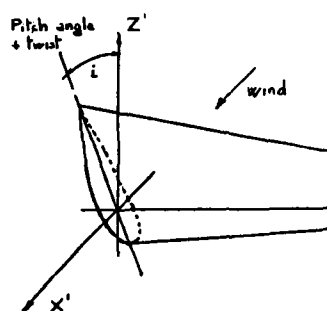
FIG. 3

Blade axes
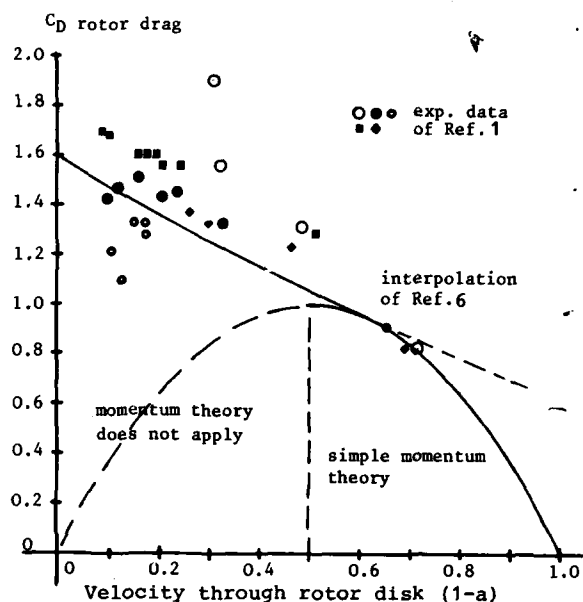
FIG. 4

Relation between the rotor drag and the average velocity through the rotor disk.
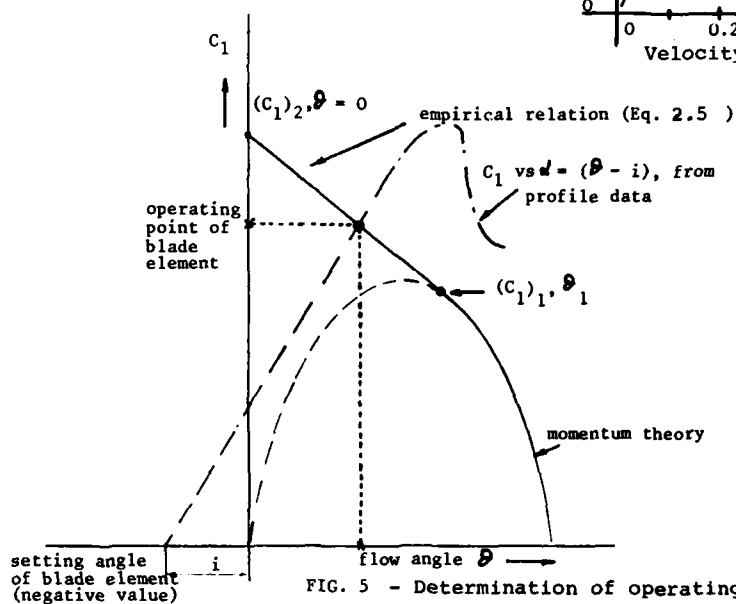
FIG. 5 - Determination of operating point of blade element
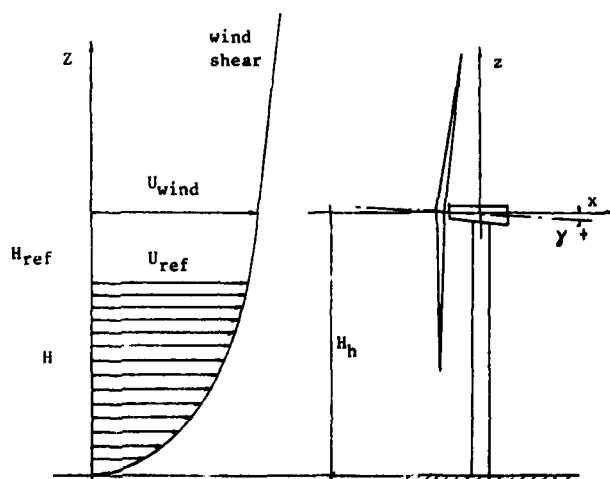
FIG. 6

Wind shear and tilt angle
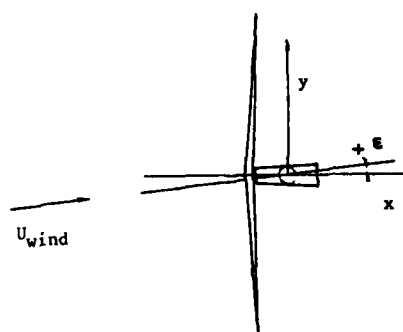
FIG. 7

Yaw angle
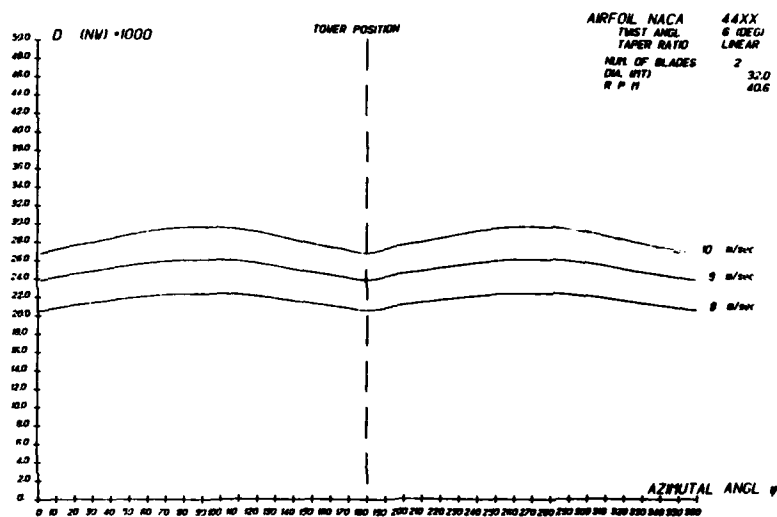
FIG.8
Rotor Drag
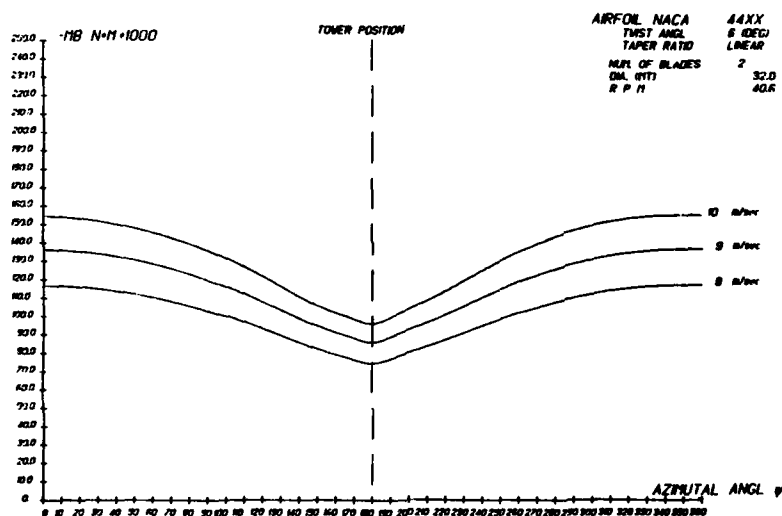
FIG.9

Flatewise moment
at the root blade
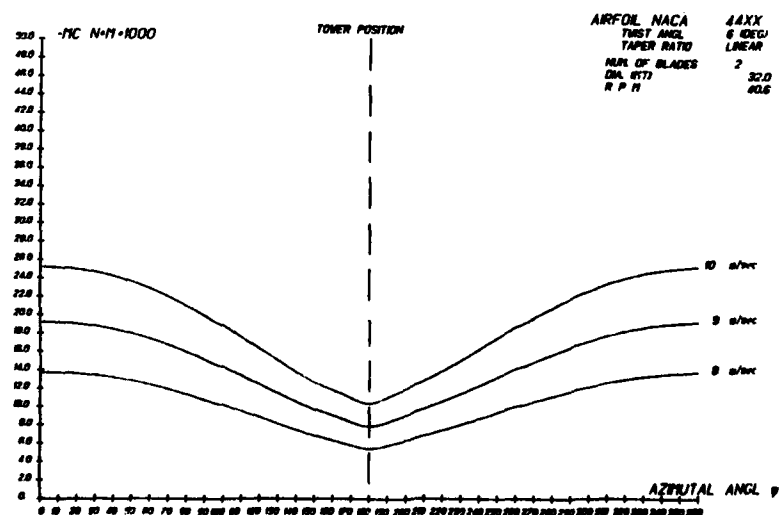
FIG.10

Chordwise moment
at the root blade

MT N·M

TOWER POSITION

AIRFOIL NACA   44XX
TWIST ANGL   6 (DEG)
TAPER RATIO   LINEAR
NUM. OF BLADES   2
DIA. (MT)   32.0
R P M   40.6

10 m/sec
9 m/sec
8 m/sec

AZIMUTAL ANGL ψ
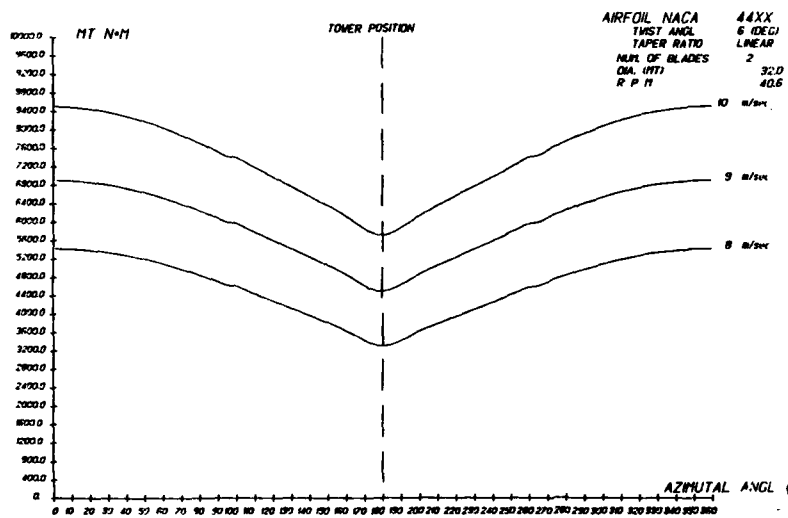
FIG. 11

Torsion moment at
the root blade on
25% of chord

MY(N·M) ·1000

TOWER POSITION

AIRFOIL NACA   44XX
TWIST ANGL   6 (DEG)
TAPER RATIO   LINEAR
NUM. OF BLADES   2
DIA. (MT)   32.0
R P M   40.6

10 m/sec
9 m/sec
8 m/sec

AZIMUTAL ANGL ψ
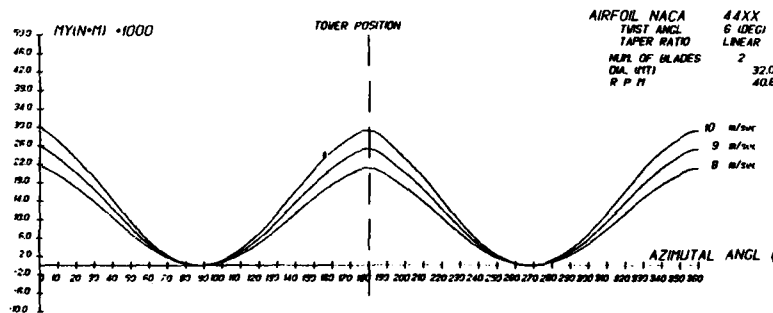
FIG. 12

Rotor tilting moment

MZ(N·M) ·1000

TOWER POSITION

AIRFOIL NACA   44XX
TWIST ANGL   6 (DEG)
TAPER RATIO   LINEAR
NUM. OF BLADES   2
DIA. (MT)   32.0
R P M   40.6

AZIMUTAL ANGL ψ

FIG. 13

Rotor yaw moment

Y (NW)

TOWER POSITION

AIRFOIL NACA   44XX
TWIST ANGL   6 (DEG)
TAPER RATIO   LINEAR
NUM. OF BLADES   2
DIA. (MT)   32.0
R P M   40.6

10 m/sec
9 m/sec
8 m/sec

AZIMUTAL ANGL ψ
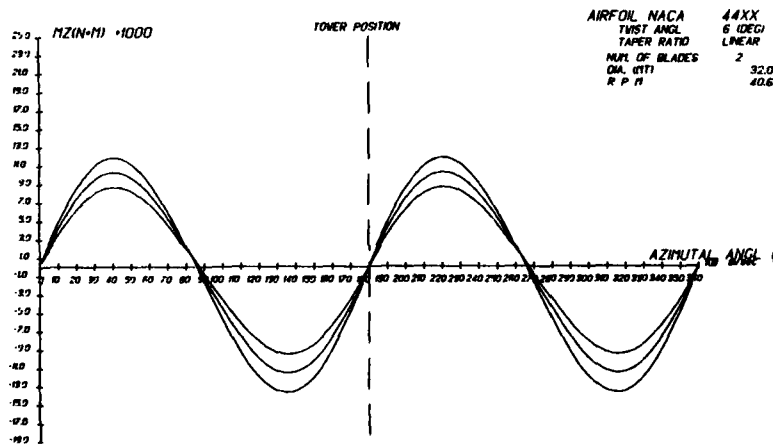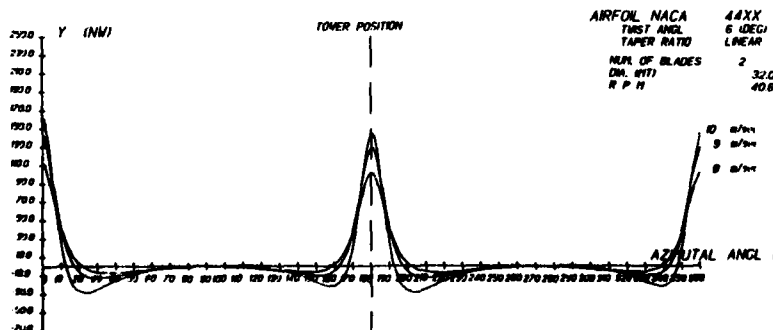
FIG. 14

Lateral force Y
considering only
the tower disturbance

PREDICTION ET VERIFICATION EXPERIMENTALE
DU CHAMP DES VITESSES D'UN ROTOR
EN VOL STATIONNAIRE

C. MARESCA, Maître de Recherche au C.N.R.S.
M. NSI MBA, Attaché de Recherche à l'I.M.F.M.
D. FAVIER, Chargé de Recherche au C.N.R.S.

Institut de Mécanique des Fluides. LA 03 du C.N.R.S.
1, rue Honnorat, 13003 Marseille, FRANCE

SOMMAIRE

L'étude dont il est fait état ici a pour objet de tester les hypothèses et les limites de validité d'un code de calcul relatif aux performances d'un rotor d'hélicoptère en vol stationnaire.

Ce calcul, mis au point à l'origine par la S.N.I.A.S. Marignane, est basé sur le principe de mise en équilibre partielle d'un sillage initialement prescrit à partir de lois empiriques et permet de déterminer le champ de vitesses instantané et les performances associées. L'expérience a consisté en des mesures des trois composantes du vecteur vitesse à l'aide d'anémomètres à fils chauds croisés et à laser et en la détermination des lignes tourbillonnaires d'extrémité par visualisation et anémométrie à fils chauds croisés. Les efforts globaux (traction et couple) ont été de même mesurés.

Les confrontations calcul-expérience ont été réalisées dans une grande gamme de variation des paramètres : nombre de pales, pas général, vrillage (linéaire et non linéaire), géométrie de l'extrémité. Le résultat de ces confrontations montre que pour certaines configurations, le calcul est satisfaisant, (quadripale, forte charge, vrillage linéaire, extrémités rectangulaires ou effilées). Par contre, il est à revoir pour les autres configurations. La prise en compte d'un sillage lointain mieux modélisé et d'une structure évolutive du noyau tourbillonnaire mise en évidence par l'expérience s'avèrent indispensables dans le modèle de calcul.

NOTATIONS

a_o : conicité

b : nombre de pales

c : corde des profils (0,05 m)

C : couple du rotor

C_Q : coefficient de puissance : $\dfrac{C}{\rho \pi R^3 (V_e)^2}$

C_T : coefficient de traction : $\dfrac{T}{\rho \pi R^2 V_e^2}$

C_z : coefficient de portance des profils

C_{z_M} : coefficient moyen de traction : $\dfrac{6\, C_T}{\sigma}$

F.M. : figure de mérite : $\dfrac{T^{3/2}}{\sqrt{2\ \rho \pi R^2}\ C \Omega}$

OZYZ : trièdre défini dans la figure 5

r : abscisse radiale comptée à partir du moyeu

r_t : rayon du noyau tourbillonnaire d'extrémité

R : rayon du rotor

t : temps

T : traction du rotor

u :
v : composantes radiale, tangentielle et axiale : voir figure 5
w :

V_e : vitesse en extrémité de pale (ΩR)

$\tilde{z}$: traction réduite : $\dfrac{200\, C_T}{\sigma}$

σ : plénitude du rotor : $\dfrac{b.c}{\pi R}$

$\theta_{0,75}$: pas général

θ_V : vrillage

ψ : azimut ou phase (Ωt)

Ω : vitesse angulaire du rotor

ρ : masse volumique de l'air (1,225 kg/m3)

Γ : circulation

1. INTRODUCTION

Depuis plusieurs décades, les aérodynamiciens des rotors d'hélicoptère développent des codes de calcul de plus en plus sophistiqués afin de relever le défi lancé pour améliorer les performances de ces rotors. En particulier, le cas du vol stationnaire, qui présente une étape importante vers l'étude plus ambitieuse du vol d'avancement, a retenu l'attention de nombreux chercheurs. L'effort déployé pour déterminer les caractéristiques aérodynamiques liées à ce type de vol porte essentiellement sur la modélisation

du sillage et principalement sur la détermination de la ligne tourbillonnaire d'extrémité de pale qui est l'un des paramètres fondamentaux dans les calculs entrepris.

Une première génération de ces calculs a consisté à introduire dans les codes un sillage du rotor "prescrit" préalablement par des équations empiriques tirées d'expériences effectuées sur de nombreux rotors. Les travaux de Landgrebe[1][1'], ainsi que ceux présentés dans la référence 2 (voir par exemple Cheney et al, Gray et al, etc...) donnent un vaste aperçu de ce qui a été fait concernant cette première génération. On citera de même la référence 1" qui concerne des rotors à faible paramètre d'avancement.

Ces dernières années, une seconde génération de calcul a été lancée aux Etats-Unis par Kocurek et al[3], Scully[4], Gohard[5], Summa et al[6] et en France par Courjaret et al[7] puis Pouradier et al[8]. La principale innovation consiste en ce que le sillage est assujetti à affecter une géométrie "libre" définie sous l'influence de l'établissement des vitesses induites.

Ainsi la connaissance de mise en équilibre du sillage conduit à une détermination des charges subies par les pales et par suite à une optimisation qui sont plus proches de la réalité.

Le code de calcul développé par la S.N.I.A.S.[9] avec l'appui expérimental de l'O.N.E.R.A. a déjà donné lieu à une série de vérifications destinées à fixer les limites du calcul et éventuellement à le faire évoluer.

Dans le même esprit, l'I.M.F.M., avec le soutien de la Direction des Recherches Etudes et Techniques, a entrepris un vaste programme d'études destiné à tester le code de calcul existant relativement à divers paramètres tels que : le nombre de pales, le pas général, le vrillage (linéaire et non linéaire), la géométrie de l'extrémité. Le but du présent document est donc de montrer sur un très grand nombre de cas, les confrontations réalisées entre calcul et expérience et d'en dégager les enseignements.

Après avoir présenté dans le paragraphe 2 le calcul des vitesses induites dans le sillage en faisant ressortir ses avantages et ses faiblesses, le paragraphe 3 fait état du programme d'essais effectué et des techniques de mesure mises en oeuvre : a) anémomètres à fils chauds croisés et à laser utilisés pour la détermination des lignes tourbillonnaires d'extrémité et des vitesses induites ; b) visualisations pour la détermination des lignes tourbillonnaires très près du plan de rotation des pales, ainsi que pour la détermination de la variation avec la phase du noyau tourbillonnaire. La comparaison entre le calcul et l'expérience est effectuée sur différentes configurations de rotors dans le paragraphe 4. Les enseignements qui en sont tirés, permettent de fixer les limites du calcul exploité et d'en présenter les modifications futures à y apporter.

2. CALCUL

Les hypothèses faites et les méthodes de résolution de ce modèle de calcul sont développées en détail dans les références (7) et (8). Nous nous contenterons ici d'en retracer les grandes lignes.

La pale est assimilée à une ligne portante située au quart avant, et la distribution tourbillonnaire suivant cette ligne est supposée continue.

Le programme de calcul consiste en une mise en équilibre partielle du sillage; la ligne tourbillonnaire marginale peut être mise en équilibre depuis son départ de la pale émettrice jusqu'à son passage sous la pale suivante correspondant à la phase $\psi = 2\pi/b$; au-delà, la ligne tourbillonnaire est supposée descendre et se contracter selon les lois expérimentales définies dans les références (1) et (10), jusqu'à la phase $8\pi/b$. Le reste du sillage est remplacé par un anneau tourbillonnaire de rayon 1,2 R placé à une distance axiale correspondant à $8\pi/b$ et dont l'intensité est quatre fois celle de la ligne d'émission d'extrémité.

Les données d'entrée du calcul sont : la configuration géométrique du rotor, les polaires stationnaires des profils constituant la pale et le coefficient de traction.

Différentes étapes de la mise en équilibre :

1ère étape

La ligne marginale de départ ou géométrie initiale du sillage est fixée en fonction du vrillage et du coefficient de traction par application des lois de descente et de contraction de la nappe tourbillonnaire et de la ligne marginale ; ces lois ont été déterminées expérimentalement par Landgrebe[1], puis affinées par Kocurek et Tangler[10].

La distribution de circulation sur la pale est approximée par un développement en cosinus dont les coefficients sont déduits à partir des polaires stationnaires et de la donnée des vitesses incidentes. Les vitesses induites sont ensuite calculées en chacun des points de la ligne tourbillonnaire marginale par application de la loi de Biot et Savart.

2ème étape

Une nouvelle géométrie du sillage est obtenue par l'intégration des vitesses induites suivant un incrément de temps, ou encore suivant $\Delta\psi$.

- Les étapes 1 et 2 sont répétées jusqu'à ce que la ligne tourbillonnaire marginale soit tangente en chacun de ses points aux vitesses induites calculées sur ces points. On dit alors que le sillage s'est mis "librement" en équilibre sous l'effet du champ de vitesses induites développé.

3ème étape

La mise en équilibre précédente conduit à la détermination de nouvelles vitesses incidentes sur les différents profils de pale donc à une nouvelle distribution de circulation sur la pale donnée par la loi de Kutta-Joukowski qui est compatible avec la nouvelle géométrie de sillage obtenue.

- Les étapes 1 à 3 sont répétées jusqu'à ce que la circulation obtenue à l'étape 3 soit compatible avec celle donnée à l'étape 1.

A chaque itération de la circulation, on change le pas général de manière à conserver constant le coefficient de traction fixé au départ. La figure 1 donne l'organigramme du calcul précédemment décrit. Pour

l'instant, il n'a pas été apporté de grandes modifications au modèle exploité dans les références (7) et (8) en raison du temps qu'a demandé la comparaison calcul - expérience sur un nombre de cas qui s'est voulu le plus grand possible afin de pouvoir tester le code sur une large gamme de paramètres.

Faiblesses du calcul

Bien que la ligne tourbillonnaire se mette en équilibre sous l'effet des vitesses induites, cette mise en équilibre s'effectue seulement entre $\psi = 0$ et $\psi = 2\pi/b$. Pour $2\pi/b < \psi < 8\pi/b$, on fait appel à une loi empirique[1]. La géométrie du sillage lointain ($\psi > 8\pi/b$) n'est pas définie mais remplacée artificiellement par un anneau de recirculation.

- La structure des noyaux tourbillonnaires n'intervient pas dans le calcul. Il est fait l'hypothèse que le rayon du tourbillon r_t est constant tout au long de la ligne d'extrémité et égal arbitrairement à $5.10^{-3}R$. La figure (2) représente l'influence de la variation du rayon du noyau tourbillonnaire sur les lignes marginales d'émission obtenues. Les courbes en pointillés donnent les variations avec la phase de r/R et z/R pour 2 valeurs de $r_t/R = 5.10^{-3}$ et $2,5.10^{-3}$. On n'a décelé aucune différence dans les résultats de calcul : les deux séries de courbes sont confondues. Par contre, lorsque le rayon r_t/R est pris égal à 10^{-2}, on obtient les courbes en traits continus qui attestent une contraction des lignes marginales plus grande que celle obtenue avec une valeur arbitraire de $r_t/R = 5.10^{-3}$ (courbe 1) et une vitesse de descente des tourbillons plus grande.

- En ce qui concerne la technique de calcul, le fait d'avoir modélisé la pale par une ligne portante interdit, comme le montre Kocurek dans la référence (3), d'appliquer le calcul à des extrémités en flèches,en raison des indéterminations de vitesse qui apparaissent aux points de calcul choisis sur la pale.

- Le calcul des vitesses induites par intégration numérique de la formule de Biot et Savart repose sur la méthode de Gauss qui utilise un nombre fini de points de calcul le long de la pale et de la ligne tourbillonnaire marginale. Un nombre de points de calcul égal à 11 s'avère suffisant dans le cas de rotors quadripales. Une optimisation de ce nombre de points de calcul est actuellement en cours pour des rotors tripales et bipales.

- Enfin, l'exploitation a été jusqu'à présent effectuée au Centre de Calcul du Pharo de l'Université d'Aix-Marseille II, qui dispose d'un ordinateur IRIS 80.Les Universités du Sud-Est de la France ont,à présent, la possibilité d'être reliées au Centre de Calcul de Montpellier (C.N.U.S.C.) qui dispose d'un ordinateur nettement plus puissant (IBM.3033). A titre d'exemple, la mise en équilibre et le calcul des vitesses induites dans un plan du sillage nécessite actuellement un temps de 20 mn C.P.U. dans les cas extrêmes (convergence difficile). Ce temps sera ramené à 1 mn C.P.U. sur l'IBM de Montpellier.

3. EXPERIENCES

3.1. Le rotor

Le rotor de 1,5 m de diamètre, articulé en battement et en traînée, est décrit en détail dans la référence (11). La figure 3 montre des vues du montage réalisé dans la veine de la soufflerie elliptique de l'I.M.F.M. Les essais présentés par la suite sont relatifs à des vitesses en bout de pales de l'ordre de 107 m/s.

3.2. Jeux de pales utilisés

Les différents jeux de pales, en fibre de carbone et de fabrication S.N.I.A.S., sont répertoriés sur la figure 4. Les rotors ont été numérotés de 1 à 6 suivant les pales qui les équipent. La corde c est égale à 0,05 m.

3.3. Techniques de mesure

- La mesure des efforts (traction et couple) s'effectue globalement à l'aide de jauges de contraintes disposées sur le tube de support du rotor.

- La détermination des vitesses induites est réalisée à l'aide d'une sonde à fils chauds croisés dont le support est monté sur un chariot explorateur (voir figure 3) se déplaçant en r et z. Le signal de sortie, linéarisé avec la vitesse, est numérisé et exploité sur ordinateur HP 9345 B. Le vecteur vitesse résultant en fonction du temps est déduit de deux positions de mesure successives de la sonde, comme indiqué sur la figure 5. Cette technique est utilisée pour la zone interne du sillage jusqu'à la frontière dé finie par la nappe tourbillonnaire marginale. Au-delà de cette zone, la mesure des vitesses, notamment celle des courants de retour, est effectuée à l'aide d'un vélocimètre à laser bidimensionnel, fonctionnant en rétrodiffusion et muni d'une cellule de Bragg. Les optiques d'émissions ont des focales de 1000 mm et 1800 mm, permettant une exploration complète du champ aérodynamique.

La figure 6 représente l'implantation du vélocimètre proprement dit dans la veine pour la photo du haut, et le système d'acquisition et d'exploitation des données pour la photo du bas.

- La détermination des lignes marginales tourbillonaires a été effectuée à l'aide de la sonde à fils chauds croisés dans les régions où les risques de collision des pales avec la sonde n'est pas trop grand (en général $\psi > 70°$ ou $80°$). La sonde est amenée dans un plan z du sillage et le voltage de sortie de la sonde, proportionnel à la composante W, est envoyé sur un oscilloscope dont le balayage est synchronisé sur la rotation de la pale (la phase $\psi = 0$ correspond au passage d'une pale au droit de la sonde). Il est alors procédé à un déplacement radial du chariot depuis l'extrémité de la pale vers le moyeu. Durant ce déplacement, l'observation de la trace de l'oscilloscope ainsique celle du niveau de turbulence permet de localiser le passage du tourbillon sur la sonde qui se manifeste par un niveau de turbulence maximum et un pic de vitesse important. Le chariot est alors arrêté et la variation de W au cours d'une période est enregistrée, permettant ainsi de déterminer le déphasage du passage du tourbillon par rapport à la pale qui l'a largué. La ligne marginale est donc complètement déterminée par la mesure de r, z et ψ.

Afin de déterminer cette ligne dans des zones plus proches du plan de rotation, il a été fait appel à une technique de visualisation. La fumée blanche constituée par de l'air chargé de chlorhydrate d'ammonium est émise de manière continue à l'aide d'un émetteur profilé placé en aval du plan de rotation dans la zone de courants de retour.

Un système vidéo (caméra- moniteur - magnétoscope permettant l'arrêt sur image et par suite une

photographie de l'écran du moniteur) complété par un éclairage stroboscopique synchronisé sur la rotation des pales est utilisé pour la mise en évidence des lignes d'émissions de l'écoulement qui peut être réalisée à toute phase ψ. Les photographies de la figure 7 montrent un exemple de deux lignes d'émission obtenues aux phases $\psi \simeq 0°$ et $10°$. Ces lignes visualisent parfaitement l'intersection des lignes tourbillonnaires d'extrémité avec le plan diamétral dans lequel la fumée est émise. Il est alors aisé, à l'aide des photographies prises à différentes phases entre $0°$ et $90°$ de mesurer la position du tourbillon en r et z et donc de compléter les mesures faites à la sonde à fils chauds.

De plus, il est possible de mesurer le diamètre du noyau tourbillonnaire et d'en donner son évolution en fonction de la phase. A titre d'exemple, la figure 8 présente les variations avec la phase des rayons r_t mesurés suivant cette technique. Les résultats reportés ici sont relatifs aux rotors 1,3,4,5 et à un pas général $\theta_{0,75} = 10°$. On constate que durant la fraction de temps séparant le largage du tourbillon ($\psi = 0°$) et la première interaction ($\psi = 90°$), le rayon du tourbillon subit de fortes variations puisqu'il passe grosso-modo du simple au double. Ce résultat montre clairement que l'hypothèse de calcul d'un noyau de dimension constante durant la mise en équilibre est à améliorer.

3.4. Programme d'essais

Le programme d'essais a été résumé sur le tableau de la figure 9. Les résultats relatifs au rotor n°6 n'ont pas encore été exploités. Lors de tous ces essais, la vitesse en bout de pale a été maintenue constante à 107 m/s.

Les mesures de vitesses induites à l'anémomètre à fils chauds croisés ou au laser ont concerné généralement 2 à 3 plans dans le sillage correspondants aux phases $\psi = 4/3 \ \pi/b$, $2\pi/b$, $3\pi/b$. En chacun de ces plans, les variations de la vitesse avec le temps ont été enregistrées pour une dizaine de valeurs de la coordonnée radiale ; le pas entre ces mesures radiales a été resserré à l'approche de la position du tourbillon marginal.

4. RESULTATS. COMPARAISON CALCUL-EXPERIENCE

Les résultats présentés ici testent le code de calcul sur cinq rotors par confrontation à l'expérience (voir tableau de la figure 9). Il est donc possible de juger de l'influence des paramètres suivants : pas général, nombre de pales, vrillage, extrémités, dans la limite de variation de ces paramètres. Quand le calcul l'a permis, la confrontation porte sur les performances (figures de mérite), les lignes tourbillonnaires marginales, et les vitesses induites dans le sillage.

4.1. Figures de mérite

Les valeurs expérimentales des figures de mérite sont comparées dans le cas de rotors quadripales (rotors 1,4 et 5)) sur la figure 10 en fonction de $\bar{Z}$ ou C_{z_M}, avec $10 < \bar{Z} < 20$. (Le rotor 2 n'est pas reporté ici, la valeur du couple n'ayant pas été mesurée). Avant de comparer le calcul à ces valeurs, on remarquera l'avantage de l'extrémité en flèche sur une extrémité purement effilée pour $\bar{Z} > 15$ avec inversion des tendances pour $\bar{Z} < 15$. Aux fortes valeurs de $\bar{Z}$ ($\bar{Z} > 20$), les pales à vrillage linéaire et à extrémité droite semblent plus performantes.

Evidemment le paramètre nombre de pales n'a pas été pris en compte ici, mais les essais actuellement en cours à l'I.M.F.M. permettront de poursuivre l'analyse faite à la lumière de ce nouveau paramètre.

Il est de plus à noter que pour des $\bar{Z} < 16$, les tendances dégagées ci-dessus sont en accord avec les résultats présentés dans la référence (12) qui sont relatifs à des vitesses en bout de pale de 196 m/s. L'influence de ce paramètre V_e ne semble donc pas se manifester sur la répartition des figures de mérite tout au moins tant que $\bar{Z}$ reste inférieur à 16 ($C_{z_M} < 0,5$).

Les tableaux ci-dessous résument la confrontation effectuée sur les figures de mérite.

Rotor 1

	$\theta_{0,75}$	F_M	$\theta_{0,75}$	F_M
essai	10	0,74	8	0,629
calcul	11,05	0,705	8,61	0,649

Rotor 3

	$\theta_{0,75}$	F_M	$\theta_{0,75}$	F_M
essai	10	0,7136	8	0,6227
calcul	12,45	0,789	convergence non obtenue après 40 itérations	

Rotor 5

	$\theta_{0,75}$	F_M	$\theta_{0,75}$	F_M	$\theta_{0,75}$	F_M
essai	10	0,6826	8	0,5961	6	0,512
calcul	13,19	0,7619	10,60	0,573	convergence non obtenue après 40 itérations	

On remarque que dans toutes les configurations de rotor étudiées, le calcul surestime les pas généraux de l'ordre de 10 % pour le rotor 1, de 24 % pour le rotor 3 et de 32 % pour le rotor 5.

Pour le pas général de 10°, l'efficacité sustentatrice F_M est donc sous-estimée pour le rotor 1, tandis que le calcul donne un gain de cette efficacité de 11 % pour le rotor 3, et de 12 % pour le rotor 5. Par contre, pour le pas général de 8°, on a une sous-estimation de sustentation pour le rotor 5 de l'ordre de 3 % tandis qu'un gain du même ordre est observé pour le rotor 1.

4.2. Lignes tourbillonnaires marginales

La confrontation générale effectuée sur les lignes tourbillonnaires marginales et présentée sur le tableau de la figure 9 permet de dégager quelques lois d'ensemble. Il ressort que pour des pas et un nombre de pales relativement élevés (10° et 4 respectivement), l'accord calcul-expérience est bon dans tous les cas testés sauf pour le vrillage non linéaire (rotor 3). Nous reviendrons par la suite sur ce point.

Pour des pas plus faibles (8° et 6°) seuls les rotors à vrillage linéaire et extrémité rectangulaire (1 et 2) ont été étudiés pour l'instant. Le calcul donne des résultats acceptables à $\theta_{0,75}$ = 8°, et mauvais à $\theta_{0,75}$ = 6°.

A titre d'exemple, sont présentés dans ce qui suit, quelques résultats obtenus sur les lignes marginales dans le cas particulier $\theta_{0,75}$ = 10° et b = 4 :

- Rotor n°1

La figure 11 donne, dans cette configuration de rotor, une comparaison du calcul avec l'expérience. On constatera d'une part que les résultats expérimentaux obtenus aux fils chauds croisés et par visualisation se complètent et se recoupent parfaitement. D'autre part, l'accord calcul-expérience, qui est bon dans le proche sillage ($0° < \psi < 90°$), se détèriore sensiblement dans le sillage lointain ($\psi > 150°$).

- Rotor n° 3

Les résultats présentés sur la figure 12 attestent en premier lieu un mauvais recoupement entre les expériences déduites des fils chauds et des visualisations. En effet, lors des essais effectués sur les pales à vrillage non linéaire, il a été observé une instabilité spatiale et temporelle de la ligne marginale, ce qui a rendu particulièrement difficile la détermination aux fils chauds des phases et de la position des tourbillons. Il s'est avéré nécessaire de moyenner sur 200 cycles les enregistrements d'oscilloscope. Il a par contre été plus aisé de choisir au cours du défilement de la bande enregistrée des visualisations, le moment où le tourbillon est parfaitement formé sur l'écran, ce qui conduit à des mesures de position du tourbillon plus fiables par ce dernier procédé.

En second lieu, les écarts observés entre calcul et expérience conduisent à revoir le calcul pour ce type de rotor. Une amélioration peut être apportée en tenant compte de la variation du noyau tourbillonnaire dans la zone $0° < \psi < 90°$. Les variations expérimentales de r_t/R relatives au rotor n°3 ont été reportées sur la figure 8 et montrent que par rapport au rayon constant r_t/R = 5.10^{-3} utilisé dans le calcul, le rayon réel est inférieur à cette valeur jusqu'à $\psi = 40°$ environ et supérieur ensuite. Si on se reporte à présent à la figure 2, on constate qu'un rayon plus faible introduit dans le calcul ne change pas le résultat déjà obtenu (courbes en pointillés); par contre l'introduction d'un rayon plus fort déplacera la ligne des z/R vers le bas et celle des r/R vers l'intérieur (courbes continues). Ces évolutions reportées sur la figure 12 amélioreront donc notablement l'accord calcul-expérience en particulier dans la zone de forte variation de rayon r_t du noyau tourbillonnaire ($\psi > 30°$).

- Rotor n° 4

Bien que le calcul actuel ne soit pas opérationnel pour ce rotor, les résultats purement expérimentaux ont été présentés sur la figure 13, afin de montrer l'allure des lignes tourbillonnaires marginales dans le cas d'une extrémité en flèche. On notera dans ce cas une contraction radiale du sillage nettement plus faible que celle précédemment observée sur les rotors 1 et 3 (Figs. 11 et 12).

- Rotor n° 5

En ce qui concerne le rotor à extrémité effilée, la figure 14 donne la comparaison calcul - expérience ; il semble que le sillage lointain soit bien modélisé. L'introduction de la variation du noyau tourbillonnaire pour $0 < \psi < 90°$ devrait, comme dans le cas discuté sur le rotor 3, améliorer le résultat du calcul.

4.3. Vitesses induites dans le sillage

La lecture du tableau de la figure 9 permet de dégager une vue d'ensemble sur l'efficacité du calcul. Remarquons qu'une bonne confrontation calcul-expérience sur les lignes tourbillonnaires d'extrémité ne conduit pas toujours à une bonne concordance sur les vitesses (rotor 5, rotor 1 en tripale). Ce fait est certainement dû à la non efficacité de la modélisation du sillage lointain (position et intensité de l'anneau de recirculation) dans certaines configurations.

Les composantes du vecteur vitesse u,v,w ont été mesurées en différents plans de coupe z et suivant différentes sections radiales r/R en fonction du temps, c'est-à-dire de la phase.

Il a semblé plus intéressant de comparer calcul et expérience à un z donné, et à une phase donné, la variation de la vitesse étant portée en fonction de l'abscisse radiale r/R .

Les commentaires qui suivent concernent, à titre d'exemple, le rotor n°1 en configuration quadripale, à $\theta_{0,75}$ = 10°. Deux phases ψ = 0° et 60° ont été sélectionnées pour caractériser les comparaisons réalisées sur la composante axiale w. Les points expérimentaux qui découlent de mesures faites aux anémomètres à fils chauds croisés et à laser sont comparés aux résultats du calcul sur les figures 15 et 16. Deux types d'anémomètres laser ont été utilisés durant ces essais : celui de l'I.M.F.M. et celui de l'Institut de Saint-Louis. On constatera le bon accord sur les niveaux de vitesse entre calcul et expérience. Le léger décalage du pic de vitesse en r/R observé sur la courbe de la figure 16 entre calcul et expérience était prévisible en raison des légers écarts observés à ψ = 60° sur la ligne tourbillonnaire d'extrémité de la figure 11.

Une autre série de courbes relatives au rotor 5 ($\theta_{0,75}$ = 10°, b = 4) fait l'objet des figures 17 à 19 pour les phases ψ = 0°, 40° et 80°. L'allure des points expérimentaux (fils chauds seulement) et des points de calculs sont en bon accord. Le tourbillon qui pour z/R = - 0,0066 se situe à ψ = 90° (ou 0°) et à r/R = 0,89 (voir figure 14), se matérialise par un pic de vitesse marqué sur la figure 17, à r/R ≈ 0,89

à la fois pour les courbes expérimentale et calculée.

On remarquera que l'approche du tourbillon à $\psi = 80°$ (figure 19) donne lieu sur la courbe expérimentale à un profil caractéristique à double pics, alors que le calcul ne prévoit pas cette allure.

On notera enfin que sur les trois figures présentées, il y a un décalage systématique du calcul sur l'expérience, le calcul sous-estimant l'expérience. Comme cela a déjà été mentionné, la bonne détermination de la ligne tourbillonnaire dans le sillage proche n'est pas suffisante pour conduire à des bonnes répartitions de vitesses induites ; cette insuffisance pouvant être attribuée à un mauvais modèle du sillage lointain.

Les appréciations portées dans le tableau de la figure 9 sont également valables pour les composantes tangentielle et radiale.

5. CONCLUSION

Un code de calcul des performances d'un rotor en vol stationnaire a pu être testé par comparaison à des expériences relatives à la position des lignes tourbillonnaires marginales et aux vitesses induites dans le sillage. Le champ d'investigation, bien qu'encore limité, a toutefois permis de se faire une première idée de l'influence de paramètres tels que : nombre de pales, pas général, vrillage (linéaire et non linéaire) forme de l'extrémité.

Le calcul est tout à fait performant dans la mise en équilibre des lignes tourbillonnaires marginales pour une phase comprise entre 0 et $2\pi/b$ dans le cas de rotors quadripales à pas général relativement élevé ($\theta_{0.75} = 10°$) et à vrillage linéaire. Dans le cas d'un vrillage non linéaire, il est montré que l'accord entre calcul et expérience est défectueux et que le calcul peut être amélioré en introduisant la variation avec la phase du rayon du noyau tourbillonnaire qui pourrait être définie par une formule empirique tirée d'expériences réalisées pour de nombreux rotors.

Il est aussi montré que, même lorsque le calcul prévoit de façon satisfaisante le proche sillage, comme c'est le cas des rotors à extrémités de pales effilées, le champ des vitesses induites n'est pas prédit précisément par manque d'un modèle de sillage lointain adéquat.

Les confrontations effectuées sur les rotors à vrillage linéaire et à extrémité rectangulaire ont montré de plus, le peu d'efficacité du calcul à faible nombre de pales et à faible pas général.

Enfin, le calcul n'est pas opérationnel pour des extrémités en flèche et demanderait à être étendu à ce type de géométrie dont les expériences en cours à l'I.M.F.M. pourraient fournir un support empirique à de nouveaux modèles de calcul par la position des lignes tourbillonnaires marginales et par la détermination des dimensions des noyaux tourbillonnaires.

REFERENCES

(1) A.J. LANDGREBE
"An analytical and experimental investigation of helicopter rotor hover performance and wake geometry characteristics", U.S.A. AMRDL Technical Report 71-24, June 1971 (Summarized in : "The wake geometry of a hovering helicopter and its influences on rotor performances" J.A.H.S., Vol.17, n°4, Oct.1972).

(1') A.J. LANDGREBE, T.A. EGOLF
"Prediction of helicopter induced flow velocities using the rotorcraft wake analysis", 32nd A.H.S. Forum Proceedings, Washington, May 1976.

(1") A.J. LANDGREBE, R.B. TAYLOR, T.A. EGOLF, J.C. BENNET
"Helicopter airflow and wake characteristics for low speed and hovering flight from rocket interference investigations", 37th A.H.S. Forum Proceedings, New-Orléans, 1981.

(2) "Aerodynamics of rotary wings", AGARD Conference n°111. Fluid Dynamics Panel Specialists'Meeting, Marseille, Sept. 1972.

(3) J.D. KOCUREK, L.F. BERKOWITZ, F.D. HARRIS
"Hover performance methodology at Bell helicopter Textron", A.H.S. Forum Proceedings, Washington D.C., May 1980.

(4) M. SCULLY
"Computation of helicopter rotor wake geometry and its influence on rotor harmonic airloads", MIT ASRL TR 178-1 March 1975.

(5) J.D. GOHARD
"Free wake analysis of wind turbine aerodynamics", MIT ASRL TR 184-14, Sept. 1978.

(6) J.M. SUMMA, D.R. CLARK
"A lifting surface method for hover/climb airloads", A.H.S. Forum Proceedings, Washington D.C., May 1976.

(7) R. COURJARET, A. CASSIER
"Aérodynamique des rotors : calcul des performances au point fixe avec sillage expérimental figé", Contrat D.R.E.T n° 75/276, lot n°2, H/DE-EC.

(8) J.M. POURADIER, A. BREMOND, J. GALLOT
"Aérodynamique des rotors en vol stationnaire : mise en équilibre", Contrat D.R.E.T. n°75/276, lot n°2, H/DE-EC.

(9) J.M. POURADIER, E. HOROWITZ
"Aerodynamic study of a hovering rotor", Proceedings of 6th Europ' Rotorcraft and Powered lift Forum, Bristol, September 1980.

(10) J.D. KOCUREK, J.L.TANGLER
"A prescribed wake lifting surface hover performance analysis", 32nd Annual Forum of the American Helicopter Society, May 1976.
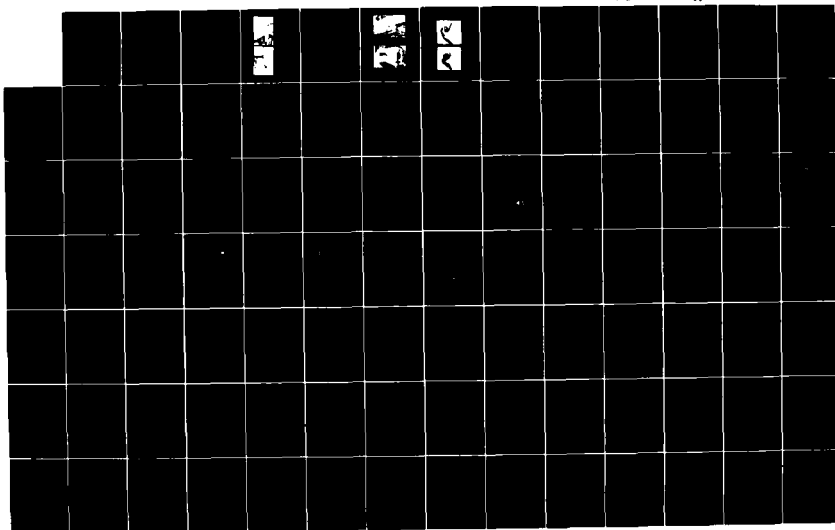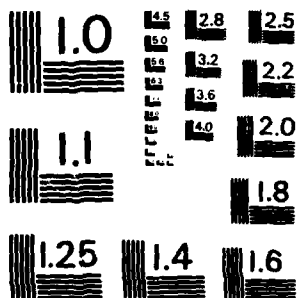
MICROCOPY RESOLUTION TEST CHART

NATIONAL BUREAU OF STANDARDS-1963-A

(11) M. NSI MBA, D. FAVIER, C. MARESCA, J. REBONT
"Calcul et mesure du champ des vitesses induites par un rotor d'hélicoptère (vol stationnaire),
Contrat D.R.E.T., n°78/456, Décembre 1980.

(12) J.P. SILVANI, A. VUILLET
"Aerospatiale survey of wind tunnel testing of small and large scale rotors", Proceedings of 7th
European Rotorcraft and Powered lift Aircraft Forum, Garmisch, September 1981.
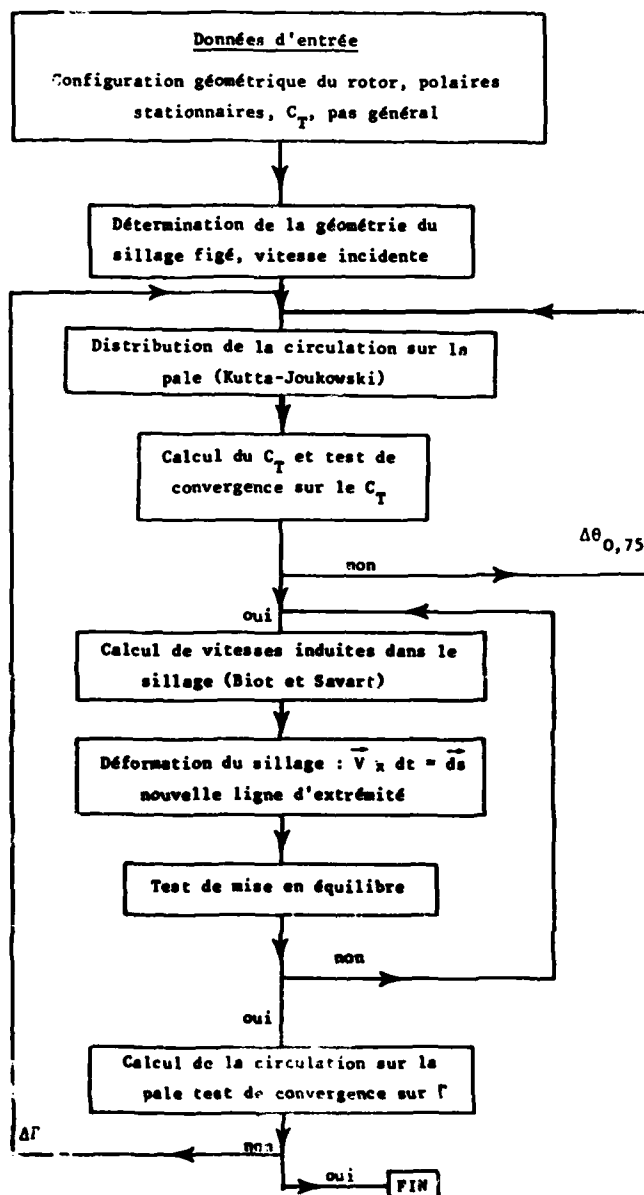
Figure 1 Organigramme du calcul
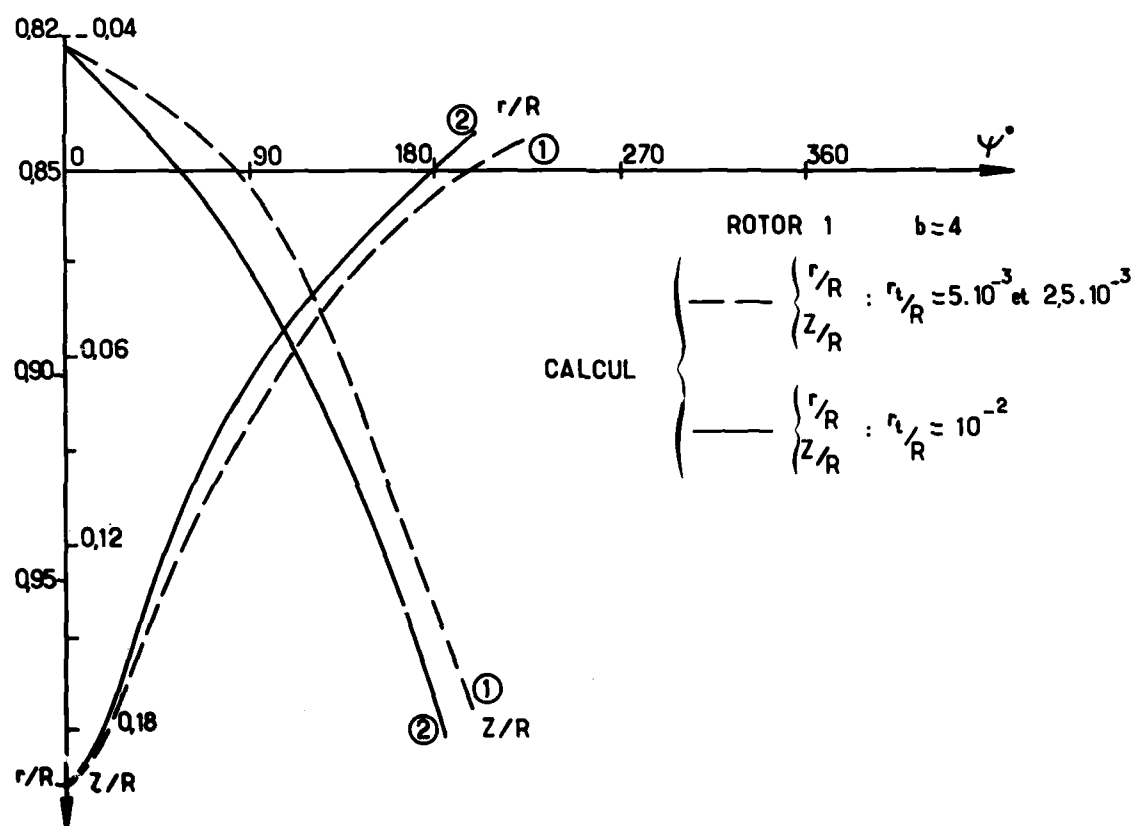
Figure 2 Variation de la ligne tourbillonnaire marginale avec le rayon du noyau tourbillonnaire

MONTAGE DU ROTOR
EN SOUFFLERIE
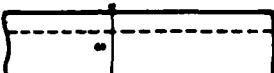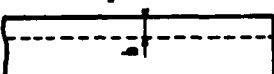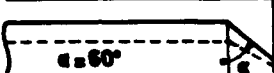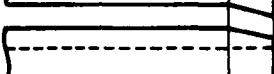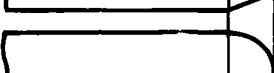
VUE DE DESSUS

ROTOR

PORTE SONDE

CHARIOT EXPLORATEUR

Figure 3 Montage en soufflerie et déplacement de la sonde à fils chauds

Numéro du rotor	Vrillage	Forme en plan	Profil
1*	_8°		BV 23010
2*	_14°		BV 23010
3**	Non linéaire		OA 209
4**	_8,3°	α=60°	OA 209
5**	_8,3°		OA 209
6**	_8,3°		OA 209

* Profil étudié dans la référence 11

** Etude en cours

$a = 0,15c$
$b = 0,25c$
$d = 0,60c$

Figure 4   Différents types de pales utilisées
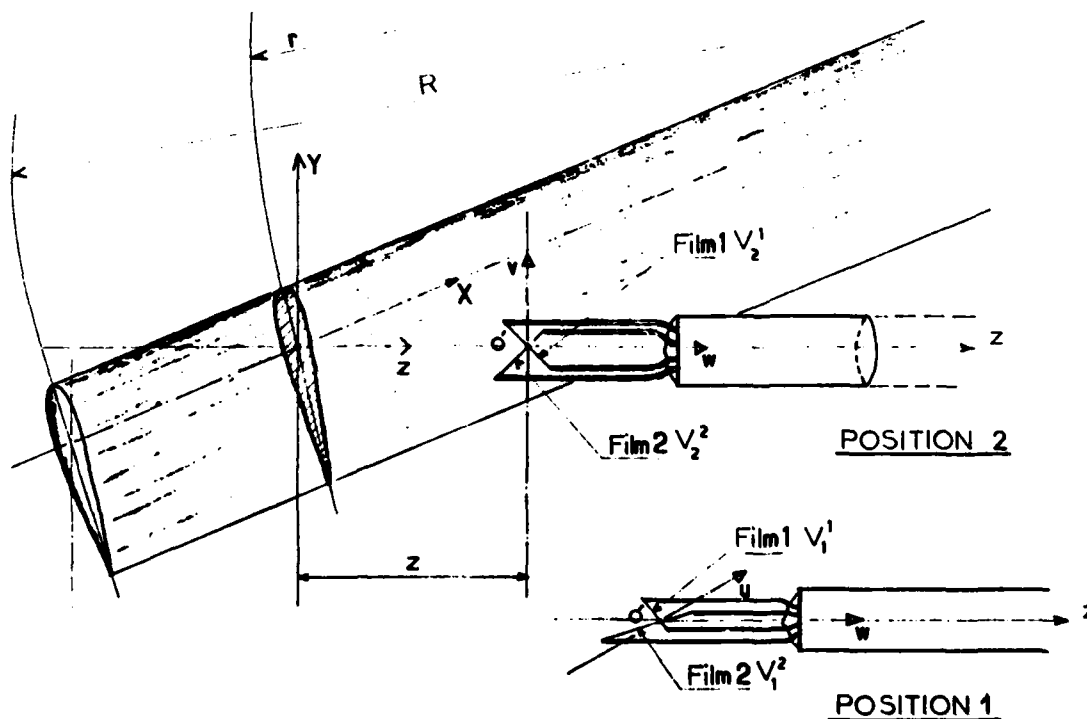
Figure 5   Positions de la sonde à fils chauds
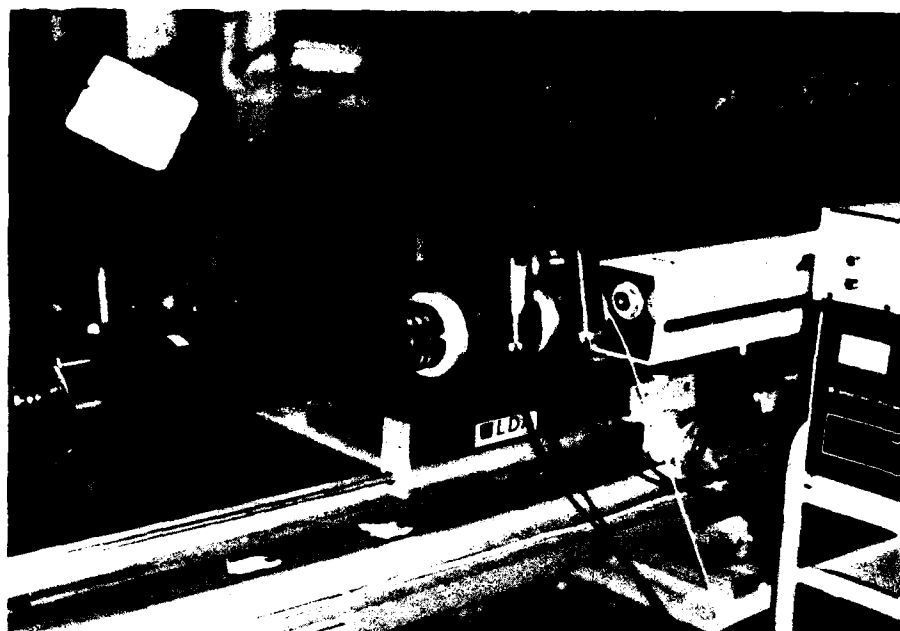
VELOCIMETRE LASER

ACQUISITION DES DONNEES

Figure 6 Vélocimètre laser et acquisition des données

EXEMPLE DE VISUALISATION DES NOYAUX TOURBILLONNAIRES

PALE $\psi \simeq 0°$

$\psi = 20°$

ROTOR 1

Figure 7 Visualisation des noyaux tourbillonnaires
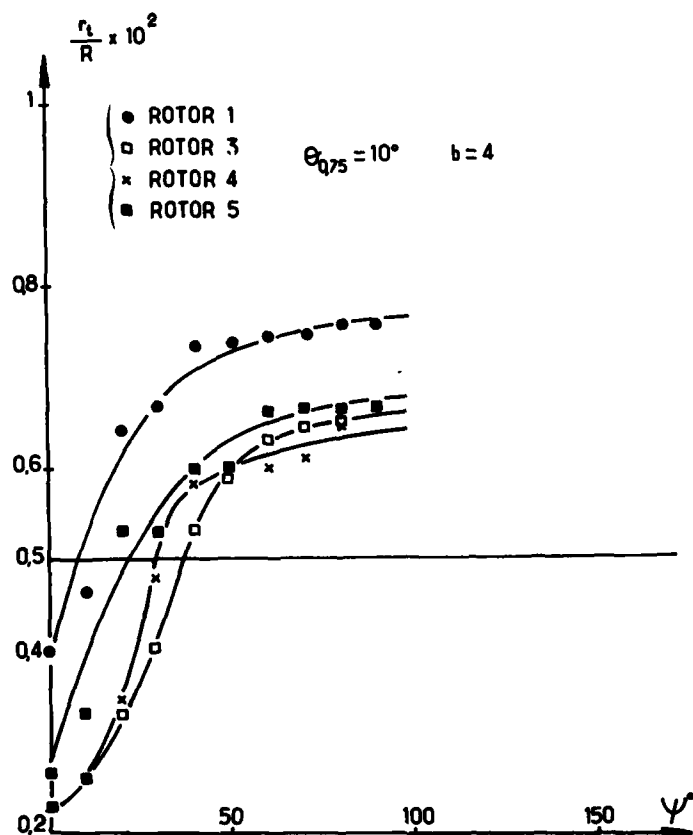
Figure 8   Variation du rayon du noyau tourbillonnaire marginal déduite des visualisations

PAS GENERAL Θ$_{0,75}$	10°							8°					6°	
Nombre de pales : b	4					2		4		3	2		4	2
N° du rotor (voir fig.4)	1	2	3	4	5	1	2	1	2	1	1	2	1	1
$\bar{Z}$	17,10	17,10	16,42	19,46	19,47	21,91	21,91	13,85	13,85	12,80	18,70	18,70	11,70	11,52
TOURBILLONS D'EXTREMITE — Expériences	FC V	FC V	FC V	FC V	FC V	FC	FC	FC	FC	FC	FC	FC	FC	FC
TOURBILLONS D'EXTREMITE — Compar. calcul-expér.	+	+	−	Calcul non opérat.-onnel	+	X	X	+	X	X	Calcul non convergé	X	−	Calcul non convergé
VITESSES INDUITES — Expériences	FC L	FC L	FC	FC	FC	FC L	FC	FC	FC	FC L	FC	FC	FC	FC
VITESSES INDUITES — Compar. calcul-expér.	+	+	−	Calcul non opérat-onnel	−	−	X	+	+	−		X	−	

FC : Fils chauds , L : Laser , V : Visualisation
+ : Bon , X : Acceptable , − : Mauvais

Figure 9   Tableau des résultats d'essais
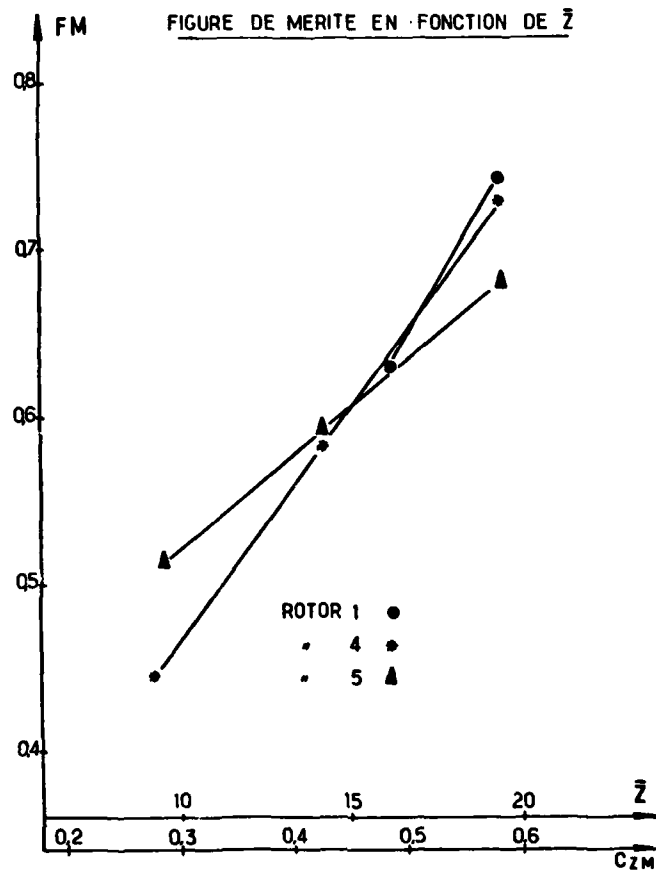
Figure 10 Figures de mérite
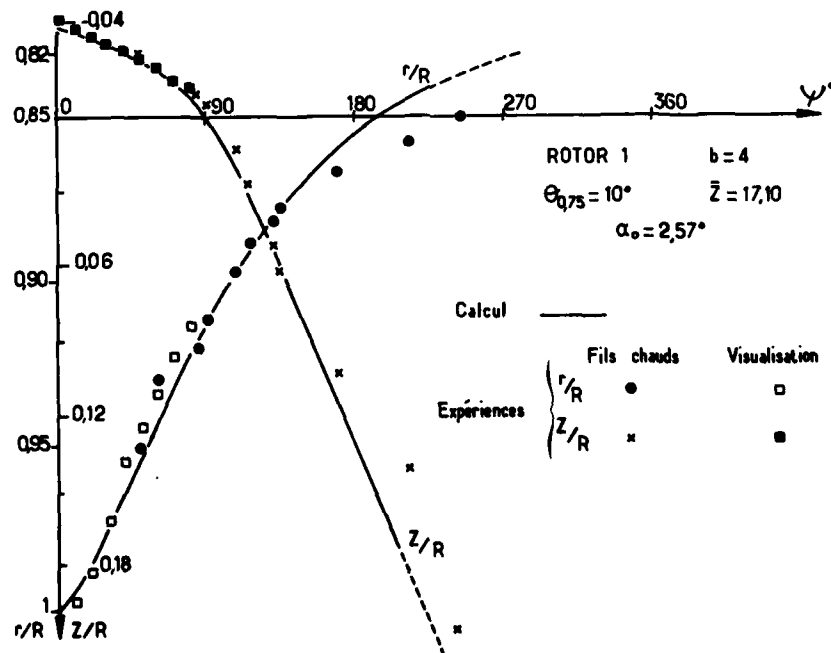
Figure 11 Positions de la ligne tourbillonnaire d'extrémité avec la phase. Rotor 1
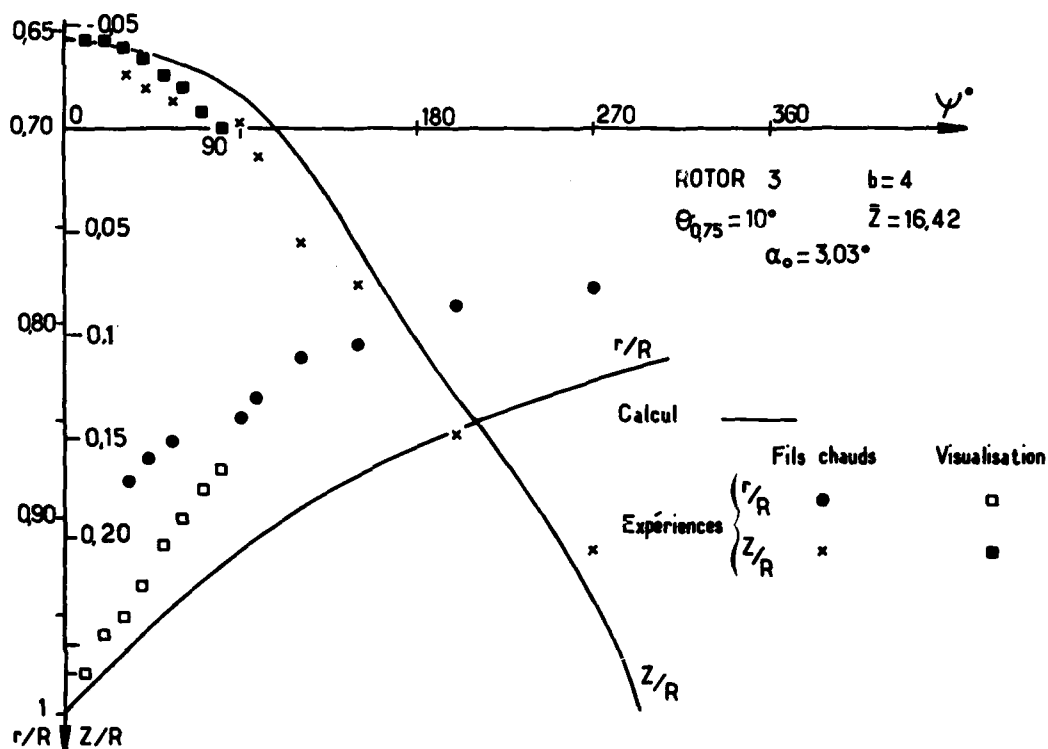
Figure 12 Positions de la ligne tourbillonnaire d'extrémité avec la phase. Rotor 3
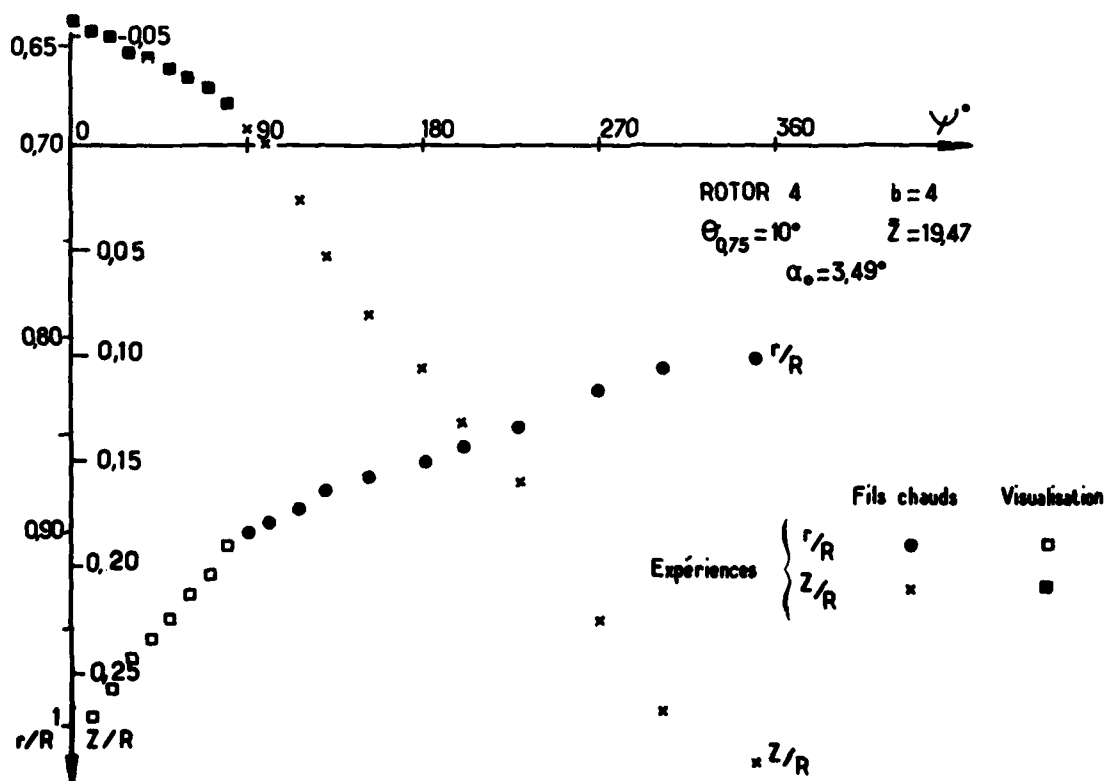
Figure 13 Positions de la ligne tourbillonnaire d'extrémité avec la phase. Rotor 4
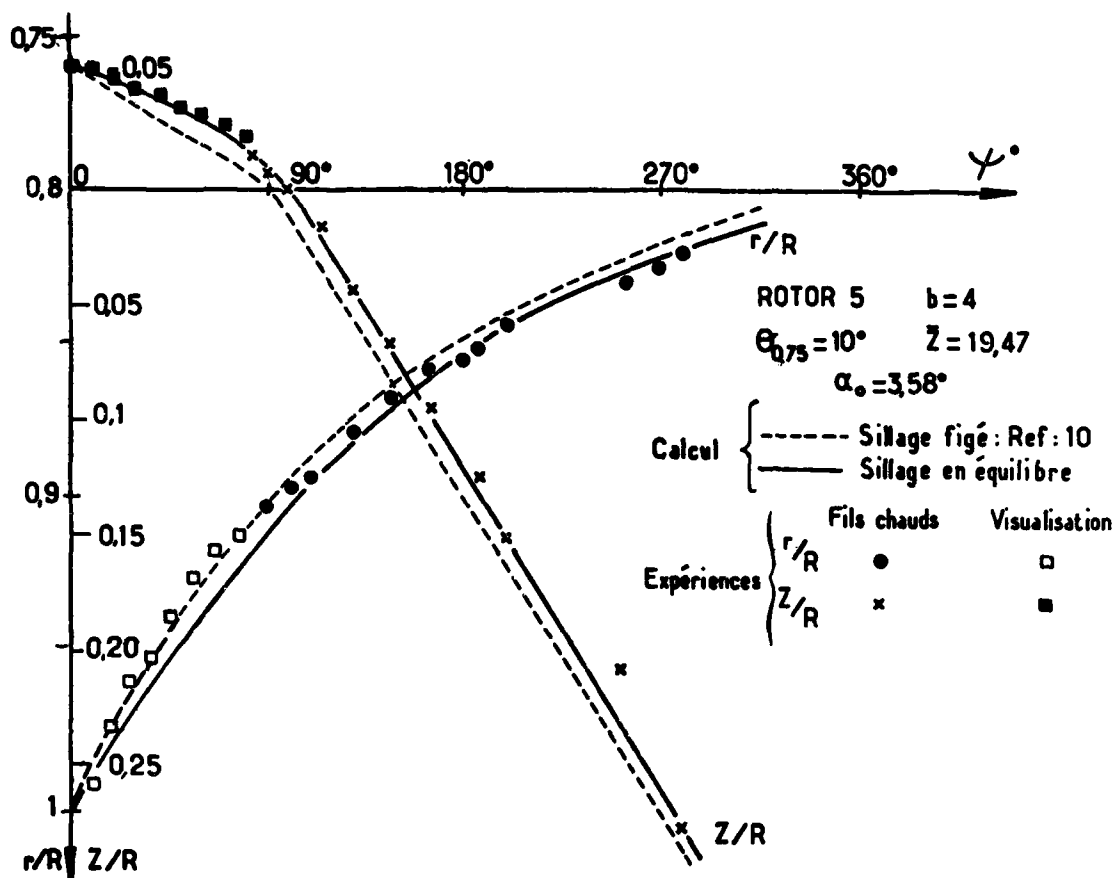
Figure 14 Positions de la ligne tourbillonnaire d'extrémité avec la phase. Rotor 5
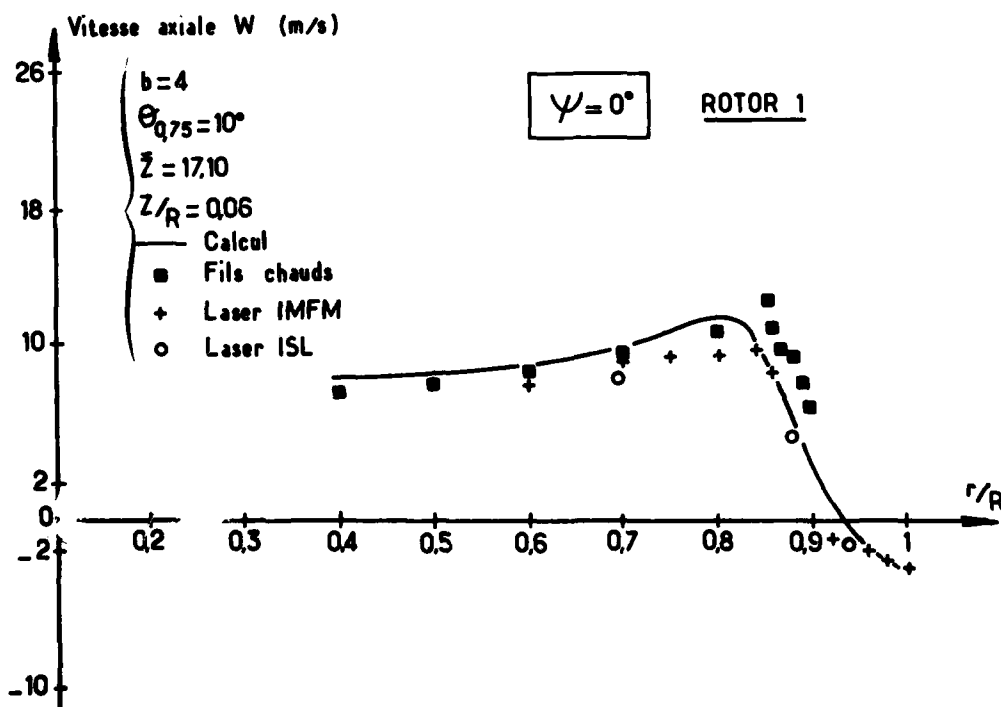
Figure 15 Répartition radiale de la composante axiale W. Rotor 1 ; $\psi = 0°$
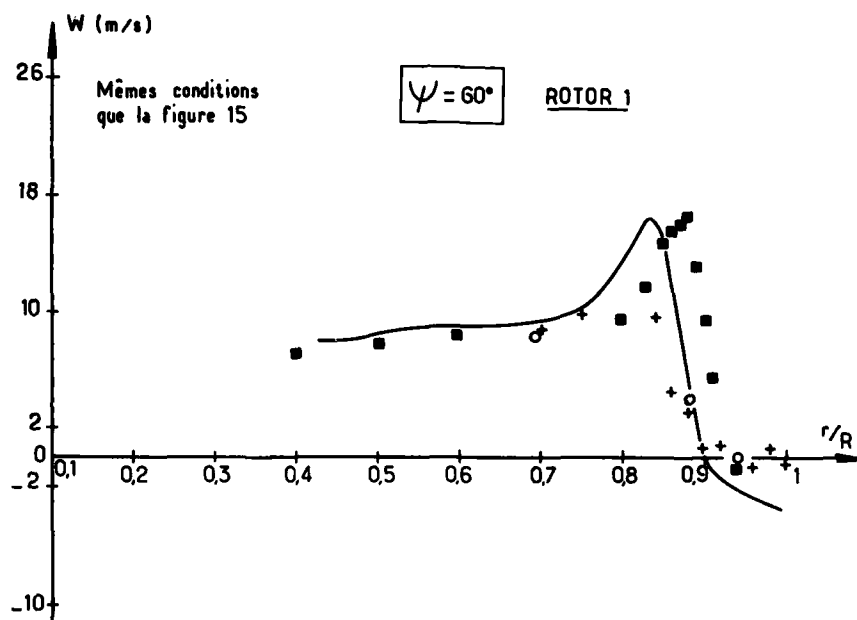
Figure 16 Répartition radiale de la composante axiale W. Rotor 1 ; ψ = 40°
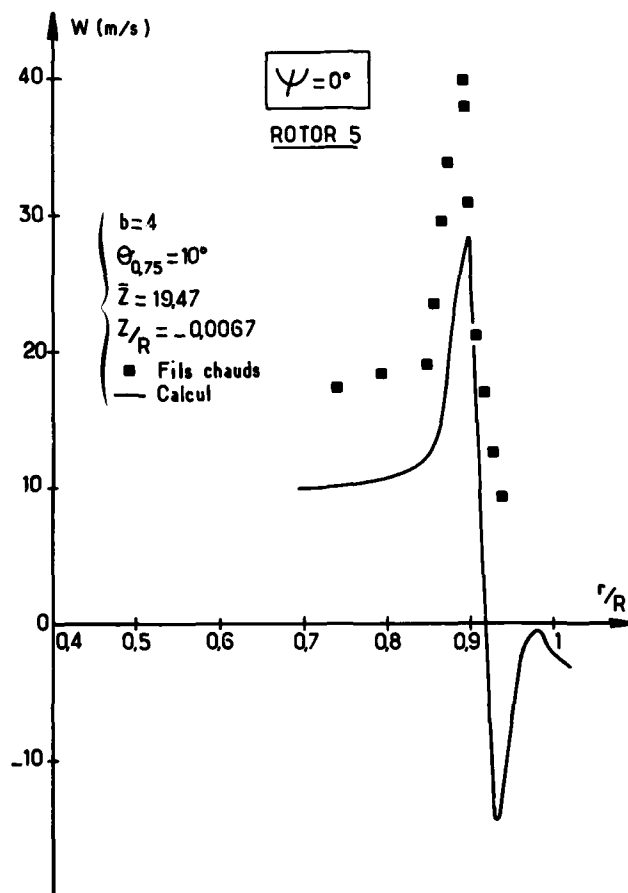
Figure 17 Répartition radiale de la composante axiale W. Rotor 5 ; ψ = 0°

W (m/s)

40

30

20

10

0

-10

$\psi = 80°$

ROTOR 5

Mêmes conditions
que la figure 17

r/R

0,4   0,5   0,6   0,7   0,8   0,9   1

Figure 19 Répartition radiale de la composante axiale W. Rotor 5 ; $\psi = 80°$

W (m/s)

40

30

20

10

0

-10

$\psi = 40°$

ROTOR 5

Mêmes conditions
que la figure 17

r/R

0,4   0,5   0,6   0,7   0,8   0,9   1

Figure 18 Répartition radiale de la composante axiale W. Rotor 5 ; $\psi = 60°$

VELOCITY COUPLING - A NEW CONCEPT
FOR HOVER AND AXIAL FLOW
WAKE ANALYSIS AND DESIGN

J. David Kocurek
Group Engineer, Aerodynamics Technology
and
Lenard F. Berkowitz
Aerodynamicist
Bell Helicopter Textron, Inc.
P. O. Box 482
Fort Worth, Texas
76101
USA

SUMMARY

The distorted prescribed wake method has evolved in the United States as the standard for rotary wing hover performance calculations as evidenced by its wide acceptance not only for advanced design applications but also for routine analysis as well. A review of the history and development of the method is provided as introduction to velocity coupling, a new approach defining the key parameters of the wake in hover and axial translation. This technique is formulated from the concept of principal wake induced velocities which are calculated iteratively as simple functions of loading and key geometric characteristics of the near wake tip vortex spirals. This velocity coupled wake model is shown to predict the hovering rotor's wake geometry in greater detail as compared to earlier methods. Also, correlation with a rotor in axial climb demonstrates the successful application of the method to this regime. These examples illustrate how the velocity formulation isolates the major interactions of the wake elements, by not only clarifying experimentally observed characteristics, but also providing a physical basis for systematic refinement of the prescribed wake method.

1. INTRODUCTION

Recent progress in the area of rotor hovering wake analysis has matured a reliable, working methodology for aerodynamic design and performance prediction, as typified by the lifting surface method with distorted prescribed wake of Reference 1. This technology foundation, with first level consistency throughout, affords research opportunities to again focus on refinement of details which clarify modeling, extend validity, and allow new applications to be challenged. It is, therefore, appropriate to again examine the central element of the performance analysis, the wake model itself.

With the prescribed wake approach the complex distorted wake geometry is economically computed in terms of basic parameters which are themselves iteratively coupled to some primary variable of the analysis, such as thrust level, tip vortex strength, or principal wake induced velocities as will be shown. These coupling relationships are derived from experimental measurements of wake geometry, or subsequent numerical experiments which identify relationships between geometry and variables more detailed than thrust.

This paper focuses on the development of velocity coupling, a refinement in hover prescribed wake modeling. The velocity coupling concept is a third generation prescribed wake, but the first to rely entirely on fundamental wake physics as the basis for developing the generalized expressions which describe the wake's behavior. As such, it lends considerable insight into experimentally observed wake characteristics. Additionally, the formulation clearly demonstrates the interaction of the key wake elements and thus systematic refinements can now be made to improve the analytical model's faithfulness for modern blades which go beyond the experimental prescribed wake data base (References 2, 3). Also, because of its velocity formulation, it is a unified technique which permits a natural transition of the hovering wake analysis into axial flight, from the low speed helicopter vertical climb regime through that of cruising propellers. The method is also extendable in concept to vertical descent.

To preface the discussions on velocity coupling, this paper first highlights the development progress of the distorted prescribed wake and its basic features. Following this, the concept of principal wake induced velocities is introduced and used to formulate velocity coupling. This new wake model is then demonstrated within the methodology of Reference 1, which will be referred to throughout the paper as the global analysis. Comparisons are made to earlier wake coupling methods, and the extension of the hover wake to axial translation is developed with detailed results shown for a rotor in climb. The paper is concluded with comments on this new technology and specific recommendations for research programs to further improve hover and axial flow methodology.

2. THE EXPERIMENTALLY PRESCRIBED WAKE

The first generation distorted prescribed wakes were developed with guidance from several benchmark experimental studies which focus on defining the important tip

vortex trajectory in the near wake region. The basic structural features of these wake models are still in current usage and follow those originally conceptualized by Gray (References 4 and 5) from smoke studies of a single-bladed rotor. Gray hypothesized that the trailed vortex sheet from the rotor blade rapidly splits into inboard and outboard portions at the radial blade station assumed to correspond to maximum blade bound circulation. The inboard sheet then settles axially as the outboard sheet quickly rolls about the forming tip vortex to complete its development. This original concept is compared in Figure 1 to the computational model of Reference 1. Gray also developed expressions which describe the radial and axial coordinates of the tip vortex trajectory in the wake. These trajectory expressions have since evolved to simpler forms in terms of the now familiar parameters k_1, k_2, and λ_1, as illustrated in Figure 2, and as given by

$$z/R = k_1 \psi \qquad\qquad 0 \leq \psi \leq 2\pi/b \quad (1)$$

$$z/R = k_1(2\pi/b) + k_2 (\psi - 2\pi/b) \qquad \psi > 2\pi/b$$

$$r/R = A + (1-A)e^{-\lambda_1 \psi} \qquad \psi > 0$$

As observed in Figure 2, from the time the tip vortex forms ($\psi=0$) until the following blade passage ($\psi=2\pi/b$), it translates downward at the initial settling rate k_1. As the tip vortex passes beneath the first following blade, the impulse from that blade and its trailing wake system increases the axial displacement to k_2. The initial radial contraction of the tip vortex behaves exponentially with increasing wake azimuth. The contraction is described by the rate parameter λ_1 and an effective minimum nondimensional radius A. The task in the prescribed wake method is thus to conveniently define these key parameters.

Based on observations of full-scale and model rotor wakes, Jenney, et al, (Reference 6) proposed that the major inadequacy of classical methods was their discrepant modeling of the wake trajectory details. This point was illustrated through calculations made using a lifting line analysis with prescribed wake which demonstrated the high sensitivity of rotor performance to placement of the tip vortices in the wake model. This approach to wake modeling was extended and popularized by Landgrebe (Reference 3) who reported the first generalized analytical model derived from extensive experimental study of hovering rotor wake geometry behavior. This data base includes wake characteristics of model rotors with two through eight linearly twisted blades of constant chord and moderate to high aspect ratio. The progression of methodology through this period is narrated in detail with emphasis on the rotor wake in the survey by Landgrebe and Cheney, (Reference 7).

The experimental data base was expanded and clarified by Kocurek and Tangler using schlieren flow visualization, (Reference 2). This study documented wake shapes for rotor configurations of from one through four blades of constant chord with twist rates of up to 24 degrees. Because of the consideration of single-bladed rotors and both high and low blade aspect ratios this work revealed wake sensitivity to thrust coefficient, number of blades, and twist not previously identified and resulted in improved generalizations for the trajectory parameters.

The experimental prescribed wake was thus accepted as a powerful and essential addition to rotor aerodynamic analysis. However, further development of the wake model was sought for several reasons beyond technical curiosity. First, confident application of the method in the practical environment was limited to the class of rotors for which experimental generalizations were available. Second, but of equal importance, was that these purely empirical generalizations are based on measurable and derived quantities. Although certainly relevant, these are not necessarily the physical parameters governing the wake. For instance, with the class of rotors described above, the measured settling rates correlated well as functions of thrust coefficient C_T and linear twist rate θ_1, but were easily observed to follow the tip loading as noted in Reference 1. Observations of rotors with more complex configuration, such as nonlinear twist and tapered planform, showed similar influences and thus make the merits of attempting to further generalize the experimental wake highly questionable.

3. SECOND GENERATION REFINEMENTS

Numerical experiments with prescribed wake analysis and analysis based on classical momentum and vortex theories, as described in References 1 and 8, demonstrated that tip vortex strength could be isolated as prominently governing the wake parameters. The second generation, circulation coupled wake models were derived from these studies, and have since become the standard for hover performance analysis.

Since circulation coupling is derived from the experimental wake, it is still entirely dependent upon the accuracy of that data base. Also, it is well to remember that although definite trends can be identified for certain configuration characteristics, quantification of those trends in the wake model can imply a level of accuracy not achievable in the guiding measurements. Nonetheless, the texture of the circulation coupled model is consistent with available data, and the model offers the

systematic trendin~ needed for evaluation of rotor aerodynamic performance. Bene-
ficial features of the approach include:

- Wake settling rate and contraction parameters become functions of the itera-
  tively calculated tip vortex strength Γ_{tv} rather than C_T,

- No explicit influence of blade configuration appears, and

- The range of the experimentally documented wake data base is extended to
  rotors beyond those tested, subject to the assumption that the wake is
  solely dictated by Γ_{tv}.

The importance of this first benefit is that the quality of predicted wake para-
meter correlation to C_T then depends upon the correctness of all elements of the
global analysis which influence Γ_{tv}. In fact, the effects of these influences are
magnified. This consequence can be used, therefore, to identify sensitivity to such
elements as modeling of the tip vortex rollup process, or the far wake, which would be
masked if the wake were modeled based on C_T, an integrated parameter.

4. IDENTIFICATION OF PRINCIPAL VELOCITIES

The initial concept for velocity coupling was disclosed in Reference 1, and
development progress was discussed in Reference 9. The work was motivated by the
insight into the wake's behavior gained during the development of circulation
coupling, and by the desire to extend that wake into axial flow. As described
earlier, the circulation coupling relations give the wake parameters, which are
actually transport velocities, in terms of Γ_{tv} through correlated proportionalities.

For k_2 the proportionality is recognized as the momentum induced velocity associated
with a constant radial loading Γ_{tv}. For k_1 and λ_1 the relationship to such a funda-
mental velocity is not clearly seen. But, the success and simplicity of the technique
suggested that principal velocities exist which, if identified, could form the basis
for an improved wake model which meets the goal of being based directly on first level
considerations.

Several other researchers have also approached this problem with notable results.
For their prediction of rotor performance in axial flight, Moffitt and Sheehy (Refer-
ence 10) developed a semiempirical wake model based on intuitive modifications of
experimentally determined hover wake geometries. To account adequately for variations
in k_1 they found it necessary to relate k_1 to the average induced velocity distri-
bution over the outer ten percent of rotor radius. Very recently, Miller (References
11 and 12) has demonstrated the feasibility of predicting hover wake geometry with
very simple free wakes, one that is two-dimensional and one that uses vortex rings.
From these analytical solutions, Miller notes that geometry is influenced by two major
factors. The initial trajectory is determined primarily by the induced velocity from
all vortices lying below and generated by preceding blade passages; that is, by the
tip vortex spirals and not the inboard wake. Then, as the following blade passes, the
higher downward rate is imparted by the newly formed vortex. This work further sup-
ports the concept of principal velocities.

The search for simple velocities which would describe the wake parameters
directly began by exercising the global analysis with circulation coupled wake. The
velocity field in the blade tip region was traced ultimately to two major components.
The first is that velocity induced by the radial load distribution acting through the
trailed near wake of the generating blade. The second velocity is that due to the
discrete tip vortices acting at key azimuths along their trajectory. These velocities
were examined for their relationship to the wake parameters. This approach yielded a
remarkably simple expression for the contraction parameter. For prediction of
settling rates this approach has resulted in a purely analytical scheme which in-
corporates the principal velocity concept.

5. RADIAL CONTRACTION PARAMETER

The principal velocities are calculated from very simple idealizations of the
wake. To calculate that resulting from blade loading, a flat fixed-wing type semi-
infinite trailed wake is assumed, as shown in Figure 3. Based on this wake and the
radial circulation distribution, the lateral loading velocity v_ℓ as used to determine
λ_1 is calculated at the position of first vortex passage, as shown in Figure 4. The
second velocity is the mutual induction, or interference, of the discrete tip vorti-
ces. As also illustrated in Figure 4 for λ, a lateral velocity v_i is calculated at
the same position as before, but now due to a straight line infinite vortex at the
position of next vortex passage. These velocities were calculated for several of the
model rotors from Reference 2, based on analysis with circulation coupled wake.
Standard linear regression techniques were then used to assess the relationship
between the velocities and λ_1. The excellent results are illustrated in Figures 5
through 7. The first two of these show the calculated variation of the circulation
coupled λ_1, with the principal lateral velocities. Figure 7 shows that λ_1 correlates

to a linear combination of v_ℓ and v_i, thus indicating the simple balance mechanism in the field. The correlation is itself linear and explicity independent of number of blades.

Of the two terms, the dominant one is v_i which contains the influence on contraction of all of the tip vortices beneath the calculation point. This term's dominant effect is consistent with the observation that most of the wake's contraction occurs at an early age. The loading component v_ℓ serves to appropriately balance the contraction to zero in the coupling relationship given by

$$\lambda_1 = -6.4096\ v_\ell/(\Omega R) - 18.7615\ v_i/(\Omega R) \qquad (2)$$

Note that with velocity coupling the wake's outer boundary is no longer restricted to being uncontracted in the limit of $\Gamma_{tv} \to 0$.

6. SETTLING RATES

Equally interesting relationships were discovered between simple velocity calculations and settling rates. However, these led to an analytical model which approaches a free wake in nature, but considers only mean inflow and interference velocities based solely on considerations of the tip vortices. This was possible since tip vortex strength and position cause the variations in loading, and thus the variations in axial velocity due to loading which were found to be related to settling rates.

6.1 Interference Component

The interference velocity w_i is again the mutual induction of the discrete tip vortices, taken in the axial sense, and calculated as illustrated in Figure 8. This velocity represents the interaction in the initial wake between the newly formed tip vortex and the adjacent spiral. This velocity is described by Γ_{tv} and the characteristic spacing as shown, from the blade tip to the point of first vortex passage (r_1, z_1) in the $\psi=0$ reference plane of the wake, and as given by

$$\frac{w_i}{\Omega R} = \frac{\Gamma_{tv}/(\Omega R^2)}{2\pi(r_1/R-1)}\left[\frac{1}{1+\left(\dfrac{z_1/R}{r_1/R-1}\right)^2}\right] \qquad (3)$$

The choice of this mutual induction as a principal velocity is substantiated in Figure 9 which shows the increment in settling rate from k_1 to k_2 to be acceptably linear with w_i. This result again demonstrates the influence of number of blades to be implicit through the radial and axial spacing of the near wake vortices.

The concept is further developed by thinking of the tip vortex as settling at some mean rate which is initially retarded by w_i prior to first blade passage (the k_1 region), and then increased after first blade passage by w_i to the final settling rate (the k_2 region), as sketched in Figure 10. This idea is placed in traditional perspective in Figure 11 which for constant chord, untwisted blades shows that k_1 is linear with the simple difference between the momentum induced velocity $(C_T/2)^{1/2}$ and w_i. For rotors with different planform or twist, this result will not hold as should be expected from the experience with circulation coupling which showed the dependence of settling rate on tip loading. However, combining this knowledge with the observation in Figure 11, a form for the initial settling rate is suggested as

$$k_1 = k_m - k_i \qquad (4)$$

where k_m is that rate associated with the mean inflow, and with Eq. (3)

$$k_i = w_i/(\Omega R) \qquad (5)$$

Combining this further with the rate increment from Figure 9, taken approximately as

$$k_1 - k_2 = -2k_i \qquad (6)$$

then the secondary settling rate becomes the simple sum of the two principal axial velocities,

$$k_2 = k_m + k_i \qquad (7)$$

6.2 Mean Inflow Component

The problem is now reduced to one of defining k_m from an idealization based on first level physics which captures the variation of the tip region mean inflow with

Γ_{tv}, and which permits straightforward calculation. It was shown for the special case of Figure 11, that the mean settling rate is that due to the average momentum induced velocity. This velocity can be derived equally as well from the classical vortex theory which assumes an uncontracted wake cylinder. For the present application such a cylinder must replace, on the average, the distorted tip vortex trajectory surface of the actual wake. The distorted wake of the global analysis is modeled in near and far wake regions as sketched in Figure 12. The near wake is the stable region from generation to the point of maximum contraction, taken as the wake azimuth of $8\pi/b$. This approach is based on schlieren flow visualization which indicates that regardless of the number of blades, generally four well defined tip vortex passages appear beneath the reference blade prior to the onset of tip vortex instability and diffusion. Beyond the near wake, the outer wake boundary is characterized by random interaction and merging of adjacent tip vortices and by vortex diffusion. This far wake region is modeled by a continuation of the near wake vortices on a nominal trajectory, representing the shear layer which thickens radially with increasing axial displacement much like an expanding free jet. Through extensive performance correlation study it was found that this expanding wake model must be finite in effect to produce the proper level of induced velocity at the disk. As also shown in Figure 12, an effectively sized vortex cylinder could serve to model this complex geometry for the purpose of calculating an average inflow.

Based on these observations, the mean inflow component of the axial settling rates is derived from consideration of a vortex cylinder as illustrated in Figure 13. The radius r_1/R of the cylinder is assumed to represent the nominal radius of the tip vortex trajectory surface of the actual wake. In addition, the idealized cylinder is assumed to be of finite length z_m/R.

Following Reference 13, the axial velocity w_m in the vicinity of the mouth of the cylinder is

$$w_m = \frac{1}{4\pi} \frac{d\Gamma}{dz}\left[\omega(z_m) - \omega(0)\right] \tag{8}$$

where $d\Gamma/dz$ is the strength of the vorticity and $\omega(z)$ is the solid angle at a point in the cylinder's mouth subtended by an element of the cylinder at z. For the infinite length cylinder it can be shown that the radial distribution of induced velocity is everywhere uniform. For the finite cylinder it is assumed that the mean velocity is adequately modeled by the velocity along the axis. Then as shown in Figure 14, the solid angle is equal to the portion of the surface of a sphere of unit radius which is cut out by the conical surface with vertex at the origin and with base as the perimeter of the cylinder's far end. With this geometry in mind, then

$$\omega(z_m) = 2\pi\left[1 - \frac{z_m/r_1}{[1+(z_m/r_1)^2]^{1/2}}\right] \tag{9}$$

$$\omega(0) = 2\pi$$

and

$$w_m = \frac{1}{2}\frac{d\Gamma}{dz}\left[\frac{-z_m/r_1}{[1+(z_m/r_1)^2]^{1/2}}\right] \tag{10}$$

The cylinder strength is easily expressed in terms of the problem variables of interest in defining the actual tip vortex spiral. The axial density $d\Gamma/dz$ is equivalent to the rate $d\Gamma/dt$ at which circulation is added to the wake, ratioed to the rate of axial displacement dz/dt of the wake elements. For the rotor with finite number of blades b and tip vortex strength Γ_{tv}.

$$\frac{d\Gamma}{dt} = \frac{d\Gamma}{d\psi}\frac{d\psi}{dt} = \left(\frac{b\Gamma_{tv}}{2\pi}\right)\Omega \tag{11}$$

and

$$\frac{dz}{dt} = \Omega \frac{dz}{d\psi} \tag{12}$$

Since the greater portion of the tip vortex spiral settles at the secondary rate k_2 it is assumed that this rate is satisfactory for the required displacement term. Thus,

$$\frac{d\Gamma}{dz} = \frac{b\Gamma_{tv}}{2\pi R k_2} \tag{13}$$

And finally with the mean settling rate defined as

$$k_m = w_m/(\Omega R) \tag{14}$$

then

$$k_m = \frac{b\Gamma_{tv}/(\Omega R^2)}{2\pi \, k_2} \left[\frac{-z_m/r_1}{[\,1 + (z_m/r_1)^2\,]^{1/2}} \right] \qquad (15)$$

6.3 Determination of Cylinder Length

The nonlinear equation system now developed was studied as a function of Γ_{tv}, with λ_1 determined from circulation coupling. By comparing these calculations with measured settling rates it was apparent that the vortex cylinder length z_m was systematically influential. The length parameter for calculation of k_m was therefore calibrated by sweeping values of z_m until satisfactory correlation with experimental settling rates was achieved. These values of z_m were then examined in relationship to a number of problem variables in order to identify any functional behavior. The result is given in Figure 15, and shows z_m to vary as a function of $(z_1/R)/(r_1/R-1)$, the ratio of the translation component increments from vortex generation until blade passage. The cylinder length required increases systematically until $z_m \to -\infty$ asymptotically at $(z_1/R)/(r_1/R-1) = 1$. Beyond that value the length remains infinite. The data symbols shown in Figure 15 are those calculated as described, and indicate the very close correspondence of z_m with $(z_1/R)/(r_1/R-1)$. The functional variation is approximated by the fairing as indicated and as given by

$$z_m/r_1 = -1.4913 \left[\frac{\left[(z_1/R)/(r_1/R-1) \right]^2}{1 - (z_1/R)/(r_1/R-1)} \right]^{0.4} \qquad (16)$$

This curious relationship suggests several physical interpretations, especially in view of the asymptotic behavior. It is first noted that the induced velocity due to a vortex ring in a plane parallel to the ring and displaced by z_1 has a maximum at the point r_1 when $z_1/R = r_1/R-1$. Thus it can be argued that the ratio represents the potential for maximum settling rate, and thus maximum wake extent, as a consequence just of the cylindrical wake structure. However, the asymptotic nature also implies strongly that $(z_1/R)/(r_1/R-1)$ is a measure of the stability, and thus, persistence of the wake. That is, below the critical unity value of the ratio, the persistence is influenced by the proximity of the first following blade and the abruptness by which its additional downward induced velocity accelerates the tip vortex from the k_1 rate to k_2. These results and observations could also be the key to better understanding and reducing the empiricism of the truncation of the far wake model of the global analysis, and for sure merit further attention.

7. SOLUTION WITH VELOCITY COUPLED WAKE

At the stage in the iterative solution of the global analysis when the wake geometry requires updating, Γ_{tv} and the loading information for calculation of the velocities which give λ_1 are available from the most recent blade circulation solution. With Γ_{tv} and λ_1, the settling rates k_1 and k_2 can be solved from the nonlinear set of Eqs. (5), (15), and (16) using standard numerical techniques. This updating process is repeated until compatibility between loading and wake geometry is obtained, and except for the intermediate iteration to obtain k_1 and k_2, does not differ from that when using either the experimentally prescribed or circulation coupled wake models.

The velocity coupled wake does, however, show a greater level of detail in results than do the previous models. Before comparing to those methods, the correspondence of k_m to the momentum induced velocity is reiterated in Figure 16. These calculations are for constant chord, untwisted blades, and are made with the global analysis. The important point for this special case is not the correspondence of the magnitude of k_m to the momentum level, for this is probably coincidence, although noteworthy. What is significant beyond the intriguing relationship itself is that the analysis with its comparatively greater complexity and higher degrees of freedom relative to momentum concepts has reproduced this simple linear correlation. Variations in k_m for twisted rotors show similar results, but with offsets in C_T reflecting the radial shift in loading.

Attention is now focused on comparing wake parameter calculations using velocity coupling to those made with experimentally prescribed and circulation coupled wakes. These comparisons are facilitated by viewing the parameters as functions of Γ_{tv} to place them on a common basis which highlights differences. Figures 17, 18, and 19 show calculations of λ_1, k_2, and k_1 respectively. The data symbols are those points

calculated with the experimental generalizations of Reference 2. These are in fact the calculations from which the circulation coupling of Reference 1 was developed, and the dashed fairings depict those results. The solid fairings are the results of velocity coupling. It should be recalled that for the experimental wake, single fairings were selected to represent the λ_1 and k_2 parameters. This was dictated by the high degree of scatter and difficulty in measurement of these terms, especially λ_1. In the calculated variation of λ_1 and k_2 with Γ_{tv} some variation with number of blades is evident, but again single fairings were selected for the circulation coupled generalizations. The calculations with the present method again show a trend with number of blades which for k_2 is consistent with the earlier calculation, and which therefore implies that the trend is indeed a valid result. Excellent results are also obtained from k_1 as seen in Figure 19 where the spread with number of blades is well duplicated.

8. EXTENSION TO AXIAL TRANSLATION

Modification of the velocity coupled hover wake for application to rotors in axial translation requires only the addition of the advance ratio in terms of the rate

$$k_a = -V_a/(\Omega R) \qquad (17)$$

to the expression for mean settling rate k_m. The axial translation velocity V_a is taken positive in climb and modifies the mean settling rate to

$$k_m = k_a + \frac{b\Gamma_{tv}/(\Omega R^2)}{2\pi\, k_2} \left[\frac{-z_m/r_1}{[\,1 + (z_m/r_1)^2\,]^{1/2}} \right] \qquad (18)$$

All influences of translation on the wake parameters are implicit through the additional displacement caused by k_a. The advantage of the velocity basis for the wake is thus clearly demonstrated in providing this unified model for the axial regime. In climb, for example, k_a directly increases the magnitudes of k_1 and k_2 through its addition in k_m. However, these increases are partially offset by the feedback also through displacement, since the increase in k_m is reduced through the inverse proportionality to k_2. Also in climb, the interference component k_i is reduced through its dependence on displacement, with attendant effects on k_1 and k_2. Radial contraction is similarly modified by axial translation through its implicit displacement influence. In the limit of large axial advance ratio such as that of a propeller in cruise, it is easy to see that k_i and the induced portion of k_m will tend to zero such that k_1 and k_2 will approach k_a. Also in that limit, the radial contraction will approach zero, leaving the wake geometry dependent as it should be only on the kinematics of the problem. These trends are illustrated in Figure 20 which shows k_i, the induced portion of k_m, and λ_1 as functions of V_a normalized by the momentum induced velocity in hover at the thrust level indicated. The result from momentum theory is also shown for reference. These calculations are based on a 0.25 scale model AH-1G helicopter tail rotor which was tested in the NASA Langley 30- by 60-foot wind tunnel as part of the program reported in Reference 14. Calculated performance is compared to measurements from these tests in Figure 21. The velocity coupled wake analysis shows very good agreement with slight but consistent optimism in power. The influences of the wake are explored further by viewing the radial distributions of axial induced velocity shown in Figure 22. As the rotor initially moves from hover to increasing climb speeds, the decrease in the magnitude of induced velocity is most rapid. The relative upwash from the tip vortex spiral also diminishes as the climb speed increases and the wake stretches out.

9. CONCLUSIONS AND RECOMMENDATIONS

This paper has introduced a new and unified approach to prescribing the wake of a helicopter rotor in vertical and hovering flight. Velocity coupling captures the essence of a free wake analysis, and achieves this generality with minimum complexity. By deriving the geometry of the wake from formulations in the velocity domain, this method satisfies similar equilibrium criteria of the computationally demanding free wake while retaining the simplicity of the prescribed wake. As an added benefit from its velocity basis, the model is equally applicable not only to hover, but also to axial flight as well. This consistency of theory is achieved through the implicit effects of these flight variables on wake geometry. These influences act through the changes in displacements of key wake elements which then effect changes in the characteristic convective velocities.

As the result of the development of the velocity coupled wake, the following observations are noted:

1. Radial contraction can be expressed in terms of principal lateral velocities, and is a strong function of tip vortex strength with second order effect due to loading.

2. Settling rates can be expressed in terms of principal axial velocities which are identified with mean inflow and the mutual induction, or interference between adjacent spirals of the near wake tip vortices.

3. The mean inflow component of the settling rates can be modeled by a vortex cylinder which is sized to approximate the real wake tip vortex trajectory surface.

4. The interference velocity can be described with a simple two-dimensional approximation of the near wake tip vortex elements.

5. The details required in the vortex cylinder model used in the present study are similar to observed far wake characteristics and strongly support the requirement for analytical wake models with systematically varying truncation.

6. The formulation of velocity coupling allows a natural transition into axial translation. As in hover, the wake geometry is implicitly modified through the feedback between the principal velocities and the displacements from which they are calculated.

7. Correct wake modeling only requires agreement between wake parameters and blade loading. Correlation of wake parameters with rotor performance characteristics then necessitates adequate representation of all aspects of the problem, including tip vortex rollup process, tip vortex structure, and far wake influences.

Additional development of hover and axial flow methodology would be accelerated by research focusing on poorly understood physical details, and increasing the amount of benchmark experimental data available for correlation. Several specific technology programs which would guide future development are:

1. Simultaneous measurements of wake geometry characteristics, blade load distribution, rotor thrust, and rotor torque need to be made. This data is necessary for complete assessment of the wake model and global analysis.

2. To improve understanding of its behavior and influence, the rotor far wake should be investigated experimentally. The far wake has been shown to be an influential element which has not received adequate attention.

3. Performance and wake measurement of isolated rotors in axial translation should be made. The importance of low speed axial climb characteristics on helicopter performance assessment is in great contrast to the very limited amount of quality data available for correlation of methodology.

4. The prescribed wake method should be extended to the descent regime. Wake analyses are essential for investigation of this important regime such as experienced by a tail rotor in sideward flight.

REFERENCES

1. Kocurek, J.D., Berkowitz, L.F., and Harris, F.D., "Hover Performance Methodology at Bell Helicopter Textron," Presented at the 36th Annual National Forum of The American Helicopter Society, Washington, D.C., May 1980.

2. Kocurek, J.D., and Tangler, J.L., "A Prescribed Wake Lifting Surface Hover Performance Analysis," Presented at the 32nd Annual National Forum of the American Helicopter Society, Washington, D.C., May 1976.

3. Landgrebe, A.J., "An Analytical and Experimental Investigation of Helicopter Rotor Hover Performance and Wake Geometry Characteristics," USAAMRDL Technical Report 71-24, Eustis Directorate, U.S. Army Air Mobility Research and Development Laboratory, Fort Eustis, Virginia, June 1971. (Summarized in "The Wake of a Hovering Helicopter Rotor and Its Influence on Hover Performance," Journal of the American Helicopter Society, Vol. 17, No. 2, October 1972, p. 3).

4. Gray, R.B., "On the Motion of the Helical Vortex Shed From a Single-Bladed Hovering Model Rotor and Its Application to the Calculation of the Spanwise Aerodynamic Loading," Princeton Aeronautical Engineering Department Report No. 313, September 1955.

5. Gray, R.B., "An Aerodynamic Analysis of a Single-Bladed Rotor in Hovering and Low Speed Forward Flight as Determined from the Smoke Studies of the Vorticity Distribution in the Wake," Princeton Aeronautical Engineering Department Report No. 356, September 1956.

6. Jenney, D.S., Olson, J.R., and Landgrebe, A.J., "A Reassessment of Rotor Hovering Performance Prediction Methods," Journal of the American Helicopter Society, Vol. 13, No. 2, April 1968, p. 1.

7. Landgrebe, A.J., and Cheney, M.C., "Rotor Wakes-Key to Performance Prediction," AGARD Conference Proceedings No. 111 on Aerodynamics of Rotary Wings, Fluid Dynamics Panel Specialists Meeting, September 1972.

8.   Landgrebe, A.J., Moffitt, R.C., and Clark, D.R., "Aerodynamic Technology for Advanced Rotorcraft - Part I," Journal of the American Helicopter Society, Vol. 22, No. 2, April 1977.

9.   Kocurek, J.D., "Development of the Velocity Coupled Prescribed Wake," Presented to the Round Table on Helicopter Rotor Wakes, NASA Ames Research Center, Moffett Field, California, November 1980.

10.   Moffitt, R.C., Sheehy, T.W., "Prediction of Helicopter Rotor Performance in Vertical Climb and Sideward Flight," Presented at the 33rd Annual National Forum of the American Helicopter Society, Washington, D.C., May 1977.

11.   Miller, R.H., "A Simplified Approach to the Free Wake Analysis of A Hovering Rotor," Presented at the Seventh European Rotorcraft and Powered Lift Aircraft Forum, Garmisch-Partenkirchen, Federal Republic of Germany, September 1981.

12.   Miller, R.H., "Rotor Hovering Performance Prediction Using the Method of Fast Free Wake Analysis," Presented at the AIAA 20th Aerospace Sciences Meeting, Orlando, Florida, January 1982.

13.   Knight, M., and Hefner, R.A., "Static Thrust Analysis of the Lifting Airscrew," N.A.C.A. Technical Note No. 626, Washington, D.C., December 1937.

14.   Yeager, W.T., Young, W.H., and Mantay, W.R., "A Wind Tunnel Investigation of Parameters Affecting Helicopter Directional Control in Low Speed Flight in Ground Effect," NASA TN D-7694, November 1974.

GRAY'S WAKE, ADAPTED
FROM REFERENCE 5

COMPUTATIONAL AERODYNAMICS
MODEL OF REFERENCE 1.
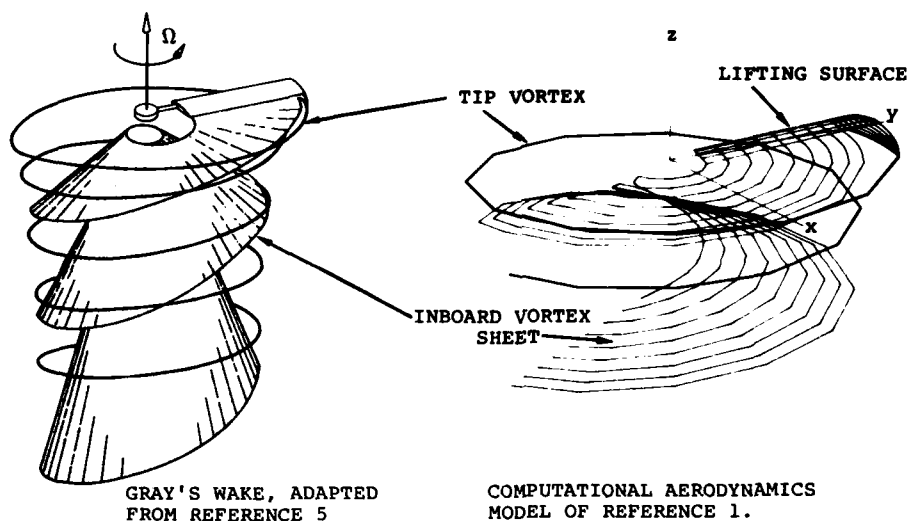
Figure 1.   Rotor wake in hover as conceptualized by Gray (Reference 5), and as modeled in the methodology of Reference 1.
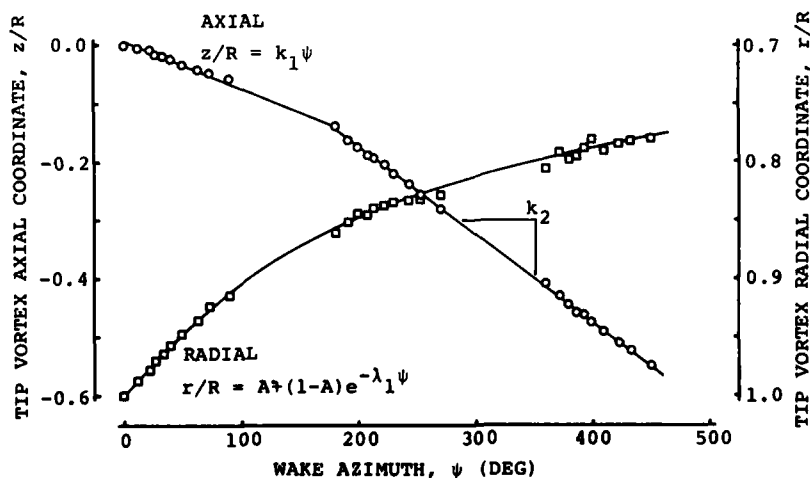
Figure 2.   Two-bladed model rotor tip vortex trajectories.
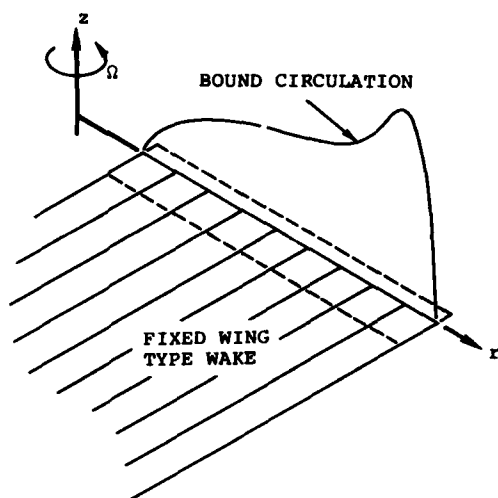
Figure 3. Simple near wake model used to calculate principal velocities.

Figure 4. Principal lateral velocities are calculated at position of first vortex passage.

Figure 5. Calculated variation of contraction parameter with principal velocity due to loading.
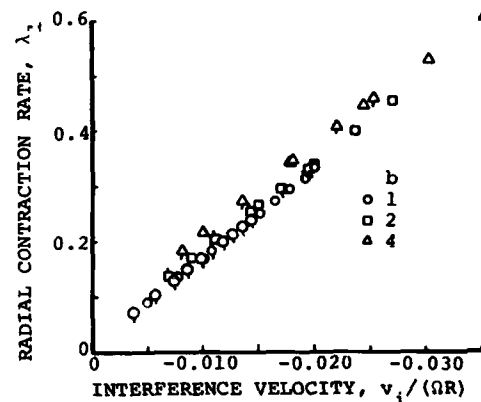
Figure 6. Calculated variation of contraction parameter with principal velocity due to successive tip vortex passages.

Figure 7. Radial contraction is a linear function of principal lateral velocities.
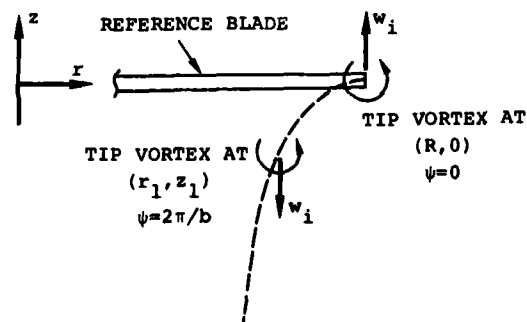
Figure 8. Geometry for calculation of axial interference velocity.
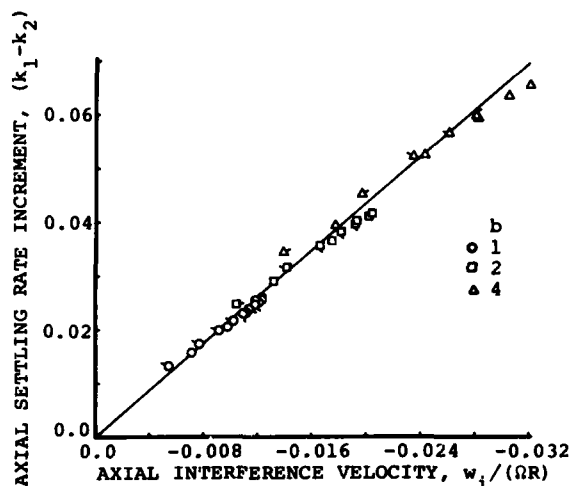
Figure 9. The increment in settling rate from k_1 to k_2 is a linear function of the axial interference velocity.

Figure 10. Axial settling is due to mean inflow modified by axial interference velocity.

Figure 11. Initial settling rate correlates with momentum induced velocity retarded by axial interference velocity.
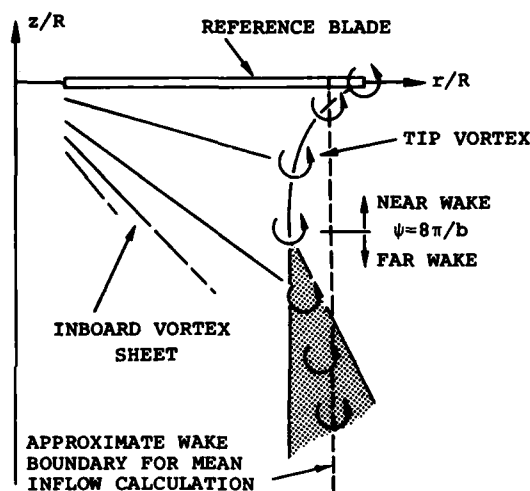
Figure 12. Near and far wake regions of prescribed wake model of global analysis, and approximate cylinder for mean inflow calculation.

Figure 13. Detailed geometry of vortex cylinder for mean inflow calculation.
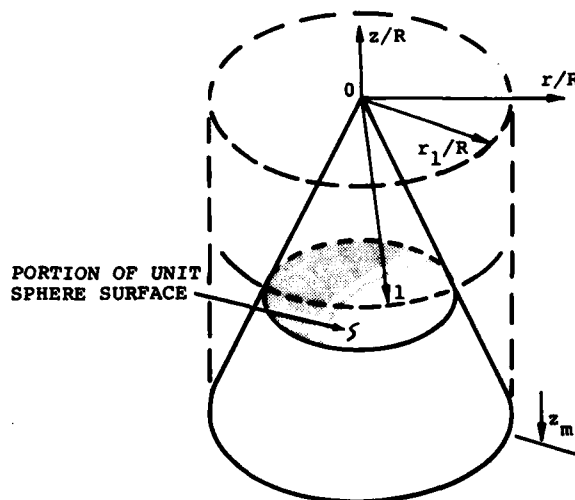
Figure 14. The solid angle is the surface of the unit sphere cut out by the conical surface as shown.
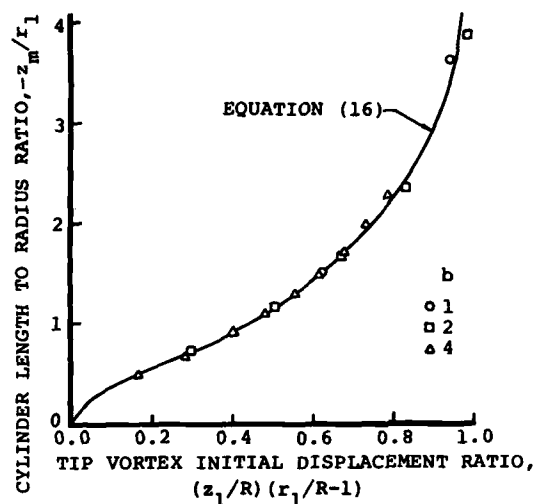
Figure 15. Cylinder length is a systematic function of tip vortex position at first blade passage.

Figure 16. Calculated mean settling rate correspondence to momentum induced velocity.

Figure 17. Calculated variations of contraction parameter with tip vortex strength.
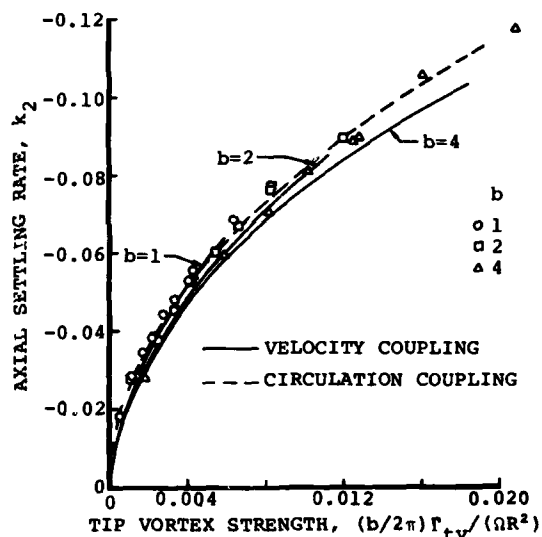
Figure 18. Calculated variation of secondary settling rate with tip vortex strength.

Figure 19. Calculated variation of initial settling rate with tip vortex strength.
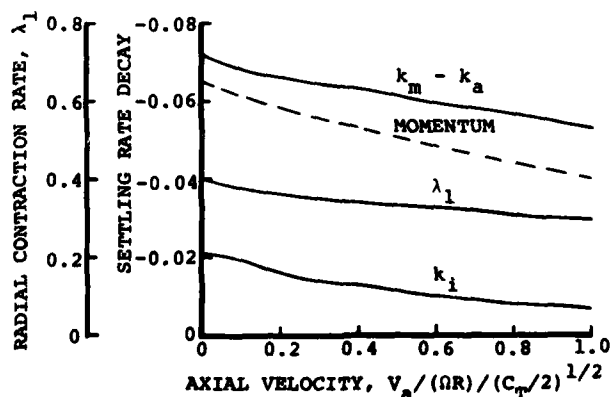
Figure 20. Induced components of velocity coupled wake parameters show correct variations toward high advance ratio limit in climb.
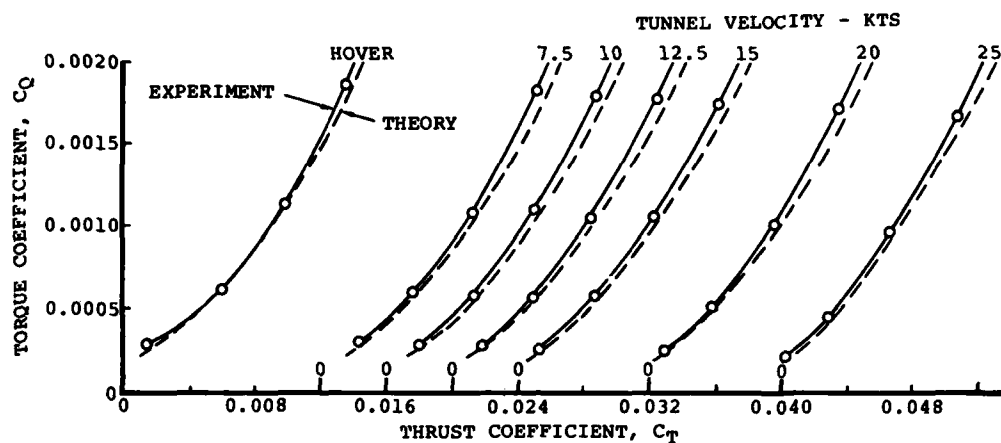
Figure 21. Climb performance calculated with velocity coupled wake correlates well with tests of model scale tail rotor.
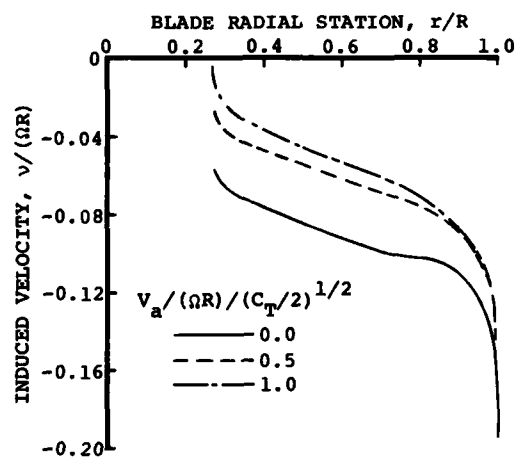
Figure 22. Calculated axial induced velocity distributions in climb show diminishing magnitudes and interference.

STUDIES ON BLADE-TO-BLADE
AND ROTOR-FUSELAGE-TAIL INTERFERENCES

by

H. Huber
G. Polz

Messerschmitt-Bölkow-Blohm GmbH
Postfach 80 11 40
8000 München 80, Germany

SUMMARY

With the increasing sophistication of modern helicopter designs the problems arising from the interactional aerodynamic flow field around the helicopter has become more acute. Interactional aerodynamics are, by origin, of utmost complexity, because many of the interactions involve viscous processes, the flow usually is unsteady and the interactions are strongly interdependent.

The paper focusses on some specific areas out of the many existing problems. First major problem is the blade-to-blade vortex interaction phenomenon, where the unsteady pressure fluctuations, due to the vortices impact, result in highly impulsive blade loadings, excessive dynamic hub forces/moments, and impulsive noise signatures. The paper describes MBB's analytical modelling techniques, including prescribed-contracted-wake analysis, and free-wake-models, and discusses results of analytical investigations. Experimental results obtained from in-flight blade modal bending measurements are also presented.

As a second category, the interactional aerodynamic flow from the fuselage to the rotor blades is treated. Due to flow displacement effects around the fuselage contour, large up-wash and aownwash components can be produced, resulting in significant changes of the local angle-of-attack within the rotor disc plane. The paper describes analytical investigations on this type of interference, using a singularity model for the flow calculation around the fuselage body. Parametric influences of the rotor-fuselage separation distance are shown.

As a third category, interference flow effects between the rotor head and fuselage to the tail area are investigated. The wake pattern, particularly that of the upper components results in a reduction of the steady flow pressure, and in reductions of the vehicle stability characteristics. Significant unsteady components contained in the wake flow may cause substantial structural loading, and severe aircraft vibrations. For the analytical representation of the steady interference flow a model, containing separated flow calculation, is used. Experimental results including steady pressure contours and dynamic pressure and flow angle fluctuations at the empennage/tail rotor area will be shown including WT-model and full-scale flight test results.

1. INTRODUCTION

In recent years considerable attention has been devoted to and significant steps have been accomplished in the aerodynamic design of helicopters. Advanced research and development work on rotor blade airfoils allowed increasing the Figure of Merit and the maximum lift-to-drag ratios at high speed significantly. Streamlining and other refinements of fuselage contours were successful in reducing the parasite drag of helicopter substantially. Increase of the engine air intake efficiency also contributed to better performance achievements.

With the increasing sophistication of modern helicopter designs, the interactional aerodynamic phenomena between the various passive and active components have become more and more acute. Many of the former and todays helicopter designs were or are suffering from problems arising from some of the multifarious interactional events. The state of the art in this field - relating both to the knowledge of the basic mechanisms, and to the potentials of design improvements - seems to be not as far developed when comparing with the field of the more classical aerodynamic problems.

Analytical methods for predicting the rotor inflow have been developed at various levels of accuracy, and their potentials were demonstrated by many authors (References 1 to 7, for example). It seems, however, that the most powerful free-wake vortex models in use today are not yet fully applied during practical vehicle design and development programs. Until fairly recently, many of the problems of interactional aerodynamics were not even fully recognized, although substantial problems and drawbacks resulting from interactional flow anomalies were experienced by many helicopter designs.

Fundamental work on this area was contributed just a few years ago (Reference 8), which systematically describes the scope of the interactional aerodynamic processes and the various flow anomalies in the flow field of a helicopter.
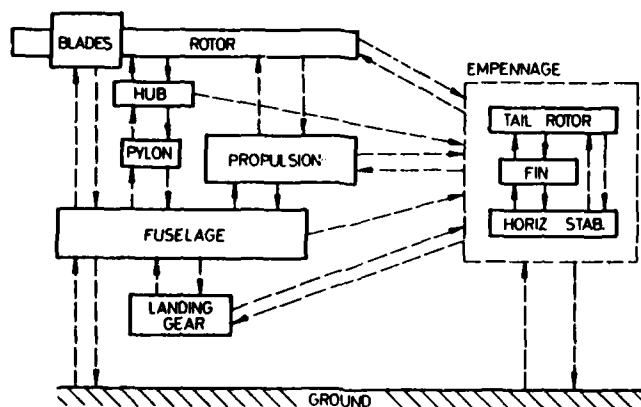
FIGURE 1   Helicopter Aerodynamic Interactions (Schematic)

Figure 1, taken from Reference 8 and slightly modified, presents a schematic overview of the broad scope of aerodynamic interactions. The following work will focus on some of the areas shown, and will contribute recent results obtained at MBB, from both analytical work and from experiments.

These three areas are

- Blade-to-Blade Flow Interaction

- Fuselage-to-Rotor Interaction

- Rotor/Fuselage-to-Tail Area Interferences.

2.   BLADE-VORTEX INTERACTIONAL AIRLOADS

2.1   ANALYTICAL MODELLING

The flow field around the helicopter rotor blades is significantly influenced by the rotor wake, especially when flying in the near hovering and low to moderate flight speed region. The accurate prediction of performances, and the reliable estimation of rotor blade loading and fuselage vibratory excitation require a precise modelling and prediction of the rotor wake structure.

The evolution of the analytical methods started from the quite simple Goldstein analysis, followed by actuator disc and blade momentum theories. Emphasis was then placed on prescribed wake theories, taking into account wake contraction effects. The mostly developed representation were then achieved by free-wake models.

Several methods of rotor downwash calculations are in use today at MBB (Reference 7). In an experimental-prescribed contracted wake model (Figure 2) the blade is represented
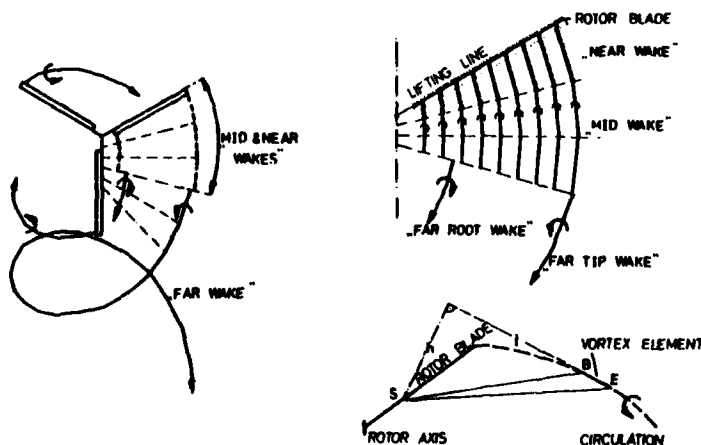
FIGURE 2   Wake Structure of the Prescribed-Contracted-Wake Model
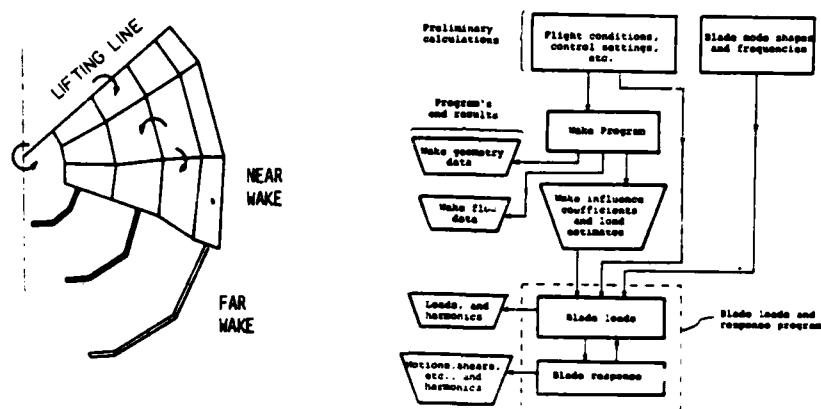
FIGURE 3 Wake Structure and Flow Diagram of the Free-Wake Model (Sadler)

by a lifting line and the wake is divided into an inboard section and a tip vortex section. In the near wake, the inboard root vortex is formed by meshes of trailed and shed vortices, and the tip vortex is formed by a bundle of trailing vort ces. In the mid wake the shed vortices are omitted and in the far wake section the wake is modelled by two single root and tip vortices. The wake geometry is based on the experimental work done by Landgrebe, Reference 5 . Although this wake geometry has initially been evaluated for the hovering condition, it was extended for forward flight by introducing the wake geometry according to the free stream velocity.

A major advance in the wake modelling is achieved by the free-wake analytical represen- tation, such as described by Reference 6 , and indicated in Figure 3. The near wake is calculated by an array of discrete trailing, and shed vortices generated with vortex strengths corresponding to radial and azimuthal blade circulations; the far wake is formed by an arbitrary number of trailing vortices. The vortex elements are allowed to convect in the velocity field they create, until they take up positions which are consistent with the resultant free stream and vortex induced velocities.
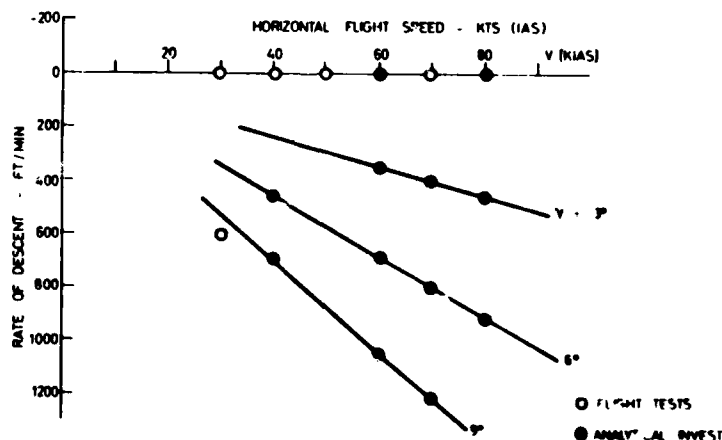
FIGURE 4 Range of Intensive Blade-to-Blade Vortex Interaction

2.2 RESULTS OF ANALYTICAL INVESTIGATIONS

One of the primary practical applications of such rotor wake models is to calculate harmonic blade airloads, necessary for blade strength analysis and rotor hub forces/ moments, for example. Thereby, a prime area of interest, showing significant blade-blade vortex interactions, is the range of low-to-moderate flight speeds, and, particularly, the range of medium rates of descent (Figure 4).

An analytical study was conducted investigating flight speeds of 40 to 80 kts and rates of descent between zero and 1200 ft/min, which corresponds to glide slope angles of up to 9 degrees. Figure 5 shows calculated time histories of the local thrust distribu- tion at different blade spanwise stations. The abscissa axis reference is the azimuth angle of the subject blade. Forward flight speed is 60 kts. In the horizontal flight condition , left side of Figure 5, the local thrust variation at the several radial stations is marked by only slight vortex interactions: One mild tip vortex interference is seen
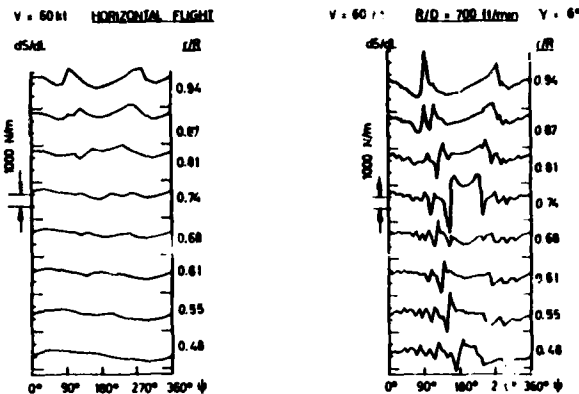
FIGURE 5 Calculated Time Histories of Local Lift (left: 60 kts level flight, right: 60 kts, 700 ft/min descent rate)
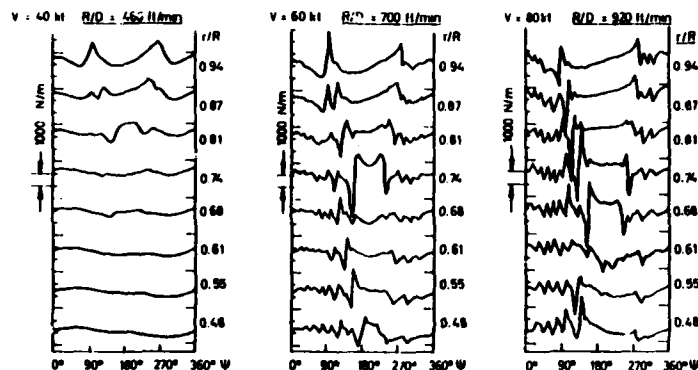
FIGURE 6 Calculated Time Histories of Local Lift for Different Flight Speeds, Constant Glide Slope 6 Degrees

starting slightly before the 90 degrees azimuth position at the blade tip, and moving inboard with the blade azimuthally progressing to the 180 degrees position, and then moving outward again, when the blade is passing the 270° azimuth position. In contrast to this variation, the time trace for the flight case 60 kts, 700 ft/min descent rate, (Figure 5 right diagram) indicates strong blade tip vortex interactions progressing from the tip to the inboard locations and moving outboard again around the blade retreating position.

Figure 6 shows a comparison of airload traces for different flight speeds at identical glide slope angles (6°). The trend indicates that, as forward speed is increased, the loci of maximum vortex interference effectively move inboard on the rotor disc.
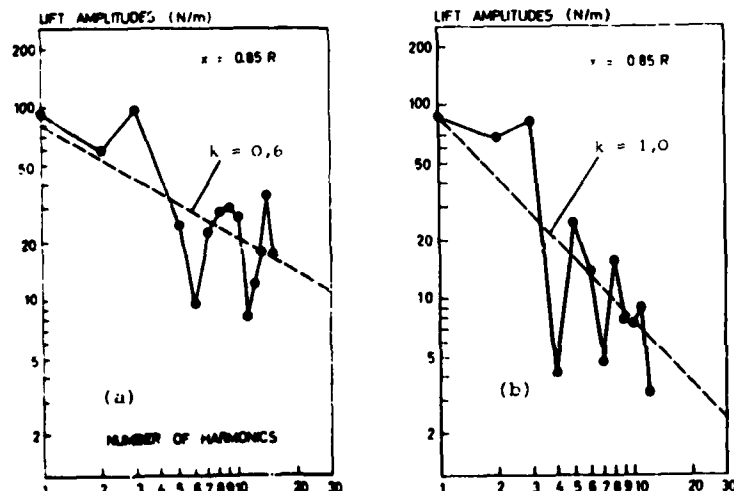
FIGURE 7 Calculated Harmonic Airloads at 85 % of Radius, Flight Condition 60 kts/6°, and 80 kts/3°

The local thrust distributions were frequency analyzed in terms of harmonics of the rotor rotational frequency. Figure 7(a) shows local thrust amplitudes as a function of the number of harmonics, for a radial station near the tip (0.85 R); a range of harmonics of 1Ω to 15Ω is covered. Flight condition is 60 kts, 700 ft/min rate of descent, corresponding to the right picture of Figure 5 . The occurance of large high harmonic airloads relative to the low frequency loads is evident. When describing the harmonic airloads decay versus frequency by the exponential function

$$L_n = L_1 \cdot n^{-k},$$

an exponent as low as 0,6 can be derived from this diagram. Figure 7(b) presents the frequency spectrum for the 80 kts, 450 ft/min descending rate case, showing an exponent of about 1.0. In contrast, airload decay exponents in the magnitude of 2.0 to 2.5 are obtained for the horizontal flight conditions.

2.3 EXPERIMENTAL STUDIES

Theories and analytical methods available today can roughly cope with the principal blade-vortex interactional problems, and are capable of indicating the main parametric influences. Experimental work, however, is of utmost importance in order to support existing theories,and to accomplish a more complete understanding in the required depth.

Experimental work at MBB was directed towards full-scale inflight testing on the BO 105 hingeless rotor. The approach taken was no direct airload measurement, but was concentrated on blade moment measurements, and subsequent derivations of aerodynamic forces. The area of investigations included horizontal flight speeds of 30 to 70 kts, climb and descent rates equivalent to 30 to 50 percent torque setting, as well as transient flight conditions during landing flares, see Figure 4.
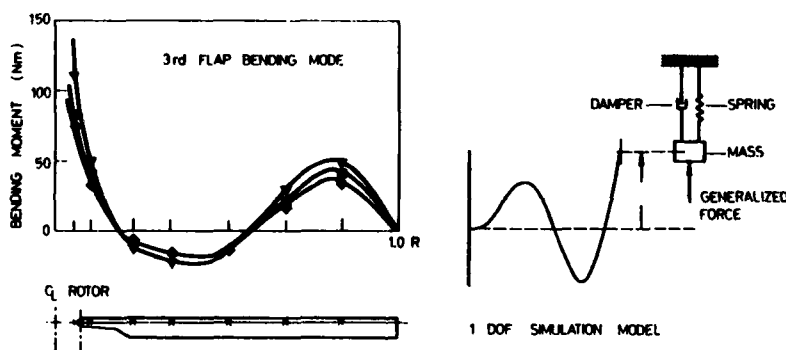
FIGURE 8   Simulation Model for Airloads Evaluation from Measured Bending
Moment Data

Blade bending moments were measured at seven stations over the blade radius (Figure 8), and aerodynamic forces were determind by use of a simplified one-degree-of-freedom spring/ mass-damper model. Details of this modal approach have been described in References 9 and 10 and will not be covered in detail here.
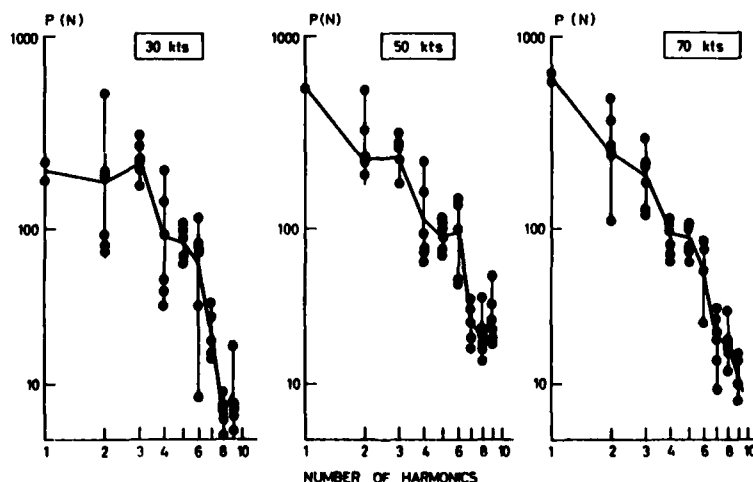
FIGURE 9   Harmonic Airloads for Different Horizontal Flight Speeds
(from Blade Bending Measurements)
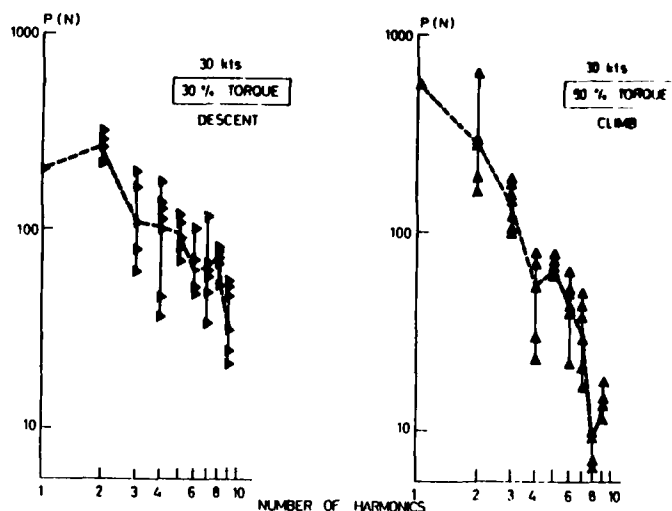
FIGURE 10   Harmonic Airloads during Climb and Descent Conditions at
30 kts

Discussion of Results: Figure 9 shows results of harmonic airloads as a function of
multiples of the rotating frequency for 30, 50, and 70 kts horizontal flight speeds. A
comparison of the results indicates a similar harmonic decay for the different airspeeds,
whereas the absolute magnitudes of amplitudes increase with lower flight speeds.

Figure 10 shows corresponding spectrographs for variations in the vertical speed com-
ponent , i.e. climb and descent at 30 kts airspeed. In climb the harmonic airloads show
a strong decay versus frequency, indicating that nearly no vortex-interactions occur. In
contrast to this favourable variation, the curve for the descent case is marked by large
amplitudes at high harmonics, indicating severe vortex interactions, which support the
flight vibration observations quite well.

Further interesting results from the transient flight conditions are shown in Figure 11,
comparing the aerodynamic exciting forces during a landing flare condition. Two things are
seen from the charts. First, the higher harmonic amplitudes evident in the diagram are even
exceeding the 1Ω and 2Ω trim loads. Furthermore, it should be noted from these charts that
aerodynamic exciting forces do change quite rapidly within one second during this flight
condition.
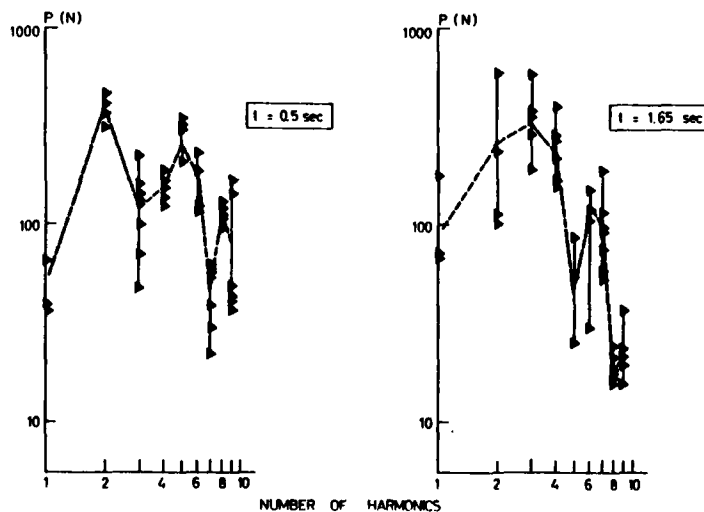
FIGURE 11   Harmonic Airloads during Landing Flare, Transient Condition
(From Blade Bending Measurements)

3.   FUSELAGE FLOW TO MAIN ROTOR INTERACTION

The interaction of the fuselage flowfield with the flow in the rotor disc plane is another important problem area, as indicated in the schematic diagram of Figure 1. These matters and its consequences have received considerable attention during several recent helicopter developments.
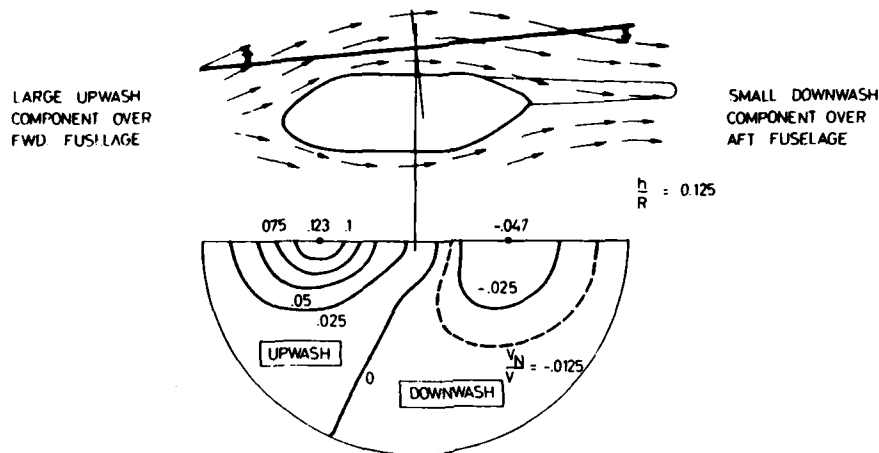
FIGURE 12   Principle of Fuselage Flow Interaction into the Rotor Plane

Figure 12 gives the prinicpal geometric relationship of the fuselage flowfield and the resultant normal velocity component in the rotor disc, shown for a high forward speed flight condition. In principle, the flow around ^he fuselage upper nose section produces an upwash flow component in the front parts of the rotor disc, and the flow around the aft section produces a downwash component at the rear parts of the rotor disc. It is evident that due to the steeper nose shapes the upwash flow components in the front parts usually are higher than the downwash components in the rear parts.
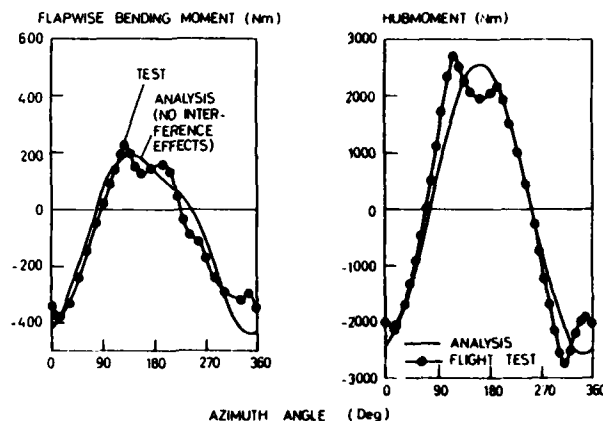
FIGURE 13   Blade Root and Hub Bending Moment in Forward Flight
(BO 105, 100 kts)

One reason for considering these aerodynamic effects is the potential direct effect on blade loads and on airframe vibratory exciting forces. Figure 13 shows a time history of the blade flapwise bending moment on one blade (left diagram) versus the rotor azimuth angle. An impulsive bending mode exc.tation at a 135 degrees azimuth position is evident in the trace, which damps out in the following half rotorrevolution. A correspon- ding dip in the curve of the main rotor hub moment (right part) is also observed. The harmonic analysis shows that this higher harmonic content of the hub moment is one main source of fuselage vibrations. As will be shown in the subsequent section, the aerody- namic mechanism certainly involves the flow distortion in the front part of the rotor disc due to the fuselage upwash flow components.

In this respect, the trend to more compact helicopter designs, having lower clearance between rotor and fuselage, certainly contributes to aggravating the interference inten- sity. As modern helicopter designs, in addition, tend to more slender and longer fuselage configurations, the displacement effect of the front part of the fuselage influences more the outer parts of the rotor blade and, therefore, a region with higher dynamic pressure.

Another effect is the impact of the blade tip vortices on the airframe creating strong
impulsive pressure fluctuations, which can result in annoying vibrations and noise in the
cockpit region, as shown in References 8, 11. These effects become important especially
for the high speeds and higher blade loadings of modern helicopter concepts, as discussed
in Reference 12.

    Analytical Studies: A prinicipal parametric study has been conducted at MBB, considering
a modern type of fuselage shape (Figure 12). A panel method was used for the calculation
of the fuselage flowfield. Fig. 14 shows the representation of the body contour by panel
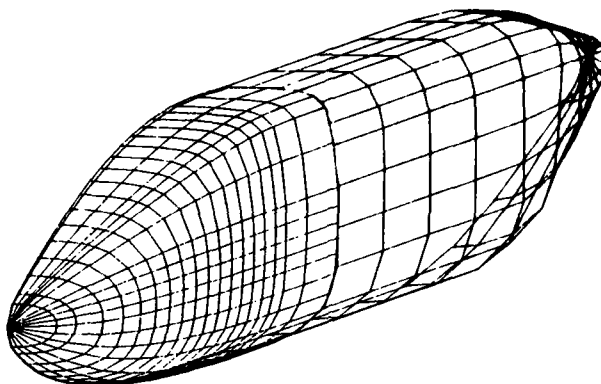
FIGURE 14   Panel Representation of the Fuselage Body

elements. The fuselage induced normal velocity component in the rotor plane is introduced
in a rotor program. The rotor model used for this study is based on the blade element
theory, simulating the induced downwash by a local momentum theory. Flow components from
the fuselage flowfield are iteratively combined with the rotor induced velocities;
reactions from the rotorflow components down to the fuselage flowfield are neglected.
Within the aerodynamic loads calculation procedure, blade deflections are taken into
consideration by a simplified method representing only the first flapwise bending mode.
For the subsequent calculation of blade structural loads, and of rotor hub excitation
forces and moments a separate coupled bending mode shape analysis is used.

    In Figure 15, a typical influence of the rotor-fuselage clearance on the vertical flow
component distribution is shown for a high speed forward flight condition. Because of the
steeper inclination angle, the maximum fuselage induced upwash velocity on the front part
of the rotor disc is 2-3 times higher than the corresponding maximum downwash on the rear
part. It is seen from the figures, that maximum vertical velocity components increase with
a decrease of the rotor-fuselage clearence, whereas the boundary between the upwash and
downwash areas remain nearly unchanged.
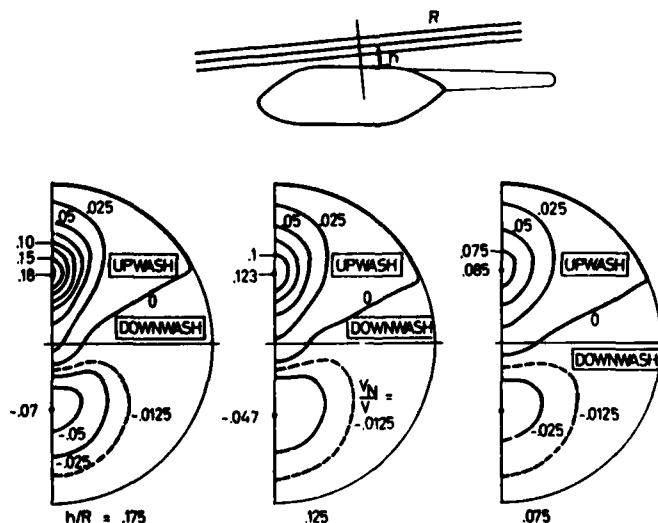
FIGURE 15   Fuselage induced Upwash/Downwash in the Rotor Plane as a
            Function of Rotor-Fuselage Clearance (Calculated)

In the real case the downwash on the rear part of the rotor disc is further reduced due to the separated flow behind the fuselage and rotor shaft/hub area, which prevents the confluence of the flow behind the fuselage body.

As a result from the change of normal flow component, the effective local angle of attack is changed, especially at the front and aft positions of the rotor disc (Figure 16). At the forward blade position ($\psi = 180^\circ$), a substantial increase of local angles is seen, with the maximum occuring at about 40% of blade radius. For the smallest rotor-fuselage clearence the static stall boundary of the blade airfoil is nearly reached. At the outer radius positions, the change of the angle of attack diminishes due to the higher inplane velocity component. At the blade tip the angle is even reduced with increasing fuselage influence, an effect resulting from the superposition of the vertical velocity component of the blade's flapping motion at the same aircraft trim condition.

Corresponding influences on the blade lift distribution over blade radius are seen from Figure 17. Maximum load increase due to fuselage upwash occurs at about 50% of radius
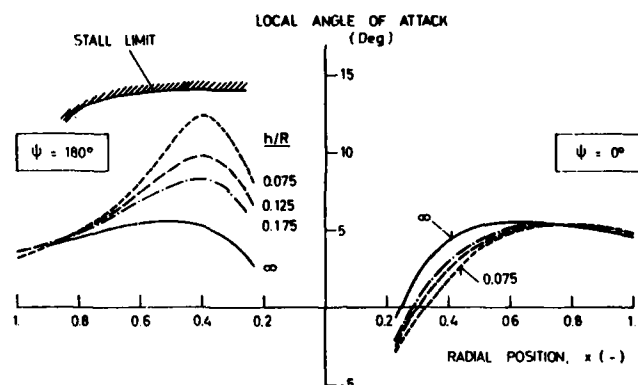
FIGURE 16 Fuselage Flow Influence on local Angle of Attack at the Blades, V = 150 kts
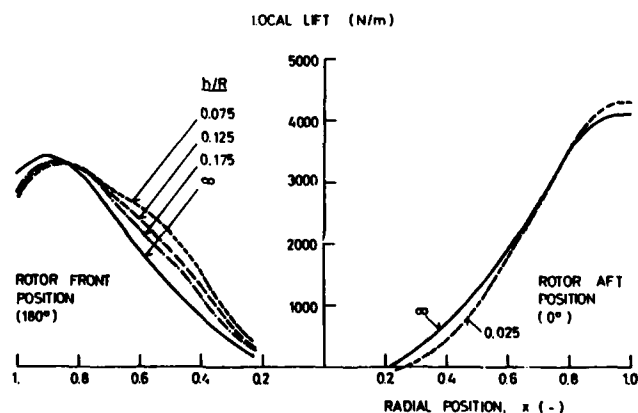
FIGURE 17 Effect of Fuselage Flow on Local Lift Distribution

at the front rotor position, the local lift being twice the value of the isolated rotor calculation without fuselage interference. As fuselage induced velocities differ significantly between the fore and aft rotor position, a slight influence on rotor torque is also obtained by calculation, lower rotor positions being more favourable.

In Figure 18 the azimuthal variation of local thrust at a 40% radial position is shown, and frequency analysis results are compared. The blade spanwise position of 40 to 50% radius is particularly important due to the fact, that this station usually corresponds with the antinodes of oscillation of the 2nd and the 3rd natural flap bending mode shapes. From the harmonic analysis results in Figure 18 a strong increase of the 2nd to 5th harmonic local lift is evident.
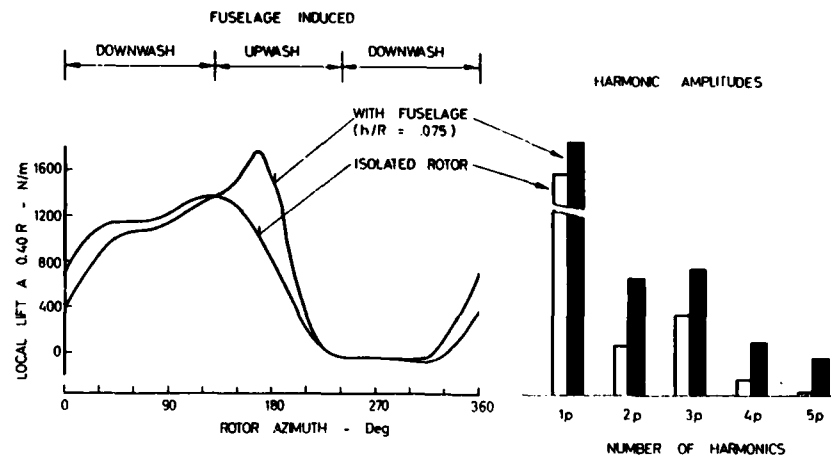
FIGURE 18 Effect of Fuselage on Blade Local Lift, Calculated for 150 kts

4.   FUSELAGE/HUB-TAIL INTERFERENCE PROBLEMS

4.1   THE FLOW PROBLEM

A field of increasing importance is the interference problem between the fuselage/pylon/hub area, and the tail area. Adverse interference effects result primarily in a reduced efficiency of the tail surfaces and tail rotor and in severe dynamic structural loadings, and aircraft vibrations (References 8, 13 to 17). They usually occur in horizontal forward flight as well as in descent flight. Figure 19 illustrates the main interference effects in forward flight. The fuselage wake hits mostly the horizontal tail, thereby reducing its efficiency due to the loss in dynamic pressure. The wake of the rotor hub/mast affects the flow on the tail rotor and side fin, thereby impairing their effectiveness. Also "tail shake" phenomena can be caused by this wake, especially when the frequency content coincides with a natural frequency of the tail surfaces or tail boom, as discussed later.
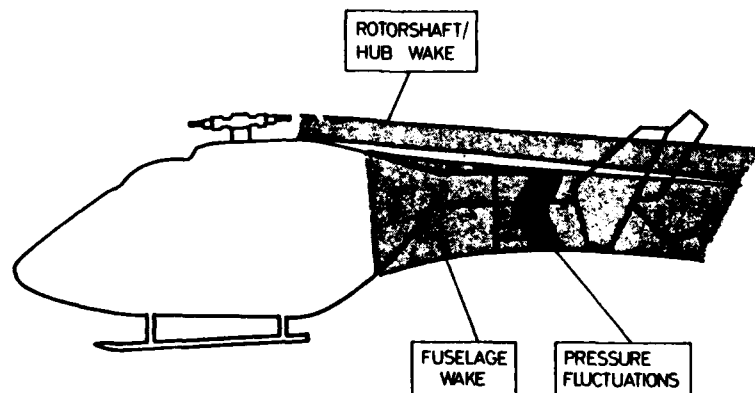
FIGURE 19 Main Interference Effects between Fuselage/Hub and Tail Area

In Figure 20 an overview of the different interference sources and the resulting aerodynamic effects is given. Besides the steady pressure loss in the fuselage wake, large unsteady flow components can occur due to periodic flow separation on the aftbody. In addition, the high frequency turbulence in the wake can reduce the efficiency of the tail surfaces due to the increased tendency toward flow separation, especially in the case of a thick airfoil section. Furthermore, the upwash/downwash combined with the fuselage lift reduces the lift curve slope of the horizontal tail and thus its effectiveness. In a similar manner, the fuselage induced side wind changing with the yaw angle reduces the efficiency of all vertical tail surfaces. In addition, a flow spillage on the engine inlets can cause flow separation on the outer surface of the cowling, and can therefore intensify the wake. A strong wake, and therefore severe interference effect, is caused by the main rotor hub/shaft region, which includes unfavourable aerodynamic shape components. Improvements can be achieved by applying particular attention in the design and by suitable modifications of the components. So, for example, a mast fairing (pylon) can diminish the wake of the rotor shaft significantly. With a suitable surfboard-shape of the pylon roof top, a vortex pair is created, whose downwash deflects the wake in the tail

		STEADY PRESSURE LOSS	DISCRETE UNSTEADINESS	TURBULENCE	VORTICES	VERTICAL FLOW DEFLECTION	LATERAL FLOW DEFLECTION
FUSE-LAGE BODY	SHAPE	X	X	(X)			
	LIFT/DOWNLOAD				(X)	X	
	YAWING ANGLE						X
ENGINE COWLING	INLET SPILLAGE	X					
	EXHAUST FLOW			X		(X)	
PYLON					X[1]	X[1]	
ROTOR HUB / SHAFT		X		X	X[2]	X[2]	
APPENDAGES		(X)	(X)	(X)	(X)	(X)	

[1] WITH SURFBOARD-SHAPED ROOF TOP   [2] WITH HUB CUP

FIGURE 20 Sources of Interferences and Main Aerodynamic Effects

area preventing this region from considerable pressure loss. A similar effect can be achieved by the installation of a hub cap, which directs "fresh" air into the wake immediately behind the rotor hub.

Theoretical methods can provide a basic knowledge of these interference effects, however wind tunnel investigations or flight tests are often required to supplement the analytical studies.

4.2 ANALYTICAL AND EXPERIMENTAL RESULTS

STEADY FLOW EFFECTS

Several methods for the calculation of the fuselage flow have been developed in recent years (References 18, 19). A model developed by MBB is based on a panel method for the fuselage flow displacement effects and vortex distribution in the wake (Figure 21). In this model the growth of the wake with increasing distance from the fuselage, as well as the vortex system combined with the fuselage lift is taken into account. Figure 22 shows the flow around the BK 117 fuselage together with the wake boundaries and the momentum loss inside.
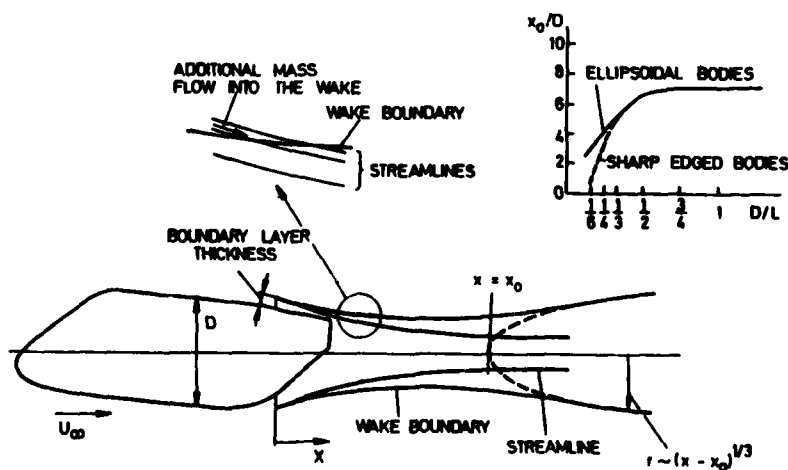
FIGURE 21 Analytical Model for Separated Fuselage Flow Calculation
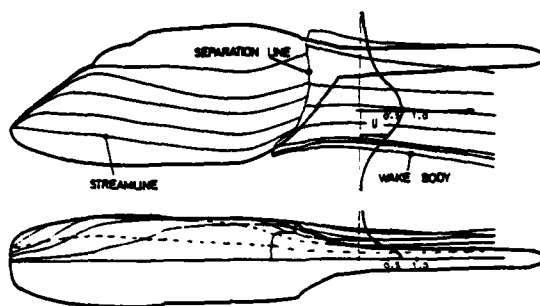
FIGURE 22 Calculated Flow Field on BK 117 Fuselage (α = -5 degrees)

An important aerodynamic effect results from the fuselage upwash or downwash associated with the fuselage vertical force. In Figure 23 the velocity distribution (wind tunnel measurement) over the tail section area of a specific helicopter fuselage shape and the resulting upwash distribution over the span of the horizontal tail are shown for a fuselage angle of attack of -5 degrees. The increase of the mean angle of attack at the horizontal tail due to this upwash is about 4 degrees. Zero fuselage lift and, therefore, zero upwash occurs at an angle of attack of +8 degrees; this means, that the lift curve slope of the horizontal tail is reduced by about 30 % due to the fuselage upwash/downwash effect.
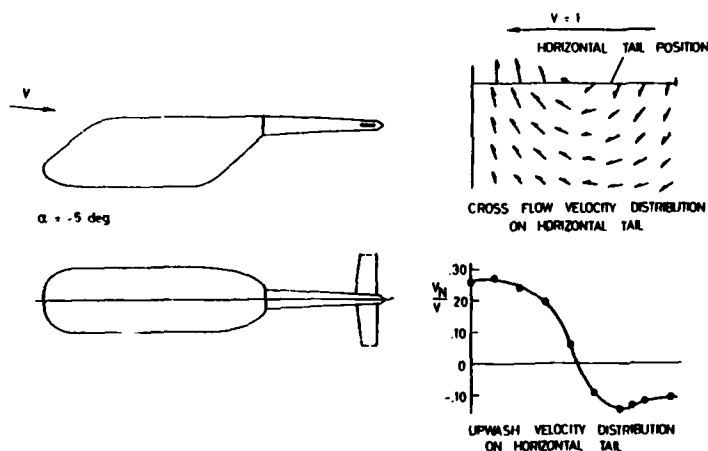
FIGURE 23 Fuselage induced Upwash in the Tail Area, WT-Measurements
(α = -5 degrees)

For the investigation of the main rotor hub wake, the pressure losses at the tail rotor and tailplane positions have been measured during BK 117 model wind tunnel tests, Reference 20. To reduce the adverse effect of the hub wake on the tail fin, the aircraft has been fitted with a hub cap. In Figure 24 the improvement of the dynamic pressure on the vertical tail due to the bent down hub wake produced by the hub cap can be clearly seen.
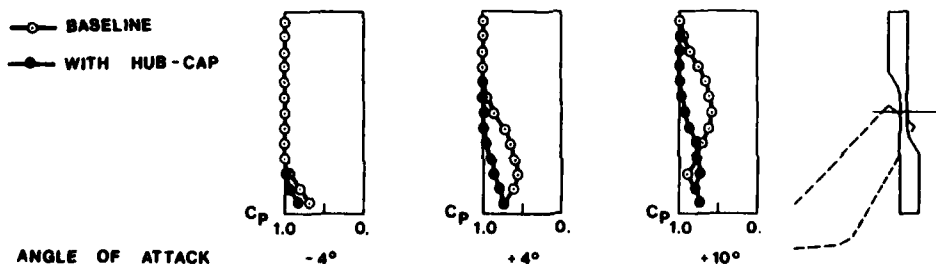
FIGURE 24 Total Pressure Distribution at Tail Area; Influence of Main
Rotor Hub (WT-Test Results)

AIRCRAFT AFT VIEW
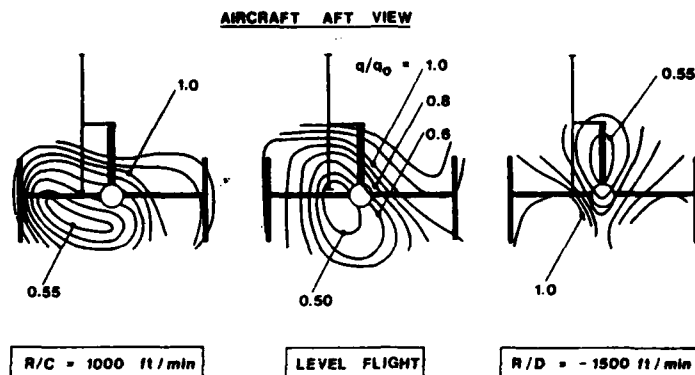
FIGURE 25   In-Flight Pressure Measurement at Tail Area, V = 80 kts

Inflight measurements of the flow situation at the empennage and tail rotor area were conducted on a BK 117 experimental aircraft, Reference 17. Fifteen pitot-tubes were fitted for dynamic pressure measurements, and flow angle indicators at 90 degrees to one another were installed to sense the vertical and lateral flow angles at both sides of the horizontal tail end-plates. Figure 25 shows dynamic pressure maps, for climbing, level flight and descending flight condition as interpolated from the test points. The curves indicate a large depression area, which obviously moves downward during climb rates, and moves upward during descent rates. These results are in agreement with the findings in References 15. The flow angle measurements further indicated, that a constant lateral flow angle of about 8 degrees, obviously resulting from the trim sideslip angle, and from the tail rotor induced lateral velocity component, occurs at the right endplate station.

UNSTEADY COMPONENTS

Interactional aerodynamics gets still more complex when taking into account the unsteady flow phenomena, usually contained in the wake structure. Fluctuating flow components can, in many cases,be more troublesome than steady flow distortions. At the downstream positions of the rotor and of the fuselage usually rotor-harmonic contents, resulting from the blade passage interaction,and also non-rotor harmonic components, resulting from turbulent wake, are experienced. Especially the fluctuating flow elements can be the source of severe structural loadings, and of excessive aircraft vibrations. The "tail-shake" phenomenon encountered by many helicopters in early flight test programs (References 14 to 17), is one of the well-known problems in this area.

Theory is not capable up to now to account for dynamic wake phenomena, and today's work is, therefore, mainly related to experimental investigations. Figure 26 shows results of the above mentioned inflight measurements. Time histories of vertical and lateral flow angles, and of the dynamic pressure at one horizontal tail station are shown. Very large dynamic amplitudes are evident in these traces, and it is also seen that flow conditions on both sides of the fin area differ significantly.
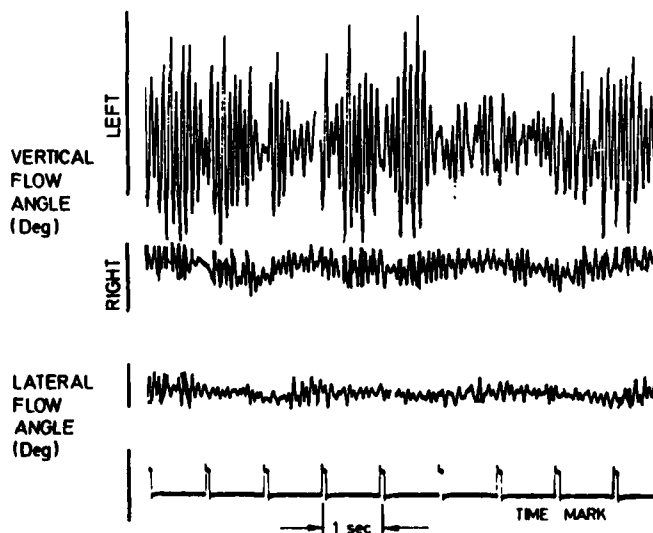
FIGURE 26   Time Traces of Flow Angle Measurements at Tail Area;
V = 100 kts, right sideslip condition

A frequency analysis, using the Fast Fourier Transform method, was used to obtain spectrographs of the flow parameters. Typical examples are presented in Figure 27, showing the frequency diagram of the vertical and lateral flow angles, and of the fluctuating pressure signal for two different flight speed conditions. A frequency range of zero to 70 Hz is covered. Both blade passage frequency components $(4\Omega, 8\Omega)$, and non-harmonic frequency contents are evident from these frequency diagrams. The influence of airspeed is clearly seen, indicating a substantial increase of the unsteady flow angle fluctuations with higher speed. Usually the range of exciting frequencies coincides with some natural frequencies of the tail boom and tail surfaces, so that strong amplifications in the resulting airframe oscillations can occur.
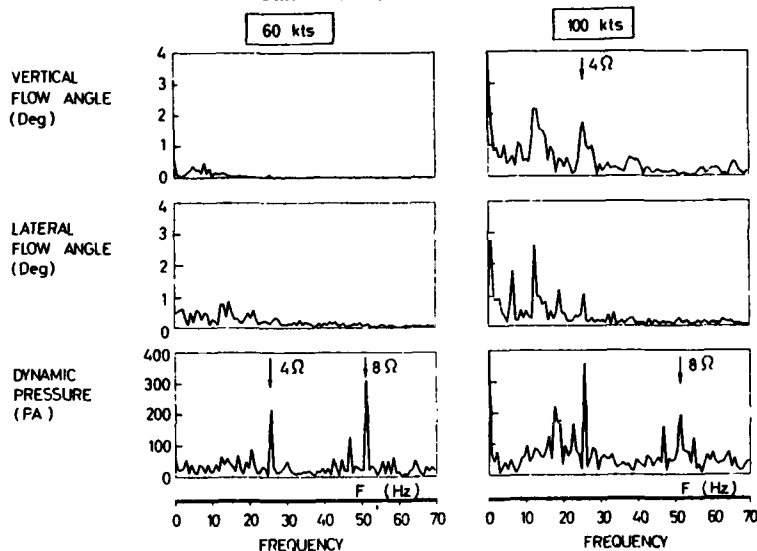
FIGURE 27 Frequency Spectra of Flow Angles and Dynamic Pressure for
60 and 100 kts Level Flight Speed

A summary of the prevailing frequencies of the flow angles and of the pressure signals both from wind-tunnel and flight testing is given in Figure 28. Natural frequencies of tail components and the lower rotor-harmonics are also indicated. The diagram shows a fairly conclusive picture about the wake quality with variation of airspeed. Correlation with Strouhal-Number relationship $(f = S \cdot v_\infty/d)$ roughly indicates the components characteristic dimensions responsible for the production of the wake.
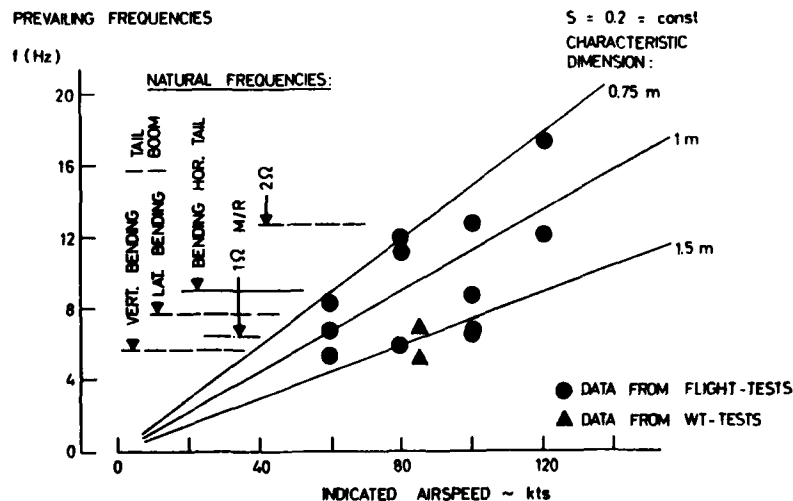
FIGURE 28 Prevailing Wake Frequency Content vs Air Speed

Flight tests have been undertaken to investigate various devices which could be of benefitial influence on the wake impingement. The diagrams shown on Figure 29 demonstrate the effect of a hub-cap installed on the main rotor hub, and the effect of removing a rear fuselage spoiler, initially installed for directional stability improvement. The diagrams show a comparison of the oscillating bending moments, which effectively proved to be a direct measure for the vibrations felt in the cabin. Both small configuration changes greatly improved the tail shake situation, both in level flight and, particularly, at descent rates (right diagram of Figure 29).
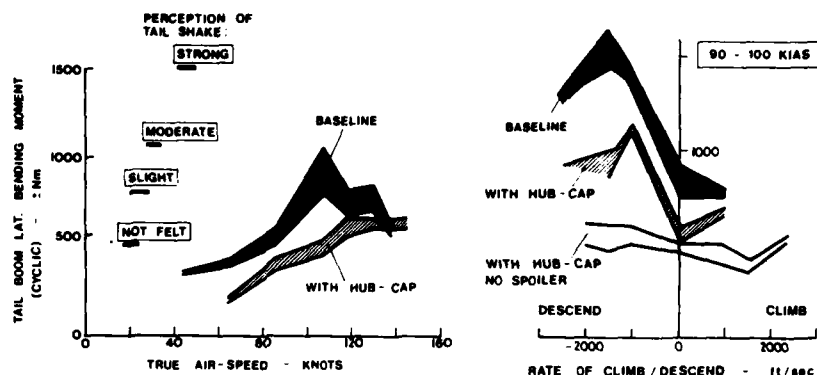
FIGURE 29   Effect of Airframe Configuration Changes on Tail Shake
during Horizontal Flight and Rates of Climb/Descent
(Measured Data)

5.   CONCLUSIONS

From the multifarious aerodynamic interactions of the helicopter three areas have
been investigated, and the following conclusions can be drawn:

- Blade-vortex interactional airloads are most severe in the flight conditions of low
  to moderate flight speed, particularly under medium rates of descent. Existing rotor
  wake models are capable of calculating the main features of vortex interactions, the
  higher harmonic airloads show good correlation in the harmonic decay with experimen-
  tal data.

- Interactions of the fuselage flowfield into the rotor disc plane are of substantial
  impact on the rotor flow conditions. Combination of analytical fuselage flow models,
  and rotor calculation models allows for determining the effects of fuselage flow
  interaction on local inflow conditions, and higher harmonic airloads of the rotor.
  It is shown that interference effects are generally reduced with an increase of
  the rotor-airframe clearance.

- Flow interactional effects between the rotor hub and fuselage parts, and the tail
  section are of great influence on aircraft behaviour. The steady pressure loss,
  resulting in a reduced effectiveness of the tail rotor and tail plane components
  can be simulated by existing analytical methods if the separation phenomena are
  included. Additionally, strong fluctuating components are observed in the wake flow
  which can result in severe airframe oscillations. Theories for calculating the un-
  steady flow phenomena are not available today, so that an understanding of the pheno-
  mena and problem solutions are mainly based on experimental work.

- Analytical results presented in this paper were mostly obtained from special purpose
  working models. As it seems, a combination of such models into a fully coupled model
  will certainly improve the reliability of the results, and will provide a usefull tool
  for practical design work.

6.   REFERENCES

1. Glauert, H.   On the Vertical Ascent of a Helicopter,
                             Aeronautical Research Council (Great Britain), R&M No. 1132, 1927

2. Goldstein, S.   On the Vortex Theory of Screw Propellers,
                             Royal Society Proceedings, Ser. A 123, 1929

3. Scully, M.P.   Approximate Solutions for Computing Helicopter Harmonic
                             Airloads, Massachusetts Institute of Technology, TR 123-2,
                             1965

4. Joglekar, M.   An Actuator-Disc Analysis of Helicopter Wake Geometry and
    Lowey, R.   the Corresponding Blade Response,
                             USAAVLABS Technical Report 69-66, 1970

5. Landgrebe, A.J.   An Analytical and Experimental Investigation of Helicopter
                             Rotor Hover Performance and Wake Geometry Characteristics,
                             USAAMRDL Technical Report 71-24, 1971

6. Sadler, S.G.   Development and Application of a Method for Predicting Rotor
                             Free Wake Positions and Resulting Rotor Blade Air Loads,
                             NASA CR-1911, 1971

7. Stricker, R.   Rotor Prediction with Different Downwash Models,
    Gradl, W.   4th European Rotorcraft and Powered Lift Aircraft Forum,
                         1978

8. Sheridan, P.F.   Interactional Aerodynamics - A New Challenge to Helicopter
    Smith, R.P.   Technology,
                         35th Annual Forum of the AHS, 1979

9. Daughaday, H.   An Approach to the Determination of Higher Harmonic Rotor
    Kline, J.   Blade Stresses,
                         9th AHS Forum Proceedings, 1953

10. Huber, H.   Ermittlung von höherharmonischen Erregerkräften und Blatt-
                         biegemomenten am BO 105-Rotor,
                         MBB TN D126-7/72, 1972

11. Landgrebe, A.J.   Aerodynamic Technology for Advanced Rotorcraft,
    Moffit R.C.   AHS-Symposium, Essington, Pensylvania, 1976

12. Wilby, P.G.   An Investigation of the Influence of Fuselage Flow Field on
    Young, C.   Rotor Loads, and the Effects of Vehicle Configuration,
    Grant, J.   4th European Rotorcraft and Powered Lift Aircraft Forum, 1978

13. Schultz, K.J.   Fluctuating Surface Pressure Characteristics on a Helicopter
    Splettstoesser, W.R. Fuselage under Hover and Forward Flight Condition,
                         4th European Rotorcraft and Powered Lift Aircraft Forum,
                         1978

14. Fradenburgh, E.A.   Aerodynamic Design of the Sikorsky S-76 SPIRIT Helicopter,
                         34th Annual Forum of the AHS, 1978

15. Roesch, P.   Aerodynamic Design of the Aerospatiale SA-365 N Dauphin 2
                         Helicopter,
                         6th European Rotorcraft and Powered Lift Aircraft Forum,
                         1980

16. Roesch, P.   New Designs for Improved Aerodynamic Stability on Recent
    Vuillet, A.   Aerospatiale Helicopters,
                         37th Annual Forum of the AHS, 1981

17. Huber, H.   Flight Characteristics Design and Developement of the MBB/
    Masue, T.   KHI BK 117 Helicopter,
                         7th European Rotorcraft and Powered Lift Aircraft Forum,
                         1981

18. Clark, D.R.   An Analysis of Airframe/Rotor Interference in Forward
                         Flight,
                         7th European Rotorcraft and Powered Lift Aircraft Forum,
                         1981

19. Polz, G.   Separated Flow Around Helicopter Bodies,
    Quertin, J.   7th European Rotorcraft and Powered Lift Aircraft Forum,
                         1981

20. Nakano, M.   Wind Tunnel Test Result of the BK 117 Airframe,
    Ikebe, Y.   Kawasaki Heavy Industries Ltd., Report KKA-78-088, 1978

ROTOR-FUSELAGE INTERFERENCE ON ENGINE INTERNAL AERODYNAMICS IN MANEUVERING HIGH-SPEED ROTORCRAFT

by

Dino Dini
Istituto di Macchine, Università di Pisa
56100 Pisa, Italy

SUMMARY

Unsteady loads resulting from rotor blade vortex interactions and aerodynamic interference effects with the fuselage in high flight speed rotorcraft are here considered from the point of view of the influence on engine internal aerodynamics. Moreover, inertial forces and gyroscopic moments during rotorcraft maneuvers, inducing cyclic bending of the rotating disks, blades and shafts of the engines, are investigated.

Engine damages or failures due to certain combinations of frequencies, very close to aerodynamics resonance, cause rotorcraft accidents. In such cases, inputs are given by interference of aerodynamics loads. This specific area requiring further effort is identified by the present paper.

Integration of transient aerodynamic phenomena makes possible engine malfunctioning or flame out. Ways for the solution, at the design stage, of such critical interferences are here suggested.

The propulsion system is shown to be responsible to fail because of its original deficiency in satisfying instantly excessive loading factors imposed on the cyclically variable rotor torque during the pilot transitional inputs from a flight segment to another. Moreover, it is shown as limitations have to be imposed up on the operations of rotorcraft as a result of the high aeroelastic vibration levels encountered in flight, and transmitted to the driving engines.

INTRODUCTION

When the helicopter is in flight, the rotors, engine and drive shafts, cause vibrations which are transmitted to the structure. Each component has its own natural vibration, one of which is affected by its mass, flexibility or rigidity, its shape, dimensions and material used.

For the whole aircraft this results in complex vibrations which can sum up or subtract. When the natural frequency matches that of vibrations originating from the main rotor, at each blade rotation these vibrations receive an other reflected pulse. The vibration amplitude increases very rapidly. These divergent vibrations and the resulting oscillations can cause significant transient loadings of the engine structure itself and may introduce alternating stresses and fatigue effects on the engine components, through the main gear box suspension unit and the main rotor head, figures 1 and 2.

Because of the rotor-fuselage integration, aeroelastic instabilities have to be predicted for a reliable engine control design. Fatigue limits imposed on helicopter engines are more severe than in other automotive application, because of the vibration level induced in the engine core. Periodic aerodynamic and inertial blade loadings may have serious consequences with respect to the shafts and the discs to which these blades are attached. Flutter, with either random or uniform phasing between adjacent blades, may exert oscillatory root reactions that integrate for the entire disc and excite a shaft resonance. Unsteady loads resulting from rotor blades vortex interactions and aerodynamic interference effects with the fuselage in high flight speed rotorcraft are here considered from the point of view of the influence on engine internal aerodynamics.

THE MECHANISM LIMITING HIGH-g MANEUVERS

Adverse flight characteristics are encountered in certain high normal load factor maneuvers, such as transient engine torque pressure (changes during high roll rate maneuvers). Cyclic control force feedback at high load factors has to warn the pilot that the maneuver should be limited in severity.

Avoidable maneuver limitations include such problems as inadequate altitude margins to recover from high-g turns at low airspeeds, figure 3.

The boundaries of the flight envelope are not defined by structural limitations, as other limits are encountered first. Among these are the aerodynamic limit of the rotor.

In maneuvers, with mean normal load factors in excess of 1.3 g, like banked turns at constant or varying airspeed and altitude, as well as rolling or symmetric pullups, variables have to be chosen to describe the aircraft trajectory and to indicate the loading, power and vibration levels.

Helicopter maneuverability can be studied from the point of view of simulation on a computer. A series of fixed-collective symmetric pullups have to be simulated to determine the thrust levels at which certain maneuver limiting phenomena occur. The pullups may be simulated at different advance ratios, with different maximum mean normal load factors achieved varying the rate at which the longitudinal cyclic stick position is changed.

Operationl fixed-collective maneuvers are entered by diving from level flight cruise at a certain power setting. The simulation of symmetric pullups determines: the value of C_T/σ at which the onset of re-

treating blade stall occurs as a function of advance ratio, the thrust levels at which the maximum contin-
uous engine horsepower and steady transmission torque rating in exceeded. The flapping stop and cyclic
force feedback limits are found. Finally, a control system fatigue limit (based on the oscillatory pitch
link axial force) and the absolute aerodynamic limit are determined. An increase in required horsepower
and oscillatory pitch link axial force also occurs at the onset of retreating blade stall, but at slightly
different values of C_T/σ.

The maximum lift capability of the rotor establishes the absolute aerodynamic limit. This limit is deter-
mined by increasing the severity of the maneuver until no further gain in maximum mean normal load is
achieved.

The designer needs to understand the phenomena occurring during high-g maneuvers so that ways may be
found to improve maneuverability.
The maximum normal load factor achievable in a symmetric pullup can be influenced by the way the maneuver
is terminated. If the pullup ends with a pushover, the pilot will start recovery early. This avoids low-g
hover, with its loss of control effectiveness. Higher normal load factors can be attained in the pullup
it is ended by a right roll similar to a wing-over maneuver.
High cockpit vibration levels are an indication of stall. A strong correlation between oscillatory normal
load factor and chordwise bending moments are a good indication of stall. But, rotor stall is not the only
cause of high cockpit vibration. Vertical vibration and blade bending moments show high frequency compo-
nents which are associated with the rotor intersecting its own wake. The occurrence of wake crossing, fig-
ure 4, is dependent on the airspeed and fuselage and rotor angular rates and is not entirely repeatable.
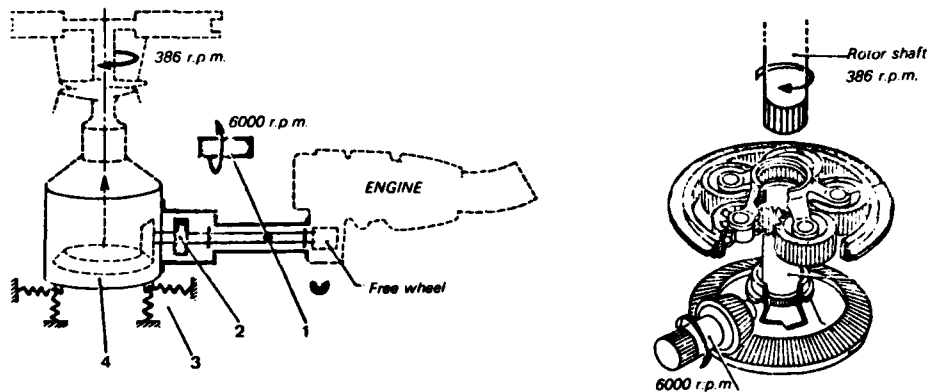
Fig. 1 - Power transmission to main rotor.

This aerodynamic effect cannot be modified, but a vibration isolation system can postpone the onset of cock-
pit vibration to higher normal load factors.

Transient engine torque pressure surges as large as 90 kPa may be encountered during maneuvers initi-
ated at high power settings. The engine torque pressure will tend to increase whenever: the rotor pitch
rate is negative, the rotor roll rate is negative, or the cyclic stick moves forward.
Engine torque pressure surge and the absolute aerodynamic limit are the only phenomena which limit the max-
imum normal load factor. Control force feedback has been designed into the aircraft to force the pilot to
limit maneuvers to load levels that will not decrease the useful life of the vehicle. Cockpit vibration
has been found to restrict some maneuvers.

However, the load factor capability is most important in maneuverability. The limits are: engine power
in a steady turn, and rotor stall in a deceleration turn. For future helicopters, g levels over 3, up to
high speeds, will be required.
While the relationship between maneuverability and the functional mechanism is well understood, frequent
and abrupt changes in speed place severe stresses on the engines, gears, and all dynamic parts, which are
reflected in special engine requirements.
From positive acceleration, as large as + 2 g, during pull up in a terrain avoidance compound maneuver,
the three dimensional mission is going on through negative acceleration (sometimes in between - 1 g and
- 0.5 g in the push-over/rolling maneuver, figure 5.

Military helicopters require a maneuver capability beyond a hover out-of-ground-effect condition:
a power/maneuver margin equivalent to a vertical rate of climb of 150 meters per minute. But, higher tur-
ulence levels are encountered with vertical component of 300 mpm, as in advanced attack helicopters.
The rapid change of load factor, roll and pitch angles, rolling and pitching speeds, Ref. 1, up to their
extremes, will result in high loads. Nearly half of all accidents can be attributed to factors related to
inadequate performance or control capability.

Peak engine power is required to make rapid changes in flight path and altitude under the precise

control of the pilot, as in hovering, acceleration and deceleration, and target acquisition.

Fig. 2 - Main rotor.
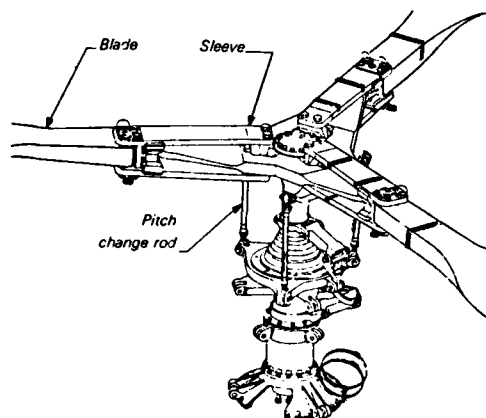
Fig. 3 - Helicopter terrain avoidance maneuver.

A typical turn maneuver is described on figure 6.

The propulsion systems is often responsible to fail because of its original deficiency in satisfying instantly excessive loading factors imposed on the cyclically variable rotor torque during the pilot transitional inputs from a flight segment to another. The computerized fuel control is effectively inadequate to establish continuous equilibrium between shaft drag torque and delivered engine torque, in that resulting excessive rpm inertial dissipation.

Moreover, limitations are imposed up as a result of the high aeroelastic vibration levels encountered in flight, and transmitted to the driving engines. The associated periodic loads on the engine rotating parts, particularly during the so called transition flight regime between hovering and forward flight and during high-speed flight, are contributing substantially to material fatigue and consequently high rate of replacement and maintenance of component parts. Extreme flight conditions are right and left turns, rolling pull-outs, longitudinal reversal, cyclic and collective pull-ups, slope landings and starts.

Fig. 4 - Intersection of following blade with tip vortex trailing from a leading blade for μ = 0.3.

Fig. 5 - Typical terrain avoidance compound maneuver.
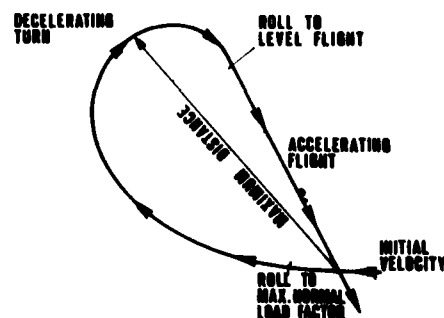
Fig. 6 - Typical tur maneuver.

ENGINE RESPONSE DURING MANEUVERS

In maneuvering flight, where sharp turn and abrupt pull-ups may be required, severe blade stall can be encountered, because of rotor rpm decay or high load factors. Reduction of collective pitch and/or increasing rotor and engine speed will help.

Engine output shaft rpm cannot generally vary more than 10%, and gas turbine engine operation may become critical at the minimum rpm values, with a consequential loss of rotor thrust.

Surge still exists in engines that have been abused. Repeated surging and the accompanying transient torsional loads from the engine can cause damage to the airframe components.

The interstage bleed system, automatically relieving the compressor of a small amount of air during the period of the engine acceleration cycle, may encounter higher loss of power than usually. The entire sequence operation could not be controlled by the fuel control sensing gas producer speed, fuel flow and pilot demand, therefore not ensuring proper opening and closing of the interstage air-bleed. The fuel control is a hydro-mechanical device, with fuel regulator and power turbine governor. The acceleration and deceleration fuel flow control may be in excess of the engine's ability to immediately produce the desired power. The amount of fuel added to the air in the combustor may be not exact at all times to get a good performances, Ref. 4.

As a result, the engine should be brought through transitory condition as rapidly as possible, keeping the rotorcraft out of dangerous mixtures. Boost pumps, check, metering, dump, pressurizing, and shutoff valves, and pressure regulators, of the automatic fuel flow system, are a very complex matter, susceptible of possible malfunctioning failure during rapidly changing operation. The emergency fuel system must be operated with some care to avoid engine damage. The transient air-bleed control on the compressor rotor of the gas producer turbines is not able to operate correctly during power turbine rotor acceleration. Unsteady airloads on the helicopter main rotor might be so high to stop at all the combustion process.

At high speeds, the load factors in maneuvers with sharp edged gust impact are relatively high, and the effect on the engines become critical. Significant transient loading of compressor structure would usually be associated with a gross change in the throughflow, that is either truly aperiodic. The problem of sudden changes in througflow is closely related to the aeroelastic problem of a single airfoil passing through a sharp-edge gust front in the atmosphere, such as might be produced by a remotely originated blast wave, Ref. 3.

If the compressor is operating in a cyclic surging or stalling condition, the required number of cycles for fatigue and consequent failure could be accumulated in a short period of time. Low cycle fatigue might so be encountered in compressor rotor blades, nowadays subjected to exceedingly high centrifugal stresses.

Distorted flow into a helicopter gas turbine, as a consequence of turbulence in maneuvers, can trigger engine instabilities. Among the propulsion system margins are buzz or inlet unstart, compressor stall, turbine inlet temperature, and mixture ratio limits to maintain combustor flame stability, Ref. 3.

Indirect effects of severe inlet distortion are also producing potentially harmful aerodynamic environments for blading at operating conditions. Examples of such indirect effects are the ones arising from the thick annulus boundary layer and the degradation of flow quality. The first one may stall the compressor rotor blade tips and give rise to a rotating stall pattern of limited radial extent, giving rise to periodically reversing throughflow and surge (in the case of massflow reversal); the sudden forward travelling of the compressor discharge pressure, coexisting with the flow reversal, implies a pressure wave, the so-called hammershock, going through the compressor into the inlet. The second one may induce usually high turbulence levels and thick wakes on the stator and rotor airfoils, producing negative incidence in some stages of the axial compressor.

The degradation of flow in an axial turbomachine may lead to the onset of self excited blade vibration (stall flutter) or self-excited fluid oscillation (stall propagation).

High-performance gas turbine engines are sensitive to not only self-induced cyclically changing loads but also to extremely induced loads which result from helicopter maneuvers. The engine is expected to operate in a very hostile environment, being exposed to extremes of temperatures, pressure, vibration, and mechanical forces within the engine. In addition, the engine is exposed to a variety of accelerations in all directions, thus imposing large inertial and gyroscopic forces on an already complex loading environment. The engine is expected to function under all conditions with small clearances between rapidly moving and stationary parts and to exibit little degradation in performance after long period of operation.

An engine stall is expecially bad in a helicopter because of the rapid load reversal which occur in the rotor drive system. A stall is indicated by a sudden drop in compressor discharge pressure accompanied by an increase in exhaust gas temperature.

The complex combination of external and internal operating forces and maneuver forces presents a big obstacle to determining the distortions occurring in the engine during helicopter flight. Because of rotor movement, case bending and ovalization, rotor shaft and blade bending, blade extensions, and thermal stresses, it is difficult to predict the relative movement of engine components under all flight maneuvers. Abnormal vibrations in an engine installation may be caused by malfunctioning engine-mounted airframe accessories, engine mounts and other external connections, as well as by impulsive flow phenomena caused by blade-vortex interaction on the advancing side of the rotor disk. External airloads may be so highly unsteady to produce engine instabilities, going from the accompanying the distinctive "blade slap" acoustic signature of some helicopter rotors to those determining engine fatigue, failures and stop.

DESIGN CRITERIA FOR ENGINE/AIRFRAME COMPATIBILITY

The structural characteristics, the inertial characteristics, and the aeroelastic behaviour of the rotary wing are involving the compatibility of the major multidegree-of-freedom systems: rotor, control, airframe, drive train, and powerplant, Ref. 2.

Power transmission to main rotor, figure 7, for the Aerospatiale AS 350 and figure 8 for the Agusta A 129, is under conditions that the drive shaft transfers only engine torque to the main gear box, while other loads are picked up by the housing and barrel junction assembly. The main rotor head absorbs the forces induced by the rotation (centrifugal force, flapping and /lag loads).

1) Fixed ring gear
2) Planet gear
3) Planet gear spherical bearing
4) Thrust washer
5) Sun gear
6) Oil jets
7) Power input casing
8) Bevel pinion
9) Taper roller thrust bearing
10) Cylindrical roller bearing
11) Oil level sight gauge
12) Magnetic drain plug
13) Oil pump
14) Taper roller bearing
15) Lower casing
16) Oil relief valve
17) Main casing, ribbed, double wall
18) Bevel ring gear
19) Vertical shaft
20) Oil pump drive gear
21) Taper roller bearing
22) Oil fuller plug
23) Oil jet

Fig. 7 - AS 350 - power transmission to the main rotor.
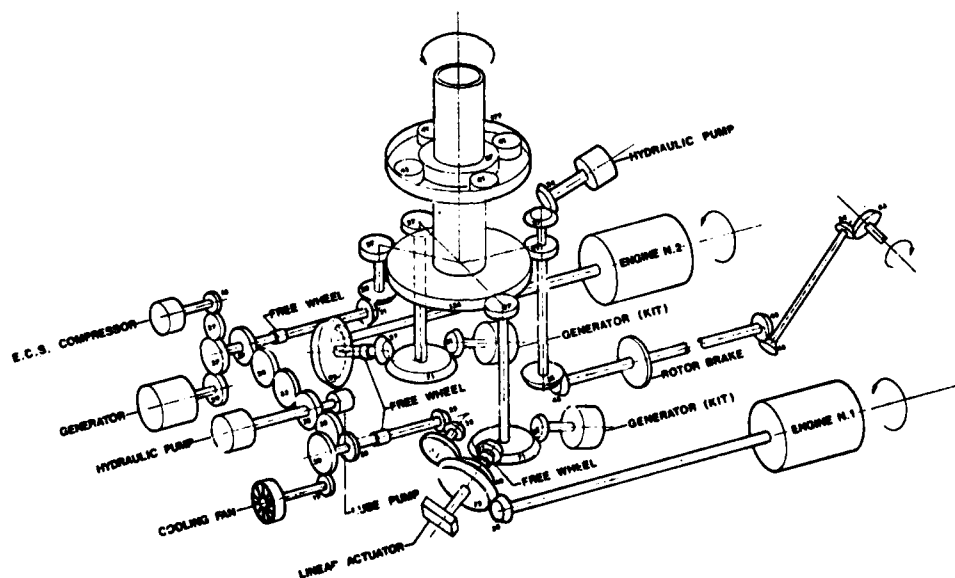
Fig. 8 - A 129 - drive system schematic.

Helicopter engine/drive system torsional instability can be prevented if care is taken for accurately represent both engine and rotor in the torsional analysis. Particular attention should be paid to proper lag damper representation, including hydraulic compressibility effects.

When considering a helicopter under the aspect of dynamics, it consists of a complex system of anelastic fuselage and the rotating rotor. They represent an oscillating system which can be subjected to self-excited oscillations under certain circumstances. They can occur either on ground or in the air and are called the classical ground and air resonance.
Up to the present time, the frequency difference between rotor blade motions and fuselage oscillations has been sufficiently great to allow then to be considered separately. But, recent studies have indicated that, because of the increased coupling between blades and fuselage as a result of increased hinge stiffness, this is no longer the case.

It is therefore evident that it is not always possible to establish cause and effect relationships for the prediction of engine/drive/ariframe compatibility. However, through a combination of analysis and testing, proper compatibility is usually achieved. Analysis and rotor/drive/engine system integration testing is required to establish optimum operation procedures, expecially in maneuvering. Airframe panel excitation due to fluctuating aerodynamic pressures at rotor sequencies should be evaluated with a finite-element model of the entire airframe structure in order to establish the resonant frequencies and the forced-response stresses. Helicopter engine/drive system torsional instability can be prevented if care is taken to accurately represent both engine and rotor/systems in the torsional analysis. Particular attention should be paid to proper lag damper representation, including hydraulic compressibility effects.
Self-excited vibrations of transmission-mounted components can be minimized by using finite-element analytical methods in the design stage and by test verification of the initially received hardware. Analsys and testing should not be limited to rotor, but should include gear tooth mesh frequency excitation as well.

Structural analysis, based upon finite element model calculations, is employed for stress and vibration evaluations of structural components. It essentially consists in substituting the actual structure with an equivalent assembly set up in a series of simple solid and elastic elements for vibration analsys. The method of structural analysis, applied to complex configuration mechanical pieces, permits to obtain an excellent approximation of the real strain and stress distribution. Applied to a structure, it permits, through the solution of dynamic equations, the establishment of matural modes and frequency of the fuselage and the rotor coupling.
Methods of analysis of helicopter blade flutter for both hinged and hingeless blades are formulated.
The instability associated with the stall flutter is due to the adverse time phasing of the aerodynamic torsional moment resulting from the loss of blade bound vorticity during torsional motion at high angle of attack. The complex nature of the phenomena precludes an analytical representation of the unsteady airloads at the present time, but the prediction of regions of instability is made possible by the application of experimental data. The high pitch-link loads which occur in stall flutter may be a serious obstacle to increased flight speeds. The most profitable way of reducing these loads is to use aerfoil sections, which have high dynamic-stall angles, so that they can operate in the retreating blade region below the stall angle as much as possible.

Vibration in helicopters may lead to excessive levels of fatigue. It is common practice to design, as far as it is possible, the fuselage such that the natural frequencies of the major normal modes are well separated from the rotor forcing frequency. The analysis may be applied to the problem od determining which part of the fuselage structure of a particular helicopter is most effective in reducing the roto induced vibrational response in the region of the pilot's seat. The vibration levels are kept to a minimum by introducing vibration absorbers and also modification of the fuselage structure, or by designing the gearbox and engine mountings so that the transmission of oscillatory forces is suppressed.

Accurate finite-element method analyses and/or shake testing of all engine installations, whether hard-mounted, detuned, or isolated, are required to determine potential vibration and stress problem areas. It is desirable to formulate engine/airframe manufacturer interface agreement during the early design stages in order to obtain a timely resolution of the potential interface dynamic problems.

The realistic rotary-wing aeroelastic problem is obviously the interblade mechanical coupling, or the coupling between rotor and the fuselage, or the coupling between the rotor/fuselage and the control system.
Prediction methods for estimating total aircraft dynamic stability and response characteristics have been developed by starting with a minimum number of degrees of freedom to describe the system.
Airloads in forward flight or in maneuver are considered as result of an empirically modified uniform inflow which is dependent from the rotor ratio and shaft movement and from the unsteady blade aerodynamics due to angle of attack cyclically variable, flight Mach number and blade shape.
The analysis becomes the simulation of a complete rotorcraft which involves a detailed dynamic description of the rotor and control system, as well as conventional six degrees of freedom body dynamic description which operates both in a prescribed flight condition and in transient loads imposed by pilot inputs.
In the first case, the aircraft is constrained to uniform flight, while the controls are engaged to obtain a force and moment equilibrium of the vehicle at that static condition, operating directly on main collective and cyclic pitch, tail rotor and aircraft attitude. In the second case, rotor, control and airframe, are free to respond dynamically to external inputs.
The rotorcraft may be simulated dynamically in thirty coupled degrees of freedom: six for the body, four

for the hub (pitch, roll, height displacement for deformation, and rotational speed), four for the combination of the control gyro/swash-plate. Motion of each of the four main rotor blades are simulated by two flap-wise and one inplane modes and a pitch horn bending degree of freedom which couples blade feathering to the control gyro. In addition to these thirty degrees of freedom, it may be considered a first torsion mode for each blade. Since the frequency of this mode is usually over 4 Ω, quite higher in comparison to the other dynamic mode of interest, a dynamic representation of this mode increases the computation complexity. This mode is included as a massless elastic response to blade torsion moments with a first order lag.

The model with thirty degrees of freedom may be written in matrix form, and can handle hover, forward flight, and maneuver flight conditions, Ref. 2.

Efficient design practice for rorocraft, which includes appropriate vibration analysis, requires: an estimation of rotor loads on the fuselage structure based on fully aeroelastic analysis; an adequate knowledge of the structural characteristics to determine coupled natural frequencies and mode shapes; an evaluation of inflight vibration and fuselage response.

This work takes a very high, long and expensive, work, for instance at the IBM 370/168-type, computer time. In such a way, the hub supporting structure can be properly designed to minimize the transfer of high periodic forces and moments, into the basic rotorcraft structures, imposed particularly during the so-called transition flight regime between hovering and forward flight and high-speed flight.

Inclusion of the lay damper mathematical model (with hydraulic spring effect) into the torsional stability computer simulation of the rotor/engine control accurately reproduce the torque oscillation with the original fuel controls. Frequency of oscillation, phasing, and magnitude of damper force, shaft torque oscillation, and fuel flow fluctuations, are simulated accurately.

EFFECTS ON THE ENGINE OF ROTOR/FUSELAGE TRANSIENT AERODYNAMICS

Unsteady loads resulting from rotor blade vortex interactions and aerodynamic interference effects with the fuselage in high speed rotorcraft are influencing the engine internal aerodynamics. As a limit, if the engine is overloaded, the maximum power will drop with decreasing rpm. Since overload conditions are accompanied by speed decreases, a sufficient margin to the "surge line" has to be maintained and the engine output will be automatically limited. In this operating range, free power turbine engines, figure 9, are less critical than single shaft engines. In a free-turbine engine, however, changes in engine performance because of load changes will also require changes of the gas generator rpm. Due to the inertia of the gas generator rotor, these changes in power will require a longer period as compared to a single-shaft engine, in which only the relatively quick-acting fuel valve is to be adjusted and no rotor masses must be accelerated. This difference will result in larger rpm variations under changing loads in a free-turbine engine as compared to a single-shaft engine.
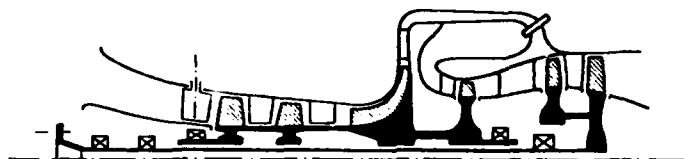
Fig. 9 - Engine concept improvement.

In the case of moderate helicopter advance ratio (forward speed/blade tip speed = $V\cos\alpha/\Omega R$) and of local incidences lower than that of profile stall, the azimuthal evolution of the blade local loads are presented on figure 10 for different blade sections (at radius r in respect to tip radius R). The maximum level flight speed is limited by power availability, stall, compressibility, and aeroelastic stability effects.

Accuracy in calculations of engine-rotor performance in calculations of engine-rotor performance is required because the engine could be not able to support instabilities due to unsteady airloads on the helicopter rotor.

With the development of helicopters capable of higher flight speeds, the problem of blade stall flutter has become one of major importance for the engine operation. Classical flutter involves coupling between two, or more, natural modes of vibration. In stall flutter, the flutter frequency tends to become equal to the natural torsional frequency. This implies that in this case the torsional motion predominates.

Large high-frequency oscillations in torsional moment (TM), lift and aerodynamic moment coefficients, on the retreating side, were detected in flight-test data taken from a rotor blade during a maneuver, as shown in the plot of figure 11. This response was the result of dynamic stall induced by previously formed tip vortices, which, under that particular maneuver flight conditions, pass under the blade at the azimuth positions indicated in figure 11. High vibration levels are established by aerodynamic loading, and aeroelasticity of the rotor blades, and resonance of the structure. Increased periodic forces are occurring when the rotor thrust is increased, during transition from hovering to forward flight, and at

higher tip-speed ratios. The harmonics above the fourth are generally below 20 percent of the principal harmonic force. In turn, the magnitude of the harmonic forces other than the n-th one for n-blade rotor is generally below 50 percent of the principal n-th harmonic.
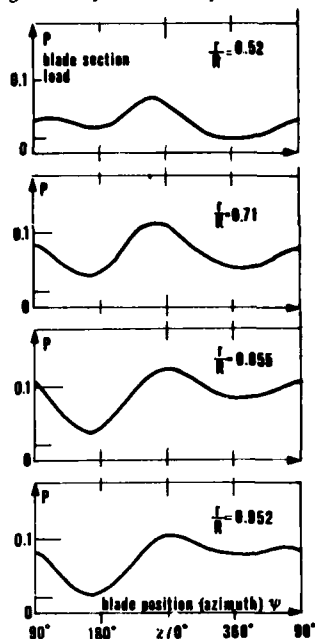
Fig. 10 - Blade local load for a rigid three blade rotor.

Fig. 11 - Measured time history of section loading and moment coefficient and blade torsional response.

The analysis of blade torque moments indicates the magnitude of the harmonic components to be about 4 ÷ 5 percent, respectively, of the steady components of the moments.

But, still now, rotorcraft are operated at reduced speeds, as much as 20% below the forward velocity that they might otherwise achieve, because of vibratory environments. However, the understanding of the sources of vibration is more and more required for reaching forward speed as high as 370 km/h.

Adimensional amplitude $\Delta Q/Q$ and angular velocity Ω/Ω_{av} cyclic variations of the rotor torque may be, near the maximum acceptable flight speed, respectively, of the order of 0.1 and 0.05, as compared with the measured value of $\Delta C_\ell/C_\ell{}_{av}$, $\Delta C_T/C_T{}_{av}$ and $\Delta C_m/C_m{}_{av}$ (respectively related to the lift, thrust and moment coefficients), as in figures 10 and 11.

The flow disturbances due to the fuselage affect the loads and motion experienced by the rotor. Hub forces and moments are important from the vibration point of view, and figure 12 gives the predicted azimuthal variation of pitching moment, axial force and in-plane force for rotor alone and with fuselage effects. The amplitude of the fore and aft in-plane force is doubled by the presence of the fuselage, whereas the pitching moment and axial force amplitudes are slightly decreased. Calculations indicate that fuselage upwash can provide a perturbation to aerodynamic forces which leads to a significant blade and hub response in a form depending upon the stiffnesses of the rotor blades, even when blade stall is not precipitated. In transition flight regimes and extreme flight maneuvers, as in the acceleration maneuver time history on figure 13, the rotor drag torque Q is varying abruptly during each revolution, because of: sudden airloads overimposed to the cyclic pitch control of the rotor thrust; vibration and blade flexibility effects, overimposed to stall flutter and flap-lag-torsional blade aeroelasticity; effects on the engine of the strongly aeroelastic system corresponding to the rotor-fuselage integration.

Such cyclically variable main rotor drag and induced torque Q is reduced in amplitude and disuniformity to the shaft ot the free (power) turbine. The speed reduction ratio between engine and main rotor is ranging, for the present rotorcraft, from 70 to 80 : 1 and will be increased in the foreseable future. About in the same ratio, the main rotor torque and frequency disuniformities are reduced to the gas turbine engine shaft. Fortunately, the rotor unsteadiness during a single revolution is spread in 70 ÷ 80 engine shaft revolutions!

The damping action of the transmission layout, from the main and tail rotors to the gas turbine engine, is necessary for a reliable continuous power availability. From the other hand, the lifed items in a rotorcraft transmission system, for example as complex as in figure 8, must be replaced, due to possible fatigue damage after expiry of a fixed flying time, typically a few thousands hours.

The reduction of gas turbine powerplant weight, in comparison to previous reciprocating engines, has made possible to install enough power for good performance. Unfortunately, the same kind of revolution has not taken place in the power transmission, where some components are operating at very high angular velocity and acceleration. Since both gas turbine and helicopter rotors operate at a tip speed based on Mach number, the rotational speed of the engines will increase with advanced technology engines, where the turbine inlet temperatures will increase appreciably. The speed reduction ratio will also increase.

The gas turbine engines that have been designed for present helicopter use, such as the General Electric T-58 on the Agusta Bell 204AS, the Lycoming T-53 and the Allison T-63, were required to have an integral gear-box to reduce the output speeds to approximately 6 500 rpm, because it was believed this was as high a speed as could be conveniently handled by rotorcraft.

Inertia loadings of gears, shaft and bearings, of the transmission system may be serious consequences with respect to the attached gas turbine engine. A rich variety of vibration phenomena gives rise to distorted throughflow in the engine. Mechanical and aeromechanical excitations exert, in such a way, dangerous oscillatory root reactions on the blades, Ref. 5.

With rotor torque Q reduced about 70 ÷ 80 times to the free (power) turbine shaft, its periodic disuniformity, created by moderate speed forward flight at limited vibrational and aeroelastic effects, is practically absorbed through the engine gear box (between power shaft and drive shaft) and the planetary gear unit (between drive shaft and rotor shaft), with passive heat production, Ref. 6.

But, when the forward speed is so high to start blade stall vibration and large amplitude aeroelastic effects, the engine is quite largely influenced and cannot compensate the required power fluctuations through the automatic fuel control action. We may expect in this case considerable compressor-turbine and free (power) turbine vibration and engine flow distortion. In absence of a self acting automatic control, to avoid high flight speeds and too abrupt maneuvers, or in the case of pilot error, engine failures and/or flame-outs could be involved.
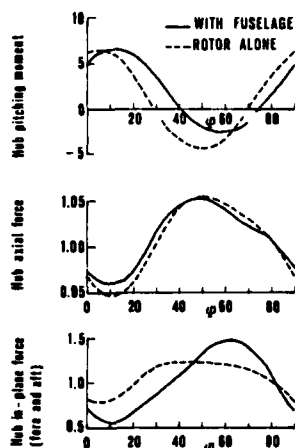
Fig. 12 - Predict hub moment and forces with and without fuselage flow effects, as a multiple of mean value for rotor alone.
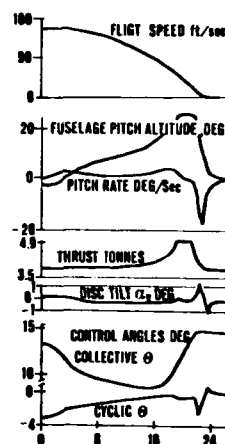
Fig. 13 - A deceleration maneuver time history.

With Q_e and ω_e corresponding to instantaneous values of the power turbine shaft torque and the shaft angular velocity, and η and Ω, respectively, to the mechanical efficiency due to power dissipation through the reduction gears, and to the main rotor angular velocity, the corresponding engine torque (considering the average torque Q_{av} for such flight condition)

$$Q_e = Q \cdot \Omega/\omega_e \cdot \eta = (Q_{av} \pm \Delta Q)\Omega/\omega_e \cdot \eta \qquad (1)$$

is cyclically variable, depending upon the rotor torque and the changing mechanical behavior (expressed by the value of η).

At constant forward flight speed, the control fuel setting is such to deliver, with a fuel flow G, (N/s), at net heat value K , (J/N), a fuel power GK, (W), corresponding to the following mechanical balance

$$G \cdot K = (Q_{av} \cdot \Omega_{av} + Q_c \cdot \omega_{ec})/\eta_t \cdot \eta_m \cdot \eta \qquad (2)$$

where Q_c , ω_{ec} η_t and η_m , are torque and angular velocity of the compressor turbine, and thermal and mechanical efficiencies.

Now, the periodically variable power turbine rotational acceleration $d\omega_e/dt$ is depending upon the inability of the fuel control system to vary instantaneously the delivered power, and it may be expressed

$$\pm d\omega_e/dt = \Delta Q \cdot \Omega/\omega_e \cdot (J_e + J_1 + J_2 + J_3 + J_r) \qquad (3)$$

where: J_e is the power turbine rotor system moment of inertia, and J_1, J_2, J_3, J_r, are the moments of inertia reduced (through the square rotation speed ratios $(\Omega/\omega_e)^2$) to the power turbine shaft, respectively, of engine box gear, drive shaft, planetary unit gear, and rotorcraft main rotor. (In a complete drive system, it has to be taken into account the tail rotor torque disuniformity and the reduced moment of inertia of the relative drive components).

The rotational acceleration is cyclically variable according the expression of ΔQ and Ω. Practically, such acceleration is also influencing the gas producer turbine speed, introducing flow distortions and aeromechanical effects on all the engine.

A problem of first priority is to determine the natural frequencies and mode shapes of all the modes that have potential resonances over the engine operating range. Aerodynamic and mechanical resonance vibrations are typified by frequencies that, when in proximity to peak resonance response, will be exact multiples of rotor speed and "track" with slight rotor variations. A mechanism of separation and re-attachment of flow, referred to as "separated-flow vibration", characterized by non-periodic amplitude modulation in the fundamental modes at their natural frequencies, independent of rotor speed, increases both amplitude and amplitude modulation until the cascade develops a rotating stall and propagates surge. Turboblading response to surge is of special importance since the mechanism results in brief but damagingly high overstress ratios.

But, the most destructive type of vibration encountered is the self excited (flutter) vibration, characterized by subtle indications of onset and explosive amplitude build-up to levels that can approach $2 - 3$ times endurance limits. Frequencies correspond to the natural frequency at onset and are independent of rotor speed.

Flight in turbulence and abrupt maneuvers might induce distorted inlet flows and engine performance degradations. The combination of these phenomena to high amplitude (and/or frequency) rotor torque fluctuations may have serious consequence on the engine operation.

The collapse of axialsimmetry of the flow in the compressor, at rotational speed lower than the nomminal speed, causes rotating stall. Although this phenomenon is confined only to a part of the compressor at a given moment, as in a abrupt maneuver in air turbulence, and does not severely affect the performance map of the compressor, it is more dangerous than other unsteady phenomena to the survival of the compressor. In fact, the rotating stall is comprised of a wide range of exciting frequencies which can include self frequency of one of the blade rows. The rotating stall usually occurs close to the compressor surge line, where the blade boundary layers are thick. In this region, a wall stall or surge configuration usually appears before the rotating stall can stabilize.

Blade stalls and rotor-induced surges are then occurring when the distortion intensity is such that steady or surge pressure ratio limits are reached.

During engine surge, dynamics loads stress fixed and moving blades and components.

Compression and expansion wave over and under-pressure relative to pre-surge steady levels occur as a consequence of flow breakdown within the compressor of the gas producer.

Possible indirect effect are the beam-like vibrations of the shaft, and the flexural modes of forced vibrations of the discs. These disc modes, or blade and disc modes of blade disc assemblies, consist of alternating patterns of axial displacements with increasing numbers of diametral modal lines and circular modal lines for higher natural frequencies. Failure prediction can then be conducted by comparing with the results of rotating disc fatigue, testing under controlled conditions of energy input.

The transmission,(from the main rotor to the engine) damping, is an important means of reducing blade amplitudes. The phenomenon implies the dissipation of energy and the reduction of wear of a critical part in the case of structural damping or the generation and propagation of cracks along the internal grain boundaries of metallic alloys. The axial machines have to be designed to withstand more severe vibration environments by using composite materials.

Engine new technology is developing dynamic components (which have greater efficiency, reliability and ease of maintenance), advanced materials (metals and composites), and advanced lubrication concepts, Ref. 6.

High dynamic rotor loads in turbulence limit the high speed and maneuverability capabilities of helicopters. Dynamic loads influence the reliability and maintainability characteristics of a rotorcraft and, hence, its life-cycle cost. The goal of the techonology program is therefore to predict engine dynamic performance capabilities during high speed forward flight and transient maneuvers.

The main rotor incremental torque ΔQ, in respect to the average torque Q_{av}, is determining the torque Q_e and the rotational acceleration $d\omega_e/dt$ of power turbine shaft approximately according eqs. (1) and (3), for each azimuthal angle of the main rotor.

Even though only experimental data and directly measured values could help to solve the problem, analytical approximate procedures may be as it follows.

Rotor torque in forward flight

With the blade assumed as a rigid beam with a flapping hinge, figure 14, the total induced air velocity W relative to a blade element distant r from the no-feathering axis (as resultant of the induced airspeed, the forward velocity V of the rotorcraft, and the rotational velocity $\Omega \cdot r$) has a chordwise component U_T (comprehensive of $\Omega \cdot r$)

$$U_T = - V \cos\alpha \sin\psi - \Omega \cdot r = - \Omega \cdot r(x + \mu \sin\psi) \qquad (4)$$

(with: advance ratio $\mu = V \cos\alpha / \Omega \cdot R$, and $x = r/R$) and a component U_p perpendicular to the chord, having ignored the spanwise component).

In the region of the advancing blade ($0 < \psi < 180°$), the relative chordwise wind due to rotational speed

is increased by a component of V; in the region of the retreating blade ($180° < \psi < 360°$), the component of V reduces the relative wind. The wind is blowing from the trailing edge to the leading edge in the part of the retreating blade, where the forward speed component is greater than that due to the rotational speed, eq. (4). This happens, Ref. 2 and eq. (4), in a circular "reversed flow" region whose diameter is μ R, figure 14.
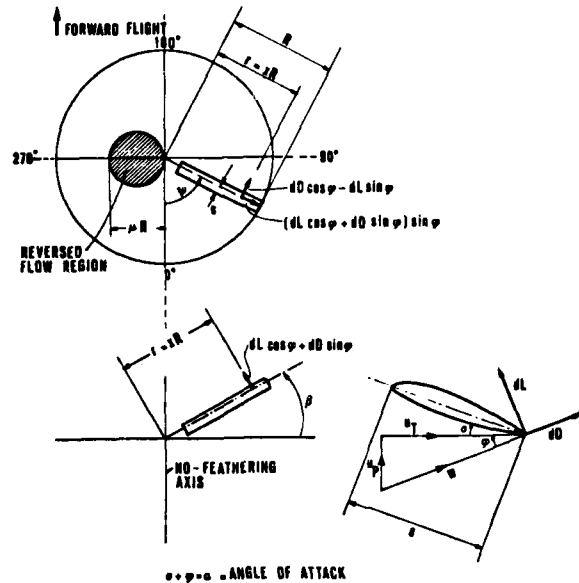
Fig. 14 - Vibration of blade torque with azimuthal angle
in forward flight.

The contribution from this region is usually very small; for $\mu = 0.3$, the area of the reversed-flow region is only 2.5 per cent of the total rotor area (with very small velocities). But, when $\mu = 0.6$ and more (well above the top speeds of present-day helicopters), the reversed-flow region begins to assume importance.

The torque dQ on a blade element ($c \cdot dr$) is, figure 14, as function of the lift dL and the drag dD

$$dQ = r(dD \cdot \cos\varphi - dL \cdot \sin\varphi) \tag{5}$$

It is, with $W^2 = U_T^2 + U_P^2 \simeq U_T^2$, $\cos \simeq 1$, $\sin \simeq U_P/U_T$, C_L and C_D corresponding to drag and lift coefficients

$$dQ = r(C_D - C_L U_P/U_T) \tfrac{1}{2} \rho U_T^2 \tag{6}$$

where, the first term denotes the blade element torque dQ_d due to profile drag, and the second term corresponds to the blade element torque dQ_i due to rotor induced lift.
Eq. (6) becomes, in respect to the azimuthal angle ψ and the dimensional ratio $x = r/R$

$$dQ = dQ_d - dQ_i = \frac{x^3 R^4 \Omega^2 \rho c}{2} (x + \mu \sin\psi)^2 \cdot (C_D - C_L \cdot U_P/U_T) \, dx \tag{7}$$

The rotor thrust dS on a blade element ($c \cdot dr$) is, figure 14,

$$dS = (dL \cos\varphi + dD \sin\varphi) \cos\beta \simeq dL \simeq \frac{x^2 R^3 \Omega^2 \rho c}{2 U_T} (x + \mu \, \text{sni}\psi)^2 C_L U_P \, dx \tag{8}$$

The values of the lift and drag coefficients in eqs. (7) and (8) may be deduced, with simple ideas of induced velocity calculated on the assumption of the rotor regarded as a lifting surface, in function of the local angle of attack $\alpha = \theta + \varphi$. The angles θ and φ, for each blade azimuth ψ, are depending upon the blade pitch "collective and cyclic" control (pitch control by feathering, figure 14, contemporarely all the blades and individually each blade) and the amplitude of the total induced velocity W (see the induced

velocity distribution according to Mangler's theory, Ref. 4).

For instance, figure 15 shows that the rotor blade of a particular helicopter in forward flight, $V = 260$ km/h, at advance ratio $\mu = 0.33$ operate at angles of attack which vary periodically each revolution. On the advancing side, the angles of attack are small, while, on the retreating side they are large and, for the greater part, correspond to angles well above static stall angle of a typical blade section. As a given blade advances, the tip vortex from the preceding blade may pass closely underneath it, as indicated in figure 4 for $\mu = 0.2$, and the point of intersection moves inward along the blade as the azimuthal angle ψ increases.

It is so possible, at the cruise forward speed of a rotorcraft requiring a total rotor thrust S for supporting its weight and air drag, to evaluate appropriate values of C_L, C_D, U_p and U_T as necessary for applying eq. (7).

For each azimuthal angle ψ (referred to a blade of the rotor) and for all the blade elements, and the b blades of the rotor, we may get the total torque $\Sigma\, dQ$ required to overcome the induced drag and the profile drag. Adding to such a total torque that one necessary to turn the tail rotor, the value of $(Q_{av} \pm \Delta Q)$ in eq. (1) is obtained. The periodic distribution of the rotor torque is shown on figure 16.
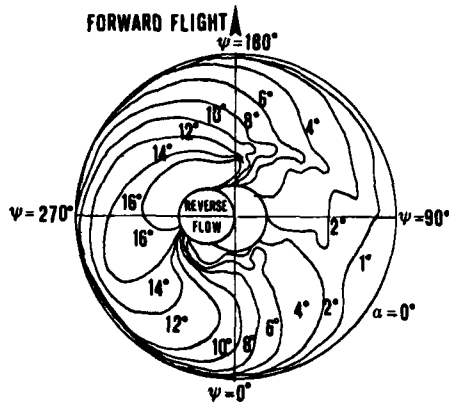
Fig. 15 — Angle of attack distribution with no uniform downwash for $\mu = 0.33$.
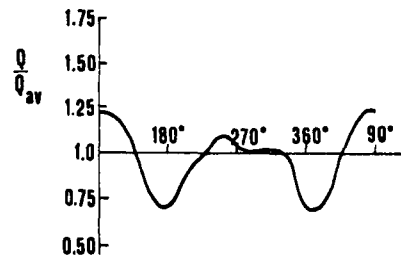
Fig. 16 — Variation of blade loading with azimuthal angle.

The average torque $Q_{d\ av}$ for b constant chord blades, due to profile drag, is

$$Q_{d\ av} = (b/2\pi) \int_0^R \int_0^{2\pi} \tfrac{1}{2}\, \rho\, U_T^2 \cdot C_D \cdot c \cdot r \cdot dr \cdot d\psi =$$

$$= (b/4\pi)\rho\ c\ \Omega^2\ R^4 \int_0^1 \int_0^{2\pi} C_D (x + \mu\, \sin\psi)^2 \cdot x \cdot dx \cdot d\psi = \qquad (9)$$

$$= \rho \cdot b \cdot c \cdot \Omega^2\ R^4 \cdot C_{D\ av}(1 + \mu^2)/8$$

assuming an average value $C_{D\ av}$ of the drag coefficient.

The average torque $Q_{i\ av}$ for b constant chord blades, due to rotor induced drag, is

$$Q_{i\ av} = -\ (b/2\pi) \int_0^R \int_0^{2\pi} \tfrac{1}{2}\, \rho\, U_T \cdot C_L \cdot U_p \cdot c \cdot r \cdot dr \cdot d\psi =$$

$$\qquad (10)$$

$$= -\ (a\ b\ \rho\ c\ R^2/4\pi) \int_0^1 \int_0^{2\pi} (U_T\, U_p\, \theta + U_p^2)\, x \cdot dx \cdot d\psi$$

where it has been considered $C_L = a(\theta + \varphi)$, with a constant slope lift a.

To solve eq. (10), it is necessary to introduce the rotor thrust dS on each blade element as expressed by eq. (8), the force component dH perpendicular to the no-feathering axis, i.e.

$$dH = (dD\cos\varphi - dL\sin\varphi)\sin\psi - (dL\cos\varphi + dD\sin\varphi) \cdot \sin\beta \cdot \cos\psi \qquad (11)$$

and the air induced velocity profile.

The average torque Q_{av}, as in eq. (1), is obtained adding the required tail rotor torque to the values carried out with eqs. (9) and (10).

Finally, for each azimuthal angle ψ, the values of $\pm\Delta Q$ and $\pm\Delta Q \cdot \Omega/\omega$, as in eq. (1) and figure 16, and $\pm d\omega_e/dt$, as in eq. (3), are obtained for the engine (and the transmissions) transient response.

Rotor torque in "over-speed" forward flight and in transient maneuvers

During "over-speed" forward flight and in transient maneuvers, vortex wakes spring from the individual blades and form a complicated downwash pattern, as the vortex elements spiral downwards below the rotor plane because of high Mach number and changing incidences. Moreover, effects of flexibility may determine complex blade bendings and coincidence between the frequencies of the blade motion with the frequencies of forced motion or the natural frequencies of other parts of the rotorcraft.

The periodically varying aerodynamic loads along the rotor blades transmit vibrations to the hub. Aero-elastic coupling of rotor blades determines flap-lag instability, pitch-lag instability, pitch-flap flutter, blade weaving, and stall flutter.

Large high-frequency oscillations in pressure, torsional moment, lift and aerodynamic moment on the retreating side, are detected during a maneuver. This response is the result of dynamic stall induced, figure 4, by the previously formed tip vortices, which, under the maneuver flight condition, pass under the blades at the azimuthal positions over there indicated.

Rotor aerodynamics simulation programs are under development for a broad range of high speed and transmission flight conditions. From them, it will be possible to perform detailed analysis of rotor torque variation, more critical than that on figure 16. Such aeroelastic rotor analysis contains the following items: accurate representation of the rotor dynamics, including the effects of the centrifugal force field, blade twist, mass distribution, stiffness distribution, and the coupling effects between in-plane, out-of-plane, and torsion displacement of the blades; the blade element aerodynamic coefficients C_L and C_D for stalled and unstalled conditions; the rotorcraft's response to pilot control inputs, gust and other externally applied forces.

However, prediction of the rotor torque Q azimuthal signature for "over-speed" forward flight and transient maneuvers is a complex task involving a high degree of idealization and many assumptions. When the rotor system concerned is hingeless, or semi-rigid, the complexity of this task is amplified by a strengthening of the inter-relationships that exist between the three fundamental loading actions of overall aircraft trim balance, rotor system oscillatory loading and vibratory forcing of the airframe.

From the other hand, the rotor torque, Q and Q_e, azimuthal signatures, as in eqs. (1) and (4), may be directly measured in flight. The collected data can be used to analyze the engine component behaviour and the aerodynamic load distribution in "over-speed" forward flight and transient maneuvers.

According test flights, limitations are established for each type of helicopter. For instance, in any kind of maneuver, the flight speed must never overcome the maximum forward speed in the same condition.

Quite high inertial loads derive, in military helicopters, from maneuvers like the ones shown on figure 3, 5 and 6. With load factors as high as 3.5 g, sometimes istantaneously higher up to 10 g, serious mechanical damages and failure on engines may be involved. With negative load factors, as the ones on figure 4, the distorted inlet flow may cause induced engine instability.

Large gyroscopic moments are created when a spinning body such as the turbo-engine rotates about some axis oti than its spin axis. The size of these moments is a function of the body spin speed, mass and distribution of mass of the spinning parts about their spin axes (as transmission systems with roller gear reduction unit), and the rotorcraft pitch/yaw rate. The resultant forces cause damaging cyclic bending of the rotating disks, blades and shafts. Gyroscopic moments of military helicopters may be of the order of 270 m-kN. It should be noted that gyroscopic forces are generated not only by helicopter maneuvers but can also be induced on engine. With the per cent occurrence of the standard maneuvers loads spectrum, the calculated lifetimes may be more than 5 000 hours for the rotor shaft, 11 000 hours for the rotor hub and 22 000 hours for the blades, and much less for the gas turbine engine.

LIST OF SYMBOLS

V   = forward speed

W   = total induced velocity

Q   = torque

T, L, D = thrust, lift, drag

10-14

Ω = rotor angular velocity

ω = turbine angular velocity

J = mass moment of inertia

η = efficiency

α = angle of attack

C_T = thrust coefficient

σ = solidity

n = number of g

av = average

other symbols clearly explained in the test.

REFERENCES

|1| D. Dini, "Problems of Engine Response during Transient Maneuvers", AGARD Conference Proceedings No.302, Toulouse (France), May 1 981.

|2| D. Dini, "Prediction of Aeroelastic Instabilities in Rotorcraft Engine Design", AGARD Conference Proceedings No. 248, Cleveland (USA), October 1 978.

|3| D. Dini, A. Di Giorgio and S. Cardia, "Gas Turbine Transient Operating Conditions Due to an External Blast Wave Impulse", AGARD Conference Proceedings No. 177, Monterey (USA), September 1 975.

|4| D. Dini, "Innovazioni nei Motori per Elicotteri e loro Responso in Manovra ad Alta Velocità", 6° Congresso Nazionale della Associazione Italiana di Aeronautica e Astronautica, Roma, Giugno 1 981.

|5| D. Dini and L. Giorgieri, "Testing Simulation of Damages Occurred in Service", AGARD Conference Proceedings No. 215, The Hague (Netherlands), April 1 977.

|6| D. Dini, "Self Active Pad Seal Application for High Pressure Engines", AGARD Conference Proceedings No. 237, London, April 1 978.

COMMENTARY FOR SESSION II

WAKE AND AERODYNAMIC INTERFERENCE EFFECTS
OF ROTORCRAFT AND WIND TURBINES

By

Anton J. Landgrebe

Manager, Aeromechanics Research
United Technologies Research Center
East Hartford, CT 06108
USA

The technology pertaining to wakes and aerodynamic interference effects is fundamental to the prediction of the aerodynamic loads of rotorcraft and wind turbines. Significant advances in this technology have been made in recent years as exemplified by the six papers presented at this session. The following commentary contains a summary of the key features of each reported study, brief comments on the technical approach and results, and recommendations for future activity. The order of presentation herein is consistent with the order of the papers in this AGARD Conference Proceedings.

Aerodynamic Research of Tipvane Wind Turbines
(G. J. W. van Bussel, Th. van Holten, G. A. M. van Kuik)

An interesting concept for improving the performance of wind turbines is presented with emphasis on the analytical method used to represent the complex aerodynamics of the tipvane turbine. Key features of the method are listed below.

Key features:

- Acceleration potential, asympotic expansion
  approach

- Predicts airload distribution on "T-tail" tipvane
  configuration

- Complex aerodynamics of interfacing surfaces require
  boundary condition assumptions

- Accounts for oversynchronous and undersynchronous
  operation

- Predicts vortex annihilation for oversynchronous
  operation resulting in no induced drag

The accurate analytical modeling of oversynchronous as well as undersynchronous operation is a primary requirement of the method, for the principal performance benefit of the tipvane concept is dependent on achieving oversynchronous operation where the tipvane of each blade is situated in the wake of the previous blade's tipvane. A movie shown during the session, clearly indicated the interaction of the vortex from the upstream edge of a tipvane with the vortex from the downstream edge of the following tipvane. The two vortices were synchronized by tip speed ratio to place them in the immediate proximity of one another and thereby produce a mutual diffusion process influenced by their opposing rotational sense. It is stated in the paper that "in oversynchronous situations the vortex annihilation is almost perfect (no induced drag)." It was stated during the presentation that power coefficients above 1.0 are hopefully anticipated. Considering, a typical peak power coefficient of conventional wind turbines near 0.5, this would be a significant accomplishment. The degree of achievement of the high power coefficient remains to be demonstrated by test. Also, the sensitivity of the power coefficient to off-design tip speed ratios (nonoptimum synchronization) should also be determined by test. It was mentioned that the viscous drag can be high due to tipvane flow separation if the tipvane is not tilted properly. Thus, experimental determination of the sensitivity of power coefficient to off-design tip speed ratios for a fixed tilt angle is also recommended.

Overall, the complex aerodynamics of the tipvane concept, resulting from interfacing surface (blade/vane) interacting vortices, and predominant viscous drag contributions, present a formidable challenge to the accuracy of the acceleration potential, asymptotic expansion approach which assumes small disturbance, potential flow behavior coupled with the applicability of two-dimensional airfoil characteristics to include viscous effects. The need for a test program is recognized by the authors.

Recommendation:

· Conduct a systematic experiment with power, flow
  visualization and airload distribution measurements
  to provide validation data for each component of analysis
  and check boundary condition assumptions.

Aerodynamic Load Calculation on Horizontal Axis Wind Turbine in Nonuniform Flow
(E. Lupo)

The classical blade-element momentum approach for predicting the performance
characteristics of horizontal axis wind turbines is extended to include the contributors
to nonuniform flow. Empirical relations are included where momentum theory is inapplicable.
Key features of the method are listed below.

Key features:

· Blade-element momentum theory

· Predicts rotor loads, moments, performance

· Nonuniform flow due to yaw, tilt, atmospheric boundary
  layer, tower reflection

· Upwind rotor

The accuracy of the method presented cannot be assessed from the contents of the
paper due to the lack of comparison of the theoretical predictions with experimental data.
Also, the presented results are limited to a small yaw angle of 5 degrees. Blade root
bending and torsion moments are aerodynamic moments and do not include the blade
aeroelastic contributions (a rigid blade is assumed).

The power variation of wind turbines with changing yaw angle has been expressed in
several wind turbine references as proportional to $\cos^n \epsilon$, where ϵ is the yaw angle
and the exponent has been assumed or determined empirically. However, due to limited
test results and/or design differences, values of n have been inconsistent. An assessment
of this method by comparing the predicted power versus yaw variation with reliable test
data would be of interest. Considering the assumptions made in the momentum theory, and
the neglect of flow nonuniformity perpendicular to the rotor disk, it is likely to be
found that this method is restricted to small cross flows and yaw angles.

The above comments lead to the following recommendations.

Recommendations:

· Experimental validation required

· Include aeroelastic blade representation for blade
  bending and torsion moments

· Demonstrate analysis at more severe yaw angles where
  nonuniform flow is more significant

· Calculate power variation with yaw angle and compare with
  available data and $\cos^n \epsilon$ relationship

Prediction and Experimental Verification of the Resultant Induced Velocity Field of a Hovering Rotor
(C. Maresca, M. Nsi Mba, D. Favier)

Experimental studies of the hover performance and wake an . airflow characteristics
of model rotors with tip design variations are presented, and the results are compared
with wake analysis predictions. Key features of the study are listed below.

Key features:

· Combined free wake and prescribed wake analysis

· Experimental performance, wake geometry, core size, flow
  velocities (flow visualization, laser anemometer, hot film
  anemometer)

·Tip shape and twist variations

·Correlation ranges from good to poor

The results indicate how experimental and theoretical techniques are being applied and expanded in France to acquire a better understanding of hovering rotor aerodynamics for improved predictive capability. An interesting result of the application of smoke flow visualization techniques is the determination of the variation of tip vortex core size with tip design and tip vortex age. Specifically, core size was shown to increase with vortex age and be consistently smaller for the three designs representing tip and nonlinear twist variations from the conventional rectangular tip blade. Comparisons of measured figure of merit for three rotors indicate a change from performance benefit to performance decrement as thrust is increased for a rotor with a tapered tip design. Comparisons of tip vortex geometry predictions from a combined near free wake/prescribed far wake method with test data indicate good to poor correlation. The poorest correlation was for a rotor with nonlinear twist blades. Continued model rotor testing, as planned, to provide correlation data and empirical models for wake geometry and vortex characteristics will be valuable.

In order to further assess the analytical method, the following is suggested.

Recommendations:

·Use prescribed experimental wake to check analysis
 for performance and flow velocity prediction

·Compare blade loading for nonlinear twist rotor with that
 of a circulation coupled analysis

·Compare predicted blade loading with available test
 results

·Test is required for combined performance, blade loading, wake
 geometry and flow velocity measurements for theory validation

Velocity Coupling - A New Concept for Hover and Axial Flow Wake Analysis and Design
(J. D. Kocurek, L. F. Berkowitz)

A velocity coupled wake model is described which defines the key wake parameters that are required to predict induced velocities, blade spanwise airloading, and rotor performance for hover and axial translation flight. The key features of the velocity coupling technique are listed below.

Key features:

·Generalized wake geometry parameters described in
 terms of principal velocities calculated from simplified
 wake representations

·Calculates hover and axial climb performance and wake
 features

·Provides additional insight for physical mechanisms of
 hovering wake and flow velocities

The velocity coupling approach is an alternative to the prescribed wake and circulation coupled approaches now in use. Similar to the other approaches, a key objective is to provide wake geometry. It is not necessarily more accurate than the other methods, but it can provide fundamental insight for the hovering rotor wake and flow field. The insight provided by the method may identify improved wake modeling procedures through a better understanding of the flow field characteristics. An interesting example is the results of Fig. 16 where it is shown that the mean settling rate in the wake, $(k_1 + k_2)/2$, is simply the momentum induced velocity which is independent of number of blades.

The accuracy of the velocity potential approach remains to be demonstrated through a more extensive correlation study than the one model tail rotor application reported in the paper. Several hover performance methods have demonstrated acceptable performance correlation for classical blade designs. The current need is for a hover method that can accurately predict blade airloading and performance for blades with advanced tip designs. It is not apparent at this time that the velocity coupled approach will offer an improvement over other methods regarding this objective.

Recommendations:

·Validation study of wake geometry, blade
 loading and performance for a wide range of
 rotors

·Current hover methods have been demonstrated as
 sufficient for conventional rotor designs. Demon-
 stration of degree of applicability to advanced
 designs is required (particularly tip shape).

Studies on Blade-to-Blade and Rotor-Fuselage-Tail Interferences
(H. Huber, G. Polz)

A comprehensive description of MBB experimental and analytical activities in the
area of helicopter aerodynamic interaction is presented. Results are presented for three
categories: blade-to-blade vortex interaction, fuselage interference at the main rotor,
and fuselage/hub interference at tail surfaces. The results show the value of conducting
and relating analytical and experimental programs to gain an understanding of the aero-
dynamic mechanisms involved in helicopter interactional effects. It is also demonstrated
that current wake modeling technology can be used to predict many aerodynamic interaction
characteristics. Key features of the paper are presented below.

Key features:

·Blade-Vortex Interactional Airloads - - Wake analysis
 can predict the harmonic decay of higher harmonic airloads
 similar to test data for flight conditions with blade-vortex
 interaction. Harmonic amplitudes are large for such conditions.

·Fuselage to Main Rotor Interaction - - Analytical prediction of
 aerodynamic interference of fuselage at rotor for varying rotor
 height is demonstrated.

·Fuselage/Hub - Tail Interference - - Sources of steady and
 unsteady interference are identified. In-flight pressure
 measurements, model wind tunnel measurements, and an analytical
 fuselage panel method with fuselage/hub/shaft wake representation
 indicate significant steady tail interference effects. Flight
 test results indicate large n/rev tail interaction due to main
 rotor wake and the feasibility to relieve tail shake with
 airframe configuration changes such as hub cap and spoiler.

The analytical results presented, based on current wake methodology, are encouraging.
However, considerable fundamental wake modeling research and methodology development
remains to be done before comprehensive, accurate interactional aerodynamic methods are
available for routine use in helicopter design. For example, the high sensitivity of the
amplitude of blade and fixed lifting surface airloads to vortex distance and analytical
vortex representation, for close vortex interaction, must be addressed through fundamental
experiments and improved vortex interaction modeling. Also, wake geometry prediction
methods must be very accurate for close vortex interaction calculations.

The fuselage to main rotor interaction results of Figures 15 to 17 are similar to
those presented in Reference 1*. The influence of wake distortion and the fully coupled
solution for the fuselage/rotor interaction remains to be studied.

It is mentioned in the tail interference section of the paper that "theory is not
capable up to now to account for dynamic wake phenomena" and "theories for calculating
the unsteady flow phenomena are not available today". A method was recently developed
at the United Technologies Research Center for predicting rotor wake induced empennage

---

*Reference 1:

Landgrebe, A. J., R. C. Moffitt, and D. R. Clark: Aerodynamic Technology
for Advanced Rotorcraft. Journal of the American Helicopter Society, Vol.
22, Nos. 2 and 3, April and July 1977 - - Parts I and II. Also, Proceedings
of the National Symposium on Rotor Technology, American Helicopter Society,
Mideast Region. August, 1976.

airloads contributing to tail shake, as reported in Reference 2*. In this method the
UTRC Rotorcraft Wake Analysis was combined with a local vortex interaction model and
lifting surface representation of the empennage to predict both the unsteady induced
velocities at the tail due to the passage of the main rotor tip vortices and the resulting
unsteady airloads. Reasonable theory-test correlation of the 6 per rev unsteady airloads
for the 6-blade CH-53A helicopter was demonstrated. Additional test results, such as the
MBB unsteady tail flow angle and dynamic pressure data, presented in Fig. 27, confirm the
n/rev airload amplification and are required for continued theory validation.

Recommendations:

·Continue simultaneous theory development, model test, and flight
test to provide a fully-coupled helicopter aerodynamic interaction
prediction method and validation data.

·Fundamental experiments are needed to guide the analytical modeling
of close blade-vortex interaction, fuselage and tail-vortex interaction
and the unsteady fuselage wake.

Rotor-Fuselage Interference on Engine Internal Aerodynamics in Maneuvering High-Speed Rotorcraft
(D. Dini)

This paper provides a description of the sources of engine damage and failure related
to the unsteady loads resulting from rotor blade vortex interactions, aerodynamic inter-
ference effects with the fuselage, and other mechanisms. The influence on both the engine
internal aerodynamics, the unsteady torque transmitted to the engine shaft, and the
vibratory excitation of the engine are considered in the discussion. Unlike the previous
papers, new methodology or experimental results are not presented. Instead, several
topics are discussed which provide a qualitative understanding of the external mechanisms
which limit engine performance and structural life.

It is described that blade-vortex interaction effects, particularly in high speed
maneuvers, can influence all three of the above-mentioned factors. Nonuniformity of
the engine inlet flow produced by wake induced effects, turbulence, and maneuvering flight
flow conditions can result in compressor rotating stall. Also, unsteady cyclic rotor
torque variations can be produced which can be transmitted to the engine. When the
forward speed is high enough to produce blade stall and large amplitude aeroelastic
effects, the torque fluctuations can be transmitted through the gear box to the engine
resulting in compressor and free turbine vibration.

A primary implication of the paper appears to be that many of the same concerns
for rotor and fuselage vibratory loads and unsteady airflow that are of interest in the
helicopter design process are also of significance for engine considerations, and similar
methodology is required to predict the engine inlet flow and vibratory excitation. For
example, a combined rotor dynamics and wake analysis applicable to high speed maneuvers is
needed to predict the vibratory excitation from the rotor shaft, the cyclic shaft torque,
and the wake-induced component of the engine inlet distortion. A method accounting for
the rotor-fuselage aerodynamic interaction is needed to predict the engine vibratory ex-
citations transmitted from the rotor and fuselage.

---

*Reference 2:

Gangwani, S. T., Determination of Rotor Wake Induced Empennage Airloads,
Proceedings of the American Helicopter Society National Specialists'
Meeting on Helicopter Vibration, Hartford, CT, Nov. 1981.

PREDICTION OF AERODYNAMIC LOADS ON ROTORCRAFT

COMMENTARY ON SESSION II:*

"Wakes and Aerodynamic Interference Effects of Rotorcraft and Wind Turbines"

by
B. Maskew
Vice President, Research
Analytical Methods, Inc.
Redmond, Washington 98052
U.S.A.

1. INTRODUCTION

First, let me acknowledge the valuable contributions given to this commentary by two of my colleagues at Analytical methods, Inc.; namely, David Clark and Mick Summa, both of whom had the opportunity to read most of the preprints for this session.

Predicting the effects of wakes and aerodynamic interference on rotorcraft and wind turbines is, of course, a difficult non-linear problem. For the purpose of the commentary on the papers of this session, I have considered the problem in four main elements shown in Figure 1: rotor blade model; tip-edge vortex; wake model; and rotor/wake/surface interaction.

2. ROTOR BLADE MODEL

The shape of the rotor blade, of course, largely determines the way the wake is formed in the first place--this in turn affects the way the wake develops, how it interacts with the blade, especially at first blade passage, and how it interacts with other surfaces on the rotorcraft or support structure. The way the blade is represented in a theoretical model, therefore, strongly influences how well we can predict the detailed effects of wake and aerodynamic interference. Certainly, if we are attempting to predict the detailed performance changes of the various advanced blade shapes--of which we have seen several examples in both Session I and the present Session covering swept, tapered and parabolic tips, non-linear twist and also tip vane devices--then the blade geometry must be modelled in close detail, especially in the tip region.

In the first paper of this session we saw the benefits of tip vanes on wind turbine performance. The model used for this analysis was based on the acceleration potential formulation. The authors were careful to point out the small perturbation assumption of this approach, and yet, in the optimum synchronous state, when the interaction between the edge vortex system and the downstream vane is at its peak, the velocity perturbations are likely to be high. If further development of the tip vane concept is to be pursued analytically, e.g., to optimise shape, orientation, etc., then a lifting-surface model at least should be considered.

If we wish to predict in detail the performance (i.e., distributions of pressure, thrust and torque as well as the integrated force and moment) of blades having advanced features, then the blade geometry must be adequately represented in the methematical model. In this respect, lifting-line models cannot be expected to treat the complicated three-dimensional flow fields present in the tip region and during a vortex/surface encounter. I think Dr. Maresca's paper demonstrated that. Inadequate blade modelling probably contributed to the substantial differences between measured and calculated collective pitch, although the far-wake model was almost certainly the major culprit.

A lifting-surface model is a minimum requirement for treating advanced features of planform and twist and offers direct coupling between the wake and the blade loading. Modern airfoils with reflex camber, local tabs, etc., require even more detailed modelling. At AMI we find a surface singularity panel method offers a very practical approach giving complete pressure distributions--albeit with limitation regarding transonic effects. It also leads to practical treatment of viscous effects via boundary layer methods and this gives predicted edge separation lines for tip-edge vortex modelling, Figure 2.

3. TIP-EDGE VORTEX

The way the loading is shed near the rotor tip strongly affects the tip vortex location and character; i.e., whether it is intense or diffuse. This has a major impact on rotor performance, noise and behavior at first blade passage. Adequate treatment of this effect again requires detailed modelling of the blade in the tip region. The benefits of the tip-vane model in the first paper of this session are directly tied to the interaction between the tip vortex system and the following vane.

4. WAKE MODEL

As hypothesized by Gray and demonstrated practically by Landgrebe, the hovering rotor wake quickly separates into two major parts: an inboard sheet of weak vorticity and an outer tip sheet that rapidly rolls up to form a strong tip vortex. This had lead to the use of simplified "prescribed wake" models summarised and extended here in Dr. Kocurek's paper. Prescribed wake models are in wide use for practical calculations and are also used for setting up initial wakes for subsequent free-wake analyses--Dr. Maresca used such an approach in his paper and this is also done in AMI's hover analysis programs, except we favor a semi-infinite wake model representing a set of concentric cylinders of uniform vorticity. This far-wake model has proven to be very effective in giving accurate performance predictions with considerably reduced computing effort. It is not argued that the wake does not eventually dissipate, only the details far down-stream are not of general interest. The far-wake model is merely a convenient and adequate representation of the actual wake. It is felt that the added parameter of wake length in Dr. Kocurek's method offers a means of compensating for deficiencies between the prescribed wake model and the actual wake; e.g., as regards inflow and loading shape and wake geometry.

One of the conclusions in Dr. Kocurek's paper should be emphasized; namely, the need for a wider data base. The prescribed wake models are clearly very effective within the range of the experimental data base, but we should exercise caution when going outside this data base--as we saw in Dr. Maresca's paper. To demonstrate this further, Mick Summa has provided some calculated results. Figure 3 compares the calculated circulation distribution for three rotor geometries at approximately the same thrust coefficient. Simple element momentum and prescribed wake (circulation-coupled) methods predict a large performance gain going from the rectangular to the tapered case. These gains do not materialize when proper account is taken of the free-wake and lifting-surface effects. The tip vortex strength is reduced but the vortex actually moves closer to the blade, Figure 4 (for the same thrust coefficient); consequently, the induced power reduction does not appear.

In addition to this, whereas AMI free-wake calculations (with semi-infinite wake model) on standard rectangular blades agree very well with prescribed wake analyses, Figure 5, large differences occur for tapered blades. First, the load distribution, Figure 6, relates to a non-linear inner sheet, Figure 7, and the weakened tip vortex moves closer to the blade than the prescribed wake locations shown in Figure 8. These movements are well within the scatter of experimental measurements.

5. ROTOR/WAKE/SURFACE INTERACTION

The fifth paper of this session examined the more general problem of the interaction between a rotor, its wake and configuration surfaces. The interference of the fuselage acting on the rotor is calculated using a source panel method: this only represents the displacement effect. A panel method based on source and doublet singularities is recommended for this task: this represents the effects of circulation as well as displacement and is more amenable for modelling the separation zones using free vortex sheets.

It is evident that the fuselage can have a strong effect on rotor loading distribution, but the paper only discusses a one-way interaction; i.e., first-order effects. The mutual interactions of the rotor, wake and fuselage need to be represented as these lead to important higher-harmonic effects.

6. CONCLUSIONS

Prediction methods are advancing and are providing a means for more detailed modelling of rotor, wake and configuration. However, experimental data will continue to play a large part in the application of these methods. In this respect, there is a need for more data on general blade configurations, including measurements of wake geometry and surface pressures as well as loads and moments. Such data would fulfill a requirement to expand the data base for semi-empirical procedures such as prescribed wake analyses and at the same time would help validate more advanced calculation methods. In addition, experimental evidence will continue to provide insight into ways of modelling the complex flow phenomena associated with rotor-craft. Areas requiring particular attention include blade/vortex interaction and rotor wake impingement on fuselage/tail.

1. Rotor Blade Model

2. Tip-Edge Vortex

3. Wake Model

4. Rotor/Wake/Surface Interaction

Figure 1.   Four Elements in the Prediction of Wake and Aerodynamic
Interference Effects on Rotorcraft and Wind Turbines.
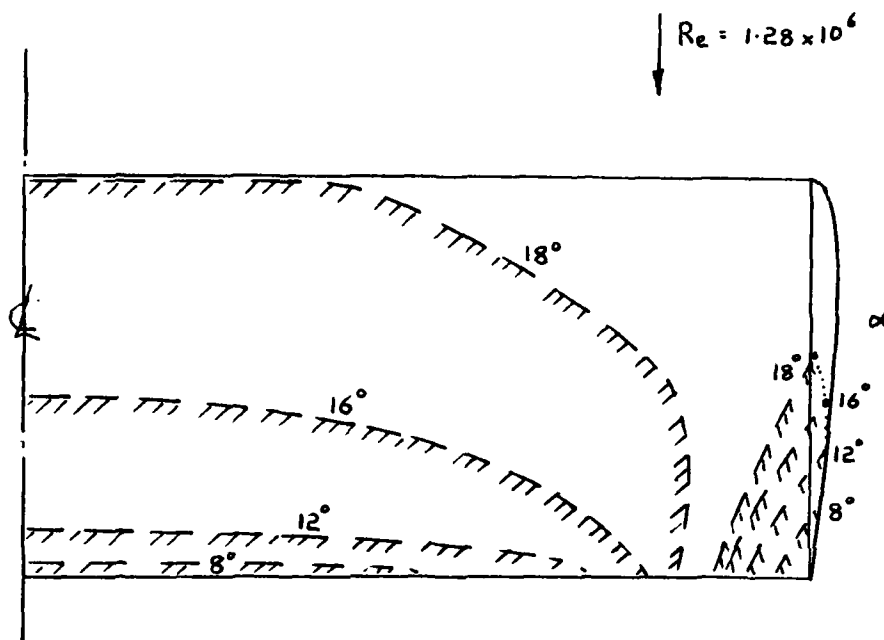
$$R_e = 1.28 \times 10^6$$

Figure 2. Calculated Separation Boundaries for a Range of α at a Reynolds Number of 1.28×10^6.

SPANWISE DATA

UH-1H	CASE1	✕
Tapered	CASE2	△
Ogee	CASE3	▫

Y / RADIUS
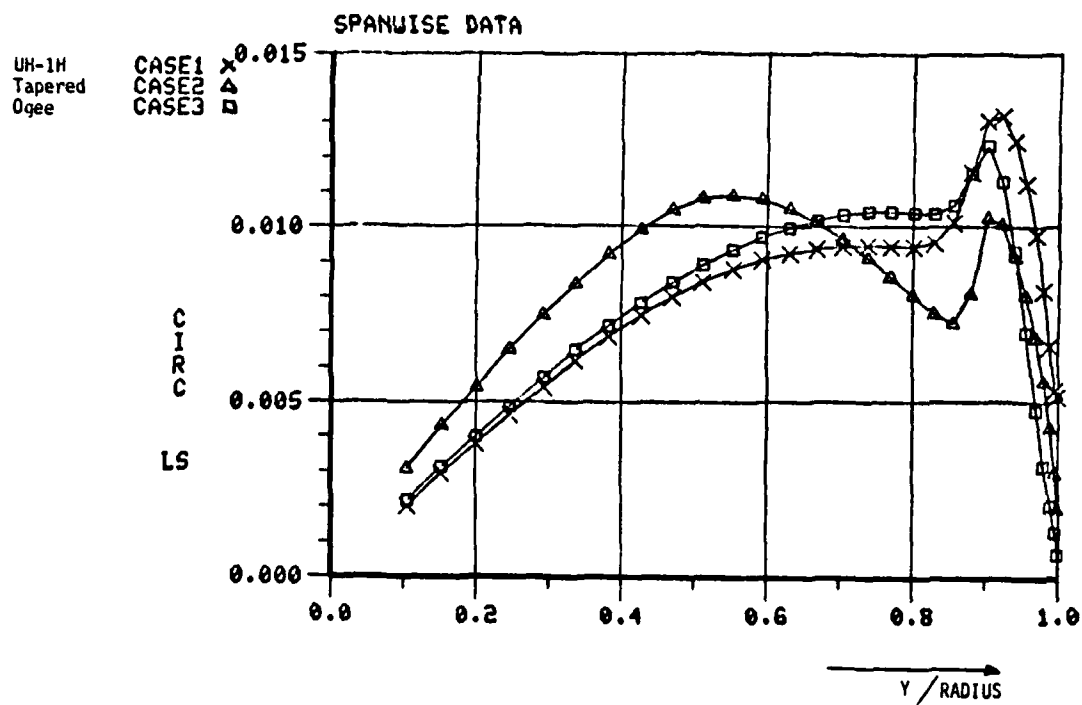
Figure 3. Comparison of Calculated Radial Circulation Distribution for Rectangular, Tapered and OGEE Rotors.
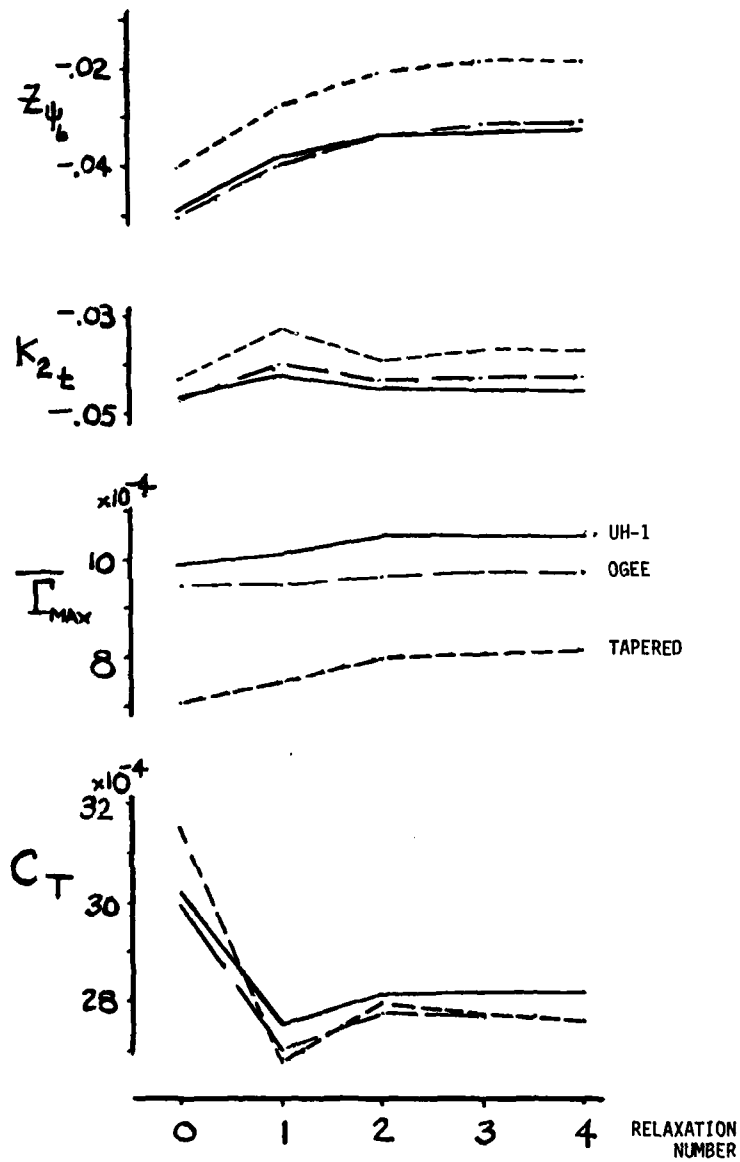
Figure 4. Behavior of Key Rotor Properties with Relaxation Iteration.
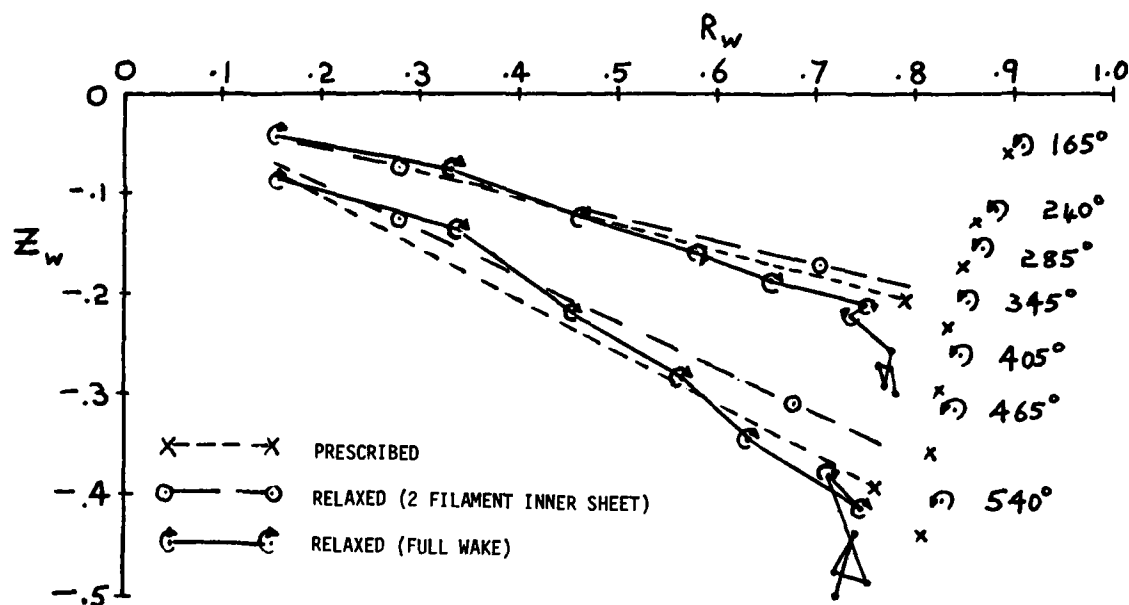
Figure 5. Wake Geometry Comparison (Rectangular Blade, AR = 13.7, $\theta_1 = 0$, $\theta_{75} = 8°$).
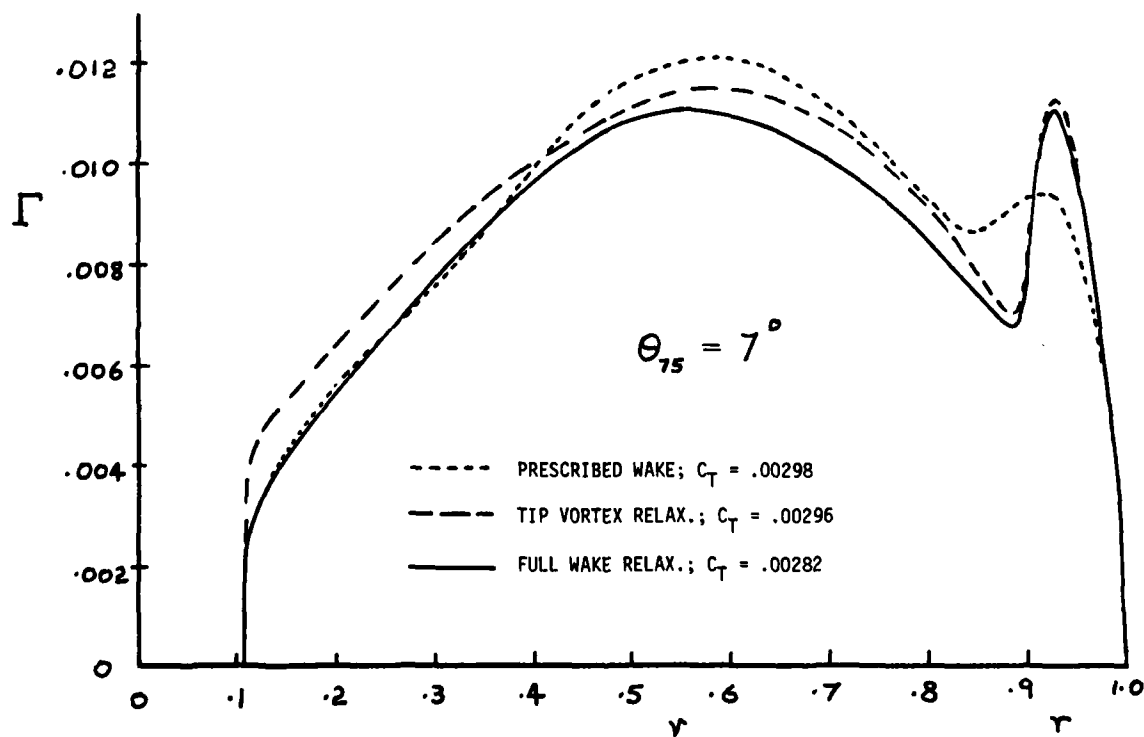
Figure 6. Calculated Tapered Rotor Circulation Distribution (TR = 3:1 from R = 0.5, $\theta_1 = -14°$).
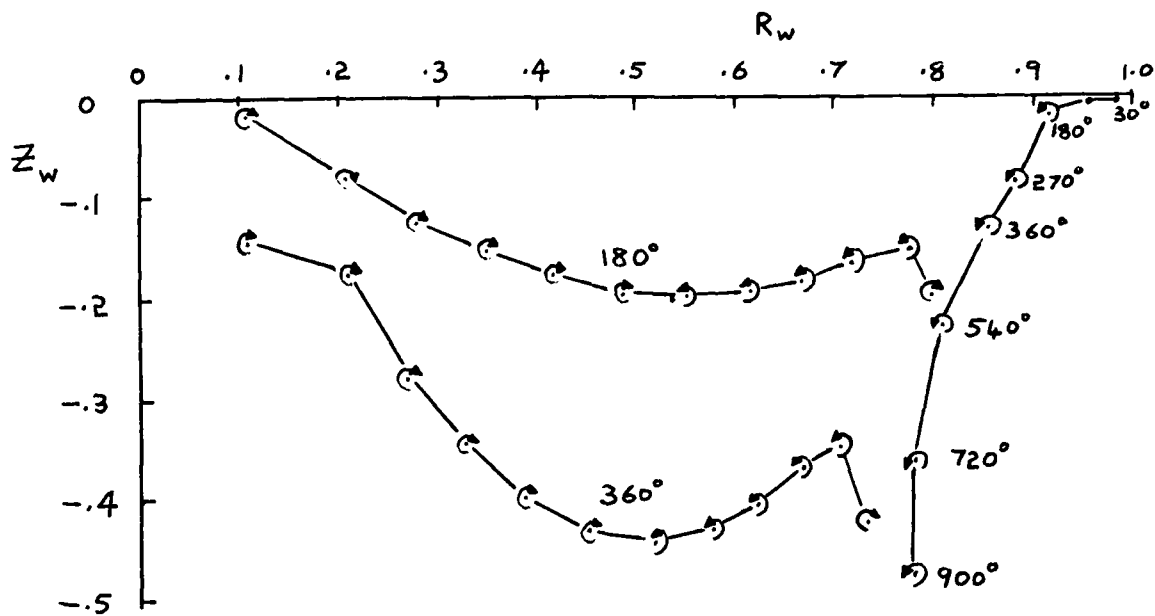
Figure 7. Calculated Tapered Rotor Wake Geometry (Full Wake Relaxation).
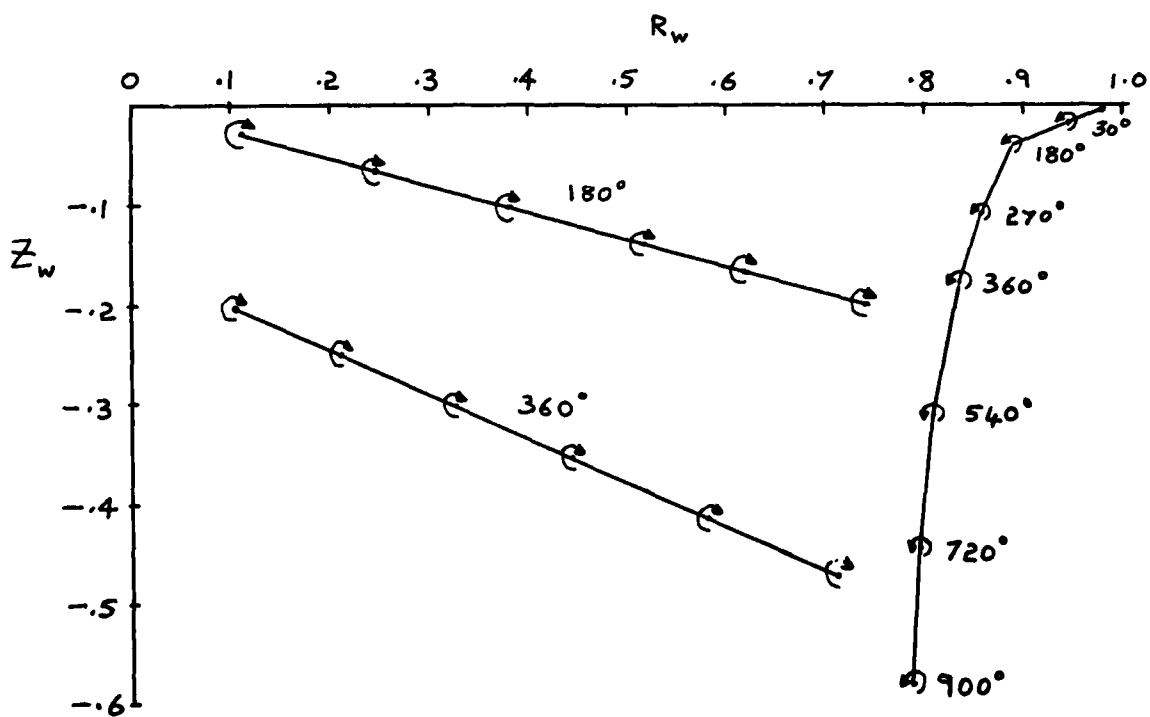
Figure 8. Prescribed Tapered Rotor Wake Geometry.

DEVELOPMENT OF THE VORTEX RING WAKE MODEL AND ITS INFLUENCE ON
THE PREDICTION OF ROTOR LOADS

by

C. Young
Structures Department, Royal Aircraft Establishment
Farnborough, Hampshire, GU14 6TD, UK

SUMMARY

The vortex ring wake model is widely used by RAE and Westland Helicopters Ltd in the prediction of helicopter rotor loads. The evolution of the model is traced from the original form developed over ten years ago to the current version which includes the distortion due to the aircraft fuselage and an interactive near wake. The effects of improvements in the model are illustrated at each stage with comparisons between flight test data obtained with the Puma helicopter at RAE Bedford. The predicted and measured hub forces and moments for the Lynx helicopter are also compared.

1   INTRODUCTION

The wake trailed by the blades of a helicopter rotor plays an important part in determining the loads and the vibrational forces and moments transmitted to the fuselage. The vortices forming the wake in forward flight have a cycloidal shape extending below and behind the rotor. Modelling the wake matnematically is not easy but considerable advances have been possible due to developments in high speed digital computers. Methods are now available, for example, in which the wake, represented by short vortex elements, is allowed to distort under its own induced velocity field until it is force free[1], but in general, simpler techniques are used for day to day work. Typical of these methods are the prescribed wake analyses in which the wake is assumed to have some predetermined geometry or simply follows an undisturbed spiral path. The vortex ring method described here belongs to the simpler group of wake models but cycloidal vortices are not used and the spiral path is approximated by vortex rings.

Development of the vortex ring model began over ten years ago. The aim was to devise a method that represented the main features of the wake but was computationally efficient, and these criteria have always applied to subsequent changes. The original model, described in section 2, has undergone fairly extensive modification. The positioning of the rings relative to the blade has been improved, section 3, and the vertical displacement of the rings from the plane of the disc made more representative, section 4. The most recent change has been to introduce some degree of interaction between the load on the blade and the strength of the trailing vortices. The so-called 'interactive near wake' is described in section 5.

The effect of the various modifications and improvements will be demonstrated by comparing the blade stresses measured on a Puma helicopter with those calculated by the second generation RAE/WHL rotor loads analysis. The dynamics of the blade and the mathematical representation of the rotor has been kept the same for all the calculations thus the changes seen are due solely to the effect of the different wake models.

The vibration level of helicopters is becoming increasingly important. Some comparisons are presented in section 6 on how the ability to calculate hub forces and moments has changed since the vortex ring model was introduced using the Lynx helicopter as an example. Finally some areas where the representation of the wake can be further improved are described in section 7.

2   THE ORIGINAL VORTEX RING WAKE

The original vortex ring model developed by WHL[2] represented the wake by a half ring originating at the reference blade and typically 12 complete vortex rings extending downstream, Fig 1. Only two systems of rings were used, representing the root and tip vortices, but only the tip vortex is shown in the figure for clarity.

The centres of the rings were displaced at equal intervals vertically and downstream from the tip path plane. The non-dimensional vertical separation of the rings was

$$\Delta z = 2\pi (\mu_N + \lambda_0)/b$$

where b is the number of blades, μ_N the free stream velocity normal to the disc, and λ_0 the mean momentum value of the induced velocity. Similarly, the separation of the rings downstream was

$$\Delta x = 2\pi \mu_T/b$$

where μ_T is the tangential component of the flight velocity.

The bound circulation was assumed to be constant along the blade so the root and tip vortices had the same strength but of opposite sense. The magnitude of the circulation was determined by assuming that the blade flapping was zero, and setting the moment of the aerodynamic forces about the flap hinge to a constant. The resulting expression was

$$\gamma = \gamma_0 (1 - 1.5\mu \sin \psi)$$

where γ_0 is the mean circulation and is related to the thrust, rotor geometry, and flight speed, *ie*

$$\gamma_0 = T\Big/\rho b\Omega R^2 \left(0.5 - 0.1875\mu_T^2\right) \ .$$

The trailing vortex strength was therefore constant with a superimposed first harmonic content. This variation of vortex strength meant that the velocity induced by the rings could be evaluated in closed form using elliptic integrals, and undoubtedly contributed to the efficiency of the method.

The impact of the vortex ring model on the calculation of blade loads is shown in Fig 2 for the Puma blade at an advance ratio of 0.32. The measured flatwise bending moment is compared with that calculated using the vortex ring model and the trapezoidal Glauert downwash distribution. Both calculations were made with the new RAE/WHL rotor loads analysis which is briefly described in the Appendix. The dynamic representation of the blade was identical for the two calculations and in each case the rotor was trimmed to the same thrust and first harmonic flapping angles. The differences between the two theoretical bending moment distributions are therefore due entirely to the change in the induced velocity.

The peak-to-peak bending moment is better predicted by the vortex ring model. The waveform also has more higher harmonic content than the calculation with the Glauert distribution although the magnitude and phasing is not correct. Further inboard, however, the situation is not quite so satisfactory, Fig 3. The calculated bending moments at 35% radius on the retreating side of the disc show a double peak compared to the single peak of the measurements. The fault does not seem to lie with the vortex ring model as the calculation with the Glauert distribution shows similar behaviour although the effect is less pronounced. The source of the discrepancy, though not the reason for it, can be found from Tables 1 and 2 which list the harmonic content of the bending moment at 35% and 75% radius respectively. The fifth harmonic is greatly overestimated at the inboard station and this is responsible for the dip in the bending moments at about 270° azimuth. Note also that the third harmonic component is also severely underestimated at both radial positions.

3   IMPROVEMENTS IN THE HORIZONTAL POSITION OF THE VORTEX RINGS

The first major change to the wake geometry was made when a representation of unsteady aerodynamics and a model of the dynamic stall process was included in the old rotor performance calculation. The development of the torsional oscillation on the retreating side of the disc following the initial stall can be damped or divergent depending on the torsional frequency of the blade and the phasing of the vortex interactions[3]. Unfortunately, there is a considerable error in the position of the blade-vortex inter-sections viewed in plan, Fig 4, when the vortex rings are placed on a line extending downstream compared to the intersections of a spiral wake. The error is greatest over the rear of the disc and had to be corrected to improve the prediction of stall phenomena.

The improved wake model positions the centre of any ring which has an intersection with the blade so that the radial position of the intersection and the tangency of the ring to the blade corresponds to the intersection of the undistorted spiral path of the wake. The centre of the rings therefore no longer lie on a straight line although the vertical displacement is still uniform. The size of the rings was also changed, being larger than the rotor radius on the advancing side of the disc and smaller on the retreating side. Provision was also made to allow the effective origin of the tip vortex to lie inboard of the blade tip. The half vortex ring trailing from the reference blade, however, always originates from the tip.

The mathematics needed to make the changes are not presented here since it involves some tedious geometry. The effect on the blade bending moments at the two radial positions considered previously, however, is shown in Fig 5 at 75%R, and Fig 6 at 35%R. The calculations with the original vortex ring model shown in Figs 2 and 3 are also presented so that the differences can be readily seen.

The most significant improvements at the outboard station, Fig 5, occur on the advancing side of the disc. The trends are better predicted but the peak bending moment on the retreating side is now underestimated. There is a slight improvement at 35%R, Fig 6, since the magnitude of the fifth harmonic component has been halved, Table 1. The third harmonic contribution, however, at both radial stations remains underestimated and incorrectly phased.

4   IMPROVEMENTS IN THE VERTICAL POSITION OF THE VORTEX RINGS

The next modification to the vortex ring wake model introduced the effect of a fuselage. The fuselage generally induces an upwash over the front of the rotor disc which increases the loading on the inboard portion of the blade and can lead to premature

blade stall. There may also be a downwash over the rear of the disc depending on the rotor geometry and the shape of the fuselage. The change in loading tends to excite the second and third flap modes and the second lag mode of the rotor which can have an important influence on the aircraft vibrational levels. The secondary effect of the fuselage, which is the main concern of this section, is to change the velocity field through which the trailing vortices pass. The upwash around the front of the disc keeps the tip vortex from the preceding blade closer to the reference blade which enhances its effect. A proper representation of the fuselage in the rotor analysis was therefore one reason for completely revising the procedure used to calculate the vertical displacement of the vortex rings.

The distance travelled below the rotor by a trailing vortex filament depends on three factors; the free stream velocity normal to the tip path plane, the rotor induced velocity, and the fuselage induced velocity. The vertical separation between the vortex and the point at which the velocity is evaluated will also depend on the blade flapping motion. All four contributions are now considered in the revised wake model originally developed by WHL[4] and subsequently modified at RAE.

Consider an element of vorticity on a tip vortex situated at (x_1, y_1, z_1) in a system of axes with the origin at the rotor hub and aligned with the tip path plane, Fig 7. The vortex has two possible points of origin, A and B, with angular location $\psi_p = \psi_1$ or $\pi - \psi_1$. The transformation from the axes parallel to the tip path plane (X_{TP}, Y_{TP}, Z_{TP}) to the fuselage axes (X_F, Y_F, Z_F) requires knowing the vertical displacement of the vortex. A first approximation to this distance can be found by assuming that the blade has only first harmonic flapping and that the vortex has travelled in a uniform velocity field, thus

$$z_1 = x_1 (\lambda_0 + \mu_N)/\mu_T + \beta + z_b$$

where β is the flapping displacement, $\beta = a_0 - a_1 \cos \psi_p - b_1 \sin \psi_p$, and z_b is blade precone at the tip.

The co-ordinates of the point (x_1, y_1, z_1) in the fuselage axes (x_f, y_f, z_f) are

$$x_f = x_h + x_1 \cos(i + a_1) - y_1 \sin(i + a_1) \sin b_1 + z_1 \sin(i + a_1) \cos b_1$$

$$y_f = y_1 \cos b_1 + z_1 \sin b_1$$

$$z_f = z_h - z_1 \sin(i + a_1) - y_1 \cos(i + a_1) \sin b_1 + z_1 \cos(i + a_1) \cos b_1$$

where i is the shaft angle and x_h, z_h are the co-ordinates of the rotor hub in the fuselage axes. Similar expressions for the co-ordinates of the point at which the vortex was shed can also be written down (x_p, y_p, z_p).

The first approximation to z_f is now refined by calculating the distance the vortex would have travelled if the mean velocity were replaced by a more representative velocity. The vortex travel is

$$z = z_p + \frac{1}{\mu_T} \int_{x_p}^{x_f} \frac{\bar{V}(z)}{\Omega R} \, dz$$

where (z) is the total velocity with components $V(z)$ due to the rotor downwash, the free stream, and the fuselage flow field.

The rotor induced velocity is assumed to be the Glauert downwash distribution inside the disc, and twice the mean downwash outside the disc,

$$\frac{V(z)}{\Omega R} = \lambda_0 \left(1 + E(x - x_h) \right)$$

or

$$\frac{V(z)}{\Omega R} = 2\lambda_0 \ .$$

The velocity due to the free stream is

$$\frac{V(z)}{\Omega R} = \mu_N$$

thus

$$z_f \approx z_p + \int_{x_D}^{x_f} \left\{ \frac{\mu_N}{\mu_T} + \frac{\lambda_0}{\mu_T} \left(1 + E(x - x_h) \right) \right\} dx \quad .$$

The fuselage flow field is normally calculated by a panel method but a simpler expression with an analytic form for the induced velocity is required to calculate the displacement of the vortices. A single source is used whose strength and position are chosen to match, as far as possible, the front of the fuselage. The induced velocity then becomes

$$\frac{V(z)}{\Omega R} = \left(\frac{d}{R}\right)^2 \frac{\mu_T}{16} \frac{z}{(x^2 + y^2 + z^2)^{3/2}}$$

and

$$\Delta z = \int_{x_p}^{x_f} \left(\frac{d}{4R}\right)^2 \frac{z}{(x^2 + y^2 + z^2)^{3/2}} \quad .$$

The vortex height, however, is an unknown function of x and the integral has to be solved iteratively.

Transforming from the fuselage axes to the original axes gives the distance the vortex has travelled vertically,

$$z_v = (x_f - x_h) \sin(i + a_1) \cos b_1 + y_f \sin b_1 + (z_f + \Delta_z - z_h) \cos(i + a_1) \cos b_1$$

and the distance between the point on the blade at which the induced velocity is required, z_i , and the vortex is

$$z_s = z_i - z_v + z_c$$

where z_i includes the blade precone, and z_c is a correction term to account for the difference between the assumed first harmonic flapping and the true blade flapping, and the difference between the flapping at the point on the blade and the flapping when the vortex was shed.

Several approximations have been made in the analysis to avoid lengthy iterations and the need to integrate along the path of the vortex, but the validity of the approach has been confirmed by flight measurements.

The main rotor of the Puma helicopter is well separated from the fuselage and the effect of including the fuselage flow field is smaller than for some other aircraft such as the Lynx. The inclusion of a more representative rotor induced velocity instead of the previously assumed mean value, however, does affect the displacement of the vortex rings. The change in the calculated bending moment at 75%R due to the distortion of the wake can be seen in Fig 8. There is generally an improvement in the correlation though the effect is not large. A bigger change occurs further inboard, Fig 9, but the improvement here is probably due more to the change in modal forcing from the different loading than from the distortion of the wake. The blade bending moment in the first quadrant is now well predicted, and the improvements on the retreating side arise from a further reduction of the fifth harmonic component, Table 1. The dip in the measured bending moment at about $180°$ azimuth was thought to come from the close passage of the tip vortex from the preceding blade which intersects the reference blade at about 50%R. The calculation, however, does not show this feature even though the vortex is now closer to the blade than in the previous calculation due to the reduction in the assumed induced velocity over the front of the disc.

5   THE INTERACTIVE NEAR WAKE

The most recent innovation to the wake model is the interactive near wake. The original model assumed only a first harmonic variation of the root and tip vortex strength which was not directly related to the spanwise load on the blade. This is no longer satisfactory for rotors in which a higher harmonic loading is deliberately introduced by aeroelastic tailoring or pitch input. The predicted load near the tip of the advancing side of the disc was also somewhat unrealistic since the trailing vortex could have a positive circulation strength while the load was negative. In reality, the vortex would change sign to give an upwash in the tip region which would reduce the magnitude of the negative loading. This has important consequences for swept tips where incorrectly predicted loads would give the wrong torsional response of the rotor. The interactive near wake was an attempt to correct for some of the deficiencies but the primary concern was that the efficiency of the method should not be compromised.

The method eventually adopted was to replace the half rings originating from the root and tip of the reference blade with more half rings distributed over the blade span as shown in Fig 10. The rest of the wake, *ie* the system of complete vortex rings, remained unchanged. The strength of the half rings is related to the blade load and therefore varies with azimuth, but at any given azimuth angle, the circulation does not vary along the ring, *ie* the history of the loading is neglected. This assumption is necessary to avoid integrating along every vortex at each azimuth angle which would take an excessive amount of computer time. The error however should be small as the velocity induced at the calculation points is dominated by the part of the ring closest to the blade and this has the correct strength.

The number of half rings used depends on the number of positions x_{b_j} specified on the blade where the aerodynamic characteristics are evaluated, Fig 10. The first station is always at the blade root, the last at the tip, with the load at both points set to zero. The blade is divided into N segments with x_{b_3} to x_{b_N} at the mid points of segments 2 to $N-1$. The first segment extends from the blade root to the point midway between x_{b_2} and x_{b_3}, and the last from the midpoint of $x_{b_{N-1}}$ and x_{b_N} to the tip. The trailing vortices originate from the tip of the blade and from the root of each segment. The strength of the first trailing vortex is Γ_1 corresponding to the load evaluated at x_{b_2}, and the strength of the tip vortex is Γ_N corresponding to the load evaluated at $x_{b_{N+1}}$. The strength of the intermediate vortices is related to the loads on adjacent segments.

The non-dimensional radius of each half ring is

$$x_{v_j} = x_j + \mu_T \sin \psi$$

where x_j is the origin of the vortex on the blade. The rings are therefore larger on the advancing side of the disc, smaller on the retreating side, and initially correspond to the spiral path.

The bound vorticity Γ_j on the blade at radial position j is

$$\Gamma_j = \mu_j c_j C_{L_j} \Big/ 2R$$

where C_{L_j} is the lift coefficient, μ_j the blade tangential velocity, and c_j the blade chord. The lift coefficient is determined by the blade pitch, the velocity terms, and the unsteady aerodynamic corrections, so that C_{L_j} can be written

$$C_{L_j} = a_j \left(\theta_j + t_j + \alpha_{u_j} + \frac{\lambda_{h_j} + \lambda_{c_j}}{\mu_j} - \alpha_0 \right)$$

where a_j is the aerofoil lift curve slope at the appropriate Mach number, θ_j is the blade pitch, t_j the blade twist, α_{u_j} is such that $a_j \alpha_{u_j}$ represents the lift increment due to unsteady effects, λ_{h_j}, λ_{c_j} are the induced velocities from the half rings (near wake) and complete rings (far wake), and α_0 is the zero lift angle. Separating the near wake velocity terms and substituting C'_{L_j} for the remainder of the expression gives

$$C_{L_j} = C'_{L_j} + a_j \lambda_{h_j} \Big/ \mu_j$$

and

$$\Gamma_j - a_j c_j \lambda_{h_j} \Big/ 2R = \mu_j c_j C'_{L_j} \Big/ 2R \quad .$$

The near wake velocity λ_{h_j} is the sum of the velocities induced by all the half rings,

$$\lambda_{h_j} = \sum_{k=1}^{N+1} \sigma_{jk} \gamma_k$$

where γ_k is the trailing vortex strength and $\sigma_{jk} \gamma_k$ is the velocity induced at the jth blade station by the kth trailing vortex. The trailing vortex strengths are related to the bound vortex strengths

$$\gamma_k = \Gamma_{k-1} - \Gamma_k$$

thus

$$\lambda_{h_j} = \sum_{k=1}^{N} (\sigma_{jk+1} - \sigma_{jk})\Gamma_k$$

and

$$\Gamma_j - \frac{a_j c_j}{2R} \sum_{k=1}^{N} (\sigma_{jk+1} - \sigma_{jk})\Gamma_k = \mu_j c_j C'_{L_j}\Big/2R \qquad j = 1,\ldots,N.$$

The bound vortex strengths can therefore be found from a solution of the N simultaneous equations. The influence coefficients σ_{jk} are particularly simple for a half vortex ring and can be evaluated analytically using elliptic integrals.

The interactive near wake has a considerable effect on the calculated bending moments, Figs 11 and 12. A disturbance is now apparent between 120° and 180° azimuth at 75%R, and the peak is sharper on the retreating side of the disc. Further inboard the changes are even more marked, Fig 12. The minimum bending moment is now correctly positioned at about $\psi = 100°$ and a small dip is visible between 180° and 240° azimuth. The predicted bending moment in the fourth quadrant is also much improved. Reference to Tables 1 and 2 shows that the harmonic content of the oscillations are better predicted; the third harmonic contribution in particular is now closer to the experimental values.

The two radial stations examined so far, 35%R and 75%R, were not chosen because they give the best comparison with experiment but because they are representative of the inboard and outboard sections of the blade. The interactive near wake generally gives an improvement over the whole blade. Comparisons at two other radial positions, 65%R and 83%R, are shown in Figs 13 and 14. The prediction using the original vortex ring model is included in Fig 13 so that the effect of all the changes made to the wake rather than the incremental change can be seen. The improvement in the correlation is quite dramatic considering that the dynamic model of the rotor has remained unaltered and the changes are due solely to the downwash distribution. The calculation made with the latest wake model only is shown in Fig 14 at 83%R. Agreement is excellent although the ninth harmonic component which is responsible for the ripple on the measured distribution is underestimated.

Attention has concentrated on the flatwise bending moment distributions since there were more measuring stations than for the other blade stresses. The torsion moment was recorded at only two radial positions and the edgewise bending moment at one position but comparisons with some of this data are made in Fig 15. The torsion moment is generally well predicted with only a slight error in the phase of the fifth harmonic component. The correlation with the edgewise bending moment, however, is not quite so good. The higher harmonic content is reasonably accurate, particularly the fourth, but the phasing of the first harmonic component is poor.

6   HUB FORCES AND MOMENTS

The loads transmitted to the fuselage by the rotor in the form of vibration are becoming increasingly important to operators of helicopters in all fields. Civil operations require helicopters to have the ride qualities of fixed wing aircraft while the military require low vibration levels to reduce the failure rate of delicate equipment and to provide a stable weapon platform. Vibration levels have reduced as the helicopter has matured but new requirements are becoming very demanding. The trend in the past has been to fit vibration absorbers to the blades and hub or to isolate the rotor system from the fuselage to allow only steady forces to be transmitted. The need for such devices could be obviated or reduced if the vibration levels could be accurately predicted in the design stage when remedial action is easier to take. Predicting vibration levels requires accurate modelling of the rotor and fuselage since the two cannot be treated in isolation. The forcing from the rotor is the predominant ingredient however and reliable methods are essential. This section examines how the ability to predict the hub forces and moments has progressed over the past ten years or so. The helicopter considered is the Westland Lynx and the comparisons will cover all the advances made in modelling both the dynamics and aerodynamics of the rotor.

The measured and calculated fixed co-ordinate 4Ω hub forces and moments are compared in Figs 16 and 17. The calculations were made at only two speeds, 122 and 161 knots, using two methods. The first generation analysis did not include unsteady aerodynamics or fuselage effects and had a fairly simple dynamic representation of the blade. The aerofoil section was constant along the blade and the induced velocity was calculated with the original vortex ring model. The second generation rotor analysis is described in the Appendix. The calculations shown in Figs 16 and 17 included unsteady aerodynamics, fuselage effects, and employed the interactive near wake model. The hub moments are more accurately predicted with the new calculation method. The trend with increasing forward speed for the pitching moment in particular is closer to the measurements. The hub forces show a similar improvement with the exception of the longitudinal shear, Fig 17. Further investigation is needed to determine the reason for this but previous calculations for the Lynx have shown that the in-plane shears are very sensitive to the representation of the fuselage and some improvements may be required. The second lag mode frequency could also be in error since no allowance was made for flexibility in the gear box and the calculated mode frequency could be too high. With this one possible exception, therefore, the prediction of vibratory forces and moments have become more accurate. The improved

level of correlation, however, cannot be ascribed to any particular change in the methods or wake model. All the refinements in the second generation analysis have made a contribution, thus reliable estimates of rotor vibrational levels need detailed attention to all aspects of the rotor dynamics and aerodynamics.

7   FUTURE DEVELOPMENTS

One of the main advantages of the vortex ring method is its computational efficiency. A typical calculation to evaluate the induced velocity at 800 points requires only 15 seconds on a VAX 11/780 computer. It is therefore difficult to envisage any further major changes to the model that does not compromise this efficiency. One possible minor change that would not increase the processor time significantly, would be to vary the size of the vortex rings in the far wake more smoothly. At present the rings are large on the advancing side of the disc and small on the retreating side with an abrupt change at $\psi = 0°$ and $180°$. A better representation might be obtained by calculating the size of the rings to match the curvature of the spiral wake at the blade-vortex intersection points. The current model, however, has been shown to be accurate enough for day to day calculations and perhaps what is needed is a completely new and more thorough treatment of the wake for use on those occasions when greater accuracy is required.

8   CONCLUDING REMARKS

The development of the vortex ring wake model has been traced from its conception over ten years ago to the present day. The predicted bending moments for the Puma blade were compared with flight test measurements at each stage to demonstrate the effect of the improvements. The current version of the wake model gives quite accurate predictions of the blade stresses, and comparisons with the hub forces and moments measured on the Lynx helicopter have shown an improved capability to estimate rotor vibrational levels.

REFERENCES

1   S.G. Sadler: "Development and application of a method for predicting rotor free wake positions and resulting blade air loads." Vol.1 - Model and results, NASA CR-1911, 1971

2   C.V. Cook: "Induced flow through a helicopter rotor in forward flight." WHL Research Paper 374, 1970

3   T.S. Beddoes: "Retreating blade stall flutter." WHL Research Paper 531, 1976

4   R.V. Smith: "Some effects of wake distortion due to a fuselage flow field on rotor thrust limits." ARO Workshop on rotor wake technology, 1979

Table 1

HARMONIC CONTENT OF THE BENDING MOMENT AT 35%R, μ = 0.32

	Measured	Glauert	Original vortex ring	Improved vortex ring	Improved vortex ring + fuselage	Interactive near wake
a_1	203	192	140	204	268	204
b_1	-257	-302	-328	-317	-302	-276
a_2	-24	99	69	67	29	48
b_2	123	191	141	178	204	110
a_3	-44	52	27	78	1	-82
b_3	228	-11	-12	8	68	140
a_4	25	0	-40	14	7	21
b_4	8	1	-5	-16	3	13
a_5	-28	-58	-64	-71	-18	16
b_5	-31	80	160	45	24	-34

Table 2

HARMONIC CONTENT OF THE BENDING MOMENT AT 75%R, μ = 0.32

	Measured	Glauert	Original vortex ring	Improved vortex ring	Improved vortex ring + fuselage	Interactive near wake
a_1	223	253	252	274	312	197
b_1	-311	-338	-374	-350	-334	-265
a_2	-279	-114	-229	-160	-189	-201
b_2	24	75	6	57	61	-39
a_3	-63	100	80	118	56	-11
b_3	230	48	26	74	125	158
a_4	-80	28	49	-11	-22	-63
b_4	69	12	48	51	26	22
a_5	6	14	15	7	21	49
b_5	48	60	-13	44	52	25

Appendix

A BRIEF DESCRIPTION OF THE RAE/WHL ROTOR ANALYSIS

The new rotor analysis used to make the calculations presented was developed jointly by WHL and RAE. The method of calculating the blade modes and the forced response equation were derived by WHL while RAE interfaced the dynamics and aerodynamics and wrote the main computer program for solving the equations of motion and calculating the blade loads.

The analysis will treat a very general blade with various root conditions and secondary load paths. The locus of shear centres consists of a series of straight lines orientated in any direction so that kinked blades can be represented. Each secondary load path can be modelled by up to three rotational and three linear springs either attached to the blade or located at the end of weightless arms. Point flexibilities set anywhere in the blade are also allowed. The blade root may be either built-up or hinged in up to three mutually perpendicular directions with or without restraint. A lumped mass approximation is not used and the equations for the blade modes are solved by integrating from the root to the tip with the appropriate transformations being made whenever there is a discontinuity in the orientation of the shear centre. The modes can also be calculated with steady loads imposed.

The forced response equation is fully compatible with the modes and is correct to second order. The equation is solved by a forward integration scheme based on the Z-transform in which the blade is cycled around the azimuth until the modal displacements converge. Unsteady aerodynamics are included with two models of the dynamic stall process, and up to eight aerofoil sections are allowed along the span of the blade. Fuselage effects, as described in section 4, are modelled and various downwash options are available including the interactive near wake. Blade and hub loads are presently calculated by modal summation but force integration is being considered as an alternative.
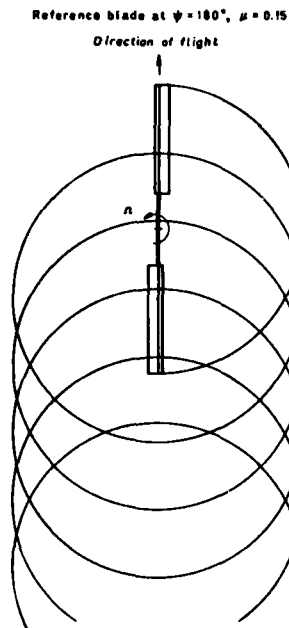
Fig 1 Disposition of the vortex rings in the original model
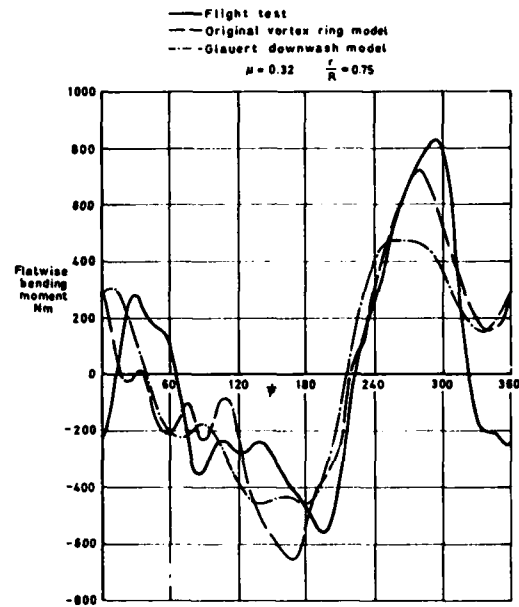
Fig 2 Flatwise bending moment calculated with the original vortex ring model and Glauert downwash compared with experiment
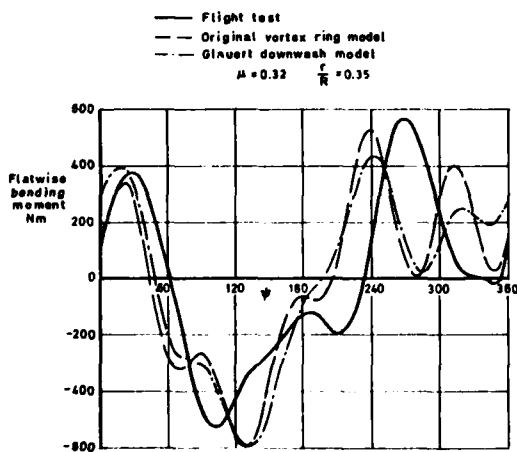
Fig 3 Flatwise bending moment calculated with the original vortex ring model and Glauert downwash compared with experiment
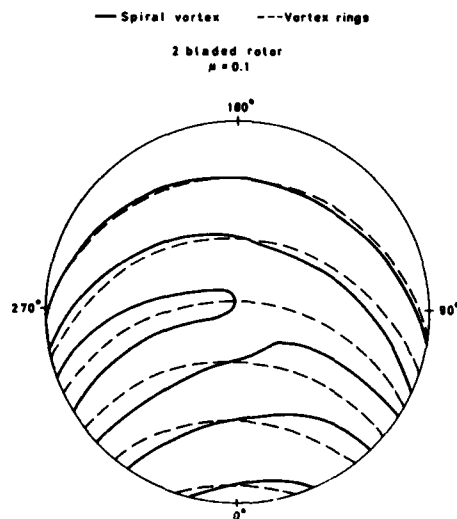
Fig 4 Blade-vortex intersection points
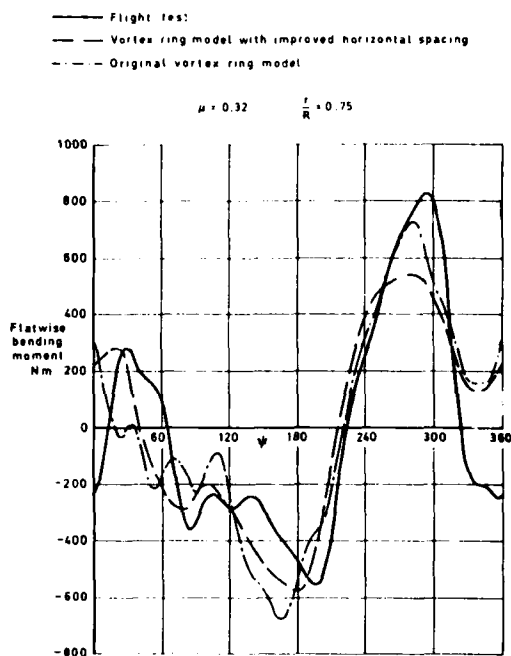
Fig 5 Measured flatwise bending moment compared
with those calculated by the improved and
original vortex ring models

Fig 6 Measured flatwise bending moment compared
with those calculated by the improved and
original vortex ring models
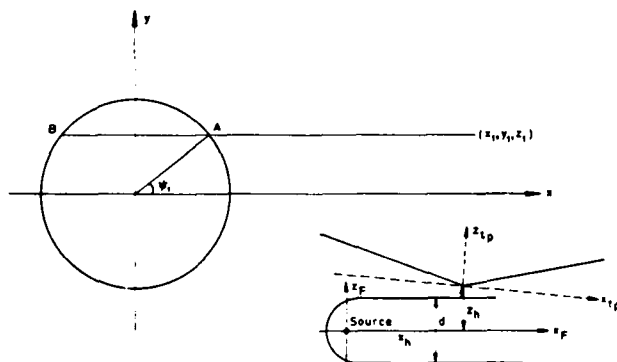
Fig 7 Geometry to evaluate the vertical displace-
ment of a tip vortex

Fig 8 Measured flatwise bending moment compared
with those calculated by the improved
vortex ring model with and without
fuselage effects
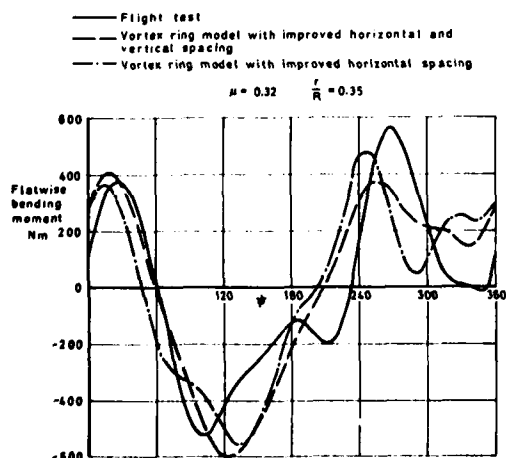
Fig 9 Flatwise bending moment calculated with and
without fuselage effects compared to flight
test

Fig 10 Bound and trailing vortex strengths for the interactive near wake

Fig 11 Flatwise bending moment calculated with the interactive wake model compared to flight test

Fig 12 Flatwise bending moment calculated with the interactive wake model compared to flight test

Fig 13 Effect of all the changes in the vortex ring model on the predicted bending moment distribution

Fig 14 Measured and calculated bending moment at 83%R

Fig 15 Calculated and measured torsion moment and edgewise bending moment
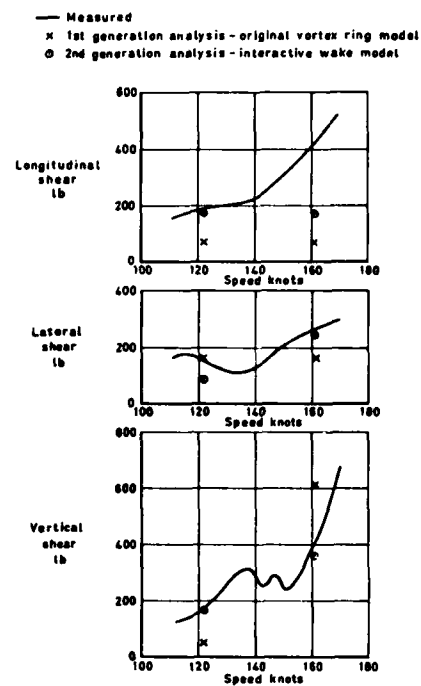
Fig 17 Calculated and measured fixed coordinate 4Ω shear forces at the hub for the Lynx
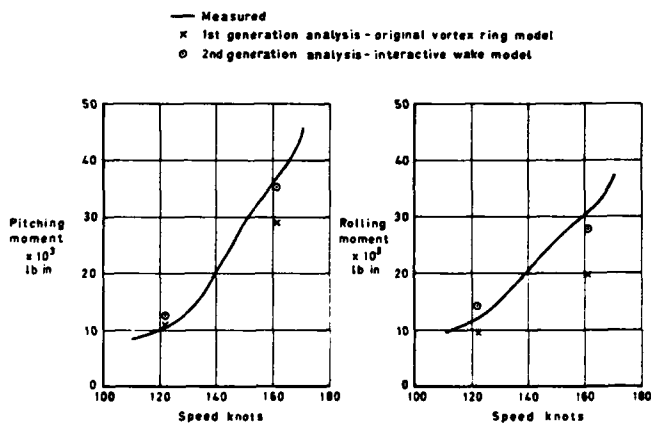
Fig 16 Measured and calculated fixed coordinate 4Ω hub moments for the Lynx

EQUILIBRE AEROELASTIQUE D'UN ROTOR D'HELICOPTERE EN PRESENCE

DE FORCES AERODYNAMIQUES NON LINEAIRES

par Jean-Joël COSTES

Office National d'Etudes et de Recherches Aérospatiales (ONERA)
92320 Châtillon (France)

RESUME

        Un code de calcul incluant les couplages aéroélastiques en fluide
décroché est représenté dans cet article. Le point le plus important est la
modification de l'aérodynamiques tridimensionnelles linéaire pour y inclure
les phénomènes de décrochage. Les forces aérodynamiques non linéaires provien-
nent de modèles mathématiques pour des profils bidimensionnels. Diverses mani-
pulations permettent d'aboutir à un système non linéaire unique dont on peut
trouver une solution approchée par une méthode pas à pas. Quelques comparaisons
théorie-expérience sont données en exemple.

AEROELASTIC EQUILIBRIUM OF AN HELICOPTER ROTOR

WITH NON LINEAR AERODYNAMIC FORCES

SUMMARY

        This paper presents a computer code which includes aeroelastic cou-
plings for stalled flight cases. A key point is the modification of the clas-
sical linear aerodynamics to include stall. The non linear forces are given by
some available mathematical models. After a few manipulations, one obtains a
single non linear system of equations, written in a form suitable for a step
by step resolution. As a matter of example, a few comparisons between theory
and experiment are given.

I - INTRODUCTION

Le but de cet article est de présenter un code de calcul incluant les couplages aéroélastiques sur un rotor d'hélicoptère, en tenant compte du décrochage éventuel sur la pale reculante. On examinera en premier lieu un exemple d'équations de la mécanique des pales. Ces équations sont quasi linéaires en fonction des portances même non linéaires. L'aérodynamique examinée ensuite est fondée sur le potentiel d'accélération en fluide compressible. Les pales sont schématisées par une ligne portante au 1/4 avant, l'influence de tous les sillages est incluse. Cette théorie linéaire est modifiée pour prendre en compte les résultats expérimentaux bidimensionnels sur profils décrochés. Le système non linéaire complet, incluant les couplages aéroélastiques, est transformé par diverses manipulations pour une résolution plus aisée à l'aide d'une méthode de Newton généralisée.

II - EQUATIONS DE LA MECANIQUE DES PALES

Les pales des rotors d'hélicoptères actuels sont attachées au moyeu par des articulations complexes, qui permettent des mouvements de battement et de traînée aussi bien que des rotations adaptant le calage de la pale aux paramètres de vol désirés. La commande de pas impose des mouvements cycliques actuellement limités au premier harmonique, mais susceptibles dans le futur de comporter des harmoniques de rang supérieur. Dans les rotors classiques, les mouvements de battement et de traînée se font autour d'articulations rigides, mécaniquement complexes et coûteuses à l'entretien.

Les moyeux futurs seront en matériaux stratifiés souples assurant les divers mouvements, mais dans tous les cas, on peut supposer en première approximation, que la partie empennée de la pale se comporte comme un corps rigide. Il est ensuite possible de rajouter autour du mouvement de corps rigide des déformations élastiques de faibles amplitude, pour tenir compte de la souplesse de la pale. Pour simplifier l'exposé du problème, on se limitera au cas d'une pale rigide articulée en battement et en traînée. Les repères de référence sont donnés figure 1. L'axe de battement est $O_1 x_1$ et l'axe de traînée est $O_2 z_2$. La pale peut changer de calage par rotation autour de l'axe $O_2 y_2$. Si on suppose les angles de battement β et de traînée θ petits, en négligeant les forces d'inertie engendrées par le pas cyclique, les équations de Lagrange fournissent le système différentiel régissant le mouvement de la pale. Ce système se réduit ici à deux équations linéaires :

Système 1
$$\begin{cases} \ddot{\beta} I_{xx} + \Omega^2 \beta (I_{33} - I_{yy} + \mathcal{M}_s n_b) = -\mathcal{M}_s g + \mathcal{C}_1(t) \\ \ddot{\theta} \mathcal{J}_{33} + \Omega^2 \theta \mathcal{M}_{y_6} (n_b + n_t) = \Omega^2 \mathcal{M} x_6 (n_b + n_t) + \mathcal{C}_2(t) \end{cases}$$

où l'on a : n_b distance OO_1 , n_t distance $O_1 O_2$

I_{xx} = inertie de la partie empennée + manchon $O_1 O_2$ autour de l'axe de battement

I_{yy} = inertie de la partie empennée + manchon $O_1 O_2$ autour de l'axe longitudinal (inertie faible)

I_{33} = inertie de la partie empennée + manchon $O_1 O_2$ autour de l'axe $O_1 z_1$ $(I_{33} \simeq I_{xx})$

$\mathcal{M}_s$ = moment statique de la partie empennée + manchon autour de l'axe de battement

$\mathcal{J}_{33}$ = inertie de la partie empennée autour de l'axe $O_2 z_2$

$\mathcal{M}_{y_6}$ = moment statique de la partie empennée autour de l'axe $O_2 z_2$

$\mathcal{C}_1 \, et \, \mathcal{C}_2$ = forces aérodynamiques généralisées.

Ce système n'est valable que pour de petits mouvements du fait de la linéarisation. On peut le compléter en supposant de petits mouvements autour d'un mouvement de grande amplitude connu, ce qui introduit des termes correctifs non linéaires au deuxième membre. La solution approchée du système 1 s'obtient comme suit : On suppose le régime établi, les travaux des forces aérodynamiques aussi bien que les éventuels termes correctifs non linéaires deviennent périodiques avec la période de rotation du rotor. On suppose le contenu harmonique des termes du 2ème membre limités à un ordre peu élevé (dans les calculs présentés : 6). Le système différentiel est linéaire et à coefficients constants et de ce fait les fonctions inconnues $\beta(t)$ et $\theta(t)$ ont également une décomposition harmonique limitée à l'ordre 6. On pose par exemple :

(2)
$$\beta(t) = a_0 + a_1 \cos \psi + a_2 \sin \psi + \ldots + a_{11} \cos 6\psi + a_{12} \sin 6\psi$$

$$\theta(t) = b_0 + b_1 \cos \psi + b_2 \sin \psi + \ldots + b_{11} \cos 6\psi + b_{12} \sin 6\psi$$

$\psi = \Omega t + \varphi$ est la position azimutale de la pale

On exprime ensuite le système 1 en 13 positions azimutales équidistantes, c'est-à-dire en 13 instants t, ce qui donne le système matriciel suivant :

$$\begin{bmatrix} K \end{bmatrix} \begin{bmatrix} a_0 \\ \vdots \\ a_{12} \\ b_0 \\ \vdots \\ b_{12} \end{bmatrix} = \begin{bmatrix} \mathcal{C} \end{bmatrix}$$

Dans le cas simplifié exposé ici la matrice K est creuse, dans le cas général où les équations en β et θ sont couplées, la matrice K est pleine. On peut aussi avoir d'autres mouvements de pales et des déformations élastiques mais K reste à coefficients constants. Le deuxième membre comporte aussi bien les travaux des forces aérodynamiques, que d'éventuels termes correctifs introduits pour tenir compte des non linéarités dues aux amplitudes finies des mouvements. Ce système matriciel est de dimension réduite ce qui rend sa résolution aisée. On obtient :

$$(3) \qquad \begin{bmatrix} a_o \\ \vdots \\ a_{12} \\ b_o \\ \vdots \\ b_{12} \end{bmatrix} = \begin{bmatrix} K^{-1} \end{bmatrix} \begin{bmatrix} \mathscr{C} \end{bmatrix}$$

De ce fait le mouvement de la pale autour d'une solution approchée $\beta_o(t)$, $\theta_o(t)$ donnée, s'exprime linéairement en fonction des forces aérodynamiques. Si un état d'équilibre approché n'est pas connu, on peut tout d'abord supposer $\beta_o = \theta_o = 0$, résoudre (3) et linéariser ensuite autour de ce premier mouvement. Les termes correctifs non linéaires sont faibles et n'entrainent aucun problème de stabilité. Le système (3) est sous cette forme bien adapté pour l'élimination des inconnues $\beta(t)$ et $\theta(t)$ entre les équations de la mécanique et celles de l'aérodynamique exposées dans les deux chapîtres suivants.

III - AÉRODYNAMIQUE LINÉAIRE

III.1 - Détermination de la portance

Les calculs d'aérodynamique linéaire forment la base de la méthode de calcul des charges aérodynamiques et doivent fournir les corrections tridimensionnelles dans les cas non linéaires étudiés au chapître suivant. On trouvera en référence (1) et (3) un exposé complet de la méthode. Celle-ci est dérivée des travaux sur la stabilité aéroélastiques des avions, elle utilise le potentiel d'accélération et une schématisation par ligne portante unique. On définit une surface hélicoïdale engendrée par une ligne qui se déplace en se translatant et en tournant (voir figure 2). On choisit ordinairement la ligne du 1/4 avant, qui est aussi l'axe de pas, les mouvements de battement et de traînée sont négligés, on ne retient que la rotation et la translation d'ensemble du rotor. La surface engendrée sera prise comme une zone de discontinuité pour la vitesse du fluide. La partie empennée de la pale est rabattue sur la surface hélicoïdale et se projette à l'instant t sur la surface Σ qui porte, dans le cas général, une répartition surfacique de doublets de pression. Du fait de l'approximation par ligne portante unique, les doublets de pression sont concentrés sur une seule ligne situé au 1/4 avant de la pale. Comme cette même ligne engendre le sillage, on évite les déformations de Σ au cours du temps. Les points de collocation, où l'on calcule la vitesse normale induite, sont situés au 1/4 arrière de la pale et projettés sur le sillage. On exprime en ces points de collocation les relations habituelles de glissement instationnaire, en tenant compte cette fois de tous les mouvements de la pale : conicité, battement, traînée, torsion, déformations élastiques. La portance le long de la pale est décomposée, avec des coefficients à déterminer, sur une base de fonctions dépendant de la position radiale et du temps. On a choisi :

$$(4) \qquad F(r,t) = \sqrt{1-\eta^2} \left[\sum_{i=1}^{n} Z_i \, L_i(r) + \sum_{i=1}^{n} \sum_{j=1}^{m} X_{ij} \, L_i(r) \cos j\psi + \sum_{i=1}^{n} \sum_{j=1}^{m} Y_{ij} \, L_i(r) \sin j\psi \right]$$

avec
$$\eta = \frac{2r - R_1 - R_o}{R_1 - R_o} \qquad ; \qquad \psi = \Omega t + \varphi$$

r coordonnée radiale $\qquad R_o, R_1$ coordonnée radiale des extrémités de la pale

$L_i(r)$ est un polynôme de Lagrange égal à 1 pour le coordonnée radiale r_i.

n = nombre total de polynômes de Lagrange ($n = 5$)

m = nombre d'harmoniques ($m = 6$)

ψ est l'azimut de la pale, φ est une constante dépendant de la pale considérée. Les forces aérodynamiques étant périodiques et les mêmes pour toutes les pales, un simple déphasage donne dans (4) la portance pour chacune des pales.

Les Z_i, X_{ij}, Y_{ij} sont des coefficients inconnus au nombre total de 65 pour les applications numériques envisagées. Ces coefficients sont assez mal adaptés aux futurs calculs non linéaires, car ils n'ont pas d'interprétation physique immédiate. Si on considère $(2m+1)$ positions azimutales équidistantes de la pale (figure 3) et en chaque azimut la valeur de la portance F aux n positions radiales r_i déjà utilisée pour les polynômes de Lagrange, les $n(2m+1)$ valeurs de F peuvent être utilisées en lieu et place des Z_i, X_{ij}, Y_{ij}. On aura dans un classement déterminé :

$$(5) \qquad \begin{bmatrix} F_1 \\ \vdots \\ F_{n(2m+1)} \end{bmatrix} = \begin{bmatrix} C \end{bmatrix} \begin{bmatrix} Z \\ X \\ Y \end{bmatrix}$$

C étant une matrice de changement de base non singulière.

Chaque fonction de base telle que $L_i(r) \cos j\psi$ induit dans l'espace des vitesses dépendant du temps et du point considéré. On calcule la composante normale au sillage pour les $n(2m+1)$ points de collocation; points du 1/4 arrière de la pale pour les $(2m+1)$ positions azimutales équidistantes déjà citées. Cette composante de vitesse normale est calculée pour chacune des fonctions de base, ce qui donne en définitive une matrice $[A_e]$ de coefficients d'influence. Du fait de la linéarité, la vitesse induite totale W est la somme des vitesses induites par chaque fonction de base. On aura l'équation matricielle suivante :

$$(6) \qquad \begin{bmatrix} A_e \end{bmatrix} \begin{bmatrix} Z \\ X \\ Y \end{bmatrix} = \begin{bmatrix} W \end{bmatrix}$$

et par combinaison avec (5), en posant $[A] = [A_e][C^{-1}]$ on a :

(7)
$$\begin{bmatrix} & & \\ & A & \\ & & \end{bmatrix} \begin{bmatrix} F_1 \\ \vdots \\ F_q \end{bmatrix} = \begin{bmatrix} W_1 \\ \vdots \\ W_q \end{bmatrix}$$

où l'on a posé $q = n(2m+1)$

Dans (7) le vecteur deuxième membre $[W]$ est donné par le condition de glissement. Pour le rotor à pales rigides articulé en battement et en traînée, à une distance radiale r et à une position azimutale ψ donnée, W est la projection de la vitesse de la pale sur la normale locale.

(8)
$$W = \left(-U_\infty \cos\Lambda \sin\psi \sin i - \Omega r \sin i + U_\infty \sin\Lambda \cos i\right) + \beta\left(U_\infty \cos\Lambda \cos\psi \cos i - \Omega r_L\right)$$
$$+ \dot\beta (r - r_b)\cos i + \theta\left(-U_\infty \cos\Lambda \cos\psi \sin i\right) - \dot\theta (r - r_b - r_t)\sin i$$

avec i fonction donnée de r et de t et $\psi = \Omega t + \varphi$

Il suffit de remarquer que dans (8) interviennent les inconnues donnant le mouvement de la pale, ici β et θ , leurs dérivées $\dot\beta$ et $\dot\theta$, ainsi qu'un terme d'excitation forcée connue. Comme au chapître précédent on décompose $\beta(t)$ et $\theta(t)$ en série de Fourier suivant les relations (2). Ainsi le vecteur colonne $[W]$ peut s'écrire sous la forme :

(9)
$$\begin{bmatrix} W_1 \\ \\ W_q \end{bmatrix} = \begin{bmatrix} W_{01} \\ \\ W_{0q} \end{bmatrix} + \begin{bmatrix} & & \\ & W_{ij} & \\ & & \end{bmatrix} \begin{bmatrix} a_0 \\ \vdots \\ a_n \\ b_0 \\ \vdots \\ b_n \end{bmatrix}$$

Si le mouvement de la pale est connu, par exemple mesuré au cours d'une expérience, on calcule le vecteur colonne $[W]$ par la relation matricielle (9) et en reportant dans (7) on obtient un système d'équations linéaires dont la résolution fournit la colonne des forces F_j .

III.2 - Détermination de la portance et de la traînée

Dans le cadre d'une théorie linéarisée au 1er ordre, une surface nommée sillage est une zone de discontinuité pour les vitesses normales. Une partie Σ de cette surface est à l'instant t une zone de discontinuité pour la pression. L'élément de surface Σ est la projection de la surface portante sur le sillage. La surface portante est supposée très voisine de Σ (infiniment petit du premier ordre), on ne peut donc faire de distinction entre un saut de pression sur Σ ou sur la surface portante. En outre, les pressions au bord d'attaque ne pouvant être justifiables d'une théorie linéarisée, on ne peut avoir d'effet de succion, ce qui exclu un calcul rigoureux des traînées de portance. Comme celles-ci sont nécessaires pour obtenir la puissance à fournir pour faire tourner le rotor, on est ammené à compléter les résultats de la théorie linéaire par des extensions semi-empiriques dont l'origine remonte à Prandtl. On fait l'hypothèse suivante :

La surface portante se comporte localement comme un profil bidimensionnel, lorsque l'on tient compte des influences de tous les sillages tourbillonnaires, en particulier le paradoxe de d'Alembert est vérifié, la portance est normale à la vitesse locale. Sous une autre forme celà revient à dire que pour un profil bidimensionnel à l'incidence α_p la force de portance F est inclinée de l'angle α_p vers le bord d'attaque par rapport à la normale à l'axe neutre (voir figure 4). Ceci n'est valable que pour un profil non décroché, dans un fluide non visqueux et en stationnaire.

Dans la théorie du potentiel d'accélération appliquée aux rotors d'hélicoptère on peut obtenir une bonne valeur pour le module de $F(r,t)$, au moins lorsque les hypothèses de linéarisation sont valables (rotor peu chargé). La portance varie en fonction de la position azimutale de la pale, mais les fréquences réduites restent très modérées, ce qui permet de faire une hypothèse quasi stationnaire. Connaissant le module de la portance et la vitesse normale locale V_T due principalement à la rotation de la pale et à la translation de l'hélicoptère, on détermine $\alpha_p(r,t)$ par la relation :

(10)
$$\alpha_p(r,t) = \frac{F(r,t)}{\pi \rho c V_T^2} \cdot \sqrt{1 - M_T^2}$$

M_T étant le nombre de Mach local.

A son tour la relation (10) permet de définir l'orientation de la portance F (r,t) par rapport à la normale au profil laquelle est déterminée par la forme géométrique de la pale et son mouvement au cours du temps. On peut également rajouter une force de traînée de frottement T dirigée suivant l'axe neutre avec :

$$T = \frac{1}{2} \rho c V_T^2 C_x \qquad C_x \simeq 0,01$$

III.3 - Solution du problème couplé

Dans le cas général, les forces aérodynamiques aussi bien que le mouvement de la pale sont inconnus. Si l'on reprend l'exemple simple d'une pale rigide articulée en battement et en traînée, on peut maintenant expliciter dans le système 1 les travaux des forces aérodynamiques.

On aura en négligeant les traînées de frottements :

(11)
$$\mathcal{G}_1(t) = \int_{R_o}^{R_1} (r - r_t) \, F(r,t) \cos(i - \alpha_P) \, dr$$

$$\mathcal{G}_2(t) = -\int_{R_o}^{R_1} (r - r_b - r_t) \, F(r,t) \sin(i - \alpha_P) \, dr$$

$i(r,t)$ est le calage du profil local déterminé par le vrillage de la pale et le pas cycli-
que. L'incidence aérodynamique α_P n'est pas connue et sa détermination par la formule (10) conduit à des
non linéarités. On sait que α_P est un angle de quelques degrés et on le déterminera par un calcul pas à
pas. Au premier pas on prend $\alpha_P = 0$ et on calcule $F(r,t)$ suivant la méthode qui sera exposée plus loin, par
(10), on obtient une valeur approchée de $\alpha_P(r,t)$ et on fait ensuite une nouvelle détermination de $F(r,t)$.
Les calculs convergent sans aucune difficultés, seul le mouvement de traînée étant mal estimé au premier
pas.

Supposons que l'on ait une valeur approchée $\alpha_{P_o}(r,t)$ pour $\alpha_P(r,t)$, il faut ensuite remplacer
dans (11) $F(r,t)$ par sa valeur déduite de (4). A un instant t donné, on effectue les intégrations suivant
la distance radiale r, les travaux $\mathcal{G}_1(t)$ et $\mathcal{G}_2(t)$ sont alors des fonctions linéaires des coefficients Z, X, Y.
En exprimant ces relations pour les $(2m+1)$ valeurs de l'azimut déjà citées, le vecteur colonne $[\mathcal{G}]$ du
système (3) devient :

(12)
$$\begin{bmatrix} \mathcal{G} \end{bmatrix} = \begin{bmatrix} \mathcal{G}_o \end{bmatrix} + \begin{bmatrix} T_{ij} \end{bmatrix} \begin{bmatrix} Z \\ X \\ Y \end{bmatrix}$$

Dans la relation matricielle (12), le vecteur colonne $[\mathcal{G}_o]$ et la matrice $[T_{ij}]$ sont connus. Le
vecteur colonne des Z, X, Y est à déterminer, mais il est équivalent d'utiliser les $n(2m+1)$ valeurs de
F. Par combinaison avec (5) la relation (12) devient :

(13)
$$\begin{bmatrix} \mathcal{G} \end{bmatrix} = \begin{bmatrix} \mathcal{G}_o \end{bmatrix} + \begin{bmatrix} T_{ij} \end{bmatrix} \begin{bmatrix} C^{-1} \end{bmatrix} \begin{bmatrix} F_1 \\ \vdots \\ F_q \end{bmatrix}$$

Les équations de la mécanique traduites par le système (3) deviennent maintenant :

(14)
$$\begin{bmatrix} a_o \\ \vdots \\ a_{12} \\ b_o \\ \vdots \\ b_{12} \end{bmatrix} = \begin{bmatrix} K^{-1} \end{bmatrix} \begin{bmatrix} \mathcal{G}_o \end{bmatrix} + \begin{bmatrix} K^{-1} \end{bmatrix} \begin{bmatrix} T_{ij} \end{bmatrix} \begin{bmatrix} C^{-1} \end{bmatrix} \begin{bmatrix} F_1 \\ \vdots \\ \vdots \\ F_q \end{bmatrix}$$

Les équations (14) déterminent le mouvement de la pale en fonction des efforts en $n(2m+1)$
points du disque rotor. Il suffit maintenant de combiner les systèmes linéaires (7), (9) et (14) pour ob-
tenir le nouveau système :

(15)
$$\left[\begin{bmatrix} A \end{bmatrix} - \begin{bmatrix} W_{ij} \end{bmatrix} \begin{bmatrix} K^{-1} \end{bmatrix} \begin{bmatrix} T_{ij} \end{bmatrix} \begin{bmatrix} C^{-1} \end{bmatrix} \right] \begin{bmatrix} F_1 \\ \vdots \\ F_q \end{bmatrix} = \begin{bmatrix} W_{o1} \\ \vdots \\ W_{oq} \end{bmatrix} + \begin{bmatrix} W_{ij} \end{bmatrix} \begin{bmatrix} K^{-1} \end{bmatrix} \begin{bmatrix} \mathcal{G}_o \end{bmatrix}$$

Tous les termes du système (15) sont connus ce qui détermine la valeur des forces de portance.
On reporte ensuite dans (14) pour avoir le mouvement de la pale et dans les équations appropriées pour obte-
nir les performances globales du rotor. Les faibles non linéarités, d'origine aérodynamique comme α_P et la
traînée de frottement, ou d'origine mécanique, mouvements importants en battement et en traînée, amortisseurs
etc..., nécessitent quelques pas de calcul pour la détermination précise des forces de portance. L'expérien-
ce acquise en ce domaine permet de dire combien de calculs sont suffisants. On n'a jamais rencontré de dif-
ficultés de convergence pour l'aérodynamique linéaire avec la méthode qui vient d'être exposée.

III.4 - Exemple de résultats

Un rotor expérimental de la SNIAS, à pales rigides articulées en battement et en traînée sans
pas cyclique, a été essayé à Modane en Juillet 1970 dans la soufflerie S1. Bien que ces expériences soient
déjà anciennes elles constituent encore la base des confrontations théorie-expérience, aussi bien pour l'aé-
rodynamique linéaire que dans les cas avec décrochage sur la pale reculante. Quatre sections de la pale ont
été instrumentées, chacune comporte 10 capteurs différentiels et la portance intégrée est normalisée par rap-
port à la pression statique en veine P_o. Le cas de vol présenté en figure 5 a un rapport d'avancement de
$\mu = 0,44$. Un rapport d'avancement aussi élevé est considéré comme limite pour la théorie linéarisée avec li-
gne portante unique. De plus, l'étendue du cercle d'inversion devient importante. A l'intérieur du cercle
d'inversion et dans son voisinage, les vitesses de la pale sont faibles ce qui a conduit à supposer la for-
ce de portance nulle à cet endroit. Le manque de résultats expérimentaux dans le cercle d'inversion ne per-
met pas de meilleures hypothèses. En particulier, il aurait été utile de pouvoir estimer les traînées. En
dépit de toutes les approximations, la comparaison théorie-expérience reste encore acceptable. Le niveau des
forces est assez bien prévu, mais l'analyse harmonique met en évidence des erreurs importantes sur les phases.

La méthode qui vient d'être exposée peut être étendue au cas d'une pale flexible. Des expériences ont été réalisées en vol sur un hélicoptère d'essai de la SNIAS, le SA 349Z Gazelle. Les pales étaient instrumentées avec des jauges de contraintes. Un étalonnage des jauges a été réalisé à l'ONERA en relevant la réponse de ces jauges aux modes propres de la pale encastrée au mur. Au cours du vol le mouvement de la tête du rotor a été mesuré par des accéléromètres, il peut ß+re introduit comme donnée dans les calculs. La comparaison entre la théorie et l'expérience porte sur l'évolution le long de la pale des ampl'-tudes des harmoniques des moments de battement. La figure (6) extraite de la référence 5 donne un exc.aple type de résultats.

IV - AERODYNAMIQUE NON LINEAIRE

IV.1 - Aérodynamique stationnaire bidimensionnelle

A - Etude expérimentale - Incidence du profil

L'incidence aérodynamique du profil est par définition en bidimensionnel stationnaire, l'angle entre la direction du vent à l'infini amont et l'axe de portance nulle. Si on convient de définir le calage ou incidence géométrique du profil comme étant l'angle entre l'axe de portance nulle et l'axe de la soufflerie.les deux incidences géométriques et aérodynamiques sont confondues.Pour des profils minces, des incidences aérodynamiques petites et des vitesses modérées, la portance est indépendante du profil considéré. Par contre, lorsque l'incidence augmente des décollements apparaissent et chaque profil est caractérisé par une courbe de C_{zo} stationnaire (voir figure 7). Si le sillage et la zone décollée au-dessus du profil (voir figure 8) ont des épaisseurs qui restent modérées, tout se passe comme s'il existait pour le profil un nouvel axe neutre dont l'incidence aérodynamique serait plus faible. Pour ce nouvel axe neutre, les formules linéaires seraient valables. On pourrait en particulier calculer les vitesses induites comme en aérodynamique linéaire et appliquer une condition de glissement pour le nouvel axe neutre fictif du profil décroché.

B - Définition de l'incidence efficace

On cherche à traduire, dans une formulation mathématique, les hypothèses physiques données plus haut pour un profil décroché.

Soit un profil à l'incidence aérodynamique α_p . En l'abscence de décollements, la force de portance par unité de longueur F est donnée par la formule 16.

$$(16) \qquad F = \pi \rho c \, V_\infty^2 \frac{\alpha_p}{\sqrt{1-M^2}}$$

c est la corde du profil, M le nombre de Mach, ρ la masse volumique du fluide non perturbé.

Si l'incidence aérodynamique α_p est grande, on mesurera une force $\overline{F}$ inférieure à F du fait des décollements. On considère alors F comme engendrée par un profil fictif calé à l'incidence aérodynamique $\alpha_{peff.}$ telle que :

$$(17) \qquad \alpha_{peff.} = \frac{\overline{F}\sqrt{1-M^2}}{\pi \rho c \, V_\infty^2} \qquad \text{avec} \qquad |\alpha_{peff.}| \leqslant |\alpha_p|$$

$\alpha_{peff.}$ est l'incidence aérodynamique efficace. Les décollements ont provoqué pour le profil une perte d'incidence égale à $\alpha_p - \alpha_{peff.}$. Pour un profil donné, à un nombre de Mach et à un nombre de Reynolds donnés, les courbes de C_{zo} expérimentales permettent de définir, au moins de manière implicite, la relation :

$$\overline{F} = f(F)$$

ayant $\overline{F}$, on en déduit l'incidence aérodynamique efficace par (17).

IV.2 - Aérodynamique stationnaire tridimensionnelle

De nombreux résultats expérimentaux sont disponibles pour des profils bidimensionnels, mais on ne connais pas, le plus souvent, le comportement de ces profils sous l'effet des influences tridimensionnelles d'un rotor réel. Un problème non encore totalement résolu est le calcul des forces aérodynamiques sur une pale d'hélicoptère à partir des résultats expérimentaux bidimensionnels sur les profils. On a essayé de fonder une méthode théorique, permettant le passage du bidimensionnel au tridimensionnel, sur l'hypothèse de Prandtl déjà présentée lors du calcul des traînées. Si l'on retranche les influences de tous les sillages, le profil se comporte comme en bidimensionnel pour le calcul des traînées. L'hypothèse correspondante pour les décollements sera la suivante : une fois retranchée l'influence de tous les sillages, la perte d'incidence aérodynamique due aux décollements sera la même que celle mesurée dans des conditions analogues pour un profil 'id mensionnel. En outre, si l'épaisseur des sillages est faible, leur influence peut se calculer au moyen e l. théorie linéarisée. Pour préciser ces idées, on étudiera en détail le cas d'une aile rectangulaire d'enve gure finie en translation (voir figure 9). Dans le cadre de la théorie linéarisée du chapitre III, l'aile est schématisée par une ligne portante située au 1/4 avant. En ne tenant pas compte des termes instationnaires de la formule 4, la portance r unité de longueur est décomposée sur une base de fonctions suivant l'expression :

$$(18) \qquad F(y) = \sqrt{1-\eta^2} \sum_{i=1}^{n} z_i \, _{-i}(y)$$

$$\text{avec} \quad \eta = \frac{2y - Y_1 - Y_0}{Y_1 - Y_0}$$

Dans le cas de la figure 9, on a pris $n=5$. On calcule en 5 points situés sur la ligne du 1/4 arrière les vitesses induites par chacune des 5 fonctions de force : $\sqrt{1-q^2}\, L_i(y)$. Soit a_{ij} cette vitesse induite au point P_j. En désignant par α_j le calage du profil à l'ordonnée y_j la condition de glissement est donnée par :

$$(19) \qquad V_\infty \alpha_j = \sum_{i=1}^{n} a_{ij} z_i$$

Dans le cas linéaire la résolution du système 19 donne les n valeurs de z_i et par 18 la force $F(y)$. Plutôt que d'utiliser les inconnues z_i, on aurait pu raisonner à partir des F_i, valeur de la portance à l'ordonnée y_i avec :

$$(20) \qquad z_i = \frac{F_i}{\sqrt{1-q_i^2}}$$

Le système 19 s'écrit en fonction des nouvelles inconnues :

$$(21) \qquad \sum_{i=1}^{n} \frac{a_{ij}}{\sqrt{1-\eta_i^2}}\, F_i = V_\infty \alpha_j$$

Dans un cas décroché la force de portance devient $\overline{F}(y)$, qui s'exprime suivant la formule 18, en fonction des $\overline{F}_i = \overline{F}(y_i)$ par :

$$(22) \qquad \overline{F}(y) = \sqrt{1-q^2}\, \sum_{i=1}^{n} \frac{\overline{F}_i}{\sqrt{1-q_i^2}}\, L_i(y)$$

En supposant les sillages et les zones décollées d'épaisseurs modérées, les vitesses induites se calculent comme en linéaire. Au point de collocation P_j elles sont égales à :

$$(23) \qquad w_j = \sum_{i=1}^{n} \frac{a_{ji}}{\sqrt{1-\eta_i^2}}\, \overline{F}_i$$

Mais du fait du décollement des filets fluides on a $w_j \neq V_\infty \alpha_j$, la condition de glissement ne s'applique plus. C'est ici qu'intervient l'hypothèse de la perte d'incidence aérodynamique. Pour un profil bidimensionnel à l'incidence α_P on aurait sans décollement une force de portance par unité de longueur donnée par (16), du fait des décollements la perte d'incidence est égale à :

$$(24) \qquad \Delta\alpha_P = \frac{(F - \overline{F})\sqrt{1-M^2}}{\pi \rho c V_\infty^2}$$

ou encore de façon équivalente, on peut dire que les décollements engendrent une perte de vitesse induite égale à :

$$(25) \qquad \Delta w = \frac{(F - \overline{F})\sqrt{1-M^2}}{\pi \rho c V_\infty}$$

$\overline{F}$ est une fonction connue de F

Dans le cas d'une aile tridimensionnelle, on écrit que la somme des vitesses induites par les portances réelles $\overline{F}(y)$, augmentée de la perte bidimensionnelle de vitesse induite, traduit encore la condition de glissement classique et de ce fait on a, en sommant (23) et (25) :

$$(26) \qquad V_\infty \alpha_j = \sum_{i=1}^{n} \frac{a_{ji}\overline{F}_i}{\sqrt{1-\eta_i^2}} + \frac{(F_j - \overline{F}_j)\sqrt{1-M^2}}{\pi \rho c V_\infty}$$

avec $\qquad \overline{F}_j = f(F_j)$

Le système 26 est fortement non linéaire puisque la relation $\overline{F}_j = f(F_j)$ est donnée par les courbes de Cz_0 expérimentales. De plus, on ne peut en général, pas inverser cette expression car $F_j = g(\overline{F}_j)$ n'est pas déterminée en tout point de façon unique. De ce fait, le choix des inconnues principales est imposé, on utilisera les Fj qui une fois connus permettent le calcul des $\overline{F}$j. On réécrit le système (26) sous la forme suivante :

$$(27) \qquad \sum_{i=1}^{n} \frac{a_{ji} F_i}{\sqrt{1-\eta_i^2}} = V_\alpha \alpha_j + \sum_{i=1}^{n} \frac{(F_i - \overline{F}_i)a_{ji}}{\sqrt{1-\eta_i^2}} - \frac{(F_j - \overline{F}_j)\sqrt{1-M^2}}{\pi \rho c V_\infty}$$

On remarque que le système non linéaire (27) apparait comme dérivé du système linéaire (21) par une perturbation du deuxième membre. On rajoute un facteur correctif non linéaire w_j^* égal à :

$$(28) \qquad w_j^* = \sum_{i=1}^{n} \frac{(F_i - \overline{F}_i)a_{ji}}{\sqrt{1-\eta_i^2}} - \frac{(F_j - \overline{F}_j)\sqrt{1-M^2}}{\pi \rho c V_\infty}$$

Pour justifier une méthode de résolution pas à pas du système 27, il faut démontrer que le terme correctif w_j^* reste modéré dans les cas pratiques. On observe tout d'abord que dans un cas non décroché on a $F = \overline{F}$, ce qui entraîne $w_j^* = 0$, quels que soient les indices i et j. Dans un cas décroché, pour une aile de grand allongement peu vrillée, on peut également démontrer que w_j reste de valeur modérée. Si l'aile est de grand allongement, au milieu de celle-ci tout se passe comme en bidimensionnel. Supposons cette aile chargée par la portance $F(y) - \overline{F}(y)$, la vitesse induite au point Pj au milieu de l'aile est donnée par w'_j avec

$$w'_j = \sum_{i=1}^{n} \frac{(F_i - \overline{F}_i)a_{ji}}{\sqrt{1-\eta_i^2}}$$

mais w'_j est égal aussi à la vitesse induite au 1/4 arrière d'un profil bidimensionnel chargé par $F_j - \bar{F}_j$ on a :

$$w'_\delta = \frac{(F_j - \bar{F}_j)\sqrt{1-M^2}}{\pi \rho c \, V_\infty}$$

De ce fait w^*_j donné par 28 est nul au milieu de l'aile.

Le raisonnement n'est plus valable aux extrémités mais on sait que les incidences aérodynamiques s'annullent aux extrémités libres. Comme il n'y a pas de décrochage pour des incidences faibles, on a $F = \bar{F}$ et w^* est nul aux extrémités. De ce fait, w^* reste modéré partout sur l'aile de grand allongement et le système 27 peut être résolu par une méthode pas à pas. Le premier pas est un calcul linéaire avec $w^*_\delta = 0$, on obtient F, puis $\bar{F}$, ce qui fournit une première estimation de w^*. On continue jusqu'à convergence. Le système (27) étant un système non linéaire quelconque, on ne peut être assuré, ni de la convergence, ni même de l'unicité de la solution. La méthode qui vient d'être décrite a l'avantage de rechercher une solution au voisinage de la solution linéaire, ce qui est d'un grand intérêt dans les applications pratiques, en particulier pour les rotors d'hélicoptères souvent modérément décrochés.

IV.3 - Aérodynamique instationnaire bidimensionnelle

A - Mise en forme des résultats expérimentaux bidimensionnels

Les résultats expérimentaux, dont on dispose généralement, sont relatifs à des profils en mouvement de tangage sinusoïdal avec une vitesse à l'infini constante. Pour être utilisables, ces expériences doivent couvrir une gamme très complète de nombre de Mach, d'amplitudes et de fréquences réduites. En outre les résultats doivent être modélisés par une méthode si possible peu coûteuse en temps de calcul, cette méthode doit pouvoir interpoler les résultats et les étendre à des mouvements quelconques, par exemple périodiques avec de nombreux harmoniques en tangage, le tout ajouté à une variation cyclique de la vitesse du vent. En général, on ne possède pas de résultats expérimentaux pour des mouvements aussi complexes. Une étude des méthodes de reconstruction sortirait du cadre de cet article, on trouvera en référence (4), (9), (10), des précisions sur les deux méthodes qui ont été utilisées pour les calculs de rotor. La figure (10) montre deux exemples de reconstructions de boucles de Cz instationnaires, on doit se garder de toute conclusion sur la qualité des résultats.

B - *Utilisation des résultats expérimentaux*

Dans les calculs par la méthode des doublets, on est amené à introduire une relation entre la portance expérimentale $\bar{F}(t)$ et la portance $F(t)$ théorique calculée sans décollements. Dans le cas général, $\bar{F}(t)$ dépend non seulement de la valeur instantanée $F(t)$, mais aussi de toutes les valeurs prisent par $F(\tau)$ entre $\tau = -\infty$ et $\tau = t$. Pour les applications au rotor d'hélicoptère en vol stabilité, la vitesse du profil peut être considérée comme périodique ainsi que le mouvement de tangage et de pompage. De plus, on ne considère qu'un nombre restreint d'harmoniques, par exemple m = 6. De ce fait, pour une vitesse dans la soufflerie $V(\tau)$ donnée, $F(\tau)$ est déterminée par 2m + 1 valeurs $F_j = F(\tau_j)$ à des intervalles de temps constants. On peut écrire :

$$\bar{F}_i = f_i (F_1 \ldots \ldots F_{2m+1})$$

Il y a 2m + 1 fonctions f_i et $\bar{F}_i = \bar{F}(\tau_i)$

Les expériences ou les méthodes mathématiques de reconstruction permettent la détermination des fonctions f_i

C - Perte de vitesse induite en instationnaire décroché

En linéaire instationnaire, on décompose la force $F(\tau)$ sur une base de fonctions périodiques, au nombre d'harmoniques limité, égales à l'unité pour une valeur τ_i du temps et égales à zéro pour les autres valeur τ_j .

Les τ_j sont des valeurs du temps qui divisent la période en intervalles égaux. Soit $g_i(\tau)$ une de ces fonctions de base. On peut écrire :

$$(29) \qquad F(\tau) = \sum_{i=1}^{2m+1} F(\tau_i)\, g_i(\tau)$$

On trouvera, pour illustrer ce genre de décomposition, en figure 11, la fonction $g_i(t)$ périodique, de période T et comportant 3 harmoniques.

On peut calculer les vitesses induites au 1/4 arrière du profil à un instant t pour les fonctions $g_i(\tau)$ avec $-\infty < \tau < t$. Soit $W_i(t)$ cette vitesse induite. Les instants t peuvent être pris dans l'ensemble des τ_j déjà utilisé. En outre si $\alpha(t)$ et $V(t)$ sont les vitesses et le calage du profil à l'instant t, on aura pour l'aérodynamique linéaire :

$$(30) \qquad V(t)\alpha(t) + \frac{c}{2}\frac{d\alpha}{dt}(t) = \sum_{i=1}^{2m+1} F(\tau_i)\, W_i(t)$$

c est la corde du profil.

On écrit l'équation 30 pour (2m+1) valeurs de t, le système obtenu où V, c et W_i sont connus, permet la détermination de $F(\tau_i)$, puis par (29) de $F(\tau)$. Il s'agit d'un calcul discrétisé d'autant plus précis que le nombre d'harmoniques m est grand. Pour le même profil, à la même vitesse et avec la même

variation d'incidence, en fluide décroché, la portance est donnée par $\overline{F}$ (τ) qui est décomposée elle aussi suivant la formule (29) :

$$(31) \qquad \overline{F}(\tau) = \sum_{i=1}^{2m+1} \overline{F}(\tau_i) \, g_i(\tau)$$

Lorsque les hypothèses d'épaisseur modérée pour la zone décollée et pour le sillage sont réalisées, on peut calculer les vitesses induites de façon analogues à ce qui a été fait en linéaire. La vitesse induite au 1/4 arrière à l'instant t est W(t) donné par :

$$(32) \qquad W(t) = \sum_{i=1}^{2m+1} \overline{F}(\tau_i) \, W_i(t)$$

avec $\overline{F}(\tau_i) = f_i(F_1 \ldots \ldots F_{2m+1})$ supposé connu

La perte de vitesse induite en bidimensionnel est obtenue par différence entre (30) et (32) et s'écrit :

$$(33) \qquad W'(t) = \sum_{i=1}^{2m+1} \left[F(\tau_i) - \overline{F}(\tau_i) \right] W_i(t)$$

IV.4 – Aérodynamique instationnaire tridimensionnelle

A – Application à l'aile en translation à vitesse constante

La vitesse du vent à l'infini est constante. L'aile a des mouvements d'oscillation de tangage. En linéaire, le problème est résolu en décomposant la portance sur une base de fonctions dépendant à la fois de l'envergure et du temps. Il suffit de combiner ce qui a été fait pour l'aile en stationnaire et pour le profil en instationnaire. On écrira :

$$(34) \qquad F(\tau,y) = \sqrt{1-\eta^2 y} \sum_{i=1}^{2m+1} \sum_{j=1}^{n} \frac{F_{ij} \, L_j(y) \, g_i(\tau)}{\sqrt{1-\eta_j^2}}$$

$$F_{ij} = F(\tau_i, y_j)$$

On peut calculer les vitesses induites $W_{ij}(t,y)$ pour un point P de la ligne du 1/4 arrière situé à l'ordonnée y, à l'instant t. Ces vitesses induites sont calculées pour chacune des fonctions de base

$$\frac{\sqrt{1-\eta^2}}{\sqrt{1-\eta_j^2}} L_j(y) \, g_i(\tau)$$

La vitesse induite totale est la somme de chacune des vitesses induites par les fonctions de base. Si $\alpha(t,y)$ est le calage de l'aile à l'ordonnée y et à l'instant t on aura :

$$(35) \qquad V\alpha(t,y) + \frac{c}{2} \frac{\partial \alpha}{\partial t}(t,y) = \sum_{i=1}^{2m+1} \sum_{j=1}^{n} F_{ij} \, w_{ij}(t,y) = w(t,y)$$

La condition de glissement comporte des termes instationnaires dépendant de la dérivée de l'incidence.

Dans le cas d'une aile décrochée la portance est écrite sous la forme :

$$(36) \qquad \overline{F}(\tau,y) = \sqrt{1-\eta^2 y} \sum_{i=1}^{2m+1} \sum_{j=1}^{n} \frac{\overline{F}_{ij} \, L_j(y) \, g_i(\tau)}{\sqrt{1-\eta_j^2}}$$

avec $\overline{F}_{ij} = \overline{F}(\tau, y_j)$

Les hypothèses d'épaisseur modérée, pour la zone décollée sur l'aile et pour les sillages, permettent le calcul des vitesses induites comme en linéaire. On aura :

$$(37) \qquad \overline{w}(t,y) = \sum_{i=1}^{2m+1} \sum_{j=1}^{n} \overline{F}_{ij} \, w_{ij}(t,y)$$

Ici $\overline{w}$(t,y), la vitesse induite totale n'est plus donnée par une condition de glissement du fait du décollement. Pour poursuivre, on suppose que la perte de vitesse induite pour le profil d'ordonnée y est la même que celle advenant en bidimensionnel dans les mêmes conditions similaires. On entend par conditions similaires un profil bidimensionnel dont la portance serait $\overline{F}$(τ,y) lorsque τ varie de $-\infty$ à t. Cette perte de vitesse induite est donnée par (33). On aura alors en combinant (33), (35) et (37) la nouvelle relation :

$$(38) \qquad V\alpha(t,y) + \frac{c}{2} \frac{\partial \alpha}{\partial t}(t,y) = \sum_{i=1}^{2m+1} \sum_{j=1}^{n} \overline{F}_{ij} \, w_{ij}(t,y) + \sum_{i=1}^{2m+1} \left[F(\tau_i,y) - \overline{F}(\tau_i,y) \right] W_i(t)$$

La relation (38) est ensuite exprimée pour les instants $t = \tau_k$ appartenant à l'ensemble des temps équidistants, qui ont servi à la définition des $g_i(\tau)$. De même, les ordonnées y seront prises dans l'ensemble servant de base à la définition des polynômes de Lagrange. En écrivant (38) pour toutes les ordonnées y_ℓ et pour tous les instants τ_k, on aboutit au système non linéaire suivant :

(39)
$$V\alpha(\tau_k,y_\ell) + \frac{c}{2}\frac{\partial\alpha}{\partial t}(\tau_k,y_\ell) = \sum_{i=1}^{2m+1}\sum_{j=1}^{n} \overline{F}_{ij}\, w_{ij}(\tau_k,y_\ell) + \sum_{i=1}^{2m+1}\left[F_{i\ell}-\overline{F}_{i\ell}\right]W_i(\tau_k)$$

avec
$$\overline{F}_{i\ell} = f_{i\ell}\left(F_{1\ell}, F_{2\ell}, \dots\dots, F_{(2m+1)\ell}\right)$$

Dans le cas d'un même profil tout le long de l'aile la fonction $f_{i\ell}$ ne dépend plus de ℓ.

Diverses méthodes de résolution sont possibles pour le système (39). En s'inspirant de ce qui a été fait en stationnaire, l'une d'elle consiste en le fait de rajouter et de retrancher le système li-néaire (35). On obtient alors :

(40)
$$\sum_{i=1}^{2m+1}\sum_{j=1}^{n} F_{ij}\, w_{ij}(\tau_k,y_\ell) = V\alpha(\tau_k,y_\ell) + \frac{c}{2}\frac{\partial\alpha}{\partial t}(\tau_k,y_\ell) \longrightarrow$$
$$+ \sum_{i=1}^{2m+1}\sum_{j=1}^{n}(F_{ij}-\overline{F}_{ij})w_{ij}(\tau_k,y_\ell) - \sum_{i=1}^{2m+1}\left[F_{i\ell}-\overline{F}_{i\ell}\right]W_i(\tau_k)$$

avec
$$\overline{F}_{i\ell} = f_{i\ell}\left(F_{1\ell}, F_{2\ell}, \dots\dots, F_{(2m+1)\ell}\right)$$

Les inconnues principales sont les Fij, une fois déterminés, les expériences ou les méthodes de reconstruction permettent de remonter aux forces non linéaires $\overline{F}$ij, l'inverse n'est pas vrai. Au premier pas de calcul le terme correctif :

(41)
$$w^*(\tau_k,y_\ell) = \sum_{i=1}^{2m+1}\sum_{j=1}^{n}(F_{ij}-\overline{F}_{ij})w_{ij}(\tau_k,y_\ell) - \sum_{i=1}^{2m+1}\left[F_{i\ell}-\overline{F}_{i\ell}\right]W_i(\tau_k)$$

est pris égal à zéro ce qui n'est vrai que pour des cas non décrochés.

Dans le cas général w^* est différent de zéro, il serait souhaitable que sa valeur reste modérée comme en stationnaire. On peut bien entendu traiter des cas stationnaires à l'aide de la théorie instation-naire en rendant le calage indépendant du temps. A ce moment, les Fij et $\overline{F}$ij ne dépendent plus de l'indice i et le terme correctif instationnaire se réduit au terme correctif stationnaire de la formule (28) dont il est une discrétisation dans le temps. Les remarques qui ont été faites sont toujours valables et on est assuré d'avoir w^* de faible valeur. Malheureusement, pour des cas instationnaires sévères comme ceux ren-contrés sur un rotor d'hélicoptère, la fonction $\overline{F} = f(F_1 \dots F_{2m+1})$ a un comportement tellement erratique dû aux boucles de décrochage, qu'elle compromet la stabilité d'une méthode de résolution pas à pas fondée sur l'estimation successive des termes correctifs w^*. On est amené à utiliser une méthode de Newton géné-ralisée, elle s'établit comme suit :

Soit Fij une solution approchée du système (40). On en déduit les forces non linéaires $\overline{F}$ij ainsi que l'erreur pour chacune des équations du système. On recherche ensuite une nouvelle solution sous la forme (Fij + δFij), ce qui pour les forces non linéaires donne ($\overline{F}$ij + $\delta\overline{F}$ij) avec :

(42)
$$\delta\overline{F}_{ij} = \sum_{\ell=1}^{2m+1}\frac{\partial f_{ij}}{\partial F_{\ell j}}\,\delta F_{\ell j}$$

L'évaluation de (42) doit être indépendante de la méthode de modélisation des forces expérimen-tales choisie, c'est pourquoi on calcule les dérivées partielles par différence finie. On a :

$$\frac{\partial f_{ij}}{\partial F_{\ell j}} = \frac{f_{ij}(F_{1j},\dots,F_{\ell j}+\Delta F_{\ell j},\dots,F_{(2m+1)j}) - f_{ij}(F_{1j},\dots,F_{\ell j},\dots,F_{(2m+1)j})}{\Delta F_{\ell j}}$$

On prend pour $\Delta F_{\ell j}$ environ 1 N/m., ce qui est une valeur petite par rapport aux forces mises en jeu dans ce type de problème. Par cette technique, le système non linéaire (40) devient un système li-néaire en δFij, les nouvelles inconnues. Au pas de calcul suivant, on part de la nouvelle solution (Fij + $\lambda\delta$Fij). Le paramètre λ est un paramètre de relaxation égal ou inférieur à 1. Dans certain cas très diffi-ciles λ peut descendre jusqu'à 0,1. A chaque pas, on évalue également la valeur absolue de l'erreur et on poursuit les calculs jusqu'au minimum local le plus proche en partant de la solution linéaire. Comme on ne peut être assuré de l'existence et de l'unicité de la solution de (40), la méthode utilisée a le mérite de fournir une solution approchée plausible.

B - Application à l'hélicoptère en vol avançant

Au paragraphe précédent, on a supposé que le profil se comportait localement comme en bidimensionnel une fois déduit divers vitesses induites. Le comportement bidimensionnel est donné par l'expérience et si la méthode de reconstruction est bonne, on peut espérer obtenir, pour une vitesse à l'infini constante et pour des variations sinusoïdales du calage de l'aile, une bonne évaluation des forces de portance. Pour l'hélicoptère en vol avançant, la composante de la vitesse normale à la pale est une fonction sinusoïdale de l'azimut. Les variations sont de grande amplitude mais heureusement à fréquence faible, on ne dispose en général pas de valeurs expérimentales pour un tel mouvement. La méthode de reconstitution des boucles de C_z devra alors inclure une extension au cas d'une vitesse à l'infini variable. Cette extension se fait à partir d'hypothèses quasi stationnaires, le résultat est pratiquement invérifiable, les forces sur un rotor réel étant le résultat de conditions trop complexes pour être isolées. De plus, on néglige les effets centrifuges exercés par la rotation des pales sur la zone de fluide décollé et entraîné. De même l'influence sur le décrochage de la composante radiale de la vitesse d'avancement de l'appareil est mal connue (référence 10).

Avec toutes les réserves précédentes, les hypothèses d'épaisseur modérée des sillages et des zones décollées, permettent le calcul des vitesses induites au 1/4 arrière de la pale comme en aérodynamique linéaire. Si on suppose ensuite, que la section considérée se comporte comme un profil bidimensionnel dont les forces de portance sont données par une extension hardie des résultats expérimentaux, on obtient alors un système non linéaire analogue à (40), qui se résout suivant les mêmes principes. Un exemple de résultat est donné en figure 12. Il s'agit de la série d'essais effectués à Modane et déjà utilisés en figure 5 pour la théorie linéaire. Cette fois le rapport d'avancement est de μ = 0,3 mais le cas de vol est très chargé, le décrochage apparait sur la pale reculante. Le mouvement de la pale est mesuré en cours d'essai et imposé dans les calculs pour isoler les effets aérodynamiques. La théorie linéaire donne dans la zone de la pale reculante des forces de portance trop grande ; la simple utilisation des courbes de C_z statique améliore les résultats. Le décrochage instationnaire est modélisé par la méthode de Boeing pour le profil NACA 0012, son introduction dans les calculs rapproche sensiblement la théorie des résultats expérimentaux, sauf en extrémité de pale où les faibles incidences aérodynamiques ne peuvent donner lieu à du décrochage suivant la théorie exposée ici. On constate pourtant un fort décrochage sur la pale reculante, sans doute doit-il être expliqué par l'influence des gradients de pression dans le sens radial ou par la centrifugation du fluide mort.

C - Exemple d'utilisation - Choix d'un profil

Les profils sont étudiés par la théorie en bidimensionnel stationnaire jusqu'à l'incidence de décrochage, ils sont ensuite passés en soufflerie pour l'instationnaire. Quelques programmes de calculs partant des équations de Navier-Stockes permettent des études en instationnaire décroché, mais le temps machine est voisin de la demi-journée et ils ne sont guère utilisés dans l'industrie. Bien que cette situation soit loin d'être satisfaisante, de nouvelles familles de profils sont développées et l'expérience prouve qu'ils sont susceptibles d'améliorer les performances et le comportement vibratoire des hélicoptères. La méthode de calcul qui a été décrite dans les paragraphes précédents permet le passage du bidimensionnel au tridimensionnel, elle peut en dépit de ses imprécisions apporter une aide appréciable dans le choix des profils dont l'épaisseur est variable le long de la pale. A titre d'exemple, on trouvera en figure 14 des comparaisons d'évolution de C_z pour deux profils d'épaisseur 12%. L'un est le profil classique NACA 0012 modélisé par la méthode de Boeing, l'autre est le profil ONERA-AEROSPATIALE OA 212 utilisé actuellement sur une partie des pales du Dauphin et modélisé par la méthode ONERA avec des équations différentielles couplées. Bien qu'il n'ait pas été possible de modéliser les profils à l'aide du même modèle, on peut espérer que les deux modèles mathématiques donnent des résultats voisins de la réalité, ce qui permet de comparer les deux profils. On a choisi des pales de même forme géométrique que celles des expériences de Modane, le profil est le même tout le long de la pale, le rapport d'avancement est de μ = 0,3 et le mouvement de pale est imposé. Pour ne pas compliquer l'interprétation des résultats, on a tout d'abord effectué un calcul linéaire qui fournit la loi d'incidence et on examine ensuite le comportement du profil pour cette évolution d'incidence fixée. Il s'agit en fait du premier pas de calcul de la méthode exposée dans cette article.

On constate, pour les deux distances radiales présentées en figure 14, une amélioration sensible de la valeur du C_z fournie par le OA 212 à l'azimut 270°. A la distance r/R_1 = 0,81, on obtient pratiquement le C_z linéaire et on ne peut donc chercher à améliorer le profil, par contre à la distance r/R_1 = 0,61, des gains considérables sont encore possibles, en particulier à partir de l'azimut 310°. On peut aussi mettre en doute la manière dont les différents modèles mathématiques prévoient le recollement. En extrémité de pale les incidences sont faibles et il n'y a pas de différence entre les deux profils, au moins en théorie. Les calculs présentes en figure 14 peuvent être poursuivis jusqu'à convergence et même être effectués pour un cas plus proche de la réalité incluant le couplage avec les mouvements de la pale.

5 - COUPLAGES DES MOUVEMENTS DE PALE AVEC L'AERODYNAMIQUE NON LINEAIRE

A - Méthode de calcul

On a déjà vu en chapître II que le mouvement de la pale s'exprimait de façon quasi linéaire en fonction des forces aérodynamiques, ce fait est toujours valable pour les cas décrochés, mais cette fois il faut remplacer les forces linéaires Fij par les forces non linéaires $\overline{F}$ij. Il existe cependant une différence, en linéaire les forces de traînées sont faibles et sont introduites par un terme en C_{x_0}. Dans le cas de décollements, les traînées sont importantes, on connait en général la valeur du coefficient de traînée en stationnaire, mais les résultats expérimentaux instationnaires font défaut et il n'existe pas de modèle mathématique disponible. Il faut alors se contenter d'introduire des traînées quasi stationnaires pour estimer l'accroissement de puissance nécessaire pour compenser les pertes dues aux décollements. Si $\mathcal{T}$ (r, t) est la force de traînée en Newton/mètre, les relations (11) deviennent :

$$\mathcal{C}_1(t) = \int_{R_0}^{R_1} (r - r_b) \left[\overline{F}(r,t) \cos(i - \alpha_p) - \overline{T}(r,t) \sin(i - \alpha_p) \right] dr$$

(43)

$$\mathcal{C}_2(t) = \int_{R_0}^{R_1} (r - r_b - r_t) \left[\overline{F}(r,t) \sin(i - \alpha_p) + \overline{T}(r,t) \cos(i - \alpha_p) \right] dr$$

On a persisté pour les calculs présentés à introduire les $\overline{T}$ (r, t) comme des termes correctifs évalués à chaque pas de calcul, en effet, ils interviennent peu dans le mouvement de battement et les mouvements de traînée de pale, où ils sont prépondérents, sont toujours de faible amplitude.

Comme $\overline{F}$ (r, t) est décomposé sur la base déjà introduite pour F (r, t) dans la relation (4), si on classe dans un ordre déterminé les $\overline{F}_{ij}$, les relations (13) et (14), où l'on remplace Fi par $\overline{F}_i$, sont toujours valables. De même, la condition de glissement donnée par (9) reste inchangée. Par contre, le système d'équations d'origine aérodynamique est changé, c'est maintenant le système (40) qui s'écrit sous la forme matricielle suivante :

(44)
$$\left[A_e \right] \left[\begin{matrix} F_1 \\ \vdots \\ F_q \end{matrix} \right] = \left[W \right] + \left[A'_e \right] \left[\begin{matrix} F_1 - \overline{F}_1 \\ \vdots \\ F_q - \overline{F}_q \end{matrix} \right]$$

et par combinaison avec (9) il devient :

(45)
$$\left[A_e \right] \left[\begin{matrix} F_1 \\ \vdots \\ F_q \end{matrix} \right] = \left[\begin{matrix} W_{o1} \\ \vdots \\ W_{oq} \end{matrix} \right] + \left[w_{ij} \right] \left[\begin{matrix} a_o \\ a_{12} \\ b_o \\ b_{12} \end{matrix} \right] + \left[A'_e \right] \left[\begin{matrix} F_1 - \overline{F}_1 \\ \vdots \\ F_q - \overline{F}_q \end{matrix} \right]$$

Si on combine (45) avec le système (14) où l'on a remplacé les Fi par des Fi comme il a été dit plus haut, il vient :

(46)
$$\left[A_e \right] \left[\begin{matrix} F_1 \\ \vdots \\ F_q \end{matrix} \right] = \left[\begin{matrix} W_{o1} \\ \vdots \\ W_{oq} \end{matrix} \right] + \left[w_{ij} \right] \left[K^{-1} \right] \left[\mathcal{C}_o \right] + \left[w_{ij} \right] \left[K^{-1} \right] \left[T_{ij} \right] \left[C^{-1} \right] \left[\begin{matrix} \overline{F}_1 \\ \vdots \\ \overline{F}_q \end{matrix} \right] + \left[A'_e \right] \left[\begin{matrix} F_1 - \overline{F}_1 \\ \vdots \\ F_q - \overline{F}_q \end{matrix} \right]$$

On posera

$$\left[B \right] = \left[w_{ij} \right] \left[K^{-1} \right] \left[T_{ij} \right] \left[C^{-1} \right]$$

$$\left[Q_o \right] = \left[w_{ij} \right] \left[K^{-1} \right] \left[\mathcal{C}_o \right] + \left[\begin{matrix} W_{o1} \\ \vdots \\ W_{oq} \end{matrix} \right]$$

$$\left[A_e^* \right] = \left[A_e \right] - \left[B \right]$$

$$\left[A_e'^* \right] = \left[A'_e \right] - \left[B \right]$$

Le système (46) peut alors s'écrire sous la forme :

(47)
$$\left[A_e^* \right] \left[\begin{matrix} F_1 \\ \vdots \\ F_q \end{matrix} \right] = \left[Q_o \right] + \left[A_e'^* \right] \left[\begin{matrix} F_1 - \overline{F}_1 \\ \vdots \\ F_q - \overline{F}_q \end{matrix} \right]$$

Au deuxième membre, on voit apparaître des termes correctifs dus aux non-linéarités aérodynamiques. En outre, le vecteur colonne Q_o doit être réactualisé à chaque pas de calcul pour tenir compte des traînées. Comme il a été dit au chapitre précédent pour l'aérodynamique non linéaire sans couplage mécanique, on ne peut résoudre (47) par approximation successives du terme correctif. Il faut utiliser une méthode de Newton généralisée.

A partir d'une solution approchée (F, $\overline{F}$), on recherche une solution $(F + \delta F)$, $(\overline{F} + \delta \overline{F})$ par linéarisation des termes $\overline{F}$. Le système (42), qui traduit les résultats bidimensionnels instationnaires décrochés, peut se mettre sous la forme matricielle équivalente :

$$(48) \quad \begin{bmatrix} \delta\bar{F_1} \\ \vdots \\ \delta\bar{F_q} \end{bmatrix} = \begin{bmatrix} & \mathcal{F}^\circ & \end{bmatrix} \begin{bmatrix} \delta F_1 \\ \vdots \\ \delta F_q \end{bmatrix}$$

On obtient alors un nouveau système linéaire où les inconnues sont les δF. La résolution de ce système fournit les δF. On reprend les calculs à partir d'une nouvelle solution $F + \lambda\,\delta F$ où λ est un facteur de relaxation et on réactualise le vecteur Q_0. On évalue à chaque pas de calcul l'erreur et on arrête les calculs sur un minimum local de l'erreur. Comme au premier pas, on part de la solution linéaire $(F-\bar{F}) = 0$, on converge ensuite vers un minimum voisin de la solution linéaire, ce qui fournit une solution physiquement admissible.

B - _Exemple de résultats_

Pour le cas de vol 855 au rapport d'avancement, μ= 0,3 , déjà présenté en figure 12 pour l'aérodynamique non couplée, on trouvera en figure 13 des calculs couplés, c'est-à-dire avec la pale en équilibre. Deux calculs sont présentés, l'un avec une aérodynamique linéaire et l'autre avec les décollements instationnaires reconstruits par la méthode de Boeing. Bien que des différences soient notables entre les conditions de calcul avec pale en équilibre et mouvement imposé, l'allure générale des résultats est inchangée et l'accord reste assez bon.

VI - LIMITATIONS ET DEVELOPPEMENTS FUTURS

VI.1 - _Limites des calculs théoriques actuels_

Le code de calcul, dont la théorie a été présentée aux chapîtres précédents, est limité au cas d'une pale rigide articulée en battement et en traînée, mais possède une aérodynamique non linéaire. Un autre code de calcul tient compte de la souplesse des pales, caractérisée par l'ensemble des modes propres mesurés à l'arrêt, pale encastrée au mur. Ce programme est limité à une aérodynamique linéaire et en particulier le moments des forces de portance autour du 1/4 avant est nul. Dans les cas décrochés, les mouvements de torsion peuvent devenir très importants et entraîner des variations d'incidence non négligeables. Le programme non linéaire présenté n'inclu pas le calcul des moments , dans les cas expérimentaux testés la pale était très rigide en torsion et de plus la modélisation des moments par la méthode de Boeing est très imprécise. Quelques tentatives ont été effectuées sur des modèles simplifiés à partir de la méthode ONERA dans des buts d'étude de la stabilité des rotors (voir référence 8). L'introduction des moments _est possible dans le code de calcul présenté_, lorsqu'il n'y a pas de couplage avec la torsion de la pale, puisque l'incidence aérodynamique est connue. Il faut toutefois disposer d'un modèle mathématique du décrochage assez précis. D'autres limitations sont plus sérieuses, en particulier le passage du bidimensionnel en tridimensionnel pour le fluide décollé n'inclu pas l'équilibre radial dans la zone fluide entraînée par la pale. Il faudrait une relation non linéaire de la forme :

$$\bar{F}(\pi,t) = f\left[\, F(\tau,\pi) \,,\, \frac{\partial F}{\partial \pi}(t,\pi)\,\right]$$

τ variable _de_ $-\infty$ _à_ t

En d'autres termes, il faut inclure dans l'hypothèse de Prandtl un effet de gradient d'incidence le long de l'envergure.

Même lorsque la condition de glissement est vérifiée sur la pale, d'autres limitations peuvent intervenir. L'une d'elles est particulièrement gênante, il s'agit de l'hypothèse de ligne portante unique qui limite le domaine d'utilisation des calculs théoriques au rapport d'avancement μ= 0,35 . Multiplier le nombre de lignes portantes n'arrangerait pas les choses, à moins d'augmenter aussi le nombre de points en envergure. Une autre cause d'erreur est la déformation des sillages, en particulier le sillage de la pale précédent immédiatement la pale de référence. Certains codes de calcul utilisant le potentiel de vitesse (tourbillon en incompressible) permettent d'introduire les déformations de sillage. Leurs limitations, maillage assez lâche, incompressibilité, temps de calcul, sont sévères. Dans la pratique, il faut se contenter d'une forme de sillage prescrite à l'avance. Dans la théorie du potentiel d'accélération utilisée à l'ONERA, seules les déformations de sillage dites "cylindriques" peuvent être incluses. Les cas de vol stationnaire, où les contractions de sillages sont importantes, ne peuvent être traités convenablement, de plus dans ce cas particulier, la perturbation créée par la présence du fuselage doit être particulièrement forte. En pale avançante une autre limitation se fait jour : l'apparition d'effet transsoniques se traduit par des ondes de choc. Les ondes de choc changent radicalement la répartition de pression sur le profil et l'hypothèse de ligne portante unique au 1/4 avant n'est plus justifiée. Enfin, le temps de calcul requis par toutes les méthodes de prévision du comportement aéroélastique des rotors est important, ce qui réduit le nombre de cas de vols qui peuvent être examinés. Quelle que puisse être la précision d'une théorie, un cas de calcul isolé est le plus souvent sans valeur dans la pratique industrielle. Tout au plus, un cas isolé peut servir de vérification dans une situation déjà bien connue. Pour le code de calcul auquel cet article fait référence, il se décompose en deux étapes, dont la première est un calcul d'aérodynamique linéaire qui permet d'obtenir la matrice des vitesses induites. La matrice est obtenue au prix de une demi-heure d'unité centrale sur UNIVAC 1110. Cette matrice est ensuite utilisée dans un programme d'aéroélasticité, elle est valable pour différents pas (général, cyclique multicyclique), pour différentes caractéristiques mécaniques de la pale, pour différents profils. Le temps de calcul est alors variable suivant la complexité du problème traité. On peut donner les temps approximatifs suivants :

10 mm	en linéaire mouvement de pale imposé
15 mm	en linéaire avec couplage aéroélastique
30 mm	non linéaire méthode Boeing avec couplage aéroélastique
45 mm	non linéaire méthode ONERA avec couplage aéroélastique

La tendance actuelle étant au raffinement de la théorie, on ne peut espérer d'amélioration du temps de calcul que par une augmentation de la rapidité des ordinateurs. Il se pose aussi un problème d'interprétation des résultats, une liste de chiffres n'est plus suffisante dans un cas aussi complexe. Il faudrait pouvoir tracer des cartes de forces de portance, de traînée, d'incidence, des évolutions de C_z etc... ce n'est plus possible manuellement pour des applications industrielles. Les problèmes d'implantation des codes de calculs chez l'utilisateur et de couplage avec les moyens de sortie graphique de celui-ci devraient devenir de plus en plus importants dans les années à venir.

VI.2 - Développements futurs

A - Mécanique

On peut constater dans l'industrie une évolution rapide de la technologie de l'ensemble pales + moyeu par l'introduction des matériaux nouveau. Les gains en durée de vie, en entretien, en coût, sont considérables mais se traduisent aussi par des difficultés théoriques nouvelles. Les matériaux à fibres ont des caractéristiques anisotropes et des comportements mal connus, parfois même non linéaires. Des essais au sol sont actuellement utilisés pour connaitre les caractéristiques modales nécessaires aux calculs d'aéroélasticité, mais ils ne peuvent servir que de vérification une fois la pale ou le moyeu construit. Des études fondamentales théoriques et expérimentales sont entreprisent et devraient tendre à la prévision sur plan des caractéristiques mécaniques.

B - Aérodynamique théorique

Le fait le plus regrettable pour l'aérodynamique du rotor d'hélicoptère est l'absence,voire l'impossibilité pratique,d'une théorie que l'on pourrait qualifier d'unifiée. En effet il est possible de :

- traîter un fuselage isolé,
- de mettre en équilibre des sillages de tourbillons discrets,
- de faire des calculs de surface portante pour une aile en attaque oblique,
- d'introduire les effets transsoniques dans des cas non portants pour un flux à l'infini stratifié,
- de faire des expériences ou des calculs en fluide décroché pour des cas bidimensionnels.

Un rotor d'hélicoptère est tout celà, mais couplé, en tridimensionnel instationnaire et portant. En ce qui concerne l'aérodynamique utilisée dans cet article les améliorations possibles vont porter sur deux points principaux :

1 - une tentative d'introduction des effets de surface portante pour la pale avançante et la pale reculante. Le sillage serait divisé en deux parties, une partie lointaine hélicoïdale où la schématisation par ligne portante serait conservée et une partie proche où la pale se déplacerait dans un plan et serait traitée en surface portante par la méthode des singularités.

2 - une amélioration du passage du bidimensionnel décollé en tridimensionnel, en tenant compte du gradient de pression dans la zone décollée.

C - Aérodynamique expérimentale

Les améliorations théoriques doivent aller de pair avec des tests nombreux et souvent difficiles à réaliser. Les expériences permettent à la fois d'établir la théorie et de la tester dans quelques cas réels. Trois types d'expériences sont programmées dans un futur proche :

1 - Des expériences bidimensionnelles instationnaires sur une famille de profils modernes. Ces expériences serviront à la fois à l'amélioration du modèle mathématique et la constitution d'une base de données pour les applications aux rotors.

2 - Une aile rectangulaire non vrillée avec un profil OA 209 sera essayée en attaque oblique en soufflerie. Cette aile rigide sera animée de mouvements de tangage de fortes amplitudes analogues au pas cyclique d'une pale d'hélicoptère et entrera dans le domaine décroché. Des capteurs de pression, stationnaires (tuyaux) et instationnaires (membrane à semi-conducteur), seront répartis en quatre sections de l'aile. Les résultats obtenus serviront à tester dans des cas particuliers simples le passage du bidimensionnel décroché au tridimensionnel.

3 - Des expériences en vol seront réalisées sur un hélicoptère d'essai par la SNIAS. Ces expériences de réalisation très complexe auront des buts multiples, mais en particulier les mouvements des pales et les pressions en quelques sections de la pale seront mesurés. On en espère des comparaisons théorie-expérience dans des cas de vol réalistes.

D - Couplage aéroélastique

Les progrès réalisés en aérodynamique devront être intégrés dans les programmes d'aéroélasticité. Ceux-ci doivent inclure la souplesse de la pale et en particulier les modes de torsion. Bien que celà puisse conduire à des codes de calcul gigantesques il semble que l'extension des principes exposés dans cet article pour un cas simplifié, puisse se faire sans difficultés théoriques particulières. Un tel travail ne serait

10 mm	en linéaire mouvement de pale imposé
15 mm	en linéaire avec couplage aéroélastique
30 mm	non linéaire méthode Boeing avec couplage aéroélastique
45 mm	non linéaire méthode ONERA avec couplage aéroélastique

La tendance actuelle étant au raffinement de la théorie, on ne peut espérer d'amélioration du temps de calcul que par une augmentation de la rapidité des ordinateurs. Il se pose aussi un problème d'interprétation des résultats, une liste de chiffres n'est plus suffisante dans un cas aussi complexe. Il faudrait pouvoir tracer des cartes de forces de portance, de traînée, d'incidence, des évolutions de C_z etc... ce n'est plus possible manuellement pour des applications industrielles. Les problèmes d'implantation des codes de calculs chez l'utilisateur et de couplage avec les moyens de sortie graphique de celui-ci devraient devenir de plus en plus importants dans les années à venir.

VI.2 - Développements futurs

A - Mécanique

On peut constater dans l'industrie une évolution rapide de la technologie de l'ensemble pales + moyeu par l'introduction des matériaux nouveau. Les gains en durée de vie, en entretien, en coût, sont considérables mais se traduisent aussi par des difficultés théoriques nouvelles. Les matériaux à fibres ont des caractéristiques anisotropes et des comportements mal connus, parfois même non linéaires. Des essais au sol sont actuellement utilisés pour connaitre les caractéristiques modales nécessaires aux calculs d'aéroélasticité, mais ils ne peuvent servir que de vérification une fois la pale ou le moyeu construit. Des études fondamentales théoriques et expérimentales sont entreprisent et devraient tendre à la prévision sur plan des caractéristiques mécaniques.

B - Aérodynamique théorique

Le fait le plus regrettable pour l'aérodynamique du rotor d'hélicoptère est l'absence, voire l'impossibilité pratique, d'une théorie que l'on pourrait qualifier d'unifiée. En effet il est possible de :

- traîter un fuselage isolé,
- de mettre en équilibre des sillages de tourbillons discrets,
- de faire des calculs de surface portante pour une aile en attaque oblique,
- d'introduire les effets transsoniques dans des cas non portants pour un flux à l'infini stratifié,
- de faire des expériences ou des calculs en fluide décroché pour des cas bidimensionnels.

Un rotor d'hélicoptère est tout celà, mais couplé, en tridimensionnel instationnaire et portant. En ce qui concerne l'aérodynamique utilisée dans cet article les améliorations possibles vont porter sur deux points principaux :

1 - une tentative d'introduction des effets de surface portante pour la pale avançante et la pale reculante. Le sillage serait divisé en deux parties, une partie lointaine hélicoïdale où la schématisation par ligne portante serait conservée et une partie proche où la pale se déplacerait dans un plan et serait traitée en surface portante par la méthode des singularités.

2 - une amélioration du passage du bidimensionnel décollé en tridimensionnel, en tenant compte du gradient de pression dans la zone décollée.

C - Aérodynamique expérimentale

Les améliorations théoriques doivent aller de pair avec des tests nombreux et souvent difficiles à réaliser. Les expériences permettent à la fois d'établir la théorie et de la tester dans quelques cas réels. Trois types d'expériences sont programmées dans un futur proche :

1 - Des expériences bidimensionnelles instationnaires sur une famille de profils modernes. Ces expériences serviront à la fois à l'amélioration du modèle mathématique et la constitution d'une base de données pour les applications aux rotors.

2 - Une aile rectangulaire non vrillée avec un profil OA 209 sera essayée en attaque oblique en soufflerie. Cette aile rigide sera animée de mouvements de tangage de fortes amplitudes analogues au pas cyclique d'une pale d'hélicoptère et entrera dans le domaine décroché. Des capteurs de pression, stationnaires (tuyaux) et instationnaires (membrane à semi-conducteur), seront répartis en quatre sections de l'aile. Les résultats obtenus serviront à tester dans des cas particuliers simples le passage du bidimensionnel décroché au tridimensionnel.

3 - Des expériences en vol seront réalisées sur un hélicoptère d'essai par la SNIAS. Ces expériences de réalisation très complexe auront des buts multiples, mais en particulier les mouvements des pales et les pressions en quelques sections de la pale seront mesurés. On en espère des comparaisons théorie-expérience dans des cas de vol réalistes.

D - Couplage aéroélastique

Les progrès réalisés en aérodynamique devront être intégrés dans les programmes d'aéroélasticité. Ceux-ci doivent inclure la souplesse de la pale et en particulier les modes de torsion. Bien que celà puisse conduire à des codes de calcul gigantesques, il semble que l'extension des principes exposés dans cet article pour un cas simplifié, puisse se faire sans difficultés théoriques particulières. Un tel travail ne serait

toutefois justifié que si les résultats obtenus en aérodynamique sont suffisamment sûrs dans le domaine de vol considéré.

VII - CONCLUSION

        Dans les chapîtres précédents, on a examiné comment les équations de la mécanique pouvaient se coupler avec une théorie linéaire, tridimensionnelle compressible et instationnaire, modifiée pour tenir compte des résultats expérimentaux dans les cas décrochés. Les pales répondent de façon quasi linéaire aux forces aérodynamiques, même lorsque celles-ci sont fondamentalement non linéaires. Cette propriété permet l'élimination des mouvements de pale inconnus dans les équations de nature proprement aérodynamique. Il reste un système non linéaire où les seules inconnues sont des forces de portance théoriques, équivalentes à des incidences. La recherche d'une solution se fait par une méthode de Newton généralisée en partant de la solution linéaire. Les résultats obtenus ont été comparés aux portances mesurées sur un rotor testé dans la soufflerie S1 de Modane. La comparaison théorie-expérience est satisfaisante pour des rapports d'avancement modérés (inférieurs à $\mu= 0,4$). Les développements futurs de l'aérodynamique théorique concernent le comportement des extrémités de pales aux azimuts 0° et 180°, ainsi qu'une amélioration du tridimensionnel non linéaire. Des expériences seront réalisées sur une aile rectangulaire en attaque oblique animée de mouvements de rotation de grande amplitude autour d'un axe longitudinal voisin du quart avant. On en attend une meilleure prévision du décrochage au voisinage de l'extrémité libre de la pale.

REFERENCES :

1) - R. Dat
    Représentation d'une ligne portante animée d'un mouvement vibratoire par une ligne de doublets d'accélération.
    La Recherche Aérospatiale n° 133 (Nov. Déc. 1969) Traduction NASA TT-F 12 952 (1970)

2) - R. Dat
    La théorie de la surface portante appliquée à l'aile fixe et à l'hélice.
    La Recherche Aérospatiale n° 1973-4, Traduction ESRO-TT-90 (1974)

3) - J.J. Costes
    Calcul des forces aérodynamiques instationnaires sur les pales d'un rotor d'hélicoptère -1972-
    Agard report n° 595, Traduction en anglais NASA-TT-F-15039 (1973)

4) - J.J. Costes
    Introduction du décollement instationnaire dans la théorie du potentiel d'accélération. Application à l'hélicoptère.
    La Recherche Aérospatiale n° 1975-3

5) - C.T. Tran, G. Renaud
    Theoretical predictions of aerodynamic and dynamic phenomena on helicopter rotors in forward flight
    Sept. 1975, First European Rotorcraft and Powered lift Aircraft Forum Southampton (England)

6) - J.J. Costes
    Rotor Response prediction with non-linear aerodynamic loads on the retreating blade.
    Second European Rotorcraft and powered lift Aircraft Forum
    Bückeburg (RFA) - 20-22 Sept. 1976

7) - J.J. Costes
    Application of the lifting line concept to helicopter computation
    4th European Rotorcraft and poweredlift Aircraft Forum
    Stresa (Italy)   13-15 Sept. 1978

8) - C.T. Tran, D. Falchero
    Application of the ONERA Dynamic stall model to a helicopter blade in forward flight
    Présenté à Seventh European Rotorcraft and Powered lift Forum
    Garmisch - Partenkirchen (RFA), 8-11 Sept. 1981

9) - R. Dat, C.T. Tran, D. Petot
    Modèle phénoménologique de décrochage dynamique sur profil de pale d'hélicoptère.
    Communication présentée au XVIème Colloque d'Aérodynamique Appliquée (AAAF)
    Lille 13-15 Novembre 1979 - ONERA T.P. n° 1979-149

10) - R.E. Gormont
     A mathematical model of unsteady aerodynamics and radial flow for application to helicopter
     rotors.
     USA-AMRDL - TR - 72-67 (Mai 1973)

11) - J. Liiva, F.J. Davenport, L. Gray, J.C. Walton
     Two dimensional test of airfoils oscillating near stall
     USA - AVL ABS - TR 6813 (Avril 1968)

12) - R.A. Ormiston
     Comparison of several loads prediction methods for a hypothetical rotor.
     Conference présentée le 13-15 Février 1974 à Moffett Field Californie
     Rotorcraft dynamics Publications NASA SP 352

13) - Stepniewski
     Rotary wing Aerodynamics · Volume 1
     NASA Contractor Report 3082

AD-A124 360   PREDICTION OF AERODYNAMIC LOADS ON ROTORCRAFT(U)   3/4
ADVISORY GROUP FOR AEROSPACE RESEARCH AND DEVELOPMENT
NEUILLY-SUR-SEINE (FRANCE)   SEP 82 AGARD-CP-334

UNCLASSIFIED   F/G 1/2   NL
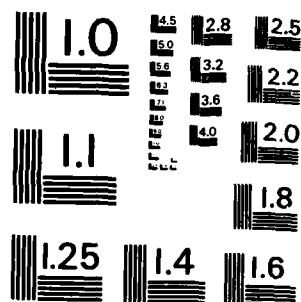
MICROCOPY RESOLUTION TEST CHART

NATIONAL BUREAU OF STANDARDS-1963-A
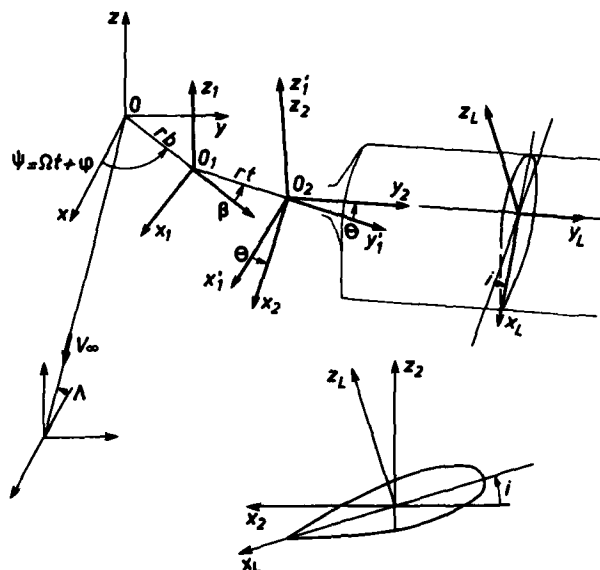
Fig. 1 — *Repère de référence pour un rotor articulé en battement et en traînée.*
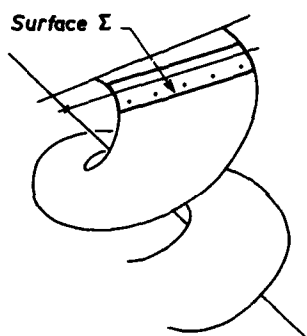
Fig. 2 — *En accord avec les hypothèses de linéarisation, la pale d'hélicoptère est rabattue sur son sillage (surface Σ).*
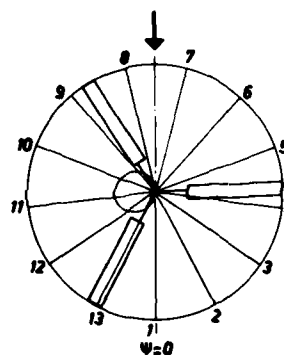
Fig. 3 — *On considère 13 positions azimutale équidistantes de la pale (ψ = 0 en position la plus arrière). Pour chaque azimut les portances en 5 positions radiales seront calculées.*
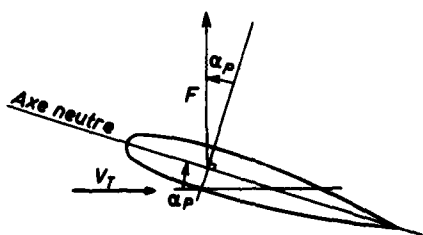
Fig. 4 — *Profil bidimensionnel. Paradoxe de d'Alembert.*

a) — Distance à l'axe de rotation r/R_1 = 0,52.

b) — Distance à l'axe de rotation r/R_1 = 0,71.

c) — Distance à l'axe de rotation r/R_1 = 0,855.

d) — Distance à l'axe de rotation r/R_1 = 0,952.
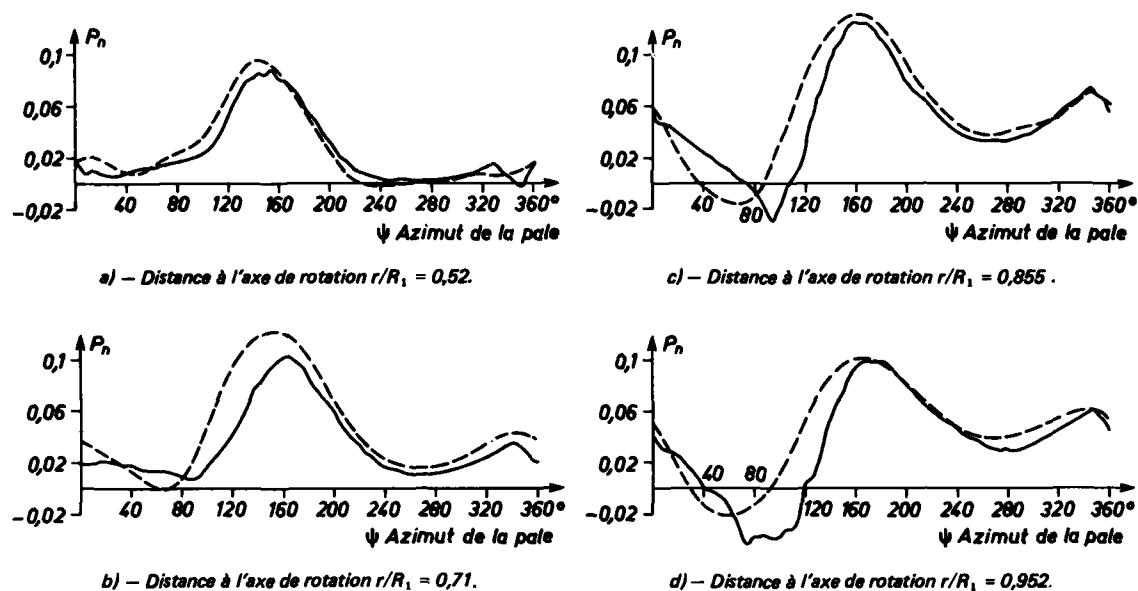
Fig. 5 — Portances normalisées pour 4 sections de la pale en fonction de
l'azimut. Expérience 841. Rapport d'avancement $\mu = 0.44$

—————— Expérience. Profile NACA 0012 sur toute la pale
— — — Calcul pale libre articulée en battement et en traînée.

$$P_n = \int_0^1 \Delta p/p_0 \ d(x/c).$$

$\cdots$ Mesure en vol
—————— Calcul avec moyeu fixe
— — — Calcul avec mouvement du moyeu imposé
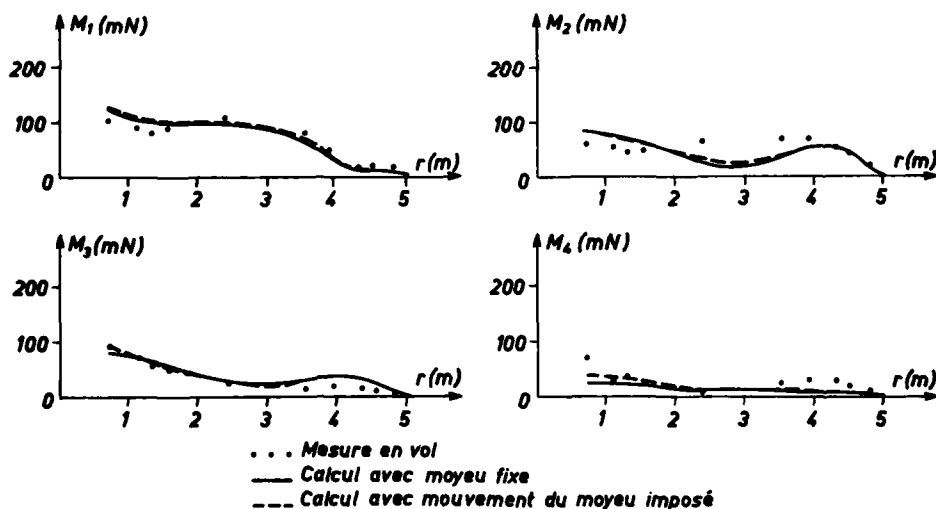
Fig. 6 — Essai en vol du SA 349 Z gazelle (μ = 0,33, CT/σ = 0,067).
· Analyse harmonique des moments de battement le long de la pale.
· Amplitude des 4 premiers harmoniques.
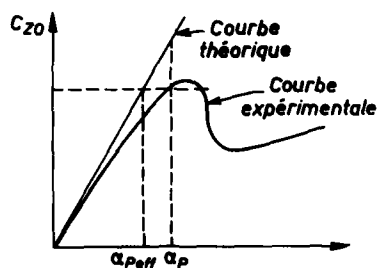
Fig. 7 — Mesure du coefficient de portance en
stationnaire.
α_P incidence aérodynamique.
α_{Peff}. incidence aérodynamique efficace.
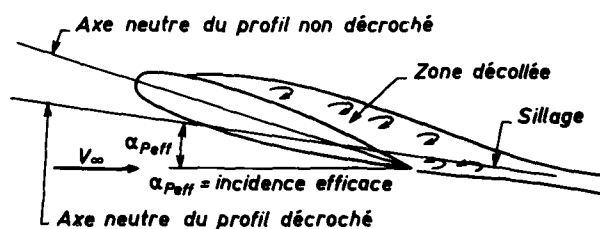
Fig. 8 — Ecoulement décollé stationnaire autour
d'un profil bidimensionnel.
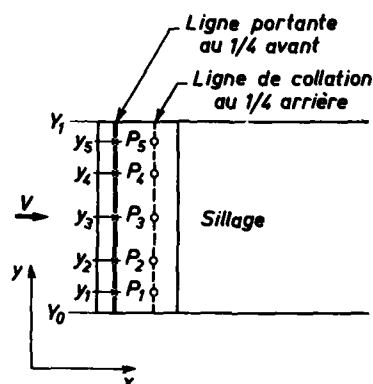
Fig. 9 — Aile rectangulaire en translation —
Schématisation par une ligne por-
tante au 1/4 avant.

Mach = 0,2 $\alpha_0 = 12,24°$
f = 16,86 Hz $\Delta\alpha = 4,84°$
k = 0,128
$k = \dfrac{\pi f c}{V}$

—— Mesures TR 68 –13A. Liiva.
Naca 12 modifié réf. 11.

--- Courbe calculée méthode
Bœing.

—— Mesures sur le profil
ONERA – AEROSPATIALE 0A 212

Mach = 0,3   k = 0,049
$\alpha_0 = 13°$ $\Delta\alpha = 6°$

--- Courbe calculée par la méthode
ONERA réf. 9.
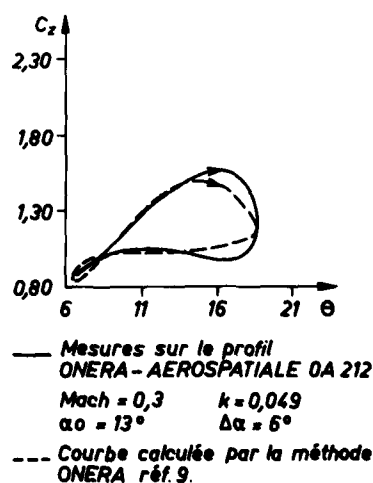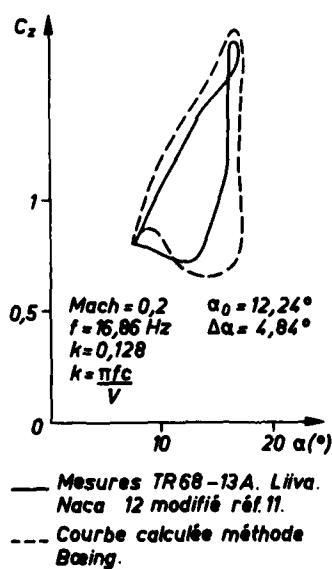
Fig. 10 — Reconstruction des boucles de Cz par deux modèles mathématiques.
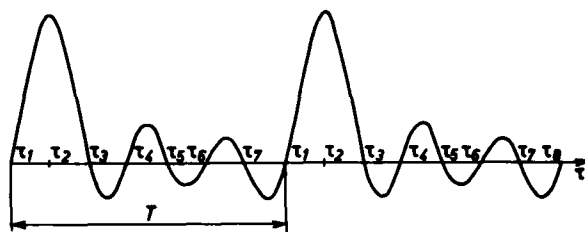
Fig. 11 — Exemple de fonction de base, la fonction $g_2 (\tau)$ égale à
1 pour $\tau = \tau_2 + nT$ et égale   à 0 pour $\tau = \tau_i + nT$
$i = 1, 3, 4, 5, 6, 7$ $g_2 (\tau)$ ne comporte que 3 harmoniques.

Expérience
Calcul linéaire
Avec décollement statique
Avec décollement instationnaire

a) Distance à l'axe de rotation $r/R_1 = 0,52$.

c) Distance à l'axe de rotation $r/R_1 = 0,855$.

b) Distance à l'axe de rotation $r/R_1 = 0,71$.

d) Distance à l'axe de rotation $r/R_1 = 0,952$.
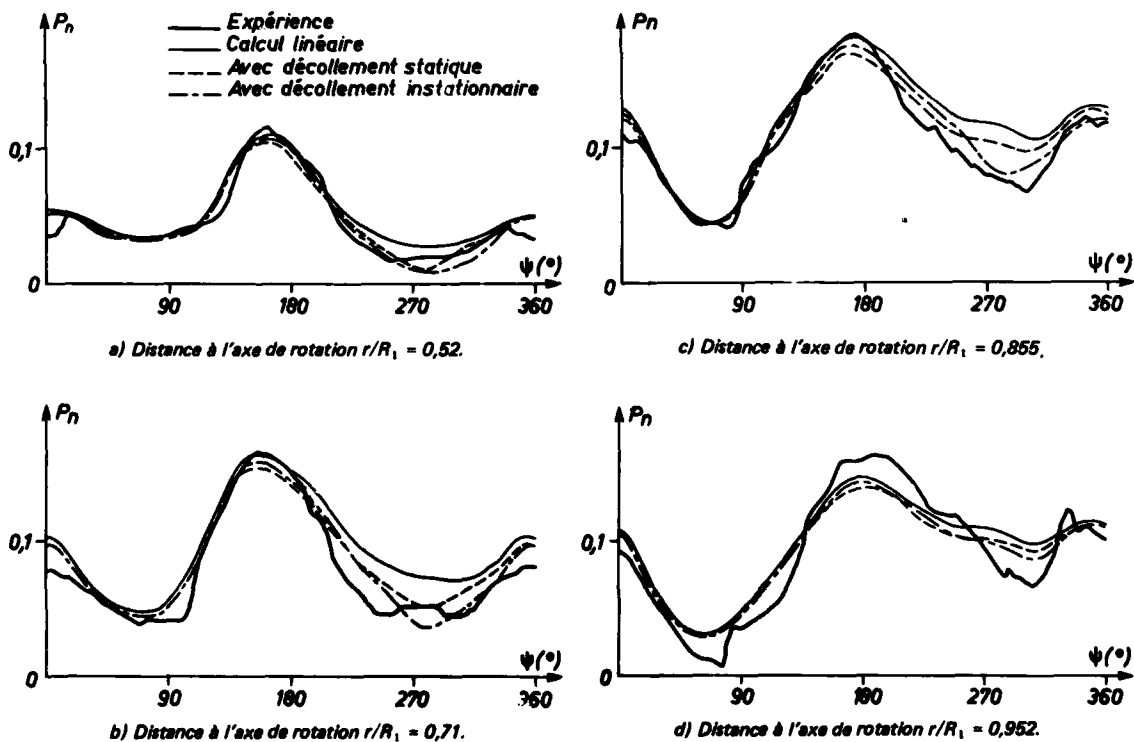
Fig. 12 — Cas de vol n° 855 - Mouvement de la pale donné par l'expérience $\mu = 0,3$.

$Pn = \int_0^1 \Delta p/po \; d (x/c)$. Profil NACA 0012 sur toute la pale.

a) Distance à l'axe de rotation r/R₁ = 0,52.

c) Distance à l'axe de rotation r/R₁ = 0,855.

b) Distance à l'axe de rotation r/R₁ = 0,71.

d) Distance à l'axe de rotation r/R₁ = 0,952.
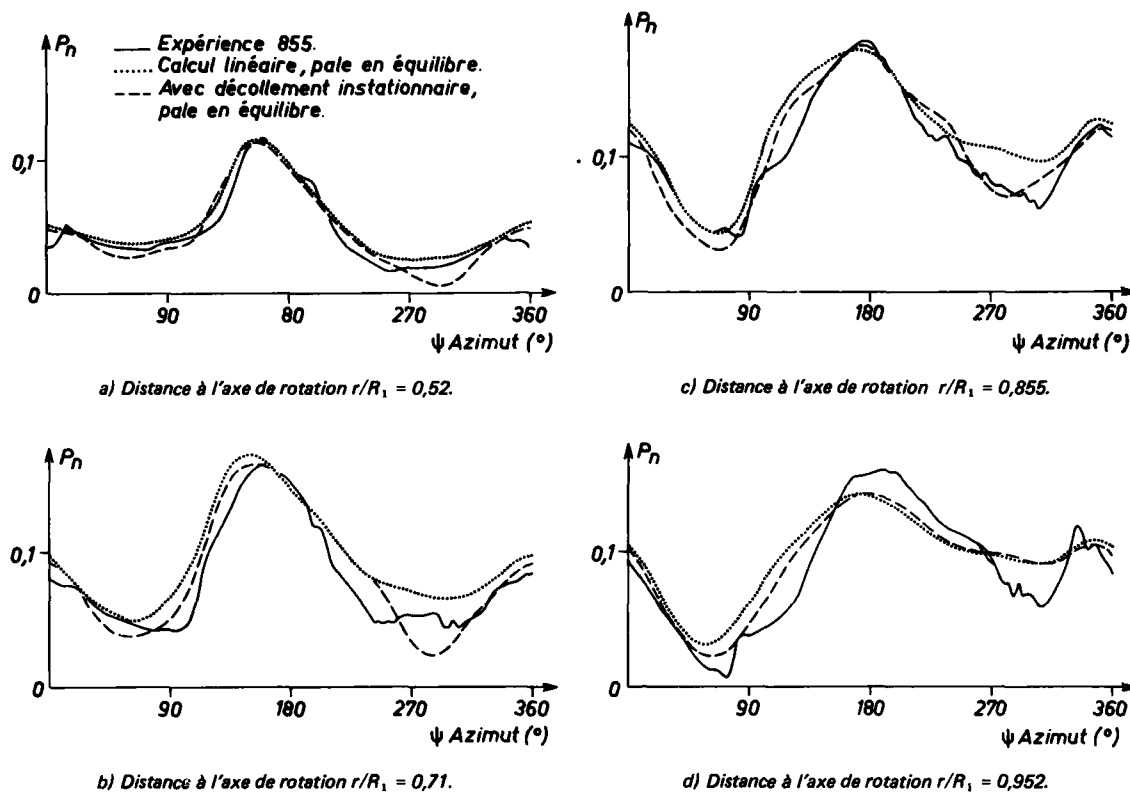
Fig. 13 — Cas de vol n° 855 - Pale en équilibre avec les forces aérodynamiques théoriques.

$$Pn = \int_0^1 \Delta p/po \; d\,(x/c) \; ; \quad profil\ NACA\ 0012\ sur\ toute\ la\ pale.$$
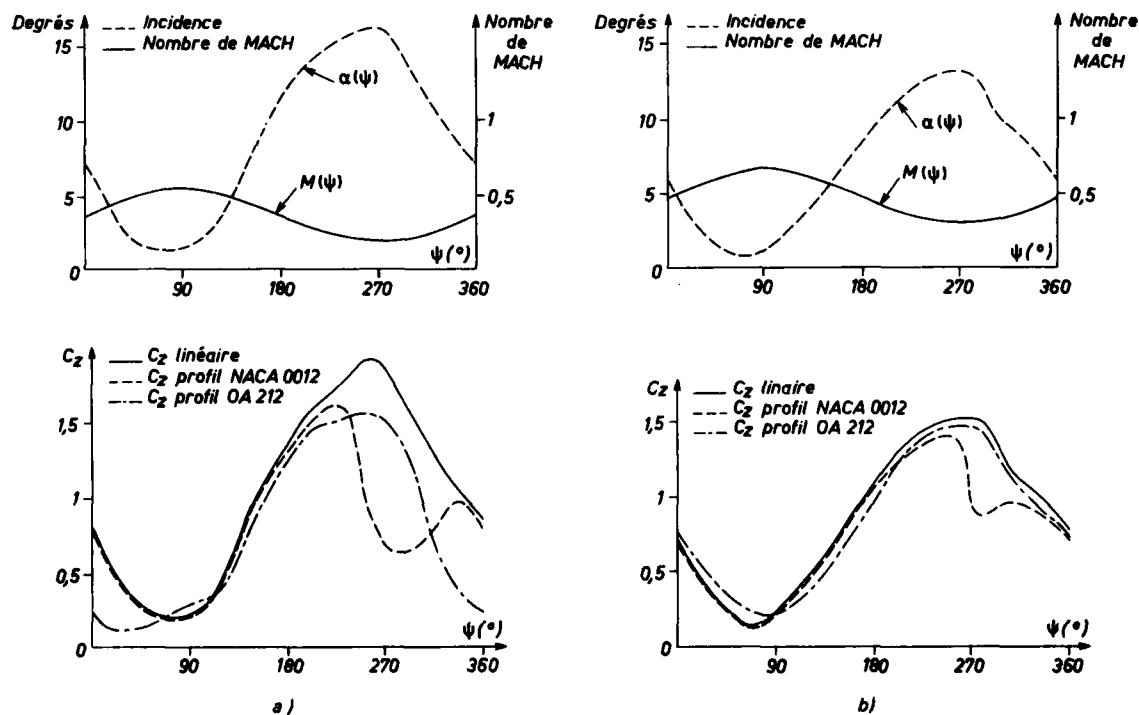
Fig. 14 — Comparaison des Cz pour deux profils d'épaisseur 12 %.

a) Évolution de l'incidence, du nombre de Mach et du Cz à la distance radiale r/R₁ = 0,61 en fonction de l'azimut.

b) Évolution de l'incidence, du nombre de Mach et du Cz à la distance radiale r/R₁ = 0,81 en fonction de l'azimut.

FIRST RESULTS FOR THE DEFINITION OF A
GENERAL ROTORCRAFT DYNAMIC PROGRAM

by

Anselmo Russo and Alberto Ceriotti
Dynamics Engineers
Costruzioni Aeronautiche G. AGUSTA
Cascina Costa – Varese
ITALY

SUMMARY

This paper describes the work done at Agusta Helicopters during these last years
in order to define a computer program able to solve the large number of problems related
to the dynamic behaviour of a rotor or a complete helicopter.
Starting from the idea of describing the analytical model by a technique similar to the
finite element analysis, the equations of motion are obtained with the aid of the general
equation of dynamics, in its standard matrix form. These matrices are updated at each
step of integration by means of the coordinates describing the reached configuration.
These operations are simply the linearization, around the actual position of dynamic
equilibrium, of the equations of motion and constrain equations.
Forcing functions can be either forces or imposed displacements depending on time as well
as on any kynematic value of other elements or their own kynematic value. A special
feature of the program permits to introduce, in an analytical way, any possible dependence
by means of a set of FORTRAN statements in the input cards.
Aerodynamic forces acting on the elements can be steady or unsteady according to the
choice by the user. The steady aerodynamic coefficients are computed from the local
incidence deduced by means of kynematic, gust, and induced velocities of the rotor wakes
introduced into the model.
Particular attention is paid to the input data both for a rational description of the
model and in order not to cause format troubles to the user; the helpful way indicated
by NASTRAN program is taken as a guideline and in some cases improved as for the forcing
functions mentioned before.

INTRODUCTION

When designing a helicopter, a large number of different computations are
necessary to predict the dynamic behaviour of the machine and its components. This set
is continually changed during this stage until a satisfactory compromise is reached
between their producibility and the initial requirements.
This approach is typical of an optimisation problem in which the desired set of parameters
minimizes a stated function, i.e. vibration level in structural points, without failure
of some geometrical constraints or imposed dependences among them (stresses or displace-
ments). In theory, this process can be developed automatically, utilizing the optimiza-
tion algorithms, but in practice the lack of an appropriate software and the exaggerated
computer time required prevent their utilization.
To overcome these difficulties, the optimization problem is solved by the experience
gained in the previous designs and/or by trying to optimize each component separately,
disregarding the effect of an optimization on the other ones, unless evident. At present,
the software required to perform all these computations is, in our Company, completely
specialized by dedicated programs for ground resonance, pitch lag instability, dynamic
behaviour of blades and so on. Each of them is based on its own hypotesis and simplifi-
cation generally derived from experience.
These limitations are sometimes unacceptable in a new design, and when this happens, a
great effort must be done in order to develop the new software, that, at the worst, is
not a generalization of the problem but only a particular case. All these reasons
suggested us to develop a methodology able to unify all these softwares in a single
program to answer questions that might arise in a new project.
This attempt can be seen as a way to generalize the dynamic problems of a system. The
selected way takes advantage from the methodology introduced by the finite elements in
which the system is thought as a set of basic elements connected in any prescribed manner.
This technique permits to build up simple as well as complicated structures according to
the problems to be analysed.

EQUATIONS OF MOTION

The basic assumption, in the development of the equations of motion, is the utilization of rigid elements (RE) to idealize the structure. The RE are connected to each other by means of stiffness, damping, structural damping matrices, hinges, springs, constraints, etc., according to the examined structure. They are loaded with known forces and moments defined as functions of time and/or any kynematic parameter. The equations of motion are deduced, at each step of integration, by the general equation of dynamics that states for a system of particles: "the reaction forces don't work for any virtual displacement"

$$\sum_i \delta \vec{r}_i \cdot \vec{R}_i = 0. \tag{1}$$

This equation, valid for the ideal constraint, leads to the Lagrange's equations.

For a system of rigid bodies, the general equation of dynamics can be riformulated in the following manner: "the reaction forces (forces and moments) don't work for any virtual rototraslatory displacement". So, for a set of rigid bodies, we can write:

$$\sum_{i=1}^{n} \{\delta r\}_i^T \cdot \left[\{F_E\} + \{F_I\} \right]_i = 0. \tag{2}$$

where:

$$\left[\{F_E\} + \{F_I\} \right]_i \qquad \text{reaction forces}$$

$$\{F_E\} = \left\{ \frac{\vec{F}_E}{\vec{M}_E} \right\} \qquad \text{resultant of external forces}$$

$$\{F_I\} = \left\{ \frac{\vec{F}_I}{\vec{M}_I} \right\} \qquad \text{resultant of inertial forces}$$

$$\{\delta r_i\} = \left\{ \frac{\delta \vec{x}_{cg}}{\delta \vec{\vartheta}} \right\} \qquad \text{virtual rototraslatory displacements of the i-th element}$$

VIRTUAL DISPLACEMENTS AND DEGREES OF FREEDOM

Let's consider an arbitrary set of reference systems (RS) of known origins P_i and orientation $[a_i^o]^T$ with respect to a fixed RS. Let's suppose now that any translation or rotation around one coordinate axis of the RS produces a rigid translation or rotation of the RS that follow it. A point x_n of the n-th RS is seen in the absolute RS solving the equation:

$$\vec{x}_o = [R_n]^T \vec{x}_n + \sum_{i=0}^{n-1} [A_i]^T \{\vec{P}_o + \Delta \vec{P}\}_{i+1} \tag{3}$$

where:

$$[R_n]^T = [A_n]^T [a_n^o]^T$$

$$[A_i]^T = \prod_{j=1}^{i} [T_j^*]^T \qquad \text{and} \qquad [A_o]^T = [U] \quad \text{(unit matrix)}$$

$$[T_j^*]^T = [a_j^o]^T [T_\alpha]_j^T [a_j^o]$$

$$[T_\alpha]^T \qquad \text{elementary rotation around x, y, or z axes (see appendix 1)}$$

$$\Delta \vec{P} \qquad \text{relative translation of the origins of the RS}$$

The absolute velocity of x_n is

$$\dot{\vec{x}}_o = [\dot{R}_n]^T \vec{x}_n + \sum_{i=0}^{n-1} [\dot{A}_i]^T \{\vec{P}_o + \Delta \vec{P}\}_{i+1} + \sum_{i=0}^{n-1} [A_i]^T \{\dot{\vec{P}}\}_{i+1} \tag{4}$$

It is easy to show that the angular velocities of the nth RS can be obtained from

$$[\Omega_\Lambda] = [R_n][\dot{R}_n]^T \qquad \text{(see appendix 1)} \tag{5}$$

$$\left[\dot{R}_n\right]^T = \sum_{i=1}^{n} \dot{\alpha}_i \left[R_{id}\right]^T$$

$$\left[R_{id}\right]^T = \left[T_1^*\right]^T \cdot \left[T_2^*\right]^T \cdot \cdots \cdot \left[T_{id}^*\right]^T \cdots \left[T_n^*\right]^T \left[a_n^o\right]^T$$

$$\left[T_{id}^*\right] = \frac{1}{\dot{\alpha}_i} \cdot \frac{d}{dt}\left(\left[a_i^o\right]^T \left[T_{\alpha i}\right]^T \left[a_i^o\right]\right)$$

Thus the coordinates of this transformation are relative coordinates and represent the local displacements. Fig 1 shows, as example, a rigid blade with flap, drag and pitch angles as considered in the analysis.

From a kynematic point of view, the position of a fixed point in the n-th RS is univocally determined once a set of relative coordinates is established, while the transformation law is prescribed by the sequence of RS choosed. Same conclusions are valid for velocities, too.

During the integration, the geometry can be updated as if the system started everytime from the last position. In this way it is possible to overcome the problem of the choice of the sequence at each step of integration, reaching the right position of the system also after that large displacements and rotations have been developed.

The infinitesimal variations of the absolute coordinates of the x_n point $\{\delta x_o\}$ and rotations of relative RS $\{\delta\theta\}$ are computed by:

$$\frac{\partial \vec{x}_o}{\partial q_i} = \frac{\partial \vec{x}_o}{\partial t} \cdot \frac{1}{\dot{q}_i} = \frac{\partial \vec{x}_o}{\partial \dot{q}_i} \qquad \text{(velocity of } \vec{x}_o \text{ for unit } \dot{q}_i) \tag{6}$$

$$\frac{\partial \vec{\theta}}{\partial q_i} = \frac{\partial \vec{\Omega}}{\partial \dot{q}_i} \tag{7}$$

$$\{\delta\vec{x}_o\} = \sum_{i=1}^{n} \frac{\partial \vec{x}_o}{\partial q_i} \delta q_i \quad ; \quad \{\delta\vec{\theta}\} = \sum_{i=1}^{n} \frac{\partial \vec{\theta}}{\partial q_i} \delta q_i \tag{8}$$

where the gradients contained in the two expressions Eq(8) are evaluated by means of the equations of the velocities Eq(4) and of the angular velocities Eq(5), utilizing the identities Eq(6)-Eq(7). The meaning of q_i can be either relative rotations $\{\alpha_i\}$ or translations $\{\Delta P_i\}$ of the previous RS.

In matrix form

$$\begin{Bmatrix} \delta\vec{x}_o \\ \delta\vec{\theta} \end{Bmatrix} = \left[c_1 \right] \{\delta q\} \qquad \text{where} \qquad c_{1kj} = \frac{\partial r_k}{\partial q_j} \tag{9}$$

Now

$$\{\dot{r}\}_i = \left[c_1 \right]_i \{\dot{q}\} \tag{10}$$

$$\{\ddot{r}\}_i = \left[c_1 \right]_i \{\ddot{q}\} + \{\ddot{r}\}_{\dot{q}=0} \tag{11}$$

The last equation will be utilized for the computation of the inertia forces and moments taking into account the dependence of the acceleration on the relative velocities $\dot{q}$ and displacements q by means of the term $\{\ddot{r}\}_{\dot{q}=0}$.

This term is equivalent to

$$\{\ddot{r}\}_{\dot{q}=0} = \frac{d}{dt} \left[c_1 \right] \{\dot{q}\} \tag{12}$$

as the gradients are function of the displaced configuration.

With this technique every RE can be characterized by means of three initial overlapped RS; each of them can rotate only around one coordinate axis with the sequence α_x, α_y, α_z, while the first RS can also translate. So the final position of the RE will be univocally determined by the displacements of the first origin and three non-orthogonal rotations. This way, for a single rigid body, coincides with Eulero's procedure with the difference that the classical Eulero's transformation utilizes the sequence α_z, α_x, α_z, while, in the aeronautical field, the sequence α_z, α_y, α_x is commonly utilized.

Starting from the RE, it is possible to construct any desired series of elements in the manner described for the series of RS. The connection points can be arbitrarely located in the RS of the RE. These are the points at which it will be possible to introduce the relative stiffness, damping and structural damping matrices. Each element can be the origin of other elements. In this way the final structure looks like a tree structure where the absolute coordinates and velocities of any point of an element can be computed by

means of the same formulas presented before. A typical example of this structure can be a helicopter with fuselage, transmission, hub and blades or a less complicated one like a single blade. The degrees of freedom (DOF) of a tree structure coincide with the unconstrained DOF introduced in the connected points and they are, therefore, Lagrange's coordinates.

When the series are interconnected, the coordinates are not Lagrangian any more but constrain equations exist among them and they must be satisfied at each step of integration. These equations are non-linear as they are function of the configuration that can be different from the initial one.

An example of this situation is represented by the link between the blade and the swash plate by means of a control rod. To solve the kynematism contained in the model of Fig. 2 the algorithm starts from the tree structure and detects the closed rings contained, checking if the last terms of the series are connected with any other element. In this case, the tree structure is composed of the following series:

$$\begin{bmatrix} 0 & 1 & 2 & 4 \\ 0 & 3 & 7 & \\ 0 & 1 & 2 & 5 & 6 \end{bmatrix}$$

(the numbers are the names of the elements) and the connected series or closed rings are:

$$\begin{bmatrix} 0 & 1 & 2 & 4 \\ 0 & 3 & \end{bmatrix} \quad \text{and} \quad \begin{bmatrix} 0 & 3 & 7 \\ 0 & 1 & 2 & 5 & 6 \end{bmatrix}$$

After this step the algorithm analyses the rings more closed to the origin, breaking the connecting element into two pieces, leaving one side attached to the first series and the other to the second one. Then defining $\Delta \vec{x}$ as the vector connecting the broken sections and choosing three of the nine director cosines of the two RS associated with the two sides of the broken element (Fig. 3), we can write the following system of equations:

$$\left\{ \begin{matrix} \Delta \vec{x} \\ \Delta \vec{n} \end{matrix} \right\} = \left[\frac{\partial \vec{x}}{\partial \vec{n}} \frac{\partial q_i}{\partial q_i} \right] \left\{ \delta q_i \right\} \tag{13}$$

where $\{\delta q_i\}$ are all the DOF permitted in the connection points of the elements of the ring (including the DOF of the broken element itself). The congruence condition requires:

$$\left\{ \begin{matrix} \Delta \vec{x} \\ \Delta \vec{n} \end{matrix} \right\} = \left\{ 0 \right\} \tag{14}$$

After the elimination of the equations always verified (zero gradients like the dz equation in the example) and those that are in linear combination (the versors of x and y axes) it is possible to express a number of DOF equal to the remain equations in terms of the other ones.

To avoid ill-conditioning of the matrix associated with the selected dependent DOF, we implement the first step of the Newton-Raphson algorithm perturbing the system with all the combinations of the independent previously evaluated DOF. The combination that predicts the closest solution to the right one (congruence) is selected. The imposed DOF are treated as independent ones and will be then eliminated after the assembling of the system of the equations of motion.

After the analysis the ring must be grounded to eliminate its DOF from the other rings. This operation is easy done eliminating all its elements from the remaining rings. In the example, the second ring, after the elimination of the elements 1, 2, 3 contained in the first ring, will become:

$$\begin{bmatrix} 0 & 7 \\ 0 & 5 & 6 \end{bmatrix}$$

which will then be analysed.(DOF of Fig. 2 are reported in Tab. 1).

All these computations are executed before the integration and permit to define, for each ring, the independent equations and the dependent DOF. During the integration the first step is the imposition of the Lagrangian DOF calculated in the previous step of the integration. Then, with the aid of the Newton-Raphson algorithm, the congruence is obtained with the appropriate dependent DOF. The gradients between the dependent and independent DOF are computed around the reached configuration. The virtual displacements of the prescribed point of a rigid element (our choice is the center of gravity) are then defined by the set of equations:

$$\{\delta r\} = [c_1]\{\delta q_c\} \tag{15}$$

$$\{\delta q_c\} = [c_2]\{\delta q_1\} \qquad c_{2kj} = \partial q_{ck} / \partial q_{1j} \tag{16}$$

Substituting

$$\{\delta r\} = [c_1][c_2]\{\delta q_1\} \tag{17}$$

The dependent velocities and accelerations then are:

$$\{\dot{q}_c\} = [c_2]\{\dot{q}_1\} \quad ; \quad \{\ddot{q}_c\} = [c_2]\{\ddot{q}_1\} \quad \text{as} \quad \frac{d}{dt}[c_2] = 0. \tag{18}$$

and the absolute velocities and accelerations are:

$$\{\dot{r}\} = [c_1][c_2]\{\dot{q}_1\} \tag{19}$$

$$\{\ddot{r}\} = [c_1][c_2]\{\ddot{q}_1\} + \{\ddot{r}\}_{\ddot{q}_1=0} \tag{20}$$

The equation of dynamics Eq(2) in terms of the Lagrangian coordinates becomes:

$$\sum_{i=1}^{n} \{\delta q_1\}^T [c_2]^T [c_1]_i^T \left(\{F_E\} + \{F_I\}\right)_i = 0 \tag{21}$$

from which, for their completely arbitrariness, it is possible to obtain the system of the equations of motion:

$$[c_2]^T [c_1]_i^T \left(\{F_E\} + \{F_I\}\right)_i = 0 \qquad (i=1,2,\ldots\ldots,n) \tag{22}$$

The problem so formulated permits to draw some considerations. The simplifications introduced with the RE are soon counterbalanced by the simplicity to operate with its characteristic parameters (Ω, $\vec{R}$, $\vec{M}$, $\delta\vec{r}$, etc.) thus reflecting in easy way the physics of the problem. Moreover, the particular choice of the DOF permits to compute automatically the matrices C_1 and C_2 of the virtual displacements from the input geometry, no matter how complicated, leaving this way the possibility to increase the number of elements until the desired approximation is reached.
Looking at the forces contained in the equations of motion we can note that they are simply the resultant of the forces and moments acting on the elements, applied in their center of mass. Thus we are able to introduce any type of forces without any concern about the application point, direction and their dependence from any parameter.

FORCES ACTING ON THE SYSTEM

INERTIA FORCES AND MOMENTS

Working at element level, it is easy to compute the inertia forces and moments starting from the classical formulation

$$\vec{F}_I = -\sum_i m_i \vec{a}_i = -M \vec{a}_{cg} \tag{23}$$

$$\vec{M}_I = -\sum_i (P_i - O) \times m_i \vec{a}_i \tag{24}$$

If the point "O" coincides with the center of mass and remembering the velocity and acceleration fields of a rigid body

$$\vec{v}_i = \vec{v}_{cg} + \vec{\Omega} \times (P_i - O) \tag{25}$$

$$\vec{a}_i = \vec{a}_{cg} + \vec{\dot{\Omega}} \times (P_i - O) + \vec{\Omega} \times \left[\vec{\Omega} \times (P_i - O)\right] \tag{26}$$

we obtain

$$\vec{M} = -[I]\vec{\dot{\Omega}} - [\Omega_\times][I]\vec{\Omega} \tag{27}$$

where [I] is the inertia matrix referred to any RS with origin in the center of mass. In matrix form

$$\{F_I\} = \left\{\begin{matrix}\vec{F}_I \\ \vec{M}_I\end{matrix}\right\} = -\left[\begin{matrix}[m] & 0 \\ 0 & [I]\end{matrix}\right]\left\{\begin{matrix}\vec{\dot{x}}_{cg} \\ \vec{\dot{\Omega}}\end{matrix}\right\} - \left\{\begin{matrix}0 \\ [\Omega_\times][I]\vec{\Omega}\end{matrix}\right\} \tag{28}$$

Substituting the expression of the acceleration

$$\left\{\frac{\vec{F}_I}{\vec{M}_I}\right\}_i = -\left[\frac{[m]\mid 0}{0\mid [I]}\right][c_1]_i\,[c_2]\{\ddot{q}_1\} - \left[\frac{[m]\mid 0}{0\mid [I]}\right]\{\ddot{r}\}_{\ddot{q}_1=0} - \left\{\frac{0}{[\Omega][I]\vec{\Omega}}\right\} \quad (29)$$

the generalized forces of inertia become

$$\{F_I\}_G = -\;[c_2]^T\;[\,c_1]_i^T\left[\frac{[m]\mid 0}{0\mid [I]}\right][c_1]_i\,[c_2]\,\{\ddot{q}_1\} +$$

$$-\;[c_2]^T\;[c_1]_i^T\left[\frac{[m]\mid 0}{0\mid [I]}\right]\{\ddot{r}\}_{\ddot{q}_1=0} - [c_2]^T\,[c_1]_i^T\left\{\frac{0}{[\Omega][I]\vec{\Omega}}\right\} \quad (30)$$

where the contribution to the mass matrix of the ith element is

$$[M]_i = [c_2]^T\,[c_1]_i^T\left[\frac{[m]\mid 0}{0\mid [I]}\right][c_1]_i\,[c_2] \quad (31)$$

ELASTIC, DAMPING AND STRUCTURAL DAMPING FORCES

This set of forces will be treated formally in the same way as they are obtained from the product of a matrix with a vector. In fact

$$\{F_E\} = [K]\{q\} \quad (32)$$

$$\{F_D\} = [D]\{\dot{q}\} \quad (33)$$

$$\{F_{SD}\} = i\,g\,\{F_E\} = i\,g\,[K]\{q\} \quad (34)$$

where $[K]$ and $[D]$ are, respectively, the stiffness and damping matrices, g is the structural damping parameter and i the imaginary unity. Let's consider now two RE connected in a point P (see Fig. 4) by means of a stiffness matrix. The imposition of the permitted displacements q_i to the point P of the element "a" generates, in the same point, the following forces and moments (action):

$$\left\{\frac{\vec{F}_E}{\vec{M}_E}\right\}_{Pa} = -[K]\{q\}_a \quad (35)$$

while on the point P thought on the element "i" the forces and moments (reaction) will be:

$$\left\{\frac{\vec{F}_E}{\vec{M}_E}\right\}_{Pi} = +[K]\{q\}_i \quad (36)$$

Reducing now the forces and moments to the same RS "i" and "a" by means of the transformation matrix and displacing them to the respective center of gravity with a transformation of the type:

$$\left\{\frac{\vec{F}_E}{\vec{M}_E}\right\}^* = \left[\frac{[U]\mid 0}{[P-CG]_A\mid [U]}\right]\left\{\frac{\vec{F}_E}{\vec{M}_E}\right\}_P \quad (37)$$

where

$$\left\{\frac{\vec{F}_E}{\vec{M}_E}\right\}^* \qquad\qquad \text{force and moment applied in the center of gravity}$$

$$\left\{\frac{\vec{F}_E}{\vec{M}_E}\right\} \qquad\qquad \text{force and moment applied in point P}$$

$[P-CG]_A$ matrix deduced from the vector multiplication $(P-CG)\times\vec{F}_E$ (see Appendix 1)

we obtain the desired expression of the elastic forces in terms of DOF

$$\left\{ \begin{matrix} \vec{F}_E \\ \vec{M}_E \end{matrix} \right\}_i^* = \left[K \right]_i^* \left\{ q \right\}_i \tag{38}$$

$$\left\{ \begin{matrix} \vec{F}_E \\ \vec{M}_E \end{matrix} \right\}_a^* = \left[K \right]_a^* \left\{ q \right\}_a \tag{39}$$

where $\left[K \right]_i^*$ and $\left[K \right]_a^*$ are the stiffness matrices reduced to the center of gravity of the respective elements. Remembering the equations of motion, the generalized forces then are:

$$\left\{ F_E \right\}_{iG} = \left[C_2 \right]^T \left[C_1 \right]_i^T \left[K \right]_i^* \left[C_1 \right]_i \left[C_2 \right] \left\{ q_1 \right\} \tag{40}$$

$$\left\{ F_E \right\}_{aG} = \left[C_2 \right]^T \left[C_1 \right]_a^T \left[K \right]_a^* \left[C_1 \right]_a \left[C_2 \right] \left\{ q_1 \right\} \tag{41}$$

where

$$\left[K \right]_{ii} = \left[C_2 \right]^T \left[C_1 \right]_i^T \left[K \right]_i^* \left[C_1 \right]_i \left[C_2 \right] \tag{42}$$

$$\left[K \right]_{ia} = \left[C_2 \right]^T \left[C_1 \right]_a^T \left[K \right]_a^* \left[C_1 \right]_a \left[C_2 \right] \tag{43}$$

are the contributions of the elastic forces applied in point P to the stiffness matrix of the whole structure. It is interesting to note that the assembling of the first contribution makes the stiffness matrix disymmetric while the subsequent assembling makes it symmetric (see Tab. 2).
This fact can be interpreted in this way: "the symmetry of a mechanical matrix comes from the third principle of dynamics, that is the equality of action and reaction". So, if we introduce only the action, like linearized aerodynamic forces or control system forces, the matrices will become disymmetric and if these forces are in phase within their causes, the system an be unstable.
The ground can be thought as a further element, the displacement of which is then consider ed zero. Thus, the elements connected to the ground make the mechanical matrices symmetric.
It is possible to introduce springs and dampers among any element of the structure. The way to compute the contribution to the stiffness and damping matrices is quite similar to that presented before. While the stiffness, damping matrices are considered linear, these scalar elements can be described with non-linear characteristics. The non-linear algorithm presented in this work linearizes them around the position of dynamic equili-brium reached. The stiffness, damping and structural damping in the connection points are introduced into the computer program by means of input cards. Their evaluation is easy done with specialized program like NASTRAN, etc., starting, if desired, from tri-dimensional structures and condensing the obtained matrices to the desired points. These condensed matrices must then be calculated in the relative coordinates suitable for the input. The example of Fig. 5 shows a tridimensional channel structure built up with bi-dimensional plate elements monodimensionalized by the computations of the axes of the shear centers and the stiffness matrix in relative coordinates.
This method permits to avoid the development of complicated elements like beam elements, curved and twisted, suitable for rotor blades and to analyse new materials, like composit, in an easy manner.

GENERAL FORCES

Any other type of forces follows the method indicated before. Their dependence on any desired parameters (displacements, velocities, accelerations, Eulerian angles, angular velocities, etc.) of the elements are easily introduced into the program.
A special feature of the input data permits to introduce these dependences in an analy-tical way by means of a set of FORTRAN statements (see Fig. 6). This set of statements can be a complete program with subroutines the final results of which are the desired forces and/or moments. These parameters can be evaluated both in real time and also by keeping into account any delays specified by the operator (like pilot inputs).

IMPOSED MOTION

Among the forcing functions there is the possibility to impose desired displacements, velocities or accelerations of the DOF. The algorithm considers, in the first stage, these DOF as Lagrangian ones. So the equations of motion, before the computation of the unknown accelerations, have the following matrix form:

$$\left[\begin{array}{c|c} M_{11} & M_{12} \\ \hline M_{21} & M_{22} \end{array}\right]\left\{\begin{array}{c} \ddot{q}_1 \\ \ddot{q}_2 \end{array}\right\} + \left[\begin{array}{c|c} B_{11} & B_{12} \\ \hline B_{21} & B_{22} \end{array}\right]\left\{\begin{array}{c} \dot{q}_1 \\ \dot{q}_2 \end{array}\right\} + \left[\begin{array}{c|c} K_{11} & K_{12} \\ \hline K_{21} & K_{22} \end{array}\right]\left\{\begin{array}{c} q_1 \\ q_2 \end{array}\right\} = \left\{\begin{array}{c} F_1 \\ F_2 \end{array}\right\} \tag{44}$$

where q_2 are the imposed DOF and q_1 are the unknown ones. Solving the system

$$M_{11}\ \ddot{q}_1 + B_{11}\ \dot{q}_1 + K_{11}\ q_1 = -M_{12}\ \ddot{q}_2 - B_{12}\ \dot{q}_2 - K_{12}\ q_2 + F_1 \tag{45}$$

the forcing forces that arise from the imposed q_2 displacements are:

$$F_F = - M_{12}\ \ddot{q}_2 - B_{12}\ \dot{q}_2 - K_{12}\ q_2 \tag{46}$$

These q_2 are introduced into the program as the forces, both in terms of displacement or velocity or acceleration and as a function of any other parameters and time by means of tables, FORTRAN statements and so on.

AERODYNAMIC FORCES

The RE representing an aerodynamic element of the helicopter is defined by means of a straight leading edge arbitrarely oriented in the RS of the element. The chords are perpendicular to this axis and twisted in a prescribed manner around the leading edge starting from the chord lying in the xy plane of the element according to the right hand rule (Fig. 7).
In every local profile, the incidence is computed at 3/4 of the chord by means of the contribution of three different velocities field: kynematic, gust, induced velocity of the rotor wake contained into the model. The kynematic field is computed by means of the equation Eq(25) taking into account the relative motion of the profile with respect to the air. The gust field is defined as a region of the absolute RS included between two planes parallel to the z axis in which a distribution of vector velocities, along any normal axis of theirs, is specified. The absolute direction and module distribution of these vectors are introduced in input data cards and the module can depend on the time in any analytical way. A gust field, so defined, can be used as an alternative way for simulating either the translation of the helicopter or transients between a flight and the other.
The program checks if the characteristic point of the section falls into this region; if this happens it adds to the point the contribution of the gust velocity deduced from the distribution introduced.
The induced velocity field, following Glauert's idea, is imagined as a circular jet of air having the same diameter of the rotor and velocity V (flight velocity) which, in corrispondence of the rotor, is deflected to the opposite side of the thrust with a mean velocity v_o and then accelerated up to a velocity $2v_0$ at a distance of the same order of the rotor radius. The value of the induced velocity is related to the thrust by the empirical formula

$$v_o = \frac{T}{2\rho A}\ \frac{1}{V'} \tag{47}$$

where $$V' = \sqrt{v^2 + v_o^2}$$

which reduces to the momentum formula for $V = 0$

$$T = 2\ \rho\ A\ v_o^2 \tag{48}$$

and to the induced velocity of an elliptically loaded wing for $V' \simeq V$

$$T = 2\ \rho\ A\ V\ v_o \tag{49}$$

So, in this simplified model, we can say that in the range of high flight velocities the rotor behaves like a wing deflecting the induced velocity by 90° from the flight velocity; closed to the hovering it behaves like a true rotor accelerating the air in the same direction of the thrust; between these two conditions no information is provided, so we

decided to join the two extreme deflections by a cubic function:

$$\delta = - 180° \ \bar{V}^3/\bar{\tilde{V}}^3 + 270° \ \bar{V}^2/\bar{\tilde{V}}^2 \tag{50}$$

where

$$\bar{V} = V/U_t \qquad ; \qquad U_t^2 = T/(2 \ \rho \ A)$$

$$\bar{\tilde{V}} = \tilde{V}/U_t \qquad ; \qquad \tilde{V} \text{ is the transition velocity}$$

If we assume that the axis of the stream tube is always tangent to the resultant velocity V', it will then be deflected to a RS with x oriented as the flight velocity, according to a function with an initial slope:

$$\text{tg } \gamma_o = v_o \sin \delta /(V + v_\delta \cos \delta) \tag{51}$$

and final slope at a distance S, taken on the axis of the tube,

$$\text{tg } \gamma_S = 2 \ v_o \sin \delta /(V + 2 \ v_o \cos \delta) \tag{52}$$

The differential equation of the axis of the tube is then

$$y' = v_o \sin \delta /(V + v_o \cos \delta) \tag{53}$$

which gives, for a linear variation of the velocity v:

$$v = v_o \cdot x/x_S + v_1 \tag{54}$$

where x_S is the coordinate of "S"

$$S = \int_o^{x_S} \sqrt{1 + y'^2} \ dx \tag{55}$$

$$\begin{cases} y = \dfrac{1}{2} \cdot \dfrac{v_o}{v} \cdot \dfrac{x^2}{x_S} + \dfrac{v_o}{v} \cdot x & \text{when } \bar{V} \geqslant \bar{\tilde{V}} \quad (\delta = 90°) \\[3mm] y = R \ x + \dfrac{T}{C} \ \ln \left[\dfrac{C \ x + D}{D} \right] & \text{when } \bar{V} < \bar{\tilde{V}} \quad (\delta = \delta(\bar{V})) \end{cases} \tag{56}$$

where

$$R = \text{tg } \delta \qquad ; \qquad \frac{T}{C} = - \text{tg}\delta \cdot x_S \cdot V/(v_o \cdot \cos \delta)$$

$$\frac{C}{D} = (v_o \cdot \cos \delta /x_S)/(v_o \cos \delta + V)$$

We further assume that the distribution of the induced velocity over the rotor disc is repeated over the discs of the wake which have the same inclination with respect to the resultant velocity V'. These local discs have their area reduced according to the equation of continuity

$$\rho \ A \ V' = \rho \ A_o \ V'_o = \text{cost} \tag{57}$$

The geometry and intensity of the wake associated to a rotor is thus completely defined once the thrust developed by the rotor and the flight velocity are known.
On the other hand, the thrust depends on the induced velocity so an iterative procedure is needed to achieve the balance between the calculated thrust and the thrust obtained by the Glauert's formula.
The thrust is defined as the mean value of the forces developed by the blades over one revolution which, in steady flight, is very closed to the sum of their instantaneus values. So, it is resonable to consider as the thrust the value deduced by the sum of all contributions of the blades at each step of the integration without deducing it from the whole revolution. This permits to follow, approximatively, the transient phenomena related to the induced velocities. In this way, at each step of the integration, for any value of the induced velocity established by convergence algorithm, the program checks if the characteristic point of the aerodynamic section falls into the wake, by evaluating first the disc containing the point according to the assumptions introduced

before and then comparing the radius of the point with the wake's. If the point is insi de the wake the induced velocity, deduced from the selected distribution, is added to the other velocities. These operations are repeated for every rotors introduced into the model. In this way we try to take into account the aerodynamic interference of one wake into the other, as,for example, the interference between the main rotor over the tail rotor, etc..

The influence of the ground effect over the mean value of the induced velocity is intro duced by means of experimental results (Ref. 1) for every flight conditions. The distri butions adopted for the induced velocity are: Glauert-Coleman, Mangler-Squire and uniform distribution. However the user can utilize his own distribution by analytical formula or tables. Knowing the local incidence, the steady aerodynamic coefficients are computed in the classical way utilizing the two-dimensional airfoil data (wind-tunnel tests) including compressibility, stall, and reversed flow effects.

The tri-dimensional correction is introduced following the ideas suggested by Harris (Ref. 2).

The skin drag forces are calculated in the direction of the resultant velocity by means of zero incidence and Mach number equal to 0.3.

To solve unsteady aerodynamic phenomena some empirical correlation techniques are used (Ref. 2÷7). These methods seek to correlate force and moment data obtained from relati- vely simple wind-tunnel tests in formulations that show the effects of the numerous relevant parameters such as airfoil shape, Mach number, amplitude and frequency of oscillations, mean angle and type of motion. Common to all the available literature re- levant to dynamic stall is the observation that unsteady effects increase with increa- sing pitch rate, that is, rate of change of airfoil incidence. It is also evident that the dynamic stall events require finite times to develop. Therefore, these parameters, introduced in dimensionless form, appear as input data for all these empirical methods. Another common aspect is that the empirical correlations are used as corrections to steady airfoil data, so that most geometrical, Reynolds number and Mach effects are on- ly accounted for insofar as they determine the static section characteristics.

COMPUTER PROGRAM

The structure and capabylity of the computer program beyond the parts descri- bed and presented in the previous chapters, consist at present solely of the integration algorithm. This foundamental part of the computation will be, in the future, utilized for generating prescribed solution directly required by the user by means of a single card.

An example of input cards is reported in Fig. 6, where the "GRID" cards contain the coordinates of the interst points of the structure and the number of the element to which these coordinates are related. The "ELEM" cards contain the informations relative to the elements: the RS, the mechanical properties, DOF, aerodynamic data and the grid points physically connected to the element. Among the various cards presented, it is possible to see the way by which we introduce the analytical formulas ("QFUNZ" cards). The variables starting with the letter "P" are the generic parameters from which the dependent variables are functions and are defined in the respective "PARAM" cards asso- ciated with the necessary informations. All the input data are checked to detect possi- ble format or logic errors and send the related messages.

Analysing all the input data, the program autogenerates the dimensions of the matrices for the subsequent steps leaving the user completely free to introduce the desired model. At present nothing is provided for an automatic output of the computed data as the logic is pending definition.

CONCLUSIONS

The report presents the basis for a general non-linear program capable to ana- lyze complicated structures including rotating elements, like rotor blades. From a gene- ral point of view the program analyzes any mechanical system without referring to a par- ticular model but deducing it from the input geometry. Load conditions are totally gene- ral and able to resolve static as well as dynamic non-linear problems according to the forces (displacements) applied to the system. The integration algorithm takes advantage of the matrix form by which the equations of motion are written, thus permitting to uti- lize the more recent developments in this field (Ref. 8-9).

A lot of work must still be done in obtaining the desidered solutions in all the diffe- rent fields to be analyzed.

REFERENCES

1. Bramwell, A.R.S., "Helicopter Dynamics", 1976, Edward Arnold Publisher.

2. Harris, F.D., Tarzanin, F.J., Jr., and Fisher, R.K., Jr., "Rotor High-Speed Performance; Theory vs Test.", J. AHS, vol. 15, no. 3, 1970.

3. Bielawa, R.L., "Synthesized Unsteady Airfoil Data with Applications to Stall--Flutter Calculations.", AHS Preprint no. 935, 1975.

4. Gormont, R.E., "A Mathematical Model of Unsteady Aerodynamics and Radial Flow for Application to Helicopter Rotors.", U.S. Army AMRDL-Eustis Directorate Report TR-72-67, 1973.

5. Ericson, L.E., Reding, J.P., "Dynamic Stall of Helicopter Blades", AHS 26th, June 1970.

6. Tran, C.T., and Petot, D., "Semi-Empirical Model for the Dynamic Stall of Airfoils in View of the Application to the Calculation of Responses of a Helicopter Blade in Forward Flight.", Paper no. 48, Sixth European Rotorcraft and Powered-Lift Aircraft Forum, Bristol, England, 1980.

7. Carlson, R.G. et al., "Dynamic Stall Modelling and Correlation with Experimental Data on Airfoils and Rotors.", Paper no. 2, NASA SP-352, 1974.

8. Hughes, T.J.R., "Recent Developments in Finite Element Methods", Nastran User's Conference, Munich, West Germany, June 1981.

9. Gerardin, M., "A Classification and Discussion of Integration Operators for Transient Structural Response", AIAA Paper 74-105.

10. Finzi, B., "Meccanica Razionale", Zanichelli Bologna Editore, 1970.

11. Gantmacher, F., "Lectures in Analytical Mechanics", MIR Publisher, Moscow, 1975.

ELEM	1-A	2-A	3-A	4-A	5-A	6-A	1-B	2-B	3-B	4-B	5-B	6-B
0	1*	2*	3*	4*	5*	6*						
1	7*	0	0	0	0	8*						
2	0	0	0	0	0	11						
4	0	0	0	0	0	9*	0	0	0	0	0	12
3	0	0	0	0	0	13						
7	0	0	0	0	0	14						
5	0	0	0	0	0	10*						
6	0	0	0	0	0	15	0	0	0	0	0	16

Tab. 1   Degrees of freedom of the structure of Fig. 2
(DOF with # are Lagrangian; without # are dependent; DOF=0 are constrained)

0.0	0.0	0.0	0.0	0.0	0.0	0.0	0.0	0.0	0.0
0.0	0.0	0.0	0.0	0.0	0.0	0.0000	-0.0000	-18.3383	0.0000
0.0	0.0	0.0	0.0	0.0	0.0	0.0000	-0.0000	-14.8444	0.0000
0.0	0.0	0.0	0.0	0.0	0.0	0.0000	-0.0000	-115.1476	0.0000
0.0	0.0	0.0	0.0	0.0	0.0	-0.0000	0.0000	14.8444	-0.0000
0.0	0.0	0.0	0.0	0.0	0.0	0.0000	-0.0000	-18.3383	0.0000
0.0	0.0	0.0	0.0	0.0	0.0	-9.3337	-4.9414	-12.9736	0.0000
0.0	0.0	0.0	0.0	0.0	0.0	-4.9414	-92.8015	-76.8281	0.0000
0.0	0.0	0.0	0.0	0.0	0.0	-10.5030	21.4275	-82.4773	0.0000
0.0	0.0	0.0	0.0	0.0	0.0	0.0000	-0.0000	0.0000	-0.0000

0.0	0.0	0.0	0.0	0.0	0.0	0.0	0.0	0.0	0.0
0.0	0.0	0.0	0.0	0.0	0.0	0.0	0.0	0.0	0.0
0.0	0.0	0.0	0.0	0.0	0.0	0.0	0.0	0.0	0.0
0.0	0.0	0.0	0.0	0.0	0.0	0.0	0.0	0.0	0.0
0.0	0.0	0.0	0.0	0.0	0.0	0.0	0.0	0.0	0.0
0.0	0.0	0.0	0.0	0.0	0.0	0.0	0.0	0.0	0.0
0.0	0.0	0.0	0.0	0.0	0.0	-9.3337	-4.9414	-10.5030	0.0000
0.0	0.0	0.0	0.0	0.0	0.0	-4.9414	-92.8015	21.4275	-0.0000
0.0	0.0	0.0	0.0	0.0	0.0	-10.5030	21.4275	-138.1422	0.0000
0.0	0.0	0.0	0.0	0.0	0.0	0.0000	-0.0000	0.0000	-0.0000

Tab. 2   Effect of action and reaction on the stiffness matrix.
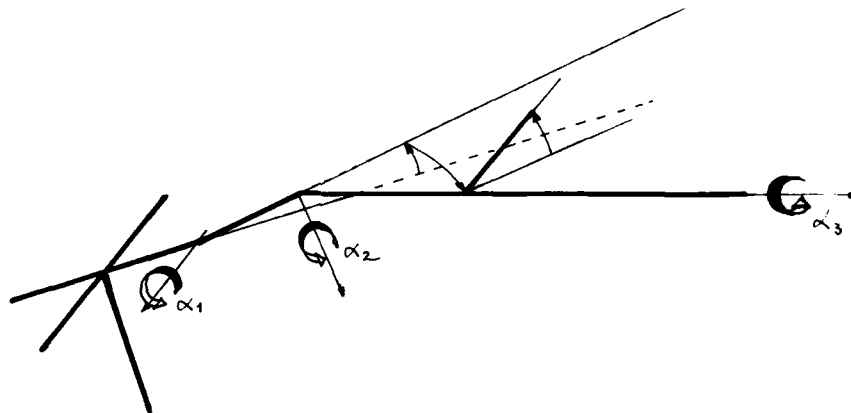
Fig. 1   Example of degrees of freedom of a rigid blade:
Flap (α_1), Drag (α_2) and Pitch (α_3) angles.
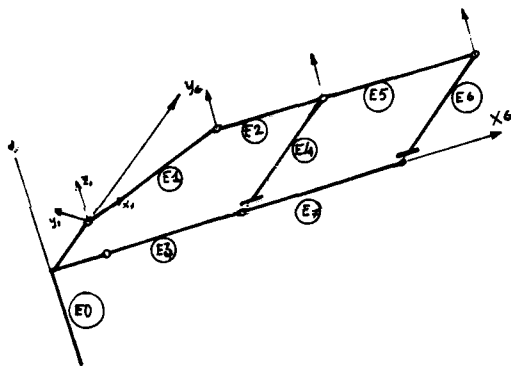
Fig. 2   Tree structure.
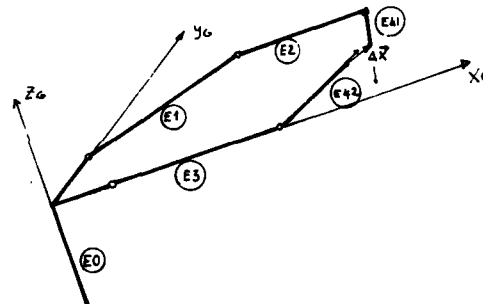
Fig. 3   Closed ring.
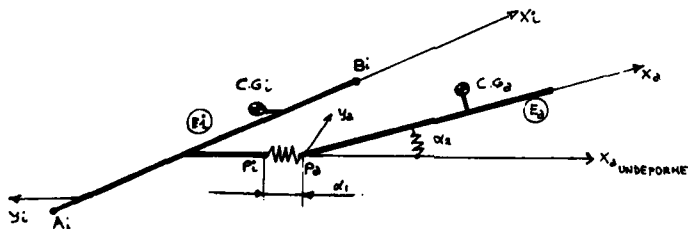
Fig. 4   Example of elastic connection.
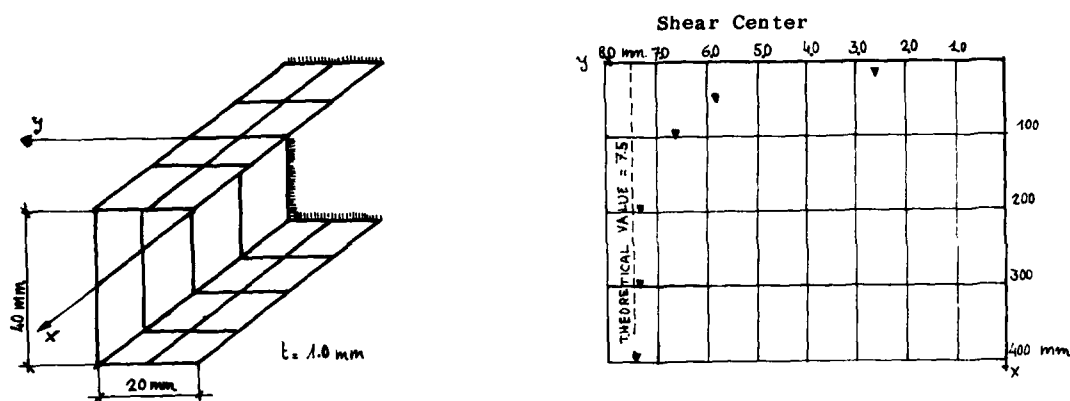
Fig. 5   Monodimensional structure vs tridimensional
structure.

```
                          E C O   D E I   D A T I   D I   I N G R E S S O
SCHEDA
NUMERO        .  1  ..  2  ..  3  ..  4  ..  5  ..  6  ..  7  ..  8  ..  9  ..  10  .
-----------------------------------------------------------------------------------------
  1-     CELAS    30      1       6       1               20.    20.    20.
  2-     ELEM     0       1       2       3      10                              ELE01
  3-     +LE01    123456                                                        ELE02
  4-     +LE02                                                                  ELE03
  5-     +LE03    4       5       ENDDATA
  6-     ELEM     1       3       6       7      10     999992  0      1         ELE11
  7-     +LE11    16      16                                                    ELE12
  8-     +LE12    0012    2.      19      0012   2.     20     10     10
  9-     FORZA    6               1       1                     20     1
 10-     FORZA    F               3       4      1      6      10
 11-     FORZA    M       2       3       4      1      6
 12-     GRID     1               0.      0.     -1.
 13-     GRID     2               0.      0.     0.
 14-     GRID     3               0.      1.     0.
 15-     GRID     4               1.      0.     0.
 16-     GRID     5               0.      -1.    0.
 17-     GRID     6               3.      4.     0.
 18-     GRID     7               0.5     3.5    0.
 19-     GRID     19      1       0.      0.     0.
 20-     GRID     20      1       4.25    0.5    0.
 21-     INERZIA  10      5.+1    1.      0.     0.                             INE01
 22-     +INE01   50.     50.     1.+2    50.    70.7106 70.7106
 23-     PARAM    COSI            P1      0.150
 24-     PARAM    COSI            FRED    200.
 25-     PARAM    COSI            AENOD   STEADY
 26-     PARAM    COSI            GRAV    9.810  -3
 27-     PARAM    COSI            VSOUND  344.
 28-     PARAM    COSI            RO      0.125
 29-     PARAM    GUST     1      4       3      -5.    50     1      2.     50
 30-     PARAM    FUGOL    1      P2      1      1      1      1      2.
 31-     PARAM    FUGOL    3      P4      3      1      6      2      0.
 32-     PARAM    RELEASE                 2      1      6      1
 33-     RIGID    10      123456  11.     22.    33.    44.    55.    66.    RIG1
 34-     +IG1     12.     13.     14.     15.    16.    23.    24.    25.    RIG2
 35-     +IG2     26.+1   34.+1   35.+74  36.    45.    46.    56.+10
 36-     TABELLA  10                                                            TAB11
 37-     +AB11    .0      0.      0.      10.    10.    100.   100.          TAB12
 38-     +AB12            1000.   1000.   ENDDATA
 39-     TABELLA  990012  CP                                                  ITA    4
183-     TABELLA  990012  CD                                                  ITA  148
426-     TABELLA  990012  CM                                                  ITA  391
571-     UFUNZ    2       PP2=P1+3*P4+DSIN(P2)
572-     UFUNZ    50      GUST=DSIN(314.*PTIME)
```

Fig. 6   Input data cards.
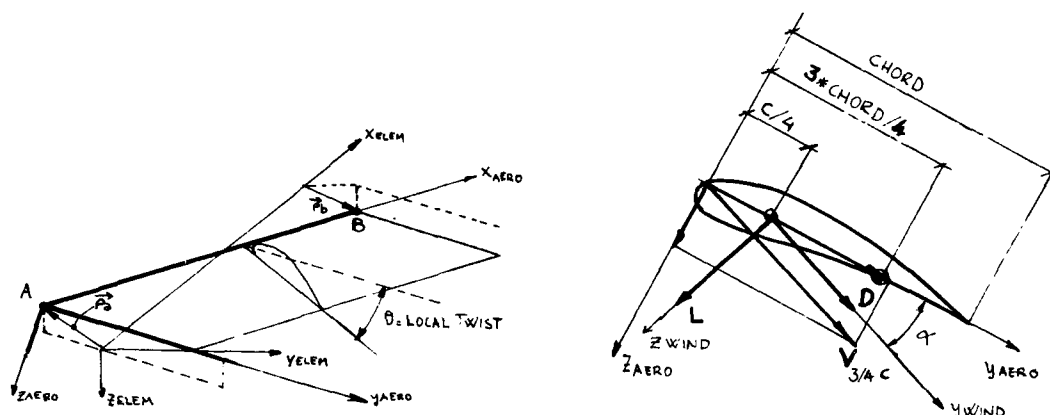
Fig. 7   Aerodynamic element and typical section.

APPENDIX 1

1. **Definition of the matrix** $[\ ]_\wedge$

$$\vec{a} \times \vec{b} = \begin{bmatrix} 0 & -az & +ay \\ +az & 0 & -ax \\ -ay & +ax & 0 \end{bmatrix} \cdot \begin{bmatrix} bx \\ by \\ bz \end{bmatrix} \qquad \text{or} \qquad \begin{bmatrix} 0 & +bz & -by \\ -bz & 0 & +bx \\ +by & -bx & 0 \end{bmatrix} \cdot \begin{bmatrix} ax \\ ay \\ az \end{bmatrix}$$

$$\Downarrow \qquad\qquad\qquad\qquad\qquad\qquad \Downarrow$$

$$[a]_\wedge \vec{b} \qquad\qquad\qquad\qquad [b]_\wedge^T \vec{a}$$

2. **Elementary transformation**

$$[T_x]^T = \begin{bmatrix} 1 & 0 & 0 \\ 0 & \cos\alpha & -\sin\alpha \\ 0 & \sin\alpha & \cos\alpha \end{bmatrix} \quad [T_y]^T = \begin{bmatrix} \cos\alpha & 0 & \sin\alpha \\ 0 & 1 & 0 \\ -\sin\alpha & 0 & \cos\alpha \end{bmatrix} \quad [T_z]^T = \begin{bmatrix} \cos\alpha & -\sin\alpha & 0 \\ \sin\alpha & \cos\alpha & 0 \\ 0 & 0 & 1 \end{bmatrix}$$

3. **Definition of the matrix** $[\Omega]_\wedge$

$$\text{Eq(3)} \quad \vec{x}_o = [R_N]^T \vec{x}_N + \vec{P}_N \qquad\qquad \text{Eq(4)} \quad \dot{\vec{x}}_o = [\dot{R}_N]^T \vec{x}_N + \dot{\vec{P}}_N$$

where $[R_N]^T$: transformation matrix from relative RS to global RS valid for any vector

         $\vec{P}_N$: absolute velocity of the origin

Reducing the absolute velocity x_o to the relative system

$$\dot{\vec{x}}_{oN} = [R_N][\dot{R}_N]^T \vec{x}_N + [R_N] \dot{\vec{P}}_N$$

and comparing with Eq(25), remembering point 1 of this Appendix, we obtain:

$$[\Omega]_\wedge \vec{x}_N = [R_N][\dot{R}_N]^T \vec{x}_N$$

and, as a consequence:

$$[\Omega]_\wedge = [R_N][\dot{R}_N]^T$$

REVIEW OF ROTOR LOADS PREDICTION METHODS

by
Peter J. Arcidiacono
Manager of Aeromechanics
and
Robert Sopher
Supervisor, Dynamic Methods
Sikorsky Aircraft
North Main St.
Stratford, Conn. 06602
U.S.A.

SUMMARY

A review of recent progress made in predicting rotor loads is presented. The period considered is that since the paper presented by Dr. Robert Ormiston at the NASA Rotor Craft Dynamics Conference in 1974. By request, only United States work has been considered. In Dr. Ormiston's paper a comparison of loads predicted using several then state-of-the-art methods was presented for a set of standard cases, and technical areas requiring further work were identified. It is the intention of this paper to review the progress that has been made in the identified areas in the intervening years. Emphasis of necessity is placed on the work accomplished at Sikorsky Aircraft and United Technologies Research Center to develop improved loads analysis. However, a survey of members of industry and the research community was made to generalize the conclusions as much as possible. Technical areas recommended for priority attention in the future are identified as well as the perception of technology opportunities that may be emerging in the relatively near future. Finally, the impact of the U.S. Government effort to develop a Second Generation Comprehensive Helicopter Analysis System (2GCHAS) is reviewed.

It is concluded that the aerodynamic aspects of rotor loads analyses generally have not changed greatly since 1974. Although progress has been made in addressing some of the fundamental aerodynamic areas, this progress has not always been integrated into the load programs. On the other hand, the structural aspects of the loads programs have been advanced, particularly with respect to consistent formulation of equations and the ability to efficiently assemble the desired dynamic elements for problems of varying degrees of complexity. The impending emergence of the U.S. Government 2nd Generation Comprehensive Helicopter Analysis System (2GCHAS) is expected to accelerate the orderly development and control of rotor loads programs of enhanced technical capability.

LIST OF SYMBOLS

c	chord, ft
C_{FM}	Flatwise moment coefficient, flatwise moment$/\rho \pi R^3 \Omega^2 R^2$
C_L	Lift coefficient
$C_{L_{max}}$	Maximum lift coefficient
C_M	Pitch Moment coefficient
C_N	Normal force coefficient
C_p	Pressure coefficient
f	Frequency of oscillation, cycles/second
GW	gross weight, lbs
k	Reduced frequency, $\frac{C\omega}{2V}$
L_{max}	Maximum lift generated by two dimensional airfoil, lb/ft
M	Mach number
M_T	Rotational tip Mach number, ΩR/speed of sound
$\bar{r}$	Radial location on blade divided by R
R	Rotor radius, ft
V	Flight or Tunnel Airstream velocity, ft/sec
X	Distance along airfoil chord divided by C, measured aft from leading edge (except in Figure 10)

x,y,z	Coordinate system as defined in Figure 10
α	Airfoil angle of attack, deg
α_M	Mean value of α, deg
$\bar{\alpha}$	½ Amplitude of α oscillation, deg
θ	Equivalent linear twist of rotor blade, deg
Λ	Sweep angle of lifting surface relative to airstream, deg.
μ	Advance ratio, $V/\Omega R$
ρ	Air density, $\dfrac{lb}{ft^4}sec^2$
σ	Rotor solidity, total blade area/rotor disc area
ψ	Blade azimuth angle measured from downstream position, deg
ω	Frequency of oscillation, rad/sec
Ω	Rotor rotational frequency, rad/sec

INTRODUCTION

The complexity of the rotary wing loads prediction problem is well recognized. The problem is aeroelastic in nature and, as such, has a high degree of coupling between the aerodynamic and structural elements of the problem. The high aspect ratio of the blade makes torsional deflections potentially very important since this degree of freedom experiences little centrifugal stiffening. Proper formulation of the torsion equation requires consistent treatment and retention of nonlinear terms. The aerodynamicists, of course, are challenged by dynamic stall, wake distortions, unsteady transonic flow and time varying sweep features of the problem. Even with the advent of high speed computers, an exact treatment of the problem is not possible. All of the analyses today therefore involve some assumptions. Permissible assumptions of course depend on the problem being addressed, with the higher frequency load problems demanding the most rigor because they require the most detailed description of the airload distribution.

In 1973-74, there appeared to be a milestone of sorts reached in the development of rotor loads analyses. Higher speed computers had allowed the latest generation of aerodynamic technology - variable inflow, sweep and dynamic stall - to be integrated into the loads programs. A review of many of the various programs, together with their correlation capabilities, was conducted in the 1973 AGARD meeting of Reference 1. This review was soon followed in 1974 by a unique comparison of primarily U.S. loads programs (Reference 2). Reference 2 was unique in that all methods were applied to the same set of standard cases for a hypothetical rotor. The results were surprising with respect to the relatively wide variation in loads predicted by the different methods. Figure 1 shows, for example, the large range in loads predicted for a typical operating condition. The methods all employed variable inflow and unsteady stall aerodynamics of one form or another. In examining the results, it was clear that differences existed in both the aerodynamic and structural formulation of the methods. Figure 2 shows that large differences existed even at the most fundamental level, namely that of steady state airfoil data. Figure 3 shows that differences also existed at the fundamental level of predicting in-vacuo blade natural frequencies. The variations seen in aerodynamic pitching moment and torsion natural frequency are particularly important because the torsional response of the blade couples most directly with the aerodynamic loading. Reference 2 concluded that: "Difficulties in the results arise from all three basic areas: Numerical solution techniques, structural dynamics and aerodynamics." Recommendations from Reference 2 were:

"1. Compare the methods on a trending basis

2. Assess in detail the validity of assumptions and semi-empirical factors used

3. Conduct fundamental research on dynamic stall, blade/vortex interactions and three-dimensional flow effects

4. Correlate (at some point) the methods with data from a well instrumented wind tunnel test of a large rotor."

It is our perception that in the intervening years since the publication of Reference 2, Recommendation 3 has received the most attention.

The objectives of this paper are to review the general limitations of the older analyses; discuss the perceived progress in (a) the underlying fundamental technology, (b) the integration of the technology into actual loads predictions programs, and (c) the acquisition of test data for validation; and finally to present limited recent correlation results. In attempting to satisfy these objectives, a survey of members of U.S. technical community was made. The following questions were posed:

1. Wnat is your perception of progress in rotor loads prediction technology since 1974 in the areas of:

    a) structural representation and
    b) aerodynamic representation?

2. To what extent have technology advances been made operational in a loads prediction program?

3. To what extent have technology advances improved correlation?

4. What areas exhibit the worst correlation?

5. What are the most critical assumptions in the analyses?

6. What are the most critical data needed to validate the analyses and understand any lack of correlation?

7. What particular improvements in rotor loads prediction capabilities are you looking for as a result of the U.S. Government 2nd Generation Comprehensive Helicopter Analysis System (2GCHAS)?

Clearly, the subject area is large and the authors do not claim to have made an exhaustive study. Apologies are extended to any whose work has not been cited and, as noted before, only U.S. work has been considered.

We are grateful for the survey inputs received and have drawn on the material but not in any formal structured manner. The specific words and emphasis of this report necessarily represent those of the authors, unless otherwise noted. Also acknowledgment is due to T. W. Sheehy, Chief of Aerodynamics at Sikorsky Aircraft for his contributions.

LIMITATIONS OF ANALYSES

As noted earlier, the problem of predicting rotor loads is a challenging one. Large computer programs are inevitably involved as are assumptions and approximations. The latter are usually driven and colored by the particular experience and data base available to the group developing the program. The need to keep computing times under reasonable control also is a contributing factor shaping the analysis used. One often finds analyses being developed almost in parallel with their application and, hence, being driven by a critical time schedule. Although the initial version of any analysis is usually rigorously derived based on clearly stated assumptions, an evolution of the analysis occurs which is often less well controlled for a variety of reasons. Documentation of changes also may not be as complete as desired because of higher priority needs and change overs in personnel for example. Checking a large analysis to verify that coding errors are not present also represents a challenge that can be quite time consuming. Often some problems of interest simply cannot be solved and new technology cannot be introduced without extensive rederivation and reprogramming to incorporate additional degrees of freedom or features. Finally, in the process of evolving the analysis to eliminate or refine certain initial assumptions, one has to recognize the possibility that compensating errors may be partially eliminated so that the newer version actually does less well than the older one. Our experience at Sikorsky has encompassed all of the problems noted above at one time or other. As stated quite well by Johnson in Reference 3: "The job could always be done better. The hard task is recognizing when it should be. Any good code will have a range of validity extensive enough to ensure it a long life. Eventually, however, problems will begin to overwhelm it and the technology will march beyond it. That is the time to begin work on the next generation of codes."

To a considerable degree it is these very considerations which have prompted the U.S. Government to undertake the 2nd Generation Comprehensive Helicopter Analysis System (2GCHAS). This should provide a framework in which (a) an orderly development of codes can take place and (b) the best available technology can be efficiently tapped. Unfortunately, we are not yet at that point. The older analyses are still evolving and newer ones are appearing. The Sikorsky Normal Modes Analysis described in Reference 1 has since incorporated yawed flow, swept tip details, and fuselage flow field effects. Boeing has incorporated in its C-60 analysis new representations of tip effects, variable inflow and fuselage flow field as well as various structural representation improvements (including redundant load paths). Bell (Reference 4) has evaluated the use of unsteady stall and free wake inflow models and incorporated redundant load paths in C-81.

In addition to the evolution of the older codes, recognition has been given to the fact that the time has arrived for newer codes based on restructuring of the problem. Several types of new large codes have appeared. References 3 and 5 are examples of comprehensive analyses, which use essentially the same basic approaches as older analyses, but which have benefited from consistent new derivations and complete reprogramming. They appear to have the same aerodynamic technology as older codes but have incorporated additional dynamic degrees of freedom and redundant blade structural elements. These methods are more limited in their ability to model dynamic configurations than the new substructure methods, exemplified by Reference 6, and described in a subsequent section of the paper.

As a result of the difficulties experienced with older programs, a better under-standing has been obtained of the procedures required to maintain and control program configurations. Presumably the 2GHAS effort will, in the near future, combine the best of the features of all of the more recent programs and at the same time enforce the discipline required to control the program validation and changes.

PROGRESS IN FUNDAMENTAL TECHNOLOGY

This section briefly reviews our perception of the progress being made in the fundamental technology underlying rotor loads prediction methods. Both aerodynamic and structural areas are considered.

Airfoil Characteristics

One of the most basic requirements in any rotor loads prediction analysis is the ability to determine the aerodynamic forces and moments at discrete blade sections. This has traditionally been done by calculating the local velocities and angles-of-attack and yaw (or sweep) and then using the measured aerodynamic characteristics for two dimensional airfoil sections. As pointed out by Dr. Ormiston in 1974, however, substantial differences are apparent even at this very basic level (e.g., see Figure 2 of this paper). Obviously, if one analysis was capable of precisely predicting the flow conditions and blade dynamic response different load predictions would still result because of uncertainty in airfoil data.

It has been demonstrated and known for some time that different characteristics very likely will be obtained for the same airfoil section tested in two or more tunnels. This can be attributed to several factors including model surface quality, Reynolds number differences, tunnel turbulence level, floor and ceiling inter-ferences, sidewall interferences, and, to some extent, data acquisition techniques.

In the belief that the Reynolds number and the tunnel floor, ceiling, and sidewall effects are the dominant factors determining the ability to obtain accurate two-dimensional data, Sikorsky developed the Tunnel Spanning Apparatus (TSA). This device, shown in Figure 4, consists of a spar that spans the width of a large test section (8 to 11 feet) to which full scale or near full scale airfoil shells are attached. An eight inch metric section located at the center (see Figure 4) allows direct measurement of three forces and three moments. Surface pressure data and wake rake data (in steady state tests) are typically acquired simultaneously to provide detailed loading information and data redundancy. Because of the relatively large distances between the tunnel floor, ceiling and sidewalls to the position at which measurements are made, the data obtained are less influenced by tunnel interferences. The TSA has been used by Sikorsky to acquire both steady-state and unsteady data in swept and unswept flow conditions. The TSA was used to address one of the questions raised by Arcidiacono in Reference 1, namely the augmentation of maximum lift cap-ability on a swept two-dimensional airfoil. Inferences had in the past been made from limited three dimensional swept wing tests. The TSA results shown in Figure 5 show that sweep does increase maximum lift by 15 to 25% beyond classical 2-D airfoil theory for two Sikorsky airfoils.

The dependency on empiricism for unsteady airfoil characteristics and, in particular, dynamic stall characteristics was also cited by Dr. Ormiston as a defi-ciency in the prediction of rotor loads. While progress has been made in this area, it has predominantly been progress in obtaining additional experimental data and in investigating the basic features of dynamic stall. Reference 8 provides a good summary of what has been learned about dynamic stall and the current status of prediction techniques.

A major contribution to the available data base and the understanding of the dynamic stall phenomenon is reported in Reference 9. This work included tests of eight airfoils and an attempt to quantify the effects of several airfoil design para-meters on the dynamic stall characteristics. Figure 6 presents the maximum lift achieved by seven of the sections tested. This figure shows that the lift increment due to deep dynamic stall (i.e., vortex dominated, large airload fluctuations) is not significantly different for the airfoils tested but that the lift increment obtained at dynamic stall onset is affected by airfoil shape. Generally, the authors of Reference 9 conclude that airfoils exhibiting trailing edge stall are preferred to those exhibiting leading edge stall.

Table I from Reference 9 provides a summary of the importance of various parameters to the dynamic stall phenomenon. Another parameter (blade sweep) is not shown in Table I and has been demonstrated to have an effect on the dynamic stall phenomenon. Figure 7 demonstrates that sweep or yawed flow effects can alter the dynamic stall characteristic. It is apparent that much needs to be done before the designer can fully exploit the benefits or cope with the disadvantages of unsteady aerodynamics.

Several prediction techniques are described and discussed by McCroskey in Reference 8. These techniques are empirical in nature and each incorporates certain symplifying assumptions and shortcomings. As pointed out by McCroskey, each method manages to reproduce reasonably well the data sets used in its development, but almost no correlation has been demonstrated in reproducing independent data sets. A new semi-empirical technique has recently been devleoped at United Technologies Research Center (UTRC) by Gangwani (Reference 10). This method explicitly accounts for the formation and streamwise movement of the vortex shed from the leading edge. It also incorporates the effects of non-zero sweep angles. The empirical coefficients used in this method are based on unsteady test data obtained in the UTRC 8 ft. high speed tunnel using the Sikorsky TSA. Figure 8 demonstrates the ability of this method to reproduce the independent data set from Reference 9. The UTRC data and the Reference 9 data were both obtained using sinusoidal pitching motion. Figure 9 shows the ability of the UTRC method to reproduce the unsteady lift and moment data for non-sinusoidal motion. Again, this method is semi-empirical but its ability to model the independent data as shown in Figures 8 and 9 is encouraging. This UTRC dynamic stall model is currently being integrated into Sikorsky RDYNE load analysis.

Inflow Modeling

The ability to determine the aerodynamic loading on the blade requires the ability to predict the flow conditions to which each section of the blade is subjected as well as the blade motions. The history of predicting the induced inflow has evolved from uniform momentum model to longitudinal skewed momentum model to longitudinal/lateral skewed momentum model to discrete vortex models (sometime including the shed wake due to the time dependent lift) and wake distortions. It was shown in Reference 1 (paper by Arcidiacono) that the non-uniform (variable) inflow associated with the vortex methods was necessary to better represent the airload character at least at some radial locations on the blade. In a later section of this paper, some results are presented that show that variable inflow does not always improve correlation. In Reference 11, it was shown that to adequately calculate blade flapping not only was a non-uniform inflow required, but below an advance ratio of .2, a distorted vortex wake (free wake) was necessary. In Reference 4, however, it is shown that a free wake does not improve the correlation of overall rotor blade load distributions. Thus, although the necessity for improved wake models is recognized, the precise requirements for acnieving accurate loads are still unclear.

In Reference 12, the ability of a calculated distorted vortex wake model to qualitatively represent the wake of a model rotor operating in water was demonstrated. Figure 10, taken from more recent work (Reference 13) demonstrates this ability for a rotor operating at a moderate advance ratio in air. The effects of the wake geometric differences shown or whatever differences may exist in the vorticity strengths are not known but are believed to be significant especially for acoustic problems. While the necessity for accurately modeling the wake structure seems to have been demonstrated, only limited verification of the analytical capability has been conducted. Most of the wake geometry verification has been done at low speeds due to the difficulty of conducting flow visualization studies at high tunnel speeds.

In addition, to the best of our knowledge, no systematic wake geometry studies coupled with inflow velocity measurments have been conducted. The growing maturity of laser velocimetry (LV) makes this type of experimental project feasible. This type of data is required in order to identify deficiencies in the wake models and the necessary refinements. Figure 11, from Reference 14, shows reasonably goou correlation of predicted inflow velocities using a free wake analysis with LV measurements at low speed.

Perhaps the most significant progress in predicting the rotor inflow field has been the ability to predict the change in the inflow velocities due to the flow field generated by the fuselage. The use of potential flow panel methods, such as that described in Reference 15, allows the calculation of the fuselage induced velocities at the rotor blade and the blade aero'ynamic analysis can then account for the change produced in local blade loading and the wake strength. Figure 12, from Reference 16, shows the experimental and calculated differences in the blade flatwise bending moment with and without the fuselage. Certain features of the fuselage effect are reasonably well predicted; however, the effects in the first and second quadrant are poorly represented. Reference 17 also describes tests in which the effect of the fuselage on rotor loads is systematically measured. As discussed previously, wake distortion has been demonstrated to have a significant effect on the loading, at least at low advance ratios. This points out a potential deficiency in the prediction of fuselage effects in that, to date, the ability to predict the wake distortion due to the fuselage has not been developed.

Finally, it should be noted that dynamic inflow effects have been shown to be important in the prediction of rotor damping (see Reference 3).

3-D Aerodynamics

The blade element approach has been the traditional method of obtaining blade loads. This method assumes that each blade section behaves as if it were on a two-dimensional wing. The method applies to steady and unsteady conditions, but begins to break down when conditions are highly three dimensional - e.g., when a vortex passes near a blade, or at the tip of a blade. Progress has been made at the fundamental level in developing three-dimensional, quasi-steady and unsteady, sub-sonic and transonic analyses. Hereafter these analyses will be referred to as blade analyses (as opposed to lifting surface analyses) to imply that thickness effects are considered.

An inviscid, non-conservative, potential flow, quasi-steady lifting blade analysis is described by Arieli and Tauber in Reference 18. This method is an extension of a full potential code developed by Jameson (Reference 19) for fixed wing applications. The method currently accounts for only a single blade and therefore the wake induced flow field is incomplete. It also cannot currently account for tip vortex rollup and makes assumptions regarding the location of the vortex sheet to facilitate the derivation of the solution in transformed space.

Results from this method are compared to experimental data and 2-D calculations for a station near the tip for a non-lifting rotor blade in Figure 13. For this station on the advancing blade, the calculation agrees well with the experiment and the three-dimensional effects are significant. Calculations for more inboard stations are presented in Reference 18 showing, as might be expected, much smaller 3-D effects. The 3-D characteristics shown near the tip could have large effects on the predicted blade loads and moments.

Another 3-D analysis under development is described in References 20 and 21. The mathematical model used in this method is a three-dimensional, unsteady (low frequency) small disturbance transonic model. Figure 14 shows the correlation of this method from Reference 22 with measured non-lifting rotor results at 90% radius and an azimuth of 120°. Good correlation is shown for the unsteady calculation whereas the quasi-steady calculation fails to model the chordwise pressure distribution. This same characteristic was shown for the Arieli and Tauber work in Reference 18 at 120° and indicates that accounting for the flow history is important.

Both the quasi-steady, lifting blade and the unsteady non-lifting blade analyses discussed have been used to analytically assess the impact of three-dimensional effects on the advancing tip. The results, to date, suggest that these effects on blade loads could be large and future efforts should concentrate on removing the present simplifying assumptions. Also, practical techniques for modeling these effects in actual load prediction programs are required. An example of a practical lifting surface implementation for the blade vortex encounter problem is contained in the analysis of Reference 3.

Structural Modeling

The aeroelastic nature of the rotor loads problem has focused attention on the rotor blade structural model as an area for introducing improvements. The accurate simulation of the structural and dynamic behavior of a rotor blade is less difficult than the accurate simulation of aerodynamic excitations. On the other hand, even at this time, the requirements for accurate structural simulation are not understood fully. There is a consensus that careful attention has to be paid to factors influencing blade torsional deflections.

Hodges in Reference 23 has derived equations valid to second order for homogeneous, isotropic beams undergoing moderate displacements. These equations are the basis of a finite element aeroelastic stability analysis, embodied in the GRASP program, now in development. Progress has been made in identifying some of the considerations for introducing more consistent normal modes coordinates in the blade response equations. Reference 24 and 25 discuss additional terms in the blade response equations required when coupled modes are employed to express the equations in normal modes coordinates. It was found in Reference 24 that additional stiffness terms arise because the blade pitches at angles different from the distribution used to obtain the coupled modes. Application of this approach described in Reference 25 did not lead to an unqualified selection of coupled or uncoupled modes, however. Nevertheless, these considerations are indicative of the attention being paid to the structural and dynamic representation.

Representations of structural redundancies characteristic of modern rotor blade designs have been introduced in several analyses available or under development in the Industry and Government. Multiple load path representations are available, for example, in the Boeing-Vertol C-60, and the Sikorsky ET499 analyses. These analyses are based on a Myklestad transfer matrix formulation and are limited to a harmonic balance solution. Rotor/fuselage coupling may be represented by means of a rotor impedance approach (see next section). At present these analyses are not able to represent transient phenomena. Figure 15 shows that moment distributions predicted by the Sikorsky ET499 program agree more closely with test data vibratory amplitude than the results obtained by the Sikorsky normal modes method of Reference 26. However, the modal analysis time history appears more correct. While systematic

study has not yet been conducted to identify conclusively the causes of the differences, the key assumptions are believed to be the use of uncoupled modes, the assumption of low twist and the use of a modal displacement method to express moments in the modal analysis.

An avenue being followed to represent structural redundancies is a formulation based on the finite element displacement method. The GRASP program (unpublished work by Hodges) mentioned above is an example of such an analysis. An advantage of this approach is its ability to permit coupling of the blade to the airframe, control system, and structural restraints by means of automated techniques suitable for assembling finite elements and substructures in the context of a displacement method. Such assembly techniques have been incorporated in the new generation of loads programs which have begun to appear in the U. S. Industry, described below.

PROGRESS IN INTEGRATION OF TECHNOLOGY INTO LOADS ANALYSES

The complex and highly coupled character of rotor dynamic and aerodynamic phenomena has motivated the continual development of analyses integrating the diverse elements necessary for an accurate representation of the total problem.

The background to present developments is that older analyses are not easily modifiable without substantial cost and time investments. The old approach to the derivation of coupled system equations involved manual derivations. The process is laborious, slow, and susceptible to error. This process inhibited the development of new features - for example, the addition of new components like vibration absorbers.

The result of these experiences and others mentioned earlier in this paper has been the identification of certain key requirements which an accurate and modifiable analysis has to satisfy. Table 2 summarizes key attributes and Table 3 details typical physical, mathematical, and software reqirements. A unified analysis employing a limited number of elements with the versatility to be applicable to a wide range of systems is obviously desirable. Such a framework should do much to limit the difficulty and cost of establishing the correctness and validity of the analysis. An automated method for synthesizing the equations of motion is desired. Automation, as will be seen, will accomplish not only a unified and versatile framework, but will enhance modifiability, and reduce the possibility of errors. A third factor is that the software should be organized in such a way as to enhance program modifiability. The links between modules should be limited and well defined. In other words, the program should be modular, a feature which can be achieved partly by a process called structured design, described in Reference 27. Finally, the growth of the program should be controlled carefully. It is seen that many of the requirements are not technological, but concern the design and management of software. The strong interdisciplinary character of the problem is clearly evident.

In the last few years, the U.S. Government has been developing, with the assistance of the U. S. Industry, a comprehensive analysis which is designed to satisfy these concerns. This system, the Second Generation Comprehensive Helicopter Analysis System (2GCHAS), and its evolution, has been responsible for spinoffs developed by the U.S. Industry, described below.

Progress in achieving a unified, versatile, and modular framework has been achieved by the employment of substructure approaches. The helicopter structure is broken up into parts whose equations may be derived independently. The computer program assembles automatically these individual parts into an integrated system. Examples of substructure programs are the RDYNE (Rotorcraft Dynamics Analysis), and the SIMVIBE (Simplified Vibration Analysis of Reference 6), both developed by Sikorsky, the COPTER program (see Reference 28), developed by Bell Helicopter/ Textron, and the DYSCO program (see Reference 29), developed by KAMAN Aerospace Corporation. The Sikorsky and Kaman programs use the Hurty method (see Reference 7) to assemble the equations of motion from the equations for the substructures. In the Sikorsky program the substructures may be assembled with arbitrary orientations relative to one another. This, and the ability to connect arbitrary numbers and types of substructures to one another, provides the analysis with considerable freedom to represent structural configurations. In the RDYNE program, substructures comprise individual blades and elastic fuselages, as examples. Figure 16 illustrates sample components which may be assembled to represent a helicopter structure. Because each blade is modeled as a distinct substructure, the analysis is well suited to modeling failure/damage induced loading and vibratory phenomena affecting the entire helicopter. For example, Figure 17 illustrates a drive train response after the occurrence of simulated damage to a main rotor blade. The structural and dynamical coupling of the rotor and fixed system is accurately represented as shown in Figure 18 which compares ground resonance stability calculations with Flocquet theory. Although the RDYNE analysis is quite general for the representing transient and steady state loadings on coupled systems, it is not the most cost-effective method for obtaining steady state phencmena. The SIMVIBE program (see Reference 6) on the other hand is dedicated to calculating steady vibratory loadings and accelerations, and was developed for the Army Structures Laboratory. The same assembly method is used in SIMVIBE as in RDYNE. The substructures, however, are different. Instead of employing single blades as substructures, the rotor is treated as an entity. Figure 19 shows the substructures available in SIMVIBE. Rotor-induced hub excitations and rotor impedance are calculated from a single blade rotor aeroelastic analysis (G400, see Reference 5), which is executed in a stand-alone mode. This

information is sent to a file which is read by the Base or Executive Program in the SIMVIBE package, which assembles the rotor dynamic properties with the properties of other substructures, such as bifilars, fixed system vibration absorbers, or elastic fuselages. Steady state motion is assumed and a harmonic balance solution for the coupled system is assumed. Blade loadings are expanded as terms for no hub motion, and terms which account for hub motion effects. This information is transmitted as vectors of forces and matrices of blade loading derivatives to the Base Program. When the hub motion is determined from the solution, blade loadings may be found by substituting hub motion data in the blade loading expression. Figure 20 shows that the fixed system dynamic characteristics can alter hub vibratory shears generated by the rotor.

A significant area which does not lend itself to the use of the automated synthesis applicable to structural elements involves the integration of aerodynamic effects into the system. Some progress has been made and the techniques for achieving aerodynamic couplings have been demonstrated in the development of the SIMVIBE package. A technique for achieving aerodynamic couplings is to transfer data among large modules dedicated to the formation of aerodynamic properties. Figure 21 illustrates this process. Rotor-induced wake data are calculated by a variable inflow program (F389) which cycles these data to the rotor aeroelastic analysis G400 to calculate a wake consistent with the blade motions. Fuselage induced aerodynamic inflow is transmitted from a potential flow analysis to F389. Rotor-induced wake effects on an empennage are calculated by an analysis with a lifting surface empennage model (see Reference 30). Harmonics of empennage loads are then transmitted to the Base Program, and are assembled with the properties of other components to calculate the coupled system response. An attribute of the method of coupling programs to each other by data transfers is that it enables parts of the system to be independently developed. If these parts are old programs, this approach will limit the cost of developing the integrated system, and will allow a more timely development of the system. Experience with the development of SIMVIBE has confirmed these attributes.

The 2GCHAS which is under development by the government is expected to provide all the features contained in Industry programs. In addition, the 2GCHAS is expected to provide the requisite design standards and management resources for maintaining and controlling the program configuration. It is expected that the 2GCHAS will also support a much wider group of technology elements than have appeared in the Industry.

In summary, the development of versatile methods for achieving the integration of structural and dynamical elements is well advanced. Many of the target attributes listed in Table 2 have been achieved in industry experimental analyses. Progress has been made in achieving structural representations for a variety of configurations and problems within a unified framework. A design can be verified for different types of responses and protected from failure and instabilities with the knowledge that the elements of the problem, such as a blade, are the same among the varied applications. Applications of such analyses are only beginning. Aerodynamics couplings are a significant area of remaining difficulties. Data transfers between independently developed aerodynamic programs appear to provide a solution to the integration of aerodynamic elements. However, it does not appear to the authors of this paper that any fundamental advances in the aerodynamic technology developed in the last 8-10 years have been incorporated in these loads analyses. The efforts to advance the basic understanding of rotor aerodynamics discussed earlier are recognized and endorsed. However, these efforts have generally resulted in very specialized analyses/programs/experiments, the results of which have yet to be integrated in a practical way into an operational rotor loads program. Thus the survey of industry mentioned earlier reveals that most of the aerodynamic advances in rotor load programs have involved relatively modest changes made within the same basic aerodynamic framework that existed at the time of the study of Reference 2.

PROGRESS IN ACQUIRING DATA FOR CORRELATION

One of the recommendations made in Reference 2 was that the predictions from the various rotor loads analyses be correlated in detail with systematic data acquired with large scale rotors equipped with instrumentation sufficient to provide insight into the various elements of the problem - both aerodynamic and structural.

Although no formal structured response to this recommendation has occurred, certain experimental rotor programs have provided at least a portion of the data which ultimately is desired. For example, the Sikorsky S-76 rotor was tested in the NASA Ames 40' x 80' wind tunnel (Reference 16). No blade pressure data were acquired, but a family of four different blade tips was tested. Probably the most extensive instrumented rotor effort is that being conducted on the two blade Bell AH-1G. This effort is continuing with more detailed pressure data being acquired in the blade tip area. In a separate program, rotor stability data have been obtained from a series of systematic model rotor tests. Reference 31 is representative of this effort. Based on the survey conducted as part of this paper, it appears that there is still a pressing need for a more complete test in which all elements of the problem: rotor wake geometry, rotor induced flow field, blade pressures, blade stresses and rotor loads, are measured simultaneously and in detail.

CORRELATION OF ANALYSES

Reference 1 presented correlation studies using the Sikorsky Normal Mode Analyses. Typically it was shown that the inclusion of variable inflow and unsteady stall aerodynamics was required to achieve reasonable correlation of flatwise, edgewise and torsional moments. Vibratory amplitudes tended to be underpredicted although time history shapes compared favorably. In the intervening years efforts at Sikorsky and UTRC to improve correlation have concentrated on acquiring better dynamic stall data for modern airfoils as opposed to the older NACA 0012. UTRC in Reference 10 has developed a more generalized dynamic stall model and this is currently being made operational in our analysis. Sikorsky has also developed techniques for including fuselage flow field effects in loads calculations (Reference 6). Another major effort at UTRC was to develop a redundant blade load path analysis (G400, Reference 5) for bearingless rotors. Finally at Sikorsky the RDYNE and SIMVIBE and Transfer Matrix Analyses have been developed.

Systematic correlation studies to assess these new programs and features are far from complete. One effect that has been correlated is the influence of the fuselage flow field on rotor loads. Figure 22 shows that the predicted effect of the flow field induced by the rotor test module used in the tests of Reference 16 was significant, increasing flatwise vibratory moments by about 25% and improving the time history signature correlation as well. It should be noted that the test module is predicted to have less of an impact on rotor loads than the typical fuselage, which is larger and closer to the rotor. (See Figure 12 of this paper taken from Reference 16.)

An area where recent correlation (Reference 16) showed a disturbing trend is shown in Figure 23. Here the inclusion of variable inflow (with a non-free wake) showed a degraded correlation relative to constant inflow predictions. This would imply the existence of compensating assumptions present in the constant inflow analysis. Including fuselage flow field effects in the variable inflow analysis does help to improve the situation as shown.

It is rare that any analysis correlates with test data on an absolute basis. Rotor loads analyses are no exception in this regard, as indicated by the preceeding figures. However, often analyses lacking absolute correlation can be used to predict trends having been anchored to some reference data point. Figures 24-26 show the application of the Sikorsky Normal Mode Analysis in this manner. Here the analysis is used to predict the effect of tip shape changes tested in Reference 16 on key blade loads. The results are normalized in terms of the rectangular tip loads at one gross weight and compared with similarly normalized data taken from Reference 16. The beneficial effects of advanced tips on flatwise moments and control loads are predicted. The detailed correlation for these two loads is reasonable but far from perfect even on this normalized basis. Edgewise moment correlation is significantly poorer than either the flatwise moment or the control load correlation. These results, while not unexpected in light of the lack of a rigorous three dimensional aerodynamic model in the analysis, do indicate the problem facing the designer as he tries to evolve more advanced rotors. The value of systematic test data is clear.

In surveying the U.S. technical community, the question was posed as to which items exhibited the poorest correlation. The consensus response was that the higher harmonic content of the blade loads, particularly at the operating conditions at the limits of the operating envelope, were least well predicted. These loads are the ones which provide the most challenge to the aerodynamicist and yet they are also the very ones which most influence the design of the blade and hub components.

Survey results as to critical ssumptions contributing to areas of poorer correlation were cited almost unanimously as aerodynamic assumptions, approximations and empiricisms. These are all well known: wake geometry, three dimensional blade aerodynamics and dynamic stall (including sweep effects). Although emphasis was on aerodynamic shortcomings, in some instances it was clear that not all structural dynamic approximations have yet been removed from some of the older analyses. The coupling, both dynamic and aerodynamic, of the rotor and the fuselage was also cited as needing to receive more attention.

Regarding the role which 2GCHAS is expected to play in improving the situation, one respondent to the survey summed it up well in the following statement:

"Currently, there are many different methods and approaches to solving components of the rotor problem. For example, there are many different methods for calculating non-uniform downwash. These include: rigid wake, prescribed wake, free wake, local momentum wake, etc., and there are significant variations of each type. Each of these methods has an advocate, each makes different assumptions, and all are useful. But, which is the best for predicting reliable, accurate vibratory airloads?

The 2GCHAS gives industry and the Government a tool for evaluating many different approaches to nonuniform downwash, holding everything else constant. Claims can be evaluated, sensitivity established and rational decisions made. The 2GCHAS tool can be used to evaluate the best unsteady theory, the best rotor/fuselage coupling, the best method for trim or the best solution approach. In short, it provides a test bed for evaluating competing technology.

This is not all. The 2GCHAS also provides a system for holding and linking the best technology. Since the system is designed for modularity, it is the logical analysis for incorporating the best technology (once we know what the best is)."

CONCLUDING REMARKS

The prediction of rotor loads represents one of the most challenging technical tasks facing the aerodynamicist and the structural dynamicist. Good progress has been made on the structural side of the problem and new, more accurate and more versatile structural formulations are being rapidly introduced into operational loads analyses. On the other hand aerodynamics progress has been concentrated on the fundamentals of the problem and the time table for introducing the next generation of aerodynamic technology into the new analyses is not yet clear. Hopefully, this will be accomplished in an efficient and controlled manner through the 2GCHAS effort. Until the aerodynamic technology makes a breakthrough of sorts, the accuracy of existing rotor loads analyses will probably not improve significantly except through refinements to empiricisms tailored to specific user problems, designs and operating conditions. Therefore, rotor aerodynamics research is heartily endorsed. However, it is imperative that the aerodynamic researcher be alert to ways to cast the results of his work in as practical a form as possible to enhance its early integration into total loads analyses. Until higher confidence loads analyses are available, it is equally imperative that testing of rotors be an important element in providing the designer and the researcher the data necessary for each to accomplish their respective tasks. The results of these tests should be employed to validate any improvement to the loads analysis - both structural and aerodynamic.

REFERENCES

1. "Specialists Meeting on Helicopter Rotor Loads Prediction Methods", Milan, Italy, AGARD Conference Proceedings No. 122, March 1973.

2. Ormiston, R. A., "Comparison of Several Methods for Predicting Loads on a Hypothetical Helicopter Rotor", Journal of the American Helicopter Society, Vol. 19, No. 4 (October 1974).

3. Johnson, W., "Development of a Comprehensive Analysis for Rotor Craft-II: Aircraft Model Solution Procedure and Applications", Vertica Vol. 5 pp. 185-216, 1981.

4. Yen, J. G. and M. Glass, "Helicopter Rotor Load Prediction", Preprint 6 American Helicopter Society Specialists Meeting on Helicopter Fatigue Methodology, March 1980.

5. Bielawa, R. L., "Aeroelastic Analysis for Helicopter Rotor Blades with Time Variable, Nonlinear Structural Twist and Multiple Structural Redundancy", NASA CR-2638, 1976.

6. Sopher, R., and S. Kottapalli, "Substructure Program for Analysis of Helicopter Vibrations", Preprint No. 24, American Helicopter Society Northeast Region Specialists Meeting on Helicopter Vibration, November 1981.

7. Hurty, W. C., "Dynamic Analysis of Structural Systems Using Component Modes, AIAA Journal, Vol. 3, pp. 678-785, 1965.

8. McCroskey, W. J., "The Phenomenon of Dynamic Stall", Presented to von Kàrmàn Institute Lecture Series on Unsteady Airloads and Aeroelastic Problems in Separated and Transonic Flows, Rhode-Saint-Genèse, Belgium, March 1981.

9. McCroskey, W. J., et al., "Dynamic Stall on Advanced Airfoil Sections", American Helicopter Society Preprint 80-1, 36th Annual Forum of the American Helicopter Society, Washington, D.C., May 1980.

10. Gangwani, S. T., "Prediction of Dynamic Stall and Unsteady Airloads for Rotor Blades", American Helicopter Society Preprint 81-1, Proceedings of the 37th Annual Forum of the American Helicopter Society, New Orleans, Louisiana, May 1981.

11. Johnson, W., "Comparison of Calculated and Measured Helicopter Rotor Lateral Flapping Angles", NASA Technical Memorandum 81213, July 1980.

12. Landgrebe, A. J. & E. D. Bellinger, "An Investigation of the Quantitative Applicability of Model Helicopter Rotor Wake Patterns Obtained in a Water Tunnel", U. S. Army AMRDL Technical Report 71-69, 1971.

13. Johnson, W., "Comparison of Calculated and Measured Model Rotor Loading and Wake Geometry", NASA TM 81189, 1980.

14. Landgrebe, A. J., R. B. Taylor, T. A. Egolf, J. C. Bennet, "Helicopter Airflow and Wake Characteristics for Low Speed and Hovering Flight from Rocket Interference Investigations", American Helicopter Society 37th Annual Forum Proceedings, New Orleans, Louisiana, May 1981.

15. Sheehy, T. W., "A Simplified Approach to Generalized Helicopter Configuration Modeling and the Predictions of Fuselage Surface Pressures", American Helicopter Society Symposium on Helicopter Aerodynamic Efficiency, Hartford, Ct., March 1975.

16. Jepson, D., R. Moffitt, K. Hilzinger, J. Bissell, "Analysis and Correlation of Test Data from an Advanced Technology Rotor System", NASA CR-152366, July 1980.

17. Freeman, C. E. and J. C. Wilson, "Rotor-Body Interference (ROBIN) - Analysis and Test", American Helicopter Society 36th Annual Forum Preprint 80-5, May 1980.

18. Arieli, R., and Tauber, M., "Computation of Subsonic and Transonic Flow About Lifting Rotor Blades", Presented at the AIAA Atmospheric Flight Mechanics Conference, Boulder, Colorado, August 1979.

19. Jameson, A., and Caughey, D., "Numerical Calculation of the Transonic Flow Past a Swept Wing", Courant Institute of Mathematical Sciences, C00-3077-140, June 1977.

20. Carradonna, F.X., and Isom, M.P., "Subsonic and Transonic Potential Flow over Helicopter Rotor Blades", AIAA Journal, Vol. IV, No. 12, December 1972.

21. Carradonna, F.X., and Steger, J.L., "Implicit Potential Methods for the Solution of Transonic Rotor Flows", Presented at the 1980 Army Numerical Analysis and Computers Conference, Moffett Field, Ca., February 1980.

22. Chattot, J.J., "Calculation of Three-Dimensional Unsteady Transonic Flows Past Helicopter Blades", NASA Technical Paper 1721, October 1980.

23. Hodges, D. H., and Dowell, E. H., "Nonlinear Equations of Motion for the Elastic Bending and Torsion of Twisted Non-uniform Rotor Blades", NASA TN D-7818, December 1974.

24. Sopher, R., "Derivation of Equations of Motion for Multi-Blade Rotors Employing Coupled Modes and Including High Twist Capability", NASA CR 137810, February 1975.

25. Hansford, Robert E., "Comparison of Predicted and Experimentation Rotor Loads to Evaluate Flap-Lag Coupling with Blade Pitch", J. AHS, Vol. 24, No. 5, pp. 3-11, October 1979.

26. Arcidiacono, P. J., "Prediction of Rotor Instability at High Forward Speeds - Volume 1 - Steady Differential Equations of Motion for a Flexible Helicopter Blade with Chordwise Mass Unbalance", USAAVLABS TR 68-18A, February 1969.

27. Stevens, W. P., Myers, G. J., and Constantine, L. L., "Structured Design", IBM Systems Journal, Vol. 13, No. 2, 1974.

28. Yen, Jing G., and McLarty, Tyce, T., "Analysis of Rotor - Fuselage Coupling and its Effect on Rotorcraft Stability and Response", Vertica, Vol. 3, pp. 205-219, 1979.

29. Berman, Alex, "A Generalized Coupling Technique for the Dynamic Analysis of Structural Systems", J. AHS Vol. 25 No. 3, pp. 22-28, July 1980.

30. Gangwani, Santu T., "Determination of Rotor Wake Induced Empennage Airloads", Preprint No. 26, Specialist Meeting on Helicopter Vibration, American Helicopter Society, Hartford, Connecticut, November 1981.

31. Bousmann, W.G., "An Experimental Investigation of the Effects of Aeroelastic Couplings on Aeromechanical Stability of a Hingeless Rotor Helicopter", Journal of the American Helicopter Society, Vol, 26, No. 1 (January 1981).

32. Beddoes, T. S., "Onset of Leading Edge Separation Effects under Dynamic Conditions and Low Mach Numbering", Preprint No. 78-63, American Helicopter Society, 34 Annual National Forum, Washington, D. C., May 1978.

33. Hammond, C. E., "An Application of Flocquet Theory to Prediction of Mechanical In Stability", American Helicopter Society Specialists Meeting on Rotor Craft Dynamics, February 1974.

34. St. A. O. Hilaire, Carta, F. O., M. R., and Jepson, W. D., "The Influence of Sweep on the Aerodynamic Loading of an Oscillating NACA 0012 Airfoil - Volume I - Technical Report", NASA CR-3092, 1979.

Table 1. Importance of the Dynamic Stall Parameters

Stall parameter	Effect
Airfoil shape	Large in some cases
Mach No.	Small below M ~ 0.2, Large above M ~ 0.2
Reynolds No.	Small (?) at low Mach No., Unknown at high Mach No.
Reduced frequency	Large
Mean angle, amplitude	Large
Type of motion	Virtually unknown
3-D effects	Virtually unknown
Tunnel effects	Virtually unknown

Table 2. Key Attributes of Integrated Analyses

- Unified and versatile analysis
    - Applicable to wide range of problems
    - Limited number of elements
- Automated synthesis of equations of motion
- Verifiable
- Easily modifiable
- Good program organization
- Management of growth

TABLE 3. Sample Physical Mathematical, and Software Requirements

Physical

- Elastic blade
- Hingeless/bearingless
- Redundant load paths
- Precone, droop, sweep
- Dynamic stall
- 3D aerodynamics
- Rotor induced variable inflow
- Fuselage induced inflow
- Control system dynamics
- Drive system dynamics
- Fuselage dynamics
- Multiple rotors
- Higher harmonic control
- Elastic Fuselage
- Failure/Damage Events

Mathematical

- Automated assembly
- Time history, harmonic balance
- Transformation to multi-blade coordinates
- Transformation to first order systems

Software

- Plot options
- Restart capability
- Tutorial mode
- Advanced Executive
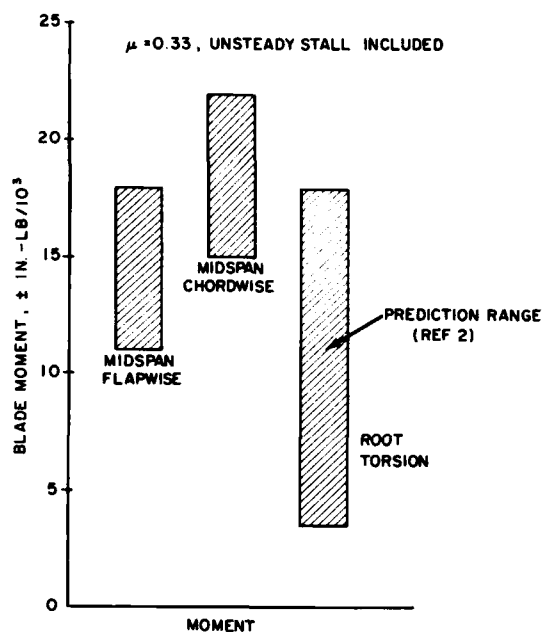
Figure 1. Analyses Differ Widely in Predicted Moments.
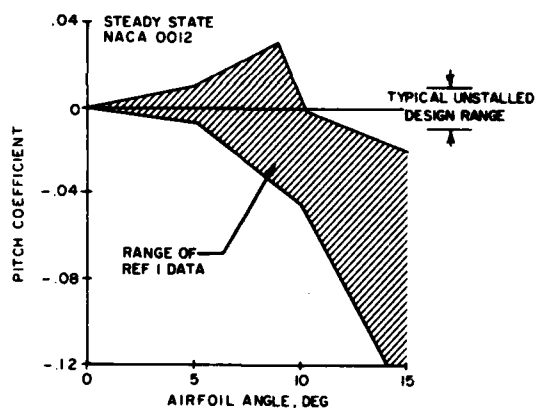
Figure 2. Critical Airfoil Data Show Large Scatter.
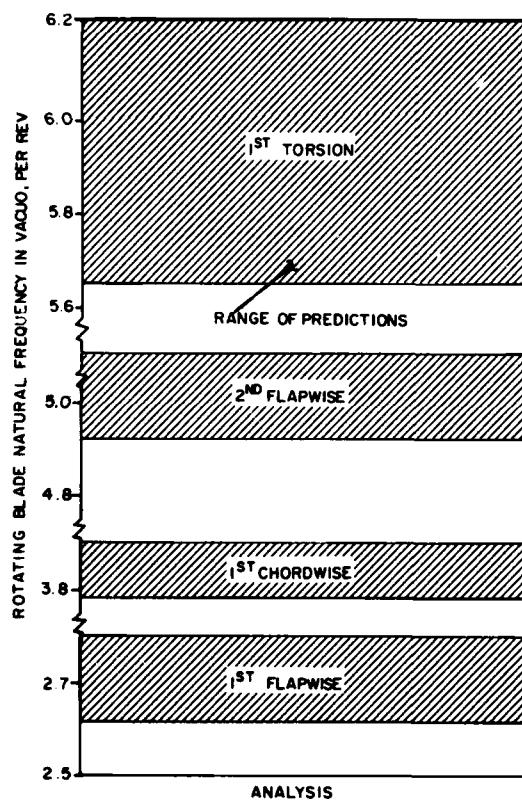
Figure 3. Reference 1 Showed Large Scatter in Predicted Natural Frequencies.
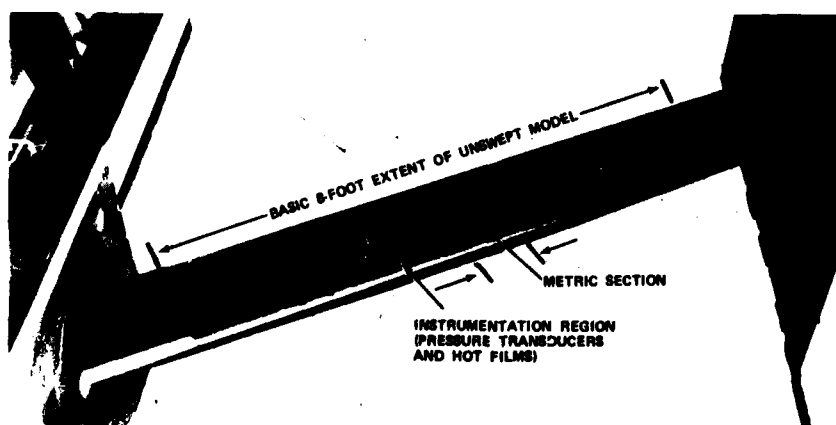
Figure 4. Tunnel Spanning Apparatus (TSA) - Swept Configuration.
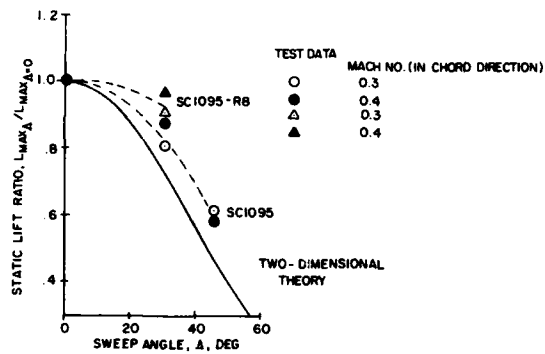
Figure 5. Tunnel Spanning Airfoil Shows 15-25% Max Lift Augmentation Due to Sweep.

SC 1095
M = 0.3
$k = 0.1$, $\alpha_M = 10°$, $\bar{\alpha} = 10°$, $\Lambda = 0°$

NASA/AMES TEST RESULTS   PREDICTION
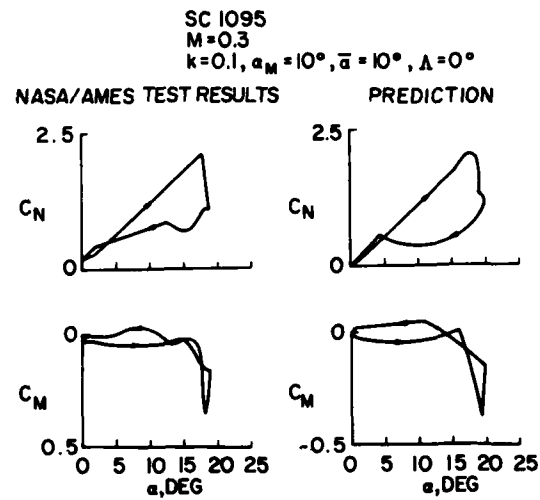
Figure 8. Comparison of Experimental Unsteady Airfoil Characteristics with Prediction Using UTRC Synthesized Data (Reference 10).

STATIC

DYNAMIC, STALL FREE

DEEP STALL

M = 0.3
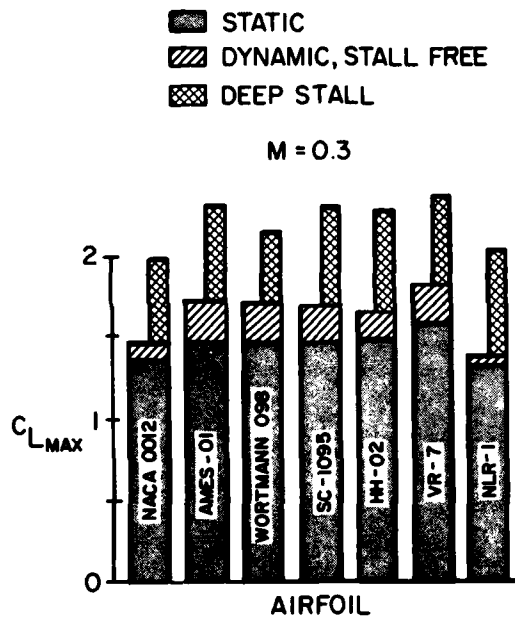
Figure 6. Comparison of Airfoil Stall Characteristics (Reference 9).

RAMP TEST(REF 32)

COMPUTED BY UTRC METHOD

Figure 9. Comparison of Computed Unsteady Data With Test Data for Ramp Function Angle of Attack Distribution (Reference 10).

NACA0012   M = 0.3   k = 0.049 $\alpha_M = 8°$ (REF 34)

Figure 7. Effect of Sweep on SC1095 Airfoil Dynamic Stall.

Figure 12. Effect of Fuselage on Blade Flatwise Bending Moment Time History. Test and Calculated Results.

Figure 10. Views of Tip Vortex Geometry in Vicinity of Blade at $\psi = 90^0$ ($V/\Omega R = 0.18$, -11^0 Twist Blade, Reference 13).
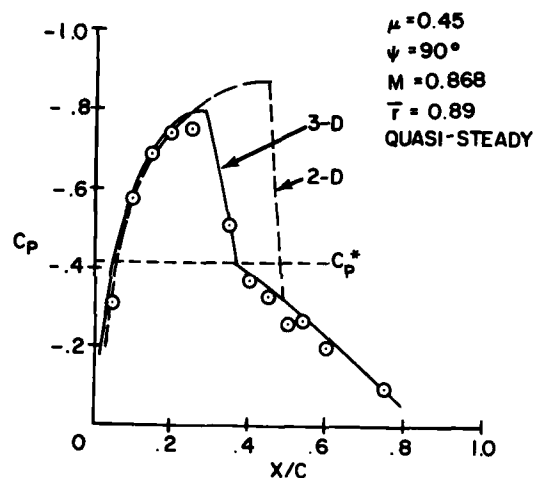
Figure 13. Comparison of Two and Three Dimensional Calculations with Measurements (Reference 18).

Figure 11. Theory Vs. Test, 15 Kts (Reference 14).
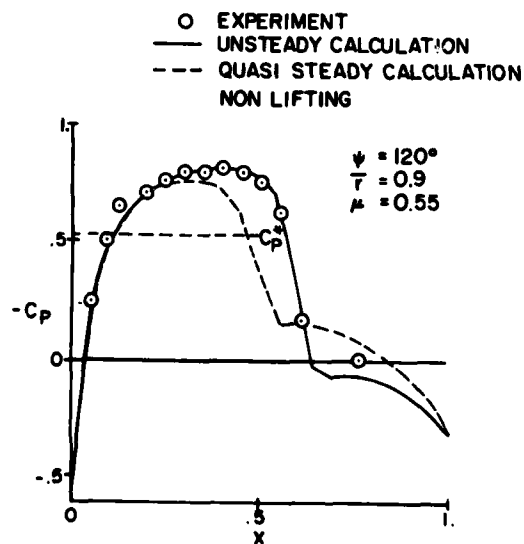
Figure 14. Comparison of Unsteady and Quase Steady Calculations with Measurements (Reference 22).

Figure 15. Comparison of Modal Analysis and Transfer Matrix Analytic Results with Flight Test.

Figure 18. Lag Damper Inoperative Stability Boundaries.

Figure 16. Sample Components Defined by Element and Connection Node Numbers.

Figure 19. Coupled Rotor/Fuselage Vibration Analysis.

Figure 17. Comparison of Drive Train Mode Time Histories.

Figure 20. Effects of Variations in Third Fixed System Mode Frequency on Rotor Hub Loads.

Figure 21. SIMVIBE Analysis Data Flows.
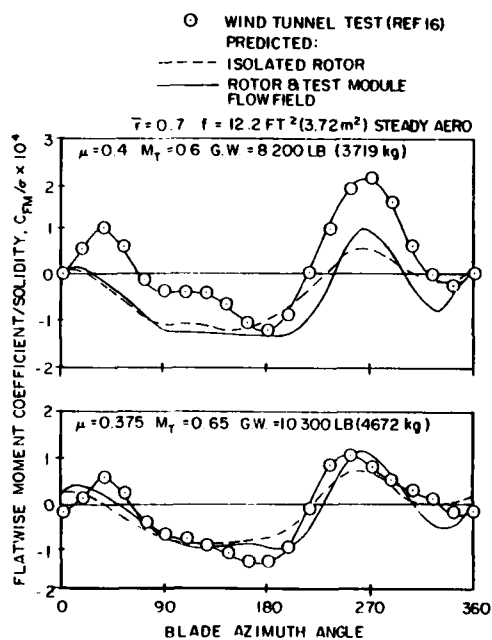
Figure 22. Inclusion of Test Module Flow Field Improves Correlation.
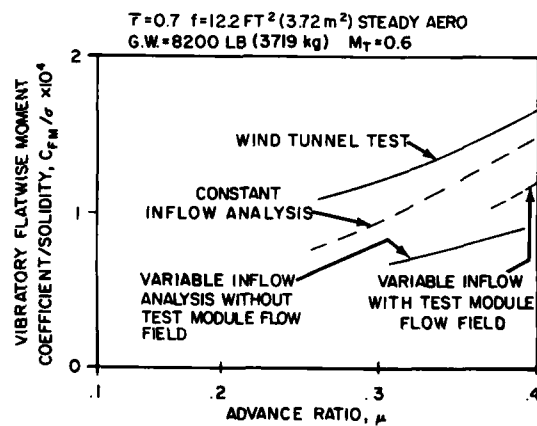
Figure 23. Comparison of Wind Tunnel Test Data with Predictions Using Various Rotor Flow Field Models.

FLATWISE
$\mu = 0.375$
$M_T = 0.65$
$\bar{T} = 7R$
$f = 12.2\,FT^2$

G.W = 7900 LB

G.W = 10 300 LB

FLATWISE MOMENT
————————————
FLATWISE MOMENT OF RECTANGULAR BLADE AT 7900 LB %

RECT TIP   TAPER   SWEEP   SWEEP & TAPER

SWEEP & TAPER

TEST

ANALYSIS
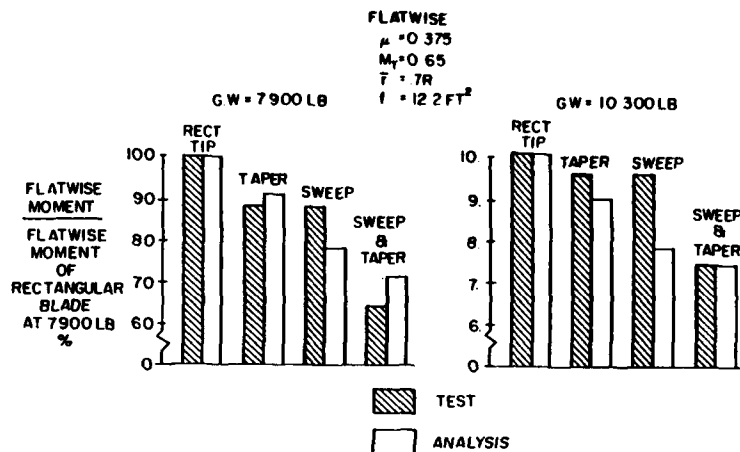
Figure 24. Comparison of Predicted & Measured Trends of Flatwise Moment with Tip Shape Changes.

CONTROL LOAD
$\mu = 0.375$
$M_T = 0.65$
$f = 12.2\,ft^2$

G.W = 7900 LB

G.W = 10 300 LB

CONTROL LOAD
————————————
CONTROL LOAD FOR RECT. TIP BLADE AT 7900 LB %

RECT TIP   TAPER   SWEEP   SWEEP & TAPER

RECT TIP   TAPER   SWEEP   SWEEP & TAPER

TEST

ANALYSIS
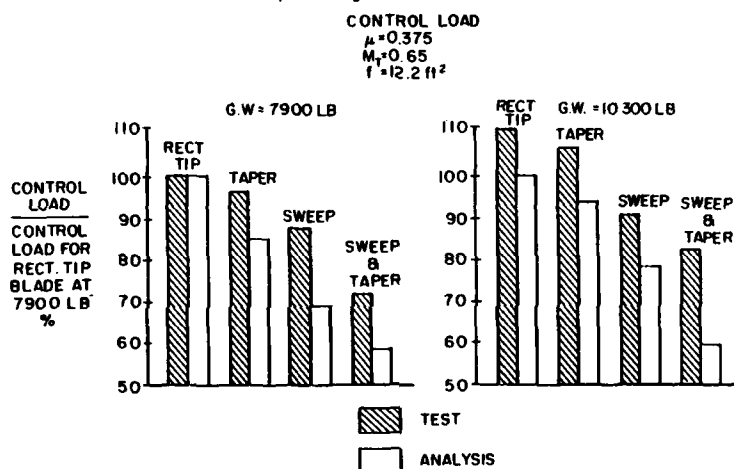
Figure 25. Comparison of Predicted and Measured Trends of Flatwise Moment With Tip Shape Changes.

EDGEWISE MOMENT
$\mu = 0.375$
$M_T = 0.65$
$\bar{T} = 0.6$
$f = 12.2\,ft^2$

G.W = 7900 LB

G.W = 10 300 LB

EDGEWISE MOMENT
————————————
EDGEWISE MOMENT FOR RECT TIP AT 7900 LB %

RECT TIP   TAPER   SWEEP   SWEEP & TAPER

RECT TIP   TAPER   SWEEP   SWEEP & TAPER

TEST

ANALYSIS

Figure 26. Comparison of Predicted and Measured Trends of Edgewise Moment With Tip Shape Changes.

THE DEVELOPMENT OF A SYSTEM FOR
INTERDISCIPLINARY ANALYSIS OF ROTORCRAFT FLIGHT CHARACTERISTICS

by

Andrew W. Kerr
US Army Research and Technology Laboratories (AVRADCOM)

and

Wendell B. Stephens
US Army Aeromechanics Laboratories

Ames Research Center
Moffett Field, California   94035

SUMMARY

A comprehensive, interdisciplinary analysis system is being developed to provide the ability to predict the technical characteristics of a wide variety rotary wing configurations. This system, which will include the analysis of rotor loads, is being created by using both an in-depth familiarity with a wide variety of "first-generation" helicopter analyses and modern software development techniques. This paper provides an overview the approach used in the development of the system and describes the software methodology used to support the development. It also includes a description of the mathematical basis for the system and presents a summary of the results of the top-level analysis and architectural design of the system. The potential ability of the system to predict rotor loads is discussed. The flexibility and extendability of the system which is a result of modern software methodology will allow the loads analyst to enhance the system without extensive restructuring or reprogramming of the system.

1. INTRODUCTION

A number of comprehensive helicopter analysis computer codes have been generated over the past 15 years to predict various technical characteristics of vehicle designs. The codes have placed particular emphasis on modeling the primary lifting rotors. Some programs such as C-81 (Reference 1), REXOR (Reference 2), and GENHEL (Reference 3) have been the outgrowth of handling qualities analysis. Other programs such as Normal Modes (Reference 4), G400 (Reference 5), C60 (Reference 6), and DART (Reference 7) have been derived as rotor loads or aeroelastic stability analyses. The analysis technology required to produce adequate loads and handling qualities preditions for of the rotor/body combination are closely related, and a considerable amount of effort b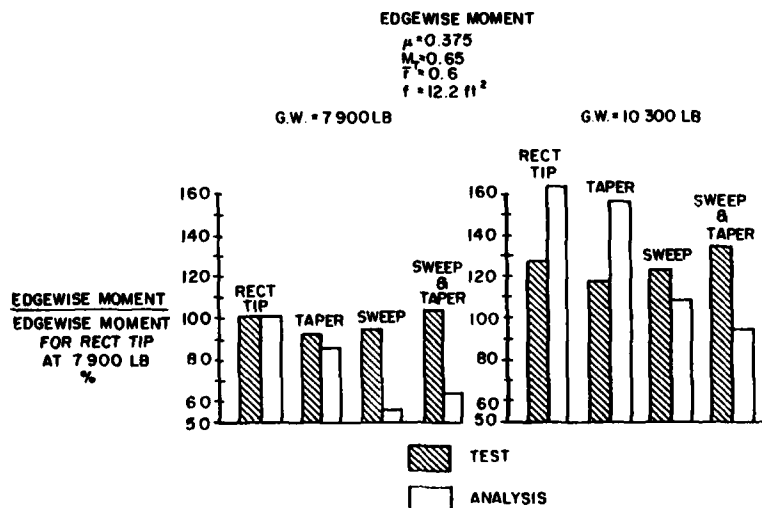y a variety of analysts has been expended on individual codes. Aerodynamics and performance analysis technology, which is often developed independently from loads anaysis, is also required to develop an accurate prediction capability for rotor loads and vibrations. Programs such as CAMRAD (Reference 8), Coupled Rotor/Airframe Vibration Analysis (Reference 9), and DYSCO (Reference 10) represent some of the recent efforts to combine these various technologies.

The US Army Research and Technology Laboratories (AVRADCOM) is developing a Second Generation Comprehensive Helicopter Analysis System (Reference 11), to be referred to in this paper as the 2GCHAS or the System. The 2GCHAS is being designed to predict performance, stability and control, loads and vibration, aeroelastic stability, and acoustics characteristics of a wide variety of rotorcraft configurations. It is being developed as an interdisciplinary analysis system to support the engineering analysis of rotorcraft through a life cycle of conceptual design, detailed design, development, and subsequent modification, and to provide a high quality software testbed for conducting research on the varied aspects of advanced rotorcraft analysis software technology. The System, which will use a finite-element approach as its mathematical basis, will contain a full range of analysis options to treat each physical component of the rotorcraft at the appropriate level of complexity required to accomplish a particular engineering analysis task. A primary consideration in the development of the System is the manner in which components of the rotorcraft, including the aerodynamics, are combined analytically to represent the vehicle as a whole. The 2GCHAS is also being structured so that its modular design will enable analysts and researchers to easily develop and insert new analysis technology into the System without adversely affecting the integrity of the System as a whole.

The "Second Generation" title for the System represents its relationship   the variety of methods developed in the late 1960's and early 1970's, References 1 through 4. These analyses and others of their vintage were derived at a time when computer capacity and software design and implementation techniques were at a much earlier stage of development than that available today. Some areas in which first generation codes failed to accurately predict aircraft response are described in References 12 and 13. The wide range of their capabilities is summarized in Reference 14. The structure of these codes has made extension difficult, and the user interface for these programs has received minimal attention, making it difficult for analysts other than the program developers to exercise the programs intelligently or effectively. More recent analysis developments, References 8 through 10, have been approached with a number of the 2GCHAS goals in mind and have had a significant influence on the 2GCHAS analysis and design.

A unique characteristic of the 2GCHAS is that it is being developed by an analysis team as opposed to a single analyst, and a large number of engineering specialists from a variety of research and manufacturing organizations will be contributing directly to the development of the System. The reason for following this approach is to insure that each element of the System is developed by a specialist with a complete understanding of the particular technology involved, and to encourage each specialist to more fully understand the interface of his technology with the other technologies required by the analysis. This approach, which is a major extension to that originally presented in Reference 15, incorporates a state-of-the-art software development process which includes structured software methodology and a product assurance methodology. The goal is to produce a clear, well-documentated, transportable computer code
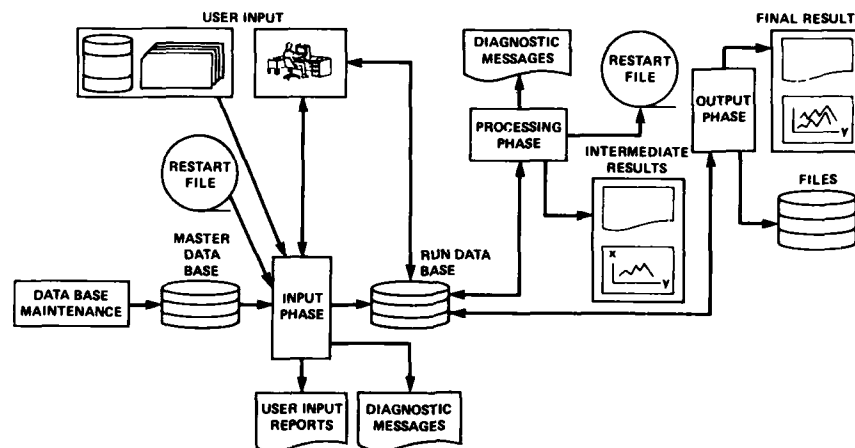
Figure 1.   User's View of the System.

which can be easily modified and extended by a wide variety of users. The System development will also stress the complete interface of the user with the system, giving him the ability to model configurations of interest, to manage and correctly assemble required input data, to interface with external computer models and data, and to construct a wide variety of formats for System outputs. A user's view of the system is shown schematically in Figure 1.

Central to any analysis of this type is the prediction of rotor loads and, ultimately, the loads on the entire helicopter. This involves the structural and aerodynamic coupling of all components. The requirement for loads prediction has been addressed in the structured analysis of the System in two ways: by evaluating the current approaches which have been developed in first generation programs and loads analyses; and by probing the research community to determine advanced approaches under investigation to insure that the constraints imposed by System architectural design do not preclude the assimilation of viable approaches into the System.

In 1976, analysts from interested Government agencies and helicopter manufacturers met in a Government/Industry Working Group (GIWG) to determine the requirements for the next generation helicopter analysis system. These requirements were subsequently studied in three predesign studies reported in References 16 through 18. A Project Office was formed at the US Army Aeromechanics Laboratory to direct the development of the System. The System requirements, updated in the predesign studies, were divided into two categories described as a Technology Complex and an Executive Complex. The Technology Complex includes the elements which form and solve the equations which model a particular rotorcraft or one or more of its component parts. The Project Office is responsible for the top-level design of the Technology Complex. The detailed design of the Technology Complex and the implementation of Technology Modules will be accomplished by a number of different developers under contract to the Project Office. Some of the Executive Complex functions include the user interface with the System, data management capabilities, control of Technology Module analysis paths, graphical display capability of analysis, and an external model interface.

Figure 2.   Structured Analysis and Design Process.

Figure 3.   Data Flow Diagram Example.

This paper addresses the software methodology being applied in developing the System, the product assurance methods to be employed in applying this methodology, the demonstration of some of the results of the initial application of the methodology to the analysis and architectural design of the Technology Complex, and the technology to be included in the System for prediction of rotorcraft loads.
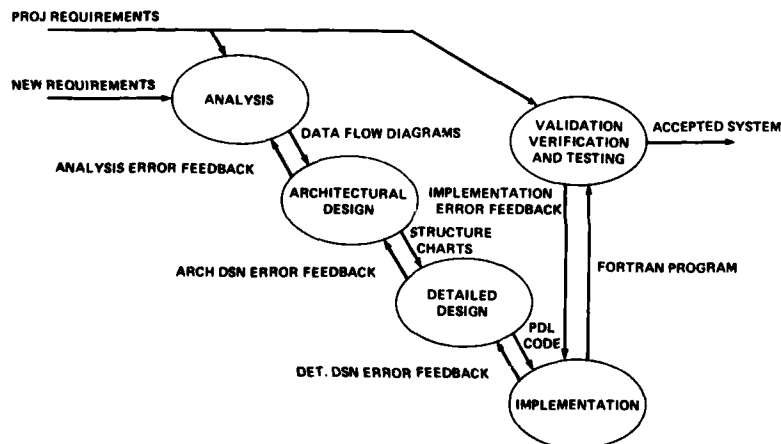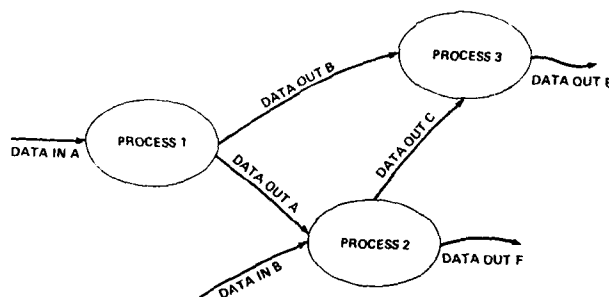
2. METHODOLOGY

A major shortcoming of many existing analysis methods is that they have grown in a somewhat randomly controlled manner, resulting in a structure that makes extending or modifying their analysis capability difficult or impractical. In most instances, coding has been undertaken well before a cohesive program architecture has been developed, partly because the requirements which the program will eventually be called upon to satisfy have not been fully defined. In the mid 1970's, software scientists developed a number of approaches and tools to structure the creation of software products to insure that the product would meet the requirements and expectations of the potential users of a program. These methods also provide a basis for insuring that the product is maintainable, modifiable, and adequately documented.

For the development of the 2GCHAS, a methodology has been adopted which makes use of a number of related methods designed to produce high-quality structured software. The schematic view of the methodology adopted is shown in Figure 2. It is divided into five basic phases which are contained in the bubbles in this figure. In the first phase, Structured Analysis, a critical review of system or subsystem requirements is carried out and those requirements are broken down to identify the specific processes involved, as well as the process data output and data input requirements. The basic tool used to carry out this analysis is the Data Flow Diagram, DFD, patterned after the work of Yourdon (Reference 19). The form of the Data Flow Diagram is shown in shown in Figure 3. Processes are identified by both a number and a name. Data inputs to and from the processes are defined by name. The analysis starts with a single process bubble and its data requirements, referred to as a the "Context Diagram" for the system being analyzed. Using a top-down approach, this diagram is broken down into progressively more complete levels of detail until the most elemental processes and their data requirements are identified. The Data Flow Diagram addresses only processes and related data transfer and does not address control of the processes involved. The control structure is addressed in later phases of the development methodology. Thus, the analysis phase addresses only what must be accomplished, but not how it is to be accomplished. Separating the process functions and data requirements from questions of implementation and control allows the overall program concept to be developed in a much more straight forward manner than that afforded by more traditional development techniques. Traditionally, the analyst often plunges right into detailed design and implementation of a computer code without a global picture of the design requirements.

In addition to the diagrams, two companion products result from the analysis: a set of Mini-Specs, and a Data Dictionary. Each bubble at every level of the analysis has a companion Mini-Specs, which is a more detailed description of the process than that contained in the few words which name the bubble on the Data Flow Diagram. The Data Dictionary includes the data items identified at all levels of the analysis, with a complete definition of each data item. The complete product of the structured analysis of the system includes a hierarchical collection of Data Flow Diagrams, Mini-Specs and a Data Dictionary. This structured analysis is then correlated with the requirements documents to insure that it both satisfies the requirements and does not exceed them. Often requirements which should have been included originally are identified during this phase, and the original requirements must be modified. Potential users of the proposed system then review the analysis for accuracy and completeness.

The next phase in the methodology is Architectural Design. In this phase, the Data Flow Diagrams become the basis for a structuring of individual functions into "modules" which will eventually be developed into computer codes. At this point, some of the required control of the processes become apparent through the structuring of the transfer of data through the modules. The tool for this process is the Structure Chart, which has the form shown in Figure 4, and is adapted from the work of DeMarco (Reference 20). The Architectural Design is a mechanicallly derived structure from the Data Flow Diagrams. This architecture is modified through stepwise refinement to achieve improvements with respect to certain metrics which insure the quality of the structure. The final product of the Architectural Design phase is a set of Structure Charts with companion Module Specs and a list of the intermodule communications (data items) for each module These products are also correlated with requirements and reviewed by potential users to insure consistency and completeness.

The third phase of the methodology is the Detailed Design of modules for the system. In this phase, each module identified in the Architectural Design phase is given detailed descriptions of their control and data structures. The control and data structures are expressed through use of a Program Design
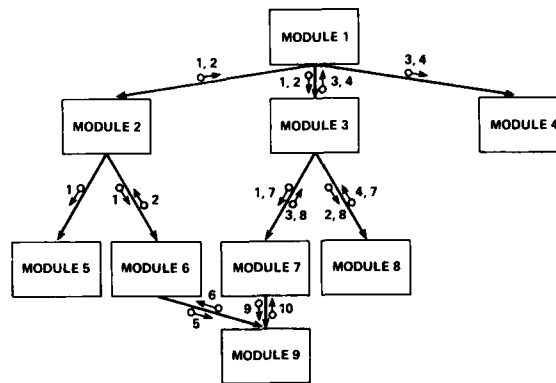
Figure 4. Example Structure Chart.

Language (PDL). The use of PDL highlights the conception process of an algorithm, leaving some complex, language-dependent idiosyncracies to the next development phase. Nine basic control structures are identified which may be used in the design and a limited number of data structures are allowed. The resulting PDL designs are then reviewed for correctness to insure that the control and data structures selected correctly implement the required function.

Up to this point in the creation of a major computer software system, not one line of actual computer code has been written. In the Implementation phase, the PDL code produced in the detailed design phase is transformed into executable code in the implementation language selected for the system (FORTRAN 77 for the 2GCHAS) with conceptual integrity, comprehensibility, efficiency, and memory requirements in mind. The products of the Implementation phase are executable implementation language code with appropriate commentary for documentation within the code. This is accomplished through the transformation of control structures, the development of data structures, the construction of utility subprograms, and packaging of the final code.

The fifth phase in the development methodology is Validation, Verification, and Testing, which is required to insure that the implementation has been successfully accomplished. Testing is the process of executing a program or subprogram with the intention of uncovering errors. Testing is not meant as a process to demonstrate the validity or correctness of the algorithms and models programmed, but to insure that the code itself is free of errors. This process is to be performed with economy in mind, both in terms of programmer time and hardware time. The design of test cases emphasizes the choice of a limited number of useful tests to reveal a maximum number of errors.

The 2GCHAS development methodology must be very orderly because of the requirement to have a large number of module developers make contributions to the System, working independently in many different locations. The top-level structured analysis and architectural design of the Technology Complex are being developed by the 2GCHAS Project Office. This analysis and architectural design has been taken to a very low level in order to insure that the requirements for the system can be met by higher level module definitions. Modules will be assigned contractually to developers at a relatively high level in the structure, and the developers will repeat the analysis and architectural design of their modules to further optimize the structure of the System. Detailed design, implementation and testing by individual module developers will then be accomplished. The modules will be integrated with the Executive Complex and System testing completed. It is anticipated that the product resulting from this effort will have a correct and flexible structure which will allow its application to a wide variety of problems by the user community.

3. SOFTWARE PRODUCT ASSURANCE

Software Product Assurance is the term applied to the actions performed to insure that software products developed meet specified all requirements. The term Product Assurance is based on the work of Bersoff, Henderson, and Siegel (Reference 21). However, the specifics of the Software Product Assurance Program for the 2GCHAS Project have been tailored to meet what are considered to be the unique needs of an engineering-oriented software system and have been drawn from many sources. Software Product Assurance is defined to consist of the three major functions shown in Figure 5: Software Quality Assurance; Software Configuration Management; and System Test and Evaluation.

The objectives of the 2GCHAS Product Assurance Program are to insure that the 2GCHAS Project produces quality software products, that adequate control is placed over the configuration of these products, and that all products have integrity as demonstrated by the results of test and evaluation. These three elements (quality, configuration, and integrity) are the cornerstones of the Program; each element is defined and expanded upon below.

The term quality is used in a strict sense to imply conformance to standards (i.e., excellence) which may be either attained or not attained in the development of a product. A product which does not meet the quality standards imposed will be refined, within practical time and cost constraints, until it meets the standards or rejected as inferior. In this context, quality applies to the content, format, and functionality of individual products whereas integrity applies to the functionality of and correctness of results from the product.
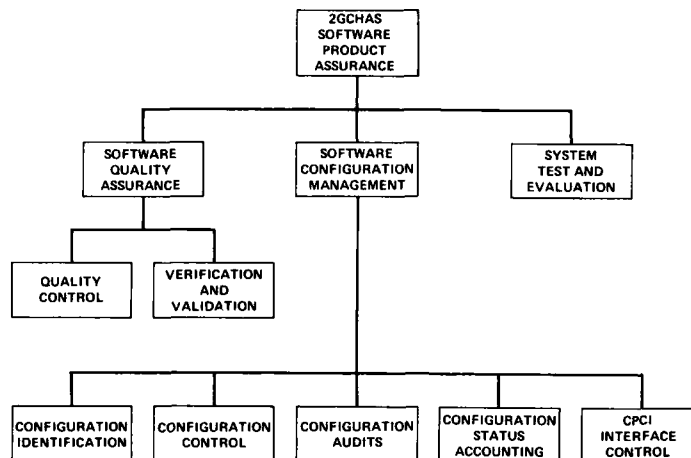
```
                          ┌──────────┐
                          │  2GCHAS  │
                          │ SOFTWARE │
                          │ PRODUCT  │
                          │ASSURANCE │
                          └────┬─────┘
          ┌────────────────────┼────────────────────┐
    ┌──────────┐         ┌──────────────┐      ┌──────────┐
    │ SOFTWARE │         │   SOFTWARE   │      │  SYSTEM  │
    │ QUALITY  │         │CONFIGURATION │      │ TEST AND │
    │ASSURANCE │         │  MANAGEMENT  │      │EVALUATION│
    └────┬─────┘         └──────┬───────┘      └──────────┘
    ┌────┴──────┐               │
┌─────────┐ ┌────────────┐      │
│ QUALITY │ │VERIFICATION│      │
│ CONTROL │ │    AND     │      │
│         │ │ VALIDATION │      │
└─────────┘ └────────────┘      │
    ┌───────────┬──────────┬──────────────┬────────────┐
┌───────────┐┌───────────┐┌───────────┐┌─────────────┐┌──────────┐
│CONFIGURATION││CONFIGURATION││CONFIGURATION││CONFIGURATION ││   CPCI   │
│IDENTIFICATION││  CONTROL  ││   AUDITS   ││   STATUS    ││INTERFACE │
│           ││           ││           ││ ACCOUNTING  ││ CONTROL  │
└───────────┘└───────────┘└───────────┘└─────────────┘└──────────┘
```

Figure 5.   2GCHAS Software Product Assurance.

The term configuration is used to mean the conceptual relationship between the parts of a product plus the physical representation of the relationships. Examples of some relationships, parts, and products and their physical representations include the following: printed listings of source code or program design language; encoding of source code, object code, or load modules on a storage device such as a tape or disk; printed pages of documents or publications; diagrams or charts which depict the analysis or design of the System. Any changes which are made to the relationships or the parts must be strictly controlled to insure that no errors are introduced into a product after the product has been judged adequate for a particular stage (i.e., baselined) and that the potential user of a product knows the histories of error correction and of enhancement incorporation.

The term integrity is used here to imply a specific state of the product. In this context, a product with integrity is defined to be a product which meets all the System functional requirements and produces correct answers. Integrity is ultimately demonstrated by successful test and evaluation at the System level.

The key aspects of the Product Assurance (PA) work and the responsibilities of the 2GCHAS PA Team are summarized as follows: developing an overall methodology for assuring the quality, configuration, and integrity of all software products; assuring that a methodology for development of all 2GCHAS software products is prepared; assuring that appropriate software tools are acquired or developed to support the application and enforcement of the development and product assurance methodologies; and assuring that the development methodology is used in the development of all software products for the System through the enforcement of the product assurance methodology. The enforcement procedures are contained in a Product Assurance Manual with its attendant procedures and standards.

The following is a list of procedures and standards which are planned for inclusion in the 2GCHAS PA Manual. It is included to show the level of involvement of the PA function required for System development.

Procedures: Standards:

Procedure for Monitoring Development of Software Products   Documentation Standard
Procedure for Review of Specification Requirement   Programming Standard
Structured Analysis Procedure   Engineering Nomenclature Standard
Architectural Design Procedure   Derivation of Equation Standard
Detailed Design Procedure   Structured Analysis Standard
Implementation Procedure   Architectural Design Standard
Testing Procedure   Detailed Design Standard
Configuration Management Procedure   Implementation Standard
                                                                Testing Standard

In addition, automated tools are being selected or developed to support development methodology and product assurance efforts.

Quality Assurance activities which have been designated as necessary for the successful implementation of the 2GCHAS have been divided into two top-level categories, as shown in Figure 6: Quality Control, and Verification and Validation (V&V). Quality Control differs from V&V in that it is accomplished by the on-going monitoring and overseeing of project activities whereas V&V determines through Documentation Testing and Inspection whether the performance of a Software Product is satisfactory. The V&V process seeks through inspection and development testing to compare the software product at a given point in its development to its immediately previous specification (via verification), as well as to the original system requirements (via validation). 2GCHAS development via the Builds approach (Reference 16), calls for a certain level of V&V Testing and Evaluation to be carried on throughout the development. The effort is focused in Build Qualification Audits, Functional Configuration Audits, Functional Qualification Reviews, and Physical Configuration Audits just prior major System releases. V&V includes both inspection and development testing.
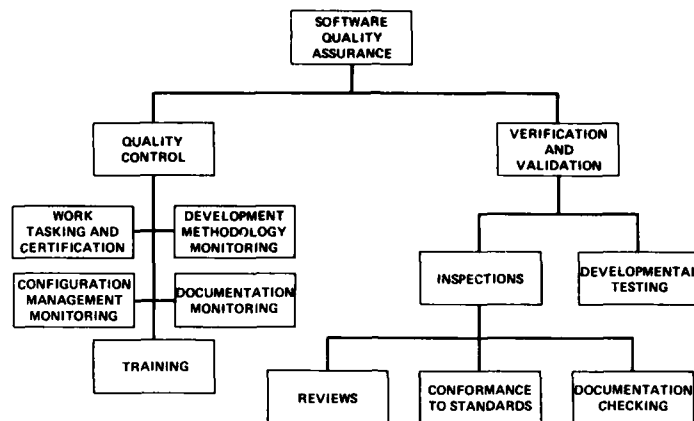
Figure 6.   2GCHAS Software Quality Assurance.

The primary function of Software Configuration Management (CM), Figure 5, is to insure that each final Computer Program Configuration Item (CPCI) is identified, controlled, and accounted for in accordance with the design requirements and/or specifications. A CPCI is a subprogram or set of subprograms developed as a unit for the System. Achievement of this objective is facilitated through the application of technical and administrative direction and surveillance in order to identify and document the characteristics of the CPCI, control changes to those characteristics, and record/report on the implementation of approved changes to the CPCI throughout its life cycle. The configuration of the software is identified and established at discrete points (baselines) during the CPCI life cycle so that subsequent changes to the configuration can be evaluated an d systematically controlled. Thus, effective configuration management maintains the integrity and traceability of the software throughout the life cycle of a system. Configuration Management addresses the five major functional areas shown in Figure 5.

System Test and Evaluation for the 2GCHAS will involve the exercising of the System by a wide range of users in various engineering disciplines and in both Government and industry design and research organizations. The results of early field testing of the System will be fed back to direct the development of improvements to be made available with subsequent system builds. This is where the final validation of the capabilities of the System to adequately model rotorcraft characteristics will be assessed, and where the quality of the user interface with the system will meet its ultimate test by a wide variety and level of users.

The basic challenge to be met in the area of PA is to develop a methodology and a program which will provide a major increase in software and documentation quality over that found in first generation analyses without constructing a labyrinth of confusing requirements which will stifle the creativity and productivity of the developers of the System. Considerable effort in this regard is being applied to meet this challenge.

4. ANALYSIS OF 2GCHAS TECHNOLOGY COMPLEX

In order to develop a good architectual design for the System at a relatively high level, it has been necessary for the Project Office to carry the structured analysis and architectual design activity to a very detailed level. This effort also affords the opportunity to review the System requirements for completeness prior to dividing the System into packages to be supplied by a large number of contributing developers. In this section of the paper, some of the results of this analysis are presented to describe the process and to show the level of technology intended for loads prediction capability.

The first phase of the analysis process was to establish the context diagram for 2GCHAS technology. The context diagram shown in Figure 7 defines the basic output required of the technology complex of the
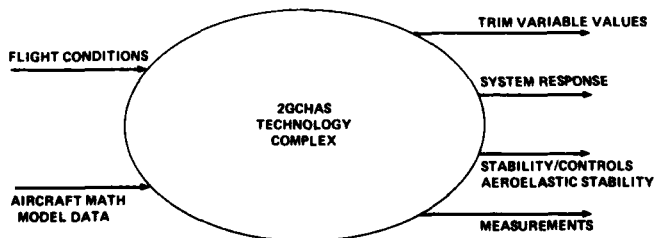

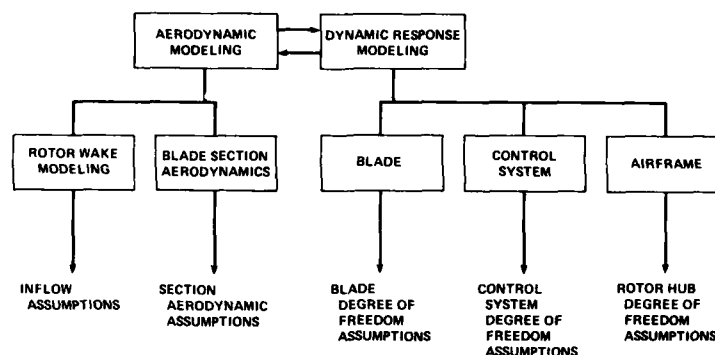Figure 7.   Technology Complex Context Diagram.

Figure 8. Basic Elements of Rotor Loads Problem.

System as well as the input in general terms. The input/output data flows and the processes are decomposed in further incremental refinements of the problem. It is recognized that the fundamental approach to the structural dynamics-aerodynamics interface, presented in Reference 22 and shown in Figure 8, has changed little. The approach used is to iterate between solving for the structural dynamic response and solving for the aerodynamic response. The basic problem is conceived of as a nonlinear structural dynamics problem which has an aerodynamic load contribution which is a function of the structural dynamic response. Thus, the general system set of equations of motion has the form

$$M(x,t)\ddot{x} + C(x,t)\dot{x} + K(x,t)x = F(x,\dot{x},u,t) \qquad (1)$$

which includes both structural dynamic and aerodynamic terms. Here x is the set of system degree of freedom, t is the independent time variable, and u is a set of free parameters which must be prescribed or determined from a set of System constraints. The dots indicate derivatves with respect to time.

There are number of solutions to Eq. (1) which are of interest to the helicopter analyst. They include determining the system steady state response (trim); integrating the nonlinear equations in time for prescribed values of u (transient response); and perturbing the equations about a steady state solution to develop perturbation equations which may be be solved to determine system stability. The decomposition of the context diagram to accomplish these functions is shown in Figure 9. At this point in the analysis it is immaterial what mathematical process is used to accomplish these objectives; i.e., whether the equations are integrated in time directly or whether they transformed to a set harmonic equations and solved as a set of algebraic equations. It is important, however, to recognize that the problem has been separated into two parts: the mathematical solutions to the system equations, and the model building required to obtain the system equations. In Figure 9 only the former part is exposed and further decompositions are needed to reveal the model building processes.

The dynamic response of the system, i.e., the displacements, x, velocity, $\dot{x}$, and accelerations, $\ddot{x}$, as well as the aerodynamic response are not often in a form directly usable by the engineering analyst or designer. The processing of this data to the particular form the engineer desires is referred to as obtaining the response characteristics of the system modeled. For example, the trim response characteristic can include: trim variable values, u, performance, vibrations, loads, and acoustics. Transient response characteristics would encompass these as well as frequency spectra analysis of the resulting dynamic response or loads. Stability measurements would include: frequency, damping and time constant parameters obtained from eigenvalue reduction; amplitude/frequency functions (used in Bode plots); eigenvector analysis; and linear transient response.
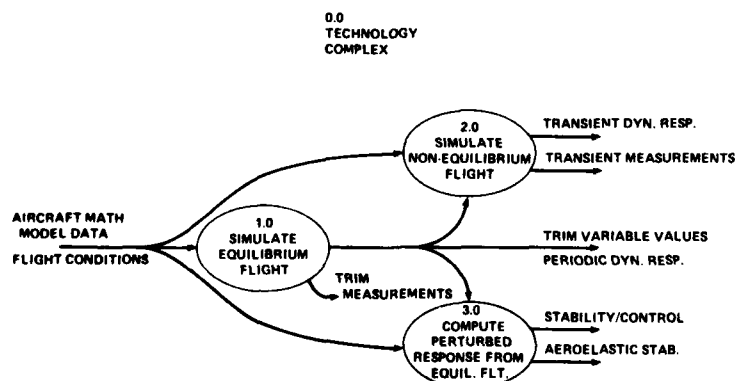

Figure 9. Decomposition of Context Diagram.

The complete analysis of the Technology Complex for the 2GCHAS System is too detailed to present in this paper. However, a further discussion of the trim process will be pursued further. Each analysis Data Flow Diagram (DFD) requires a process definition statement to define what functions the process must perform. For example, the trim process is decomposed into iterate-to-trim and fly-to-trim. The mathematical representation of iterate-to-trim in the mini-spec may be presented as follows. Transform Eq. (1) to a first order system such that

$$A(y,t)\dot{y} = f(y,u,t) \qquad (2)$$

where

$$y = \begin{Bmatrix} x \\ \vdots \\ \dot{x} \end{Bmatrix}$$

The ordinary differential equations, Eq. (2), have more unknowns, y and u, than equations. Additional equations are obtained from time-averaged response. Constraints over the period, T, are shown in Eq. (3).

$$\int_{o}^{T} g(y,\dot{y},u,t)dt \lesssim \varepsilon_2 \qquad (3)$$

Also, the system must be constrained such that over the period, T, to assure periodicity. The periodicity constraint is

$$y(o) - y(T) \lesssim \varepsilon_1 \qquad (4)$$

where ε_1, ε_2 are suitably small values to assure convergence. Here Eq. (3) is generally interpreted as the sum of the forces and moments for unaccelerated flight at the system center of gravity. Other constraints such as those involving rotor power, or blade moment balance may also be included in Eq. (3). Thus, the problem now becomes one of solving the transient response Eq. (2) over a period, T, with u and the initial conditions, y(o), estimated and then solving the set of nonlinear algebraic Eq. (3) and (4), to obtain a new set of values for u and initial conditions, y(o). The iteration continues until Eq. (3) and (4) are satisfied with reasonable limits.

Thus far, the discussion involves the mathematical solution of a set of equations and is not restricted to helicopters per se. However, it is necessary to simulate the helicopter with the mathematical model of the helicopter components. Thus, obtaining the nonlinear Eq. (1) and the constraints, Eq. (3) and (4), requires three basic steps as indicated in Figure 10: building second order equations of motion; reducing system degrees of freedom to element degrees of freedom; and coupling (and transforming) second order differential equations. In linear systems, the second step is not required.

The concept used in building the system equations of motion is a tree structure as shown in Figure 11. Any juncture (node) of the tree may have an arbitrary number of branches. The tree is not conceptually limited by either the number of levels (substructures) or by the number of branches at a node. The equation of motion at the lowest level (node) are obtained from either an internal finite element library,
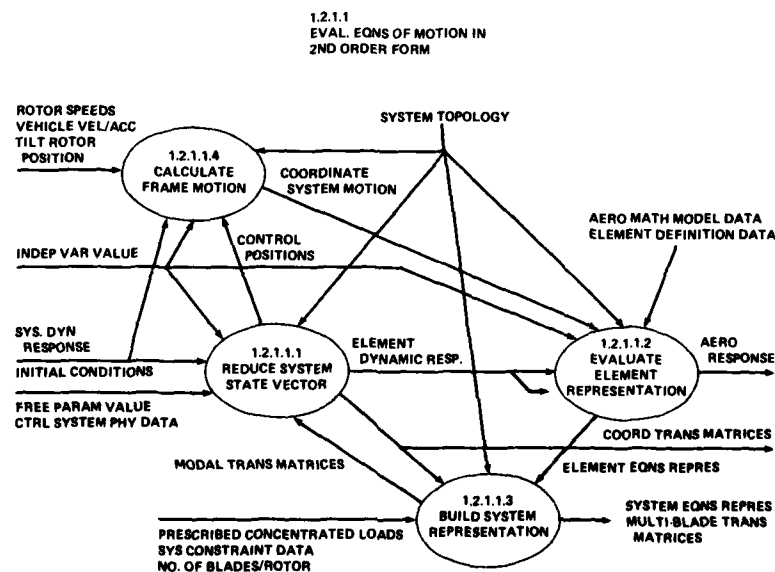

Figure 10. Data Flow Diagram for Evaluating Equations in Second Order Form.
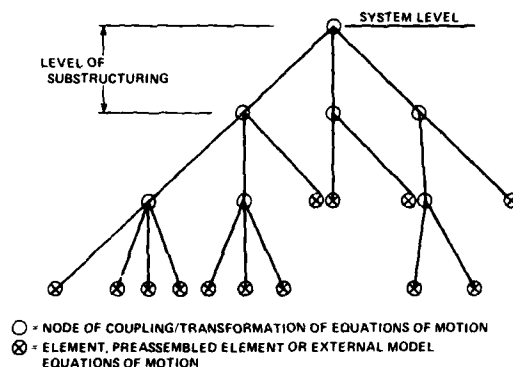
O = NODE OF COUPLING/TRANSFORMATION OF EQUATIONS OF MOTION
⊗ = ELEMENT, PREASSEMBLED ELEMENT OR EXTERNAL MODEL
EQUATIONS OF MOTION

Figure 11. Tree Structure for Building Equations of Motion.

preassembled "element" models, transfer functions, or external model interfaced with the System. The finite element library will include basic one-dimensional elements such as rods and beams, as well as rigid mass-damper-stiffness elements. Preassembled elements to represent subsystems such as rotor systems, control systems, or vibration control devices will also be developed for the element library. A sophisticated nonlinear beam element (Reference 23), for application to blades is also included. The structural element definition will include inertial and dynamic nonlinearities. The general transfer function capability similar to that in NASTRAN (Reference 24), and other codes (Reference 25), will be included. Also, some of the equation building/modeling features similar to those available in the IBM Continuous System Model Program (CSMP) will be included.

At each node of the tree in Figure 11, the user will be able to prescribe the coupling of the branches and to specify transformation of the resulting equations of motion. The transformations which must be available are: transformation from rotating to fixed degrees of freedom, multiblade coordinates (MBC); transformation from physical to modal degrees of freedom; and condensation of equations. Thus, the element definition, coupling, and transformations are based on well-known concepts used in finite element programs. However, the approach used in the System makes some improvements over previous approaches. These improvements are: remove restrictions on the depth or width of the tree structure (multilevel substructuring); for a nonlinear beam elements, allow the user to define the order of the shape function and, therefore, derive the mass, damping stiffness terms internally; and allow multiple transformations at any node (MBC, Modal, condensation). For nonlinear behavior, the element mass, stiffness, damping and forcing terms will be functions of the element response, $x_e, \dot{x}_e, \ddot{x}_e$. Thus, the system variable values $(x, \dot{x}, \ddot{x})$ must be reduced to element variable values $(x_e, \dot{x}_e, \ddot{x}_e)$ by using the inverse of the transformations and couplings used to obtain the system equations of motion. Therefore, in traversing down the tree in Figure 11, the system response is reduced to element response whereas in traversing up the tree the element equations of motions are coupled to obtain the coupled system equations.

To fully define the element equations of motion an aerodynamic generalized force for the element must be included. This is accomplished by calculating the aerodynamic response of the complete aircraft model. The aerodynamic response is defined as both the flow field velocities and the resulting aerodynamic load distribution over the aerosurfaces. The concept for aerodynamics used in 2GCHAS is to provide for different grids to be used for dynamic and aerodynamic response calculations, to couple aerosurfaces as desired, and to allow different levels of sophistication in modeling the flow field for each component. In order to allow for different dynamic and aerodynamic grids the problem is separated into dynamic and aerodynamic problems with the interface indicated in Figure 8. Coupled aerosurfaces with differing levels of modeling sophistication is illustrated in the DFD shown in Figure 12. This figure shows that the
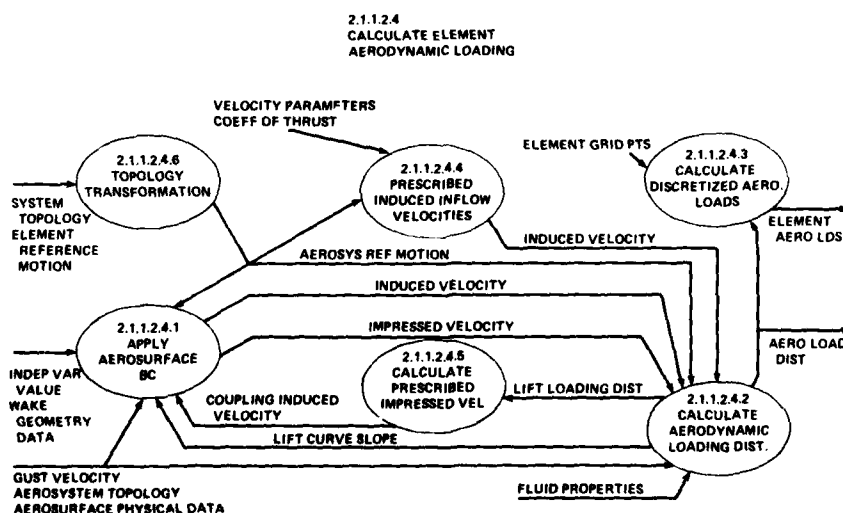

Figure 12. DFD for Aerodynamic Element Loads.

2.1.1.2.4.1
APPLY AEROSURFACE
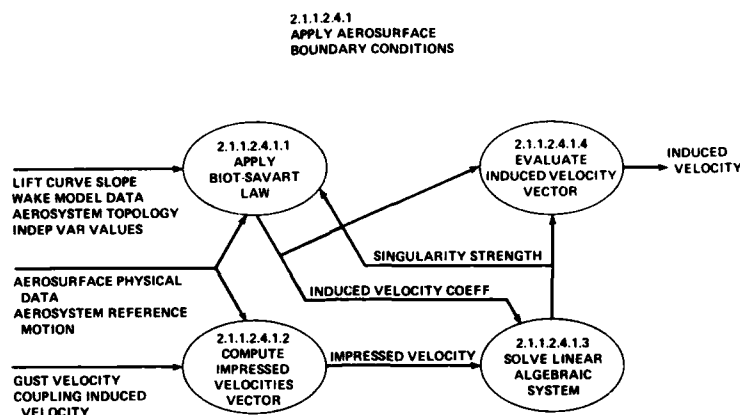BOUNDARY CONDITIONS

Figure 13. DFD for Aerosurface Boundary Condition Decomposition.

induced velocity field may be either prescribed or calculated for a component. If it is calculated, the strength of the singularities are estimated by an application of the Biot-Savart law as shown in Figure 13. The wake geometry for the Biot-Savart law application may be either rigid, empirical, semi-empirical or corrected iteratively to approximate a relaxed (free) wake.

The aerodynamic loading distributions may be obtained using either lifting line or lifting surface approaches. Typical aerodynamic singularity strength calcuations for a component are characterized by an equation of the form

$$\Gamma = ac(\dot{x} + v_i \cos \alpha + v_G + \sin \alpha \, v_F) \qquad (5)$$

where

$\dot{x}$ = plunging velocity
v_G = gust velocity
v_i = induced velocity
v_F = vehicle flight velocity
a = $dC_L/d\alpha$, lift curve slope
α = angle of attack
c = chord

The Kutta-Joukowsky relation is

$$v_i = \sigma_i \Gamma \qquad (6)$$

By substituting Eq. (6) into Eq. (5), a general expression for the calculating Γ has the form

$$\Gamma_i + \sum_j \sigma_{ij}(\alpha)\Gamma_j = b_i \qquad (7)$$

where

Γ_i = strength of the singularities along the blade and over the azimuth j, stations, i
σ_{ij} = coefficients as a function lift curve slope
b_i = impressed velocity; sum of vehicle, rotational, gust and component response velocities

Equation 7 can be extended to couple the effects of velocities induced by all other aerosurfaces. The equation would then have the form

$$\Gamma_i^m \sum_{k=1}^{n} A_{mk}^{ii} = b_i^m - \sum_{j \neq i} A_{kk}^{ij} \Gamma_j^m - \sum_{k \neq m} \sum_{j \neq i} A_{mk}^{ij} \Gamma_j^m \qquad (8)$$

where

$A_{ij} = \delta_{ij} - \sigma_{ij}$
m,k = are aerosurface indices
i,j = are component aerodynamic grid indices

The terms with $m \neq k$ account for the aerosurface component coupling. In aerodynamic coupling the coefficients, A, are explicitly derived whereas in kinematic coupling the degrees-of-freedom, x, are explicitly related. The aerodynamic coupling, therefore, is a tree structure only one level deep, but with no conceptual restriction on the width (i.e., the number of aerosurfaces). A matrix representation of the aerodynamic formulation of Eq. (8) is illustrated by Eq. (9).

$$
\begin{bmatrix}
A_{11} & 0 & 0 & 0 & 0 \\
A_{21} & A_{22} & A_{23} & A_{24} & A_{25} \\
A_{31} & A_{32} & A_{33} & A_{34} & A_{35} \\
A_{41} & A_{42} & A_{43} & A_{44} & A_{45} \\
A_{51} & A_{52} & A_{53} & A_{54} & A_{55}
\end{bmatrix}
\begin{Bmatrix}
\Gamma_1 \\ \Gamma_2 \\ \Gamma_3 \\ \Gamma_4 \\ \Gamma_5
\end{Bmatrix}
=
\begin{Bmatrix}
b_1 \\ b_2 \\ b_3 \\ b_4 \\ b_5
\end{Bmatrix}
\tag{9}
$$

Here, the first row represents the components with prescribed induced velocity, v_i. These equations uncouple from the components for which the induced velocity is to be calculated. The population of first column, A_{j1}, indicates the prescribed induced velocities may affect the components $j > 1$. However, flow from these components will not affect component 1 since A_{1j} is zero for $j > 1$. After uncoupling the equations the following systems of equations are to be solved

$$
A_{11} \, \Gamma_1 = b_1 \tag{10}
$$

$$
\begin{bmatrix}
A_{22} & A_{23} & A_{24} & A_{25} \\
A_{32} & A_{33} & A_{34} & A_{35} \\
A_{42} & A_{43} & A_{44} & A_{45} \\
A_{52} & A_{53} & A_{54} & A_{55}
\end{bmatrix}
\begin{Bmatrix}
\Gamma_2 \\ \Gamma_3 \\ \Gamma_4 \\ \Gamma_5
\end{Bmatrix}
=
\begin{Bmatrix}
b_2 \\ b_3 \\ b_4 \\ b_5
\end{Bmatrix}
-
\begin{Bmatrix}
A_{21} \, \Gamma_1 \\ A_{31} \, \Gamma_1 \\ A_{41} \, \Gamma_1 \\ A_{51} \, \Gamma_1
\end{Bmatrix}
\tag{11}
$$

In the illustration of this five component model, any of components two through five may be represented by either lifting line or lifting surface theory. Indeed, there is nothing conceptually different between panel methods and lifting surface theory, and, therefore, by implication panel methods are included as well.

In Eq. (8) and (9) the coupled strengths can be calculated simultaneously for the components. It is realized that this approach may be impractical for certain configurations and that further research is needed to fully develop a single, unified approach to rotorcraft aerodynamics modeling. For example, a problem, which remains somewhat intractable for 2GCHAS is the multiple rotor problem where the rotor diameters are of different size. Typical tail rotor may be turning three times as fast as the main rotor. Therefore, if a 15° azimuth grid is suitable for the main rotor wake geometry, a corresponding 45° grid for the tail rotor will be too crude. A scheme for integrating in different time domains remains an obvious challenge to this approach. Since Eq. (9) can always be solved iteratively as well as simultaneously, however, the thrust of this 2GCHAS formulation will proceed and even with some initial shortcomings should significantly advance the state-of-the-art in rotorcraft aerodynamics analysis.

5. LOADS PREDICTION

The prediction of the loads and performance characteristics from the structural dynamic and aerodynamic responses is a prime concern to the rotorcraft designer. Traditionally, rotorcraft analyses have taken advantage of the rotor blade force-free boundary condition at the tip and integrated the aerodynamic distribution along the blade to find the root loads and time-averaged rotor loads (Reference 8). The load calculations have been based on integrating the aerodynamic load distributions directly. General finite element codes usually calculate loads from displacements (Reference 24); that is, they determine the strains and curvatures from finite-difference representations of the displacements and then use stress-strain laws to determine the resultant loads. In Reference 26, these two methods were compared for application to rotor blades. The displacement method was found easier to implement, whereas the force integration method was found to be more accurate. The accuracy problem was illustrated for cases where concentrated loads were applied and where blade elastic properties had abrupt changes. The basic method for predicting overall vehicle loads proposed for 2GCHAS is the more general displacement method. However, in most rotorcraft analysis disciplines it is necessary to predict the rotor loads accurately. Therefore, the System will include the option for blade/rotor loads to be calculated by the force integration method. This is indicated in the DFD in Figure 14.
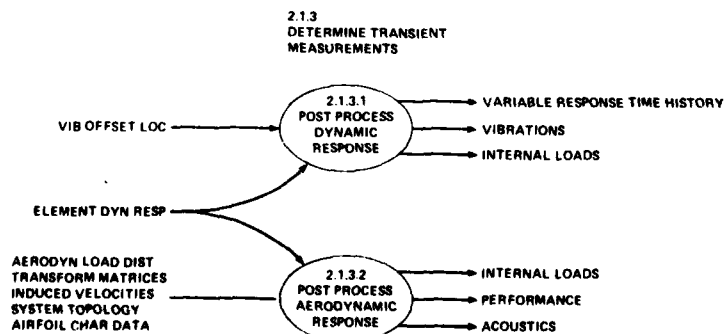
Figure 14. DFD for Measurements Decomposition.

6. ARCHITECTURAL DESIGN OF THE 2GCHAS TECHNOLOGY COMPLEX

The next step in the methodology is to convert the DFD network into structure charts. The initial implementation of the structure charts is mechanical. However, in order to optimize the system structure the designer is concerned with module communication (coupling) and minimizing duplication of functions (cohesion). This leads the system designer to employ two major metrics in the design process: low coupling, and high cohesion. In using these metrics as well as other secondary metrics in structured design methodology, the design process has yielded the structure shown in Figure 15. In the strict sense, this figure is not a structure chart since the intermodule communications (data in and data out) are omitted to simplify the presentation in this paper. These charts do reveal, however, the emerging shape and hierarchy of the Technology Complex of the 2GCHAS System. A study of the structure shows that the upper portions of the hierarchy are mathematically oriented rather than helicopter specific. The lower

Figure 15. Structure Chart for the Architectural Design of Technology Complex.

Figure 16. Control Model Overview of Architectural Design.

levels of the hierarchy, however, become increasingly helicopter specific. These levels deal with accepting the physical data and building the system equations of motion. The upper hierarchy deals with solving constrained equations (trim or steady state); integrating initial value problems (transient response); or perturbing, linearizing and solving stability equations.

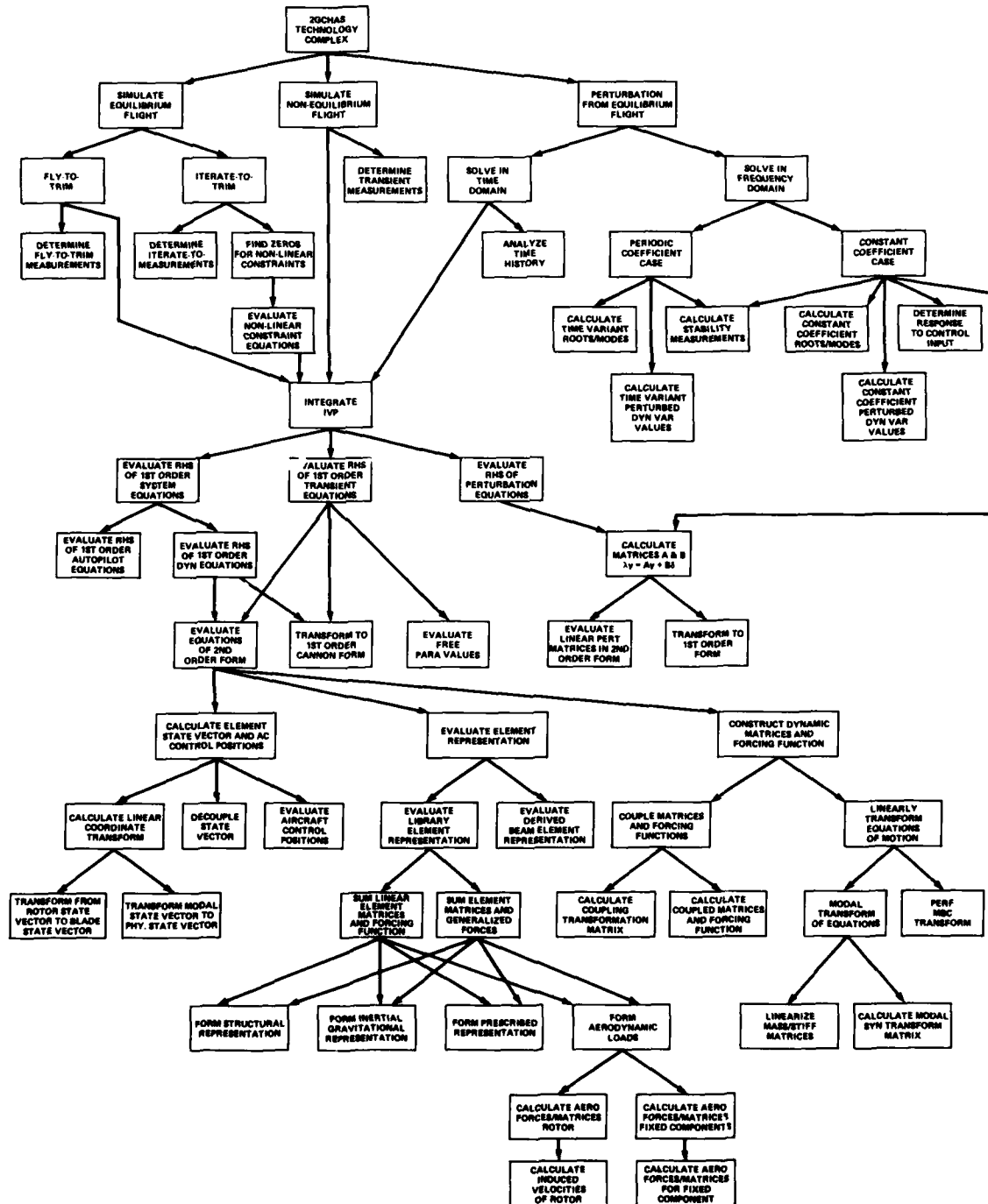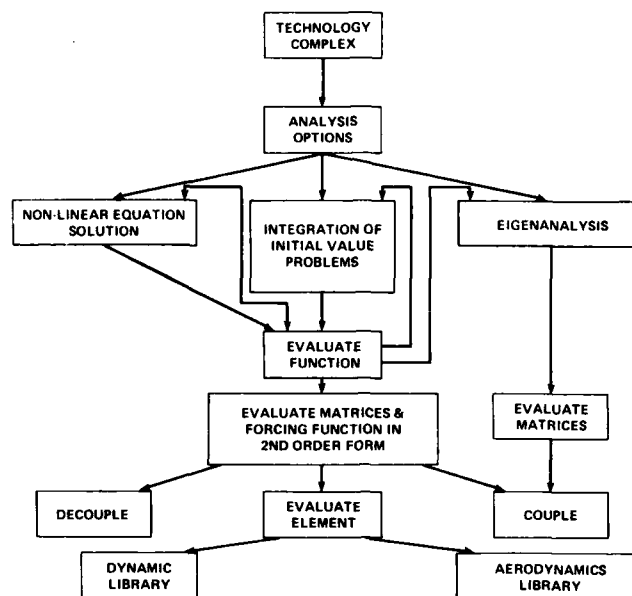This structure is further illustrated in the condensed control model diagram in Figure 16. This diagram is part flowchart and part structure chart and is developed to emphasize the mathematical processes in the upper hierarchy and the helicopter modeling and equation building functions of the lower hierarchy. The control aspects illustrated by the flowcharting indicates the temporal order in which the functions are used. This condensed figure as well as Figure 15 illustrates the modifiability of the system. The mathematical modifiability of the upper portion can occur any point above the "EVALUATE FUNCTION" level either by modifying the control logic of a particular algorithm or by implementing a new solution technique; for example, using an Adams-Basforth integration scheme instead of a Runge-Kutta scheme. The model building modification can occur most directly through the library modules. New coupling/transformation schemes may be added as they are developed. The flexibility built into the design is very general and improvements are expected to the be primarily in additions to the structural dynamic and aerodynamic libraries.

7. CONCLUSIONS

The Second Generation Comprehensive Helicopter Analysis System is being developed to provide an extensive, integrated, interdisciplinary rotorcraft analysis capability. Modern software development and product assurance techniques are being used in order to insure the correctness of the implementation of the analysis technology in the System. The technology included in the System, in most cases, is not unique to the System, but the ability to couple a wide range of analysis technology in a single software entity will provide the analyst with a significantly advanced analysis tool. The development methodology which leads to a highly structured product will allow for straight-forward extension of system analysis capabilities in any individual technology area.

Products of structured analysis and architectural design of the System presented show the basic capabilities which will allow prediction of rotorcraft loads with the 2GCHAS. The design has revealed a concept which is finite-element based for modeling rotorcraft. The system equations of motions result from a tree-structure concept which is not limited conceptually to the number of elements or the number of substructures. The aerodynamic response is calculated from a single level of coupled flow field representations. The aerodynamic components may be modeled using prescribed inflow, lifting line or lifting surface (panel) methods. Corrections for unsteady behavior can be included. The loads at any point may be recovered using a displacement method. In addition, for the rotor system, loads may be calculated using a force integration scheme. The flexibility to model various aspects of the problem at different levels of sophistication and to extend individual elements of the analysis easily with verified and validated, high-quality code will provide a valuable tool for the improvement of rotorcraft loads prediction technology.

8. REFERENCES

1. Van Gaasbeck, James R.: Rotorcraft Flight Simulation Computer Program C-81 With DATAMAP Interface, Vol. I - User's Manual, USAAVRADCOM-TR-80-D-38A, October 1981.

2. Reaser, J.S.; and Kretsinger: REXOR II Rotorcraft Simulation Model Vol. I - Engineering Documentation, NASA CR 145331, June 1978.

3. Sopher, R. and Howlett, J.: Normal Modes and GENHEL Description, Workshop on Unified Equations for Rotorcraft Systems Modeling Sponsored by Aeromechanics Laboratory, US Army Research and Technology Laboratories, (AVRADCOM), NASA Ames Research Center, Moffett Field, CA., February, 1979.

4. Arcidiacono, Peter, J.: Prediction of Rotor Instability at High Forward Speed, USAAVLABS TR-68-18A, February, 1969.

5. Bielawa, Richard L.: Aeroelastic Analysis for Helicopter Rotor Blades With Time Variable Nonlinear Structural Twist and Multiple Structural Redundacy - Mathematical Derivation and Program User's Manual, NASA CR 2638, October 1976.

6. Gabel, Richard: Current Loads Technology for Helicopter Rotors, Specialists' Meeting on Helicopter Rotor Loads Prediction Methods, AGARD Conference Proceeding No 122, Milan, Italy, March 1973.

7. Banerjee, D., and Johnston, R.A.: Integrated Technology Rotor Methodology Assessment, Proposed NASA CR.

8. Johnson, Wayne: A Comprehensive Analtical Model of Rotorcraft Aerodynamics and Dynamics, Part 1: Analysis Development, NASA-TM-81182, USAAVRADCOM, TR 80-A-5, June 1980.

9. Sopher, Robert; Studwell, R.E.; Cassarino, S.; and Kottapalli, S.: Coupled Rotor/Body Vibration Analysis, Proposed NASA CR.

10. Berman, Alex: A Generalized Coupling Technique for the Dynamic Analysis of Structural Systems, AIAA/ASME/ASCE/AHS 20th Structures, Structural Dynamics and Materials Conference, St. Louis, MO., April 4-6, 1979.

11. Kerr, Andrew W., and Davis, John M.: A System for Interdisciplinary Analysis -A Key to Improved Rotorcraft Design, Presented at the 35th Annual National Forum of the AHS, paper No. 79-8, Washington, D.C., May 1979.

12. Ormiston, R.A.: Comparison of Several Methods for Predicting Loads on a Hypothetical Helicopter Rotor; Conference on Rotorcraft Dynamics, NASA SP-352, Ames Research Center, Moffett Field, California, February 13-15, 1974.

13. Schrage, Daniel P.: An Overview of Technical Problems in Helicopter Rotor Loads Prediction Methods, AIAA Paper No. 79-0816, presented at the 20th AIAA/ASME/AHS SDM Conference, St. Louis, MO., April 1979.

14. Johnson, Wayne: Comprehensive Helicopter Analysis - A State of the Art Review, NASA TM - 78539, Nov. 1978.

15. Kerr, Andrew W., Potthast, A.J., and Anderson, W.D.: An Interdisciplinary Approach to Integrated Rotor/Body Mathematical Modeling, AHS Symposium on the Status of Testing and Modeling for V/STOL Aircraft, Philadelphia, PA., October, 1972.

16. Predesign of the Second Generation Comprehensive Helicopter Analysis System; Computer Sciences Corporation, USARTL-TR-78-41, October 1978.

17. Predesign of the Second Generation Comprehensive Helicopter Analysis System; Control Data Corporation, USARTL-TR-78-43, October 1978.

18. Predesign of the Second Generation Comprehensive Helicopter Analysis System; Science Applications, Inc., USARTL-TR-78-42, October 1978.

19. Yourdon, Edward and Constantine, Larry L.: Structured Design, 2nd edition, Yourdon Press, New York, N.Y., 1979.

20. DeMacro, Tom: Structured Analysis and Systems Specification, Yourdon Press, New York, N.Y., 1978.

21. Bersoff, Henderson, and Siegel: Software Configuration Management, Prentice Hall, 1980.

22. Arcidiocono, Peter J., and Calson, Raymond G.: Helicopter Loads Prediciton, Specialist Meeting on Helicopter Rotor Loads Prediction Methods, AGARD-DP-122, Milan, Italy, 1973.

23. Hodges, Dewey: A Small-Strain, Large-Rotation Beam Theory for Helicopter Rotor Blades, to be published.

24. MacNeal, Richard H., editor, The NASTRAN Theorectical Manual (Level 15.5), MacNeal-Schwendler Corp., December 1972.

25. Perry III, B., Knoll, R.I., Miller, R.D., and Goetz, R.C.: Capabilities and Applications of a Computer Program System for Dynamic Loads Analyses of Flexible Airplanes With Active Controls (DYLOFLEX), AIAA/ASME/ASCE/AHS 20th Structures, Structured Dynamics and Materials Conference, St. Louis, MO., April 4-6, 1979.

26. Bielawa, Richard L.: Blade Stress Calculation - Mode Deflection vs. Force Integration, Journal of the American Helicopter Society, July 1978.

COMMENTS ON SESSION III

ROTOR AIRLOAD PREDICTION PROGRAMS

by

I. C. Cheeseman
Southampton University
Southampton S09 5NH - Hants
United Kingdom

The five papers presented fall into four categories. That by Arcidiacono and Sopher is a review of programs in use and projected in the USA and is a valuable state-of-the-art exposition. The papers by Russo and Ceriotti and by Kerr and Stephens describe programs which are at an advanced stage of construction but, at the time of writing, have not been tested. Costes' paper deals with a program which has had the aerodynamic forces prediction method improved and it reports on a comparison of the theory with experiment, while Young's paper is attempting to produce a simple model of the rotor downwash which gives a reasonable prediction of rotor loads and it also includes useful comparisons of the theory with experiment. This paper is an excellent example of the evolution of a method of prediction by improving various details in a systematic way as disagreement with experiment is found.

Behind all the papers' theme is the theme of cost effectiveness of the exercise which can be measured in terms of the accuracy of the prediction relative to the computing cost. There must therefore be a requirement for a number of models ranging from the simple, which can be used extensively in initial project assessment, to the most sophisticated required for final design. A question which is raised by the presentation is whether there should be one large program which can be run at various levels from the very simple to the most complex, or a series of programs - the arguments in favour of each course of action must vary with the intended users and the facilities available.

In improving blade load prediction, Arcidiacono and Sopher reported the Ormiston recommendations of 1974 which were:-

(1) to compare the available methods on a trading basis,

(2) assess the validity of assumptions and semi-empirical factors used,

(3) conduct fundamental research on dynamic stall, blade/vortex interactions
     and three-dimensional flow effects,

and (4) correlate the methods with data from a well-instrumented windtunnel test
          of a large rotor,

and commented that for the United States work, item (3) had received most attention.

If one regards the three papers from Europe as representing the development here, then that conclusion would appear to be equally true.

What conclusions can be drawn from the work presented on aerodynamics? There are results quoted by Costes, Young and from Jepson, Moffitt and Hilzinger by Arcidiacono and Sopher which give the flatwise bending moments at about $r/R = 0.75$ for $\mu = 0.3$ (Costes actually gives section loads). Jepson et al show the rotor alone loads prediction and measurement indicating only moderate agreement over the whole azimuth and showing improved agreement when fuselage effects are included. The greatest discrepancies occur from $\psi = 330°$ to $170°$. Young compares predictions with flight measurements and his work suggests that discrepancies are significant between $\psi \approx 330°$ to $90°$. The similarity of the errors is at first surprising in view of the different basic flow models but it does expose the region of the rotor where many flow models are inadequate. In the Costes paper two interesting results are presented in figures 12 and 13. In the first case, the motion of the blade is taken to be that measured and the aerodynamic loads calculated using unsteady blade section data, while in the second figure the blade was allowed to find its own equilibrium under the action of the calculated aerodynamic forces. In both cases the calculated aerodynamic loads were compared with measured results. In the case where the actual blade motion was used, the predicted and measured loads were reasonable for $0 < \psi < 180$ and $r/R < 0.855$ but overestimated the answer for $180 < \psi < 360$. The use of the unsteady aerodynamic data markedly improved the agreement in the region $180 < \psi < 360$. At $r/R = 0.952$ the agreement was generally poorer and the different aerodynamic models gave roughly the same answer. This underlines the correct emphasis which has been given to modelling flow at the tip of the blade. When the motion of the blade was calculated the agreement with experiment is less good over the whole of the azimuth. It will be noted that for $0 < \psi < 180$ the estimate of the loads is higher than the experimental results whereas for $180 < \psi < 360$ the calculated values sometimes exceed and at other times underestimate the measured values. Thus, the resultant bending moment in the region $180 < \psi < 360$ has a better chance to be correct than over $0 < \psi < 180$. This makes it likely that the bending moment conclusion for Costes' rotor would be the same as noted above for the US and UK results. If this is the correct

interpretation of the results from these three reports, then the implication is that the aerodynamic refinement is in advance of the structural modelling. This conclusion must, of course, be related to the structural model used and Costes has used a simple model appropriate to the experimental rotor tested. This is a conclusion which is at variance with that suggested by Arcidiacono and Sopher who say in their conclusion that "good progress has been made on the structural side of the problem and new, more accurate and more versatile structural formulations are being rapidly introduced ..." This statement is supported in the text by references to a range of programs developed by the various US manufacturers and the Government laboratories. However, while some representations, like multiple load paths, have now been achieved, the paper records that there are still important items - like transient response - which cannot currently be handled. It is therefore open to question as to whether the structural or aerodynamic representation is the more advanced. The development of the finite element approach is welcomed and clearly has considerable development potential.

In that situation, one turns to examine the remaining two papers, by Kerr and Stephens and by Russo and Ceriotti. Both of these papers describe general programs into which individual techniques to simulate structural and aerodynamic functions can be inserted as they are developed. Their objectives are the same - namely to have a program which given the physical characteristics of the helicopter or part of the helicopter, will formulate the equations of motion and forcing functions and produce the relevent solutions. While generally supporting such an approach, the dangers must be clearly underlined. Computer programs are of tremendous power to the composer but may be a two-edged sword to the third party user. This is because the limitations of the program in terms of the original design may not be appreciated by the user and the programmer may have failed to consider all the cases which may be tried. With the reservations on the aerodynamics and structural reservations which exist, the case for the very courageous and ambitious approach of Kerr requires more justification than could be given in the presentation. The paper by Russo and Ceriotti with its more limited objective - namely, a finite element structural approach initially accompanied with simple aerodynamics (which can and certainly will have to be improved) - is perhaps more useful if it can achieve the universal acceptance which Kerr rightly seeks. I would feel much happier when using these more elaborate calculations if the program automatically simplified the question to something which could readily be physically comprehended and then gave an answer which would be a yardstick against which to judge the final answer of the program. This may be what is implied by the feedback loops in figure 2 of Kerr and Stephens' paper if it is made a requirement by the user but that is not the impression left by the text.

Now consider what steps should be taken for the future. It seems important that the real state of the current loads prediction programs should be determined as a matter of urgency. It is normal for all established programs to correlate with experiment. However, the experiments which are usually used are the ones which have been analysed to provide the inputs to the aero-dynamic and/or structural models. Agreement may not therefore be as significant as might at first be thought.

Therefore the programs available at the time should be judged against an agreed set of experimental data. This implies that a set of definitive tests have to be conducted, preferably both in a wind tunnel and in flight, in order to cover the whole speed range. It will probably be necessary to use both an articulated and a semi-rigid rotor to cover the various areas which are known to be important. If predictions in advance of the tests are made by the protagonists of each program, then the prediction capacity will be demonstrated. Subsequently, if experimental data, like blade motion, is made available to each predictor it should be possible to ascertain the areas of strength and weakness of the various parts of each modelling and this will cover the other points made by Ormiston which have not been already examined. It is appreciated that such a programme will be expensive and may involve disclosure of company confidential material. Kerr pointed out in the discussion that a great deal of data exists which has not been put in a form for general release. If a suitable selection of this information could be published and a series of trials of existing programs arranged, this would highlight general deficiencies in knowledge plus particular weaknesses in individual programs. The value of an exercise like that of Kerr and Stephens could then be assessed. Maybe an AGARD working party could oversee the production of the agreed data and the trials.

METHODES DE CALCUL DES CHARGES SUR ROTOR
UTILISEES A L'AEROSPATIALE ET RECOUPEMENTS
EXPERIMENTAUX

par
B. MASURE et A. VUILLET
Société Nationale Industrielle Aérospatiale
Marignane Cédex
13725
France

RESUME

Une connaissance relativement précise des charges statiques et alternées est nécessaire pour dimensionner au mieux et avec le maximum de sécurité les rotors d'hélicoptère . Le problème de la prédiction des contraintes dès le stade du dessin est complexe compte-tenu de l'environnement aérodynamique dans lequel fonctionnent les pales et des interactions aéroélastiques dues aux efforts et aux déformations importantes auxquels elles sont soumises. Au niveau des données, les caractéristiques aérodynamiques des profils et les propriétés des matériaux et des assemblages ne sont pas toujours connues avec la rigueur souhaitée.

Ce papier présente tout d'abord les méthodes de calcul employées à l'Aérospatiale pour estimer les charges statiques et dynamiques : méthode modale, méthode des azimuts, méthode simplifiée pour le calcul des charges statiques. Les hypothèses simplificatrices retenues, communes à ces trois méthodes, sont rappelées et les équations de base établies sous forme condensée. Les caractéristiques principales des trois méthodes sont décrites.

La qualité de ces méthodes prévisionnelles est ensuite analysée grâce à des recoupements avec des essais en vol sur la GAZELLE prototype 349 Z et sur le SUPER PUMA AS 332 : pour le premier appareil, la comparaison ne porte que sur les efforts dynamiques, pour le deuxième sur les efforts dynamiques et statiques. Les seuls vols envisagés sont des vols stabilisés avec ou sans facteur de charge. L'accord est en général satisfaisant mais certaines anomalies apparaissent quelquefois pour les efforts statiques en pied de pale ainsi que pour les moments de torsion. Pour ce dernier cas, la mauvaise qualité des recoupements doit être attribuée du fait que les phénomènes aérodynamiques instationnaires, non modélisés dans les applications numériques présentées dans ce papier, jouent un rôle non négligeable.

1. INTRODUCTION

Une connaissance relativement précise des charges statiques et alternées est nécessaire pour dimensionner au mieux et avec le maximum de sécurité les rotors d'hélicoptère.

Au stade de la prévision, ces charges peuvent être estimées au moyen de méthodes de calcul qui, tout en retenant un certain nombre d'hypothèses simplificatrices, requièrent néanmoins l'utilisation d'ordinateurs de grosse capacité.

Plusieurs méthodes sont utilisées à l'Aérospatiale pour estimer ces charges : méthode des azimuts, méthode modale, méthode simplifiée pour traiter le cas particulier des charges statiques. Ces méthodes vont être décrites brièvement en ne retenant que l'essentiel afin d'éviter au lecteur les développements mathématiques qui sont toujours très longs dans ce domaine et qui risquent de masquer l'essentiel.

Divers cas concrets sont ensuite traités : le calcul du champ des vitesses induites sur le rotor en vol d'avancement est commenté et présenté avec des comparaisons sur les coefficients de portance calculés et mesurés en soufflerie, qui montrent un bon accord dans le cas du vol stabilisé courant. L'application des diverses méthodes de calcul sera ensuite décrite pour deux hélicoptères : la GAZELLE 349 Z (prototype) et le SUPER PUMA AS 332 et les résultats obtenus seront comparés à des mesures effectuées en vol.

On constatera que les charges dynamiques et statiques sont à peu près correctement estimées en ce qui concerne les distributions des moments de battement et des moments de traînée mais que des progrès restent à faire en ce qui concerne les moments de torsion et les efforts dans les commandes qui en résultent. Ces comparaisons, effectuées dans le cas de vols stabilisés en translation, peuvent laisser penser que le problème de la prévision des charges est en partie résolu. Il ne faut pas oublier néanmoins que les situations critiques sont celles où l'hélicoptère évolue avec un facteur de charge élevé. Dans ce dernier cas, les méthodes prévisionnelles restent relativement correctes pour les charges statiques mais, pour l'évaluation des charges dynamiques, on a recours, pour l'instant, aux mesures en vol.

2. METHODES DE CALCUL UTILISEES A L'AEROSPATIALE POUR L'EVALUATION DES CHARGES SUR LES ROTORS

Deux méthodes principales sont utilisées à l'Aérospatiale pour évaluer les charges : la méthode modale et la méthode des azimuts. Ces deux méthodes ont en commun un certain nombre d'hypothèses simplificatrices qui, une fois retenues, conduisent à des équations de base où interviennent des dérivées par rapport à une seule variable d'espace (dérivées premières comme on le verra plus loin) et des dérivées temporelles première et seconde. Dans le cas du vol stationnaire, les termes d'excitation dynamique disparaissent ou sont très faibles. La méthode de calcul consiste alors d'une part à évaluer la déformée statique (indépendante du temps), d'autre part à analyser les petits mouvements possibles autour de cette déformée statique (modes «naturels» ou encore modes «propres» qui comportent en général un terme d'amortissement).

Dans le cas du vol d'avancement, des termes d'excitation apparaissent aux seconds membres des équations. Il est alors po ible, moyennant certaines hypothèses complémentaires, de considérer que la solution stationnaire (c'est-à-dire périodique et de pulsation égale à la vitesse angulaire Ω du rotor) est égale à la superposition d'un certain nombre de modes naturels (méthode modale). Il est aussi possible de traiter la question sans utiliser les modes propres en mettant en oeuvre une méthode d'intégration directe : la méthode des azimuts.

Nous allons tout d'abord rappeler brièvement les équations de base et les hypothèses simplificatrices, communes aux deux méthodes et décrirons ensuite les caractéristiques propres à chacune d'entre elles.

2.1. Hypothèses et équations de base

2.1.1. Décomposition d'un rotor en ses constituants

Les pales, le moyeu et les composants de la commande de pas sont considérés comme un ensemble de **pièces** en rotation : chacune de ces pièces est assimilée à une poutre hétérogène et est repérée, avant toute déformation, dans un référentiel qui lui est propre et qui prend en compte les précalages éventuels en position et orientation.

Pour chacune des pales, l'un des axes du référentiel est constitué par la ligne des centres des sections droites (en général ligne des 25 %). Le long de cette ligne sont données les caractéristiques géométriques, élastiques, dynamiques et aérodynamiques par unité de longueur.

Chacune des pièces constitutives du rotor peut être à son tour décomposée en divers **éléments** de longueur **finie** dont les extrémités constituent les noeuds de l'assemblage. En chacun de ces noeuds doivent être respectées un certain nombre de conditions aux limites qui traduisent la nature des liaisons entre les éléments successifs : encastrement, articulation, liaison souple avec ou sans amortissement et raideur. Le mouvement du centre du moyeu constitue une condition aux limites particulière.

2.1.2. Vecteur d'état à douze composantes et déformée de la pale

L'hypothèse de base associée à l'hypothèse «poutre» est qu'une section droite reste plane (pas de gauchissement) et non déformée (dans son plan).

La transformation géométrique, exprimée dans le référentiel initial propre à chacun des éléments avant toute déformation, est alors entièrement définie par la donnée :

— des 3 composantes u, v, w (vecteur $\vec{d}$) du déplacement du centre de chaque section

— des 3 angles de rotation $\theta_1, \theta_2, \theta_3$ (vecteur $\vec{\delta}$) du référentiel local lié à chacune des sections et qui est confondu, en l'absence de déformation, avec le référentiel initial.

La partie d'un élément située au-delà d'une section droite donnée, exerce sur la partie de l'élément située en-deçà de cette même section, un torseur de forces de liaison dont les éléments de réduction au centre de la section sont représentés par une force $\vec{T}$ (composantes T_1, T_2, T_3) et un moment $\vec{M}$ (composantes M_1, M_2, M_3). L'ensemble des 12 variables :

$$
\begin{array}{cccc}
u, v, w & \theta_1, \theta_2, \theta_3 & T_1, T_2, T_3 & M_1, M_2, M_3 \\
\longleftarrow \vec{d} \longrightarrow & \longleftarrow \vec{\delta} \longrightarrow & \longleftarrow \vec{T} \longrightarrow & \longleftarrow \vec{M} \longrightarrow
\end{array}
$$

constitue le vecteur d'état dont l'évolution, à un instant donné, le long de la ligne des centres définit la déformée totale à cet instant.

Les notations adoptées dans la suite du papier sont les suivantes :

$$
\text{déformation} \quad [D] = [[d], [\delta]] \quad \text{avec} \quad
\begin{cases}
[d] & \text{déplacement } (u, v, w) \\
[\delta] & \text{rotation} \quad (\theta_1, \theta_2, \theta_3)
\end{cases}
$$

$$
\text{effort} \quad [F] = [[T], [M]] \quad \text{avec} \quad
\begin{cases}
[T] & \text{force} \quad (T_1, T_2, T_3) \\
[M] & \text{moment} \quad (M_1, M_2, M_3)
\end{cases}
$$

$$
\text{vecteur d'état} \quad [X] = [[D], [F]] \qquad \text{12 composantes}
$$

2.1.3. Lois de l'élasticité appliquées aux forces de liaison

Si $[D]$ est la «déformation», à l'abscisse x, de la section droite d'un élément, la «déformation» de la section droite voisine d'abscisse $x + dx$ est :

$$
[D] + \frac{\partial}{\partial x}[D] \, dx \equiv [D] + [D]' \, dx
$$

où la notation $\left[\ \right]'$ représente la dérivée spatiale par rapport à la variable x . La déformation géométrique (élongation, cisaillement) de chacune des fibres élémentaires qui relient les points homologues de deux sections droites voisines est alors entièrement connue, grâce à l'hypothèse de non déformabilité des sections droites, à partir de $[D]$ et $[D]'$

A ces déformations géométriques élémentaires (élongation, cisaillement) correspondent des efforts de liaison élémentaires (effort normal, effort tranchant) que l'on calcule en appliquant les lois de l'élasticité linéaire et dont les éléments de réduction au centre de la section sont $[T]$, $[M]$. Les lois de l'élasticité peuvent donc être écrites sous la forme condensée :

$$\left[F\right] = f\left([D], [D]'\right) \qquad \text{ou encore sous la forme :}$$

$$\left[D\right]' = \emptyset\left([D], [F]\right) \tag{1}$$

2.1.4. Equilibre dynamique

Une tranche élémentaire d'épaisseur dx est soumise aux efforts suivants :
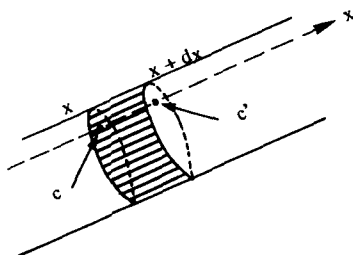
a) efforts de liaison au point C : $-\vec{T}$; $-\vec{M}$

b) efforts de liaison au point C' : $\vec{T} + \vec{T}'\,dx$; $\vec{M} + \vec{M}'\,dx$

c) forces d'inertie, y compris la gravité, dont les éléments de réduction au point C sont : $\vec{t_i}\,dx$; $\vec{m_i}\,dx$

d) efforts aérodynamiques dont les éléments de réduction au point C sont : $\vec{t_a}\,dx$; $\vec{m_a}\,dx$

L'équilibre dynamique de la tranche conduit aux deux relations :

$$\left.\begin{array}{l} \vec{T}'\,dx + (\vec{t_i} + \vec{t_a})\,dx = 0 \\[2mm] \vec{M}'\,dx + \vec{CC'} \wedge (\vec{T} + \vec{T}'\,dx) + (\vec{m_i} + \vec{m_a})\,dx = 0 \end{array}\right\} \tag{2}$$

Dans la deuxième relation, le terme $\vec{CC'} \wedge \vec{T}'\,dx$, du second ordre, peut être négligé.

Le calcul des efforts d'inertie $\vec{t_i}, \vec{m_i}$ nécessite d'évaluer l'accélération absolue $\vec{\gamma}$ de chacune des fibres élémentaires de la tranche infinitésimale considérée. Cette accélération peut s'exprimer au moyen de la «déformation» $[D]$ et de ses dérivées temporelles première et seconde $[\dot{D}]$ et $[\ddot{D}]$.

Les forces aérodynamiques qui s'exercent sur la peau externe de la tranche élémentaire sont calculées, pour les résultats présentés dans ce papier, en admettant une aérodynamique quasi-stationnaire et en utilisant les caractéristiques bidimensionnelles des profils mesurés en soufflerie (fichier de polaires). Quant à la vitesse induite, elle est calculée au moyen des formules semi-empiriques de Mejer Drees. Il est alors possible de calculer $\vec{t_a}$ et $\vec{m_a}$ en fonction de $[D]$ et $[\dot{D}]$.

En conséquence, les relations (2) peuvent être écrites sous la forme :

$$\left[F\right]' = \psi\left([D], [\dot{D}], [\ddot{D}], [F]\right) \tag{3}$$

2.1.5. Equations de base

Nous pouvons maintenant réunir les équations (1) et (3) sous une forme unique pour le vecteur d'état $\left[X\right]$ (nous rappelons que $[X] = \left[[D], [F]\right]$).

On obtient l'équation de base :

$$\left[X\right]' = G\left([X], [\dot{X}], [\ddot{X}]\right) \tag{4}$$

à laquelle il est nécessaire d'associer les conditions aux limites aux extrémités des différents éléments qui constituent l'assemblage étudié.

En appelant $\left[Y\right]$ la **réunion** des vecteurs d'état $\left[X\right]$ aux extrémités des éléments, l'ensemble des conditions aux limites peut être écrit au moyen de la relation condensée unique :

$$C\left([Y], [\dot{Y}]\right) = 0 \tag{5}$$

L'ensemble de (4) et (5) forme les équations de base. La formulation détaillée peut être établie en s'aidant de la référence [1] par exemple.

2.2. Résolution des équations de base

L'équation de base $[X]' = G \; (\; [X] \; , \; [\dot{X}] \; , \; [\ddot{X}] \;)$ associée aux conditions aux limites $C \; (\; [Y] \; , \; [\dot{Y}] \;) = 0$ forme un système d'équations non linéaires dont la résolution est conduite en deux étapes :

2.2.1. Déformée statique

On calcule tout d'abord la déformée statique qui, par définition, est indépendante du temps. Nous devons remarquer que cette déformée statique n'a de sens que si l'arbre d'entraînement du rotor est vertical et s'il n'y a aucun mouvement horizontal de la tête rotor. Les relations (4) et (5) prennent alors la forme :

$$\begin{cases} \left[X\right]' = G \; (\; [X] \; , \; [0] \; , \; [0] \;) & \text{(4bis)} \\[2ex] C \; (\; [Y] \; , \; [0] \;) = 0 & \text{(5bis)} \end{cases}$$

La résolution de (4bis) compte-tenu des conditions aux limites imposées par (5bis) est effectuée par une méthode d'intégration numérique pas à pas (méthode de Runge - Kutta par exemple) et nécessite des itérations successives car le choix des conditions initiales en début d'intégration n'est pas connu a priori.

Appelons X_0 la solution obtenue (état E_0). On a alors :

$$\begin{cases} \left[X_0\right]' = G \; (\; [X_0] \; , \; [0] \; , \; [0] \;) & \text{(4ter)} \\[2ex] C \; (\; [Y_0] \; , \; [0] \;) = 0 & \text{(5ter)} \end{cases}$$

2.2.2. Calcul des modes

On calcule ensuite les petits mouvements autour de la solution indépendante du temps, c'est-à-dire les mouvements «naturels» ou encore les modes propres. Ces petits mouvements autour de l'état statique $\left[X_0\right]$ sont obtenus par linéarisation des équations $[4]$ et $[5]$. Posons à cet effet :

$$\left[X_1 \; (x \, , t)\right] = \left[X_0 \; (x)\right] + \left[X \; (x \, , t)\right] \qquad \text{où } X \; (x \, , t) \text{ représente l'écart, considéré comme}$$

petit, entre le vecteur d'état *instantané* $X_1 \; (x \, , t)$ solution de (4) + (5) et le vecteur d'état statique $X_0 \; (x)$ solution de (4bis) + (5bis).

La linéarisation de (4) et (5) autour de l'état statique $\left[X_0\right]$ (état E_0) fournit les équations que vérifie $\left[X \; (x \, , t)\right]$:

$$\begin{cases} \left[X\right]' = [X] \; \alpha_0 \; + [\dot{X}] \; \beta_0 \; + [\ddot{X}] \; \gamma_0 & \text{(6)} \\[2ex] \left[Y\right] \; \lambda_0 \; + \; [\dot{Y}] \; \mu_0 = 0 & \text{(7)} \end{cases}$$

où $\alpha_0 \; , \; \beta_0 \, , \; \gamma_0 \, , \lambda_0 \, , \; \mu_0$ sont des matrices carrées qui ne dépendent que de x et qui sont associées à l'état statique E_0. Ces équations forment un système linéaire homogène. Appelons $[Z]$ la réunion de l'ensemble des vecteurs d'état des sections droites successives distantes de Δx. Alors, l'ensemble des équations (6) et (7) précédentes est équivalent à :

$$\left[\ddot{Z}\right] \; \Gamma_0 \; + \; \left[\dot{Z}\right] \; B_0 \; + \; \left[Z\right] \; A_0 = 0 \tag{8}$$

$\Gamma_0 \, , \; B_0 \, , A_0$ sont ici encore des matrices carrées qui, comme plus haut, sont liées à l'état statique E_0 mais qui ne dépendent plus de x. Leur dimension est d'autant plus élevée que le pas choisi Δx est plus petit.

La solution générale du système d'équations (8) est :

$$\left[Z\right] = \sum_j k_j \; e^{r_j t} \; \left[Z_j\right] \tag{9}$$

où chacune des solutions $e^{r_j t} \left[Z_j\right]$ vérifie l'équation :

$$\left[Z_j\right] \; (r_j^2 \; \Gamma_0 \; + r_j \; B_0 \; + A_0) = 0$$

Pour éviter la solution banale $\left[Z_j\right] = 0$, il est nécessaire que :

$$\text{Déterminant de } (r_j^2 \; \Gamma_0 \; + r_j \; B_0 \; + A_0) = 0 \tag{10}$$

C'est l'équation caractéristique.

Dans la solution générale donnée par (9) les diverses grandeurs ont les significations suivantes :

k_j constantes arbitraires

r_j racines de l'écuation caractéristique (10). Ce sont des nombres complexes qui s'écrivent

$r_j = \alpha_j \pm i\ \omega j$ où ω_j est la pulsation propre du mode j et où α_j est le facteur d'amortissement (si $\alpha_j < 0$) de ce même mode.

Les couples (α_j , ω_j) sont obtenus par une méthode itérative à deux variables du type Newton.

$\left[Z_j \right]$ définie à une constante multiplicative près représente la forme du mode associé à r_j .

Remarques :

1. Le calcul de α_j permet de déceler l'apparition éventuelle d'une instabilité linéaire d'un rotor en vol stationnaire.
2. La déformée $\left[X_j (x) \right]$ associée à une racine r_j de l'équation caractéristique (10) peut être calculée directement par intégration de (6) où l'on remplace $\left[\dot{X} \right]$ et $\left[\ddot{X} \right]$ par $r_j \left[X \right]$ et $r^2_j \left[X \right]$ respectivement.

Cette déformée est définie à un facteur multiplicatif près.

Le calcul des modes est très utilisé pour la définition élastique des pales et le positionnement relatif des fréquences propres : des applications ont été présentées en $\left[2 \right]$.

2.3. Méthode modale

La méthode modale est l'application de la méthode de variation des constantes pour les équations différentielles linéaires à coefficients constants. Elle peut être appliquée au cas du vol d'avancement dans la mesure où il est possible de définir un état statique moyen (donc indépendant de l'azimut $\psi = \Omega t$) autour duquel seront calculés, grâce à une combinaison appropriée des modes, les petits mouvements engendrés par les excitations provenant de l'aérodynamique et du pas cyclique. Nous admettons que les conditions d'applicabilité de cette méthode sont remplies. La méthode nécessite donc le calcul préliminaire de la suite des modes. Ceux-ci sont associés, par principe, à un vol vertical et un pas général donnés. Rappelons maintenant le principe de la méthode modale.

Soit $\left[X_o (x) \right]$ l'état statique moyen de référence, solution de (4bis) et (5bis) par hypothèse. Le vecteur d'état complémentaire $\left[X (x, t) \right]$ qui représente les petits mouvements possibles autour de l'état de référence vérifie une équation du même type que (6) mais où apparaît maintenant un terme complémentaire périodique $\left[f \right]$ provenant des excitations liées à l'aérodynamique et au pas cyclique et dont la pulsation fondamentale est celle du rotor. Cette équation est :

$$\frac{\partial}{\partial x} \left[X \right] = \left[X \right] \alpha_0 + \left[\dot{X} \right] \beta_0 + \left[\ddot{X} \right] \gamma_0 + \left[f \right] \qquad (11)$$

Elle doit être associée à nouveau à des conditions aux limites qui se traduisent par une équation du même type que (7) mais où apparaît maintenant une fonction du temps $\left[g \right]$ elle-même périodique et de même période que $\left[f \right]$:

$$\left[Y \right] \lambda_0 + \left[\dot{Y} \right] \mu_0 + \left[g \right] = 0 \qquad (12)$$

Par un processus identique à celui qui a été décrit au paragraphe 2.2.2., on peut rassembler (11) et (12) en une seule équation qui prend la forme :

$$\left[\ddot{Z} \right] \Gamma_0 + \left[\dot{Z} \right] B_0 + \left[Z \right] A_0 = \left[F \right] \qquad (13)$$

où le deuxième membre $\left[F \right]$ qui prend en compte $\left[f \right]$ et $\left[g \right]$ représente l'excitation.

En posant $\left[\dot{Z} \right] = \left[V \right]$, (13) peut s'écrire :

$$\left[\left[\dot{Z} \right] , \left[\dot{V} \right] \right] \begin{pmatrix} 1 & 0 \\ 0 & \Gamma_0 \end{pmatrix} + \left[\left[Z \right] , \left[V \right] \right] \begin{pmatrix} 0 & A_0 \\ -1 & B_0 \end{pmatrix} = \left[\left[0 \right] , \left[F \right] \right] \qquad (14)$$

dont l'équation caractéristique :

$$\text{Déterminant} \begin{pmatrix} r.1 & A_0 \\ -1 & r.\Gamma_0 + B_0 \end{pmatrix} = \text{Déterminant} \begin{pmatrix} r^2 \Gamma_0 + r B_0 + A_0 \end{pmatrix} = 0$$

est identique à (10).

A chaque racine caractéristique r_j de l'équation précédente correspond une solution $\left[\left[Z_j \right] , \left[V_j \right] \right]$, définie à un coefficient près, de l'équation (14) où l'on suppose nul le second membre ($\left[F \right] = 0$).

La solution de (14) sans second membre s'écrit alors :

$$\left[[Z] , [V]\right] = \sum_j \lambda_j \cdot e^{r_j t} \left[[Z_j] , [V_j]\right] \tag{15}$$

La solution générale de (14) avec second membre, obtenue par la méthode de variation des constantes, conduit à écrire :

$$\sum_j \dot{\lambda}_j \cdot e^{r_j t} \left[[Z_j] , [V_j]\right] \begin{pmatrix} 1 & 0 \\ 0 & \Gamma_0 \end{pmatrix} = \left[[0] , [F]\right] \tag{16}$$

Pour résoudre (16) on met à profit la propriété d'orthogonalité des modes propres que nous rappelons.

Posons tout d'abord :

$$Q(r) = \begin{pmatrix} r \cdot 1 & A_0 \\ -1 & r \cdot \Gamma_0 + B_0 \end{pmatrix}$$

On sait alors que, pour $r = r_j$ (valeur propre) :

$$\left[[Z_j] , [V_j]\right] \cdot Q(r_j) = 0$$

Si nous introduisons alors le vecteur propre adjoint

vérifiant :
$$Q(r_j) \cdot \begin{Bmatrix} \{T_j\} \\ \{U_j\} \end{Bmatrix} = 0 \text{ , les relations d'orthogonalité des modes propres s'écrivent pour } r_j \neq r_k :$$

$$[Z_j] \left((r_j + r_k) \Gamma_0 + B_0 \right) \{U_k\} = 0 \tag{17}$$

En conséquence, si nous posons de plus (pour $r_j = r_k$) :

$$[Z_k] \left(2 r_k \Gamma_0 + B_0 \right) \{U_k\} = \Lambda_k \tag{18}$$

nous obtenons, en post-multipliant la relation (16) par $\begin{Bmatrix} \{T_k\} \\ \{U_k\} \end{Bmatrix}$ et en tenant compte de (17) et (18) :

$$\dot{\lambda}_k = \frac{1}{\Lambda_k} e^{-r_k t} [F] \{U_k\} \tag{19}$$

En intégrant (19) et en réinjectant les fonctions $\lambda_j(t)$, maintenant connues, dans (15), on voit que le vecteur d'état $[Z]$ est la somme de termes évanescents (si $\mathcal{R}_e \, r_j < 0 \; \forall_j$) et de termes périodiques de pulsation fondamentale Ω dont chacun, pris séparément est, **spatialement**, un mode propre.

Discussion sur la méthode modale

La méthode modale suppose implicitement qu'il existe un état statique moyen et, corollairement, que les mouvements autour de cet état statique moyen sont suffisamment petits pour que la linéarisation soit admissible. On discerne ainsi les limitations de la méthode. C'est la raison pour laquelle une autre méthode de calcul, la méthode des azimuts, a été développée à l'Aérospatiale. C'est cette méthode que nous allons maintenant décrire.

2.4. Méthode des azimuts

Nous repartons des équations de base (4) et (5) que nous rappelons :

$$\frac{\partial}{\partial x} [X] = G \left[[X] , [\dot{X}] , [\ddot{X}] \right] \tag{4}$$

$$C ([Y] , [\dot{Y}]) = 0 \tag{5}$$

Ces équations, non linéaires comme nous l'avons dit précédemment, sont valables que l'on soit en vol stationnaire ou en vol d'avancement.

La méthode des azimuts suppose que l'état stabilisé est atteint pour le rotor, c'est-à-dire que le vecteur d'état $[X]$, qui dépend a priori de x et de t, est une fonction périodique du temps et de période fondamentale T égale à celle du rotor

$$(T = \frac{2\pi}{\Omega})$$

La méthode est donc applicable au cas des **vols stabilisés**. Dans ce cas et quoique cela n'apparaisse pas explicitement dans les équations (4) et (5), les fonctions G et C contiennent, en plus des inconnues $[X]$ et $[Y]$ et leurs diverses dérivées, des variables qui dépendent de <u>façon connue</u> du temps : par exemple le pas qui est relié au temps par la loi :

$$\theta = \theta_0 - \theta_1 \cos \Omega t - \theta_2 \sin \Omega t$$

ou encore la vitesse d'attaque «horizontale» v de l'écoulement qui est donnée par :

$$v = \Omega r + V \sin \Omega t$$

Ces variables, périodiques, constituent les diverses sources d'excitation (forces aérodynamiques, plateau cyclique).

Compte-tenu de la périodicité supposée de $[X]$, il est possible d'éliminer les dérivées $[\dot{X}]$ et $[\ddot{X}]$ de la façon suivante.

Soit z une fonction périodique de période 2π. Cette fonction peut donc être développée en série de Fourier. En limitant à l'ordre n ce développement, on obtient :

$$z = a_0 + \sum_{k=1}^{n} (a_k \cos k\,\psi + b_k \sin k\,\psi) \tag{20}$$

Ce développement dépend des $2n+1$ coefficients $a_0, a_1, b_1, \ldots, a_n, b_n$. Supposons connues les valeurs de z pour $2n+1$ valeurs de ψ également réparties sur le segment $[0, 2\pi]$, à savoir, en posant $\Delta\psi = 2\pi/2n+1$:

Valeurs de ψ		Valeurs de z
$\psi_0 = 0 . \Delta\psi$	$\longrightarrow$	z_0
$\psi_1 = 1 . \Delta\psi$	$\longrightarrow$	z_1
$\psi_2 = 2 . \Delta\psi$	$\longrightarrow$	z_2
$\vdots$		
$\psi_{2n} = 2n.\Delta\psi$	$\longrightarrow$	z_{2n}

On peut alors montrer très facilement que :

$$a_0 = \frac{1}{2n+1} (z_0 + z_1 + \ldots + z_{2n})$$

$$a_k = \frac{2}{2n+1} \sum_{i=0}^{2n} z_i \cos (k . i \, \Delta\psi)$$

$$b_k = \frac{2}{2n+1} \sum_{i=0}^{2n} z_i \sin (k . i \, \Delta\psi)$$

Le développement (20) peut donc encore s'écrire :

$$z = \sum_{i=0}^{2n} z_i \, \lambda_i (\psi) \tag{21}$$

avec

$$\lambda_i (\psi) = \frac{1}{2n+1} + \frac{2}{2n+1} \sum_{k=1}^{n} \cos k (\psi - i \, \Delta\psi) \tag{22}$$

Dans les expressions (21) et (22), z peut être considéré comme l'une des 12 composantes du vecteur d'état.

Pour un azimut donné ψ, cette composante est indépendante du temps par hypothèse. Le temps n'intervient donc dans (21) et (22) que sous la forme $\psi = \Omega t$.

En dérivant (22) par rapport au temps, on obtient successivement :

$$\dot{\lambda}_i (\psi) = - \frac{2\Omega}{2n+1} \sum_{k=1}^{n} k \sin k (\psi - \psi_i)$$

$$\ddot{\lambda}_i \; (\psi) = - \; \frac{2\,\Omega^2}{2n+1} \; \sum_{k=1}^{n} \; k^2 \; \cos k \; (\psi - \psi_i) \tag{24}$$

D'où, à partir de (21), les dérivées $\dot{z}_j$ et $\ddot{z}_j$ pour un azimut $\psi_j = j \,.\, \Delta \psi$ quelconque :

$$\dot{z}_j = \sum_{i=0}^{2n} \; z_i \; \dot{\lambda}_i \; (\psi_j) \tag{25}$$

$$\ddot{z}_j = \sum_{i=0}^{2n} \; z_i \; \ddot{\lambda}_i \; (\psi_j) \tag{26}$$

Les relations (25) et (26), compte-tenu de (23) et (24), montrent que les dérivées temporelles $\dot{z}_j$ et $\ddot{z}_j$ à l'azimut $\psi_j = j \,.\, \Delta \psi$ sont connues à partir de $z_0 , z_1 , \ldots , z_{2n}$.

Si nous revenons maintenant au problème de base, c'est-à-dire la résolution du système des équations (4) et (5), il suffit d'écrire ces équations pour l'ensemble des azimuts choisis $\psi_0 , \psi_1 , \ldots , \psi_{2n}$, de remplacer les dérivées temporelles des variables par les combinaisons des valeurs de ces variables aux $2n+1$ azimuts choisis et de remplacer enfin les fonctions connues du temps qui traduisent les excitations par leurs valeurs en ces mêmes azimuts.

Le processus utilisé pour l'intégration est alors le même que celui qui est mis en oeuvre pour le calcul d'une déformée statique à cette différence près que l'intégration est menée simultanément sur l'ensemble des $2n+1$ azimuts alors que, dans le cas du calcul d'une déformée statique, l'intégration ne porte que sur un rayon.

Discussion sur la méthode des azimuts

La méthode des azimuts peut atteindre toute la précision désirée ; D'ailleurs, à partir d'une certaine valeur de n, les harmoniques *deviennent négligeables*. La seule limitation risque d'être la puissance de l'ordinateur utilisé. En effet, alors que le calcul d'une déformée statique nécessite l'intégration de $12 + 12^2 = 156$ équations différentielles et que le calcul d'un mode effectué dans le plan complexe en exige le double, il faut intégrer, dans le cas de la méthode des azimuts, $12\,(2n+1) \; + \; \left[12\,(2n+1) \right]^2$ équations, ce qui nécessite une forte capacité en mémoires.

Par contre, la méthode ne fait appel à aucun calcul préliminaire et semble applicable à n'importe quel cas de vol stabilisé moyennant l'hypothèse fondamentale que la périodicité de l'état du système est celle du rotor.

2.5. Méthode simplifiée pour le calcul des composantes statiques des efforts en vol d'avancement

D'après la description qui en a été faite précédemment (paragraphe 2.3.), la méthode modale ne permet pas d'évaluer de façon satisfaisante les composantes statiques des charges sur un rotor. Ces composantes peuvent être obtenues au moyen de la méthode des azimuts mais nous venons de voir que cette méthode nécessite des calculs assez longs.

Une méthode simplifiée dont la rigueur n'égale sans doute pas celle des méthodes de calcul présentées précédemment peut être utilisée pour évaluer certains efforts statiques. Elle consiste essentiellement à ramener le cas d'un vol d'avancement stabilisé à celui d'un vol stationnaire «équivalent».

Cette méthode est fondée sur la constatation expérimentale que les efforts statiques enregistrés en vol d'avancement en battement, par exemple, sont peu différents de ceux enregistrés à même portance, en vol stationnaire. Il en est de même en traînée, à même puissance. Le schéma est le suivant : une fois estimées la portance et la puissance avec le programme d'équilibre appareil, la répartition des efforts aérodynamiques de battement et de traînée sont estimés séparément en vol stationnaire, avec le pas correspondant. Compte tenu des caractéristiques élastiques de la pale et des déports principaux dans les sections, on calcule le transfert du vecteur d'état à 12 composantes de l'extrémité vers le pied par itérations successives, jusqu'à ce qu'on retrouve les conditions aux limites imposées par le moyeu : le calcul permet ainsi d'estimer la déformée de pale et les efforts statiques locaux de battement et de traînée en vol de palier stabilisé, ou en vol avec facteur de charge constant.

3. CALCUL DES CHARGES AERODYNAMIQUES

La méthode employée le plus fréquemment (*cf. paragraphe 2.1.4.*) *est une méthode approchée*, utilisant la formulation de Mejer Drees pour le champ des vitesses induites et le schéma itératif suivant dont la convergence est obtenue après stabilisation sur un tour du mouvement correspondant à la réponse du premier mode de battement aux excitations :

- calcul des vitesses dues au déplacement de la pale
- calcul des incidences et des nombres de Mach locaux
- calcul des C_x , C_z , C_m par interpolation dans les fichiers des polaires de profil (polaires mesurées à la soufflerie transsonique S3 MODANE de l'ONERA)
- calcul des charges aérodynamiques.

Des comparaisons calcul - essais avaient été effectuées, il y a quelques années, sur un rotor tripale de 4 m de diamètre essayé à S1-MODANE en similitude de nombre de Mach et équipé de capteurs de pression différentiels extrados - intrados. Les coefficients de portance locaux sont obtenus par intégration des pressions. Ces essais sont décrits dans la référence [3] .

L'analyse effectuée, référence [4] , concluait à un bon accord, même jusqu'à des configurations correspondant à la VNE en piqué sur appareil. Dans les cas de vol avec décrochage, la corrélation est moins bonne.

Une comparaison plus récente est présentée Figure 1. Les essais ont été effectués par l'ONERA sur un rotor tripale, de diamètre 1,74 m, à la soufflerie S2 de CHALAIS-MEUDON en similitude de nombre de Mach aux sections 0,85 R , 0,90 R et 0,95 R. Les conditions simulées correspondent à un vol de palier à grande vitesse ($\Lambda = 0,4$) et charge moyenne ($C_{z\,m} = 0,45$) en basculement libre, sans pas cyclique. Les valeurs mesurées par intégration des pressions dans ces zones voisines de l'extrémité de pale sont un peu supérieures aux valeurs calculées. L'écart en moyenne nous paraît néanmoins suffisamment faible pour justifier le fait que l'on utilise cette méthode approchée pour calculer les charges aérodynamiques.

Si l'on veut étudier le cas des rotors fortement chargés, des méthodes plus sophistiquées ont été développées comme le potentiel d'accélération dans sa dernière version, référence [5] et la méthode tourbillonnaire avec calcul du sillage. Ces méthodes sont beaucoup plus coûteuses en temps CPU. Elles n'apportent pas grand chose pour le calcul des charges dans le domaine du vol stabilisé courant. Elles présentent l'avantage de prendre en compte les aspects tridimensionnel et instationnaire de l'écoulement, aspects qui deviennent importants et même essentiels en torsion, aux limites de fonctionnement du rotor.

Dans tous les cas, ces méthodes exigent une synthétisation ou au moins une modélisation des caractéristiques instationnaires des profils pour limiter le nombre de données. De nombreux travaux sont conduits à l'ONERA sur ces sujets ([6] , [7]) et une synthèse des problèmes d'aérodynamique instationnaire de l'hélicoptère est effectuée dans la référence [8] .

4. COMPARAISON CALCULS DE CHARGE – ESSAIS SUR HELICOPTERE SA 349 Z

Cet appareil est un prototype dérivé de la GAZELLE SA 341. Le moyeu est articulé et la commande de pas est située entre l'articulation de battement et celle de traînée, semi-rigide, qui comporte un adaptateur visco-élastique (élastomère): Le 349 Z a fait l'objet il y a quelques années, de mesures en vol pour des vitesses allant de 188 à 260 Km/h. Les pales étaient équipées de 21 postes de mesure (10 en battement, 10 en traînée, 1 en torsion). Un poste de mesure complémentaire était installé sur l'une des biellettes de commande de pas.

Nous ne présenterons ici que les résultats obtenus en vol à 260 Km/h, en vol de palier stabilisé pour lequel, dans cette gamme de vitesse et de portance, les contraintes sont les plus élevées.

Sur la Figure 2, sont présentés les mouvements dynamiques de battement pour les quatre premiers harmoniques, M_{B_1} à M_{B4}. Les calculs ont été effectués par les 2 méthodes, méthode des azimuts et méthode modale. Dans le premier cas, les commandes cycliques, longitudinale et latérale ainsi que les traction et portance du rotor ont été prises égales à celles du vol. Les valeurs de l'angle $\propto_Q$ (inclinaison de l'arbre rotor par rapport à la direction du vent relatif V_0) et du pas collectif θ_0 sont retrouvées par itération et correspondent, à 0.2° près, à celles du vol. Pour la méthode modale, les calculs ont été initialisés d'une manière un peu différente, en utilisant un programme d'équilibre appareil donnant l'assiette et l'angle $\propto_Q$. L'itération est effectuée sur les pas collectif et cyclique pour retrouver la portance et la traînée globale.

La Figure 2 conduit aux observations suivantes sur le moment dynamique de battement :

– pour l'harmonique 1, l'accord est bon à part un écart au niveau du moyeu

– pour l'harmonique 2, l'écart n'est pas très important, mais l'allure des courbes calculées est différente de celle des mesures, essentiellement au pied de pale

– pour les harmoniques 3 et 4, l'allure est meilleure, mais les écarts subsistent.

Sur la Figure 3 sont présentées de même, pour le même vol, les résultats concernant le moment de traînée : l'accord est bon pour les harmoniques 1 et 2, moyen pour les harmoniques 3 et 4.

• Des calculs ultérieurs ont été conduits pour introduire les mouvements mesurés sur la tête rotor ayant une influence sur le 3e harmonique avec une tendance à l'amélioration de la corrélation sur ce poste (méthode modale).

La modélisation du pas cyclique, délicate dans le cas de la méthode modale, explique l'écart constaté sur le premier harmonique de battement et de traînée qui reste malgré tout faible. Cette méthode se prête par ailleurs assez facilement à des couplages avec des calculs de vitesses induites plus précis et à une amélioration du schéma aérodynamique.

Sur la Figure 4, sont présentés des recoupements en torsion avec les efforts mesurés sur la biellette de pas (méthode des azimuts) en fonction de la vitesse du vol. Le niveau d'effort calculé est systématiquement mauvais, essentiellement à grande vitesse. Les résultats obtenus avec la méthode modale ne sont pas meilleurs et l'écart arrive généralement à dépasser 100 %. Deux raisons peuvent expliquer ces écarts importants :

– la modélisation incorrecte de la raideur de la chaîne de commande qui est donnée arbitrairement et intervient dans l'équilibre en torsion

– l'estimation approximative des efforts aérodynamiques en torsion et aussi l'influence des effets instationnaires qui ne sont pas pris en compte dans le calcul.

5. COMPARAISONS CALCULS DE CHARGE – ESSAIS SUR L'HELICOPTERE AS 332 SUPER PUMA

Un très grand nombre de mesures ont été effectuées sur cet appareil à l'occasion des vols de certification. Des comparaisons calculs - essais sont présentées sur les moments statiques et dynamiques de battement et de traînée. Le 332 est équipé d'un moyeu articulé avec l'ordre suivant dans les articulations à partir du centre : traînée, battement, pas. L'amortisseur de traînée est du type visco-élastique avec un terme de raideur.

Les mesures en vol sont récentes et les recoupements sur les charges dynamiques sont effectuées sur la demi-amplitude du signal, l'analyse harmonique n'étant pas disponible.

Les recoupements sur les charges statiques sont présentés également, parce que l'évaluation précise de cette composante est très importante pour le dimensionnement. La comparaison est un peu moins rigoureuse que pour les composantes dynamiques parce que l'incertitude sur les mesures est plus grande pour deux raisons :

– des erreurs sont introduites par la dérive du zéro provenant du conditionnement du signal (multiplexage, démultiplexage)

– l'étalonnage des capteurs peut être faussé par les déformations initiales.

Nous présentons les résultats sur les Figures 5, 6, 7, 8 dans le cas d'un vol stabilisé en palier à la vitesse de 260 Km/h et à la masse de 7, 8 tonnes et sur les Figures 9 et 10 dans le cas d'un vol stabilisé, en virage, à la même vitesse et à la même masse, mais avec un facteur de charge égal à 1,75.

a) Vol stabilisé en palier

Sur la Figure 5, sont données les distributions mesurées et calculées de la composante statique du moment de battement le long de la pale.

Les points expérimentaux sont repérés par des $\otimes$ et les valeurs calculées correspondent :

– pour la courbe en trait interrompu à la méthode des azimuts

– pour la courbe en trait continu à la méthode simplifiée, décrite au paragraphe 2.5.

L'accord est satisfaisant pour r > 1.5 m et en particulier dans les deux zones critiques situées à 2,3 m (début de partie profilée) et à 4 m (zone de masse additionnelle). Il est par contre mauvais, dans ce cas, lorsque l'on se rapproche du moyeu. La méthode des azimuts ne semble pas plus précise que la méthode simplifiée.

Sur la Figure 6, il s'agit de la composante dynamique du moment de battement. On a porté sur cette figure, en fonction de la distance au centre du moyeu, la moitié de l'amplitude totale de la variation, soit $1/2 \, (M_{B, MAX} - M_{B, MIN})$ où $M_{B, MAX}$ et $M_{B, MIN}$ représentent les valeurs maximale et minimale respectivement. Les valeurs mesurées et calculées sont en bon accord et les deux méthodes de calcul donnent des résultats voisins.

Les Figures 7 et 8 présentent, sous la même forme que les Figures 5 et 6, les résultats relatifs au moment de traînée. Sur la Figure 7, on observe comme sur la Figure 5 que la corrélation est satisfaisante pour r > 1.5 m mais que des anomalies apparaissent en pied de pale. Sur la Figure 8, comme sur la Figure 6, on peut considérer que l'accord entre les valeurs mesurées et les valeurs calculées est satisfaisant, la tendance étant dans ce cas à sous-estimer un peu les efforts dynamiques par le calcul.

Par ailleurs, les deux méthodes de calcul donnent des résultats voisins sauf en pied de pale.

b) Vol stabilisé avec facteur de charge n_z = 1.75 en virage

Le vol stabilisé considéré est un virage à la vitesse de 260 Km/h. Les résultats sont présentés sur la Figure 9 pour la composante statique du moment de battement et sur la Figure 10 pour la composante statique du moment de traînée. On observe sur ces deux figures un assez bon accord entre les mesures et les calculs sauf en traînée, dans la région du pied de pale (Figure 10).

CONCLUSION

Les recoupements calculs - essais présentés dans ce papier illustrent la tendance générale des résultats obtenus pour le calcul des charges sur les rotors principaux d'hélicoptère à la SNIAS. Dans la majorité des cas étudiés, qui correspondent à des mesures en vol effectuées sur SA 349 et AS 332, deux calculs, différant notablement sur le plan du schéma de résolution, sont présentés. Les méthodes sont décrites dans leurs grandes lignes au début de l'exposé. La méthode modale est maintenant classique, la méthode des azimuts l'est un peu moins.

● On retiendra que, dans le cas des vols stabilisés en palier, même jusqu'à des vitesses élevées pour les appareils actuels, les méthodes de calcul donnent une estimation assez correcte des efforts statiques et dynamiques de battement de de traînée et fournissent des résultats assez voisins entre eux. Les résultats obtenus ne sont cependant pas parfaits et il est nécessaire de continuer les travaux sur le calcul des charges tout en gardant bien à l'esprit l'importance des erreurs de mesure et la dispersion des points d'essais. La difficulté à caractériser rigoureusement les matériaux et les assemblages doit également être prise en compte et peut justifier un certain nombre d'études particulières. Sous leur forme actuelle néanmoins, ces outils de calcul sont déjà très précieux au constructeur pour le dimensionnement et la justification des pièces dans certains cas.

Des difficultés apparaissent par contre dans le calcul de la torsion. Les travaux sont donc à poursuivre également sur ce sujet dans le but de raccourcir le cycle de mise au point en vol des rotors et d'aider à étudier de nouveaux rotors comportant un centrage de pale différent des centrages habituels ou faisant intervenir fortement les couplages en torsion pour améliorer les performances.

● Un exemple de calcul simplifié visant à estimer les efforts statiques dans le cas d'un vol avec facteur de charge (vol en virage stabilisé) a été présenté. Le recoupement est correct dans les zones critiques de dimensionnement et montre qu'il est possible d'obtenir des résultats satisfaisants, au moins pour les efforts statiques, dans des cas de vol avec facteur de charge. La méthode de calcul simplifiée utilisée permet, en choisissant bien les cas les plus pénalisants, d'obtenir une bonne estimation de l'enveloppe globale des efforts statiques, ce qui est fondamental pour le dimensionnement. Quant au calcul des charges dynamiques toujours dans le cas des vols avec facteur de charge, les méthodes prévisionnelles n'en sont qu'au stade du développement.

REFERENCES

[1.] HOUBOLT, J.C. and BROOKS, G.W.

Differential equations of motion for combined flapwise bending, chordwise bending, and torsion of twisted non uniform rotor blades.
NACA Report 1346, 1958

[2.] J.P. LEFRANCQ and B. MASURE (SNIAS)

A complete method for computation of blade mode characteristics and response in forward flight
7th European Rotorcraft and Powered Lift Aircraft Forum - Garmisch - Partenkirchen, Sept. 1981

[3.] M. LECARME et C. ARMAND (SNIAS - ONERA)

Essais de rotor d'hélicoptère dans la Grande Soufflerie de Modane
7e I.C.A.S. - ROME, Sept. 1970

[4.] J. GALLOT (SNIAS)

Calcul des charges sur rotor d'hélicoptère
AGARD - CP 122 - MILAN, Mars 1973

[5.] J.J. COSTES (ONERA)

Introduction du décollement instationnaire dans la théorie du potentiel d'accélération - Application à l'hélicoptère
La Recherche Aérospatiale N° 1975-3, p. 175-188

[6.] R. DAT, C.T. TRAN et D. PETOT (ONERA)

Modèle phénoménologique de décrochage dynamique sur profil de pale d'hélicoptère
XVIe Colloque d'Aérodynamique Appliquée (AAAF) - LILLE, Nov. 1979

[7.] R. DAT and C.T. TRAN (ONERA)

Investigation of the stall flutter of an airfoil with a semi-empirical model of 2 D flow
International Symposium on Aeroelasticity - NUREMBERG, Oct. 1981

[8.] J. GALLOT (SNIAS)

Synthèse des problèmes d'aérodynamique instationnaire de l'hélicoptère
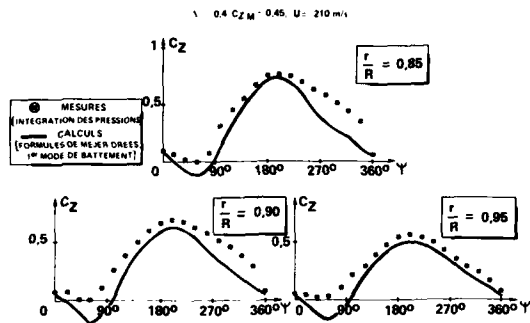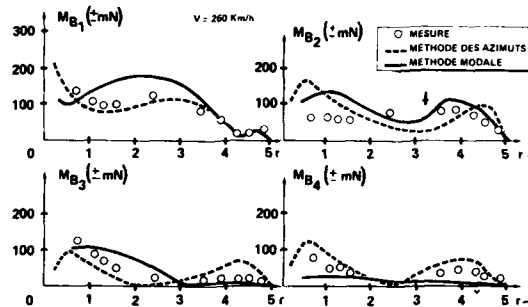15ème Colloque d'Aérodynamique Appliquée (AAAF) - MARSEILLE, Nov. 1978

FIGURE 1 : COMPARAISON EN SOUFFLERIE
DES C_Z LOCAUX

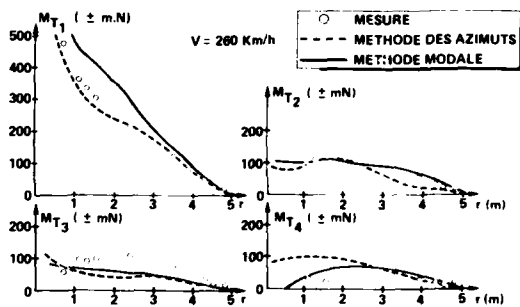FIGURE 2 : GAZELLE 349 Z - HARMONIQUES
DU MOMENT DE BATTEMENT

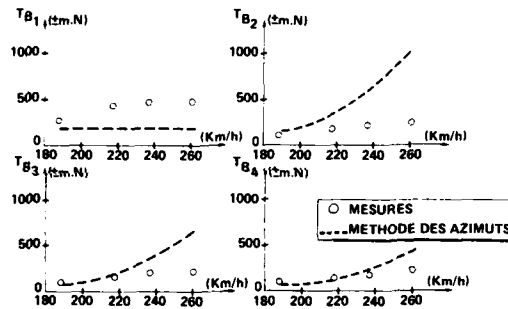FIGURE 3 : GAZELLE 349 Z - HARMONIQUES
DU MOMENT DE TRAINEE

FIGURE 4 : GAZELLE 349 Z - HARMONIQUES
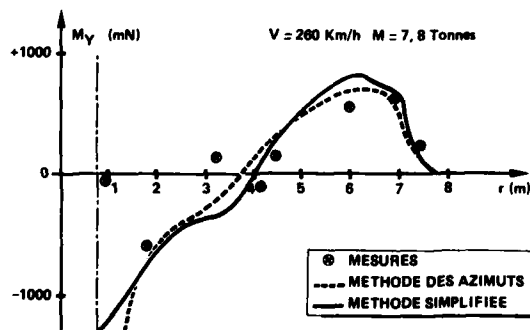DE L'EFFORT SUR LA BIELLETTE

FIGURE 5 : SUPER PUMA - COMPOSANTE
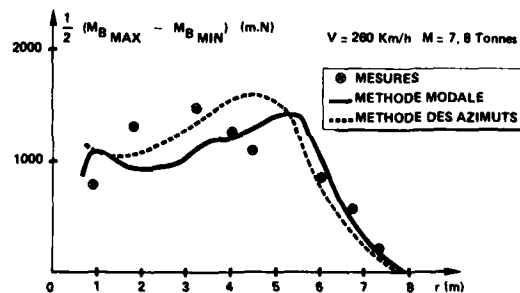STATIQUE DU MOMENT DE
BATTEMENT

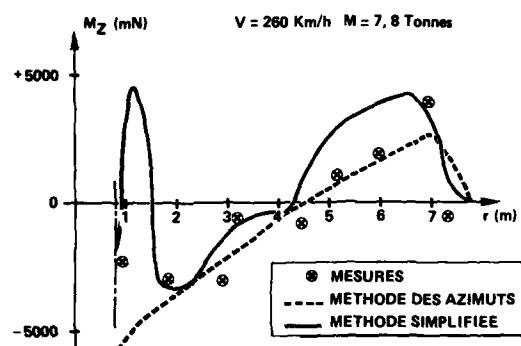FIGURE 6 : SUPER PUMA - DISTRIBUTION
DU MOMENT DYNAMIQUE DE
BATTEMENT

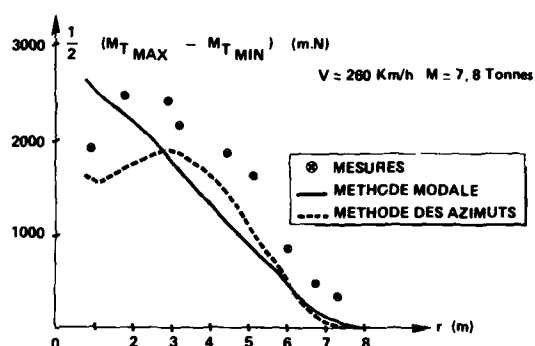FIGURE 7 : SUPER PUMA - COMPOSANTE
STATIQUE DU MOMENT DE
TRAINEE

FIGURE 8 : SUPER PUMA - DISTRIBUTION
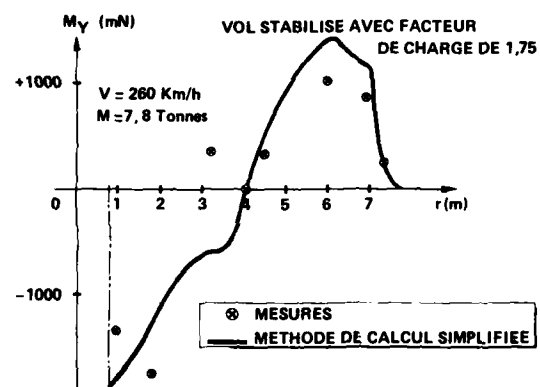DU MOMENT DYNAMIQUE DE
TRAINEE

FIGURE 9 : SUPER PUMA - COMPOSANTE
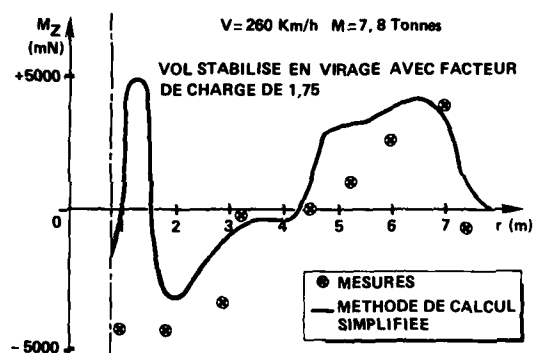STATIQUE DU MOMENT DE
BATTEMENT

FIGURE 10 : SUPER PUMA - COMPOSANTE
STATIQUE DU MOMENT DE
TRAINEE

COMPARISON OF ROTOR ANALYSIS RESULTS WITH AERODYNAMIC WINDTUNNEL DATA

by
H.-J. Langer, W. v. Grünhagen, B. Junker
Deutsche Forschungs- und Versuchsanstalt
für Luft- und Raumfahrt e.V.
Institut für Flugmechanik
D-3300 Braunschweig, Germany

SUMMARY

In recent years measurements have been conducted with a Ma-scaled rotor model: this 4-bladed hingeless rotor has a diameter of four meters and has been scaled down from the BO 105 main rotor, but exhibits certain differences in blade profile and coning angle. Measurements are presented for hub moments and blade stresses. Downwash velocities are recorded under the retreating and advancing side of the rotor.

As one part of the windtunnel measuring program was to obtain reliable data and compare these with calculations, computer programs were built up to calculate downwash as well as rotor and blade forces and moments. Different procedures are used to realize these calculations; the results are compared with windtunnel measurements.

The results of the calculation of the hub loads, blade loads, and downwash can vary considerably, so that the accuracy of the different calculation methods can be checked. As computing is a cost-intensive affair all computer programs for a future helicopter simulation program should be very fast and time-saving. As a computer program should be as simple as possible and as accurate as possible, the programs are constructed with these in mind.

1. INTRODUCTION

Measured data are obtained from both the rotating and the fixed system of the rotor. Two sensors are fixed on the rotor blade to measure the blade bending in the lagging and flapping direction. The torsion moment at the blade root is measured using pitch link load. The magnitude and phase of the blade's pitch angle are given by a potentiometer. All these data are measured at four blades, in order to detect blade differences, inaccuracies in signal transfer as well as for redundancy purposes.

The signals of the hub loads (i.e. pitching moment, rolling moment, side force, thrust and forward force) are processed by a 5-component balance. Rotor hub loads, and rotor angle of attack are measured in the fixed system. The torque is indicated by a torque meter.

In order to cover a wide data field, the measurements are varied stepwise in the $\mu - \alpha_{Ro} - \theta_o - \theta_s - \theta_c$ test regime. Thus it is possible to obtain rotor loads between these steps by interpolation.

In addition to the rotor and blade measurements, the steady state downwash velocity was resolved in three directions under the advancing and retreating blade and at low advance ratios up to $\mu = 0.2$. The results of these test runs will be shown and interpreted.

The measured downwash velocities are compared with calculated data obtained from a rigid vortex theory, which is applicable for the far-field calculation of induced velocities as well as for the near wake field calculation.

For some configurations the rotor loads are calculated and compared with measured data points. The loads are determined from the calculation of the forced blade oscillations by means of fully coupled mode shapes. The mode shapes are obtained from a finite element program based on the equations of Houbold and Brooks (Ref. 9).

The local and global momentum theories are used alternatively to calculate the blade airload and to determine the curve of the flapping angles. These data are used as input data to calculate the induced velocities by applying the rigid vortex theory. Due to the long computing time, results from the vortex theory are not fed back into the airload program.

2. NOTATION

$\underline{a}$, $\underline{\bar{a}}$	eigenvectors
C	symmetric stiffness matrix
$\underline{f}$, $\underline{f}_o$	force vectors
F_x, F_y, F_z	rotor hub forces
IF(i)	attenuation factors
K	symmetric stiffness matrix
L	triangular matrix
M	mass matrix

M_x, M_y, M	rotor hub moments, $M = \sqrt{M_x^2 + M_y^2}$
M_β	blade flapping moment
$M_{\beta 1c}$	cos-term of blade flapping moment
P_z	rotor thrust
R	rotor radius
$\underline{v}$, $\underline{v}_o$, $\bar{v}$	vectors of displacements
v_x	velocity in x-direction
w_x, w_y, w_z	downwash velocities
X	modal matrix
x, y, z	nonrotating body fixed axes
α_{Ro}	rotor angle of attack
Λ^2	diagonal matrix of natural frequencies
μ	advance ratio
Ω	rotor frequency
θ_o	collective pitch
θ_s	longitudinal) cyclic pitch
θ_c	lateral)

3. HINGELESS ROTOR PARAMETER LIST

number of blades		4
rotor diameter	[m]	4
blade chord, constant	[m]	0.121
twist, linear	[°/m]	-4
blade profile		NACA 23012 mod.
profile beginning from shaft axis	[m]	0.44
preconing	[°]	0
rotor frequency (depending on atmospheric condition)	[Hz]	17.5
blade tip speed	[m/s]	220
solidity	[-]	0.077
center of gravity of profile (relative)	[-]	0.23
spring constant, flapping	[Nm/°]	-7.266
equivalent flapping hinge offset	[m]	0.27
blade mass of flapping blade	[kg]	1.41
mass moment with respect to flapping hinge	[kgm]	1.195
moment of inertia with respect to the flapping hinge	[kgm²]	1.358
Ma-number (blade tip, hover)		0.645
Re-number/Ma-number		$1.97 \cdot 10^6$
Froude-number (blade tip, hover)		49.2
Lock-number (INA, 0 m)		4.54

4. MEASURING EQUIPMENT

The facility to measure the downwash was installed on both sides of the test stand (Fig. 1). It can be tilted simultaneously with the rotor plane. Therefore the measurements refer to the body fixed coordinates. In the lateral direction the downwash is measured along the y-axis. The distance between sensor and rotor plane is adjustable. Measurements were taken at distances between z = 0.15 m and z = 0.6 m. A variation in the x-direction has not been possible yet. The z positioning is fixed during a test series, but the sensor can be moved electrically on both sides of the rotor in the y-direction. Due to the simplification in calibration the sensors are adjustable to the main flow direction in the x-z plane. Conrad vector probes are applied in most cases (Fig. 2). The pressure signals are indicated by alcohol-filled U-shaped manometers. The difference in the level of liquid indicates the pressure.

The loads of the rotor hub are measured via a 5-component balance (F_x, F_y, F_z; M_x, M_y) consisting of seven force transducers: four in the z-direction, two in the y-direction and one in the x-direction. As the system is overdetermined (7 transducers for 5 components) it is possible to check the accuracy of the balance by applying the 'Error Compensation Method' described in Ref. 7 . Normally errors are less than four percent as regards the moments, and less than two percent as regard the thrust.

As the rotor is hingeless, at normal flight conditions the inplane hub forces are small and therefore of minor interest. Errors in hub loading measurements are higher when a force acting on one or more transducers is near zero. Such conditions can be caused by low thrust and high moment setting.

Torque is measured by a torque meter which is of high accuracy. In order to adjust the rotor angle of attack, the rotor in conjunction with the balance can be tilted by a hydraulic cylinder, and the angle is measured by a potentiometer. As the axis of tilting is 1.5 m under the rotor plane, the rotor hub is not fixed with regard to the distance from the windtunnel floor.

Measurements from the rotating system are transferred via PCM. The PCM-equipment is mounted on the rotor hub (Fig. 1). As the facility is 0.4 meters high, there may be an influence on streamlines through the rotor disk. But strain gauge measurements at the blade root show that this influence is negligible for the measurements presented in this paper.

Strain gauge bridges for flapping and lagging measurements are positioned near the root of each blade at the assumed equivalent lagging and flapping hinge. After calibration of the sensors, the blade signals sometimes show considerable differences between each other when the rotor is operating. Possible reasons for this are:

- tracking errors,
- differences in blade stiffness,
- differences in the (blade's) profile shape,
- coupling effects,
- windtunnel interferences.

It is difficult to find out which effect is chiefly responsible for divergences in the measured values, esp. for a hingeless rotor. The above reasons indicate that one cannot expect an exact coincidence when comparing measured and calculated data.

Beside the flapping and lagging measurements at each blade, all pitch link loads and the blade pitch are measured. In order to coordinate all signals a magnetic pick-up records the blade position.

5. DATA ACQUISITION AND EVALUATION

Data acquisition with the 5-hole pressure probe was realized by a photo camera. The difference in liquid level in the U-manometers, and the position and angle of incidence of the probe in the x-z plane were shot by a camera. The measurement started when the indicated pressure of the angle-position of the probe was compensated. The measuring procedure for 14 radial positions lasts three minutes.

A special facility transmits the velocity data from the photos to punch cards. The velocity data are split in the three body-fixed axes via a Fortran program.

Data from the rotating system and fixed system are transferred by two PCM systems, each with 16 channels and a bit rate of 125 kbit/s. This bit rate allows the evaluation of the data up to the 8th rotor harmonic order. For rapid analysis and quick-look a pdp 11/45 computer operates parallel to a magnetic tape which stores all test runs.

A FFT (Fast Fourier Transform) is made for each channel and for thirty rotor revolutions. As the data scatter slightly from one revolution to another the best one is printed out. The criterion for being 'the best revolution' is a minimum error in the overdetermined equation system of the balance as mentioned in the previous section.

6. WINDTUNNEL MEASURING PROGRAM

Emphasis was placed on the rotor behavior at low forward speeds; therefore most of the measurements were conducted at advance ratios of $\mu = 0.05$, $\mu = 0.1$, and $\mu = 0.15$. In order to cover a wide data field the test program consists mainly of the stepwise variation of advance ratio (μ), angle of attack (α_{Ro}), and collective ($\theta_{0.7}$), and cyclic-pitch (θ_s, θ_c). Lateral pitch (θ_c) was adjusted in most cases by maintaining a rolling moment of $M_x = 100$ Nm.

In addition, the windtunnel measuring program consists of:

- the determination of the balance loads due to windtunnel flow by variation of rotor shaft tilt without blades,
- blade tracking procedures under different thrust conditions,
- rotor balancing,
- measurements of rotor derivatives,
- comparisons of data obtained from BO 105 flight measurements and rotor model tests,
- control setting for hub moments equal zero ($M_x = M_y = 0$),
- downwash measurements.

The downwash components (w_x - positive forward, w_y - positive to the right, w_z - positive downward) were determined as a function of thrust, advance ratio, rotor angle of attack, and radial and vertical position.

The region of variation of these parameters were:

$$0.15 < y/R < 1.05$$
$$0.02 < z/R < 0.3$$
$$1000N < P_z < 5000N$$
$$0 < \mu < 0.2$$
$$-10^{\circ} < \alpha_{Ro} < +7^{\circ}$$

Only one test run was necessary for the parameter variation of y/R. Fig. 3 shows the stream vectors measured in the vicinity of the rotor.

7. CALCULATION METHODS

The calculation of the hub loads and the induced velocities is made by determining the local flow angle of attack at the rotor blade, using local momentum theory or global momentum theory.

If the flow angle distribution is known, the rotor loads and the harmonics of flapping are calculated. Normal and tangential blade forces as well as the flapping coefficients are used as input data for the rigid wake program when calculating the local induced velocities.

The following section describes the particular programs in more detail. The global momentum theory will not be described as it can be assumed to be familiar.

7.1 Local Momentum Theory

The mathematical model of the rotor is based on the concept of representing an actual aerodynamic load and downwash distribution of a blade by a series of n overlapping elliptical wings of decreasing size; each of these wings has an elliptical circulation along the span and therefore produces an uniform downwash velocity. Each elliptical wing is arranged to be drawn to one side to the blade tip. By neglecting the upwash flow outside the wings which have an elliptical circulation distribution, the induced velocities of the blade is given by the sum of the constant induced velocities of each elliptical element.

The theory takes into account:

- the upwash flow outside the rotor blade when the rotor is advancing,
- the vortex interaction between the preceding blade's tip vortex and the following blade,
- the attenuation of the circulation of the advancing blade when it is hitting the succeeding blade,
- blade flapping motion.

The theory does not take into account:

- vortex/vortex interaction,
- flow separation due to unsteady effects,
- any distortion of the rotor wake,
- the wake contraction and roll up.

Some empirically determined parameters were used in the calculations in order to adjust the calculation to rotor measurements as well as to reduce the computation time. Three influence factors are important:

IF(1)- Factor taking into account the interaction between preceding and following blade,
IF(2)- Attenuation of the tip vortex,
IF(3)- Correcting parameter. It decreases with the advance ratio and determines the rotor downwash in such a way that the measured and calculated thrust are in agreement.

On the basis of various hot-wire anemometer measurements, IF(1) was defined to be constant at 0.85. IF(2) depends to a large extent on the number of chosen segments along the blade radius.

As a tip loss factor is not taken into account and the upwash outside the blade influences the induced velocities at the blade tip, the IF(2) - influence factor has to be fixed appropriately. The factor IF(3) takes into account globally the downwash field according to a preselected thrust. This factor is comparable with the coefficient C in Ref. 6.

Furthermore, theoretical data are more reliable when the calculations take into account the flapping coefficients. The flapping coefficients are derived from calculated data. The determination of the flap angle from measurements is not very accurate owing to the characteristics of a hingeless rotor: the flapping hinge is not clearly defined, and a strong coupling exists between flapping and lagging due to changes in the blade's pitch angle. As the flapping moment is proportional to the flap stiffness in the first iteration, both the flap angle magnitude and the phase can be calculated by dividing the blade root flapping moment by the spring stiffness factor.

Another inaccuracy can arise when the windtunnel flow causes a highly distorted flow through the rotor disk at low advance ratios and at a small shaft tilt angle so

that calculation yields no reliable data.

The local momentum computer program needs a CPU-time of 6 sec (Siemens 7.870) and a memory of 80 kbyte.

The program needs the following input data:

- geometric sizes of the rotor,
- profile-data,
- windtunnel speed,
- rotor angle of attack,
- blade twist,
- rotor frequency,
- thrust,
- control angles,
- flapping coefficients (optional).

7.2 Rigid Wake Analysis

In contrast to the local momentum theory the rigid wake computer program calculates the rotor induced velocities at each point of the flow field. As it can be assumed that the rigid wake analysis is well known, only a short description is necessary.

The computation time of the rigid wake program depends on several preselectable settings:

- the number of rotor revolutions,
- the number of vortices,
- the stream contraction,
- the azimuth position where the flow field is rolled up,
- the calculation of vortex core size diameter depending on blade loading.

This version runs for about 200 sec. and has a memory of 120 kbyte. The vortices of three rotor revolutions are computed, establishing eight bound vortices and ten free vortices for a quarter of one rotor revolution. After that the whole vortex is bound and rolled up in a blade tip vortex.

The calculation of the vortex core size depends on flight conditions, and shows no substantial variation with forward speed and azimuth position (Ref. 6). Normally the the core size varies between 4 and 8 percent of the rotor radius.

7.3 Analytical Model

The real rotor system was described by a mathematical model with fully elastic blades. The fully coupled mode shapes and the eigenvalues have been calculated by a finite element procedure based upon the wellknown partial differential equation of Houbold-Brooks. This leads to a system of ordinary differential equations of the following form

$$(1) \qquad \underline{M}\,\ddot{\underline{v}} + \underline{K}\,\underline{v} = \underline{f}(\underline{v},\dot{\underline{v}},t) + \underline{f}_o$$

with the symmetric band matrices $\underline{M}$ and $\underline{K}$, the mass matrix and stiffness matrix, the vector $\underline{v}$ which contains the nodal point displacements and the slopes at the nodes. F is the vector of the aerodynamic forces and coriolis forces and depends upon the displacements of the blade elements, their velocities and the time t, $\underline{f}_o$ is a vector stemming from centrifugal forces and determines a constant deformation of the blades through these forces. The vector $\underline{v}$ is taken to be a sum of a constant vector $\underline{v}_o$ and a time dependent vector $\overline{\underline{v}}(t)$.

$$(2) \qquad \underline{v} = \underline{v}_o + \overline{\underline{v}}(t).$$

Inserting this into equation (1) one obtains

$$(3) \qquad \underline{M}\,\ddot{\overline{\underline{v}}} + \underline{K}\,\overline{\underline{v}} + \underline{K}\,\underline{v}_o = \underline{f}(\underline{v}_o,\overline{\underline{v}},\dot{\overline{\underline{v}}},t) + \underline{f}_o$$

and by choosing

$$(4) \qquad \underline{v}_o = \underline{K}^{-1}\,\underline{f}_o$$

one finally obtains

$$(5) \qquad \underline{M}\,\ddot{\overline{\underline{v}}} + \underline{K}\,\overline{\underline{v}} = f(\underline{v}_o,\overline{\underline{v}},\dot{\overline{\underline{v}}},t).$$

The symmetric mass matrix $\underline{M}$ can be decomposed into the product of two triangular matrices via the Cholesky decomposition

$$(6) \qquad \underline{M} = \underline{L}^T\,\underline{L}.$$

Assuming the solution of the form

$$(7) \qquad \overline{\underline{v}} = \underline{a}\,e^{\lambda t}$$

this leads to the following general eigenvalue problem

(8) $\qquad \lambda^2 \underline{L}^T \underline{L} \, \underline{a} + \underline{K} \, \underline{a} = 0$.

Multiplying this equation by $(\underline{L}^T)^{-1}$ from the left and substituting

(9) $\qquad\qquad\qquad \overline{\underline{a}} = \underline{L} \, \underline{a}$

yields to the special eigenvalue problem

(10) $\qquad\qquad \lambda^2 \, \overline{\underline{a}} + \underline{C} \, \overline{\underline{a}} = 0$

where $\underline{C} = (\underline{L}^T)^{-1} \underline{K} \, \underline{L}^{-1}$ is a symmetric matrix which leads to real eigenvectors. The eigenvectors of the equation (8) can be calculated via eq. (9).

For the calculation of the forced oscillations of the rotor blades the vector $\overline{\underline{v}}$ is considered to be the sum of the mode shapes $\underline{a}$ multiplied by generalized coordinates q_i

(11) $\qquad\qquad \overline{\underline{v}} = \sum q_i \, \underline{a}$

or in vector matrix notation

(12) $\qquad\qquad \overline{\underline{v}} = \underline{X} \, \underline{q}$

where $\underline{X}$ denotes the modal matrix of the eigenvectors. Inserting this into (5) one obtains

(13) $\qquad \underline{M} \, \underline{X} \, \ddot{\underline{q}} + \underline{K} \, \underline{X} \, \underline{q} = \underline{f}$.

Multiplying this equation by the transposed matrix $\underline{X}^T$ from the left the final result is

(14) $\qquad\qquad \ddot{\underline{q}} + \underline{\Delta}^2 \, \underline{q} = \underline{X}^T \, \underline{f}(\underline{q}, \dot{\underline{q}}, \underline{v}_0, t)$

where $\underline{\Delta}^2$ is a diagonal matrix with the squares of the eigenvalues.

The rows of $\underline{X}^T$ are the mode shapes and it can easily be seen that (14) is a system of harmonic oscillators which are coupled over the right side and that each upper part is decoupled from the whole system. For the calculation of the forced blade oscillations one can use the mode shapes which belong to the lower eigenvalues, because they have small discretisation errors. Thus a numerical integrable form of the differential equation of the forced blade oscillations is available. The aerodynamic forces can be calculated by taking into account the flight velocity, the rotor rotation, the elastic deformations of the blade and the element velocities.

Two downwash models are used namely a trapezoidal downwash following Payne and a downwash field which is calculated by a local momentum theory as decribed in Azuma and Kawachi (Ref. 5). For the first model only an iteration of the collective control angle was necessary to obtain a given (measured) thrust. For the second model an additional iteration of the forced blade motion was necessary because the blade flapping motion is used to calculate the induced downwash velocities.

About five iteration steps for the flapping motion lead to satisfactory results as regards steady state oscillations. To avoid numerical difficulties an appropriate stepsize for the numerical integration can be found by using a Runge-Kutta-Fehlberg integration procedure with variable stepsize.

After obtaining a steady state blade flapping and lead-lag motion the mean values of the rotor hub forces and moment were calculated by using a model with a rigid blade and a spring-restrained hinge. The degree of hinge offset and torsional spring strength was chosen to match the rotating and nonrotating lowest natural frequencies of the real blade.

The calculated blade loadings, flapping angles, normal and tangential inflow velocities were fed into another program in order to calculate induced downwash velocities by a rigid vortex theory.

8. RESULTS

Now the results will be considered that were obtained from the downwash measurements and from calculations of the fourbladed hingeless rotor at:

- $\mu = 0$; variable z/R (Fig. 4),
- $\mu = 0$; 3-component calculation and measuring (Fig. 5),
- $\alpha_{Ro} = 0$; μ variable (Fig. 6),
- $\alpha_{Ro} = -5$; μ variable (Fig. 7),
- $\alpha_{Ro} = -10$; μ variable (Fig. 8).

All measurements were made by a 5-hole pressure probe. Calculations and measurements are presented for the rotor loads.

- Torque vs advance ratio at constant thrust,
- Cyclic control vs advance ratio,
- Derivatives ($\partial M/\partial\theta_s$ and $\partial M_y/\partial\theta_s$) vs advance ratio,
- Derivative $\partial M_{\beta1c}/\partial\theta_s$ vs advance ratio.

All the rotor load calculations are executed at constant shaft tilt and with θ_c almost constant.

Figure 4 shows downwash measurements and calculations for the hovering case. The left side of the diagram shows the downwash at a distance of z/R= 0.15 (z=0.30 m) from the rotating plane. As mentioned above, two different methods are used to calculate induced velocities using the rigid wake analysis:

1. Global momentum theory (dashed line),
2. Local momentum theory (full line).

The right side (ψ= 90°) shows the induced velocities recorded at a distance of z/R= 0.3 (z=0.6 m) from the rotating plane. The measurements and calculations show the flow contraction quite well (compare the velocity components in Fig. 3).

The measured velocities are higher than the calculated at the blade tip region, and show a stronger velocity gradient. It is assumed that it is mainly at the retreating blade where the calculation makes excessive allowance for the blade root vortex. On the other hand the measurements near the blade root are influenced by the rotor hub and a fuselage-shaped body covering the rotor balance. This effect on downwash can also be seen in Figure 3 . The calculation, of course, does not allow for these effects.

The left side of the downwash field is different from that of the right side. This is a result of cyclic pitch $\neq$ 0. From the momentum theory we know that the induced velocity increases as the distance increases (up to factor two). The measurements confirm this increase.

The two curves calculated differ significantly from each other. As the vortex calculation needs the blade loads and flapping distribution as input data, the results must be different depending on whether the global or local momentum theory is used to generate these data. As expected, the local momentum theory yields better results because this theory considers in more detail the real physical situation at the blade. Thus the following calculations are made using the local momentum program to generate the input data. Figure 5 shows again a hovering condition, but the measurements and calculations are made at a distance of z/R= 0.07 from the rotating plane.

The induced velocities are split up into the x-, y- and z-directions. One part of the forward velocity vectors (left: positive, right: negative) shows the twist of the downwash. As a result of the flow under the blade in the radial direction and the strong blade tip vortex, the sideward velocity vectors increase in the direction of the blade tip. The calculated vector amplitudes in the y-direction are too high near the blade tip, because the rigid vortex calculation does not make adequate allowance for the distance between blade segment and calculated point (in the forward flight calculation especially, the measured data in the y-direction vary considerably from the calculated data). As various vortex core diameters were chosen, the vertical velocity vectors show some disturbances and the calculated curve is not as smooth as the measured curve. But nevertheless the coincidence is quite good.

More detailed measurements will be made concerning the problem of measuring the distance between blade section and vector probe. It seems that this is often a reason for the differences between the calculated and measured curves.

Figure 6 shows impressively the change in V_z-velocity at different advance ratio and at different thrust. The rotor shaft tilt is α_{Ro}= +0°. The μ= 0 curve was discussed above. The μ= 0.1 curve has only small vector-components in the z-direction. The components are higher at the right side. This is a result of the blade's pitch (θ_s= -1.2, θ_c= +3.1), the shaft incidence, and the higher tangential velocity at the advancing blade, where the blade's pitch is the main factor.

Inaccuracies in the calculation of the flapping motion as well as inaccuracies in the measured values needed as input data for the local momentum program (esp. at α_{Ro}= 0) can result in a rather large difference between measurement and calculation.

As can be seen in Figure 7 , there is the same effect between the left and the right rotor side: calculations and measured points coincide better on the left side. It can be presumed that the calculation does not make adequate allowance for the stream contraction combined with the vortex position of the preceding blade. On the other hand the distance between blade and vector probe can differ from the assumed distance so that the calculated vortex position does not coincide with the measured position.

As the downwash field has high velocity gradients in all directions it seems that good agreement between calculation and measurement depends less on the wake model used than on the position of the blade relative to the probe. As the shaft incidence increases the downwash calculation becomes more accurate, α_{Ro}= -10° (Fig. 8).

This is why the character of the flow through the rotor disk is not so disturbed as when the induced velocities are very small. Moreover, the local tangential velocities are high at the advancing blade - in contrast to the retreating blade - so that small changes in the blade's angle of attack cause large differences in the induced velocities. Therefore small deviations in the calculation of the angle of attack can result in large discrepancies in the measured data.

To sum up, there are three main reasons for the differences between measured and calculated data:

- the position of the blade relative to the vector probe is unkonwn,
- the calculation of the flapping motion (esp. phase position) can be different from the measured curve,
- the blade's effective angle of attack distribution cannot be calculated with sufficient exactitude at higher advance ratios and at a small shaft incidence.

In Figure 9 the torque is plotted versus the advance ratio. Results from the local momentum calculation (L) and the global momentum calculation (G) are compared with wind-tunnel data. The maximum tunnel speed was 55 m/s (μ= 0.25), and the rotor frequency was Ω= 110s^{-1}. Except at μ= 0 the calculation and the measurements yield nearly identical results. The higher level of the L-curve may be caused by the inaccuracies which occur when local calculations of speed, effective angle of attack, and normal and tangential components are added to determine the thrust and torque.

The measured torque at μ= 0 is considerably higher than that calculated. This is because the rotor is disturbed by its own downwash at hovering condition in the windtunnel. Calculations and measurements have been made to obtain the cyclic control curve versus advance ratio. The results are not very good; the local momentum theory in particular shows large differences (Fig.10) in θ_s. One reason is that the local momentum theory needs a special attenuation coefficient dependent on the advance ratio (Ref. 5).

Such a coefficient was assumed to be constant at each forward velocity. The classical lateral flapping curve (Ref. 2) with its peak at an advance ratio of μ= 0.1 cannot be calculated either by the global momentum theory or by the local momentum theory. The relatively simple downwash theories underpredict the magnitude of·the control angle, esp. θ_c. The local momentum curve shows a slightly better tendency than the global momentum curve because the local momentum theory allows for the tip vortex of the preceding blade hitting the following or target blade. This influence results in a local decrease in the induced velocities. When a trimmed flight is being held, the lateral control angle has to be adjusted properly. It seems that the local momentum theory underestimates the effect of vortex interaction.

As all measured points are plotted without windtunnel correction factors, better coincidence for θ_c can be expected if the angle of attack is adjusted to a higher shaft tilt. When determining the hub loads it is easier and less time-consuming to define an equivalent hinge with a torsion spring. For the calculation of the local blade loads, a fully elastic blade was assumed.

Figure 11 shows the change in the hub moment (M) and the pitching moment (M$_y$) when the longitudinal control angle θ_s is changed. The values of the measured and calculated curves in both cases indicate that the rolling moment is small. The global momentum theory yields unsatisfactory results, while the local momentum theory is in really good agreement with the measured data. The plot of pitching moment effectiveness shows no difference from the calculated values. Differences in both of the theories can be explained by the different aerodynamic assumptions used for the global and the local momentum calculations.

Figure 12 shows the flapping moment derivative ($\partial M_{1c}/\partial\theta_s$) versus the advance ratio. This presentation was chosen since the longitudinal cyclic control angle θ_s mainly influences the cos-term of the flapping moment. The curves resulting from calculations differ considerably from the measured points. But a good coincidence can hardly be achieved on account of several difficulties in both the calculation and the measurements in the case of a hingeless blade:

- the amplitude of M$_\beta$ depends on the radial position of the strain gauge sensor on the hingeless rotor blade,
- due to the blade's pitch the lagging hinge does not remain perpendicular to the rotor plane. This is in opposition to the assumptions on which the calculation is based.

For these reasons an exact agreement between the curves cannot be expected. The tendency of the measured points shows increasing values when the forward speed increases. This is an effect caused by the higher blade pitch angle θ_s, which results in a stiffer hinge as regards the rotor plane.

9. CONCLUSIONS

This paper presents various points which arise from the comparison of windtunnel data with theoretical calculations. The methods of calculation chosen had to be simple and as exact as possible, because these methods are intended for insertion in a complete helicopter simulation program and therefore low computing time is required. The following calculation methods are applied:

- global or local momentum theory, yielding the downwash aerodynamics needed to calculate the blade loads, hub loads and the flapping motion,
- rigid vortex theory, yielding local induced velocities.

The results of the calculations are:

- the measured and calculated induced velocities coincide if the flow is not highly distorted (incidence of shaft < -5°),
- the global momentum theory only yields good results for trimmed flight conditions (i.e. small hub moments). The calculation of derivatives is not so satisfactory as the theory allows only small increments for the moments,
- the local momentum theory can be applied to calculate accurately the derivatives of the hub loads (esp. the pitching moment), as the theory makes better allowance for untrimmed conditions of the rotor.

The blade loading calculation suffered from certain uncertainties regarding the measured data which cannot be avoided esp. when one is measuring at a hingeless rotor system. With the application of the local momentum theory and the rigid vortex theory the calculations show that the vortex position and the blade vortex interaction play a dominant role in the determination of induced velocities control angles, and loads.

It is not advisable to extend the downwash calculation in the direction of a free wake analysis for a complete helicopter simulation program. For flight mechanical purposes it seems to be appropriate to use a semi-empirical method on the basis of the local momentum theory which calculates the position of the tip vortex.

Efforts should be made to improve the measurements by extending the number of strain gauge sensors on each rotor blade. It would be helpful if an extended windtunnel measuring program is developed which places most emphasis on small increments in forward velocity (V_∞). One requirement for obtaining reliable measured downwash velocities is the ability to determine the distance between the passing blade segment and the vector probe.

On this basis the calculated downwash velocities for helicopter simulation programs will be acceptable.

9. REFERENCES

1. Harris, F.D.: Articulated Rotor Blade Flapping Motion at Low Advance Ratio. Journal of American Helicopter Society, Jan. 1972.

2. Johnson, W.: Comparison of Calculated and Measured Helicopter Rotor Lateral Flapping Angles. Journal of American Helicopter Society, April 1981.

3. Junker, B., Langer, H.-J.: Helicopter Rotor Downwash - Results of Experimental Research at the DFVLR-Rotor Test Stand and their Comparison with Theoretical Results. 7th European Rotorcraft and Powered Lift Aircraft Forum, Paper-No. 43, Garmisch-Partenkirchen, 8.-11. Sept. 1981.

4. Ormiston, R.A.: Comparison of Several Methods for Predicting Loads on a Hypotetical Helicopter Rotor. AHS/NASA-Ames Specialist's Meeting on Rotorcraft Dynamics. Moffett Field, Cal., 13.-15. Febr. 1974.

5. Azuma, A., Kawachi, K.: Local Momentum Theory and its Application to Rotary Wing. AIAA-Paper, No. 75-865, AIAA 8th Fluid and Plasma Dynamics Conference, Hartford, Conn., 16.-18. June 1975.

6. Crimi, P.: Prediction of Rotor Wake Flows. CAL/USAAVLABS Symposium Proceedings, Vol. 1, Buffalo, New York, 22.-24. June 1966.

7. Zurmühl: Praktische Mathematik. Springer Verlag, 1957.

8. Houbold, J.C., Brooks, G.W.: Differential Equations of Motion for Combined Flapwise Bending, Chordwise Bending and Torsion of Twisted Nonuniform Rotor Blades. NACA Report 1346, 1958.

Fig. 1: Rotor Test Stand in the
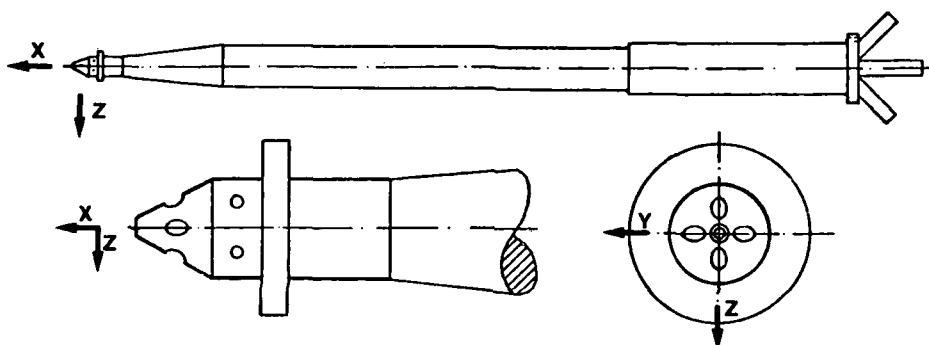Daimler-Benz Windtunnel

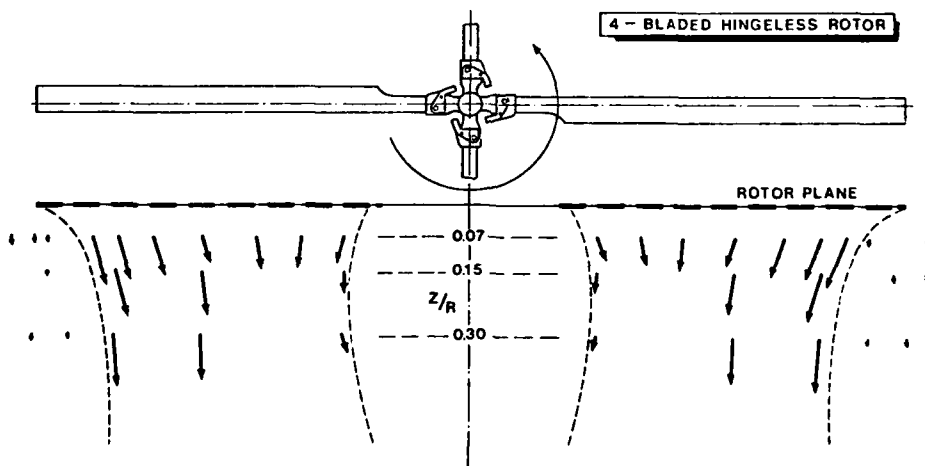Fig. 2: Pneumatic vector probe (by Conrad)

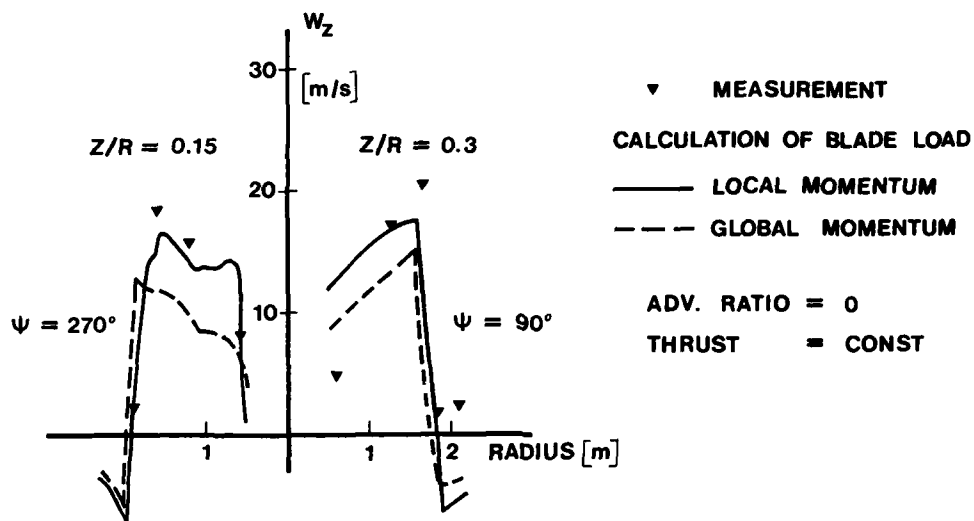Fig. 3: Velocity vectors in the Y-Z plane in hover

Fig. 4: Downwash measurements and calculations in hover
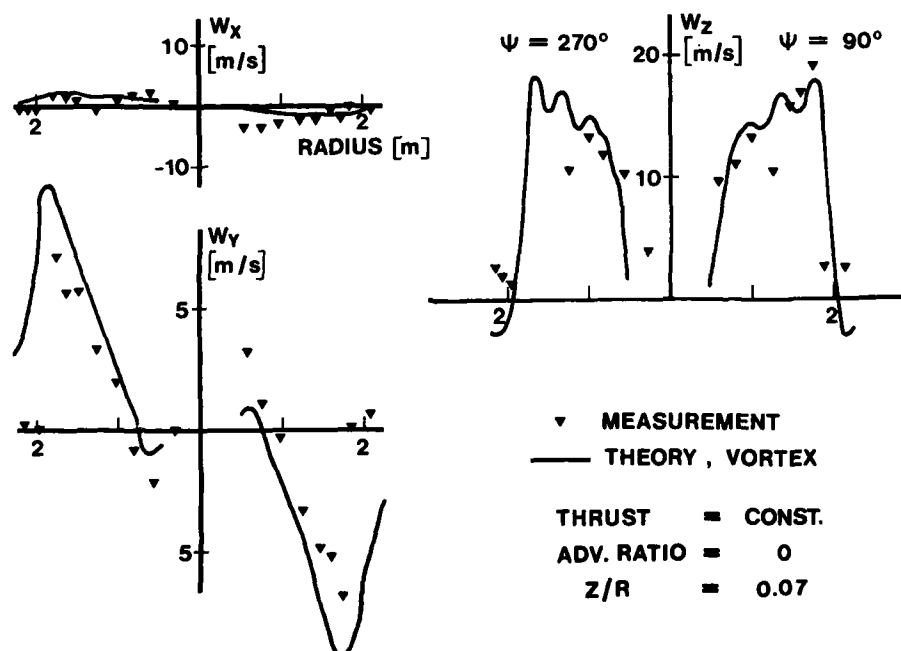at two distances from rotor plane

Fig. 5: Downwash velocities in X-, Y-, Z-direction
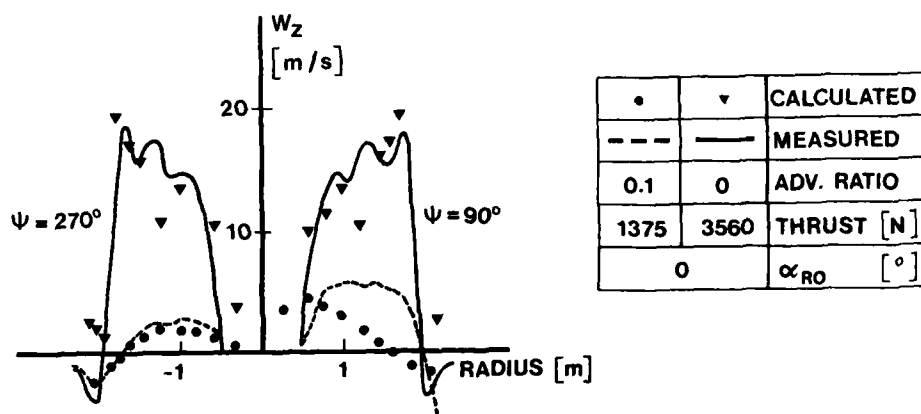(rigid vortex theory, core radius variable)

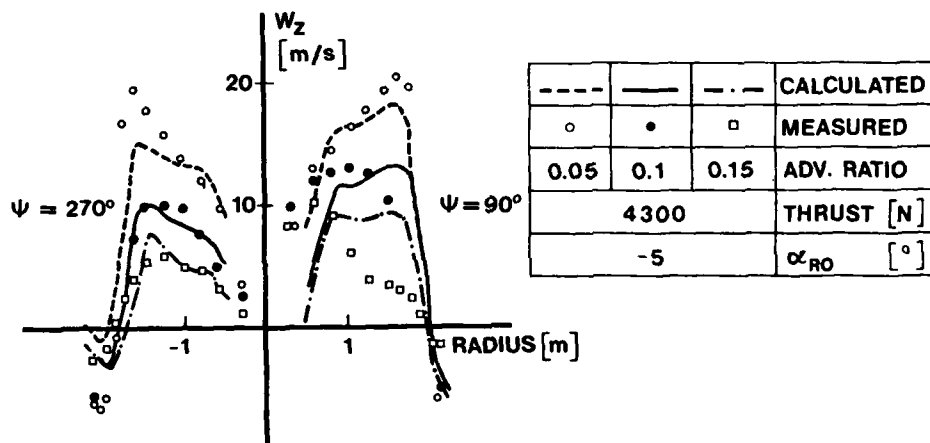**Fig. 6:** Downwash velocities at different advance ratios and constant angle of attack ($\alpha_{Ro}=0^0$)

Fig. 7: Downwash velocities at different advance ratios and constant angle of attack ($\alpha_{Ro}=-5^0$)
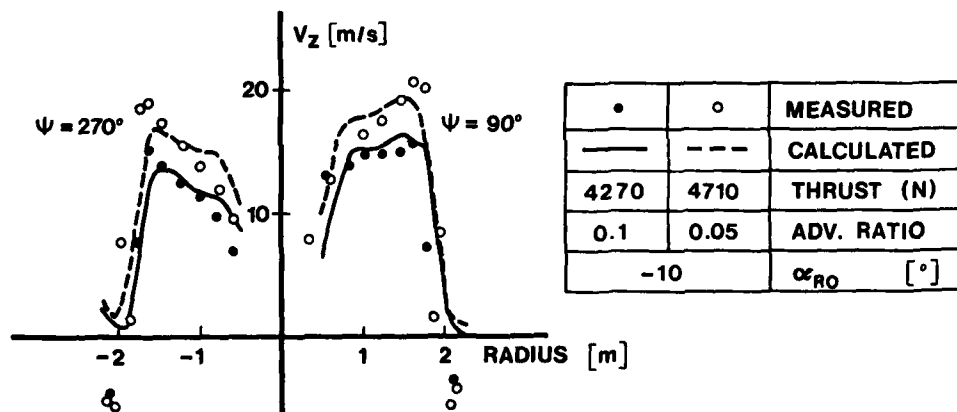
Fig. 8: Downwash velocities at different advance ratios and constant angle of attack ($\alpha_{Ro}=-10^0$)
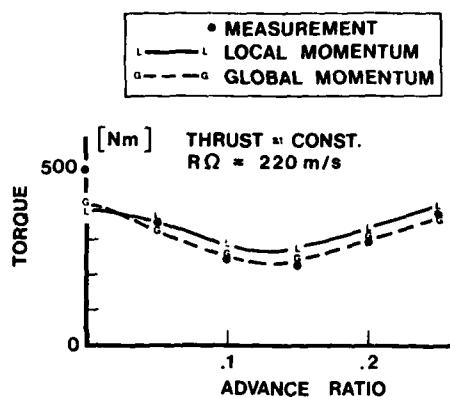
Fig. 9: Rotor torque vs. advance ratio

Fig. 10: Rotor controls vs. advance ratio
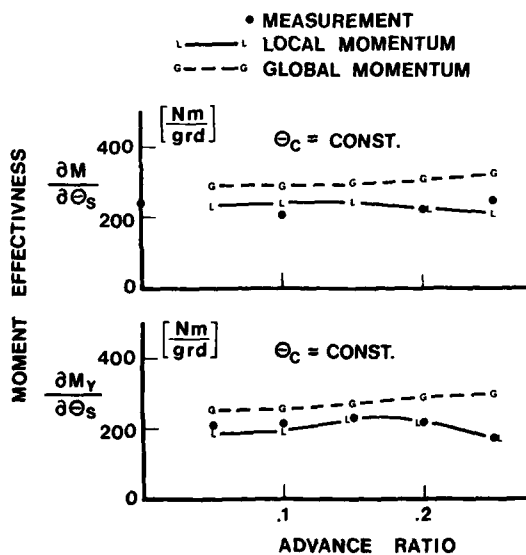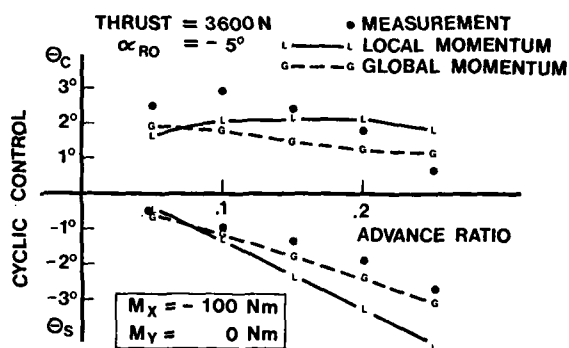
Fig. 11: Hub moment and pitching moment
vs. advance ratio

Fig. 12: Control effectiveness of 1/rev
flapping moment vs. advance ratio
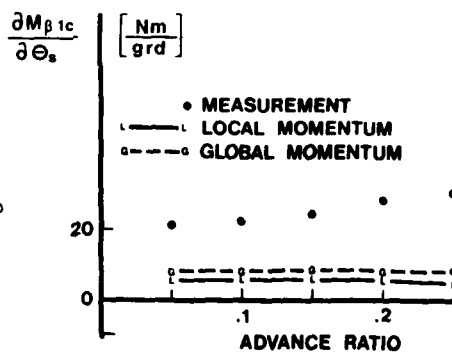
AN APPRAISAL OF ROTOR BLADE-TIP VORTEX INTERACTION AND WAKE GEOMETRY FROM FLIGHT MEASUREMENTS

by

P. Brotherhood
Flight Systems (Bedford) Department,
Royal Aircraft Establishment,
Bedford, UK

SUMMARY

The close radial spacing of leading-edge pressure transducers used as incidence and loading indicators on a Puma helicopter blade has produced a global picture of the effects of blade-tip vortex interaction. Analysis of results has enabled features of the wake geometry to be compared with prediction and the loading action of the tip vortex on the following blade assessed.

LIST OF SYMBOLS

a_{1s}	longitudinal component of blade flapping
c	blade chord
C_L	lift coefficient
C_N	normal force coefficient
$C_{p0.02}$, C_p, C_{p_m}	leading-edge pressure coefficient, suffix m, measured value
e	fraction of tip radius from which vortex trails
h	blade-vortex separation distance normal to rotor disc (Fig 8b)
k	incremental induced velocity factor
ℓ	blade-vortex separation distance parallel to rotor disc (Fig 8b)
n	blade reference number
p	blade surface pressure
q	vortex induced velocity
r	elemental blade radius
r_0	radius of reference circulation on blade
r_1	elemental vortex radius
R	tip radius
t	elapsed time
u	velocity normal to rotor disc (equation (9))
v_{i_0}	mean induced velocity
V	helicopter forward speed
$\bar{V}$	resultant velocity at blade element
V_c	chordwise velocity at blade element
V_n	velocity normal to vortex centre line
V_r	radial velocity at blade element
α	local blade incidence
α_D	rotor disc incidence
α_S	rotor shaft incidence
β_0	blade coning angle
Γ	circulation strength
θ	see Fig 8b
λ	normalised flow velocity perpendicular to rotor disc
μ	advance ratio
ν	reduced frequency $= \omega c/2V_c$
ξ	angle between blade and vortex line (Fig 8e)
ρ	air density
ϕ	see equation (2)
ψ	general azimuth angle; for meaning of suffices refer to the Appendix, section A.1
Ω	blade rotational speed

suffix 0 refers to initial conditions in the absence of blade-vortex interaction; Δ refers to vortex induced increments

1   INTRODUCTION

Using a Puma helicopter as a test vehicle, an extensive series of flight tests have provided a data bank of blade surface pressure and bending strain measurements over a wide range of operating conditions. The main objective has been to investigate blade incidence and stall distribution in the rotor disc together with blade bending moments in order to validate and extend prediction methods. Young[1] describes the vortex ring wake model used and compares predicted loads with those measured on the Puma elsewhere in this current set of papers. Aerodynamic measurements were almost entirely confined to leading and trailing-edges along the outer half of one blade. Some descriptions and results have been published in Ref 2.

Flight tests of a specially developed aerofoil have also been made on the Puma. In these the chordwise pressure distribution was measured on a small length of representative section on a modified blade[3]. Specially developed data reduction programs allow a ready access to all flight data in appropriate format.

Unsteady two-dimensional windtunnel test results of all aerofoil sections used in the various flight tests are also available.

The object of the present paper is to take various key features of the mathematical modelling of the rotor wake required for detailed blade load prediction and as far as possible test each individually using flight test results. Blade-tip vortex interaction plays an important role in producing large local excursions in incidence resulting in fluctuating loads which often limit the operational flight envelope. The global picture which the Puma results present by virtue of the close radial spacing of pressure transducers has enabled various features of the rotor wake, in which the tip vortex is a principal feature, to be investigated.

These are in particular:

(a)   the position in rotor plan view of the intersection of the tip vortex with the following blade,

(b)   the distance of the tip vortex below the following blade,

(c)   the loading action of the tip vortex on the following blade.

It had originally been intended to include a comparison of the collapse of leading-edge suction and divergence of trailing-edge pressure with the relevant break-points given by the dynamic stall model as used in the prediction method, but in the event it has not proved possible to include these results and meet the printing date for the paper.

The approach in the present paper is a pragmatic one of the flight test engineer; a first order analysis is used and any limitations or departures caused by this simplification are discussed when making comparisons with the flight results.

Before discussing the specific topics above, the experimental technique and interpretation of leading- and trailing-edge pressure coefficients will be discussed in the light of flight and tunnel data.

2   EXPERIMENTAL TECHNIQUE AND INTERPRETATION

Pressure transducers recording absolute pressure were installed in the upper surface of one of the four blades of the Puma at 2% and 91% chord at 17 radial locations along the outer half of the blade (Fig 1). A smooth profile was maintained ∵ recessing the leading-edge pressure transducers in shallow depressions in the blade spar.

The leading-edge pressures were intended to give an indication of local blade incidence, with trailing-edge pressure divergence marking the onset of separation. Since the pressure coefficient at any point on an aerofoil in steady conditions is a function of Mach number and incidence, the incidence is uniquely defined by the pressure reading if the Mach number is known. This only applies during attached flow and a more complex relationship exists on a rotor blade where oscillatory conditions apply. Figs 2 and 3 show the variation of leading $(C_{P0.02C})$ and trailing-edge $(C_{P0.9C})$ pressure coefficients from tunnel tests for NACA 0012 section. The Puma blade section is effectively a NACA 0011.4 with the existing trailing-edge tab added but the difference is not expected to produce significant errors in conclusions drawn later in the paper. The relatively low test Mach number is representative of conditions on the retreating blade and the reduced frequency $(\nu = \omega c/2V_c)$ is representative of a once per revolution variation in flight incidence. In attached flow (Fig 2), $C_{P0.02C}$ shows a simple hysteresis about the near linear quasi-steady test condition, while $C_{P0.9C}$ remains essentially constant. With penetration into stall (Fig 3), $C_{P0.02C}$ has a near linear relationship with increasing incidence leading to an increased peak value from which there is an abrupt fall accompanied by an almost simultaneous trailing-edge pressure divergence, both parameters showing pronounced hysteresis during the early stages of reducing incidence. The non-linear behaviour and extensive hysteresis makes quantitative assessment of incidence difficult to achieve when stall is present but in attached flow a single, mean-value, linear relationship between $C_{P0.02C}$ and incidence represents a reasonable, first order approximation during excursions of incidence at main rotor frequency.

With the changes in loading present during blade-vortex interaction, the effective incidence cycle may occur over some 20° of azimuth, *ie* at frequencies about 20 times greater than rotor frequency, or more. This represents a reduced frequency greater than covered during tunnel tests. Also the close passage of blade and vortex is not directly represented by changes in flow present in oscillatory testing. In order to investigate the loading action particularly during blade-vortex interaction, other flight measurements of chordwise pressure distribution are examined. These tests were not made on the NACA 0012 aerofoil but they are used here to illustrate important features used during later analysis in the present paper.

The variation of $C_{P_{0.02C}}$ and normal force coefficient (C_N) for the test section are given in Fig 4. The C_N values were obtained by integration of the 23 chordwise pressures. This particular test result is chosen to include large excursions in loading due to blade vortex interaction without appreciable stall. The detailed correlation of C_N with $C_{P_{0.02C}}$ is strikingly obvious even during blade-vortex interactions which occur in azimuth regions 90 and 270°. From this data C_N is plotted against $C_{P_{0.02C}}$ in Fig 5. Arrows show the sense of increasing azimuth and regions of blade-vortex interaction are also indicated. The hysteresis present during the large interaction at 270° azimuth is associated with incipient stall at maximum C_N. Even so, $\partial C_N / \partial C_{P_{0.02C}}$ is reasonably constant and single valued during slow and rapid changes in loading with varying Mach number. As will be discussed later, these loading changes occur as the blade passes within half a blade chord of the vortex core centre, when due to flow curvature the concept of a simple incidence change is inappropriate. Despite this, the value of $\partial C_N / \partial C_{P_{0.02C}}$ is very similar to that from tunnel tests at lower reduced frequency. These phenomena merit further attention but in the context of the present paper serve to justify the assumptions used later in sections 5 and 6 that the values of $\partial C_N / \partial \alpha$ and $\partial C_N / \partial C_{P_{0.02C}}$ obtained from appropriate tunnel tests of NACA 0012 section at lower reduced frequency may reasonably be used during first order blade-vortex interaction analysis.

3   METHOD OF ANALYSIS

An example of the variation of $C_{P_{0.02C}}$ against azimuth angle is given in Fig 6 which shows separate plots for each spanwise station, with displaced origins. The blade-tip vortex crossing points from the immediately preceding blade have been superimposed and the correlation with the waves in $C_{P_{0.02C}}$ is immediately apparent. Although not marked in the present example, the correlation of other waves with blade vortex intersections from other blades may also be made but are not discussed in the present paper as in general they produce much smaller load fluctuations. The radial variation of $C_{P_{0.02C}}$ on the retreating blade (Fig 7) shows even more graphically the characteristic positive and negative peak characteristic of incidence and loading change associated with near passage of the tip vortex. At high values of thrust coefficient and advance ratio, compressibility effects, separated flow and stall blur these characteristic features. In the following analysis of wake geometry only $C_{P_{0.02C}}$ records which display smooth, well-behaved blade-vortex characteristics are considered. The suffix 0.02C will be dropped, C_p meaning $C_{P_{0.02C}}$ unless otherwise stated.

The following simplifying assumptions are made:

(1)   vortex induced velocities are small compared with blade chordwise velocities;

(2)   maximum and minimum blade loadings occur in the outer regions of the vortex with all vorticity present enclosed within an inner, viscous core;

(3)   the time interval between positive and negative loading peaks is the same as that between corresponding incidence peaks;

(4)   three-dimensional effects in blade radial loading are neglected;

(5)   the vortex is undistorted by the passing blade;

(6)   flow conditions are linearised during the interaction, *ie* a line vortex is assumed at the appropriate angle to the blade travelling at constant speed through the vortex;

(7)   the vortex line is parallel to the rotor disc;

(8)   the local blade leading-edge pressure is proportional to incidence and the square of the local instantaneous chordwise velocity.

As mentioned earlier, this is a deliberately chosen base-line approach, variations from which are discussed and qualified when the results obtained in this manner are compared with predictions. The principles involved are discussed below and a summary of expressions used with minimal derivation is given in the Appendix.

The analysis used depends on the spacing of loading peaks with azimuth and with radius. The derivation of the vertical spacing between blade and vortex centre line from flight data (Appendix, section A.2) is based on the property that for any separation, h ,

the contrary effects of flow direction and strength produce notional maximum and minimum changes in incidence where θ is 45° and 135° as seen in Fig 8b, as the blade passes near the vortex. This property is independent of vortex strength. If the blade chord were normal to the vortex line during passage the distance travelled between positive and negative peaks would then equal 2 h. The method requires the measurement of the peak to peak separation distance from flight data.

In practice the blade chord is not normal to the vortex line and the analysis requires the angle to be known. It is derived from flight data by means of coordinates x' and y' identified in Fig 8d.

Coefficients C_p are based on chordwise velocity in the absence of blade-vortex interaction, so that when present, changes in C_p in addition to those from incidence are caused by chordwise induced velocity. The contribution is dependent on the initial value of incidence, α_0 (or C_{p_0}). Fig 9 shows the increment ΔC_p when assumed proportional to α only and also for ΔC_p proportional to $V_c^2 \alpha$ representative of high α_0 on the retreatment blade. One peak is sharpened and the other rounded out. Knowing the direction of rotation of the vortex - during the encounter the vertical position, ie whether above or below the blade may be determined in principal. In practice as discussed later this proved inconclusive. An important point to notice is that peak to peak amplitude and separation are not greatly affected by the inclusion of the chordwise velocity terms.

Having determined blade-vortex separation, it is now possible to compare the incremental blade loading during interaction with that predicted through assigning some particular strength to the vortex, based on the loading on the blade that generated the vortex. Two bound circulation strengths are chosen for this purpose, that at 0.95R as representative of the tip loading and the other the maximum value occurring at any inboard position on the blade.

Turning now to the blade-vortex geometry used in the WHL/RAE mathematical model described by Young[1]. The blade-tip vortex crossing point and angle in plan view are derived by assuming an undistorted cycloidal path originating in the blade tip (Appendix, section A.1). The element of vortex beneath each intersection point is assumed to be convected downwards with a mean value of induced velocity combined with a longitudinal wedge shaped increment leading to a 'Glauert' type distribution. With these assumptions the blade-vortex separation using measured input conditions of thrust, shaft incidence, longitudinal blade root flapping angle and coning angle has been estimated (Appendix, section A.3) and compared with the results derived from measured blade-vortex interaction characteristics previously described.

4   THE BLADE-VORTEX CROSSING POSITIONS IN PLAN VIEW

A comparison of measured and estimated blade vortex crossing points is given in Fig 10. The results are compared at four radial positions over a range of advance ratio.

Theoretical estimates of crossing position as given by a cycloidal path, have been superimposed on the flight results (Appendix, equation (A-1)), and it will be seen that vortex origins of 1.0R and 0.95R bracket the majority of results.

The measured results are based on the assumption that the vortex crossing point lies halfway between the maximum and minimum values of C_p , even though we have already seen that this is not really the case, due to the effect of chordwise velocity components from the vortex. However, this assumption was made because, as will be shown in section 5 the measured shape of the C_p variation is not always as expected and in the majority of cases the error involved is acceptably small. Errors in the value of flight speed and in particular sideslip[2] can cause biasing errors, care has been taken to minimise sideslip and any corrections required have been made. The results cover a range of thrust coefficients and the results are indistinguishable on this count. During the flight tests some were made over a range of disc loading but at constant advanced ratio, on the basis that with increasing induced velocity, the general rotor wake would show more contraction and effectively move the tip vortex origin inwards with increased disc loading. Although in the event the range of disc loading covered was limited no such trend was discernable.

The blade-vortex crossing angles obtained from flight results (Appendix, equation (A-6)) are given in Fig 11. It should be emphasised again they result entirely from consideration of the measured orientation of maximum and minimum values in the plane of the rotor disc. Theoretical estimates of vortex origin at 0.95R and 1.0R at μ = 0.263 are also included (Appendix, equation (A-2)). Agreement is good and although all results would not be bracketed by the limits, the results confirm the orthogonal properties of the flow model used to describe the blade-vortex interaction.

5   THE DISTANCE OF THE TIP VORTEX BELOW THE BLADE

The distance of the vortex below the blade at intersection obtained from flight data is given in Fig 12 for a range of advance ratio (Appendix, equation (A-7)). All results have been plotted positively, ie as occurring below the blade and this is discussed later on in the section under the validity of assumptions 5 and 8. Part of the data reduction process involves hand plotting of data which exhibits scatter between close points but

with a well-defined trend over larger intervals from which the required coordinates were obtained. The particular range of results were taken during one flight but others available show the same trend. The seeming shortage of points is of course due to the fact that only well-defined and characteristically shaped vortex crossings have been analysed. Although the Mach number is relatively low (0.4), compressibility effects at high lift coefficient distort the linear relationship of incidence with C_p and make the analysis of some data impossible in the context of the method used in the present analysis.

Theoretical estimates with vortex origin at 1.0R are also included. Reasonable agreement is obtained at $\psi = 270°$ on the retreating blade and outwards to the blade tip. Between $\psi = 90°$ and $\psi = 180°$ the trend is much flatter than predicted.

The limitations of the simplified baseline approach used are now considered using the numbering in section 3.

Assumption (1): This is not a serious limitation over the range of blade radius and advance ratio covered.

Assumption (2): Using the experimental results of Cook[4] to define the region of irrotational flow where velocity is inversely proportional to radius, the region lies roughly beyond $(h/c) = 0.2$ on the advancing blade and beyond $(h/c) = 0.3$ on the retreating blade. It will be seen that the flight results satisfy these conditions on the retreating blade but are borderline in some cases on the advancing blade.

Assumption (3): As discussed in section 2, C_N (or C_L) appears in phase with C_p, as incidence is the main forcing element this seems a reasonable assumption.

Assumption (4): This is a more serious over-simplification. The radial variation of incidence imposed by the vortex imposes a notional radial loading pattern. The resulting changes to the trailing vortices redistribute the loading, pushing the positive and negative peaks further apart and rounding them.

Hancock[5] has analysed the case of a line vortex normal to an infinite wing which approximates to blade-vortex interaction on the advancing blade. On the retreating blade interactions are oblique, ie $\xi = 40-60°$, not $90°$ as considered by Hancock. At the smallest blade-vortex separation considered by Hancock, ie $(h/c) = 0.8$, the maximum or minimum loading occurs at $(\ell/h) = 1.5$ rather than the value of near unity given by the simplified approach used in the present analysis. Assuming his analysis to hold, then the points on the retreating blade could be plotted at distances some 70% of values shown.

The points on the advancing blade are relatively much closer to the blade and lifting line methods of estimation are clearly inadequate. If, however, the flattened trend is a correct one, this is consistent with the expectation of a reduced general level of induced velocity on the advancing side of the rotor disc.

Assumptions (5) and (8): These are considered together. The condition that the chordwise velocity increment contributes to C_p (Fig 9) theoretically enables the orientation of blade and vortex, ie whether above or below to be determined. Consideration of a large number of examples has not shown this to be possible with any degree of certainty in practice. Because the results more or less agree with the theoretical trend the vortex position is plotted below the blade. The sensitivity of estimated values to possible errors in the main flight input parameters is shown in Fig 13, together with the estimated error band in measured C_p coordinates. Plotting the results inverted is well outside these sensitivities and this contrary interpretation is considered improbable particularly on the retreating blade with its higher values of h/c.

There is evidence that the second peak is frequently more rounded than the first, indicating possible distortion of the vortex or its path during the passing. On a related theme, in certain records, an uncharacteristic C_p trace or adjacent pair of traces is present during blade-vortex interaction. When it occurs it is in the region $\psi = 270°$, $(r/R) = 0.75$. The reason is unknown and until satisfactorily answered some lingering doubt must remain on the relative position of blade and vortex although plotting them below the blade gives reasonable agreement with the trend using the Glauert distribution but which of course is itself an approximation.

Assumptions (6) and (7): These are considered reasonable in the cases analysed and of lesser importance than assumption (4).

Accepting the trend of the experimental measurements but bearing in mind the qualifications and limitations discussed an assessment of the loading resulting from the blade-vortex separation is made in the following section.

6   THE LOADING ACTION OF THE TIP VORTEX ON THE FOLLOWING BLADE

To determine the loading action of the tip vortex its strength must be determined. The radial distribution of C_p is shown in Fig 14 for a typical azimuth angle at which the tip vortex will trail and interact with the following blade. A curve of the product of V_c and C_p representing the strength of the bound circulation has been included.

The maximum at 0.65R, itself a raised value due to blade-vortex interaction, is clearly visible in this case. The maximum value of C_p at this point, or elsewhere on the blade as it occurs has been used to obtain the lift coefficient, C_{L_0} , for the calculation of one reference value of circulation strength. The other is the circulation strength at 0.95R as representative of the tip loading. Using C_{L_0} values as specified above at the appropriate azimuth angle of the originating blade and the blade-vortex separation evaluated from flight results the estimated vortex induced peak to peak loading, ΔC_p , has been determined from the Appendix, equation (A-10), using a simple lifting line model in which the notional induced incidence change is directly translated into lift and can be thought of as an upper limit to the resultant loading. The measured induced loading, ΔC_{p_m} , has been normalised by the estimated value to form a loading ratio and plotted against h/c in Fig 15. Only the results from intersections on the retreating blade are presented because of their higher h/c values and increased reliability. It should be added that the magnitude of ΔC_p as calculated is independent of whether the vortex lies above or below the blade.

Supposed trend lines have been added through each set of points on the basis that both curves eventually become parallel to the 'x' axis. The higher curve based on the tip loading represents an anomaly in appearing to pass through $(\Delta C_{p_m}/\Delta C_p) = 1$ but there is insufficient data to be certain. The lower curve based on the maximum value of circulation appears as though it might approach the vicinity of unity at higher values of h/c .

It is useful to consider the length of time the portion of tip vortex has existed before interaction with the following blade. At advance ratio $\mu = 0.26$ for example, this corresponds to a minimum value of 71° of rotation of the rotor or some 17 chord lengths travelled at the tip of the advancing blade, to a maximum of 124° or 30 chord lengths at the tip of the retreating blade. The measurements of Ref 4, which were made as a full scale rotor on a test tower using hot wire anemometry indicated that the tip vortex was effectively rolled up by 70° of rotation of the rotor, there was minimal reduction in vortex peak tangential velocity after 150° ageing and the circulation in the tip vortex was approximately half that expected from the peak loading near the tip.

If in the flight test results the trend of Ref 4 were repeated and only half the maximum circulation appeared during blade vortex interaction then all the results would be expected to be below $(\Delta C_{p_m}/\Delta C_p) = 0.5$ in Fig 15 and this is clearly not so.

The loading and circulation during the rotor tower tests of Ref 4 are similar to hover conditions and exhibit a pronounced loading and circulation peak near the tip. In forward flight the circulation is generally more uniform and may give a higher relative strength of tip vortex. A more important consideration is that as previously mentioned, three-dimensional effects mean that all h/c values as plotted are expected to be over-estimated by some 30% at (h/c) = 0.8 and probably more at lower values of separation as mentioned in section 5. This effect would lower the loading ratio *pro rata* resulting in a value in the region of 0.5 at (h/c) = 0.8, and somewhat more or less depending on whether the reference circulation is taken at 0.95R or the maximum value further inboard. The flight results lie at the upper limit of what might be expected following Ref 4, particularly at the higher range of h/c but overall may be considered to show a fair measure of agreement.

At the lower values of h/c , $\Delta C_{p_m}/\Delta C_p$ has reduced markedly to the region of 0.3. It should be noted that in the calculation of ΔC_p from the Appendix, equation (A-10), the value $\partial C_p/\partial \alpha$ is required and this has been obtained from tunnel tests as described in section 2. Although it is clearly demonstrated that the derivative $\partial C_p/\partial \alpha$ is sensibly constant over a range of transient conditions, incidence as defined by two-dimensional tunnel tests may not be directly relatable to localised induced velocity changes at low h/c.

The RAE/WHL loads prediction program uses the Glauert type trapezoidal induced velocity distribution for placement of the vortex rings which represent the tip vortex. Radial blade loadings gradients are accommodated by a series of half vortex rings, which represent trailing vorticity. A vortex core diameter of 0.1C is also assumed. Attenuation of the vortex induced loading peaks is therefore represented. The 12 half rings employed were originally incorporated in the model to improve the incidence distribution on the advancing blade and the detailed effect on the tip vortex induced loading has not yet been assessed in detail.

The emphasis in the present paper is the validation and extension of the RAE/WHL loads prediction program and in certain respects the prescribed wake and lifting line methods used have prompted the approach taken. No attempt has yet been made to assess the extent to which the program produces the attenuation in vortex induced loading shown in Fig 15 or whether lifting surface methods as described by Johnson in Ref 6 are required.

7   SUMMARY AND CONCLUSIONS

The close radial spacing of leading-edge pressure transducers used as incidence and loading indicators has produced a global picture of the effects of blade-vortex interaction.

The interaction of the blade with the tip vortex trailed from the immediately preceding blade is particularly important in that it produces the largest incremental loading. Over a range of forward speed and thrust coefficient the results show that all the blade vortex intersections in plan view lie between undistorted cycloidal tip vortex loci originating at 0.95R and the extreme tip.

It has been found possible to estimate the angle between blade and vortex centre line from consideration of the radial and azimuthal spacing of vortex induced loading peaks. The results are in good agreement with estimates using cycloidal tip vortex loci at intersections with the immediately preceding blade.

Using a simplified lifting line model of the blade vortex interaction, the vertical separation of blade and vortex centre line at intersection has been derived from the spacing and orientation of vortex induced loading peaks. On the retreating blade, where the analysis is most reliable, the vertical separation derived from flight measurements agrees with prediction assuming a Glauert type induced velocity distribution. However, local changes in the distribution of trailing vorticity are neglected in the simplified derivation of separation distance. Taking trailing vorticity into account reduces the derived separation distance. The flight results therefore indicate that the Glauert type distribution used over-estimates the distance of the vortices below the blade in the region of the retreating blade.

In the region of the advancing blade tip, the derived separation is in most cases considerably less than predicted but the method of analysis is least reliable in this region.

Using the derived vertical separation and the tip vortex strength estimated from the loading on the originating blade, the vortex induced loading has been estimated using a simple lifting line model. The estimate, which may be considered an upper limit, has been used to normalise the measured loading increment to form a loading ratio. At blade-vortex separation, $(h/c) = 0.8$ on the retreating blade where the results are considered most reliable, the loading ratio is of the order 0.75. If the probable reduced separation value is used in the estimated loading, the ratio reduces to the order of 0.5. The loading ratio falls to the region of 0.25 at the lowest derived separation distances.

Overall the blade pressure and strain measurements are providing an effective tool in the validation and extension of the RAE/WHL rotor load prediction program.

REFERENCES

1   C. Young: "Development of the vortex ring wake model."

2   P. Brotherhood, C. Young: "The measurements and interpretation of rotor blade pressures and loads on a Puma helicopter in flight." 5th European Rotorcraft and Powered Lift Aircraft Forum, 1979

3   P.G. Wilby, M.J. Riley, Judith Miller: "Some unsteady aerodynamic effects on helicopter rotors." 7th European Rotorcraft and Powered Lift Aircraft Forum, 1981

4   C.V. Cook: "The structure of the rotor blade tip vortex." AGARD, Aerodynamics of Rotor Wings, 1972

5   G.J. Hancock: "Aerodynamic loading induced on a two-dimensional wing by a free vortex in incompressible flow." The Aeronautical Journal, June 1971

6   Wayne Johnson: "A lifting surface solution for vortex-induced air loads." AIAA Journal, Vol.9, No.4, April 1971

APPENDIX

A.1 THEORETICAL ESTIMATION OF BLADE AND VORTEX GEOMETRY FOR FOUR-BLADED ROTOR

Assuming the tip vortex centre line in plan view (Fig 8a) is the undistorted locus of a point in the blade tip, it can be shown that the coordinate of the point of intersection of the vortex trailed from the nth blade with blade 1 are given by the equations

$$\left. \begin{array}{l} \dfrac{r}{R} \sin \psi_1 = e \sin\left[\psi_0 + (n - 1)\dfrac{\pi}{2}\right] \\[2ex] \dfrac{r}{R} \cos \psi_1 = e \cos\left[\psi_0 + (n - 1)\dfrac{\pi}{2}\right] + \mu(\psi_1 - \psi_0) \end{array} \right\} \qquad \text{(A-1)}$$

where ψ_0 is the azimuth angle of blade 1 at $t = 0$

ψ_1 is the azimuth angle of blade 1 at intersection after time t

eR is the blade radius from which the vortex trails.

Then ψ_0 and ψ_1 may be evaluated for given values of e, r/R, μ and n .

Also the blade vortex line crossing angle is given by

$$\phi - \frac{\pi}{2} = \tan^{-1}\left(\frac{e \sin \psi' + \mu}{e \cos \psi'}\right) \qquad \text{(A-2)}$$

where $\psi' = \psi_0 + (n - 1)\dfrac{\pi}{2}$

and $\xi = \phi - \psi_1$.

A.2 ESTIMATION OF THE DISTANCE OF THE TIP VORTEX BELOW THE BLADE FROM THE MEASURED ORIENTATION OF LEADING-EDGE PRESSURE COEFFICIENT PEAKS

Flight results are reduced to coefficient form using the expression

$$p = C_{p_m}\left(\tfrac{1}{2}\rho V_{c_0}^2\right)$$

where suffix m refers to measured values, and V_{c_0} is the chordwise velocity in the absence of vortex induced velocity.

During blade vortex interaction

$$\Delta C_{p_m} = \frac{\partial C_p}{\partial \alpha} \Delta \alpha + \frac{\tfrac{1}{2}\rho C_{p_0}\left(v_c^2 - v_{c_0}^2\right)}{\tfrac{1}{2}\rho v_{c_0}^2}$$

or

$$\Delta C_{p_m} = \frac{\partial C_p}{\partial \alpha} \Delta \alpha + 2C_{p_0}\frac{\Delta V_c}{V_{c_0}} \qquad \text{to the first order.} \qquad \text{(A-3)}$$

From Fig 8b and c

$$\Delta V_n = q \sin \theta \quad \text{and} \quad \Delta V_c = - \Delta V_n \cos \xi , \quad \text{or} \quad \Delta V_c = q \sin \theta \cos \xi ;$$

$$q = \frac{\Gamma}{2\pi r_1} \quad \text{and} \quad r_1 = \frac{h}{\sin \theta} , \quad \text{or} \quad q = \frac{\Gamma \sin \theta}{2\pi h} .$$

The change in incidence α is given by

$$\Delta \alpha = \frac{q \cos \theta}{V_{c_0}} .$$

Combining expressions with equation (A-3) gives

$$\Delta C_{p_m} = \frac{\Gamma(\partial C_p/\partial \alpha)}{4\pi h V_{c_0}} \left[- 2\alpha_0(1 - \cos 2\theta) \cos \xi + \sin 2\theta\right] . \qquad \text{(A-4)}$$

Maximum and minimum values are given by

$$\theta = \tfrac{1}{2} \tan^{-1}\left(\frac{1}{2\alpha_0 \cos \xi}\right) \tag{A-5}$$

noting that when the effects of chordwise velocity increments are zero, *ie* $\alpha_0 = 0$

$$\theta_1 \quad \text{and} \quad \theta_2 \; = \; 45^\circ \text{ and } 135^\circ \text{ respectively.}$$

In order to estimate the vertical passing distance, h, the blade crossing angle, ξ, is required. This is obtained from the flight results by measurement of the coordinates x', y' of Fig 8d. A diagram of the blade vortex crossing is given in Fig 8e where $AC = \Delta r$, $BD = \bar{V}_0 \Delta t$ and $\bar{V}_0$ and Δt are the blade resultant velocity and crossing time respectively. After manipulation it can be shown that

$$\xi = \tan^{-1}\left(\frac{V_{c_0}}{V_{r_0} - (\Delta r/\Delta t)}\right) = \tan^{-1}\left(\frac{(r/R) + \mu \sin \psi_1}{-\mu \cos \psi_1 - (180/\pi R)(\Delta r/\Delta \psi)}\right) \tag{A-6}$$

where ψ_1 is the blade azimuth angle at intersection and Δr and $\Delta \psi$ correspond to the radial and azimuthal increments x' and y' of Fig 8d.

The vortex crossing velocity normal to the centre line

$$V_{n_0} = - V_{c_0} \cos \xi + V_{r_0} \sin \xi$$

$$= - \Omega r \cos \xi - V \sin(\psi_1 + \xi)$$

where V is the flight speed.

From Fig 8b,

$$h = \ell_1 \tan \theta_1 = \ell_2 \tan \theta_2$$

then

$$\Delta t = \frac{\ell_1 - \ell_2}{V_{n_0}}$$

$$= - \frac{h \cot \theta_1 - h \cot \theta_2}{\Omega r \cos \xi + V \sin(\psi + \xi)}$$

or

$$\frac{h}{c} = - \frac{\Delta \psi \pi}{180} \frac{R}{c} \left[\frac{\mu \sin(\psi_1 + \xi) + (r/R) \cos \xi}{\cot \theta_1 - \cot \theta_2}\right] \tag{A-7}$$

note that ψ_1 is related to the position of maximum and minimum C_p by

$$\frac{\ell_1}{\ell_1 - \ell_2} = \frac{\tan \theta_2}{\tan \theta_1 - \tan \theta_2} \quad . \tag{A-8}$$

A.3 THEORETICAL ESTIMATION OF THE DISTANCE OF THE TIP VORTEX BELOW THE BLADE

The rotor disc incidence α_D is given by

$$\alpha_D = \alpha_S + a_{1s}$$

where α_S is the measured shaft incidence, and a_{1s} the measured blade root flapping angle.

The mean flow through the rotor disc is given by the usual expression

$$\tan \alpha_D = \frac{\lambda}{\mu} + \frac{st_c}{2\mu(\mu^2 + \lambda^2)^{\frac{1}{2}}}$$

and

$$\lambda = \frac{V \sin \alpha_D - v_{i_0}}{\Omega R} \quad .$$

A longitudinal variation of induced velocity in which the tip vortex is imbedded has been assumed, of the form

$$u = V \sin \alpha_D - v_{i_0}\left(1 + K \frac{r}{R} \cos \psi\right) \quad .$$

In the RAE/WHL program K is a function of the wake angle and the values used in the present analysis lie in the range 1.3 to 1.5.

It is assumed that as a portion of the tip vortex travels backwards parallel to the longitudinal axis it is subject to a downward acceleration given by

$$\Delta u = K v_{i_0} \quad \text{in} \quad \frac{R}{\mu \Omega R} \quad \text{seconds}$$

or

$$\dot{u} = K v_{i_0} \mu \Omega \quad .$$

The length of time the portion of tip vortex is subject to this acceleration before intersection in plan view is

$$t = (\psi_1 - \psi_0) \frac{\pi}{180} \frac{1}{\Omega} \quad .$$

The distance of the vortex centre line below the blade non-dimensionalised by the blade chord and including the effect of coning angle β_0 is given by

$$\frac{h}{c} = \frac{t}{c}\left(u_0 + \dot{u} \frac{t}{2}\right) - \frac{R}{c} \beta_0 \left(1 - \frac{r}{R}\right) \qquad (A-9)$$

where u_0 is the value of u when $\psi = \psi'$, the blade azimuth at the generation of the intersecting portion of the tip vortex.

A.4 ESTIMATION OF THE MAGNITUDE OF VORTEX INDUCED LOADING

In this estimation the contribution to ΔC_p from chordwise induced velocity is neglected since the effect nearly cancels in its contribution to peak to peak amplitude.

On the blade from which the vortex trails

$$L = \rho (\Omega r_0 + V \sin \psi') \Gamma \quad \text{at radius} \quad r_0$$

or

$$\Gamma = \frac{c C_{L_0}}{2} (\Omega r_0 + V \sin \psi') \quad .$$

On the intersecting blade, the maximum and minimum values of incidence α occur when $\theta_1 = 45°$ and $\theta_2 = 135°$, *ie* when the blade is $\sqrt{2} h$ from the vortex centre line

or

$$v_{i_{peak-peak}} = \frac{2\Gamma}{2\pi \sqrt{2} h \sqrt{2}} = \frac{\Gamma}{2\pi h}$$

and

$$\Delta \alpha = \frac{\Gamma}{2\pi h} \frac{1}{\Omega r + V \sin \psi'}$$

or

$$\Delta C_p = \frac{\partial C_p}{\partial \alpha} \frac{C_{L_0}}{4\pi} \frac{c}{h} \frac{(r_0/R) + \mu \sin \psi'}{(r/R) + \mu \sin \psi_1} \quad . \qquad (A-10)$$
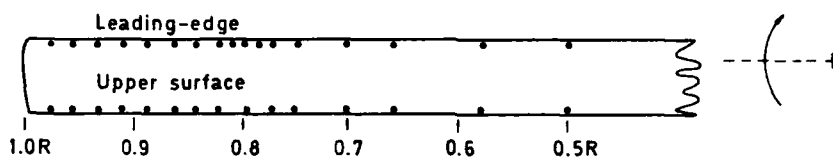
Fig 1 Location of pressure transducers
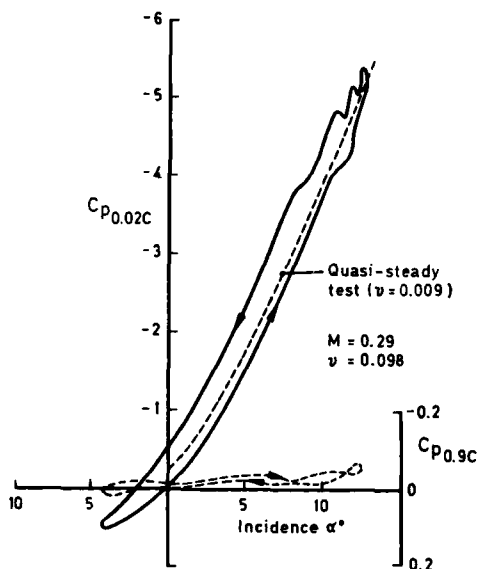
Fig 2 Leading-edge and trailing-edge pressure coefficients in attached flow
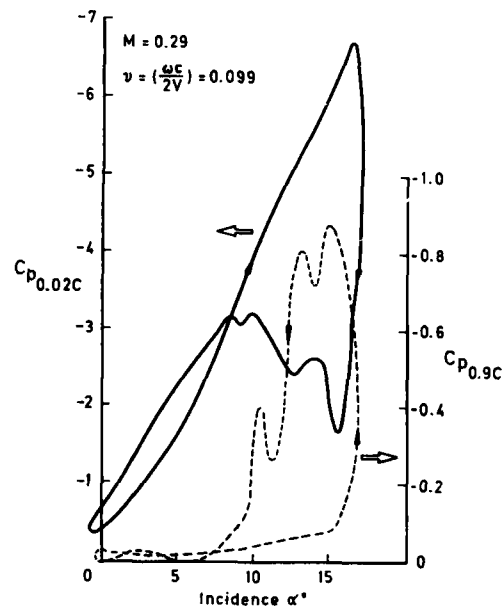
Fig 3 Leading-edge and trailing-edge pressure coefficients with separated flow
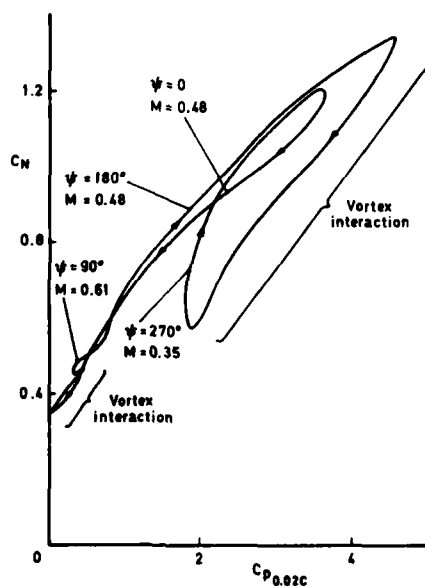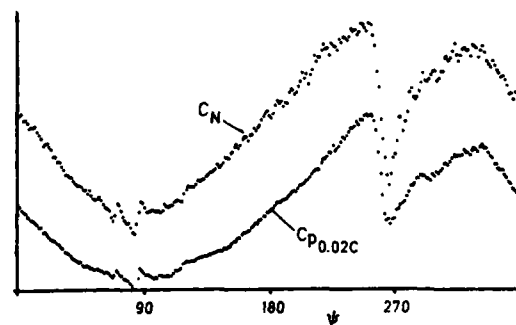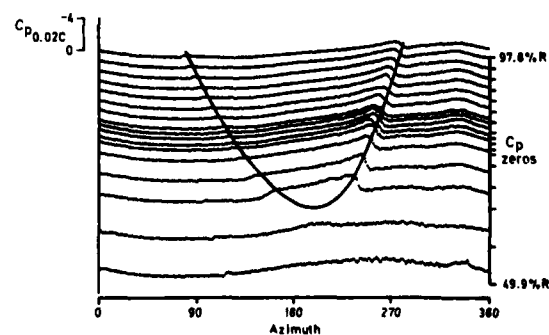

Fig 5 Variation of C_N with $C_{p_{0.02C}}$ including blade-tip vortex interaction. Flight measurements, section RAE 9647

Fig 4 Comparison of normal force coefficient and leading-edge pressure coefficient

Fig 6 Leading-edge pressure coefficients with estimated blade-tip vortex intersection superimposed $\mu = 0.24$
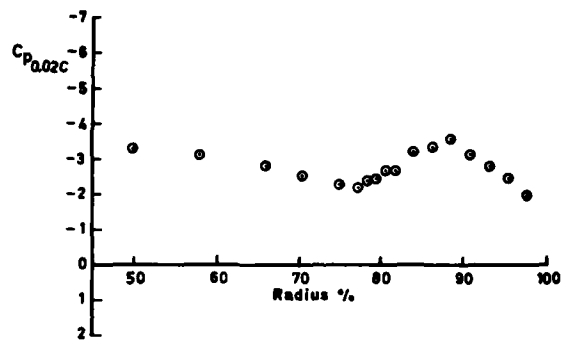
Fig 7 Example of blade-vortex interaction,
$\psi = 265°$, $\mu = 0.236$

(a)

(b)

(c)
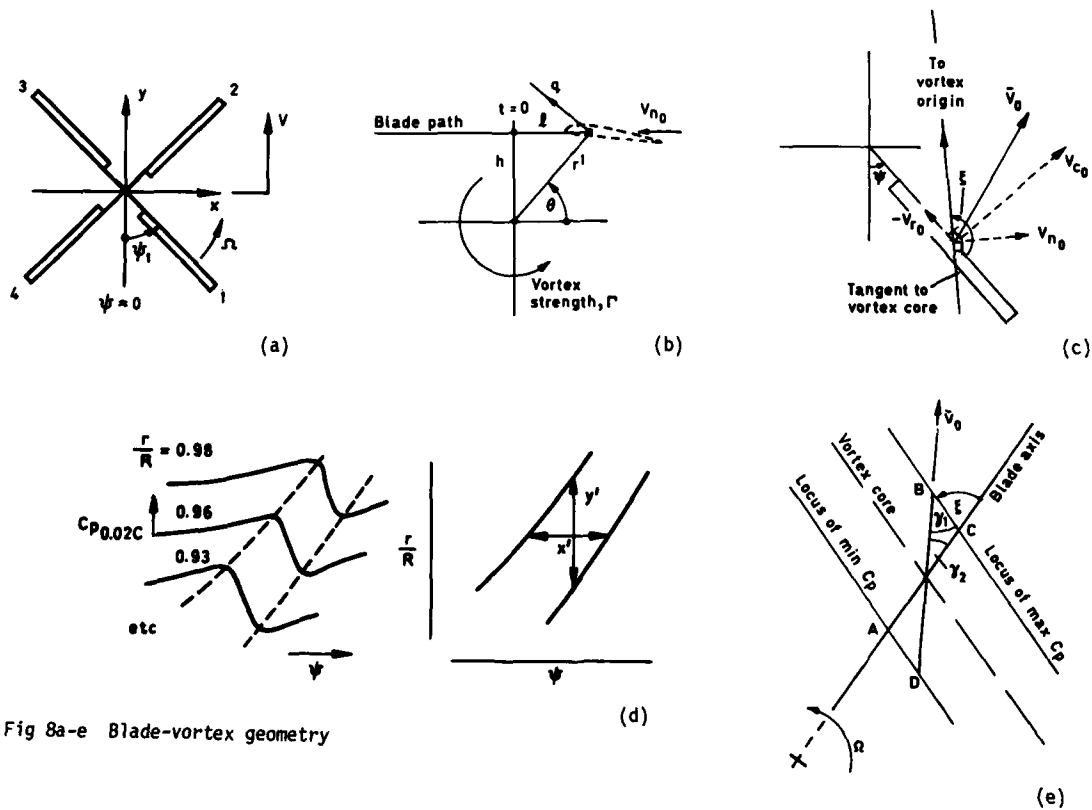
Fig 8a-e   Blade-vortex geometry

(d)

(e)
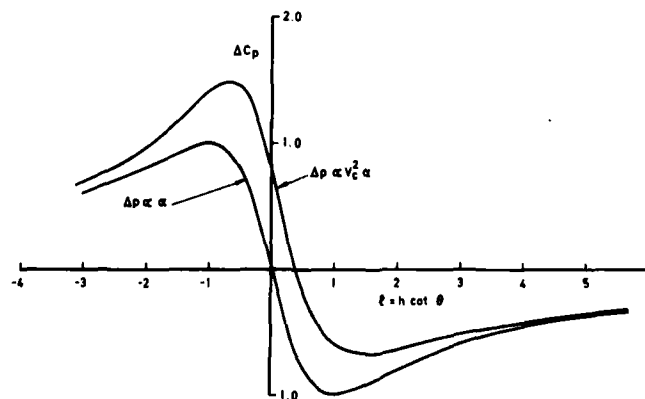
Fig 9   An example of the estimated effect of blade-vortex interaction on
leading-edge pressure coefficient
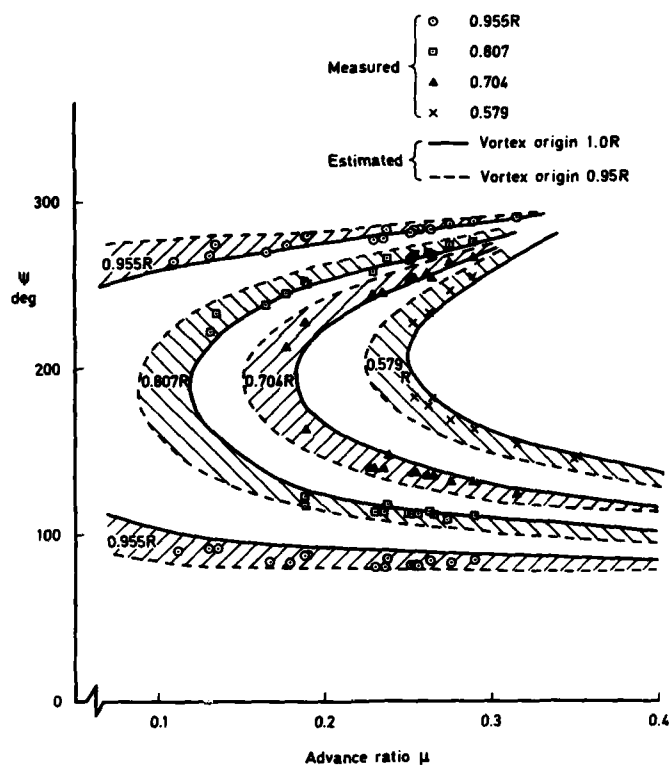
Fig 10   Comparison of measured and predicted azimuth angles at blade-vortex
intersection (in plan) from the previous blade
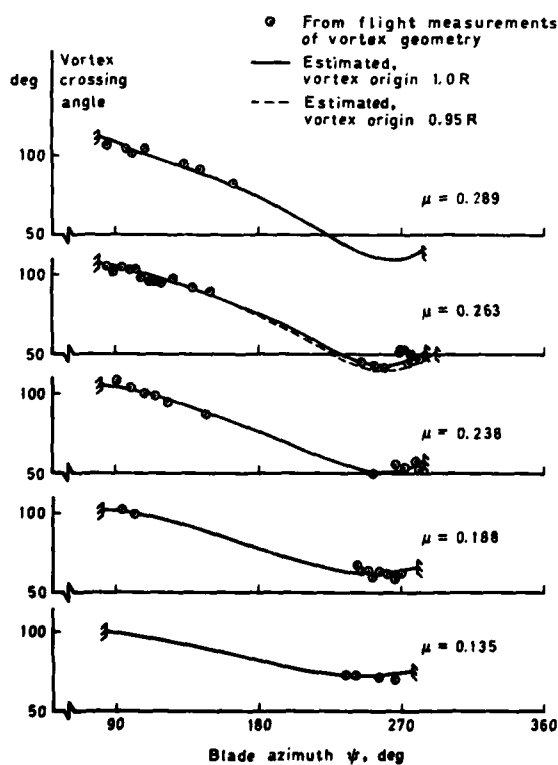
Fig 11   Blade-vortex crossing angle at inter-
section (in plan) for a range of
advance ratio
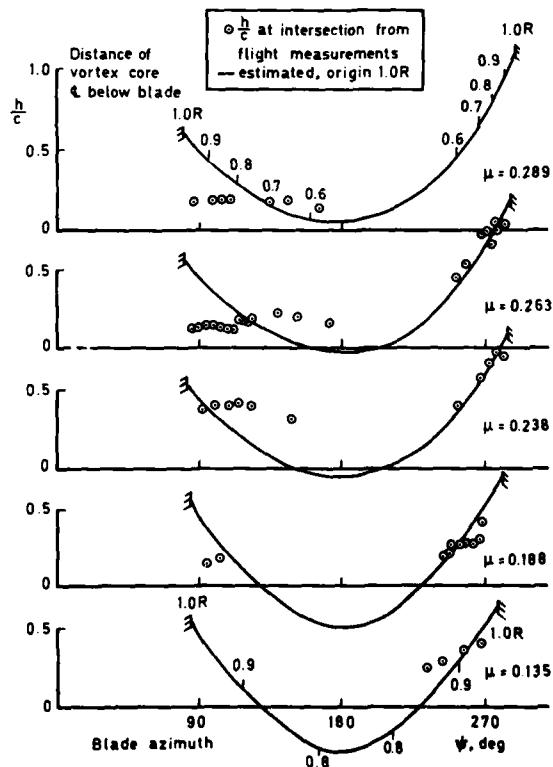
Fig 12   Distance of vortex C_L below following
blade at crossing point as a fraction
of blade chord for a range of advance
ratio
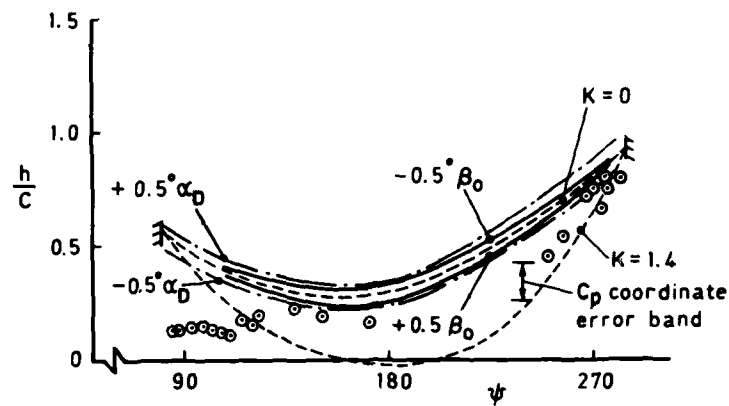
Fig 13 Sensitivity of estimated h/c to blade
coning angle, disc incidence and down-
wash factor, $\mu = 0.263$
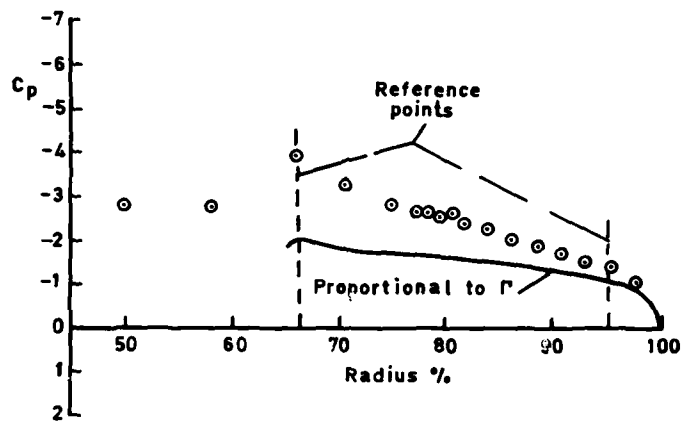
Fig 14 Example of C_p and Γ variation on
blade from which tip vortex trails

———x Maximum Γ on originating blade
‒ ‒ ‒ ⊙ Γ at 0.95R on originating blade
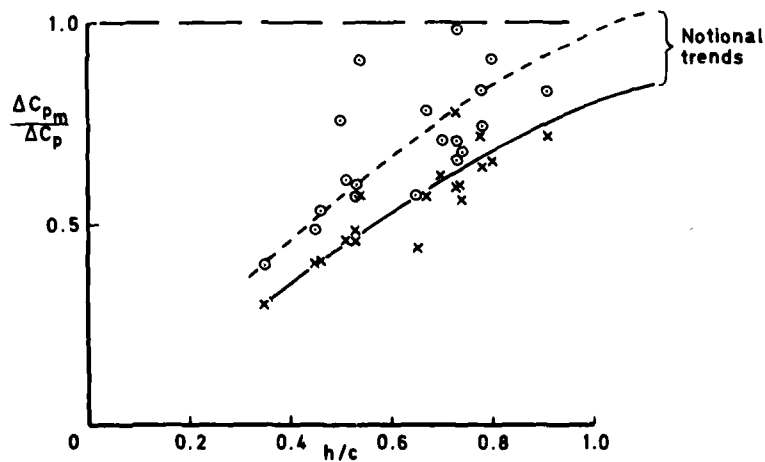
Fig 15 Loading ratio based on derived blade-vortex separation
distance and circulation on originating blade

DATAMAP AND ITS IMPACT ON PREDICTION PROGRAMS

by

Donald J. Merkley

Applied Technology Laboratory
USARTL (AVRADCOM)
Fort Eustis, Virginia 23604
USA

and

Arthur E. Ragosta

Aeromechanics Laboratory
USARTL (AVRADCOM)
Moffett Field, California 94035
USA

SUMMARY

This paper describes DATAMAP (Data from Aeromechanics' Test and Analytics--Management
and Analysis Package), a computer software system that provides direct access to large
time-history data bases (both test and analytic), performs analyses and derivations, and
displays the data in various formats, interactively or through batch processing.
Emphasis is given to the ability of directly comparing analytical, model and full-scale
test results; the care which must be taken ... n utilizing DATAMAP; and its effect on the
plans for the Second Generation Comprehensive Helicopter Analysis System (2GCHAS).
Examples of correlation of various parameters resulting from the Operational Loads
Survey (OLS) and several analytic programs are given. The OLS was a flight test program
on the AH-1G helicopter in which blade pressures, leading edge stagnation point loca-
tions, local flow magnitude and direction near the blade surface, blade accelerations,
bending moments, and the attendant responses in the control system and airframe were
measured simultaneously during operational maneuvers, providing a comprehensive data
base.

A brief description of the OLS data base is presented along with a discussion of the
development of DATAMAP. DATAMAP's versatility is shown, with emphasis on its ability to
access any time-history data base and its modular concept whereby any appropriate analy-
sis or derivation can be added to the existing capabilities as the need arises; plots
are presented which show various formats that are available to the user.

1.   INTRODUCTION

The need for the DATAMAP system is derived from the Operational Loads Survey (OLS), a
flight test conducted using a US Army AH-1G to gain experimental insight to rotor aero-
dynamic environments and structural dynamics of helicopters (Reference 1). A comprehen-
sive data base was acquired of rotor aerodynamic forces, aeroelastic loads, blade
motions, acoustics, and the attendant responses of the control system and airframe that
result from flying operational maneuvers. Continuous and simultaneous data was recorded
from 387 transducers for 224 different flight conditions. Over 72,000 separate func-
tions of time were digitized and recorded on 175 magnetic tapes. A computer program was
developed to retrieve the raw data; however, it was inconvenient and time consuming and
it discouraged potential users. It was difficult to manage such a large data base
without the proper software tools. The Applied Technology Laboratory (ATL), US Army
Research and Technology Laboratories (AVRADCOM) developed the functional descriptions
for such a software system to utilize the OLS data base and yet be general enough to be
used with other data sets, both analytical and test.

The functional descriptions required the system to provide access, data reduction, and a
variety of formats of presentation of digitized data. In addition, operation in batch,
interactive, and interactive graphics modes was required. The functional descriptions
also included a need for a high degree of user interaction and computer-generated step-
by-step explanations of user inputs, user options, and menus of data available for pro-
cessing. Most analytical methods commonly used for helicopter test data analysis,
selectable by the user in any appropriate combination, were specified. Modular design
requirements that would allow other methods to be added as the need arises were
stressed. Design requirements included execution on an IBM 360 Model 65 with Time
Sharing Option (TSO), Tektronix 4014 graphic terminal, Houston Instruments DP-1 incre-
mental plotter, and IBM 2741 typewriter terminal. The mandatory computing language was
FORTRAN IV (1966).

Bell Helicopter Textron, Scientific and Technical Computing, was selected as principal
performer to develop this software, which is now known as DATAMAP. DATAMAP meets all of
the above-mentioned design requirements with an easy-to-learn user oriented format

(Reference 2). Since it was first operational, DATAMAP has undergone a number of improvements which enhance its ability to correlate experimental data with analytics; it has been installed at different facilities on various computers and has accessed a variety of data bases, including the Army OLS, NASA Tip Aero-Acoustic Test (TAAT), Royal Aircraft Establishment (RAE) Wessex and Puma test data, Army YAH-63 Crash Test (T41), KRASH analysis program, Rotorcraft Flight Simulation Program (C81), and RAE Youngs Ring Vortex Analysis.

The OLS and TAAT data are digitized and recorded on magnetic tape in the BHT-Ground Data Center (BHT-GDC) format, which is directly read by DATAMAP. The capability exists for DATAMAP to read other time-based data stored in a specified general format called the Data Transfer File Format. This capability allows test and analytic data to be displayed in a uniform graphic format, and in many cases as curves on the same plot, which greatly facilitates correlation of test and analytics.

2. DATAMAP CAPABILITIES

DATAMAP consists of two major programs, the File Creation Program and the Processing Program, as well as several utility programs. The basic execution sequence is illustrated in Figure 1. The File Creation Program reads data from some storage medium (digital tape or disc), selectively transfers data to a direct access disc (Master File), and creates a directory of the data thus stored. Output from existing simulation programs or test data bases could be run through a format conversion program to create a Data Transfer File. The Data Transfer File format is designed to accommodate many of the different structural features of time-based data bases so that conversion of data to this format should be a reasonably simple task. Alternatively, a new simulation program could be written or an existing program could be converted to write data in Data Transfer Format directly as a primary output.

The Master File is then the data input source for the Processing Program. The Processing Program retrieves data from the Master File, accepts user commands interactively or in batch mode, processes the data, and outputs data in graphic or printed formats. The Processing Program provides the user with various analyses that may be performed on the basic data contained on the Master File; in addition, certain parameters may be derived from the basic data. The computational capabilities available to the user in the Processing Program are detailed in Figure 2. These analyses and derivations can be performed in multiple dimensions (e.g., time, chord, and radius). Sequences of analyses and/or derivations can be performed on a set of data in any appropriate combination.

Basic data and processed outputs can be presented in various formats, some of which are illustrated in the figures of this paper. Simple X-Y plots or multiple-curve X-Y plots are available. Extensive annotation for each curve on a plot is a useful option, particularily when plotting curves from different data sets. Data point representation may be accomplished by drawing symbols alone, by connecting symbols with lines, or simply by connecting the data points by lines without symbols. The user also has the options of specifying log-log or semi-log axes, scaling on X and Y, or using a plot with grids and/or tic marks. When X-Y plots are produced on the Tektronix 4014 terminal, the user may specify that the crosshair cursor be activated immediately after the plot is completed. The crosshairs may be used to evaluate points on the screen in user coordinates. Three-dimensional outputs in the form of contour plots and surface perspective drawings in rectangular and cylindrical coordinate systems are available. Auto scaling is available on all plots or the user may specify the scale values. All output options are available on a Tektronix 4014 terminal, or its equivalent, in the interactive graphics mode of operation or on an incremental plotter in the batch mode. Printed listings are available in either mode, or on an interactive typewriter terminal.

Four utility programs are provided in the system. Two of them are for file initialization in the Master and Command Sequence Files. The Command Sequence File is a permanent disc file on which sequences of command steps can be stored. Another utility program is provided for users to develop complete input sequences for the File Creation Program in an interactive mode. A File Maintenance Program is provided such that a designated data base monitor at each user installation can maintain the Master File.

DATAMAP was designed with consideration of the user. Features that assist the user in generation of command input for processing include:

- The user inputs are free-field format with logical meaning and structure, and are identical for the interactive and batch modes of operation.

- Many types of errors are detected in the input process.

- There are defaults for some entries.

- The program can list the available options, defaults, and/or meaning for each input entry if desired.

- Large numbers of data channels representing like parameters can be called by a single group name.

● Sequences of commands can be built, stored, and executed by name.

Many of these features are illustrated in Figure 13 which is an example of generating a typical DATAMAP command.

3.   CORRELATION OF TEST WITH ANALYTICS

A very versatile characteristic of DATAMAP is its ability to access various data sets during the same interactive session or batch run, which provides direct comparison and correlation between data from the different sets. Analytical results from helicopter simulations can therefore be directly correlated with actual test data to evaluate the accuracy and limitations of the analytical simulations. This feature of DATAMAP is a powerful tool that is useful to validate new analyses and to evaluate the ability of analytical simulations to model particular features under investigation; it is also useful as an engineering tool to aid the interpretation of test data.

Figures are provided to illustrate the abilities of DATAMAP to make comparisons of measured and computed data. Figures 3 through 5 show comparisons of blade bending moments at different radial stations. Each figure illustrates a choice of line type available to the user. The Rotorcraft Flight Simulation Program C81 was used to generate the computed results.

The scale for the Azimuth has been expanded in Figure 4 so that data from 0 to 100 degrees Aziumth is full frame, thus concentrating on the first rotor quadrant. This ability to window the data is available for either axis.

The Rotorcraft Flight Simulation Program C-81 is a multidisciplinary mathematical model that may be used to simulate a wide variety of helicopter or V/STOL aircraft configurations using a digital computer. Aircraft performance, stability and control, maneuver characteristics, and rotor blade loads may be estimated using this model. The following aircraft components are treated separately: the fuselage; two rotors (each with a modal pylon, aeroelastic blades, and a nacelle); a wing; four stabilizing surfaces (none of which must be purely vertical or horizontal); four external stores or aerodynamic brakes; a nonlinear, coupled control system (including a collective bobweight, stability and control augmentation system, and maneuver autopilot simulator); two jets; and a weapon with recoil. This allows detailed representation of the aircraft for design or detailed analysis applications. Six rigid-body fuselage degrees of freedom and up to six rotor blade elastic degrees of freedom for each of two rotors are accounted for. For a complete overview of C-81 capabilities and discussions of the background and development of the principal mathematical models in the program refer to References 3 and 4.

A Comparison of test data and C-81 analysis is presented in Figure 6, showing the radial distribution of blade beam bending moments. The computed bending moment is represented by a continuous line and the test measurements are represented by triangular symbols at the radial stations at which they were recorded.

The harmonic analysis feature of DATAMAP is useful for comparing multiple time histories. This analysis presumes that frequencies of interest are integral multiples of the rotor speed. The sine and cosine terms are converted to amplitude and phase in degrees. Figure 7 illustrates a graphic output of harmonic analyses performed on the blade torsional bending moment time histories from Figure 3.

The cross-plot feature allows the user to request a plot of one dependent variable versus another dependent variable as related by a common independent variable for both functions. For example, Figure 8 illustrates the relationship between two derived parameters--Normal Force Coefficient and Mach Number with the main rotor azimuth as the associating parameter. Each symbol indicates a 10-degree increment in Azimuth. A comparison of those parameters derived from OLS test measurements and from the C81 analysis is also provided in the figure.

Figure 9 compares Normal Force Coefficient distributions derived from measured data and calculated by C-81. These three-dimensional contour and surface plots provide a good qualitative view of the radial and azimuthal distributions of the data.

Figure 10 compares test data with results generated from two different analysis programs, C-81 and RAE Young's Analysis. DATAMAP has been used extensively during joint US Army/RAE cooperative exercises concentrating on rotor loads, under the auspices of TTCP (Reference 5). The RAE Young's Analysis has only a rigid blade flapping mode and one torsion mode. A representation of unsteady aerodynamics is included which uses Wagner function for attached flow and a time delay stall model for separated conditions (see Reference 6). The wake consists of a series of vortex rings displaced vertically and downstream from the tip path plane. The centers of the rings are placed so that the vortex intersections at the blade approximates radial position and tangency to the intersection of an undistorted spiral wake. Only a root and tip vortex are included and the strength of the rings has a constant value with a superimposed first harmonic variation. The analysis was never intended for teetering rotors, and it models the AH-1G as two centrally hinged blades, thus there is no carry-over from one blade to the other.
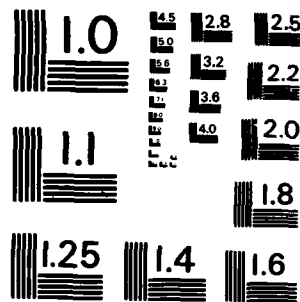
1.0

4.5 2.8 2.5
5.0
5.6 3.2 2.2
     3.6
1.1 4.0 2.0

1.8

1.25 1.4 1.6

MICROCOPY RESOLUTION TEST CHART
NATIONAL BUREAU OF STANDARDS-1963-A

● Sequences of commands can be built, stored, and executed by name.

Many of these features are illustrated in Figure 13 which is an example of generating a typical DATAMAP command.

3.   CORRELATION OF TEST WITH ANALYTICS

A very versatile characteristic of DATAMAP is its ability to access various data sets during the same interactive session or batch run, which provides direct comparison and correlation between data from the different sets. Analytical results from helicopter simulations can therefore be directly correlated with actual test data to evaluate the accuracy and limitations of the analytical simulations. This feature of DATAMAP is a powerful tool that is useful to validate new analyses and to evaluate the ability of analytical simulations to model particular features under investigation; it is also useful as an engineering tool to aid the interpretation of test data.

Figures are provided to illustrate the abilities of DATAMAP to make comparisons of measured and computed data. Figures 3 through 5 show comparisons of blade bending moments at different radial stations. Each figure illustrates a choice of line type available to the user. The Rotorcraft Flight Simulation Program C81 was used to generate the computed results.

The scale for the Azimuth has been expanded in Figure 4 so that data from 0 to 100 degrees Aziumth is full frame, thus concentrating on the first rotor quadrant. This ability to window the data is available for either axis.

The Rotorcraft Flight Simulation Program C-81 is a multidisciplinary mathematical model that may be used to simulate a wide variety of helicopter or V/STOL aircraft configurations using a digital computer. Aircraft performance, stability and control, maneuver characteristics, and rotor blade loads may be estimated using this model. The following aircraft components are treated separately: the fuselage; two rotors (each with a modal pylon, aeroelastic blades, and a nacelle); a wing; four stabilizing surfaces (none of which must be purely vertical or horizontal); four external stores or aerodynamic brakes; a nonlinear, coupled control system (including a collective bobweight, stability and control augmentation system, and maneuver autopilot simulator); two jets; and a weapon with recoil. This allows detailed representation of the aircraft for design or detailed analysis applications. Six rigid-body fuselage degrees of freedom and up to six rotor blade elastic degrees of freedom for each of two rotors are accounted for. For a complete overview of C-81 capabilities and discussions of the background and development of the principal mathematical models in the program refer to References 3 and 4.

A Comparison of test data and C-81 analysis is presented in Figure 6, showing the radial distribution of blade beam bending moments. The computed bending moment is represented by a continuous line and the test measurements are represented by triangular symbols at the radial stations at which they were recorded.

The harmonic analysis feature of DATAMAP is useful for comparing multiple time histories. This analysis presumes that frequencies of interest are integral multiples of the rotor speed. The sine and cosine terms are converted to amplitude and phase in degrees. Figure 7 illustrates a graphic output of harmonic analyses performed on the blade torsional bending moment time histories from Figure 3.

The cross-plot feature allows the user to request a plot of one dependent variable versus another dependent variable as related by a common independent variable for both functions. For example, Figure 8 illustrates the relationship between two derived parameters—Normal Force Coefficient and Mach Number with the main rotor azimuth as the associating parameter. Each symbol indicates a 10-degree increment in Azimuth. A comparison of those parameters derived from OLS test measurements and from the C81 analysis is also provided in the figure.

Figure 9 compares Normal Force Coefficient distributions derived from measured data and calculated by C-81. These three-dimensional contour and surface plots provide a good qualitative view of the radial and azimuthal distributions of the data.

Figure 10 compares test data with results generated from two different analysis programs, C-81 and RAE Young's Analysis. DATAMAP has been used extensively during joint US Army/RAE cooperative exercises concentrating on rotor loads, under the auspices of TTCP (Reference 5). The RAE Young's Analysis has only a rigid blade flapping mode and one torsion mode. A representation of unsteady aerodynamics is included which uses Wagner function for attached flow and a time delay stall model for separated conditions (see Reference 6). The wake consists of a series of vortex rings displaced vertically and downstream from the tip path plane. The centers of the rings are placed so that the vortex intersections at the blade approximates radial position and tangency to the intersection of an undistorted spiral wake. Only a root and tip vortex are included and the strength of the rings has a constant value with a superimposed first harmonic variation. The analysis was never intended for teetering rotors, and it models the AH-1G as two centrally hinged blades, thus there is no carry-over from one blade to the other.

4.   DANGERS

The analyst must be careful when using a system such as DATAMAP, since the user options of analysis, derivations, and data editing are so readily available and easy to use. It is easy to fall into a false sense of security with regard to the validity of the results. For example, it is easy for the user to mask, or edit, unwanted data time-histories simply by using the MASK command. One must be extremely cautious when masking apparently "bad" channels of data. Arbitrarily deleting "bad" data may in fact be eliminating some feature or changing the nature of real phenomena.

Digital filtering should also be done with care, so as not to obscure some highly transient event. The type of data, its frequency content, and the intent of filtering are some factors which may determine whether filtering is necessary at all. Careful consideration should be given to the choice of digital filter type, number of poles, and break frequencies when filtering is desired.

The cycle averaging option is another DATAMAP feature that may mask noncyclic transient phenomena. The cycle averaging algorithm seeks to reduce superfluous noise by averaging several contiguous cycles to form a single representative cycle.

Interpolation of data is a topic that deserves special attention, as it is normally transparent to the user and can affect the results in ways that the user should at least be aware of. DATAMAP currently uses a local cubic spline interpolation routine.

Cubic splines are prone to overshoot and to oscillate as demonstrated in Figure 11. For many interpolation applications this behavior is undesirable. The local cubic inter-polation routine in DATAMAP is more stable than a normal cubic spline interpolation inasmuch as it produces less oscillation from a sudden change in curvature; however it can still show considerable overshoot.

For a given set of function values, the cubic spline interpolation is the "smoothest" in the sense that it has the least-mean-squared curvature of all twice-differentiable interpolating functions, which implies an assumption that the original function is correspondingly smooth. However, since DATAMAP is a general-purpose system, it must process data that do not meet the smoothness criteria. Specific features of data that DATAMAP must process are:

- Sharp transitions of the physical function between measured points where the independent variable is not time. For example, tip vortex interactions cause blade pressure to change suddenly between blade pressure measurement stations.

- Noise and bias errors in flight test data are usually uncorrelated between measurement stations.

- Inoperative measurement stations can leave large "gaps" between input function values.

- Some analytic programs simulate functions that change frequency characteristics with time. These programs may increase the sample rate as high-frenquency components are introduced.

Processed results from DATAMAP are particularly affected when two-dimensional inter-polation is used to obtain a data matrix with a specified constant spacing of elements which are then plotted using surface or contour methods. Although the magnitude of interpolation overshoot and oscillation are not always large, any unusual interpolation effects are particularly disturbing in a 3-D plot because the measured data are not normally displayed separately for comparison.

A recent study of variable-power interpolation for use in DATAMAP was conducted by BHT (Reference 7). A variable power interpolation scheme was developed, although not pesently available in DATAMAP, that has desirable characteristics as illustrated in Figure 12.

5.   EVOLUTION, THE NEXT GENERATION

The state of the art of software development has been rapidly changing for several years. Programs that were considered easy to use and powerful 10 years ago are now con-sidered very difficult to use and modify. A typical class of program is a graphical/ analytical post-processor for other programs and other forms of data (such as that pro-duced by testing of hardware). This section deals with the evolution of this technology relative to codes used by the helicopter engineering community.

The first programs to post-process analytic and test data were batch-oriented, used for-matted input from cards, and produced little or no graphical output. Progress was slow; interactivity was introduced, graphics were used to a greater extent, and some programs became prompt or menu driven.

DATAMAP was a leap forward in the state of the art, incorporating advanced graphics, flexibility, enhanced user interface, and data management by the system.

The next generation is evidenced in the planning and design of the Second Generation Comprehensive Helicopter Analysis System (2GCHAS). To demonstrate this, three areas were chosen for discussion: ease of use, throughput, and model validation.

Ease of use is characterized by several attributes, including readability of input and output, extensive error handling, help messages, free-field input, and command (and/or menu) driven program control. Figure 13 shows all of these features in action in a typical DATAMAP command. Notice that an error is intercepted and rejected. No damage is done to either the data base or the user's session (including temporary files). The user can request assistance at any time to reduce the possibility of errors. A DATAMAP command is normally broken into four fields, terminated by a slash. Within a field, entries are terminated with one or more spaces, a comma, or a combination of both. Note the use of the empty field for choosing default values. Finally, notice how much more meaningful this command is than a list of numbers in (3I1, 6I4, I1) format. DATAMAP has 13 specification commands with several dozen actions, a variety of input sources, and 10 output options. A command can contain any consistent set of these parts. The resulting power and ease of use of the command interface far exceeds that which could be expected from the use of numerical switches. For 2GCHAS this concept is extended still further. In addition to the features of DATAMAP, 2GCHAS supports a wider range of commands and permits I/O to or from many places other than the program-specific files (i.e., within core, to any supported I/O device, and to operating system/FORTRAN supported file structure). The following line is an example of a command that 2GCHAS would use to perform the same functioning as the DATAMAP command in Figure 13:

CYCLE AVERAGE (1): ABS PRESSURE (FLT614,SCF1).

Although the help and error handling are not demonstrated here, there would be features similar to the features demonstrated on DATAMAP.

The readability of input and output is good in both DATAMAP and 2GCHAS by paying attention to detail on printouts and extensive use of high-quality graphics.

Throughput is the measure of the amount of productive work the programs can perform in a given period of time. Throughput may only be evaluated realistically by considerating not only the processing time but also the data preparation time and usability of the output. Many of the features already discussed under ease of use also strongly impact throughput.

DATAMAP provides logical steps with which a series of processes can be applied to a data stream. A common example of this is the sequence: cycle average absolute pressure data, derive Pressure Coefficients for this stream, integrate the Pressure Coefficients stream to yield Normal Force Coefficients, then plot the Normal Force Coefficients. The results of these steps can be saved from day to day. The 2GCHAS will provide an even more impressive data handling capability. In addition to a larger combination of analyses and derivations, a data management subsystem is envisioned which will allow manipulation of all data on the data base by file, by logical subsets (accessed by name), and by user-defined fields. An example of this capability might be to identify all flights with speeds greater than 80 knots.

Both DATAMAP and 2GCHAS enhance their own processing capabilities with a generalized interface to other programs and to data collected from other sources (e.g., from flight tests). DATAMAP does this by means of the Data Transfer File (DTF). A small program is written (or the existing program is modified) to produce a DTF in the prescribed format. An "Info" File is written to describe the contents of the DTF, the File Creation Program transfers the DTF to the Masterfile, and the default Info File is replaced. The user writes a file describing the format of the data already existing and the external model interface uses this description to input the data, storing it to the Master Data Base, or uses it directly.

Model validation is the use of the capabilities of the system to compare, evaluate, and correct application programs or the system itself. The comparisons and evaluations are performed relative to data from another program or data from an external source. The simplest, and yet perhaps the most powerful, function which supports model validation is the ability to accept input from more than one source; this capability is lacking from a vast majority of post-processors. A logical progression is that the multiple data streams must be displayable together. Statistical packages can be used to quantify trends which have been identified by inspection. Finally, analyses specifically designed for comparisions (e.g., cross correlation) can be applied. Once again, both DATAMAP and 2GCHAS excel, although in the latter two areas DATAMAP has only very basic capabilities. It is anticipated that 2GCHAS will be useable to identify trends, extrapolate some numerical conclusions based on the performance of similar types of data, and quantify the effect of a stimulus on series of analyses. Other similar types of advanced model validation techniques may also be included.

There are other areas in which DATAMAP was an intermediate step from which requirements and design for portions of the 2GCHAS were derived. DATAMAP is a state-of-the-art improvement in helicopter graphic/analytic post-processors; as a result, it has been a test bed for some new approaches. A high percentage of the implemented features of DATAMAP are very successful. In the development of 2GCHAS, the best features of DATAMAP are being retained, good features are being enhanced, and mediocre or missing features have been identified for additional development. Thus, a true evolution is taking place from outdated applications programs to DATAMAP to 2GCHAS.

The 2GCHAS is presently in development. Although the purpose of 2GCHAS is more comprehensive than DATAMAP, the portions of 2GCHAS which perform the DATAMAP-like functions have been designed around the DATAMAP structure, as can be seen by comparing Figure 1 (DATAMAP structure) to Figure 14 (2GCHAS post-processing structure).

7.   CONCLUSIONS

DATAMAP is a data analysis and management system that has been shown to be versatile and user oriented. It provides an engineering user (not necessarily computer oriented) a powerful tool for interactively analyzing and interpreting a vast amount of data which may otherwise be unmanageable. Most of the derivations and some of the analysis procedures are helicopter oriented; however, other processing capabilities, data management features, and the graphics functions can readily be used for nonhelicopter applications. Certain features of DATAMAP enable it to be used to validate new analyses and to evaluate the ability of analytical simulations to model particular phenomena; it can also be used as an engineering tool to aid in the interpretation of test data. The concepts used for the development of DATAMAP and expanded during its use have been used, or are the basis, for some of the capabilities of the Second Generation Comprehensive Helicopter Analysis System.

8.   REFERENCES

1. Shockey, G. A., Cox, C. R., and Williamson, J. W., AH-1G HELICOPTER AERODYNAMIC AND STRUCTURAL LOADS SURVEY, Bell Helicopter Textron, USAAMRDL-TR-76-39, Eustis Directorate, US Army Air Mobility R&D Laboratory, Fort Eustis, Virginia, February 1977.

2. Philbrick, R. B., THE DATA FROM AEROMECHANICS TEST AND ANALYTICS-MANAGEMENT AND ANALYSIS PACKATE (DATAMAP), Volumes I and II, Bell Helicopter Textron, USAAVRADCOM TR-80-D-30A and 30B, Applied Technology Laboratory, US Army Research and Technology Laboratories, Fort Eustis, Virginia, December 1980.

3. Van Gaasbeek, J. R., ROTORCRAFT FLIGHT SIMULATION COMPUTER PROGRAM C81 WITH DATAMAP INTERFACE, Volume I - User's Manual, Bell Helicopter Textron, USAAVRADCOM-TR-80-D-38A, Applied Technology Laboratory, US Army Research and Technology Laboratories, Fort Eustis, Virginia, October 1981.

4. Hsieh, P. Y., ROTORCRAFT FLIGHT SIMULATION COMPUTER PROGRAM C81 WITH DATAMAP INTERFACE, Volume II - Programmer's Manual, Bell Helicopter Textron, USAAVRADCOM-TR-80-D-38B, Applied Technology Laboratory, US Army Research and Technology Laboratories, Fort Eustis, Virginia, October 1981.

5. Merkley, D. J., Riley, M. J., and Young, C., JOINT ANGLO-AMERICAN EXPERIENCE OF THE ANALYSIS OF HELICOPTER ROTOR BLADE PRESSURE DISTRIBUTIONS, Seventh European Rotorcraft and Powered Lift Aircraft Forum, Garmisch-Partenkirchen Germany, 1981.

6. Beddoes, T. S., A SYNTHESIS OF UNSTEADY AERODYNAMIC EFFECTS INCLUDING STALL HYSTERESIS, First European Rotorcraft and Powered Lift Aircraft Forum, Southampton, England, September 1975.

7. Philbrick, R. B., A STUDY OF VARIABLE-POWER INTERPOLATION FOR USE IN DATAMAP, Bell Helicopter Textron Technical Data Report No. 299-099-620, Fort Worth, Texas, December 1981.
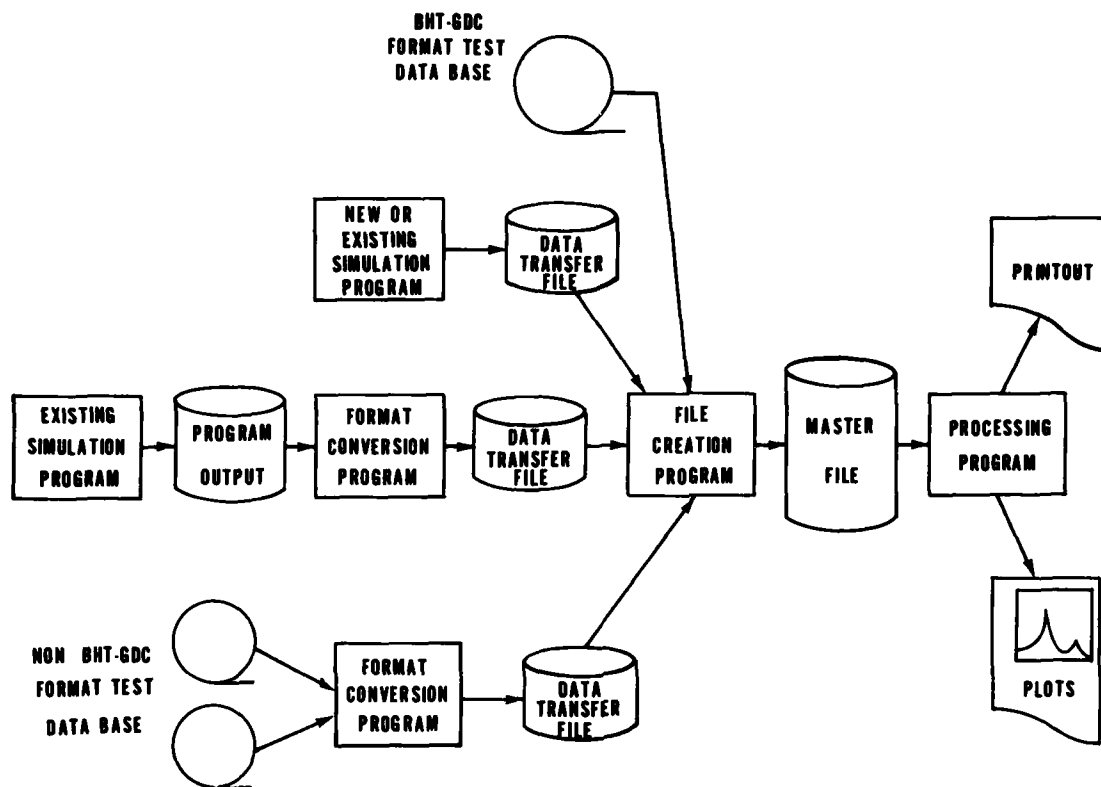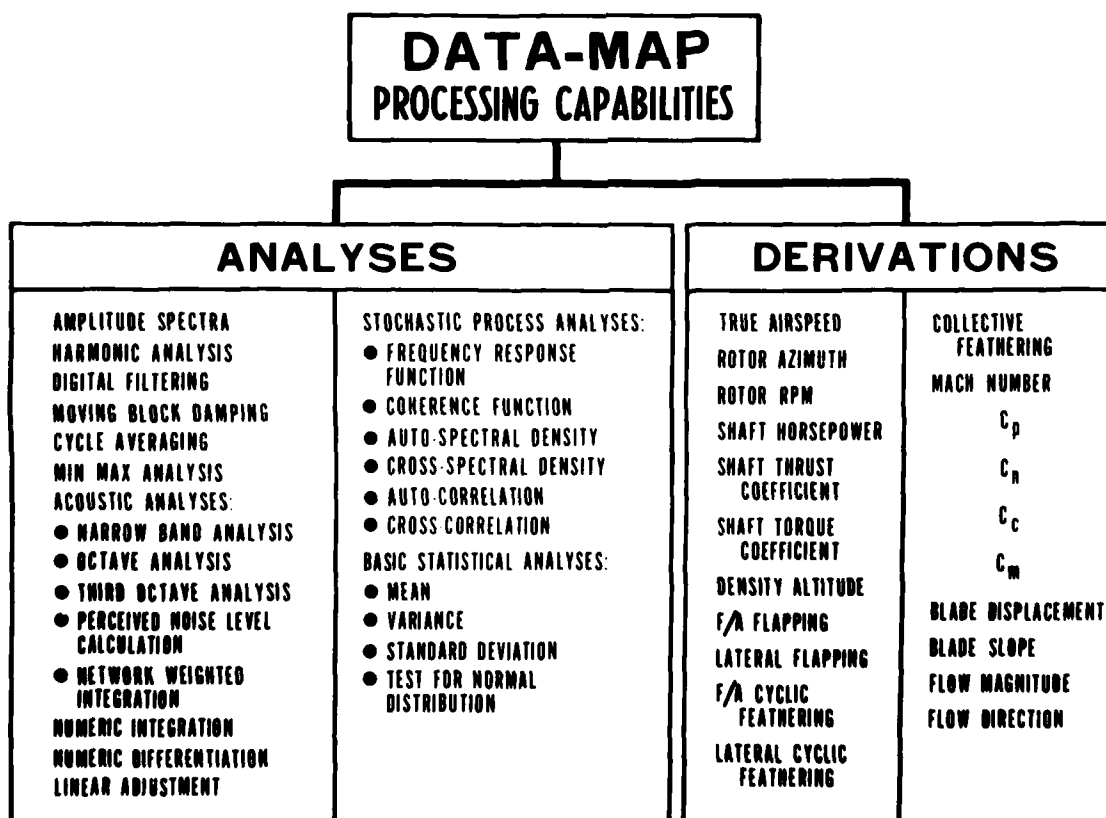
FIGURE 1. VARIOUS DATAMAP FLOW PATHS

DATA-MAP
PROCESSING CAPABILITIES

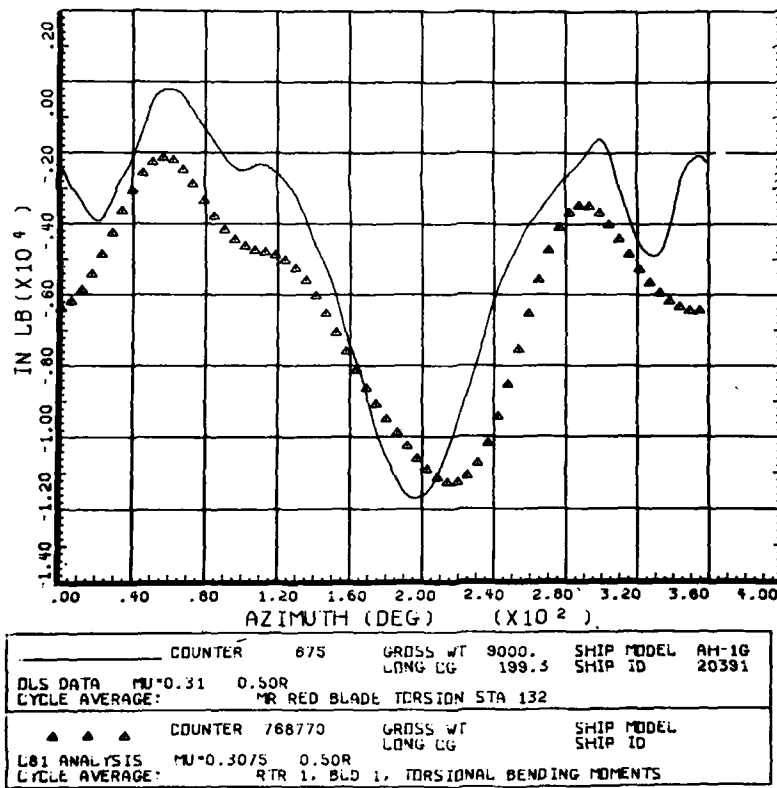| ANALYSES		DERIVATIONS	
AMPLITUDE SPECTRA	STOCHASTIC PROCESS ANALYSES:	TRUE AIRSPEED	COLLECTIVE
HARMONIC ANALYSIS	● FREQUENCY RESPONSE	ROTOR AZIMUTH	FEATHERING
DIGITAL FILTERING	FUNCTION	ROTOR RPM	MACH NUMBER
MOVING BLOCK DAMPING	● COHERENCE FUNCTION	SHAFT HORSEPOWER	C_p
CYCLE AVERAGING	● AUTO-SPECTRAL DENSITY	SHAFT THRUST	
MIN MAX ANALYSIS	● CROSS-SPECTRAL DENSITY	COEFFICIENT	C_R
ACOUSTIC ANALYSES:	● AUTO-CORRELATION		C_c
● NARROW BAND ANALYSIS	● CROSS-CORRELATION	SHAFT TORQUE	
● OCTAVE ANALYSIS	BASIC STATISTICAL ANALYSES:	COEFFICIENT	C_m
● THIRD OCTAVE ANALYSIS	● MEAN	DENSITY ALTITUDE	
● PERCEIVED NOISE LEVEL	● VARIANCE	F/A FLAPPING	BLADE DISPLACEMENT
CALCULATION	● STANDARD DEVIATION	LATERAL FLAPPING	BLADE SLOPE
● NETWORK WEIGHTED	● TEST FOR NORMAL	F/A CYCLIC	FLOW MAGNITUDE
INTEGRATION	DISTRIBUTION	FEATHERING	FLOW DIRECTION
NUMERIC INTEGRATION		LATERAL CYCLIC	
NUMERIC DIFFERENTIATION		FEATHERING	
LINEAR ADJUSTMENT			

FIGURE 2. DATAMAP PROCESSING CAPABILITIES

FIGURE 3. A COMPARISON OF MEASURED AND COMPUTED BLADE TORSIONAL BENDING MOMENTS
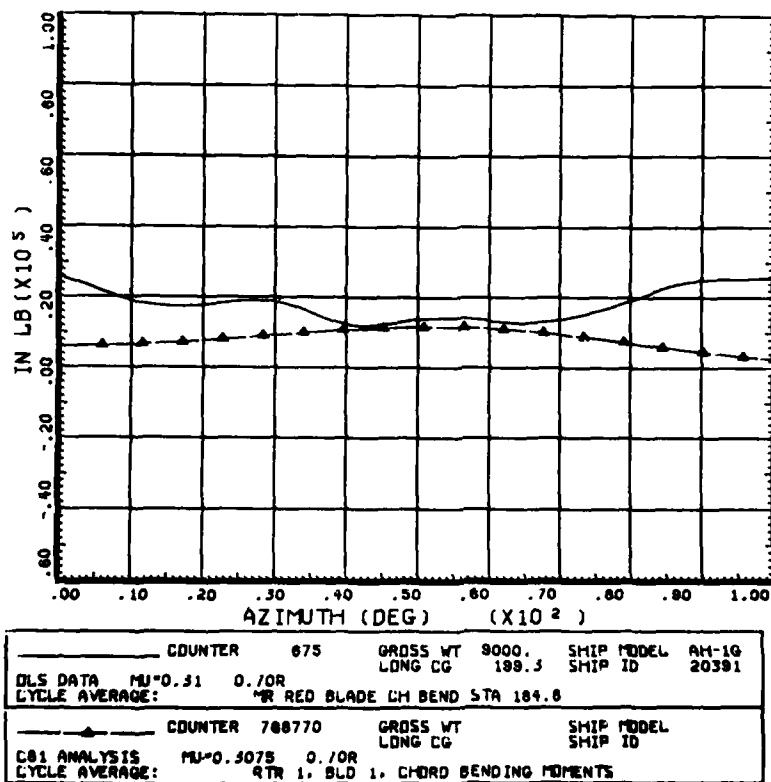
FIGURE 4. A COMPARISON OF MEASURED AND COMPUTED BLADE CHORD BENDING MOMENTS

	COUNTER	675	GROSS WT	9000.	SHIP MODEL	AH-1G
			LONG CG	199.3	SHIP ID	20391
OLS DATA	MU-0.31	.30R				
CYCLE AVERAGE:		BLADE BEAMWISE BENDING				

	COUNTER	768770	GROSS WT		SHIP MODEL	
			LONG CG		SHIP ID	
C81 ANALYSIS	MU-0.31	.30R				
CYCLE AVERAGE:		RTR 1, BLD 1, BEAM BENDING MOMENTS				
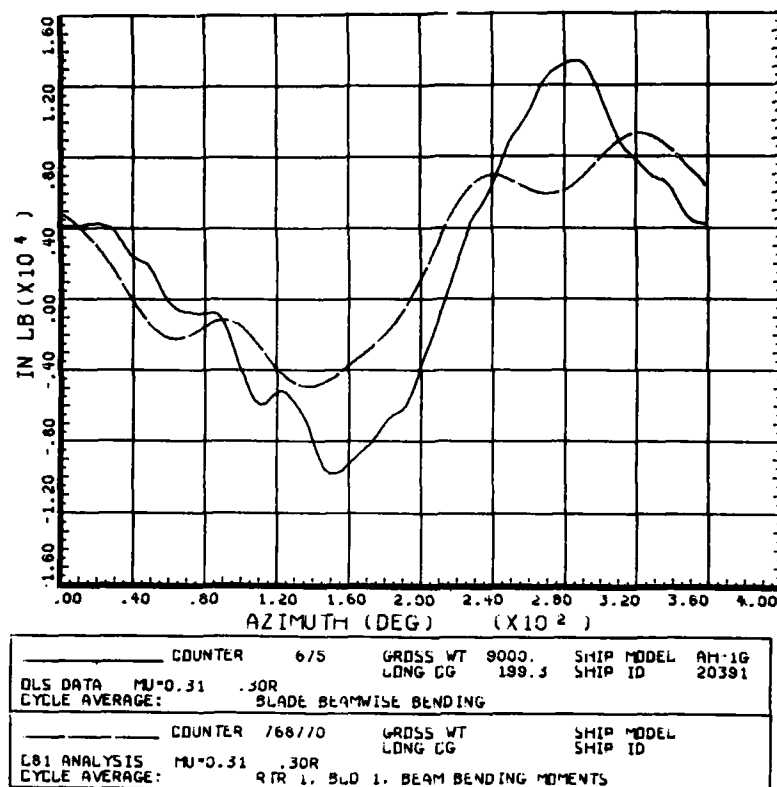
FIGURE 5. A COMPARISON OF MEASURED AND COMPUTED BLADE BEAM BENDING MOMENTS

COMPARISON OF TEST DATA AND C81 ANALYSIS

CYCLE AVERAGE: RTR 1, BLD 1, BEAM BENDING MOMENTS

COUNTER 768770 GROSS WT SHIP MODEL
  LONG CG SHIP ID

——————— 80.00 DEG. C81 ANALYSIS
▲ ▲ ▲ ▲ ▲ 80.00 DEG. OLS MEASUREMENTS
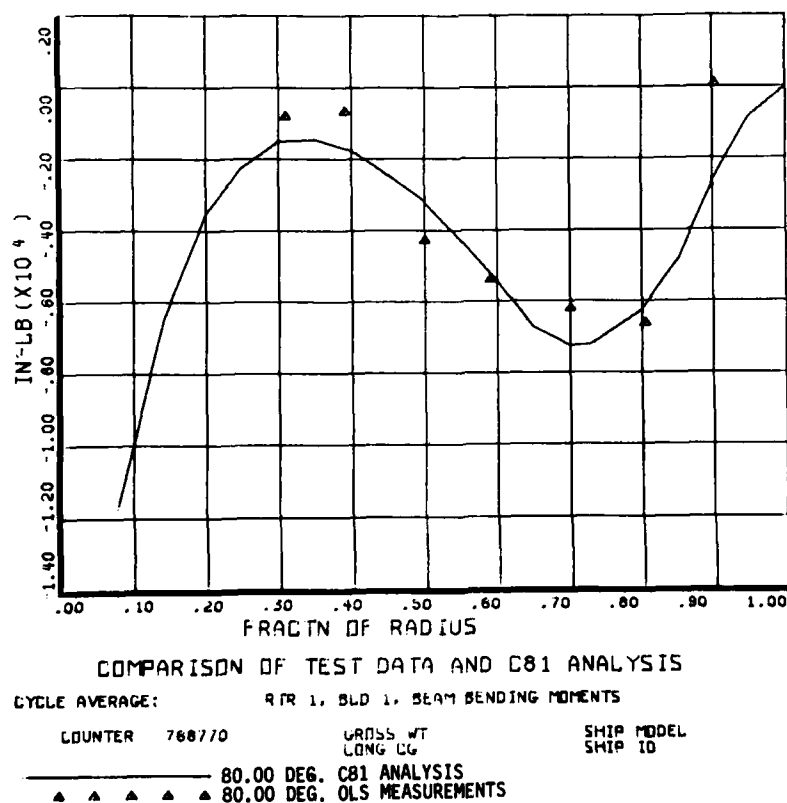
**FIGURE 6. RADIAL COMPARISON OF MEASURED AND COMPUTED BLADE BEAM BENDING MOMENTS
AT 80 DEGREES AZIMUTH**
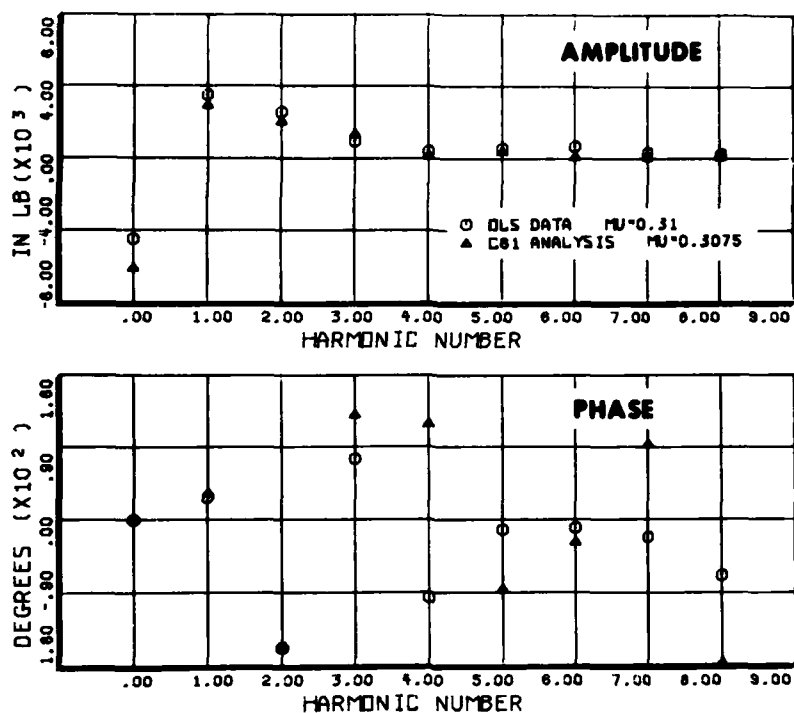
COMPARISON OF TEST DATA AND C81 ANALYSIS

FIGURE 7. HARMONIC ANALYSIS OF MEASURED AND COMPUTED BLADE TORSIONAL BENDING MOMENTS

	COUNTER	675	GROSS WT	9000.	SHIP MODEL	AH-1G
			LONG CG	199.3	SHIP ID	20391
DERIVED FROM DLS MEASUREMENTS		.864R				
ASSOCIATING VARIABLE:		AZIMUTH (DEG)		MARKING INTERVAL = 10 DEG		
	COUNTER	788770	GROSS WT		SHIP MODEL	
			LONG CG		SHIP ID	
C81 ANALYSIS RESULTS		.85R				
ASSOCIATING VARIABLE:		AZIMUTH (DEG)		MARKING INTERVAL = 10 DEG		
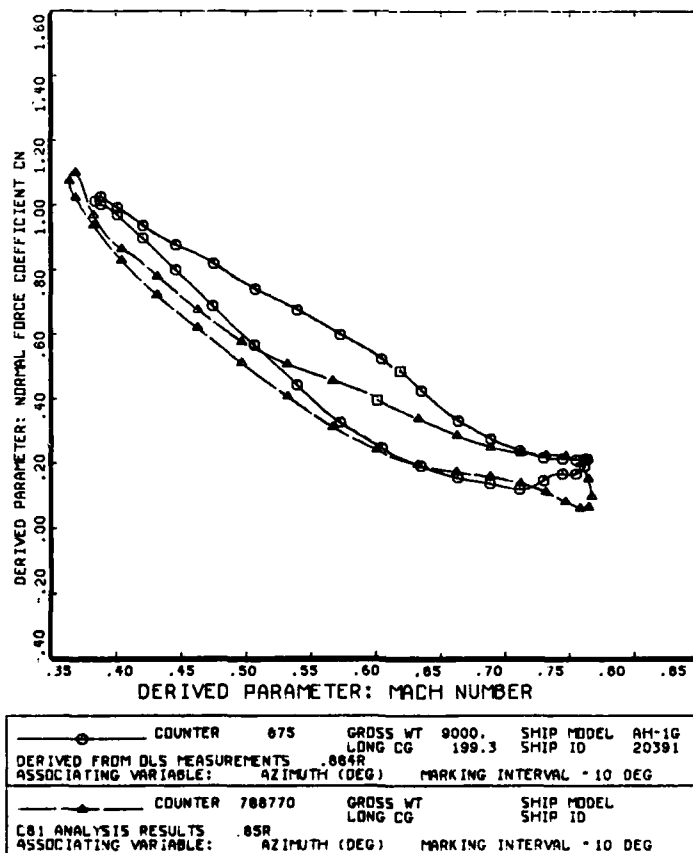
FIGURE 8. TWO DEPENDENT VARIABLES RELATED BY AN INDEPENDENT VARIABLE

OUTSIDE LIMIT
1.00 FRACTN OF RADIUS

INSIDE LIMIT
.40 FRACTN OF RADIUS

0.0 DEG

DERIVED FROM DLS MEASURED FLIGHT TEST DATA

DERIVED PARAMETER: NORMAL FORCE COEFFICIENT

| COUNTER | 075 | GROSS WT | 9000. | SHIP MODEL | AH-1G |
| | | LONG CG | 199.3 | SHIP ID | 20391 |

---------- CONTOUR LEVEL VALUES IN CN ----------

A ——— -1.0
B ——— .2
C ——— .6
D ——— 1.4
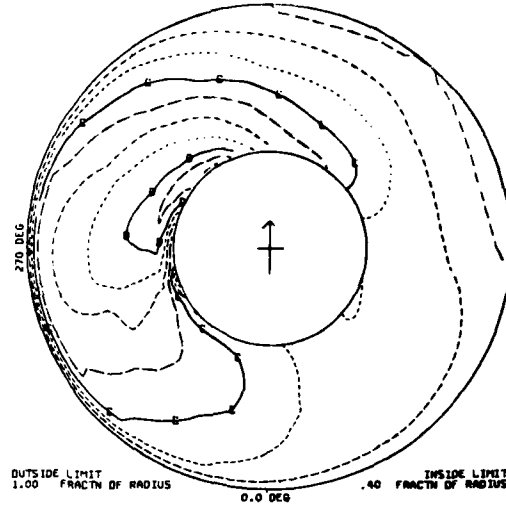
C81 ANALYSIS

CYCLE AVERAGE: RTR 1, BLD 1, NORMAL FORCE COEFFICIENT

| COUNTER | 788770 | GROSS WT | | SHIP MODEL | |
| | | LONG CG | | SHIP ID | |

---------- CONTOUR LEVEL VALUES IN ----------
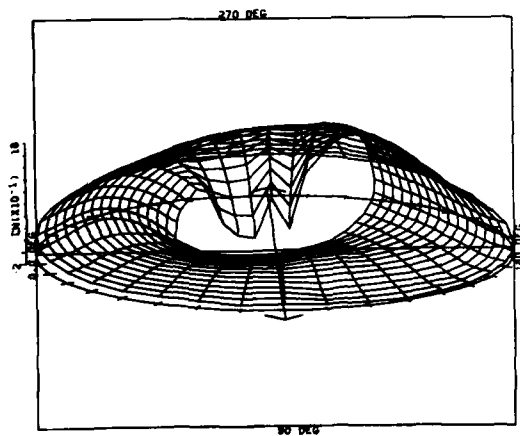
A ——— -1.0
B ——— .2
C ——— .6
D ——— 1.4

DERIVED FROM DLS MEASURED FLIGHT TEST DATA

DERIVED PARAMETER: NORMAL FORCE COEFFICIENT

| COUNTER | 075 | GROSS WT | 9000. | SHIP MODEL | AH-1G |
| | | LONG CG | 199.3 | SHIP ID | 20391 |

ANGULAR INCREMENT 10 DEG
RADIAL QUANTITY FRACTN OF RADIUS
MAX RADIUS .955
RADIAL INCREMENT .0370
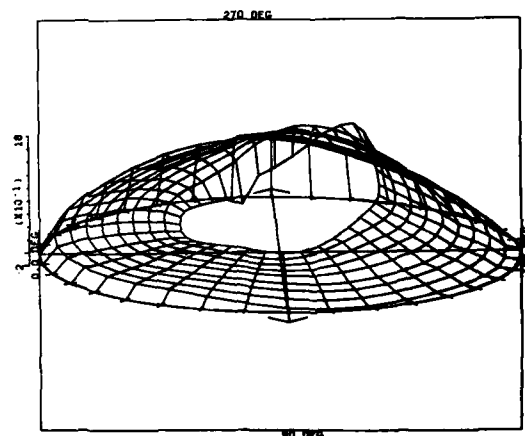
C81 ANALYSIS

CYCLE AVERAGE: RTR 1, BLD 1, NORMAL FORCE COEFFICIENT

| COUNTER | 788770 | GROSS WT | | SHIP MODEL | |
| | | LONG CG | | SHIP ID | |

ANGULAR INCREMENT 10 DEG
RADIAL QUANTITY FRACTN OF RADIUS
MAX RADIUS 1.000
RADIAL INCREMENT .0650

FIGURE 9. CONTOUR AND SURFACE PLOTS OF COMPUTED AND DERIVED MAIN ROTOR NORMAL FORCE COEFFICIENTS
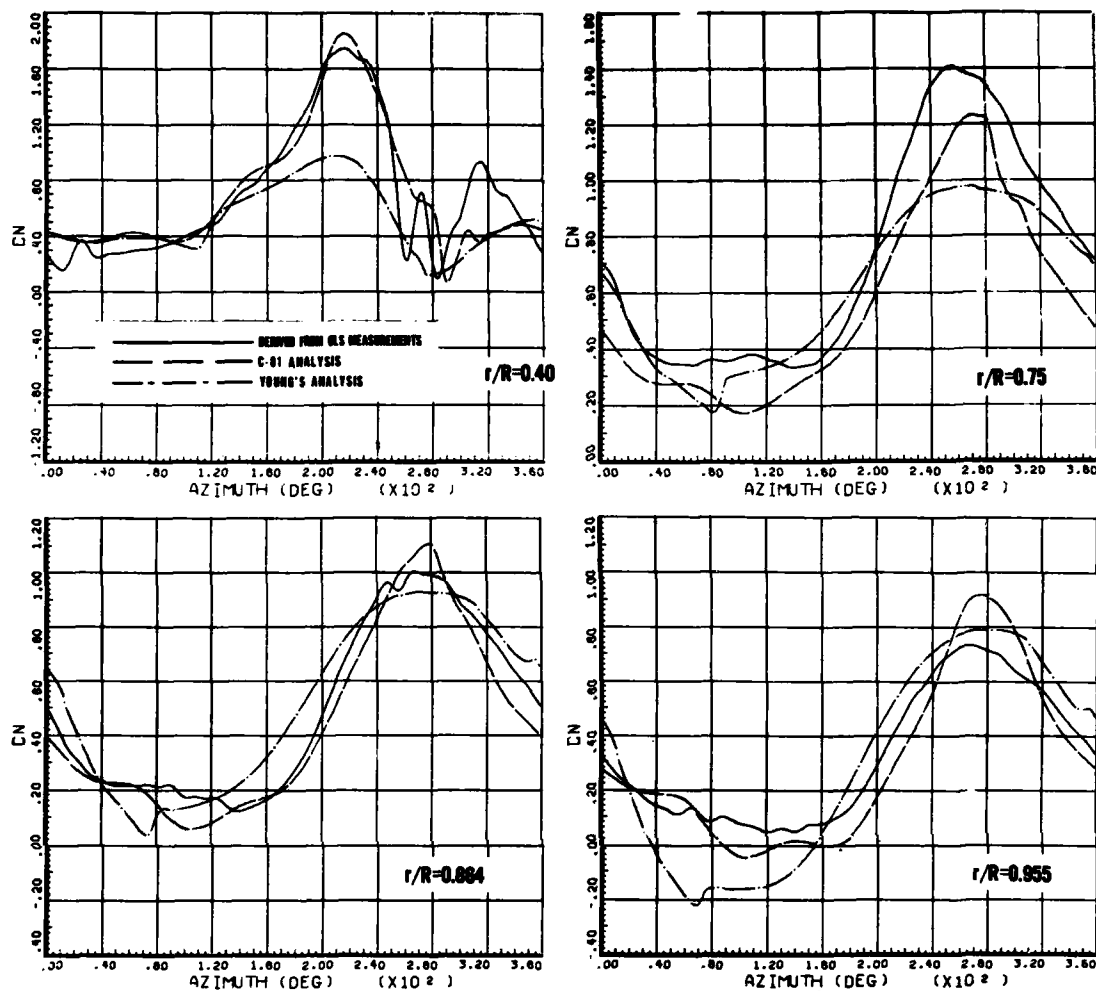
FIGURE 10. NORMAL FORCE COEFFICIENT DISTRIBUTIONS FOR VARIOUS STATIONS ON THE AH1G ROTOR
AT 0.31 ADVANCE RATIO
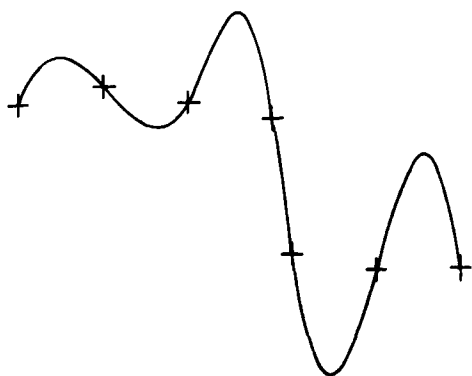
FIGURE 11. A CUBIC SPLINE INTERPOLATION SHOWING
OVERSHOOT AND OSCILLATION
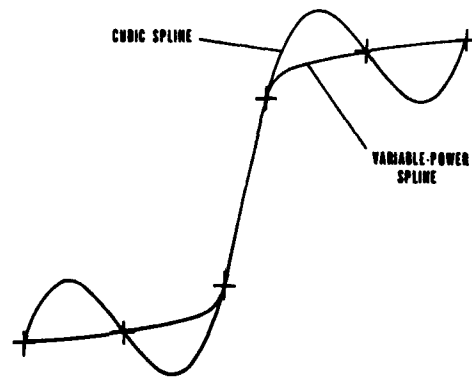
FIGURE 12. A COMPARISON OF CUBIC-SPLINE AND VARIABLE
-POWER SPLINE INTERPOLATIONS

```
anal/aber/group s2px,,,,610 0 1/keep scf1/
ENTRY UNRECOGNIZED ABER
 ACTION SUBSTEP
ENTER:- (1) OPTIONS: HARMONIC,FILTER,SPECTRUM,DAMPING,
            AVERAGE,MMAX,COHERENCE,RESPONSE,CROSS,
            AUTO,STATISTICS,ACOUSTICS,COMBINE,
            INTEGRATE,ADJUST,DIFFERENTIATE -NO DEFAULT
-----MORE ENTRIES MAY FOLLOW IN SUBSTEP-----
aver/group s2px  ?
 INPUT SUBSTEP
ENTER:- (1) DOUBLEROW OPTION: TOP,BOTTOM,BOTH-
            DEFAULT='BOTH'
        (2) ALL OR (COLUMN ELEM #)-DEFAULT='ALL '
        (3) ALL OR (ROW ELEM #)-DEFAULT='ALL '
        (4) (COUNTER)-NO DEFAULT
        (5) TIME INSTANT WITHIN ONE CYCLE BEFORE
            STARTING CYCLE (SEC) -NO DEFAULT
        (6) (# CYCLES)-DEFAULT= 1
-------MORE ENTRIES IN SUBSTEP FOLLOW-------
,,,,610 0 1/keep scf1/
ILLEGAL DEFAULT FOR SUBSTEP ENTRY  6 !!
 INPUT SUBSTEP
ENTER:- (1) (COUNTER)-NO DEFAULT
        (2) TIME INSTANT WITHIN ONE CYCLE BEFORE
            STARTING CYCLE (SEC) -NO DEFAULT
        (3) (# CYCLES)-DEFAULT= 1
        (4) AZIMUTH ANGLE(DEG)-DEFAULT= -.01
-------END OF SUBSTEP-----------------------
610 0 1/
help
 DISPOSITION SUBSTEP
ENTER:- (1) OPTIONS: PLOT,MPLOT,LPLOT,DPLOT,APLOT,
            PRIN:,CONTOUR,SURFACE,KEEP,ADD -NO DEFAULT
-----MORE ENTRIES MAY FOLLOW IN SUBSTEP-----
keep scf1/
list
ANAL/AVER/GROU,S2PX,BOTH,ALL ,ALL , 610,0, 1, -.01/KEEP
SCF1,NONE,NONE/
```

FIGURE 13. TYPICAL DATAMAP COMMAND GENERATION USING HELP FEATURES
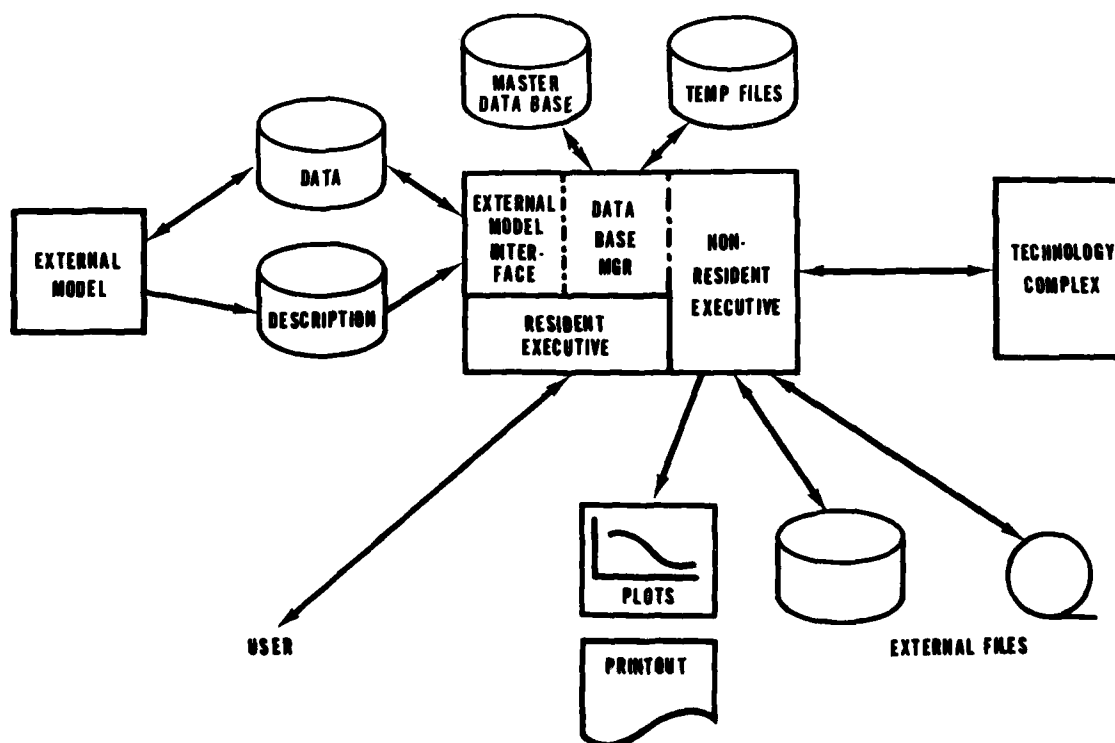
FIGURE 14. SECOND GENERATION COMPREHENSIVE HELICOPTER ANALYSIS SYSTEM POST-PROCESSING STRUCTURE

COMMENTS ON SESSION IV

EXPERIMENTAL CORRELATIONS AND VERIFICATIONS

by

S. N. Wagner
Hochschule der Bundeswehr München
Institut für Luftfahrttechnik und Leichtbau
D 8014 Neubiberg, FRG

PREPARED COMMENTS ON THE PAPERS:

It is a great pleasure for me to participate in this Specialists Meeting
on Prediction of Aerodynamic Loads on Rotorcraft and to be invited as a commentator of
Session IV.

Session IV on "Experimental Correlations and Verifications" consisted of 3 categories
of papers:

1. Comparison of flight test data with theory,

2. Comparison of wind tunnel test data with theory,

3. A software package to make such comparisons on the basis of a large variety of in-
    formations.

Before going to the detailed discussions of each paper, I would like to make some general
comments. Several of these measurements discussed in the papers were made to get some
specific information in order to substantiate or develop a special theory.

During this meeting, it was quoted occasionally that there is a lack of qualified test
data for general use. It is, therefore, suggested to collect some extra data in these
kinds of tests to get more information for general use. This data bench should also in-
clude all the background informations to be able to use the data for general comparisons.
Since wind tunnel tests and, especially, flight tests are very costly, the recording of
some more data would be negligible compared to the total costs and the experimental data
could be used more generally. I know that such a desire is critical, especially in case
of industrial measurements because of proprietory rights but, maybe, there is a way to
make such measurements usable for a greater group of users.

B. Masure and A. Vuillet (Paper 16) report on rotor load prediction methods which were
developed at Société National Industrielle Aérospatiale (SNIAS) which are used to dimen-
sion helicopter rotors. The three methods are the so-called modal method, the so-called
azimuth method and a simplified method each properly tuned to the case of application and
amount of effort. The authors show interesting comparisons between calculations of these
methods and flight measurements. They also indicate the shortcomings of these three
methods and give suggestions for further development.

The modal method postulates implicitly that there exists an average steady state and
that the movements with respect to that steady state must be small enough to allow a
linearization of the differential equations. This restriction of the method, which is
good for a first estimate of the forces and of the moments of a rotor at a flight with
medium advance ratios and low load factors, led to the derivation of the azimuth method.

The azimuth method allows to reach a desired accuracy in predicting the loads. It is
assumed that the solution vector is a periodic function and the resulting system of dif-
ferential equations has constants that are independent of time. Therefore, no instabili-
ties can be predicted. The accuracy of results can be increased by using a high number
of harmonics. However, there is a limit which is defined by the capacity of the computer.
In fact, 156 differential equations have to be integrated to calculate a static deforma-
tion. The question is whether it would be worthwhile to improve the solution procedure
and even go to higher harmonics before the physical background of the aerodynamics is
improved. It seems to me that the aerodynamic assumptions are rather conservative com-
pared to the structural part. A relatively crude inflow model (Mejer - Drees method to
calculate the induced velocity), quasisteady aerodynamics, look-up tables for compressibil-
ity and stall effects are used. Since we already know that there are strong three-
dimensional, transonic and nonsteady effects at the advancing blade, it is recommended
to improve the mathematical models for all these effects before the structural part is

even more sophisticated. This is also true for the retreating blade. The authors mention that there are problems to calculate the torsional effects with sufficient accuracy. It seems that these effects can only be predicted accurately if the influences of three-dimensional and unsteady aerodynamics can be described by an equivalent mathematical model.

The simplified method of Paper 16 is regarded a nice tool for preliminary design studies to predict the main forces and moments.

The theme of Paper 17 is to calculate the hub loads, blade loads, and downwash by various methods, and to check the accuracy of the theories by comparison with measurements on a 4-bladed hingeless rotor model in a wind tunnel. In addition, the theories used had to be both simple and as accurate as possible since they are intended for use in a complete helicopter simulation program. It is the opinion of the author that one side effect also existed concerning the wind tunnel test, namely, that the relatively young helicopter team of the DFVLR gain some experience in wind tunnel testing of helicopter models. In the future, expensive wind tunnel tests should reveal more information on the details of flow around the helicopter blade, e.g. the core size, the vertical and lateral displacement of the tip vortex as a function of time, vortex induced stall on a blade, and possibly even vortex bursting. The alcohol-filled U-shaped manometers should be replaced by pressure transducers so that the information about the downwash distribution should be available on-line.

Fig. 4 of Paper 17 shows downwash measurements and calculations in hover at two distances from rotor plane. It is explained why the local momentum theory shows better results than the global momentum theory, one reason being the flapping distribution. Despite the fact that cyclic pitch was not equal to zero in the test, it is usually small so that the influence should not be too important. The momentum methods provide a fast means of predicting overall performance, but their general success stems mainly from some compensating errors in their inflow distribution and from judicious application of empiricism by experienced users. It is, therefore, suggested that one should check David Kocurek's lifting surface theory (1) with a prescribed wake. It should be fast enough for simulation work and more accurate than momentum methods. In radial direction, more test points should be chosen to get more information about the distribution of the downwash. This is also true with respect to Fig. 5, where the influence of a trailing vortex seems to be evident.

The discrepancies between theory and measurement of Fig. 6 are partly explained by the inaccuracies in the calculation of the flapping motion. It is well-known that, with a hingeless rotor, the magnitude of the flapping response to nonuniform inflow is not greatly affected, but the phase of the response can be significantly decreased. Thus, a longitudinal inflow variation can cause both longitudinal and lateral flapping. While the longitudinal flapping might be predicted with satisfactory accuracy by a uniform inflow theory, the lateral flapping is underestimated, especially at low advance ratio. This has been demonstrated in a recent paper by Wayne Johnson (2). He showed that a calculation of the nonuniform wake-induced velocity is necessary to accurately predict lateral flapping angles. Raymond W. Prouty (3) developed a simple engineering approximation to estimate the lateral flapping angle on the basis of an average induced velocity that depends on the free stream velocity and the overall thrust. It is suggested that this approximation for quick calculations be included in helicopter simulation.

In Fig. 9 of Paper 17, the torque is plotted versus advance ratio. The good agreement between global momentum theory and experiment is again explained by some compensating errors in the inflow distribution of the momentum theory. The discrepancy between theory and measurement at an advance ratio of zero is probably caused by the flow breakdown in the wind tunnel. There are also some doubts about the validity of the data at low advance ratio because of wind tunnel wall interference effects that might occur because of the relatively large diameter of the rotor compared to the cross-section of the wind tunnel test section.

The introduction of Paper 18 gives the theme: "The objective ... is to take various key features of the mathematical modeling of the rotor wake required for detailed blade load prediction ...". In particular, the position and the effect of the tip vortex on the following blade is intended to be investigated. It is an interesting idea to use the local pressure coefficient at 2% of local chord ($C_{p0.02c}$) as an indication of local blade incidence. However, there can arise some difficulties that are connected not only with non-linear behavior when stall or non-steady effects are present at the retreating blade. Inaccuracies can also occur because of three-dimensional effects and influences of transonic, non-steady flow at the advancing side of the blade on the local pressure distribution (Ref. 5) even if the pressure coefficient of 2% of local chord is taken. It is, therefore, suggested that the local position of stagnation point, which also depends on the angle of attack, be measured. Shockey et al.(4) used hot-wire sensors on a helicopter blade to measure stagnation point location as a means to determine local aerodynamic angle of attack.

The method of measuring the distance of a tip vortex from the following blade is very interesting and deserves our attention. The discrepancy between theory and measurement of the distance of vortex below the following blade, h/c, on the advancing blade stems probably from three-dimensional and compressibility effects as well as from the simple inflow model used. The agreement between measurement and theory when determining the azimuth angles at blade-vortex intersection (in plan) and the blade-vortex crossing angle

at intersection is surprisingly good although the methods derived in the appendix of Paper 18 are relatively simple. It is only suggested that some more explanations be added how to use, for instance, eq (A1). Otherwise it might create some difficulties for rapid application.

Paper 19 describes a computer software system that enables arbitrary users to manage large data bases, to provide means of presentation of digitized data, to compare test results with theories etc. The examples shown in the paper demonstrate very clearly the versatility of the program package. If the description of the program is so clear that it can be used easily , an old dream of the engineer whether in research or in production will become reality. However, there is one danger when applying such programs: The engineer might be too indolent to check whether the results that have been produced by the computer are physically meaningful or doubtful.

REFERENCES

1. Kocurek, D.J., and Tangler, J.L.: "A Prescribed Wake Lifting Surface Hover Performance Analysis". 32nd Annual National V/STOL Forum of the AHS, Preprint No. 1001, May 1976.

2. Johnson, W.: "Comparison of Calculated and Measured Helicopter Rotor Lateral Flapping Angles". Journal of the American Helicopter Society (AHS), pp. 46-50, April 1981.

3. Prouty, R.W.: "Approximation of Lateral Flapping at Low Speed". Journal of the AHS, p. 73, January 1982.

4. Shockey, G.A.; Williamson, J.W.; and Cox, C.R.: "Helicopter Aerodynamics and Structural Loads Survey". 32nd Annual National V/STOL Forum of the AHS, Preprint No. 1060, May 1976.

5. Renaud, J., and Nibelle, F.: "Effects of the Airfoil Choice on Rotor Aerodynamic Behaviour in Forward Flight". Second European Rotorcraft and Powered Lift Aircraft Forum. Bückeburg, FRG, Paper No. 23, September 1976.

COMMENTS ON PAPERS PRESENTED IN SESSION IV OF THE FLUID DYNAMICS
PANEL ON PREDICTION OF AERODYNAMIC LOADS ON ROTORCRAFT
"EXPERIMENTAL CORRELATIONS AND VERIFICATIONS"

by

Kenneth B. Amer
Manager, Technology Department

Hughes Helicopter, Inc.
Culver City, California 90230

My comments on the papers presented in Session IV cover both general comments and specific comments. In the category of general comments, all papers should bear in mind the goals of improved prediction of aerodynamic loads on rotorcraft. Namely;

1) To improve our ability to predict blade bending loads in order to improve our ability to predict rotor blade fatigue life. Inasmuch as blade fatigue damage occurs primarily in maneuvers such as pullups and turns, it is necessary to be able to predict blade bending fatigue loads in maneuvers as well as in level flight. Thus, rotorcraft aerodynamic loads must be predictable in maneuvers as well as in level flight.

2) Another goal is to be able to predict rotorcraft vibration. Such a prediction in turn requires prediction of blade root shears and bending moments, as well as the effects of impingement of the pulsating wake on the empennage. Rotorcraft vibration is primarily of importance in level flight because of the predominant percentage of flight time. However, maneuvers such as transition from forward flight to hover tend to cause high vibration and hence are also of importance. Thus, rotorcraft loads and rotor downwash must be predictable during transition from forward flight to hover as well as in level flight.

The following specific comments apply to each of the papers presented.

Paper #17 - "Comparison of Rotor Analysis Results with Aerodynamic Windtunnel Data"

Downwash measurements and analytical correlations are always of value to improving our ability to predict rotorcraft loads. There is some confusion in this commentator's mind between "local momentum theory" and "global momentum theory." It is difficult from the verbal description to visualize the local momentum theory and a mathematical description with some figures would help. It is also not clear whether the local momentum theory referred to is the same as that incorporated in Reference 5.

There is some question as to the validity of the experimental data at an advanced ratio of 0.05. Normally for tests at this low advanced ratio, considerable attention must be made to wall effects and recirculation. Also, the poor agreement between measured and predicted main rotor torque in hover (Figure 9) is disturbing. As shown in Figure 1, the model appears to represent an actual helicopter hovering in a location only minimally affected by surrounding obstructions.

Paper #18 - "An Appraisal of Rotor Blade-Tip Vortex Interaction and Wake Geometry from Flight Measurements"

This paper is believed to be an important contribution in improving the understanding of blade/vortex interaction. The azimuthal variation of C_N and C_p presented in Figure 4 is an excellent illustration of blade/vortex interaction. The C_p data of Figures 3 and 5 are a very illuminating description of the effects of flow separation on airfoil pressure distribution. The comparison of measured and predicted azimuth angles at blade/vortex intersection shown in Figure 10 is very satisfying.

The author is to be commended for providing high quality blade/vortex data which will provide the basis for many future analytical efforts.

Paper #19 - "Datamap and Its Impact on Prediction Programs"

This paper describes and shows results of a plot package for automatically plotting computer output, both test and analytic. This should be a valuable tool in expediting comparisons between experimental data and analytical results. The contour plots of Figure 9 comparing computed and derived main rotor normal force coefficients are a highlight of the paper.

ROUND TABLE DISCUSSION
ON
"PREDICTION OF AERODYNAMIC LOADS ON ROTORCRAFT"

Dr. McCroskey

I would like to open up the floor for comments and discussions about particular things that seem to need further attention, areas in which we ought to progress, or alternatively, areas where we might seem to be going off on a tangent that is less than totally fruitful. Is there any comment now from the audience?

Mr. Vuillet

I have a question on load prediction. I would like to gather some comments from research centers and manufacturers. What is the general purpose of prediction? Is it for fatigue life estimation? In this case the methods do not show an accuracy within a 10% range, which is the minimum requirement necessary to use the data. Is it for limit loads prediction, the estimation of which is fundamental in the design procedure. In this last case, manoeuvres are the critical cases which occur at the 2 or 3 g load factor, but the methods which have been presented at this meeting only operate at 1 g load factor. May I have comments on this question please?

Dr. McCroskey

I hope you don't address that to me, because I don't make helicopters.

Mr. Brotherhood

I really would like to endorse those remarks. We have addressed most of our remarks to 1 g flight, and it is becoming obvious that there is an increased potential for the helicopter in manoeuvring flight and in the context of 'Agility' as conceived by the Army. These cases of manoeurving flight are most difficult to predict and, I would imagine, are where the least work is being done. We are just beginning to tackle these effects in our own flight research, but our RAE Westlands loads program is still strictly only applicable to 1 g rectilinear flight. It certainly needs updating to steady turning flight or steady pull-up flight, because this is an area where the helicopter has a greatly increased potential capability, and it is certainly not being adequately addressed, either from the loads side or from flight mechanics and handling aspects which are also associated with both high positive and negative load factors.

Mr. Landgrebe

I will try to respond to that from the developers standpoint, having some experience in attempting to work the maneuver problem. I use that word "attempting" in quotes because as you know, and as was just commented, most of the analyses today are directed at the steady flight condition. As was mentioned by Mr. Brotherhood, doing the analysis for maneuvers is certainly more complex. You get the problem where you have to face the computer time requirement problem in addition to the technical requirements. There are significant limitations in both areas. We saw today many instances of wake vortex interaction which gets even more severe and more complicated when you get into the maneuver situation. When you talk about free wake, inflow and airload analyses for maneuvers, there is no question that we are facing a very complicated situation. Most of the developers try to crawl before they walk and start off with the steady flight condition. We have addressed the maneuvers in a few of our programs and we started off with one which is in some ways simpler and in some ways more difficult. We took the hover condition and looked at it regarding what happens when you have an ambient wind and this ambient wind could be in the form of a gust. We moved on from there to looking at what I call a transient condition at low speed. We were successful in predicting some of the loading peaks, particularly the locations thereof, but as far as accurately predicting the magnitudes of airloads, there is still a lot to be done in that area. So, to answer the question, there is certainly a need for development for maneuver analyses. I see that coming in the normal progression of the technology, but that is an area for which a lot of the fundamental questions that were addressed at this meeting are also applicable to the level flight condition. We should get the answers to those before we move out all the way in the maneuvering flight regime.

Mr. Sopher

Accurate loads predictions for steady conditions continues to be an important need. The steady vibratory load programs are used for designing blades, and they are the only tool we have at the moment. There are things like pitch link loads and pitch link design which are attacked by means of these programs. There are other things which accurate load predictions are needed for. One is a stability prediction, for example, flap-lag and torsional response interactions. Accurate load predictions in those areas are essential. There are new areas which we haven't dealt with yet, but which you can envisage will be addressed in the future and one is vibration prediction and the configuring of aircraft to have low vibrations and the study of aircraft to examine the effects of the addition of equipment and their impact on the vibration characteristics. Finally, at the beginning of this session, Mr. Dadone discussed the need for integrating airfoil design in response programs. I expect that in the future we are going to see closer integration of airfoil designs and the use of aeroelastic response programs.

Dr. McCroskey

Thank you. I failed to mention earlier that we did have a second commentator scheduled for this session, Mr. Kenneth Amer from Hughes Helicopters. He was ill and not able to attend the meeting. I am happy to report that he was not seriously ill, but nevertheless unable to attend the meeting. He passed on to me some notes that happen to be most closely related to this question that Mr. Vuillet just raised. I would like to read a few excerpts from the notes that he passed to me.

"In the category of general comments, all papers should bear in mind the goals of improved prediction of aerodynamic loads on rotorcraft, namely;

1- To improve our ability to predict blade bending loads in order to improve our ability to predict rotor blade fatigue life. Inasmuch as blade fatigue damage occurs primarily in manoeuvres such as pullups and turns, it is necessary to be able to predict blade bending fatigue loads in manoeuvres as well as in level flight".

That is quite a challenge. Thus, rotorcraft airloads must be predictable in manoeuvres as well as in level flight.

2- "Another goal is to be able to predict rotorcraft vibration. Such a prediction in turn requires prediction of blade root shears and bending moments as well as the effect of impingement of the pulsating wake on the empenage. Rotorcraft vibration is primarily of importance in level flight because of the predominant percentage of flight time in that condition. However, manoeuvres such as transition from forward flight to hover tend to cause high vibration and hence are also of importance. Thus rotorcraft loads and rotor downwash must be predictable during transition from forward flight to hover as well as in level flight."

So he seems to say, yes, everything - fatigue, manoeuvres, transition from one flight regime to another. I think to a certain extent we all accept that is true; the question at this stage is, " with what confidence can we make such predictions?" I think that we have some distance to go in that regard.

Dr. Carlson

Coming to this meeting as a representative of the Structures and Materials Panel, I would like to add a little different perspective to that last point. Level flight predictions are extremely important because it is not the damage that they don't do, it is that they should never produce any damage. It is incumbent on the initial design not to produce a rotor system that does sustain fatigue damage in any kind of trimmed level flight, because that presents you with a catastrophe. The secondary issue is, given that, fatigue damage does not occur in 2 g trimmed flight, then how much life exists in some kind of extended manoeuvre capability. I think there is a different point to be made there, so I exhort all of you to continue with the level flight predictions, learn to walk perhaps before you run. They are extremely important.

Mr. Kerr

I guess really we have to separate two things here. One of them is the development of basic technology and the other is development of design tools. My experience has been that you often encounter a problem during a development program for which you haven't had predictive analysis capability. In order to fix the problem, you use every tool at your disposal, whether the tool was designed for that use or not. You push it, you prod it, you prop it up, and you try to solve the problem with it. In the process, you develop some confidence in the tool's ability to predict the phenomenon of interest. Then, the next time you design a helicopter, you've got a calibration on that methodology and, after adding as much technology improvement as possible, you apply it as a design tool. That is how several of the comprehensive helicopter analyses that are being used out there in industry right now have developed. They are not necessarily technically correct for every application. They may not produce good quantitative results, but you have developed confidence in them because you have applied them in solving real problems. You have confidence that you can guide your design with their use. Because we operate this way, it doesn't mean that we do not need to be going right back to basics and develop a better understanding of basic phenomena.

C-81 is a good example of an analysis which has been used for a wide range of applications. It has been a valuable tool to both the US government, the Bell Helicopter Company, and other helicopter companies which have used it. It has enabled us to go ahead with limited technology and, within its limitatins, still have a useful design tool. It wasn't many years ago that we were doing helicopter design with slide rules and desk calculators. We are now using a number of these large analyses. One reason for developing a second generation analysis is because a wide variety of first generation analyses are in use; they are used in the design room, and they will continue to be used in spite of their shortcomings. We would like to have as good a tool as the available technology can support to aid in design. We also need a way to get the new technology into the field as it is developed, not some 10 years after its development when someone gets a chance to put it in a form where it can be applied.

Dr. Mc Croskey

I prepared this slide to open the meeting. If I could have had the luxury of making a new one to conclude, I might have changed something, but at least these are my impressions on some aspects of where we stand today. I think that we have gotten a lot of mileage out of some of the older methods, but for accurate predictions, we have to move on.

(Figure 1 - McCroskey) I have listed here some methods that perhaps are still useful, but for accurate predictions they are really not adequate. I think that in the future we definitely will have to look at some of these modules that were discussed in the first day in the context of the complete rotor. I think that we will have to pay attention to stall and reattachment on the blade and transonic blade tip characteristics. It is possible in cases to put in, in modular form, transonic codes that don't compute the whole rotor environment, but that do the right thing at the right place. Certainly the wake geometry and the vortex strength are important, and I think that it is absolutely essential now to think in terms of the correct coupling of the rotor flow field with the blade motion and dynamics. Certainly the impact of modern computers will be felt evermore. Lastly, I have listed what I think are the things for which we are trying to have accurate and reliable predictions. We have spoken some of performance, vibratory stresses, and blade dynamics; we spoke not much of acoustics, but that is also important in the future. Before leaving this, I would like to make a few additional remarks.

First of all, despite all that we have heard here in the last few days, helicopters really do fly and they fly well. They do many useful missions. In some sense it may be like the weather; it really does rain and sometimes it snows, we do have periods of warm weather and sunshine and cloudy and cold weather... these exist but we are not always able to predict when they will exist and in what intensity. To a certain extent helicopters do what they are supposed to do, but we need to be able to predict these things better. We have made a tremendous amount of progress in the 10 years since the Fluid Dynamics Panel last had a meeting on this subject in Marseilles in 1972, entitled Aerodynamics of Rotor Craft. At that time, we basically had for air loads prediction, what one might tend to call the zero generation calculations. That is to say, at that time, and remember that this is only 10 years ago, we were scaling air loads data from previous flight tests. Almost nothing was analytical. The first generation air loads calculations, that is to say, analyses based on physical principles, but whose validation was limited to previous company designs, have been the innovation of the 1970's in this business. With this first generation air loads calculation, the success depends very strongly upon how close the new design is to the previous experience which that particular company might have had. Industry views these first generation analysis programs, despite their limitations, as significant advances, so that as long as a new rotor design does not depart too strongly from previous company designs, then rotor loads estimates are generally reasonable. In fact, it was at this level where the 1974 Rotor Craft Dynamics Meeting, sometimes referred to as Ormiston's Olympics, made comparisons in which for the first time these methods were applied to an arbitrary rotor. The results showed that these first generation loads calculations, if they were to be extended to a new or unrelated rotor design, would entail some considerable risk. What has happened in the last 8 years? I guess I am precluded from calling the current work second generation because that word has been coined for the effort described by Mr. Kerr; but if we consider one and one-half generation loads calculation, these would be distinguished by their ability to predict rotor loads for a wide variety of configuration types and rotor designs. There is considerable disagreement in the industry today as to how close present computer codes have actually come in meeting this objective; disagreement in how good these codes are in doing design for which they have not been fine tuned. There is a fairly unanimous feeling that the data to validate these one and one-half generation codes really do not exist, although we may be closer to it than previously thought after what has been heard today. We still have much work to do to have confidence in predicting loads on a new rotor design.

Also, I think it is important to realize that as we do go ahead in this type of work, there are potentially non-productive tangents upon which we can go and spend certain amounts of money. The program committee for this meeting consists of Prof. Steketee from the Netherlands, Dipl. Ing. Sacher from Germany, Dr. Sacerdote from Italy, M. Verne from France and Dr. David Smith from the RAE as well as myself. We the program committee in particular, and the Fluid Dynamics Panel in general, hope that some of the more fruitful paths may have been identified in this meeting. Also we hope very much that contacts have been made that will be mutually beneficial in future efforts, whether this results in direct collaboration or just exchanges of information and ideas.

To conclude I would like to thank the speakers and the commentators for the considerable efforts that they have put in in preparation for this meeting. With that I would like to turn to the Chairman of the Fluid Dynamics Panel, M. Monnerie for a few brief concluding remarks.

M. Monnerie (Translated from French)

These two days of work are nearly over. I think that we can say without any reservations that they were very interesting and that this reunion of specialists has been a success, which was indicated in particular by the number of participants and their participation. This we owe to the excellent job done by the team who have organized the meeting. All of those who have made contributions to the common work merit our recognition, and I would like to thank them on your behalf:
- First of all, the National Delegates from the United Kingdom for their friendly welcome here and the lovely environment and very nice setting for the meeting;
- Second, the Program Committee and its Chairman, Dr. McCroskey, who did very good work and for the commentators system which has been extremely efficient in drawing out the best benefits of all contributions and stimulating the discussions;
- Also of course, the commentators themselves, the session chairmen and the authors for their very interesting contributions;
- Then everyone who helped us with the meeting, including Captain Hillary and his secretary, Mrs. Scott, the interpretors, Mr. Walker who was in charge of the slides, and those who were in charge of the slides, and those who were in charge of the sound system;
- All of you who helped make the discussions extremely lively;

- Last, but not least, Mr. Rollins and his secretary, Melle Bivault, who were so careful to organize everything and to whom we owe special thanks.

Before ending, I would like to tell you about the program which has been prepared for the FDP: - Tomorrow, a specialists meeting on Wall Interference in Wind Tunnels. From 20-22 September, in Trondheim, Norway, a symposium on Missile Aerodynamics. From 21-25 March 1983, at the von Karman Institute, a special course on the Aerodynamics of Controls. From 25 April, a Symposium on Vortex Aerodynamics in the Netherlands. In May 1983, a special course on Subsonic/Transonic Interaction at the VKI and at WPAFB. Finally, in the week of 26 September 1983, a Symposium in Turkey on Windtunnels and Testing Techniques.

That is all, goodbye, have a good trip home, and I hope to see you at one of the above-mentioned activities. The meeting is adjourned.

PREDICTION OF AERODYNAMIC LOADS
ON ROTORCRAFT

CLASSICAL METHODS NOW INADEQUATE
  2-D STEADY AIRFOILS
  UNIFORM DOWNWASH OR PRESCRIBED WAKE
  RIGID BLADE DYNAMICS
  DESIGN CHARTS

FUTURE REQUIREMENTS — THE COMPLETE ROTOR
  STALL AND REATTACHMENT IN THE ROTOR ENVIRONMENT
  TRANSONIC BLADE TIP CHARACTERISTICS (3-D, UNSTEADY)
  REALISTIC WAKE GEOMETRY AND VORTEX STRENGTH
  **RELIABLE COUPLING OF ROTOR FLOW FIELD WITH BLADE MOTION
    AND DEFORMATION**
  AERODYNAMIC INTERFERENCE AND INTERACTIONS
  IMPROVED SOLUTION TECHNIQUES AND MODERN COMPUTERS

ACCURATE, RELIABLE PREDICTIONS
  PERFORMANCE
  VIBRATORY STRESSES
  BLADE DYNAMICS
  ACOUSTICS

REPORT DOCUMENTATION PAGE

1. Recipient's Reference	2. Originator's Reference	3. Further Reference	4. Security Classification of Document
	AGARD-CP-334	ISBN 92-835-0320-1	UNCLASSIFIED

5. Originator	Advisory Group for Aerospace Research and Development North Atlantic Treaty Organization 7 rue Ancelle, 92200 Neuilly sur Seine, France

6. Title	PREDICTION OF AERODYNAMIC LOADS ON ROTORCRAFT

7. Presented at	the Fluid Dynamics Panel Specialists' Meeting held at Church House, London, United Kingdom, 17–18 May 1982.

8. Author(s)/Editor(s)	9. Date
Various	September 1982

10. Author's/Editor's Address	11. Pages
Various	318

12. Distribution Statement	This document is distributed in accordance with AGARD policies and regulations, which are outlined on the Outside Back Covers of all AGARD publications.

13. Keywords/Descriptors

Mathematical prediction	Windmills
Aerodynamic loads	Aerodynamic characteristics
Helicopters	Mathematical models
Rotary wings	

14. Abstract

A wide range of aerodynamic phenomena contribute to the airloads on rotorcraft, and the accurate prediction of these loads represents a major challenge to the helicopter technical community. This Specialists' Meeting was organized for the purpose of identifying and assessing recent developments in this field. The primary theme of the meeting was the prediction and experimental verification of the steady and unsteady aerodynamic forces on the rotor blades of modern helicopters and related devices, such as wind turbines.

The Meeting consisted of four main sessions that addressed recent advances in rotor airloads prediction methods, including the evolution to the present state of the art, the capabilities and limitations of the current methodology, and the specific areas that need further effort. Nineteen invited papers were presented in the following four sessions: I Rotor Blade Aerodynamic Characteristics; II Wakes and Aerodynamic Interference Effects of Rotorcraft and Wind Turbines; III Rotor Airloads Prediction Programs; IV Experimental Correlations and Verifications.

In addition to the contributing authors, two rotorcraft specialists with broad backgrounds and experience in each of the relevant technical areas were invited to assess and critique the papers in the four sessions and to comment on advances in the state of the art in predictive capability. Written remarks by seven of these Commentators are included in these Proceedings.

At the close of the meeting a short discussion of summary remarks was recorded and is included in the volume.

AGARD Conference Proceedings No.334 Advisory Group for Aerospace Research and Development, NATO PREDICTION OF AERODYNAMIC LOADS ON ROTORCRAFT Published September 1982 318 pages A wide range of aerodynamic phenomena contribute to the airloads on rotorcraft, and the accurate prediction of these loads represents a major challenge to the helicopter technical community. This Specialists' Meeting was organized for the purpose of identifying and assessing recent developments in this field. The primary theme of the meeting was the prediction and experimental verification of the steady and unsteady aerodynamic forces on the rotor blades of modern helicopters and related devices, such as wind turbines. P.T.O.	AGARD-CP-334 Mathematical prediction Aerodynamic loads Helicopters Rotary wings Windmills Aerodynamic characteristics Mathematical models	AGARD Conference Proceedings No.334 Advisory Group for Aerospace Research and Development, NATO PREDICTION OF AERODYNAMIC LOADS ON ROTORCRAFT Published September 1982 318 pages A wide range of aerodynamic phenomena contribute to the airloads on rotorcraft, and the accurate prediction of these loads represents a major challenge to the helicopter technical community. This Specialists' Meeting was organized for the purpose of identifying and assessing recent developments in this field. The primary theme of the meeting was the prediction and experimental verification of the steady and unsteady aerodynamic forces on the rotor blades of modern helicopters and related devices, such as wind turbines. P.T.O.	AGARD-CP-334 Mathematical prediction Aerodynamic loads Helicopters Rotary wings Windmills Aerodynamic characteristics Mathematical models
AGARD Conference Proceedings No.334 Advisory Group for Aerospace Research and Development, NATO PREDICTION OF AERODYNAMIC LOADS ON ROTORCRAFT Published September 1982 318 pages A wide range of aerodynamic phenomena contribute to the airloads on rotorcraft, and the accurate prediction of these loads represents a major challenge to the helicopter technical community. This Specialists' Meeting was organized for the purpose of identifying and assessing recent developments in this field. The primary theme of the meeting was the prediction and experimental verification of the steady and unsteady aerodynamic forces on the rotor blades of modern helicopters and related devices, such as wind turbines. P.T.O.	AGARD-CP-334 Mathematical prediction Aerodynamic loads Helicopters Rotary wings Windmills Aerodynamic characteristics Mathematical models	AGARD Conference Proceedings No.334 Advisory Group for Aerospace Research and Development, NATO PREDICTION OF AERODYNAMIC LOADS ON ROTORCRAFT Published September 1982 318 pages A wide range of aerodynamic phenomena contribute to the airloads on rotorcraft, and the accurate prediction of these loads represents a major challenge to the helicopter technical community. This Specialists' Meeting was organized for the purpose of identifying and assessing recent developments in this field. The primary theme of the meeting was the prediction and experimental verification of the steady and unsteady aerodynamic forces on the rotor blades of modern helicopters and related devices, such as wind turbines. P.T.O.	AGARD-CP-334 Mathematical prediction Aerodynamic loads Helicopters Rotary wings Windmills Aerodynamic characteristics Mathematical models

The Meeting consisted of four main sessions that addressed recent advances in rotor air-loads prediction methods, including the evolution to the present state of the art, the capabilities and limitations of the current methodology, and the specific areas that need further effort. Nineteen invited papers were presented in the following four sessions: I Rotor Blade Aerodynamic Characteristics; II Wakes and Aerodynamic Interference Effects of Rotorcraft and Wind Turbines; III Rotor Airloads Prediction Programs; IV Experimental Correlations and Verifications.

In addition to the contributing authors, two rotorcraft specialists with broad back-grounds and experience in each of the relevant technical areas were invited to assess and critique the papers in the four sessions and to comment on advances in the state of the art in predictive capability. Written remarks by seven of these Commentators are included in these Proceedings.

At the close of the meeting a short discussion of summary remarks was recorded and is included in the volume.

Papers presented and discussions held at the Fluid Dynamics Panel Specialists' Meeting held at Church House, London, United Kingdom, 17–18 May 1982.

ISBN 92-835-0320-1

END

DATE
FILMED

3 - 83

DTIC